JOURNAL OF THE
MYANMAR ACADEMY
OF ARTS AND SCIENCE

Chemistry, Industrial Chemistry

Vol. XXI, No.1, November, 2024

Myanmar Academy of Arts and Science

Edition
2024, November, 200 Copies

Published by

Dr Maung Kyaw (00322) Vice-President,
Myanmar Academy of Arts and Science

ISSN 2520-0186
LCCN 2003-323143

Printed by

U Tin Soe (00171), Manager

Universities Press, Yangon, Myanmar

FOREWORD

The Myanmar Academy of Arts and Science (MAAS) was constituted on August-16, 1999 with four major fields of endeavour, namely:

(a) Introduction to Modern Methods of Teaching and Learning
(b) Promotion of Research Activities through Research Guidelines
(c) Dissemination of Knowledge and Emerging Technologies
(d) Motivating New Generation of Experts and Academics

In pursuance of these endeavours, MAAS has, since the year 2001, held Research Conferences and published research papers in the Journal of the Myanmar Academy of Arts and Science.

At the Research Conference held on 19- 21 December 2022, a total of (223) research papers were read and outstanding papers have been published in volume XXI as follows:

Vol. XXI, No.1	Chemistry, Industrial Chemistry
Vol. XXI, No.2	Physics, Mathematics and Computer Studies
Vol. XXI, No.3	Zoology, Botany, Marine Science
Vol. XXI, No.4	Myanmar, Oriental Studies, Archaeology, Anthropology and Library and Information Studies
Vol. XXI, No.5	Geography, History, International Relation, Geology, Statistics, Management Studies, Law, Journalism
Vol. XXI, No.6	Educational Theory and Management, Curriculum and Methodology
Vol. XXI, No.7	Educational Psychology

The executive committee members of Myanmar Academy of Arts and Science had been reconstituted on 4 August 2022 and again reconstituted on 8 March 2024, by the Ministry of Education with the Approval of the Government of the Union of Myanmar. Accordingly, the Publication Committee along with the Editorial Board have been formed. The primary mission of the academy is to develop and promote Higher Education in preparing future generations to meet the challenges in the 21st century.

The majority of the papers in these issues represent findings of research conducted by aspirants as well as postgraduate candidates in partial or total fulfillment of requirement for these degrees. We, the members of MAAS, do appreciate the editing work done by senior professors and scholars of high standing, these papers would prove useful, and not only for other candidates but also for all those who are interested in the results of systematic research and inquiry.

Dr Thet Lwin
President
The Myanmar Academy of Arts and Science

Journal of the Myanmar Academy of Arts and Science

Vol. XXI. No.1

Contents

Section (i) Chemistry

Section (ii) Industrial Chemistry

A FIELD STUDY ON SOIL NUTRIENTS, ENZYME ACTIVITIES, AND INSECTICIDE RESIDUE DURING PHYTOREMEDIATION*

Swe Sint[1], Phyu Phyu Myint[2], Saw Hla Myint[3]

Abstract

Phytoremediation is an eco-friendly treatment for reducing soil contamination. Cypermethrin is one of the most widely used pyrethroid insecticides against different pests, and its use causes soil contamination. A field study was conducted in cypermethrin contaminated soil to detect and monitor the changes in soil nutrients, enzyme activities, and 3-phenoxy benzoic acid (3-PBA, primary metabolite of cypermethrin insecticide). Phytoremediation was undertaken using two plant species: aster (*Callistephus chinensis* L. Nees) and Bermuda grass (*Cynodon dactylon* L. Pers.) in the absence and presence of iron oxide particles (0.01 g/kg of soil). Soil pH, soil organic carbon (SOC), total nitrogen (N), available phosphorus (P), and available potassium (K_2O) and relative metals content by EDXRF. The activities of soil urease (mg NH_4^+-N g^{-1} soil h^{-1}) and dehydrogenase (µg TPF g^{-1} soil h^{-1}) also increased in the treated soil samples as determined by the phenol-hypochlorite colourimetric method and the Triphenyl Tetrazolium Chloride (TTC) assay method. The urease enzyme activities of aster (5.363 ± 0.024) and Bermuda grass (4.816 ± 0.07) was found to be higher when compared with uncultivated soil (S_0) (3.74 ± 0.03), whereas the dehydrogenase activity of aster (0.00127 ± 0.0000) and Bermuda grass (0.00113 ± 0.0000) was also increased when compared with S_0 (0.0008 ± 0.0000) in the field experiment. Furthermore, the insecticide residue in the soil samples was determined by UV-Vis and GC-MS. The results showed the decrease in insecticide residue decrease in during phytoremediation in the presence of iron oxide particles. Phytoremediation demonstrated 96.33 % and 94.19 % PBA decrease using aster and Bermuda grass in 12 weeks period. The results demonstrated that aster and Bermuda grass showed promising potential for use as phytoremediating agents in insecticide contaminated soil.

Keywords: soil nutrients, enzyme activities, phytoremediation, aster, Bermuda grass, iron oxide particles, insecticide residue

Introduction

Cypermethrin is a highly active synthetic pyrethroid insecticide and is widely used to control insects and has been detected in organisms, including humans. Pyrethroids have been shown to pose neurotoxicity, hepatotoxicity, endocrine disruption, and reproductive risks in mammals (Wang *et al*., 2017). Cypermethrin and its metabolite, 3-phenoxybenzoic acid (PBA) have exerted adverse biological impacts on the environment; therefore, it is critically important to develop different methods to enhance their degradation (Xie *et al*., 2008). Phytoremediation is a versatile technology to treat polluted soils, pollutants, deposits, and groundwater in a profitable as well as environmentally friendly way through the usage of plants, and then thus be referred to as natural green biotechnology. The use of iron oxide particles has high potential in phytoremediation (Demangeat *et al.*, 2021).

Some species such as aster and Bermuda grass are better suited for phytoremediation due to their pre-adaption to environmental conditions of contaminated sites (e.g., weather and soil) (Swe Sint *et al*., 2021), their need for less care (e.g., frequent irrigation, and fertilizers) and their quality for restoring natural ecosystems. China aster (called "Maymyo-pan plant" in Myanmar) belongs to the family 'Asteraceae' and is native to China. China aster is one of the most popular annual flower crops cultivated widely due to its myriad colours ranging from violet, purple, magenta, pink, and white, and a comparatively longer vase life (Chaitra and Patil, 2007).

---

* Best Paper Award Winning Paper in Chemistry (2022)

[1] Department of Chemistry, University of Yangon
[2] Loikaw University
[3] Department of Chemistry, University of Yangon

Generally, asters grow best in moist, well-drained soils with plenty of sunlight. Bermuda grass (called "Myay Zar Myet" in Myanmar**)** belongs to the family 'Poaceae' and is native to Africa. Bermuda grass was evaluated for its ability to reduce oil sludge contamination in soil and the most efficient cultivar was chosen. Bermuda grass is an efficient species for phytoremediation of petroleum contaminated soil, and the selection of a more tolerant and efficient cultivar is possible. In general, Bermuda grasses are drought tolerant; that is, they survive dry soil conditions longer than most turfgrasses.

Soil enzyme activities are greatly influenced by soil properties and could be significant indicators of insecticide contaminated soil for bioavailability assessment (Xian *et al*., 2015). A reliable assessment of quality of soil contaminated with organic products is possible by testing the activities of lipase, dehydrogenase, catalase, and ureases. The main role of urease is to allow the microorganisms to use urea as a source of nitrogen (Jingjing *et al.,* 2019). Dehydrogenase occurs in all living microbial cells. It is a quick and relatively simple method to determine the overall activity of microorganisms (Wolinska *et al*., 2016). This study also focuses on the determination of urease and dehydrogenase activities in soil microorganisms. Moreover, the changes of soil nutrients and insecticidal residue were assessed during phytoremediation using aster and Bermuda grass in the presence or absence of iron oxide particles.

Materials and Methods

Soil Sample Collection Site

Soil samples were collected from the surface layer (0-20 cm depth) of an agricultural field located in Myaungtagar Village (17º 11' 45'' N latitude and 95º 59' 09'' E longitude) Hmawbi Township, Yangon Region (Figure 1). This field is usually cropped with a rose and lady's fingers rotation without treatment of any pyrethroids insecticide (including cypermethrin) for many years.

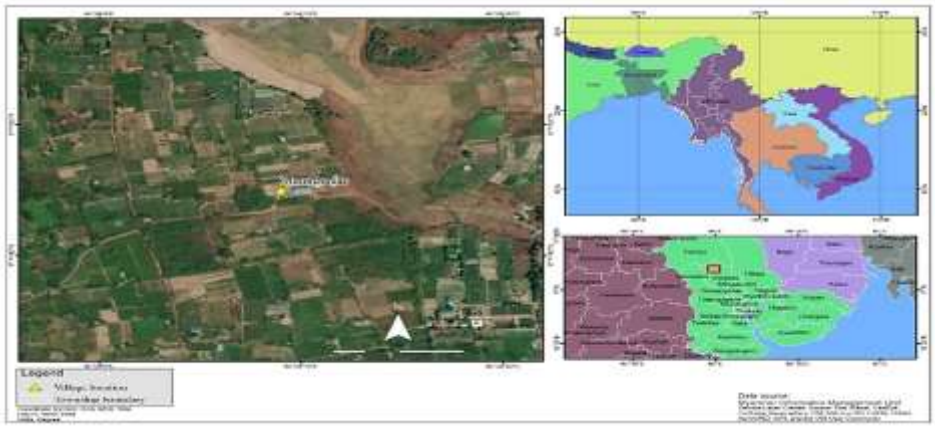

Figure 1. Sample collection site (Myaungtagar Village, Hmawbi Township, Yangon Region)

Study Design for Field Experiment

The field experiment was carried out on the farm at Myaungtagar Village, Hmawbi Township, Yangon Region from September (2021) to December (2021) to study the effect of magnetic iron oxide particles on the degradation of 3-phenoxy benzoic acid (3-PBA) in the insecticide contaminated soil. The field was prepared well by one deep ploughing, followed by three cross harrowing and planking. The field was constructed with four parallel rows of five-foot-long planting beds spaced 12 inches apart and treated with composted organic fertilizer (a mix of chicken dung and rice hull). The selected seeds were sown in another plot similarly treated with organic fertilizer.

The experiment was laid out with two treatments in a Randomized Complete Block (RCB) design by spraying with insecticide (cypermethrin) in each bed (control and treatment) and spraying with 1% iron oxide particles in the two treatment beds at the rate of 0.01 g/kg soil. Aster (Maymyo flower) plant (after the age of 20 days) and Bermuda grass (5 inches between two plants) were planted in this field. There were four rows in each field of work. The field experiments were arranged according to a random design that consisted of six treatments:

(a) **(b)** **(c)**

Figure 2. (a) Planting selected seeds (b) Preparing various treatments of the contaminated soil sample in the presence or absence of iron oxide particles (c) aster and Bermuda grass plants at 0 week

(a) **(b)** **(c)**

Figure 3. Aster and Bermuda grass plants after (a) 2 weeks (b) 8 weeks (c) 12 weeks

In the phytoremediation experiments, seedlings (2 weeks old) of the fresh plant species not previously exposed to cypermethrin were transplanted into a field containing soil contaminated with cypermethrin (100 µg/g). Plant maintenance that included watering, weeding, and pest control was done from the beginning of planting until harvest. The temperature was kept at 30 °C during the day and 27 °C at night. Water was added to the soil in each row every day to maintain the appropriate moisture content. The field study was performed with natural light. The study was continued after the screening period using two plant species that grew well in the cypermethrin-contaminated soil. Healthy plants with similar heights and biomasses of the selected species were transplanted into field plots for the main study. Samples of the soil were taken for analysis at 0, 2, and 12 weeks (with three replicates for each time) for the time of exposure to determine the amount of PBA formed, enzyme activities and the N, P, K contents over the course of 3 months.

Determination of Physicochemical Properties of Soil Sample

The moisture content of the soil sample was determined according to the oven drying method, pH value by pH meter, electrical conductivity (EC) value by electrical conductivity meter, organic matter content by Walkley and Black method based upon the oxidizable organic matter content, total nitrogen (N) content by Kjeldahl's method, cation exchange capacity by the method of Kappen (Jaremko and Kalembasa, 2014*)*, total phosphorus (P) content by spectrophotometric

method of Olsen for neutral and alkaline soil, potassium content by ammonium acetate extraction method using flame photometer, and the elemental analysis of the soil sample by EDXRF.

Determination of Enzyme Activities

The activity of the urease enzyme (mg NH_4^+-N g^{-1} soil h^{-1}) was measured by colorimetric methods (McGarity and Myers, 1967) Detail were described in the reference. Dehydrogenase enzyme activity was assayed by modified 2, 3, 5-triphenyl tetrazolium chloride (TTC) reduction technique (Casida *et al.,* 1964). Five grams of soil was placed in a beaker and carefully mixed with 0.1 g of $CaCO_3$ and 1.5 mL of distilled water added into the mixture. Then, 1 mL of 1% TTC solution was added and the beakers were incubated at 30 ºC for 24 h after plugging with cotton. The resulting slurry was filtered and triphenyl formazan (TPF) was extracted with successive aliquots of methanol in a 50 mL volumetric flask. The absorption of the pink colour was read out with spectrophotometer at 485 nm.

Extraction and Characterization of Insecticide Residue

In brief, 3-PBA was extracted from 10 g of soil samples using methanol and dichloromethane (3:1, v/v) mixture and placed in a shaker at 150 rpm for 30 min. The supernatant liquid was centrifuged at 5000 rpm for 15 min three times. The residual insecticide (as its metabolite 3-PBA) in extracted soil samples from the experimental plot was examined by using UV-Vis spectrophotometer and GC-MS.

Figure 4. Extraction of insecticide residue in various treatments over weeks

Statistical Analysis

Values were expressed as means ± standard deviation (SD). All data were tested for normality and homogeneity using Leven's test. All results were conducted with three replicates. The experimental data were statistically analyzed by one-way analysis of variance (ANOVA) using Excel.

Results and Discussion

Physicochemical Properties of Soil Sample

The soil has a sandy loam texture. This research used a soil with low nitrogen, very low organic carbon, humus, electrical conductivity (EC), high K_2O, and very high phosphorus (P) contents in order to scientifically investigate the degradation of cypermethrin. The moisture content of the contaminated soil was found to be 2.83%. The pH value of the contaminated soil was found to be 6.76. The electrical conductivity value of the contaminated soil was found to be 0.08 mS/cm. The electrical conductivity of soil informs the ionic nature of the soluble compound to supply the needs of plants. The contaminated soil had an organic carbon content of 0.66 % and a humus content of 1.13%. Humus contains every element absorbed by growing plants, but not in the same proportions as in plants. The microbes become part of the soil humus, along with materials that

have partially or entirely resisted the process of decomposition. Humus is a very important part of the ability of the soil to supply the needs of plants.

Table 1. Characteristics of the Soil Sample

Test Parameter	**Content**
Texture	Sandy loam
Moisture (%)	2.83
pH	6.76
Electrical Conductivity (mS/cm)	0.08
Organic carbon (%)	0.66
Humus (%)	1.13
Total Nitrogen (%)	0.14
CEC (meq/100 g)	11.75
Phosphorus (ppm)	81.85
K_2O (mg/100g)	24.71
Exchangeable Ca^{2+} (meq/100 g)	5.87
Exchangeable Mg^{2+} (meq/100 g)	4.56
Exchangeable K^+ (meq/100 g)	0.52
Exchangeable Na^+ (meq/100 g)	0.80

The total nitrogen content of the contaminated soil was found to be the lowest at 0.14%. Nitrogen helps plants make the proteins they need to produce new tissues. In nature, nitrogen is often in short supply, so plants have evolved to take up as much nitrogen as possible, even if it means not taking up other necessary elements. If too much nitrogen is available, the plant may grow abundant foliage but not produce fruit or flowers. The cation exchange capacity (CEC) of the soil was found to be 11.75 meq/100 g. The CEC is an essential measurement in agronomy and soil science to estimate the physicochemical state of a soil, which may be a good indicator of soil quality and productivity to supply the three important plant nutrients: calcium, magnesium, and potassium. The highest phosphorus content of the contaminated soil was found to be 81.85 ppm. Phosphorus stimulates root growth, helps the plant set buds and flowers, improves vitality, and increases seed size. It does this by helping transfer energy from one part of the plant to another. Organic matter and the activity of soil organisms also increase the availability of phosphorus.

The K_2O content of the contaminated soil was found to be 24.71 mg/100 g. Potassium is one of the three major fertilizer elements. In fertilizer and soil analyses, however, potash signifies the hypothetical potassium oxide, K_2O. In reality, there is no K_2O in fertilizers. Furthermore, K_2O is not absorbed by plants. Plant roots absorb most of their potassium as potassium ions K^+. The exchangeable calcium content of the contaminated soil was found to be 5.87 meq/100 g. Calcium is used by plants in cell membranes, at their growing points, and to neutralize toxic materials. In addition, calcium improves soil structure and helps to bind organic and inorganic particles together. The exchangeable magnesium content of the contaminated soil was found to be 4.56 meq/100 g. Magnesium is the only metallic component of chlorophyll. Without it, chlorophyll cannot capture the sun's energy, which is needed for photosynthesis.

The exchangeable potassium content of the contaminated soil was found to be 0.52 meq/100 g. Potassium improves the overall vigor of the plant. It helps the plants make carbohydrates and provides disease resistance. It also helps regulate metabolic activity. The

exchangeable sodium content of the contaminated soil was found to be 0.80 meq/100 g. Sodium cations (Na^+) are not plant nutrients, so they are not wanted by the plants. When exchangeable sodium is present in quantities greater than or equal to 5 % of (CEC), it makes the clay particles unstable in rainwater. This shows up as dispersion or cloudiness in water. Dispersive soils have poor water entry and drainage and are hard to dry. This study provides information about the nature of soil and the nutrients present in it, allowing a farmer to plan the amount of fertilizers and nutrients required to increase crop yield (Table 1).

EDXRF Analysis

The relative abundance of some elements: Si, Fe, K, Ca, Ti, Mn, Zr, Ba, Cr, Sr, Zn, Y, Cu, and Rb in insecticide-contaminated soil is determined by EDXRF (Figure 2 and Table 2). According to EDXRF, the insecticide-contaminated soil contained silicon (Si) as the major constituent and iron (Fe) as the second major constituent, followed in decreasing order by potassium (K), calcium (Ca), titanium (Ti), manganese (Mn), zirconium (Zr), barium (Ba), chromium (Cr), strontium (Sr), zinc (Zn), yttrium (Y), copper (Cu), and rubidium (Rb).

Table 2. Elemental Analysis of the Soil Sample

Element	Relative Abundance (%)
Silicon (Si)	54.729
Iron (Fe)	25.643
Potassium (K)	8.398
Calcium (Ca)	7.198
Titanium (Ti)	2.451
Manganese (Mn)	0.627
Zirconium (Zr)	0.765
Barium (Ba)	0.716
Chromium (Cr)	0.372
Strontium (Sr)	0.169
Zinc (Zn)	0.074
Yttrium (Y)	0.039
Copper (Cu)	0.078
Rubidium (Rb)	0.034

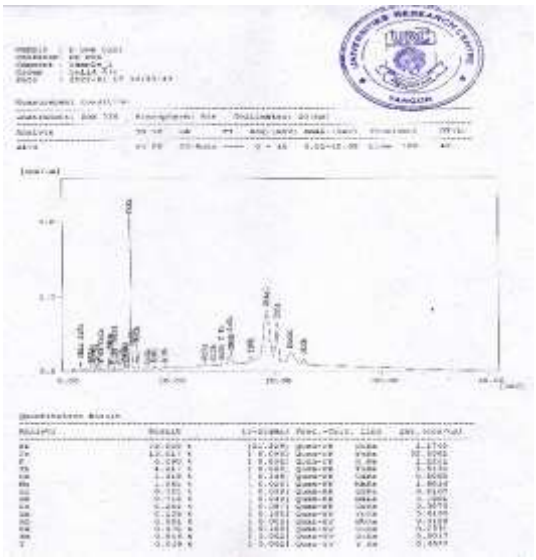

Figure 5. EDXRF spectrum of contaminated soil

The high content of silicon resists the damage to crops caused by pathogenic microorganisms and that of other elements provided as plant nutrients. Iron (Fe) is one of the major elements present in the soil, mostly in the form of oxide. Generally, the most dominant oxidation state is Fe^{3+}. Iron oxides are very important components in most soils, as they have a major influence on the chemical, physical, and microbial properties of soils. Because of their size (usually 5-200 nm), iron oxides possess a large specific surface area and highly reactive surfaces. The average particle's diameter was determined to be approximately 33.423 nm. Larger iron oxide particles degraded slowly, indicating that the reaction is surface area dependent. Potassium (K) is commonly supplied to the soil as farm manure and as commercial fertilizers.

Calcium (Ca) plays a vital role in plant growth, specifically cell wall formation, cell division, and pollination. Calcium also promotes healthy soil structure by loosening soils and stabilizing organic matter, which increases the soil's water- and nutrient-holding capacity. The more calcium is in the soil, the higher the pH of the soil can become. Titanium (Ti) is considered a beneficial element for plant growth. When plants experience Fe deficiency, Ti helps induce the expression of genes related to Fe acquisition, thereby enhancing Fe uptake and utilization and subsequently improving plant growth. The other nutrient elements, manganese (Mn), chromium

(Cr), zirconium (Zr), barium (Ba), strontium (Sr), zinc (Zn), yttrium (Y), copper (Cu), and rubidium (Rb), are used in very small amounts by higher plants, thereby justifying the name "micronutrients" or trace elements. This is due to the relatively small quantities of micronutrients in sands and organic soils and the low availability of most of these elements under very alkaline conditions.

Table 3. Characteristics of the Farm Soil Samples

Samples	Moisture %	pH	Total N %	CEC	Available Nutrients	
				K^+ (meq/100g)	P (ppm)	K_2O (mg/100g)
S_0 (0 week)	0.84	7.26	0.18	0.48	79.11	22.40
S_{Fe} (0 week)	0.77	7.39	0.20	0.73	89.07	34.47
S_{Fea} (2 weeks)	0.82	7.19	0.16	0.97	106.96	45.40
S_{Feb} (2 weeks)	0.70	7.17	0.14	0.73	74.60	34.47
S_{Fea} (4 weeks)	1.80	7.07	0.18	1.24	142.57	58.04
S_{Feb} (4 weeks)	0.84	7.06	0.16	0.97	82.74	45.40
S_{Fea} (8 weeks)	0.85	6.73	0.19	2.29	343.08	103.53
S_{Feb} (8 weeks)	0.73	7.13	0.14	1.16	151.20	54.43
S_{0a} (12 weeks)	1.016	7.05	0.142	1.28	169.86	60.66
S_{Fea} (12 weeks)	1.21	6.90	0.16	1.26	113.48	59.57
S_{0b} (12 weeks)	1.442	6.56	0.142	0.28	114.72	13.4
S_{Feb} (12 weeks)	2.68	7.68	0.13	0.43	53.442	20.34

pH and Major Nutrients of Farm Soil Samples in Different Treatments

The pH values of the contaminated farm soil at different times (0, 2, 4, 8, and 12 weeks), determined by the pH meter, are shown in Table 3. The pH values of the control soil samples at 0 week for S_0 and S_{Fe} were higher than those of the other soil samples (S_{0a}, $S_{Fea,}$ $S_{0b,}$ and S_{Feb}) for 0, 2, 4, 8, and 12 weeks, except for S_{Feb} at 12 weeks (Table 3). From these observations, the contaminated farm soil samples were found within the range of 6.5-7.68, and this range of pH is generally very compatible with plant root growth. It also affects the microbial population in soils. The optimum range for most plants is between 5.5 and 7.5. However, many plants have adapted to thrive at pH values outside this range. Therefore, the pH values measured in this agricultural soil are consistent with the determined optimum values. If the pH value is less than 5.5, it also affects the activity of soil microorganisms, thus affecting nutrient cycling and disease risk. From the study of total nitrogen percent in the contaminated farm soil samples by Kjeldahl's method, the control samples for week 0 (S_0 and S_{Fe}) were higher than those of the other soil samples (S_{0a}, $S_{Fea,}$ $S_{0b,}$ and S_{Feb}) for weeks 0, 2, 4, 8, and 12 (Table 3). Thus, the decrease in nitrogen levels reduces the leaf area, chlorophyll content, photosynthesis, and biomass production. This is because more nitrogen is consumed by the plants, which results in more nitrogen depletion in the soil.

The CEC is an essential measurement in agronomy and soil science to estimate the physicochemical state of soil, the three important plant nutrients: calcium, magnesium, and potassium. Plants use calcium in their cell membranes at their growth points and to neutralize toxic materials. In addition, calcium improves soil structure and helps to bind organic and inorganic particles together. Magnesium is the only metallic component of chlorophyll. Potassium occurs in the soil in three forms: as exchangeable (available) potassium (K^+) adsorbed onto the soil CEC; fixed by certain minerals, from which it is released very slowly into an available form; and in unavailable mineral forms. The CEC values of potassium K^+, available nutrients K_2O, and phosphorous (P) values of the control soil samples (0 week) for S_0 and S_{Fe} were found to be lower than those of the other soil samples (S_{0a}, $S_{Fea,}$ $S_{0b,}$ and S_{Feb}) for (0, 2, 4, 8, and 12 weeks), except S_{Feb} for 12 weeks (Table 3). Phosphorous (P) is a major nutrient required for energy storage and transfer, cell division, and tissue development in plants like aster and Bermuda grass. Among N, P, and K, the iron oxide-treated soil samples (S_{Fea} and S_{Feb}) for aster and Bermuda grass have the highest values of available P and K_2O.

Moisture Variation in Different Treatments

The moisture contents of the contaminated farm soil Table 3 at different times (0, 2, 4, 8, and 12 weeks) are determined by the oven drying method. The moisture contents of the control soil samples (0 week) for S_0 and S_{Fe} were lower than those of the other soil samples (S_{0a}, $S_{Fea,}$ $S_{0b,}$ and S_{Feb}) for (0, 2, 4, 8, and 12 weeks). Soil moisture is the water stored in the soil and is affected by precipitation, temperature, soil characteristics, and more. The size of the soil particles and pores affects how much water the soil can hold and how that water moves through the soil.

Enzyme Activities Variation in Different Treatments

During the incubation periods, the effects of iron oxide particles on urease and dehydrogenase activities were found to increase, as shown in Figure 6-a and b. According to this figure, the changes in urease and dehydrogenase activities depend on the dosage of iron oxide particles. The degradation of cypermethrin in soil is mostly attributed to microorganisms. Urease and dehydrogenase activities are appropriate substitute biomarkers of general microbial activities in soils. In addition to iron oxide particles, urease and dehydrogenase activities significantly increased over the course of 12 weeks.

After 12 weeks, the urease and dehydrogenase activities in the controls (or treated soil in the absence of iron oxide particles, S0) were found to reach 3.74 mg NH_4^+-N g^{-1} soil h^{-1} and 0.0008 µg TPF g^{-1} soil h^{-1}, whereas 5.975 mg NH_4^+-N g^{-1} soil h^{-1} and 0.00124 µg TPF g^{-1} soil h^{-1} were found in aster (S_{0a}) and 4.494 mg NH_4^+-N g^{-1} soil h^{-1} and 0.00124 µg TPF g^{-1} soil h^{-1} in Bermuda grass (S_{0b}). The percentages of urease and dehydrogenase activities were found to increase by 161.49 and 155 % in aster (S_{0a}) and 121.45 and 155 % in Bermuda grass (S_{0b}) compared with controls (assumed to be 100 %) through 12 weeks.

After 12 weeks, the urease and dehydrogenase activities in the presence of iron oxide particles (S_{Fe}) were found to be reached 3.8 mg NH_4^+-N g^{-1} soil h^{-1} and 0.00073 µg TPF g^{-1} soil h^{-1}, 5.363 mg NH_4^+-N g^{-1} soil h^{-1} and 0.00127 µg TPF g^{-1} soil h^{-1} in aster (S_{Fea}) and 4.816 mg NH_4^+-N g^{-1} soil h^{-1} and 0.00113 µg TPF g^{-1} soil h^{-1} in Bermuda grass (S_{Feb}). The percentage of urease and dehydrogenase activities in the presence of iron oxide particles was found to increase by 141.13 and 174 % in aster (S_{Fea}) and by 126.74 and 154.79 % in Bermuda grass (S_{Feb}) in comparison with S_{Fe} (assumed to be 100 %) for 12 weeks.

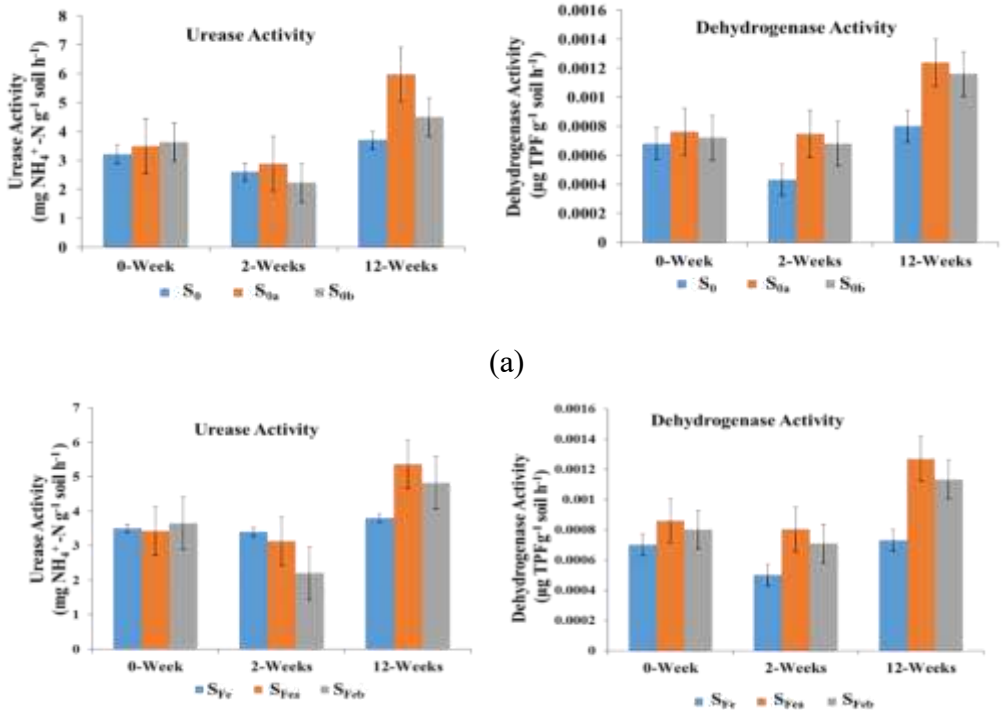

(a)

(b)

Figure 6. Soil urease and dehydrogenase activities in insecticide contaminated soil treated with aster and Bermuda grass (a) in the absence and, (b) in the presence of iron oxide particles

Insecticide Residue Percent in Contaminated Soil Samples

The effect of iron oxide particles prepared with total phenol extract from tea leaf waste as a reducing agent on phytoremediation was studied using UV-Vis and GC-MS for insecticide residue from contaminated soil.

In comparison with $S_{0\ in\ a}$ 0-week treatment, the percentages of insecticide residue in the S_0, S_{0a}, and S_{0b} treatments were found to be 213.25, 139.29, and 207.4 % PBA formed through 2 weeks of experiments and 99.2, 3.53, and 3.67 % PBA formed through 12 weeks of experiments (Figure 7-a). In comparison with S_{Fe} in the 0-week treatment, the percentages of insecticide residue in the S_{Fe}, S_{Fea}, and S_{Feb} treatments were observed to be 153.28, 170.37, and 282.35 % PBA formed after 2 weeks of experiments, and 97.89, 3.67, and 5.82 % PBA formed (no cypermethrin residue) through 12 weeks of experiments (Figure 7-b). All treatments showed phytoremediation efficiency for insecticide-contaminated soil.

At all levels of contamination of the soil, aster and Bermuda grass soil respiration was found to be significantly higher than that soil respiration. The root system and soil moisture provide a suitable environment in the soil for microorganisms, contaminants, and organic molecules nutrient interactions. (Germida *et al.*, 2002). Therefore, it seems that higher root biomass produced by aster and Bermuda grass in contaminated soils, is responsible for more microbial activity in their rhizosphere.

Aster and Bermuda grass with iron oxide particles were found to possess the greater degradation efficiency in phytoremediation. During cultivation, the plants were watered regularly. This may be because soil saturation with water decreases the oxygen levels and thus prevents the oxidation of iron oxide particles. Insecticides, which are persistent in aerobic environments, are more readily degraded under reducing conditions. The results showed that the

iron oxide particles played the most important role in the degradation of insecticide residue in the soil, compared with natural degradation in soil without iron oxide particles.

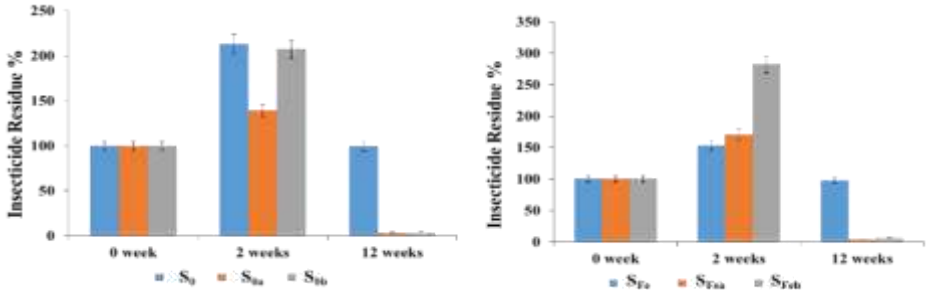

(a) **(b)**

Figure 7. Insecticide residue (PBA) percent in contaminated soil treated with aster and Bermuda grass (a) in the absence of iron oxide particles and (b) in the presence of iron oxide particles through 12 weeks experiments

Cypermethrin is relatively stable under sunlight, and, though it is probable that photodegradation plays a significant role in the degradation of the product, its effects in soils are limited. Degradation in the soil occurs primarily through cleavage of the ester linkage to give PBA and carbon dioxide. Some carbon dioxide is formed through the cleavage of both the cyclopropyl and phenyl rings under oxidative conditions. The half-life of cypermethrin in typical fertile soil is between 2 and 4 weeks. Cypermethrin is adsorbed very strongly on soil particles, especially in soils containing large amounts of clay or organic matter.

The role of functionalized iron oxide particles in nanomaterial and biomedical applications often relies on achieving the attachment of ligands to the iron oxide surface in sufficient numbers and with proper orientation (Korpany *et al*., 2017). The results of this study could be due to relationships between the ligand chemical structure and surface binding on magnetic iron oxide particles (~30 nm) for a series of related benzoic acid derivatives. The structure of the resultant ligand-surface complex was primarily influenced by the relative positioning of hydroxyl and carboxylic acid groups within the ligand. The chemical structure of benzoic acid derivatives enables fast and stable covalent binding on the surface of magnetite (Fe_3O_4) particles, which act as catchers and carriers for magnetic removal. The results of studies have shown that, with iron oxide particles applied, the levels of cypermethrin and its secondary metabolite, PBA, can be lowered.

Conclusion

The 12-week long experiment revealed an increase of available phosphorous and K_2O and enzyme activities in soil and a decrease of nitrogen content and insecticide residue. The percentage of total nitrogen content decreased from 0.18% (S_0) in 0 week to 0.16% in asters and 0.13% in Bermuda grass. The available phosphorous content increased from 79.11 ppm (S_0) in 0 weeks to 113.48 ppm in aster and decreased to 53.442 ppm in Bermuda grass through 12 weeks. The available K_2O content increased from 22.40 mg/100 g (S_0) in 0 week to 59.57 mg/100 g in asters and decreased to 20.34 mg/100 g in Bermuda grass through 12 weeks. Through a 12-week experiment, the percentage of urease and dehydrogenase activities increased 41.13 and 74.0 % in aster (S_{Fea}) and 26.74 and 54.79% (S_{Feb}) in Bermuda grass, while the percentage of insecticide residue in contaminated soil decreased from 100 % (S_0) in 0 week to 3.67 % in aster and 5.82% in Bermuda grass. The phytoremediation process increases soil urea and dehydrogenase activity.

The growth of plants with iron oxide particles in insecticide contaminated soils has favorable effects on the changes in soil nutrients, the enzyme activities, and the degradation of PBA in the contaminated soil. The findings of this study showed that aster and Bermuda grass can be recommended as native alternative options for phytoremediation in some area of the country.

Acknowledgements

The authors would like to express their profound gratitude to the Myanmar Academy of Arts and Science for giving permission to submit this paper and to Professor and Head, Dr Ni Ni Than, Department of Chemistry, University of Yangon, for her kind encouragement.

References

Casida, L. E., D. A. Klein, and T. Santoro. (1964). "Soil Dehydrogenase activity". *Journal of Soil Science,* vol. 98, pp. 371-376

Chaitra, R. and V. S. Patil. (2007). "Integrated Nutrient Management Studies in China Aster (*Callistephus chinensis* Nees) cv. Kamini". *Karnataka Journal of Agricultural Sciences,* vol. 20 (3), pp. 689-690

Demangeat, E., M. Pedrot, A. Dia, M. Bouhnik-Le-Coz, P. Roperch, G. Compaore and F. Cabello-Hurtado. (2021). "Investigating the remediation potential of iron oxide nanoparticles in Cu-polluted soil–plant systems: coupled geochemical, geophysical and biological approaches" *Nanoscale Adv,* vol.12, pp.1-13

Germida, J. J., C. M. Frick and R. E. Farrell. (2002). "Phytoremediation of oil-contaminated soils". *Developments in Soil Science,* vol. 28, pp. 169-186

McGarity, J.W. and M.G. Myers. (1967). "A Survey of Urease Activity in Soils of Northern South Wales", *Plant and Soil,* **27**, 217-238

Jaremko, D., and D. Kalembasa. (2014). "A Comparison of Methods for the Determination of Cation Exchange Capacity of Soils". *Ecological Chemistry* and *Engineering S. Journal,* vol. 21 (3), pp. 487-498

Jingjing, S., Z. Mijia, Y. Xiaoqia, Z. Chi and Y. Jun. (2015). "Microbial, Urease Activities and Organic Matter Responses to Nitrogen Rate in Cultivated Soil". *The Open Biotechnology Journal*, vol. 9, pp.14-20

Korpany, K.V., D. D. Majewski, C. T. Chiu, S. N. Cross, and A. S. Blum. (2017). "Iron Oxide Surface Chemistry: Effect of Chemical Structure on Binding in Benzoic Acid and Catechol Derivatives". *Langmuir*, vol. 33 (12), pp. 3000-3013

Swe Sint, Dr Phyu Phyu Myint and Dr Saw Hla Myint. (2021). "Iron Oxide Particles Assisted Phytoremediation of Soil Contaminated with Cypermethrin Residue", *Journal of Myanmar Academy of Arts and Science*, vol 18 (in press)

Wang, X., B. He, B. Kong, L. Wei, R. Wang, C. Zhou, Y. Shao, J. Lin, Y. Jin and Z. Fu. (2017). "β-Cypermethrin and its metabolite 3-phenoxybenzoic acid exhibit immunotoxicity in murine macrophages", *Acta Biochem Biophys Sin,* vol. 49 (12), pp. 1-9

Wolinska, A., M. Zapasek and Z. Stepniewska. (2016). "The Optimal TTC Dose and its Chemical Reduction Level during Soil Dehydrogenase Activity Assay". *Acta Agrophysica*, vol. 7 (2), pp. 303-314

Xian, Y., M. Wang and W. Chen. (2015). "Quantitative Assessment on Soil Enzyme Activities of Heavy Metal Contaminated Soils with Various Soil Properties". *Chemosphere,* vol. 139, pp. 604-608

Xie, W.-J., Z. Jian-Min, W. Huo-Yan, and C. Xiao-Qin. (2008). "Effect of Nitrogen on the Degradation of Cypermethrin and Its Metabolite 3-Phenoxybenzoic Acid in Soil". *Pedosphere*, vol. 18 (5), pp. 638-644

EFFECTIVENESS OF MODIFIED ARECA LEAF FIBER REINFORCING MATERIALS IN ECO-FRIENDLY COMPOSITES

Hnin Yu Wai*

Abstract

This research work is mainly concerned with the production of composites from 5 % NaOH modified waste areca leaf fiber with recycled polyethylene as binder and the study of their characteristics. Composites were produced by mixing each modified waste areca leaf fiber (120 g) with various compositions (10 %, 20 %, 30 %, 40 %, 50 % and 60 %) of recycled polyethylene (PE) using hot compressing molding method at 120˚C and 2200 psi. The produced composites were characterized by physicochemical and physicomechanical parameters such as modulus of rupture, thickness, density, water absorption, swelling thickness and hardness. Based on the physicomechanical properties, MAFPE 4 composite was a quality grade composite among the produced composites. It has 2679.83 psi of modulus of rupture, 0.60 cm of thickness, 0.87 g cm^{-3} of density, 23.37 % of water absorption, 33.18 % of swelling thickness and 98 D of hardness. The surface morphology of MAFPE 4 composite was studied by SEM and heat characteristic of composite by TG-DTA analyses. MAFPE 4 composite can be used in furniture and building.

Keywords: Areca leaf fiber, polyethylene, composites, modulus of rupture

Introduction

Natural fiber composites are one such kind of material. The natural fibers are widely used in the composites due to inherited properties, such as lignocelluloses, renewable, and biodegradable. There are several other reasons that favor the use of natural fibers instead of any other artificial or synthetic fibers. There are several other advantages to using natural fibers over artificial or synthetic fibers. They are lightweight materials having superior strength, competitive specific mechanical properties, high specific modulus, and reduced energy consumption. Further, they are nontoxic and nonhazardous in nature, naturally recyclable, available in abundance, flexible in usage, less expensive and that allow clean energy recovery, etc. (Raghuveer *et al.*, 2016).

To develop a composite material made from natural fibers with significantly improved strength, stiffness, durability, and reliability, it is important to have better fiber-matrix interfacial bonding. This can be accomplished through surface treatment–and the manufacturing process technology used to create the composite. Recently, broad studies on natural fibers such as sisal, jute, pineapple, banana, and oil palm empty fruit bunch fibers with thermoplastic and thermosetting materials have been carried out (Srinivasa and Bharath, 2011).

The mechanical properties of composite like tensile and bending strengths increase because of surface modification. The chemical surface modifications such as alkali, acetic anhydride, stearic acid, permanganate, maleic anhydride, silane, and peroxides given to the fiber and matrix were found to be successful in improving the interfacial adhesion and compatibility between the fiber and matrix. A strong fiber-matrix interface bond is critical for the high mechanical properties of composites. A good interfacial bond is required for effective stress transfer from the matrix to the fiber, whereby maximum utilization of the fiber strength in the composite can be achieved. Most research reviewed indicated the effect of alkali treatment in improving fiber strength, fiber-matrix adhesion, and the performance of the natural fiber composites (Dhanalakshmi *et al*., 2016).

Amongst all-natural fiber reinforcing materials, areca appears to be a budding fiber because it is inexpensive, abundantly available and has a very high potential perennial crop. The botanical name of areca is *Areca Catechu* Linnaeus, and it belongs to the Arecaceae (palmae), palm family

* Department of Chemistry, Maubin University

and Arecoideae subfamily. Arecas have superior properties such as light weight, strength, and a high strength to weight ratio. In addition, areca fibers are biodegradable, non-toxic, and eco-friendly and they have a low maintenance cost. Areca fiber is made from cellulose, lignin, and hemicellulose. Moreover, it contains minor constituents, for example, pectic, fatty and waxy matters. The main point that oversees the properties of short fiber dispersion, and fiber grid bonding. Blending the polar and hydrophilic strands with non-polar and hydrophobic matrix can bring about challenges related to the dispersion of fibers in the matrix. Additionally, the bonding between the fibers and matrix can be improved by improving the matrix with compatibilizers that adhere well to both fibers and matrix (Pavankalyan *et al*.,2018).

Synthetic polymers such as polystyrene, polyethylene, polypropylene, polyvinyl chloride etc. have higher mechanical properties, sustainability and durability compared to natural polymers. But they are not biodegradable, and they cause pollution of the environment. With this aim in mind, many researchers have developed different composites by combining natural and synthetic polymers and some of them have already been used as industrial products. Among synthetic polymers, polyethylene possesses outstanding properties like low density, low cost, good flex life, good surface hardness, scratch resistance and excellent electrical insulating properties (Miah *et al*., 2011).

It is thus the aim of the present work is to produce a polyethylene-areca leaf fiber composite using waste plastic material and modified areca leaf fiber under optimized conditions for a useful application.

Materials and Methods

All necessary research facilities were provided by the polymer department, Department of Research and Innovation, (DRI).

Collection of samples

In the experiments, waste areca leaf that is a by-product of the Nature Myanmar Company and recycled polyethylene (PE) were collected from Public waste at the Science Canteen, the Yangon University Campus, Yangon Region, and Myanmar.

Extraction of waste areca leaf fiber

Areca fibers are extracted from areca leaves after soaking them for 10-15 days. These drenched leaves are cleaned with the help of running water 5-10 times daily. The drenching process removes the dust particles. These leaves are dried in the sun for 3 days to remove the moisture content. The areca leaf fibers were cleaved into little pieces with the assistance of hand scissors. These leaves are dried in sun for 3 days to remove the moisture content. The areca leaf fibers were cleaved into little pieces with the assistance of hand scissors. After cutting, they were ground on an electric grinder obtaining a size of about 0.5-2.0 cm. The fibers were taken and dried in an oven at 70ºC. The dried samples were screened to pass through the sieve aperture of 25 meshes (0.5 mm) obtained. The sieved material was then stored in an airtight plastic bag for further experimentation.

Modification of waste areca leaf fiber

The fibers (ca. 400 g) were immersed in 6 L solution of (5 % w/v) NaOH (pH~ 13) at room temperature for 24 h, after which the fibers were washed thoroughly with plenty of water until drained water became neutral (pH~ 7). After treatment, they were dried in the sunlight and then in an oven at 70 ˚C for 3 h.

Preparation of recycled polyethylene

The collected empty drinking water bottles, made of recycled polyethylene were cut into pieces. The cut was washed thoroughly with distilled water, and then the cleaned samples were solar dried for a few days. The dried pieces were ground by a grinding machine. The particles were screened to pass through the 25 meshes (0.5 mm) of the sieve aperture. The sieved material was then stored in an airtight plastic bag for further experimentation.

Determination of physicochemical properties of modified areca leaf fiber and recycled polyethylene

The moisture content of samples was determined by oven drying method at (100 ± 5ºC), according to TAPPI-T210 om-6, 1992-1993, the solid contents of prepared samples were determined by procedure according to TAPPI-T210 om-6, 1992-1993, the ash content by ASTM test method, D 1102, 1986, the bulk density by tapping box method and the pH by using pH meter. The physicochemical properties (moisture content, ash content, solid content, bulk density, and pH) of the prepared samples were determined by conventional methods.

Characterization of areca leaf fiber, modified areca leaf fiber and recycled polyethylene

The scanning electron micrographs of areca leaf fiber, modified areca leaf fiber, and recycled polyethylene were obtained with the help of a Scanning Electron Microscope (JSM-5160, JEOL Ltd., Japan). Thermal analysis of modified areca leaf fiber and recycled polyethylene was determined by a DTA-60H (Hi-TGA 2950) thermal analyzer. TG-DTA thermogram and the description data are presented.

Production of modified areca leaf fiber-recycled polyethylene composites (MAFPE)

In this research, all the modified areca leaf fiber - recycled polyethylene composites were produced by the hot compressing molding method.

Effect of composition of recycled polyethylene (PE) on the production of modified areca leaf fiber - recycled polyethylene composites

Each modified areca leaf fiber (120 g) was mixed with (10, 20, 30, 40, 50 and 60%) recycled polyethylene before being mixed for 2 min in the Henschel mixer. The complete mixture was laid in mold. Later, this mat was carefully transferred to the hydraulic press machine for 15 min at 120 ˚C and 2200 psi. The composites from the hydraulic press were kept cool for at least 24 h and then went through a sanding process. The composites were kept at room temperature for 1 week and then the edges and both sides of the composite were trimmed and stood (15.24 cm x 15.24 cm).

Determination of the physicochemical and physicomechanical properties of modified areca leaf fiber - recycled polyethylene composites

Modulus of rupture of composites was determined according to B.S 1811:1916, thickness by Micrometer or Screw gauge, veneer clipper according to IS: 3087:1965, density by B.S 1811: 1961, water absorption by IS: 3087:1965, and swelling thickness by IS: 3087-1965. Durometer hardness by Wallance Micro Hardness Tester readings were performed according to ASTM D 2240.

Characterization of the Selected Composite (MAFPE 4)

The morphology of composite MAFPE 4 was studied by using scanning electron micrograph for analysing micro and macro pores present on the surface of samples. Thermal analysis of composite MAFPE 4 was determined by a DTA-60H (Hi-TGA 2950) thermal analyzer.

Determination of Heat Resistance of MAFPE 4 Composite

Composites were cut into 2.54 cm × 2.54 cm pieces and weighed. These pieces of composites were heated at different temperatures (100, 200, 300, 400, 500, 600 ˚C) for 5 h. Weight loss percentages were determined after.

Results and Discussion

Table 1 shows the physicochemical properties (moisture content, ash content, bulk density, and pH) of the modified areca fiber and recycled polyethylene.

Table 1. Physicochemical Properties of Modified Areca Leaf Fiber and Recycled Polyethylene

No.	Physicochemical properties	Modified areca leaf fiber	Recycled polyethylene
1.	Moisture content (%)	12.45	0.70
2.	Ash content (%)	6.78	1.30
3.	Solid content (%)	87.55	99.30
4.	Bulk density (g mL^{-1})	28.40	2.50
5.	pH	6.70	6.80

Characterization of Modified Areca Leaf Fiber and Recycled Polyethylene

SEM analysis

In Figure 1, the SEM photographs show the areca leaf fiber surface morphology before and after treatment. The micrograph of untreated fibers showed a clear network structure in which the fibrils are bound together by hemicelluloses and lignin (Figure 1 (a)). But in Figure 1 (b), when the fibers are treated with alkali, the fiber structure is formed of several bundles of filaments aligned to the plant's length. When the morphology of the treated sample is compared with the original fiber surface topography, it can be seen as a partially cleaned surface, and its roughness is formed by the partial pulling of the fibrous structure of sample. The recycled polyethylene (Figure 2), in this image has a flake like nature and is not similar in size.

Figure 1(a). SEM micrograph of areca leaf fiber

Figure 1(b) SEM micrograph of modified areca leaf fiber

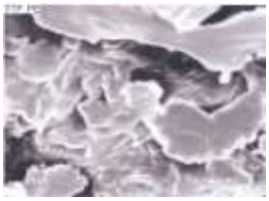

Figure 2. SEM micrograph of recycled polyethylene

TG-DTA analysis

Thermal stability of modified areca leaf fiber (Figure 3) and the interpretation (Table 2) are given. Data showed three distinct weight losses: the first one corresponded to dehydration, the second to the decomposition of small segments from cellulose and lignin and the third to the combustion.

Thermal stability of recycled polyethylene was investigated by TG-DTA analysis and the nature of the thermo gravimetric scan is shown in Figure 4 and the descriptions are shown in Table 3. Data showed two distinct weight losses: the first one attributed to the removal of moisture and the second to the combustion.

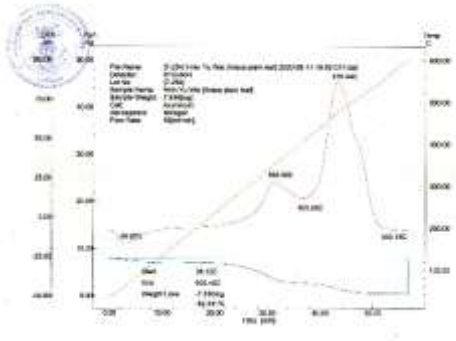

Figure 3. TG-DTA thermogram of modified areca leaf fiber

Table 2. Thermal Analysis Data of Modified Areca Leaf Fiber

TG		DTA		Remarks
Temperature range (ºC)	**Weight loss (%)**	**Peak temperature (ºC)**	**Nature of peak**	
38-100	9.29	59.87	endothermic	Dehydration due to surface water
100-380	68.33	350.99	exothermic	Decomposition of small segments from cellulose and lignin
380-500	14.68	476.34	exothermic	Combustion

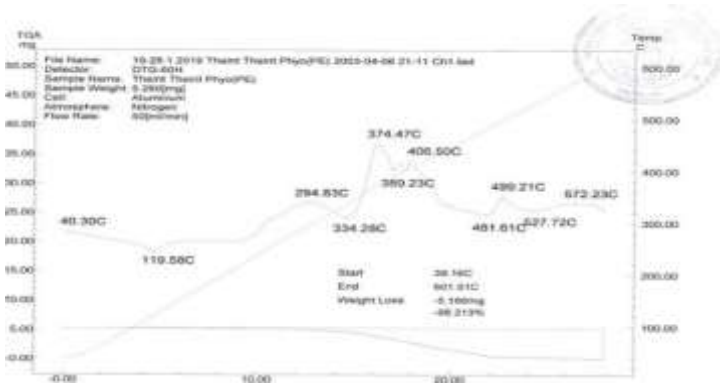

Figure 4. TG-DTA thermogram of recycled polyethylene

Table 3. Thermal Analysis Data of Recycled Polyethylene

TG		DTA		
Temperature range (ºC)	**Weight loss (%)**	**Peak temperature (ºC)**	**Nature of peak**	**Remarks**
40-360	17.68	119.58	endothermic	Removal of moisture and volatile materials
360-600	76.05	499.21	exothermic	Combustion

On the Aspect of the Production of Modified Areca Leaf Fiber - Recycled Polyethylene Composites

The composites were fabricated by hand lay-up technique. The inner cavity dimension of the mold is 15.4 cm x 15.4 cm. Each 5 % sodium hydroxide modified areca leaf fiber and various compositions of polyethylene (10, 20, 30, 40, 50 and 60 %) of recycled polyethylene were mixed by Henschel mixer for 2 min. The complete mixture of fiber and binder was laid in a mold. It was necessary to get a uniform surface of the mixture in cold section and later it was slowly transferred to the hydraulic press machine under the pressure 2200 psi and applied temperature at 120˚C. Composites of various compositions with constant fiber loading are made. The composites from the cold press were kept at room temperature for 24 h. The composites prepared for testing were cut to the conform to the dimensions of the specimen.

Effect of Composition of Recycled Polyethylene on the production of Composites

MAFPE 1, MAFPE 2, MAFPE 3, MAFPE 4, MAFPE 5 and MAFPE 6 composites were produced by mixing each modified areca fiber (120 g) with various compositions of polyethylene (10, 20, 30, 40, 50 and 60 %) at 2200 psi of pressure and applied temperature at 120 ˚C. The results of the physicochemical and physicomechanical properties of produced composites are presented (Table 4 and Figures 5, 6 and 7). It was found that the composite MAFPE 4 made with modified areca fiber (120 g) and 40 % of recycled polyethylene has the highest modulus of rupture among them. Therefore, composite MAFPE 4 was chosen to make the most suitable composite.

Table 4. Physicochemical and Physicomechanical Properties of Composites with Various Compositions of Recycled Polyethylene (PE)

Types of composite	PE (%)	Modulus of rupture (psi)	Thickness (cm)	Density (gcm^{-3})	*Water absorption (%)	*Swelling thickness (%)	Hardness shore (D)
MAFPE 1	10	1860.37	0.52	0.78	13.80	17.57	89
MAFPE 2	20	2198.12	0.54	0.82	20.36	27.89	92
MAFPE 3	30	2368.45	0.57	0.84	24.52	34.43	94
MAFPE 4	40	2679.83	0.60	0.87	23.37	33.18	98
MAFPE 5	50	2463.69	0.62	0.89	23.52	33.34	98
MAFPE 6	60	2254.23	0.63	1.14	23.98	33.76	97

*After 24 h

Applied pressure -2200 psi, Applied temperature -120 ˚C

MAFPE 1 = (120) g modified areca leaf fiber with 10 % PE

MAFPE 2 = (120) g modified areca leaf fiber with 20 % PE

MAFPE 3 = (120) g modified areca leaf fiber with 30 % PE

MAFPE 4 = (120) g modified areca leaf fiber with 40 % PE

MAFPE 5 = (120) g modified areca leaf fiber with 50 % PE

MAFPE 6 = (120) g modified areca leaf fiber with 60 % PE

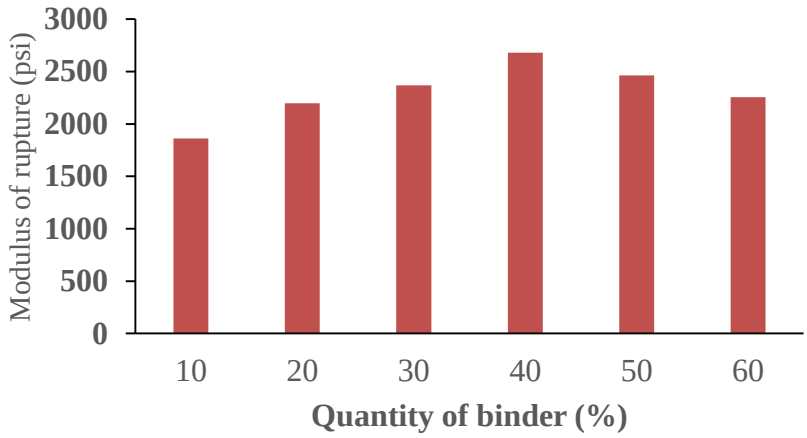

Figure 5. Modulus of rupture of MAFPE composites as a function of quantity of binder

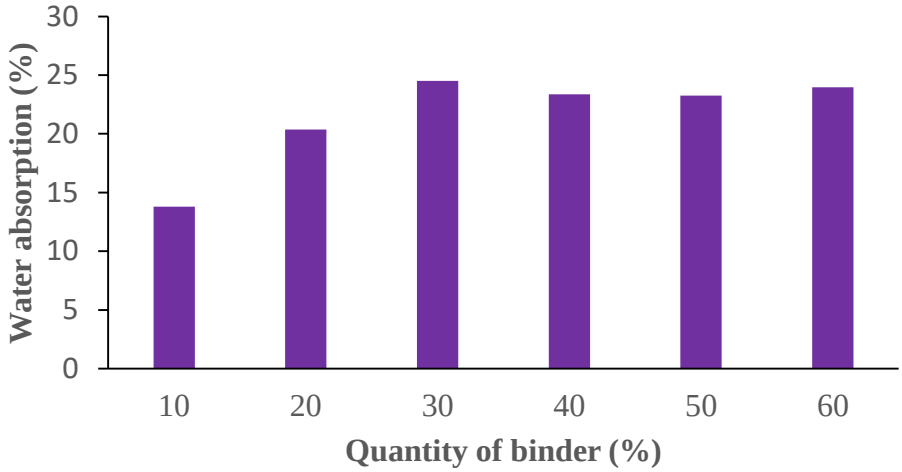

Figure 6. Water absorption of MAFPE composites as a function of quantity of binder

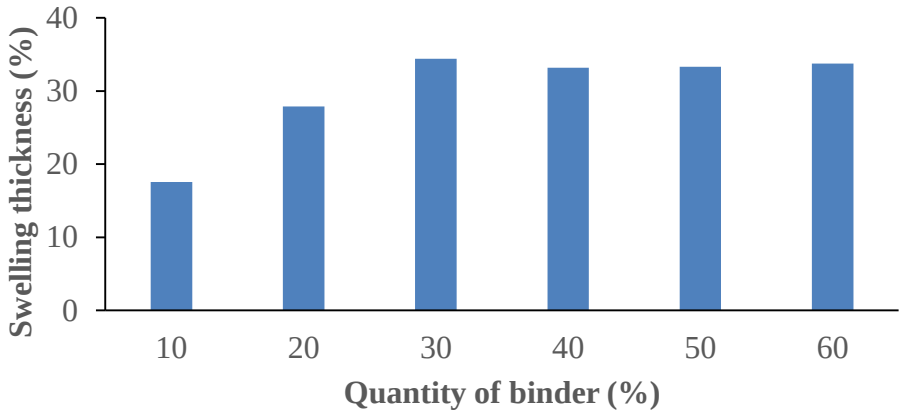

Figure 7. Swelling thickness of MAFPE composites as a function of quantity of binder

Characterization of Selected Composite (MAFPE 4)

SEM analysis

The SEM micrograph of MAFPE 4 composite showed that a longitudinal filament of fiber has been embedded in the whole surface, layer by layer presence of white sheets of matrix having different sizes on the composite (Figure 8).

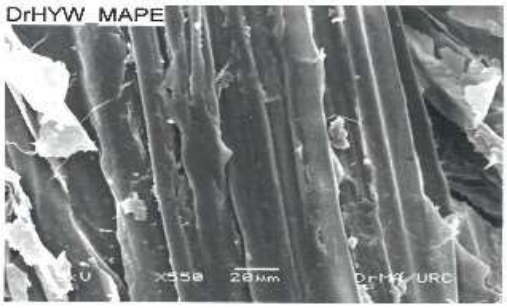

Figure 8. SEM micrograph of MAFPE 4 composite

TG-DTA analysis

Thermal stability of composite (MAFPE 4) (Figure 9) and the interpretation (Table 5) are given. Data showed three distinct weight losses: the first one corresponded to dehydration, the second to the decomposition of cellulose and lignin, and the third to the combustion.

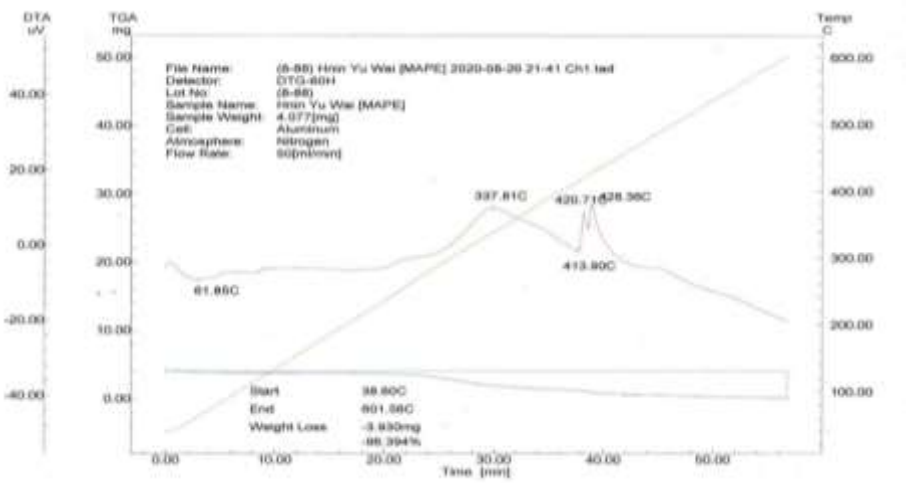

Figure 9. TG-DTA thermogram of MAFPE 4 composite

Table 5. Thermal Analysis Data of MAFPE 4 Composite

TG		DTA		Remarks
Temperature range (ºC)	**Weight loss (%)**	**Peak temperature (ºC)**	**Nature of peak**	
38-100	14.15	61.85	endothermic	Dehydration due to surface water
100-360	65.71	337.81	exothermic	Decomposition of cellulose and lignin
360-460	16.50	413.90	endothermic	Combustion
		420.71	exothermic	
		428.36	exothermic	

Heat Resistance of MAFPE 4 Composite

Table 6 and Figure 10 show the heat resistance property of the composite. When each MAFPE 4 composite was heated in the furnace at different temperatures (100. 200, 300, 400, 500, 600 ºC) changes in the colour of composites occurred. From the experimental results, the heat resistance of MAFPE 4 composite is with stand able up to 400 ºC. At 600 ºC, the composite became ash. This is due to burning at high temperature.

Table 6. Heat Resistance of (MAFPE 4) Composites at Different Temperatures

Temperature (°C)	Before heating weight (g)	After heating weight (g)	Weight loss (%)	Observation
100	3.4380	3.2540	5.30	No colour change
200	3.4324	3.0500	11.14	No colour change
300	3.4280	2.5470	31.56	Pale brown colour is formed
400	3.3950	1.9400	42.85	Brown colour is formed
500	3.3870	0.5640	83.34	Black colour is formed
600	3.3680	0.2178	92.214	Ash pale brown colour is formed

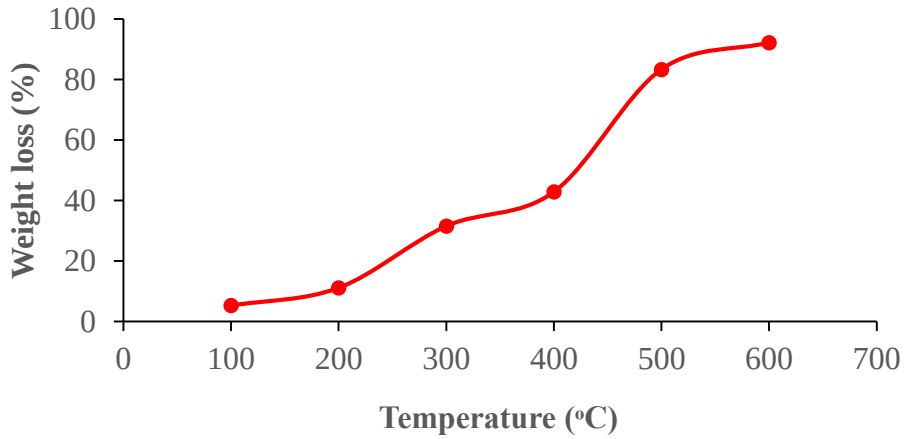

Figure 10. Weight losses (%) of (MAFPE 4) composite as a function of different temperatures

Some Possible Applications of Produced Composites

The produced composites can be used for domestic purpose like furniture, window, door, matting, civil construction etc. The photographs of produced MAFPE composites are presented (Figure 11).

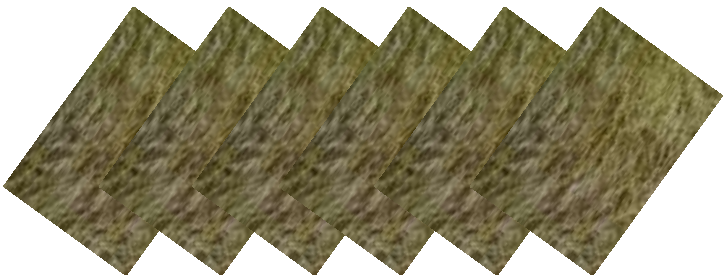

Figure 11. Photographs of MAFPE composites

Conclusion

This study reveals the use of fiber in the development of polymer composites. Improved composites were produced from 5 % (w/v) NaOH used as surface modifiers of fibers to form modified areca leaf fiber. Composites, namely MAFPE, were produced by mixing each 120 g of modified areca leaf fiber with various compositions of recycled polyethylene (PE) by using the hot-pressing method at 2200 psi and 120 ˚C. The optimal condition influencing the production of composites is based on the composition of the binder (40 %) in PE. It was found that the optimized MAFPE 4 composite possesses 2679.83 psi of modulus of rupture, 0.60 cm of thickness, 0.87 g cm^{-3} of density, 23.37 % of water absorption, 33.18 % of swelling thickness, and 98 D of hardness. Composites produced from modified areca leaf fiber are more environmentally friendly, and are used in the building and construction industries (ceiling paneling, partition boards), packaging, consumer products, etc.

Acknowledgements

The author would like to express her deepest gratitude to the Department of Higher Education, Ministry of Education, Yangon, Myanmar, for providing the opportunity to do this research and Myanmar Academy of Arts and Science for allowing to present this paper. Thanks are also due to the Polymer Department, Department of Research & Innovation (DRI) for all the necessary research facilities provided and Universities' Research Center (URC) for TG-TDA and SEM.

References

Dhanalakshmi, S., P. Ramadevi, and B. Basavaraju. (2016). "A Study of the Effect of Chemical Treatments on Areca Fiber Reinforced Polypropylene Composite Properties". *Journal of Science and Engineering of Composite Material*, vol. 9, pp. 1-20

Miah, M. J., M. A. Khan, and R. A. Khan. (2011). "Fabrication and Characterization of Jute Fiber Reinforced Low Density Polyethylene Based Composites: Effects of Chemical Treatment". *Journal of Scientific Research*, vol.3, pp. 249-259

Pavankalyan, S., R. C. Paul, K. Kamalakannan, and P. G. Scholar. (2018). "Experimental Investigation of Areca Fiber Reinforced Polypropylene Polymer Composite for Automotive Components". *International Journal of Pure and Mathematics*, vol. 118 (24), pp. 1-12

Raghuveer, H. Desai, L. Krishnamurthy, and T. N. Shridhar. (2016). "Effectiveness of Areca (Betel) Fiber as a Reinforcing Material in Eco-Friendly Composites". *Indian Journal of Advances in Chemical Science*, vol. 1, pp. 27- 33

Srinivasa, C. V., and K. N. Bharath. (2011). "Impact and Hardness Properties of Areca-Fiber Epoxy Reinforced Composites". *Journal of Materials and Environmental Science*, vol. 2 (4), pp. 351-356

STUDY ON THE APPLICATION OF UNDOPED AND SILVER-DOPED BISMUTH FERRITE SAMPLES APPLIED IN ELECTRONIC DEVICE

Thuzar Nyein[1], Zaw Naing[2], Cho Cho[3]

Abstract

In this paper, undoped bismuth ferrite ($BiFeO_3$) and silver-doped bismuth ferrite (Ag-$BiFeO_3$) samples were prepared by the sol-gel method. The resulting powder was characterized by XRD and EDXRF techniques. Comparative studies of the electrical properties of these samples were investigated by using an LCR meter in the frequency range of 20 to 100 MHz at 2 V. In this study, it was found that the AC and CD conductivities, dielectric loss tangent, dielectric constant, and capacitance depend on the frequency. The conductivity values of AC and DC increase with increasing frequency. Dielectric loss tangent, dielectric constant, and capacitance decrease with increasing frequency. These two samples demonstrated semiconducting properties in accordance with their electrical properties. In addition, Ag-$BiFeO_3$ indicates higher conductivity values than the $BiFeO_3$ sample. According to the results, both $BiFeO_3$ and Ag-$BiFeO_3$ samples could be used as touch point electrodes in a touch sensor device for electrical applications.

Keywords: $BiFeO_3$, Ag-$BiFeO_3$, electrical properties, AC and DC conductivities, touch point electrodes

Introduction

Bismuth ferrite ($BiFeO_3$, also commonly referred to as BFO in materials science) is an inorganic chemical compound with an ABO_3-type perovskite structure. In ABO_3, perovskite A is bismuth (Bi) and occupies the corner of the perovskite unit cell. B is iron (Fe), the central atom with an oxygen octahedral arrangement (Sarnatsky *et al*., 2016). Bismuth ferrite is also one of the most extensively investigated multiferroic magneto-electric compounds, in which the 6s lone pair electrons of Bi are believed to be responsible for ferroelectricity while the partially filled d orbital of Fe leads to magnetic ordering (Suastiyanti and Wijaya, 2016). Bismuth ferrite ($BiFeO_3$) has a rhombohedral structure, R3c ($\alpha = \beta = \gamma = 59.4°$, $a = b = c = 5.63$ Å) at room temperature (Awan and Bhatti, 2009). Bismuth ferrite has several applications in the fields of magnetism, memory devices, spintronics, photovoltaics, etc. (Fu *et al*., 2012). Some excellent reports have reported that $BiFeO_3$ is a very good candidate for visible light-responsive photocatalytic material and semiconductor electrodes in electronic devices (Azmy *et al*., 2017).

Touch sensors are electronic sensors that can detect touch. They operate as switches when touched. These sensors are used in lamps, touch screens on mobile devices, etc. (Catalan and Scott, 2009). Touch sensors offer an intuitive user interface. Touch sensors are also known as tactile sensors. These are simple to design, low-cost and produced on a large scale. These sensors are sensitive to any pressure, force, or touch. The principle of touch is similar to that of a switch. When there is contact or a touch on the surface of the touch sensor, it acts like a closed switch and allows the current to flow through it. When the contact is released, it acts similar to an opened switch, and there is no flow of current. With the advancement of technology, these sensors are rapidly replacing mechanical switches (Dignan *et al*., 2019).

[1] Department of Chemistry, Maubin University
[2] Department of Chemistry, Pyay University
[3] University of Yangon

Materials and Methods

Preparation of $BiFeO_3$ and Ag-$BiFeO_3$ Powder

In a mole ratio of 1:1, bismuth pentahydrate ($Bi(NO_3)_3.5H_2O$) and ferric nanohydrate ($Fe(NO_3)_3.9H_2O$) were dissolved in 2-methoxyethanol. The solution was stirred continuously for an hour at room temperature until it became translucent. As a chelating agent, citric acid ($C_6H_8O_7$) was added, and the mixture was heated and stirred at 80 °C for 2 h. The resulting mixture was then transparent, reddish-black, and clear. Additionally, the solution was placed on a hot plate at 80 °C with constant stirring for 5 h until all the liquid evaporated. Brown vapours were evolving in great quantities. A fluffy brown material (gel) was discovered in the bottom of the beaker near the end of the reaction. The resulting gel was then calcined for 4 h at 550 °C. Then, finely ground $BiFeO_3$ was obtained (Kumar, 2011).

In the chemical reduction process, polyvinyl pyrrolidone (PVP) was employed as a reductant to prepare $BiFeO_3$ powder that was doped with silver. After mixing 1.88 g of PVP with 20 mL of distilled water, the liquid was then heated to 60 °C in the air while being stirred magnetically until the PVP was completely dissolved. In a mole ratio of 5:0.3, silver nitrate ($AgNO_3$) and $BiFeO_3$ powder were dissolved in distilled water, and the PVP solution was then added. The resulting mixture was then heated at 80 °C for 2 h while being stirred continuously. Centrifugation was used to separate the product, which was subsequently cleaned with distilled water and dried in an oven at 100 °C to obtain silver-doped $BiFeO_3$ (Ag-$BiFeO_3$) powder (Lu *et al*., 2015).

Characterization

$BiFeO_3$ and Ag-$BiFeO_3$ samples were confirmed by X-ray diffraction analysis using an X-ray diffractometer (Rigaku, Japan). The average crystallite sizes of these prepared samples were calculated using the Debye-Scherrer equation. The relative abundance of elements in $BiFeO_3$ and Ag-$BiFeO_3$ powder was also determined by an energy dispersive X-ray fluorescence spectrometer (Shimadzu EDX-700, Japan).

Preparation of Pellets

The $BiFeO_3$ and Ag-$BiFeO_3$ samples were pressed into pellets with a diameter of 1.5 cm and a thickness of 0.16 cm using the MAEKAWA Testing Machine.

Determination of the Electrical Properties of $BiFeO_3$ and Ag-$BiFeO_3$

The electrical properties of $BiFeO_3$ and Ag-$BiFeO_3$ pellets were measured by the LCR-8110G meter (Inductance, capacitance, and resistance meter, GwInstek, DC 20-10 MHz). Electrical conductivity measurements were carried out at room temperature.

Fabrication of a Touch Sensor Device using $BiFeO_3$ and Ag-$BiFeO_3$ as Electrodes

The simple touch sensor processing was setup as follows: BC 547 transistor was first connected with a resistor 10 kΩ and then connected with a $BiFeO_3$ or Ag-$BiFeO_3$ electrode. The next transistor, BC 547, was connected to the first BC 547. Then, an LED of 5 mm and a resistor of 680 Ω were connected in series. The 1.5 kΩ resistor was connected to the first transistor. The two resistors, 680 Ω and 1.5 kΩ, were joined with the red wire. The first transistor, BC 547, was joined with the black wire.

Results and Discussion

XRD Analysis

Figures 1 (a) and 1(b) show the XRD diffractograms of prepared samples of $BiFeO_3$ and Ag-$BiFeO_3$, respectively. The average crystallite sizes of the $BiFeO_3$ and Ag-$BiFeO_3$ powders were calculated using the Debye-Scherrer equation. From the XRD analysis, the crystallite sizes of these samples were found to be less than 100 nm, i.e., 41.05 nm and 32.10 nm, respectively (Table 1).

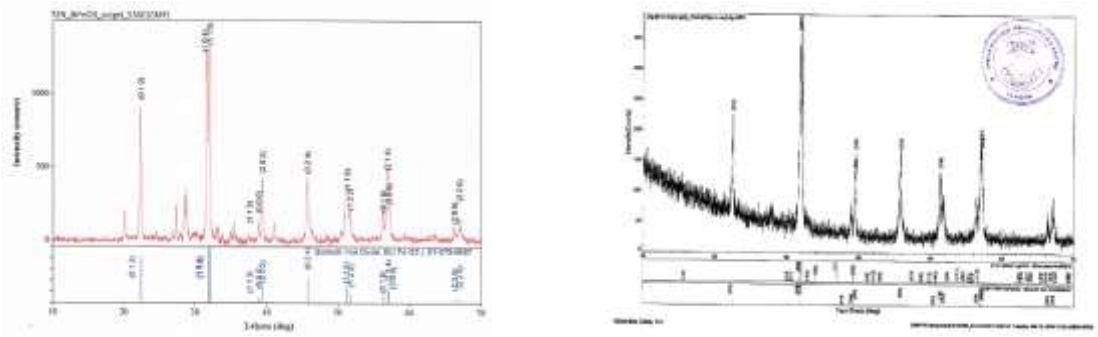

(a) **(b)**

Figure 1. XRD patterns of (a) $BiFeO_3$ (b) Ag-$BiFeO_3$ powder

Table 1. Average Crystallite Sizes of $BiFeO_3$ and Ag-$BiFeO_3$ Powder

Samples	Crystallite sizes (nm)
B**i**F**e**O**3**	41.05
Ag-B**i**F**e**O**3**	32.10

EDXRF

The EDXRF spectra of the prepared samples ($BiFeO_3$ and Ag-$BiFeO_3$) are illustrated in Figures 2 (a) and (b). Bi, Fe, and Ag are the main constituents of the prepared samples. $BiFeO_3$ is composed of 35.6 % Bi and 14.6 % Fe, while Ag-$BiFeO_3$ is composed of 26.9 % Bi, 9.98 % Fe, and 2.74 % Ag, respectively.

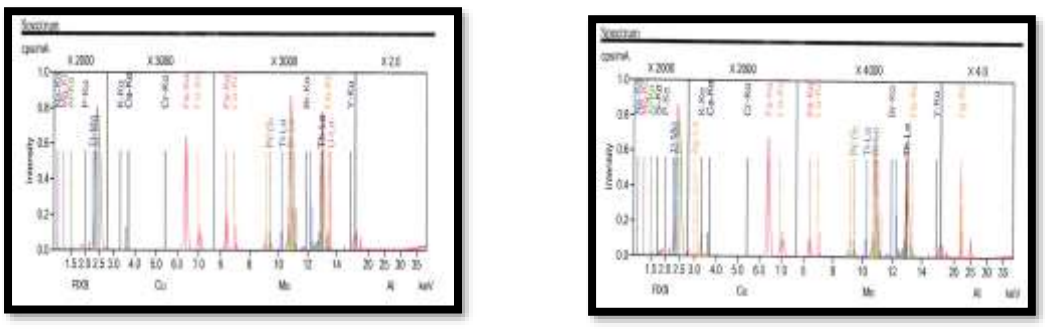

(a) **(b)**

Figure 2. EDXRF spectra of (a) $BiFeO_3$, (b) Ag-$BiFeO_3$ powder

Investigation of the Electrical Properties of $BiFeO_3$ and Ag-$BiFeO_3$ Samples

AC and DC Conductivities

An LCR meter was used to measure the variation of AC and DC conductivities of $BiFeO_3$ and Ag-$BiFeO_3$ samples at 2 V over a frequency range of 20 to 100 kHz. It was found that the AC and DC conductivities of Ag-$BiFeO_3$ were observed to be significantly higher than $BiFeO_3$ (Tables 2 and 3). So, the metal conduction behaviour increases with increasing frequency for both samples, as shown in Figures 3 (a) and (b). In addition, the AC conductivity values gradually increased with the increase in frequency of the applied alternating electric field because the increase in frequency enhanced the migration of electrons (Mubarak *et al*., 2014).

Table 2. AC Conductivity of $BiFeO_3$ and Ag-$BiFeO_3$ Samples at Different Frequencies

Samples	AC conductivity (kΩ cm^{-1})				
	20 kHz	**40 kHz**	**60 kHz**	**80 kHz**	**100 kHz**
$BiFeO_3$	0.93	1.13	1.44	1.76	1.99
Ag-$BiFeO_3$	3.51	5.95	7.90	9.82	11.35

Table 3. DC Conductivity of $BiFeO_3$ and Ag-$BiFeO_3$ Samples at Different Frequencies

Samples	DC conductivity (kΩ cm^{-1})				
	20 kHz	**40 kHz**	**60 kHz**	**80 kHz**	**100 kHz**
$BiFeO_3$	7.24	9.38	12.86	15.65	18.24
Ag-$BiFeO_3$	23.08	39.34	53.34	65.06	75.39

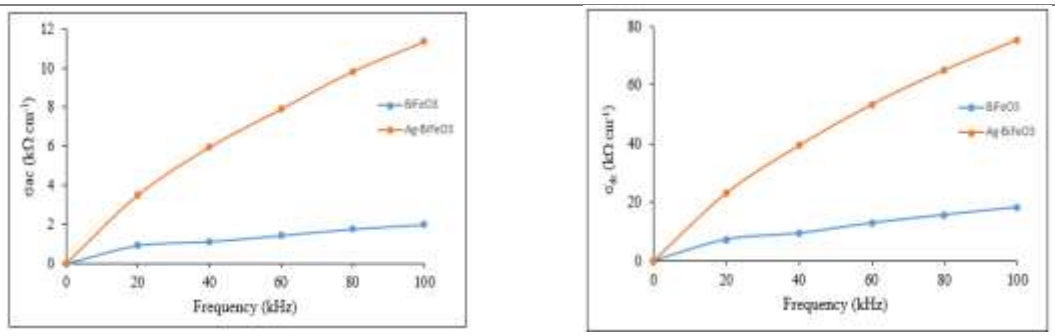

(a) **(b)**

Figure 3. Comparison of (a) AC conductivity and (b) DC conductivity of $BiFeO_3$ and Ag-$BiFeO_3$ samples

Dielectric Constant

Table 4 shows the dielectric constant values at different frequencies for the $BiFeO_3$ and Ag-$BiFeO_3$ samples. The values of the dielectric constant decrease with increasing frequency. The reduction of the space charge polarization effect caused a low dielectric constant value. So, the Ag-$BiFeO_3$ sample exhibits the highest value in dielectric constant at the lowest frequency (Figure 4).

Table 4. Dielectric Constant of $BiFeO_3$ and Ag-$BiFeO_3$ Samples at Different Frequencies

Samples	Dielectric constant				
	20 kHz	**40 kHz**	**60 kHz**	**80 kHz**	**100 kHz**
$BiFeO_3$	5.70	4.43	4.42	4.31	4.14
Ag-$BiFeO_3$	9.94	8.47	7.64	7.32	7.11

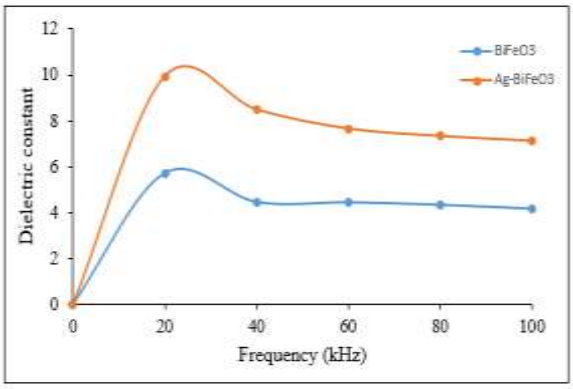

Figure 4. Comparison of dielectric constant of $BiFeO_3$ and Ag-$BiFeO_3$ samples

Dielectric Loss Tangent

The dielectric loss tangent indicates the energy dissipation in the dielectric system. The dielectric loss tangent values of $BiFeO_3$ and Ag-$BiFeO_3$ samples are shown in Table 5. The dielectric loss tangent values of Ag-$BiFeO_3$ are greater than those of $BiFeO_3$ (Figure 5). The dielectric loss tangent peaks shift towards the lower frequency side. It was believed that there was an increase in the crystalline nature of the matrix of materials.

Table 5. Dielectric Loss Tangent of $BiFeO_3$ and Ag-$BiFeO_3$ Samples at Different Frequencies

Samples	Dielectric loss tangent (tan δ)				
	20 kHz	**40 kHz**	**60 kHz**	**80 kHz**	**100 kHz**
$BiFeO_3$	0.14	0.11	0.10	0.09	0.08
Ag-$BiFeO_3$	0.32	0.31	0.30	0.29	0.28

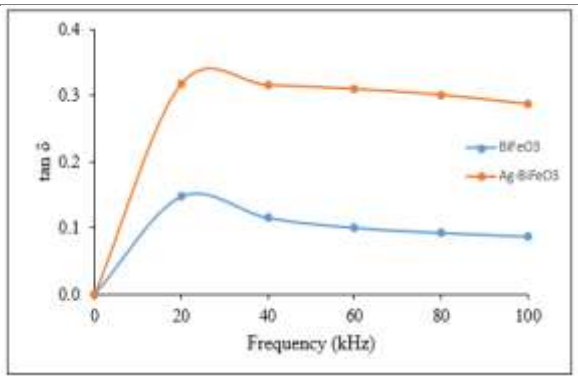

Figure 5. Comparison of dielectric loss tangent of $BiFeO_3$ and Ag-$BiFeO_3$ samples

Capacitance

The frequency-dependent capacitance of $BiFeO_3$ and Ag-$BiFeO_3$ samples is shown in Table 6 and Figure 6. It was also found that the capacitance decreased with an increase in frequency. The maximum value of capacitance was shown at the minimum frequency. This finding indicated that the capacitance decreased as the decrease of dielectric constant. Moreover, the capacitance of both samples was in the picofarad range. This meaning proved that the both samples are enabled to perform charging and recharging power in the form of electrical energy.

Table 6. Capacitance of $BiFeO_3$ and Ag-$BiFeO_3$ Samples at Different Frequencies

Samples	Capacitance (pF)				
	20 kHz	**40 kHz**	**60 kHz**	**80 kHz**	**100 kHZ**
$BiFeO_3$	4.10	3.19	3.11	3.10	2.98
Ag-$BiFeO_3$	7.17	6.10	5.51	5.28	5.12

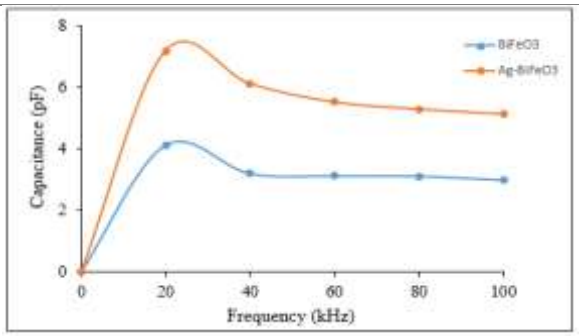

Figure 6. Comparison of capacitance of $BiFeO_3$ and Ag-$BiFeO_3$ samples

Generating Electricity in a Touch Sensor using $BiFeO_3$ and Ag-$BiFeO_3$ as Electrodes

In the touch sensor, the $BiFeO_3$ and Ag-$BiFeO_3$ samples were used as touch point electrodes (Figures 7 and 8). The black and red wires were connected to the battery. When the finger touched the $BiFeO_3$ or Ag-$BiFeO_3$ electrodes of the touch sensor, the LED lit up brightly. When the finger did not touch the electrode, the LED light faded out. So, these conducting samples could be used as touch point electrodes in touch sensor devices.

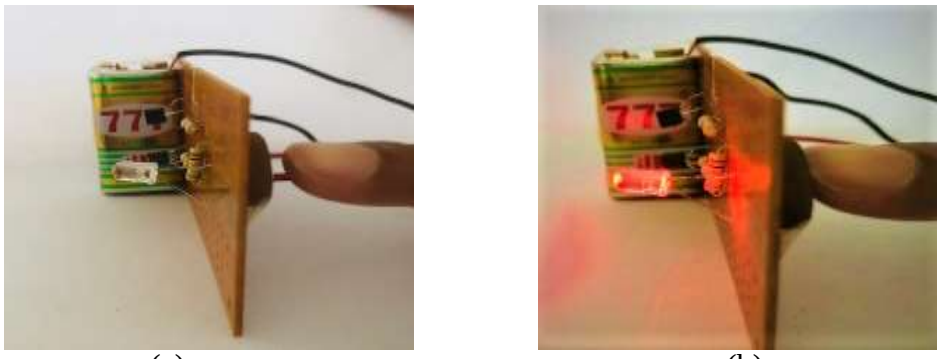

(a) (b)

Figure 7. (a) Before touch onto the $BiFeO_3$ electrode **(b)** After touch onto the $BiFeO_3$ electrode

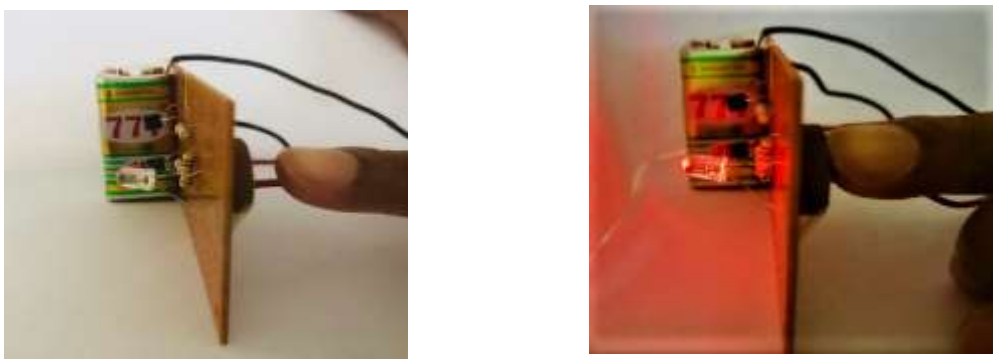

(a) (b)

Figure 8. (a) Before touch onto the Ag-$BiFeO_3$ electrode **(b)** After touch onto the Ag-$BiFeO_3$ electrode

Conclusion

Undoped bismuth ferrite ($BiFeO_3$) and silver-doped bismuth ferrite (Ag-$BiFeO_3$) powder were successfully synthesized by the sol-gel method. The electrical conductivity values of both samples gradually increased with an increase in frequency. The maximum values of AC conductivity for $BiFeO_3$ and Ag-$BiFeO_3$ samples were 1.99 and 11.35 kΩ cm^{-1}, respectively, and and those of DC conductivity were 18.24 and 75.39 kΩ cm^{-1}. These results are evident that the AC and DC conductivity values of the Ag-$BiFeO_3$ sample were higher than those of $BiFeO_3$ sample because silver possesses the highest electrical conductivity among all metals. The semiconducting properties were found out through the investigation of electrical properties. Moreover, these samples have the ability of capacitor to store energy. According to the observations, the prepared materials could be used as touch point electrodes in a touch sensor device.

Acknowledgements

The authors would like to thank the Department of Higher Education, Yangon, Myanmar for allowing to carry out this research work. Profound gratitude is especially thankful to Ministry of Education, Myanmar and Professor Dr Ni Ni Than, Head of Department of Chemistry, University of Yangon for providing all the departmental facilities.

References

Awan, M. S., and A. S. Bhatti. (2009). "Room-temperature Multi-ferrocity in Off-Stoichiometric $BiFeO_3$ Ceramics Prepared by Melt-phase Sintering". *Nucleus*, vol. 46 (4), pp. 465–471

Azmy, H. A. M., N. A. Razuki, A. W. Aziz, N. S. A. Satar, and N. H. M. Kaus. (2017). "Visible Light Photocatalytic Activity of $BiFeO_3$ Nanoparticles for Degradation of Methylene Blue". *Journal of Physical Science*, vol. 28 (2), pp. 85-103

Catalan. G., and J. F. Scott. (2009). "Physics and Applications of Bismuth Ferrite". *Journal of Advanced Materials*, vol. 21 (24), pp. 2463-2485

Dignan, J., B. Pong, A. Thesis, and P. Xiong. (2019). *Capacitance Touch Sensor Project: A Handbook for Teachers*. Columbus: Project, Department of Electrical and Computer Engineering, Ohio State University

Fu, C., M. Huo, W. Cai, and X. Deng. (2012). "Preparation of Bismuth Ferrite Nanopowders at Different Calcination Temperatures". *Journal of Ceramic Processing Research*, vol. 13 (5), pp. 561-564

Kumar, A. (2011). *Synthesis and Characterization of $BiFeO_3$ by Sol-Gel Method*. India: M-Tech (Thesis), Material Science and Metallurgical Engineering, Thapar University

Lu, H., Z. Du, J. Wang, and Y. Liu. (2015). "Enhanced Photocatalytic Performance of Ag-decorated $BiFeO_3$ in Visible Light Region". *Journal of Sol-gel Sci. Technol*., vol. 76, pp. 50-57

Mubarak, T., B. Azhdar, K. Hassan, and C. Kareem. (2014). "Effect of Temperature on Structural and Electrical Properties of Bismuth Ferrite Nanoparticles Prepared by Sol-Gel Method". *International Journal of Innovative Research in Science, Engineering and Technology,* vol. 3 (10), pp. 17034-17041

Sarnatsky, V. M., N. A. Vinokurov, Z. K. Murlieva, and N. M. R. Alikhanov. (2016). "Magnetic and Electrical

Characteristics of Bismuth Ferrite, Depending on the Impurities, Method of Preparation and Size of the Nanoparticles". *Journal of Nano and Electronic Physics*, vol. 8 (3), pp. 1-4

Suastiyanti, D., and M. Wijaya. (2016). "Synthesis of Bismuth Ferrite Nanoparticle and Single Phase by Sol-gel Process for Multiferroic Material". *Journal of Engineering and Applied Sciences*, vol. 11 (2), pp. 901-905

PREPARATION OF HYDROXYAPATITE-CEMENTED TITANIUM DIOXIDE COMPOSITE AND ITS APPLICATION

Kyi Win Mon[1], Win Pa Pa[2], Nyan Tun[3]

Abstract

Using the wet precipitation method, hydroxyapatite, $Ca_{10}(PO_4)_6(OH)_2$, was synthesized from waste crab shells in this study. The prepared hydroxyapatite and titanium dioxide with cement have been fabricated by blending to form a hydroxyapatite-cemented titanium dioxide composite at room temperature. The photodegradation capacities of composites in solar light and in the dark were studied for the degradation of dye (methylene blue) solutions with varying parameters of initial concentration of dye solution and contact time at optimal conditions**.** The results show that the kinetic study of the photodegradation reaction follows the Langmuir-Hinshelwood model equation. SEM technique was applied to characterize the prepared hydroxyapatite-cemented titanium dioxide composite. According to the SEM analysis, it was found that the pores of the composite were filled after the degradation of the dye. The photodegradation of contaminants in water collected from a fish pond near Shwedagon Pagoda was studied using composites. Composite was also found to be the most efficient and effective adsorbent for the degradation of organic pollutants from wastewater. As a result, the prepared hydroxyapatite-cemented titanium dioxide composite can be applied to the reduction of organic pollutants discharged from wastewater into aquatic environments. It would help reduce the public health risk caused by organic pollutants.

Keywords: Hydroxyapatite, Langmuir-Hinshelwood model equation, organic pollutants, photodegradation

Introduction

Hydroxyapatite (HA) is one of the inorganic materials and most methods to synthesize HA are either based on the wet precipitation method of natural sources like seashells, egg shells, fish bones and crab shells, etc. Hydroxyapatite cannot be used at load bearing-sites because of its poor mechanical strength and brittleness. Therefore, various composite materials of HA were fabricated to improve their mechanical strength, by blending with titanium dioxide (TiO_2) because titanium dioxide is an important photocatalyst due to its strong oxidation power, non-toxicity and long term photostability. Moreover, the TiO_2 catalyst can transform organic pollutants into biodegradable compounds of low molecular weight (Rajesh *et al*., 2007).

The hydroxyapatite-titanium dioxide composites were prepared by homogeneous mixing of the hydroxyapatite and titanium dioxide powders using a ball mill, followed by green compaction and then pressure-less sintering at a relatively higher temperature and soaking time 1 h (Basu and Ghosh, 2017). Hydroxyapatite-titanium dioxide composite has chemical stability of and very high activity for degradation such as dye, pesticides and fertilizer residues. Moreover, this composite may play an important role in controlling environmental pollution (Shidong *et al*., 2009).

[1] Department of Chemistry, University of Yangon
[2] Department of Chemistry, Nationalities Youth Resource Development Degree College, Yangon
[3] Department of Chemistry, University of Yangon

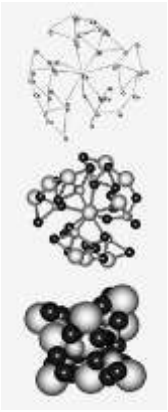

Figure 1. Structure of hydroxyapatite (HA)

The term "Langmuir–Hinshelwood mechanism" has often been used to describe the mechanism of photocatalytic reaction in suspension systems. In the field of catalysis, the reaction of two kinds of molecules proceeds on a surface on which both molecules are adsorbed at the same surface adsorption sites, with the surface reaction being the rate-determining step. The general rate equation for the L–H mechanism includes two sets of parameters for two kinds of molecules, and when one set of parameters is neglected, the equation is for a monomolecular reaction, similar to the photocatalytic reaction of a substrate adsorbed in Langmuirian fashion (Ohtani, 2011).

In this study, the hydroxyapatites were prepared from waste crab shell by using a wet precipitation technique. The prepared hydroxyapatite and titanium dioxide with cement have been fabricated by blending to form a HA-cemented TiO_2 composite. The different ratios of TiO_2 have been chosen to improve the mechanical strength and compatibility of the developed composite. The aim of the research work is to prepare the HA-cemented TiO_2 composite for the photodegradation of dye solutions and to study the photocatalytic degradation kinetics data that are fitted to the Langmuir-Hinshelwood model.

Materials and Methods

Preparation of HA-Cemented TiO_2 Composite

In the processing of composites, hydroxyapatite is prepared by reacting calcium precursor with phosphate at a Ca/P molar ratio of 1.67. Calcium oxide (CaO) was obtained as a result of calcinating crab shell powder at 900 °C and then made into a suspension in 100 mL of distilled water with a 0.3 M calcium concentration. The suspensions reacted dropwise with a 0.2 M solution of $(NH_4)_2HPO_4$. Afterward, the autoclave was quenched down through the wet precipitation method. And then trap closed chemical glass using aluminum foil to produce a suspension until pH10. The solution was then stirred for 5 h at 90 °C with a magnetic stirrer. The precipitate was filtered through filter paper and dried at 110 °C for 15 h. The pure hydroxyapatite was obtained by sintering the dried precipitate at 900 °C for 2 h. The hydroxyapatite-cemented titanium dioxide composite was performed at room temperature as follows: The fixed amount of hydroxyapatite and titanium dioxide was mixed with a glass rod for 5 min. And then cement weighing 3 g was dissolved in nearly 5 mL of distilled water by stirring with a glass rod for 5 min.

Preparation of Stock Solution of Methylene Blue

A stock solution of 100 mg L^{-1} of methylene blue (MB) solution was prepared by dissolving 0.1 g of dye in 1 L of distilled water. By serial dilution, the dye solutions of methylene blue within the concentration range of 20 to 100 mg L^{-1} were prepared. Analyses were carried out by the

colorimetric method using a UV-visible spectrophotometer and a calibration curve of methylene blue solution was plotted.

Photodegradation of Methylene Blue by Prepared HA-Cemented TiO_2 Composite

Filtration experiments were conducted to study the effect of important parameters like initial dye concentration and contact time of the composite on the photodegradation of methylene blue (MB). For each experimental run, 50 mL of different concentrations of the dye solution (20 mg L^{-1} to 100 mg L^{-1}) were contacted with the prepared HA-cemented titanium dioxide composite in the filtration unit [Figure 2 (a), (b) and (c)] and exposed to the solar light for 1 h. After 1 h, the dye solutions were taken out and their absorbance was recorded using a spectrophotometer. Similar procedures were carried out in the dark. In the contact time experiment**,** dye solution (100 mg L^{-1}) was filtrated at different time intervals (10, 20, 30, 40, 50 and 60 min) and the remaining dye concentrations were determined. The same procedures were carried out in the dark.

(a) **(b)** **(c)**

Figure 2. Photographs of (a) experimental filtration unit for the degradation of the methylene blue (b) methylene blue before and (c) after sorbed on HA-cemented TiO_2 composite

Effect of Initial Concentration on the Degradation Rate of Methylene Blue Solution by HA-Cemented TiO_2 Composite (Solar Light and Dark)

Different initial concentrations of methylene blue solution were prepared ranging from 20 to 40 mg L^{-1}. HA-cemented titanium dioxide composite was brought into contact with a fixed volume of each methylene blue solution at 50 mL prefixed for 1 h in the sunlight. After 1 h, the residual methylene blue solutions were determined by a spectrophotometer. The degradation rate of methylene blue by HA-cemented titanium dioxide composite in the dark was also determined by the above procedure. The experimental results seem to be consistent with the following equation:

$$R = -\frac{dc}{dt} = \frac{k_r K_a C_0}{1 + K_a C_0}$$

where r, k_r, K_a and C_0 are the rate of the reaction, the rate constant of the reaction of the surface-adsorbed substrate with electron, the adsorption equilibrium constant, the limiting amount of surface adsorption, and the concentration of substrate in the bulk at equilibrium, respectively. The reciprocal of initial rate ($1/R_0$) disappearance against the reciprocal of the initial concentration ($1/C_0$) was plotted by using Langmuir-Hinshelwood model equation.

Examination of Surface Morphology by SEM Technique

A scanning electron microscope (SEM) uses a beam of focused electrons of relatively low energy as an electron probe, operating at an acceleration voltage of 10 kV in vacuum with a filament current of 50 mA. The SEM studies were performed on powder sample morphology and size. These properties were based on appearance.

Photocatalytic degradation of fish pond water

The water quality parameters of water samples from near Shwedagon Pagoda, such as pH, temperature, dissolved oxygen, chemical oxygen demand, biological oxygen demand, total alkalinity, total suspended solids, chloride, sulfate, nitrite nitrogen, and ammonia nitrogen, were examined at the water and soil examination laboratory, Freshwater Aquaculture Research, Aquaculture Division, Department of Fisheries. And then, in the filtration unit, 100 mL of fish pond water sample was filled, and a prepared HA-cemented titanium dioxide composite was introduced for 2 h in solar light. The water sample's qualities were determined after 2 h.

Results and Discussion

The calibration curve for methylene blue dye solution using a spectrophotometer is presented in Table 1 and Figure 3.

Table 1. Absorbance for Different Concentrations of Methylene Blue Solution

No.	Concentration (mg L^{-1})	Absorbance
1	20	0.11
2	40	0.24
3	60	0.35
4	80	0.43
5	100	0.59

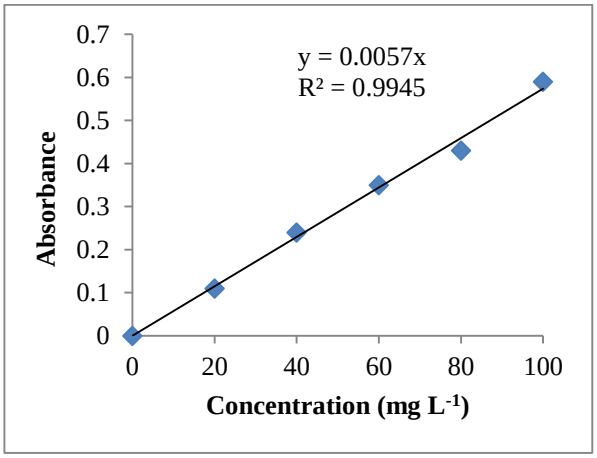

Figure 3. Calibration curve for methylene blue solution

The effect of the initial concentration of methylene blue dye on the photodegradation efficiency of the hydroxyapatite-cemented titanium dioxide composite was evaluated at different concentrations of 20, 40, 60, 80, and 100 mg L^{-1}. Table 2 and Figure 4 show that with the increase of the initial concentration from 20 mg L^{-1} to 100 mg L^{-1}, the percent degradation of dye was reduced from 91.50 % to 81.29 % in the solar light and from 82.99 % to 67.69 % in the dark. In the present study, with the decrease of the dye concentration in aqueous solution, the molecules of the dye have a better chance to react with the available active site on the composite, and as a result, the percent degradation is increased.

Table 2. The Percent Degradation of MB by HA-Cemented TiO_2 Composite at Different Initial Concentrations (Solar Light and Dark)

No.	Initial concentration (mg L^{-1})	Final concentration (mg L^{-1})		Percent degradation (%)	
		Solar light	Dark	Solar light	Dark
1	20	1.70	3.40	91.50	82.99
2	40	5.10	10.20	87.23	74.50
3	60	8.50	17.00	85.83	71.66
4	80	11.90	23.80	85.12	70.25
5	100	18.71	32.31	81.29	67.69

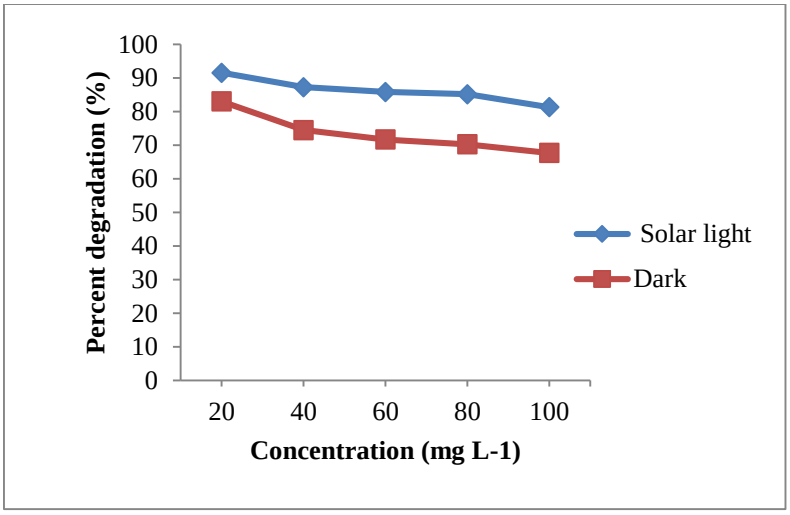

Figure 4. The percent degradation of MB by HA-cemented TiO_2 composite at different initial concentrations (solar light and dark)

From the results of Table 3, it was evident that the maximum adsorption occurred at 81.29 % in solar light and 67.69 % in the dark at 60 min. The degradation of methylene blue by HA-cemented TiO_2 composite was found to be rapid at the initial period of contact time and then slow with increasing contact time; the system reached equilibrium after 60 min. This was due to the availability of active sites that were occupied (Figure 5).

Table 3. The Percent Degradation of MB by HA-Cemented TiO_2 Composite at Different Contact Times (Solar Light and Dark)

No.	Contact time (min)	Final concentration (mg L^{-1})		Percent degradation (%)	
		Solar light	Dark	Solar light	Dark
1	10	47.62	54.42	52.38	45.58
2	20	39.11	49.32	60.89	50.68
3	30	32.31	42.52	67.69	57.48
4	40	27.21	39.11	72.79	60.89
5	50	22.11	35.71	77.89	64.29
6	60	18.71	32.31	81.29	67.69

Initial concentration = 100 mg L^{-1}

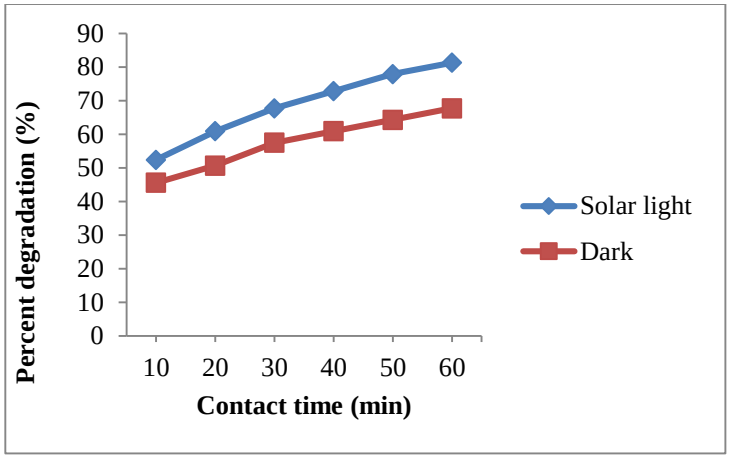

Figure 5. The percent degradation of MB in solar light and dark by HA-cemented TiO_2 composite at different contact times

Kinetic Study on Photodegradation of Methylene Blue Solution by HA-Cemented TiO_2 Composite with Langmuir-Hinshelwood Model

The kinetic study on the photodegradation of methylene blue solution by hydroxyapatite-cemented TiO_2 composite in solar light and dark was performed, and the results were fitted into the simple Langmuir-Hinshelwood mechanism. The reaction of two types of molecules on a surface in which both molecules are adsorbed at the same surface adsorption sites, with the rate-determining step being the surface reaction. Two parameters are calculated from the linear plot. One is the limiting rate of the reaction at the infinite concentration that gives maximum adsorption, that is k_r and the other is the adsorption equilibrium constant, K_a. The former parameter is a product of the rate constant and adsorption capacity of a photocatalyst, and this may be a photocatalytic activity. From this equation and plot, the value of k_r was obtained from the intercept, and then K_a was evaluated from the slope. The value of k_r in solar light was 4.885 mg L^{-1} min^{-1} and in the dark was 2.241 mg L^{-1} min^{-1}, respectively. The adsorption constant K_a for solar light was 0.0038 L mg^{-1} and 0.0070 L mg^{-1} in dark. The results are shown in Tables 4, and 5, and Figure 6.

Table 4. Effect of Initial Concentration on the Degradation Rate of MB solution by HA-Cemented TiO_2 Composite (Solar Light)

No.	C_0 (mg L^{-1})	C_t (mg L^{-1})	R_0 (mg L^{-1} min^{-1})	$1/R_0$ (mg^{-1} L min)	$1/C_0$ (mg^{-1} L)
1	20	1.4	0.310	3.225	0.050
2	25	1.9	0.385	2.631	0.040
3	30	2.64	0.465	2.193	0.033
4	35	3.38	0.527	1.897	0.028
5	40	5.08	0.582	1.718	0.025

Table 5. Effect of Initial Concentration on the Degradation Rate of MB solution by HA-Cemented TiO_2 Composite (Dark)

No.	C_0 (mg L^{-1})	C_t (mg L^{-1})	R_0 (mg L^{-1} min^{-1})	$1/R_0$ (mg^{-1} L min)	$1/C_0$ (mg^{-1} L)
1	20	3.40	0.227	3.610	0.050
2	25	4.662	0..339	2.949	0.040
3	30	6.9	0.385	2.597	0.033
4	35	7.728	0.454	2.202	0.028
5	40	10.20	2.021	2.012	0.025

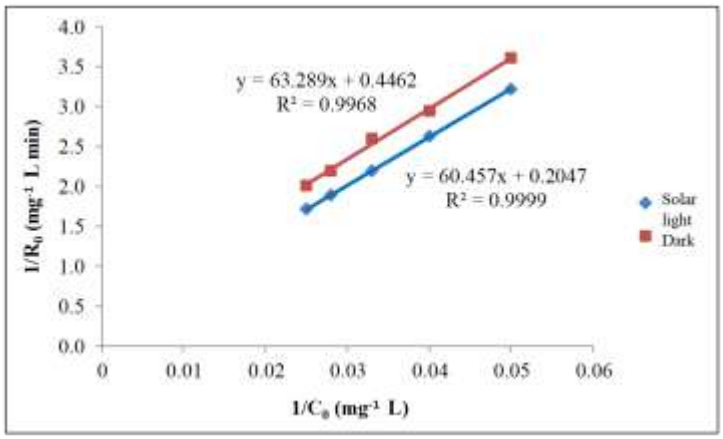

Figure 6. Plot of the reciprocal of the initial rate of MB disappearance against the reciprocal of initial concentration relevant to Langmuir-Hinshelwood model equation

Characterization of HA-Cemented TiO_2 Composite

SEM analysis

The surface morphology of the HA-cemented TiO_2 composite was examined by SEM. Figure 7 (a) shows that cement, which was used as a small granule binding source, and TiO_2, identified as anatase crystals, were deposited on HA-like crystals.

From the SEM micrographs of methylene blue-sorbed HA-cemented TiO_2 composite in solar light and dark, it can be seen that the surface of the composite is densely covered with numerous dye molecules in Figure 7 (b). Figure 7 (c) clearly shows that the dye molecules are deposited on the surface of the composite.

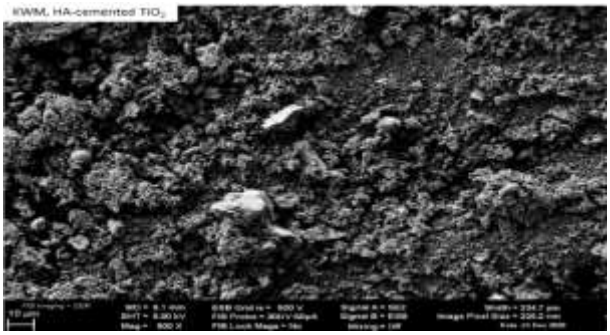

(a)

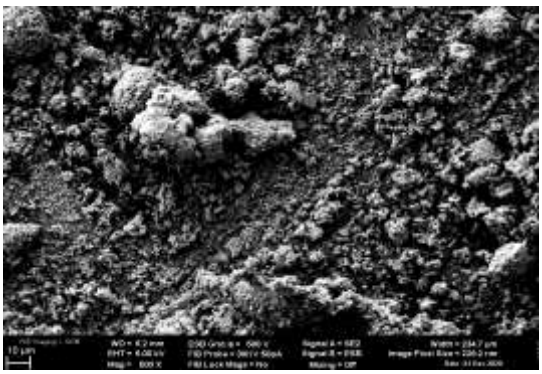

(b)

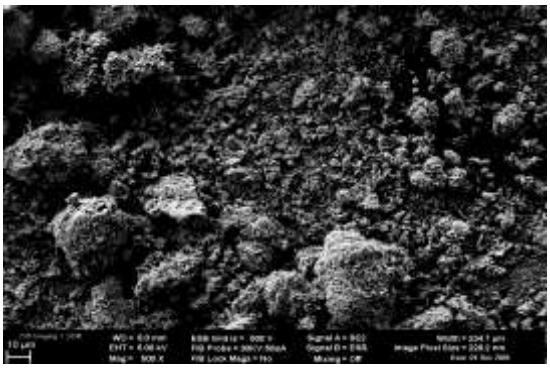

(c)

Figure 7. SEM micrographs of (a) HA-cemented TiO_2 composite (b) after MB sorbed HA-cemented TiO_2 composite (solar light) and (c) after MB sorbed HA-cemented TiO_2 composite (dark)

Treatment of Fishpond Water by HA-Cemented TiO_2 Composite

Suspended solids lead to the development of sludge deposits and anaerobic conditions when untreated wastewater is discharged into the aquatic environment. Nutrients (P, N and C) can lead to the growth of undesirable aquatic life. The water sample was collected from a fishpond near Shwedagon Pagoda and the collected water sample was treated with HA-cemented titanium dioxide composite under solar light. The quality of the collected water sample was determined before and after treatment for 2 h. Among the parameters of the water sample, before the treatment with HA-cemented titanium dioxide composite, the total suspended solid (TSS) value was 10 mg L^{-1}, and then, after treatment for 2 h, the value of TSS was reduced to 2.5 mg L^{-1}. This could be because suspended solids in the water sample were adsorbed onto the composite's surface. Therefore, the contaminants contained in water samples can be reduced by the HA-cemented titanium dioxide composite after treatment for 2 h.

Table 6. Results on Treatment of Fishpond Water by HA-Cemented TiO_2 Composite

Parameter	Unit	Before HA-cemented TiO_2	After HA-cemented TiO_2	Maximum EPA guideline*
pH	-	6.8	7.3	6.5 to 9.5
Temperature	°C	30	30	25 to 32
Dissolved oxygen	mg L^{-1}	2.75	3.25	>5
Total alkalinity	mg L^{-1}	94	92	50 to 150
Total suspended solid	mg L^{-1}	10	2.5	<25
Chemical oxygen demand	mg L^{-1}	3.31	2.21	<50
Biochemical oxygen demand	mg L^{-1}	0.50	0.50	150
Chloride	mg L^{-1}	39.99	24.99	31-50
Sulphate	mg L^{-1}	1.90	1.00	250
Nitrite nitrogen	mg L^{-1}	0.04	0.03	0 to 1
Ammonia nitrogen	mg L^{-1}	0.09	0.09	0 to 2

*USEPA, 2019

Conclusion

This study is primarily concerned with the development of an efficient photocatalyst, a hydroxyapatite-cemented titanium dioxide composite for the photodegradation of kinetic data that are fitted to the Langmuir-Hinshelwood model equation. The blending method was used to create a hydroxyapatite-cemented titanium dioxide composite with weight ratios of (40 %) titanium dioxide and hydroxyapatite and (20 %) of cement. The photodegradation of methylene blue by a prepared HA-cemented titanium dioxide composite was determined according to the parameters; initial concentration and contact time test. The effect of initial concentration on photodegradation was investigated. The maximum percent degradation of methylene blue was 81.29 % in solar light and 67.69 % in the dark for 1 h. The effect of contact time on the degradation of methylene blue solution revealed that the degradation was completed within 1 h. From this study, it is clearly seen that the percent degradation increases with increasing contact time. The kinetic study on the photodegradation of methylene blue was performed at optimum conditions. The photodegradation was found to follow the Langmuir-Hinshelwood model equation. By using this model equation, Langmuir-Hinshelwood parameters such as k_r and K_a were evaluated. The value of k_r in solar light was 4.885 mg L^{-1} min^{-1} and 2.241 mg L^{-1} min^{-1} in the dark, respectively. The contaminated water sample was collected from a fish pond near Shwedagon Pagoda. The qualities of the collected water sample parameters (pH, temperature, total alkalinity, TSS, DO, BOD, COD, chloride, sulphate, nitrite nitrogen and ammonia nitrogen) were determined before and after water treatment by using an HA-cemented titanium dioxide composite. According to the results, HA-cemented titanium dioxide composite can be effectively used for the treatment of wastewater samples.

Acknowledgements

The authors would like to express their gratitude to the Department of Research and Innovation, Myanmar, for permission to do this research and also to the Myanmar Academy of Arts and Science for allowing them to submit this research paper.

References

Basu, B., and S. Ghosh. (2017). *Case Study: Hydroxyapatite-Titanium Bulk Composite for Bone Tissue Engineering Applications*. In Biomaterials for Musculoskeletal Regeneration. Singapore*:* Springer-Verlag, pp.15-44

Ohtani, B., (2011). "Photocatalysis by Inorganic Solid Materials: Revisiting its Definition, Concepts and Experimental Procedures". *Advances in Inorganic Chemistry*, vol. 63, pp. 395-430

Rajesh, J. T., P. K. Surolia, R. G. Kulkarni and R. V. Jarsa. (2007). "Photocatalytic Degradation of Dyes and Organic Contaminants in Water Using Nanocrystalline Anatase and Rutile TiO_2". *Journal of Science and Technology Advance Material*, vol. 8 (6), pp. 455-462

Shidong, J., S. Murakami, M.Kamitakahara, and K. Ioku. (2009). "Fabrication of Titania/Hydroxyapatite Composite Granules for Photo-catalyst". *Materials Research Bulletin*. vol. 44 (4), pp. 768-774

USEPA. (2019). The EPA's Review of Nutrients in Industrial Wastewater Discharge and Treatment. Washington D.C: United States Environmental Protection Agency.

BIOLOGICAL PROPERTIES AND CHEMICAL INVESTIGATION OF *MURRAYA KOENIGII* L. SPRENG LEAVES (PYINDAW-THEIN)

Ei Ei San[1], San San Aye [2]

Abstract

In the present work, locally grown *M. koenigii* leaves were selected to investigate the chemical constituents and some bioactivities. The main aim of this research was to study the chemical constituents of essential oil and some biological activities such as antioxidant, antimicrobial, and antiproliferative activities of leaves. The preliminary phytochemical tests indicated that various types of compounds, such as alkaloids, α-amino acids, carbohydrates, cyanogenic glycosides, glycosides, organic acids, phenolic compounds, reducing sugars, saponins, steroids, and terpenoids were present in the selected leaves samples, except for flavonoids, tannins, and starch. The essential oil (2.44%) was extracted from the leaves of *M. koenigii* by steam distillation method. The total phenolic content was found to be 2.73 ± 0.004 µg GAE/mg in the ethanol extract and 2.56 ± 0.003 µg GAE/mg in the watery extract by the Folin-Ciocalteu assay. The antioxidant activity of an ethanol extract (IC_{50} = 34.84 µg/mL) was found to be more effective than watery extracts (IC_{50} = 42.92 µg/mL) by the DPPH assay. The antimicrobial activity of the leaves was screened by using the agar well diffusion method. The PE, EtOAc, and EtOH extracts showed antimicrobial activity against all tested microorganisms (16 to 18 mm). *In vitro* antiproliferative activity of ethanol and watery extracts was tested on five cancer cell lines by the CCK-8 assay. The ethanol extract inhibited the growth of MCF7 (IC_{50} 1 µg/mL), A549 (IC_{50} 1 µg/mL), Kato III (IC_{50} 15.3 µg/mL), GSU (IC_{50} 1 µg/mL), and Hela (human cervical cancer) (IC_{50} 1 µg/mL). The watery extract, was tested against MCF7 (IC_{50} > 100 µg/mL), A549 (IC_{50} 62.1 µg/mL), Kato III (IC_{50} > 100 µg/mL), GSU (IC_{50} 9.6 µg/mL) and Hela (IC_{50} > 100 µg/mL). GC-MS analysis of essential oil from *M. koenigii* leaves showed the presence of *p*-xylene, α-methyl styrene, azulene, 3-carene, methyl hexadecanoate, 9,12- octadecadienoate, 9-octadecadienoate, methyl stearate and methyl eicosanoate respectively.

Keywords: essential oil, antioxidant activity, antimicrobial, antiproliferative activity

Introduction

Plants have a significant role in maintaining human health and improving the quality of human life. The world health organization (WHO, 1999) estimated that 80 % of people rely on traditional medicine. *M. koenigii* leaf is an important leafy vegetable with many uses. It is belonging to the family Rutaceae based on semi-evergreen aromatic trees found throughout Malaysia, India, Bangladesh, Nepal, Sri Lanka, and Myanmar. It is commonly known as curry leaves. *M. koenigii* is widely used in Indian cookery for centuries and has a versatile role to play in traditional medicine. *M. koenigii* has various notable pharmacological activities in the plant such as activity on the heart, antidiabetic and cholesterol-reducing properties, antimicrobial activity, antiulcer activity, antioxidative property, cytotoxic activity, antidiarrhea activity, and phagocytic activity. The chemical composition of the fresh leaves of *M. koenigii* consists of volatile oil. *M. koenigii* is most popular on account of its diverse medicinal properties and its use as a flavorings agent in different curries and foods since ancient times. The leaves of the plant are used traditionally in the Indian Ayurveda system to treat diabetes (Pehlivan *et al*., 2012).

[1] Department of Chemistry, Bago University
[2] Department of Chemistry, University of Yangon

Materials and Methods

Plant materials

The selected sample used in this study was the curry leaves of *M. koenigii*. The sample was collected in Kamayut Township and identified at the Department of Botany, University of Yangon. The collected sample was washed with water and dried in the air. The dried pieces were made into powder by using a grinding machine. The powder sample was stored in an airtight container to prevent moisture change and other contamination.

Chemicals

Chemicals were procured from the BDH and E. Merck.

Instruments

Autoclave, incubator, distillation set, vacuum rotatory evaporator

Preliminary Phytochemical Investigation

Phytochemical tests for the leaves of *M. koenigii* were carried out according to the reported methods to investigate the presence and absence of phytoconstituents such as alkaloids, α-amino acid, carbohydrates, cyanogenic glycosides, flavonoids, glycosides, organic acids, phenolic compounds, reducing sugars, saponins, starch, steroids, tannins, and terpenoids (M-Tin Wa, 1972 Marini-Bettolo *et al.*, 1981).

Preparation of Crude Extracts

100 g of dried powdered sample was percolated in 500 mL of petroleum ether (PE, 60–80 °C) for one week and filtered. This procedure was repeated three times. Then the filtrate was concentrated by a vacuum rotatory evaporator to get the respective PE extract. Similarly, ethyl acetate and 70% EtOH extracts of the dried powdered sample were prepared according to the above procedure. The crude extract was then dried and stored in a desiccator after each solvent was removed using a rotary evaporator. In the preparation of watery extract 100 g of dried powdered sample was soaked in 500 mL of distilled water in a conical flask. These flasks were boiled in a water bath for 6 h and filtered. This process was carried out three times. The combined filtrates were dried to dryness over a water bath at 100 °C to get the corresponding watery extract.

Extraction of Essential Oil by Steam Distillation Method

The essential oil was extracted from the leaves of *M. koenigii* by the steam distillation method (Srivastava *et al.*, 2003). The sample of the fresh leaves of curry (100 g) was placed in the insert of a glass jacket. The glass jacket was filled with distilled water. The glass jacket was fitted to the set which was joined to the water condenser. When the glass jacket was heated, the condensed oil was collected in the receiver flask. The oil extracted with n-hexane was evaporated at 60-70 ˚C to get essential oil. Organic constituents in essential oil were detected by GC-MS spectroscopic method at Research and Innovation, National Analytical Laboratory.

Determination of Total Phenol Content

The total phenol content (TPC) in each crude extract was determined by the Folin-Ciocalteu reagent method (Song *et al.*, 2010). First, 0.5 mL of each extract solution was mixed with 5 mL of FCR reagent (1:10) and incubated for 30 min. 4 mL of 1 M sodium carbonate

solution was added to each tube and the tubes were kept at room temperature for 2 h. The UV absorbance reaction mixture was read at λ_{max} 765 nm. The blank solution was prepared by using distilled water instead of the sample solution. Total phenol contents were estimated as microgram gallic acid equivalents per milligram of different extracts (µg GAE / mg).

Determination of Antioxidant Activity by DPPH Assay

The DPPH radical scavenging activity of 70% ethanol and watery extracts was determined by a UV-visible spectrophotometer. The control solution was prepared by mixing 1.5 mL of ethanol and 1.5 mL of 0.002% DPPH solution in the brown bottle. The sample solution was also prepared by mixing 1.5 mL of 0.002 % DPPH solution and 1.5 mL of tested sample solution. These bottles were shaken on a shaker for 30 min and incubated at room temperature. After incubation, these solutions were measured at 517 nm and the percentage of radical scavenging activity was calculated. The antioxidant power of IC_{50} (50% inhibition concentration) values was calculated by the linear-regressive Excel program (Marinova & Batchvarob, 2011).

Antimicrobial Screening by Agar Well Diffusion Method

The antimicrobial screening of the polar and nonpolar extracts was determined by the agar well diffusion method. *Agrobacterium tumefaciens, Bacillus pumilus, Bacillus subtilis, Candida albicans, Escherichia coli, Micrococcus luteus, Pseudomonas fluorescens,* and *Staphylococcus aureus* were used as tested organisms. Four small wells of 8 mm in diameter each were cut out of the inoculated agar to place the samples to be tested. The volume of each sample placed in each well was 0.1 mL. The Petri dishes were then incubated at 37 ºC for 48 h. The diameters of the clear inhibition zones around the well were measured (Finegold & Martin, 1982).

Determination of Antiproliferative Activity

The anticancer or antiproliferative activity of ethanol and watery extracts of *M. koenigii* leaves samples was determined against five cancer cell lines such as Hela (Cervix cancer), MCF 7 (Breast cancer), Kato III (Stomach cancer), GSU (gastric cancer), and A 549 (lung cancer) by CCK-8 assay (Fatma *et al*., 2015). The tests were done at the Department of Natural Products Chemistry, Institute of Natural Medicine, and University of Toyama, Japan.

Determination of Organic Compounds in Essential Oil from the Leaves of *M. koenigii* by GC-MS Method

Gas chromatography-mass spectrometry (GC-MS) is a method that combines gas chromatography and mass spectrometry to identify different substances with a test sample (Robert and Webster, 1998). The application of GC-MS includes the identification and quantitation of volatile and semi-volatile organic compounds in complex mixtures (James and Martin, 1952). Organic constituents in essential oil from the leaves of *M. koenigii* were detected by GC-MS spectroscopic method at Research and Innovation, National Analytical Laboratory.

Results and Discussion

Phytochemical Constituents in the Leaves of *M. koenigii*

The phytochemical constituents present in the leaves of *M. koenigii* were investigated by the test tube method. The phytochemical tests revealed that alkaloids, α-amino acid carbohydrates, cyanogenic glycosides, glycosides, organic acids, phenolic compounds, reducing sugars, saponins, steroids, and terpenoids were present in the sample. However, flavonoids, starch, and tannins were not detected in the leaves of *M. koenigii*.

Total Phenol Content of Crude Extracts of *M. koenigii* Leaves

The presence of phenolic compounds in medicinal plants is responsible for their antioxidant and anti-inflammatory activities. The total phenol contents of ethanol and watery crude extracts of leaves of *M. koenigii* were evaluated with the spectrophotometric method using the Folin-Ciocalteu reagent. The principle of this method is the reduced ability of the phenol functional group. Gallic acid (3, 4, 5- trihydroxy benzoic acid) was used to construct a standard calibration curve at λ_{max} 765 nm. Total phenol content was expressed as micrograms of gallic acid equivalent per milligram (µg GAE/mg) and was detected in ethanol extract (2.73 ± 0.004 µg GAE/mg) rather than watery extract (2.56 ± 0.003 µg GAE/mg). The phenolic compounds were found to be more soluble in ethanol (Table 1).

Table 1. Total Phenol Content of Ethanol and Watery Extract from the Leaves of *M. koenigii*

No.	Extracts	TPC (µg GAE/mg ± SD)
1	Ethanol	2.73 ± 0.004
2	Watery	2.56 ± 0.003

GAE = Gallic acid equivalent

Antioxidant Activity of Crude Extracts of *M. koenigii* Leaves

The antioxidant activity of watery and 95% ethanol extracts of *M. koenigii* leaves was determined by using the DPPH assay method. The antioxidant activity was expressed as a 50% oxidative inhibitory concentration (IC_{50}). In this experiment, five different concentrations of each crude extract in 95 percent ethanol solvent were used: 31.25 µg/mL, 62.5 µg/mL, 125 µg/mL, 250 µg/mL, 500 µg/mL, and 1000 µg/mL. Butylated hydroxytoluene was used as a standard, and ethanol without crude extract was employed as a control. Determination of absorbance was carried out at a wavelength of 517 nm using a UV-visible spectrophotometer. The IC_{50} values were found to be 34.84 µg/mL for 95% ethanol extract and 42.92 µg/mL for watery extract. Butylated hydroxytoluene was used as a standard and the lower IC_{50} value of 95% ethanol extract was found to be more effective than the watery extract in free radical scavenging activity (Table 2).

Table 2. Antioxidant Activity (% RSA) of Ethanol and Watery Extracts from the Leaves of *M. koenigii*

Sample	% RSA±SD of different concentrations (µg/mL)						IC_{50} (µg/mL)
	31.25	62.5	125	250	500	1000	
Ethanol	47.27 ± 0.007	71.01 ± 0.002	92.22 ± 0.003	96.63 ± 0.0014	93.90 ± 0.015	87.39 ± 0.017	34.84
Water	31.93 ± 0.007	80.25 ± 0.004	85.08 ± 0.004	86.13 ± 0.000	86.4 ± 0.005	76.49 ± 0.039	42.92
Standard butylated hydroxytoluene	17.01 ± 0.009	31.16 ± 0.002	59.06 ± 0.023	77.09 ± 0.008	81.47 ± 0.002	87.28 ± 0.000	22.26

Antimicrobial Activity of Crude Extracts of *M. koenigii* Leaves

In the present work, the antimicrobial activity of extracts was tested on seven strains of bacteria: *Agrobacterium tumefaciens, Bacillus pumilus, Bacillus subtilis, Escherichia coli, Micrococcus luteus, Pseudomonas fluorescens,* and *Staphylococcus aureus*, and one strain of fungus, *Candida albicans.*The measurable zone diameter, including the agar well diameter (8 mm), shows the degree of antimicrobial activity. The greater the agar well diameter, the higher the antimicrobial activity. From the experimental results, it was found that PE, EtOAc, and EtOH extracts of leaves showed antimicrobial activity (16 -19 mm) against all tested microorganisms. This shows these extracts have good antimicrobial activity (15 -19 mm). However, the watery extract inhibited *E. coli, M. luteus, P. fluorescens,* and *C. albicans* (11 -14 mm). It indicates that watery extract has low antimicrobial activity (10 - 14 mm) (Figure 1 and Table 3).

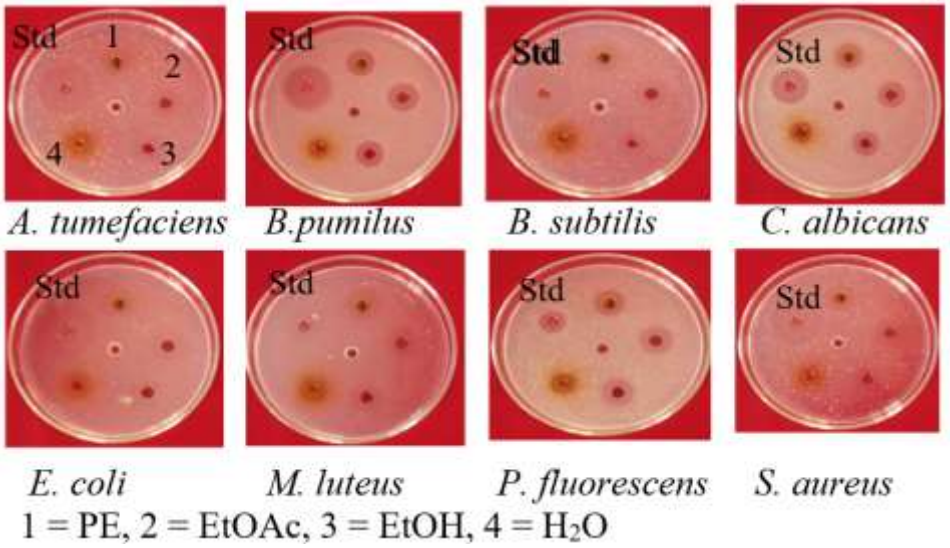

Figure 1. Antimicrobial screening of crude extracts of leaves of *M. Koenigii*

Table 3. Antimicrobial Screening of Leaves of *M. koenigii*

Microorganisms	Inhibition zone diameters of different crude extracts (mm)				
	PE	EtOAc	EtOH	Water	Standard chloramphenicol
A. tumefaciens	18(++)	18(++)	16(++)	-	29(+++)
B. pumilus	17(++)	19(++)	16(++)	-	27(+++)
B. subtilis	17(++)	17(++)	17(++)	-	29(+++)
E. coli	16(++)	17(++)	16(++)	13(+)	31(+++)
M. luteus	19(++)	18(++)	17(++)	13(+)	19(++)
P. fluorescens	17(++)	17(++)	16(++)	11(+)	15(++)
S. aureus	17(++)	18(++)	17(++)	-	29(+++)
C. albicans	17(++)	17(++)	16(++)	14(+)	22(+++)

Agar well diameter = 8 mm, No activity = (-)
10 mm ~ 14 mm = (+), 15 mm ~ 19 mm = (++), 20 mm and above = (+++)

Antiproliferative Activity of Crude Extracts of *M. koenigii* Leaves

The antiproliferative activity of ethanol and watery extracts of leaves against MCF7 (human breast cancer), A549 (human lung cancer), Kato III (human stomach cancer), GSU (human gastric cancer), and Hela (human cervix cancer) was evaluated by using the CCK-8 Assay. The anticancer effect was expressed as IC_{50} values (50% inhibitory concentration). The antiproliferative activity of ethanol and water extracts for MCF7, A549, Kato III, Hela, and GSU cell lines was evaluated as the percent cell viability of the sample at different concentrations and IC_{50} values. Ethanol extract from the leaves was found to possess the highest antiproliferative activity against MCF7, A549, GSU, and Hela cancer cell lines because of its very low IC_{50} value of less than 10 µg/mL. The water extract of the leaves exhibited low activity compared with ethanol extract because of their high IC_{50} value (> 100 µg/mL) (Table 4).

Table 4. Antiproliferative Activity of Ethanol and Watery Extracts of Leaves of *M. Koenigii* against Cancer Cell Lines

Extracts	IC_{50} µg/mL				
	MCF7	**A549**	**Kato III**	**GSU**	**Hela**
EtOH	<1	<1	15.3	<1	<1
Water	>100	62.1	>100	9.6	>100
***5FU	16.4	16.9	3.4	1.62	17.6

*5FU = Standard drug

Organic Compounds in Essential Oil by GC-MS Method

Gas chromatography-mass spectrometry (GC-MS) is the single most important tool for the separation and identification of unknown organic compounds by matching them with reference spectral. The GC-MS chromatograms of essential oil from the leaves of *M.koenigii* are shown in figures 2 to 10. The interpretation of the mass spectral was compared with their peak distributions against the database of the National Institute Standard and Technology (NIST MS 14.0, Gaithersburg, MD, USA) and those from the literature (Table 5).

Table 5. Chemical Composition of Essential Oil from the Leaves of *M. koenigii*

No.	Compound	Molecular weight	Molecular formula
1	*p*-xylene	106	C_8H_{10}
2	α-methyl styrene	118	C_9H_{10}
3	Azulene	128	$C_{10}H_8$
4	3-carene	136	$C_{10}H_{16}$
5	Methyl hexadecanoate	270	$C_{17}H_{34}O_2$
6	Methyl 9,12-octadecadienoate	294	$C_{19}H_{34}O_2$
7	Methyl 9-octadecenoate	296	$C_{19}H_{36}O_2$
8	Methyl stearate	298	$C_{19}H_{38}O_2$
9	Methyl eicosanoate	326	$C_{21}H_{42}O_2$

According to the GC-MS chromatogram (Figure 2), the peak appears at the retention time of 2.53 min, indicating the molecular weight of a compound to be 106 with the molecular formula C_8H_{10}. Therefore, it can be referred that the compound as *p*-xylene. At the retention time of 3.547 min, the GC-MS spectrum (Figure 3) shows the molecular ion peak at m/z 118, indicating the molecular formula C_9H_{10}. Therefore, the compound is α-methyl styrene. At the retention time of 6.197 min, the GC-MS spectrum (Figure 4) shows the molecular ion peak at m/z 128, indicating the molecular formula $C_{10}H_8$. Therefore, the compound is azulene.

At the retention time of 3.079 min, the GC-MS spectrum (Figure 5) shows the molecular ion peak at m/z 136, indicating the compound 3-carene with the molecular formula $C_{10}H_{16}$. At the retention time of 24.67 min, the GC-MS spectrum (Figure 6) shows the molecular ion peak at m/z 270, indicating the compound, methyl hexadecanoate with the molecular formula $C_{17}H_{34}O_2$. At the retention time of 27.77 min, the GC-MS spectrum (Figure 7) shows the molecular ion peak at m/z 294, indicating the compound is methyl 9,12-octadecadienoate, $C_{19}H_{34}O_2$. At the retention time of 28.00 min, the GC-MS spectrum (Figure 8) shows the molecular ion peak at m/z 296, indicating the molecular weight of a compound methyl 9-octadecenoate to be 296 with the molecular formula $C_{19}H_{36}O_2$. At the retention time of 28.42 min, the GC-MS spectrum (Figure 9) shows the molecular ion peak at m/z 298 which indicates the compound methyl stearate, $C_{19}H_{38}O_2$. At the retention time of 32.5 min, the GC-MS spectrum (Figure 10) shows the molecular ion peak at m/z 326 which indicates the molecular weight of a compound methyl eicosanoate with the molecular formula $C_{21}H_{42}O_2$.

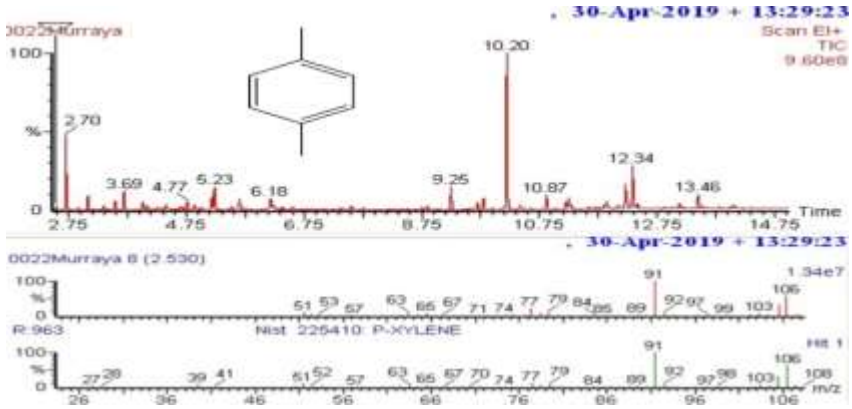

Figure 2. GC-MS chromatograms of *p*-xylene at retention time (2.530 min)

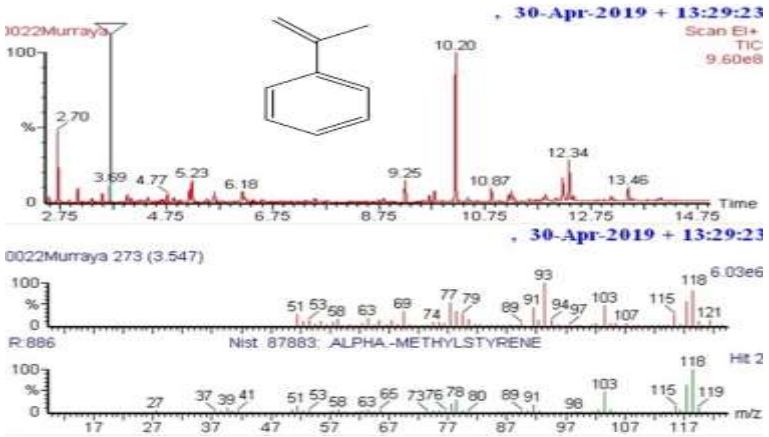

Figure 3. GC-MS chromatograms of α-methyl styrene at retention time (3.547 min)

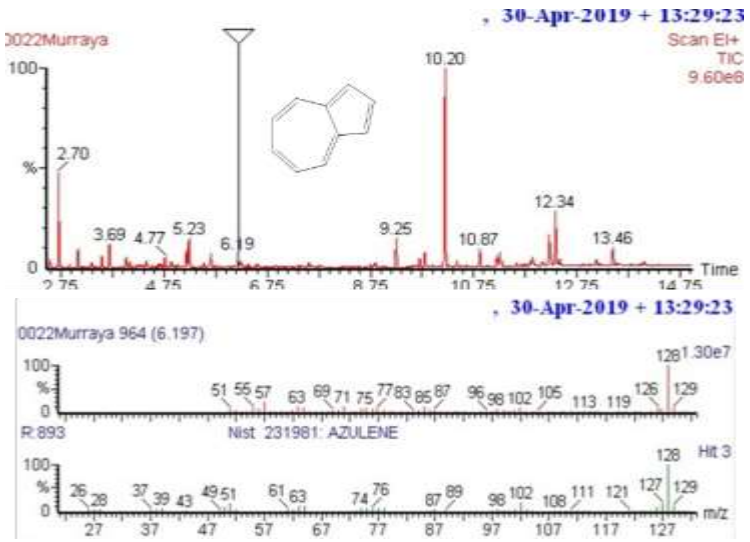

Figure 4. GC-MS chromatograms of azulene at retention time (6.197 min)

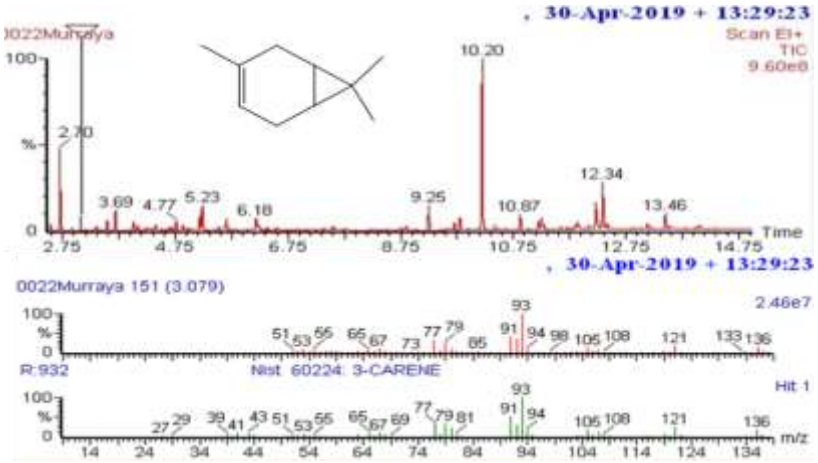

Figure 5. GC-MS chromatograms of 3-carene at retention time (3.079 min)

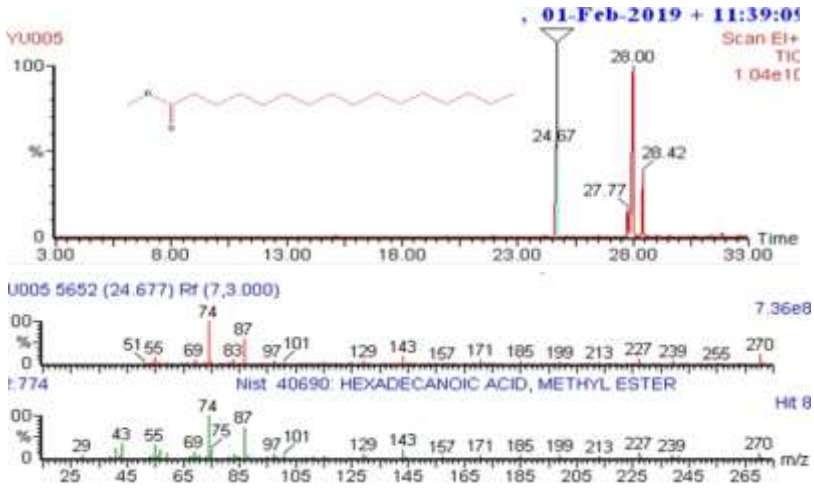

Figure 6. GC-MS chromatograms of methyl hexadecanoate at retention time (24.67 min)

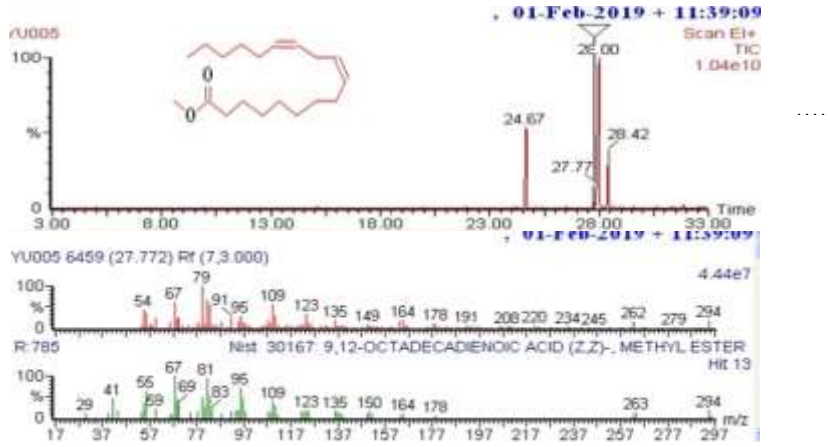

Figure 7. GC-MS chromatograms of methyl 9,12-octadecadienoate at retention time (27.77 min)

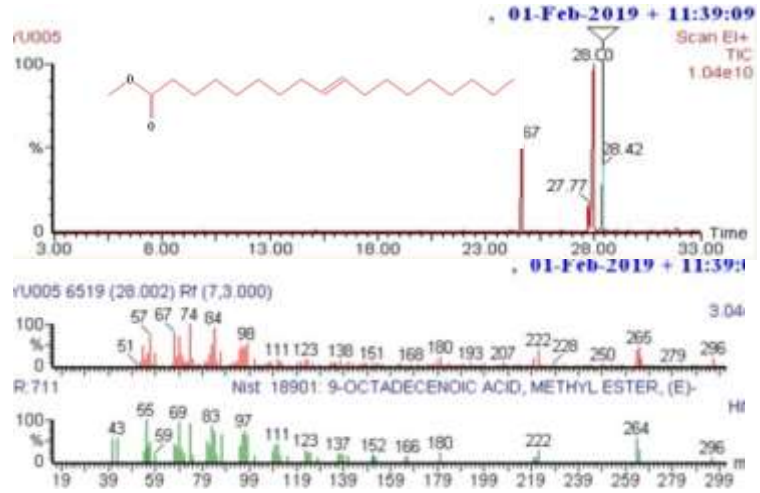

Figure 8. GC-MS chromatograms of methyl 9-octadecenoate at retention time (28.00 min)

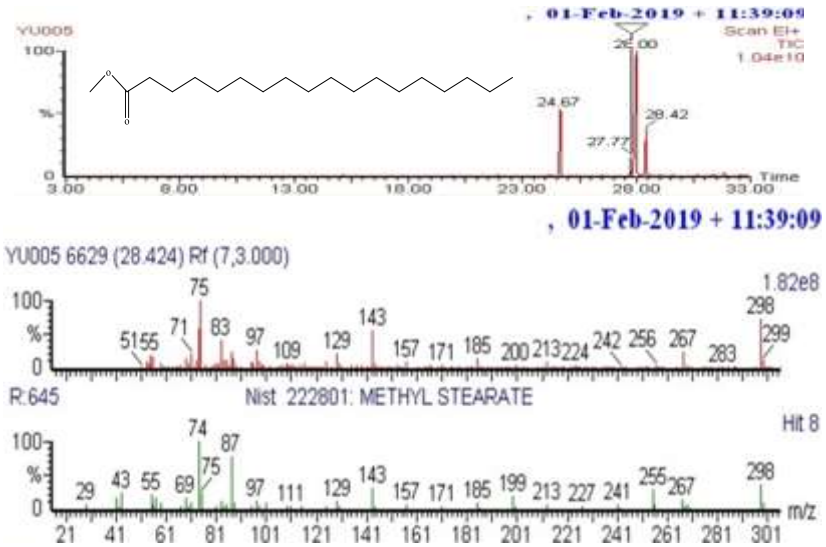

Figure 9. GC-MS chromatograms of methyl stearate at retention time (28.42 min)

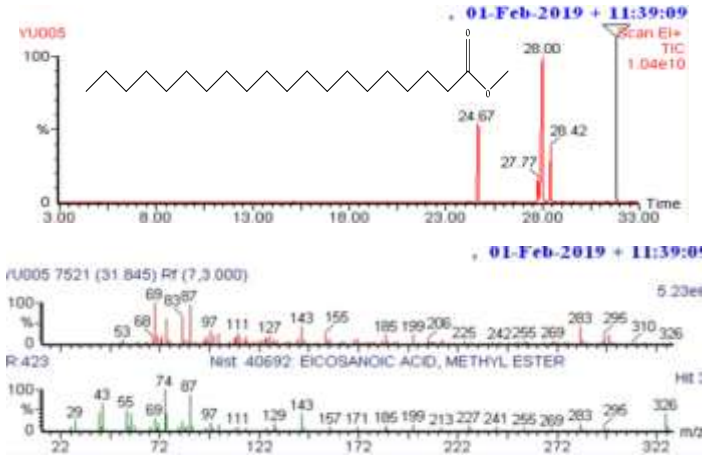

Figure 10. GC-MS chromatograms of methyl eicosanoate at retention time (31.845 min)

Conclusion

From the overall assessment of the chemical and biological investigation of curry leaves (*M. koenigii*), the following inferences could be deduced. The phytochemical tests revealed that alkaloids, α-amino acid, carbohydrates, cyanogenic glycosides, glycosides, organic acids, phenolic compounds, reducing sugars, saponins, steroids, and terpenoids were present in the sample. However, flavonoids, starch, and tannins were not detected in the leaves of *M. koenigii*. The total phenol content evaluated by the Folin-Ciocalteu reagent in terms of Gallic acid equivalent (µg/mL) in ethanol extract (2.73 ± 0.0030 µg/mL) was higher than that of watery extract (2.56± 0.0046 µg/mL). For the investigation of the antioxidant potential of ethanol and the watery extract by the DPPH assay, the IC_{50} values of ethanol and watery extracts were observed at 34.24 µg/mL and 42.92 µg/mL respectively. Therefore, the antioxidant activity of the ethanol extract is more potent than watery extract but weaker than standard BHT (IC_{50} = 22.26 µg/mL). The antimicrobial activity of the polar and nonpolar extracts was screened by using the Agar Well Diffusion method on eight microorganisms. PE, EtOAc, and EtOH extracts (16 mm - 19 mm) showed antimicrobial activity against all tested microorganisms. However, the water extract inhibited only (11mm-14 mm) against *P. aeruginosa, M. luteus, C. albicans, and E. coli*. The antiproliferative activity of ethanol and watery extracts from the leaves of *M.koenigii* were tested on five cancer cell lines by the CCK-8 assay method. It was observed that the ethanol extract was found to be more antiproliferative activity against human breast cancer) (IC_{50} < 1 µg/mL), human lung cancer (IC_{50} < 1 µg/mL), human stomach cancer (IC_{50} < 15.3 µg/mL), human gastric cancer (IC_{50} < 1 µg/mL) and human cervical cancer (IC_{50} < 1 µg/mL).In the case of water extracts, against human breast cancer (IC_{50} > 100 µg/mL), human lung cancer (IC_{50} 62.1 µg/mL), human stomach cancer (IC_{50} > 100 µg/mL), GSU human gastric cancer (IC_{50} 9.6 µg/mL) and human cervical cancer (IC_{50} > 100 µg/mL). The chemical constituents of essential oil from the leaves of *M. koenigii* were identified by the gas chromatography-mass spectrometry method. The nine organic compounds (terpenoids, esters) were found in the essential oil of leaves of *M. koenigii*. The results of the present study indicate that the leaves of *M. koenigii* L. can be used as raw material for the production of insecticides, medicines, and flavoring ingredients.

Acknowledgements

The authors would like to express their profound gratitude to the Department of Higher Education (Yangon Office), Ministry of Education, Yangon, Myanmar, for the provision of the opportunity to do this research and the Myanmar Academy of Arts and Science for allowing us to present this paper.

References

Fatma,P. K., A.B. Yildirim, R. Bayram, M.Z. Yavuz, A. Gepdiremem, and U.T. Arzu. (2015). "Antiproliferative Activity of Some Medicine Plants on Human Breast Hepatocellularulat Carcinoma Cell Lines and their Phenolic Content". *Tropical Journal of Pharmaceutical Research*, vol.14 (10), pp. 1787-1795

Finegold, S.M., and W.J. Martin. (1982). *Diagnostic Microbiology*. London: 6th Ed., C.V. Mosby Co. St. Louis, Toronto

James, A.T. and A. J. P. Martin. (1952). "Gas-Liquid Partition Chromatography; the Separation and Micro-Estimation of Volatile Fatty Acids from Formic Acid to Dodecanoic Acid". *Biochem. J*., vol.50 (5), pp. 679-690

Marini–Bettolo, G.B., M. Nicoletti, and M. Patamia. (1981). "Plant Screening by Chemical and Chromatographic Procedure Under Field Conditions". *J. Chromat*., vol.45, pp. 121-123

Marinova, G. and V. Batchvarob. (2011). "Evaluation of the Methods for Determination of the Free Radical Scavenging Activity by DPPH". *Bulg. J. Agric. Science*., vol.17**,** pp. 11-24

M-Tin Wa. (1972). "Phytochemical Screening Methods and Procedure" *Phytochemical Bulletin of Botanical Society of America Inc*., vol.5 (3), pp. 4-10

Pehlivan, K., A. Yildrim, and A. Turker. (2012). "Biological Screening of Various Medicine Plants Extracts for Antibacterial and Antitumor Activities". *Journal of Turk of Biology*, vol.36, pp. 641-652

Robert, M. S, and F. X. Webster. (1998). *Spectrometric Identification of Organic Compounds*. New York: 6th Ed., John Wiley & Sons, pp. 367-370

Song, F. L., R. Y. Zhang, Q. Xiao, L. Kuang and H. B. Li. (2010). "Total Phenolic Contents and Antioxidant Capacities of Selected Chines Medicinal Plants". *Int. J.MolSci*., vol.11, pp. 2367-2372

Srivastava, A. J., S. K. Srivastava and K.V. Syamsudar. (2003). "Bud and Leaf Essential Oil Composition of *Syzygium aromaticum* from India and Madagascar". *Flav. Fra. J*., vol.20 (1), pp. 51-53

World Health Organization. (1999). *W.H.O. Monographs on Selected Medicinal Plants.* Geneva: vol.1, pp.11-14

PURIFICATION AND CHARACTERIZATION OF POLYPHENOL OXIDASE ENZYME FROM BANANA PEELS (*MUSA ACUMINATA* SIMMONDS)

Nyein Nyein Aye[1], Myat Kyaw Thu[2], Wai Lin Oo[3]

Abstract

An enzyme called polyphenol oxidase (1.10.3.1) is responsible for the browning events that occur when handling damage to the cells. Peels from bananas were gathered in the Thiri Mingalar market in the Yangon Region. Using ammonium sulphate precipitation (20-80 %), dialysis, and gel filtration chromatography on Sephadex G-100, the enzyme polyphenol oxidase (PPO) was extracted from banana peels. Using catechol as a substrate at 420 nm, the spectrophotometric technique was used to assess the polyphenol oxidase activity. The modified Lowry's method was used to determine the protein content using a standard of bovine serum albumin (BSA) at 550 nm. The purification of polyphenol oxidase over crude extract was 3.52 folds, and 0.18 % of the protein was obtained. pH 7.0 and 30 °C were found to be the optimum conditions. It was shown that after 5h of incubation at pH 7.0, polyphenol oxidase activity remained at approximately 68.6 %. A particular pH of 7.0 was used to study the heat sensitivity of polyphenol oxidase at various temperatures of 25, 30, and 35 °C for various incubation periods (0, 1, 3, and 5 h). At 30, 25, and 35 °C, polyphenol oxidase activity was shown to be relatively stable; after 5 h of incubation, it retained 67.8, 49.6, and 26.9 % of its original activity, respectively. The activation energy (E_a) of the polyphenol oxidase-catalyzed reaction was determined to be 2.404 kcal mol^{-1}.

Keywords: polyphenol oxidase enzyme, modified Lowry's method, Sephadex G-100, activation energy

Introduction

Banana is an important food source in the developing world and is one of the most important worldwide crops (Karakus and Pekyardimci 2009). Nowadays, banana commercialization is diversifying and expanding. But, during handling, storage, and processing, its tissue turns dark brown because of the action of polyphenol oxidase (PPO). The degree of browning in bananas after cutting was associated with polyphenol oxidase activity and the concentration of free phenolic substrates (Chaisakdanugull and Theerakulkait 2009).

Polyphenol oxidases are copper-containing oxidoreductase enzymes (Aziz *et al*., 2018). Polyphenol oxidases catalyze the hydroxylation of monophenols to o-diphenols and the oxidation of o-diphenols to o-quinones using molecular oxygen, leading to the formation of black or brown pigments (Aziz and AL-Sa'ady, 2016). In the food industry, polyphenol oxidases are very important enzymes due to their involvement in the enzymatic browning of edible plants. Enzymatic browning is often undesirable and is responsible for unpleasant qualities and losses in nutrient quality. PPO plays an important role as an efficient reagent for cleaning polyphenol-containing wastewater and has many applications in the fields of medicine, food processing, and wastewater treatment. Polyphenol oxidases are a group of enzymes found in almost all living organisms, including plants, animals, and microorganisms. The aim of this research was to study the extraction and characterization of polyphenol oxidase from banana peels (*Musa acuminata* Simmonds).

[1] Department of Chemistry, University of Yangon
[2] Department of Chemistry, University of Yangon
[3] Department of Chemistry, University of Yangon

Materials and Methods

Materials

The banana (*Musa acuminata* Simmonds**)** peel sample was purchased from a local shop in the Yangon Region. Bovine Serum Albumin (BSA) was purchased from Sigma Aldrich, England. All other chemicals used were of analytical reagent grade. In all investigations, the recommended standard methods and techniques involving both conventional and modern methods were provided.

Sample Preparation and Extraction of Polyphenol Oxidase from Banana Peels

Banana peels were washed with tap water, and 50 g of each banana peel was homogenized with 200 mL of 0.05 M potassium phosphate buffer (pH 7.0) containing 1% polyethylene glycol and 0.01 M ascorbic acid in a blender for 1 min. The homogenate solution was filtered through cheesecloth and the filtrate was centrifuged at 6000 rpm for 30 min. The proteins in the supernatant were collected. The enzyme solution was fractionated with solid ammonium sulphate, and a precipitate of 20 % saturation was collected by centrifugation at 6000 rpm, for 30 min. After standing for 2 h at 4 °C, the precipitate was removed by centrifugation for 30 min at 6000 rpm, and the supernatant was collected. Solid ammonium sulphate was then added to the supernatant to achieve 80% Saturation. After standing overnight, the precipitated protein containing polyphenol oxidase was collected by centrifugation for 30 min at 6000 rpm. The pellet was redissolved in (0.05 M potassium phosphate buffer, pH 7.0) and dialyzed against the same buffer in the dialysis tubing kit (m.w. cutoff 12000 – 14000 Da). At intervals of 4 h, dialysis buffer was changed twice. The dialyzed solution was kept at 4 °C after being dialyzed to remove ammonium sulphate.

Purification of Polyphenol Oxidase Enzyme by Using Gel Filtration Chromatography

Gel filtration was carried out using Sephadex G-100. Sephadex G-100 (4 g) was dissolved in 150 mL of 0.05 M potassium phosphate buffer (pH 7.0) and kept for 1 d. Then, Sephadex G-100 was loaded into the column and pre-equilibrated. The elution rate of this column was determined by using 0.05 M potassium phosphate buffer (pH 7.0) after some cotton wool was added to the column. The eluates were collected from the column by a fraction collector after the dialyzed enzyme solution was applied to the Sephadex G-100 column. The flow rate was adjusted to 1.5 mL/7min by the mini-pump, and 1.5 mL fractions were collected per tube. The elution process was continued until no absorbance was observed at 280 nm. The protein and PPO activities of each fraction were checked by measuring the absorbance at 280 nm wavelength using a UV-visible spectrophotometer. The fraction that had the highest polyphenol oxidase activity was pooled. The pooled polyphenol oxidase fraction was measured for protein content by the modified Lowry's method, and polyphenol oxidase activity was measured. Their purification degrees were determined by measuring specific activities.

Characterization of Polyphenol Oxidase from Banana Peels (*Musa acuminata* Simmonds)

Polyphenol oxidase properties of optimum pH, optimum temperature, pH stability, thermostability, reaction time, and enzyme concentration were measured by the spectrophotometric method (Tin Tin Myo, 2009).

Results and Discussion

Extraction of Polyphenol Oxidase from Banana Peels (*Musa acuminata* Simmonds)

In the present work, the polyphenol oxidase enzyme was isolated from banana peel samples obtained from Thiri Mingalar market, Yangon Region, and was partially purified by the solid ammonium sulphate precipitation method.

Purification of Polyphenol Oxidase Enzyme by Gel Filtration Chromatography

In this study, PPO was partially purified from *Musa acuminata* Simmonds Peels using ammonium sulphate precipitation and dialysis. The PPO activity of the precipitate at 20–80 % $(NH4)_2SO_4$ saturation was found to be the highest, and this saturation point was used for all the extraction processes. The PPO enzyme obtained by precipitating with solid ammonium sulphate was dialyzed. The molecules that were smaller than 12000 Dalton are out of the dialysis tube, and the PPO enzyme is located in the tube. The fractions showing PPO activity were obtained after gel filtration chromatography.

The protein contents and polyphenol oxidase enzyme activity in different stages of purification of polyphenol oxidase were investigated. The polyphenol oxidase activity was determined by measuring the initial rate of quinone formation, as indicated by an increase in the absorbance unit at 420 nm. The polyphenol oxidase activity is defined as the increase in absorbance at 420 nm per volume of enzyme solution per reaction time (min) per 0.001 absorbance unit using catechol as a substrate.

Figure 1 shows the chromatogram of polyphenol oxidase on Sephadex G-100 gel. The protein content of the eluate was checked spectrophotometrically at 280 nm and the enzyme activity was determined at 420 nm. The fractions with the highest activity were pooled. The relative purity of the enzyme was increased by about 3.52 folds over the crude extract. The yield percent was 0.18 %. The resultant enzyme protein was dissolved in phosphate buffer (pH 7.0) and UV-visible measurement was carried out. The degree of purity of each step is show in Table 1.

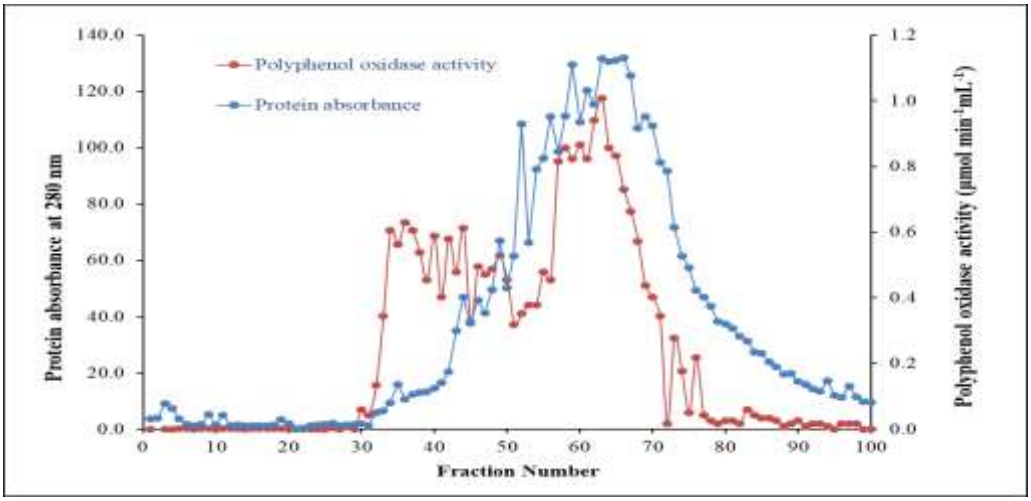

Figure 1. Chromatogram of polyphenol oxidase on sephadex G-100 gel

Table 1. Purification of Polyphenol Oxidase from Banana Peels

Fraction	Total Enzyme Activity(EU)	Total Protein Content (mg)	Specific Activity (EU/mg)	Protein Recovery (%)	Degree of Purity(fold)
Crude	611400	615.52	993.29	100	1
20 % $(NH_4)_2SO_4$ precipitation	659733	463.21	1424.24	75.25	1.43
80 % $(NH_4)_2SO_4$ precipitation	120400	49.87	2414.13	8.10	2.43
Dialysis	82983	28.80	2879.55	4.68	2.90
Sephadex G-100 gel separation	3927	1.12	3496.64	0.18	3.52

Optimum pH of Polyphenol Oxidase Activity

The enzyme is active at a limited range of pH. The activity of the enzyme is reduced and reaction rates are slower at pH levels above and below optimum pH (Hendrickson *et al*, 2007). In this work, phosphate buffer ranging from a value of 5.5 to 8.0 was used to determine the activity of the prepared polyphenol oxidase sample. The nature of the activity *vs* pH curve of the enzyme (Table 2 and Figure 2) was obviously found to be bell-shaped, and the optimum pH was obtained at pH 7.0 with catechol as substrate.

Table 2. Relationship between Polyphenol Oxidase Activity and pH of Potassium Phosphate Buffer Solution

No.	pH	Polyphenol Oxidase Activity (10^{-3}EU)
1	5.5	0.06
2	6.0	0.10
3	6.5	0.16
4	7.0	0.22
5	7.5	0.14
6	8.0	0.04

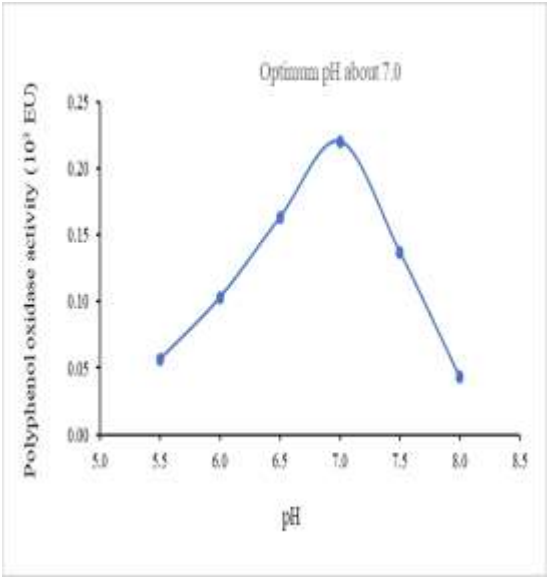

Figure 2. Plot of polyphenol oxidase activity as a function of pH of the solution

Optimum Temperature of Polyphenol Oxidase Activity

In common with other proteins, enzymes are sensitive to temperature changes (Campbell and Smith, 2000). In this study, the effect of temperature on polyphenol oxidase activity was investigated in the temperature range of 15°C to 50°C. The optimum temperature for polyphenol oxidase was found to be 30 °C in potassium phosphate buffer, pH 7.0 (Table 3 and Figure 3). It was found that the activity of polyphenol oxidase increased from 15°C to 30°C and then decreased from 30°C to 50°C.

The activation energy of the polyphenol oxidase catalyzed reaction was calculated by using the Arrhenius equation (Atkins, 1994). Table 4 shows the relationship between the temperature and velocity of the polyphenol oxidase-catalyzed reaction and the Arrhenius constant. By using the constant substrate concentration throughout the experiment, the rate constant (K) in the Arrhenius equation can be substituted by the velocity of the polyphenol oxidase-catalyzed reaction. The activation energy (E_a) was determined to be 2.404 kcal mol^{-1} from the linear regression method.

Table 3. Relationship between Activity of Polyphenol Oxidase-catalyzed Reaction and Temperature of the Solution at pH 7.0

No.	Temperature (°C)	Polyphenol oxidase Activity (10^{-3} EU)
1	15	0.27
2	20	0.30
3	25	0.33
4	30	0.36
5	35	0.31
6	40	0.29
7	50	0.12

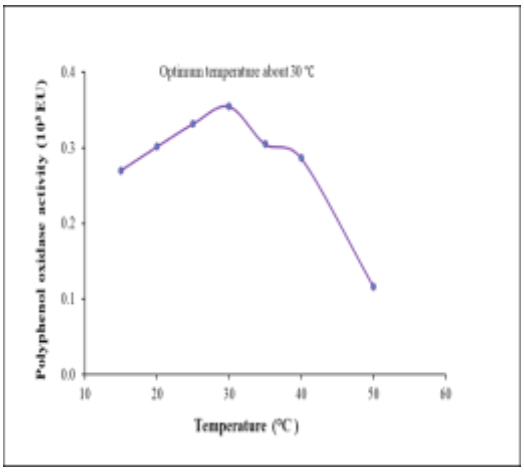

Figure 3. Plot of activity as a function of temperature of the solution at pH 7.0

Table 4. Relationship between Temperature and Velocity of Polyphenol Oxidase-catalyzed Reaction of the solution at pH 7.0

No.	Temperature (°C)	$1/T\times10^3$ (K^{-1})	Velocity (μmol min^{-1})	Log V
1	15	3.47	7.95	0.90
2	20	3.41	8.87	0.95
3	25	3.36	9.77	0.99
4	30	3.30	10.44	1.02

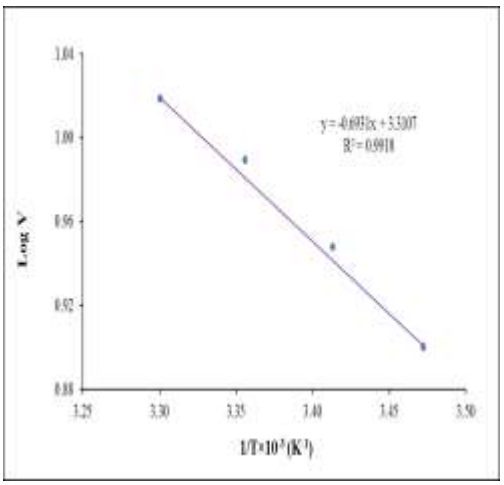

Figure 4. Plot of Log V as a function of 1/T for polyphenol oxidase activity

pH Stability of Polyphenol Oxidase activity at Different pH Values

pH profoundly affects the stability of enzymes (Sawhney and Singh, 2000). The pH stability is determined by pre-incubating the enzyme at various pH for a fixed time. The pH stability of polyphenol oxidase activity was studied by pre-incubating the enzyme at pH 6.5, 7.0, and 7.5 for 0, 1, 3, and 5 h (Table 5). From Figure 5, it can be seen clearly that the polyphenol oxidase activation at pH 7.0 was relatively stable, whereas at pH 6.5 and 7.5, activity decreased by about 60 % and 56 % of the original activity for 5 h of incubation.

Table 5. Relationship between Relative Activity of Polyphenol Oxidase Enzyme and Incubation Time at Different pH

pH	Incubation time (h)	Polyphenol oxidase activity (10^{-3} EU)	Relative activity (%)
6.5	0	0.27	100
	1	0.20	73.93
	3	0.13	48.87
	5	0.11	40.10
7.0	0	0.28	100
	1	0.24	87.92
	3	0.21	76.21
	5	0.19	68.60
7.5	0	0.23	100
	1	0.19	80.77
	3	0.15	62.82
	5	0.10	43.87

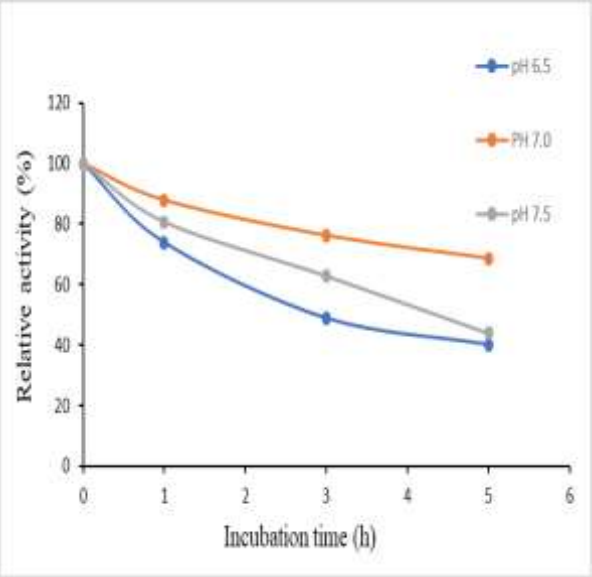

Figure 5. Plot of relative activity of polyphenol oxidase *vs* incubation time at different pH

Thermostability of Polyphenol Oxidase Activity at Different Temperatures

The maintenance of a defined functional state (chemical and structural properties that are required for activity) under extreme conditions refers to stability (Jaenicke and Bohm, 1998). The thermal stability usually increases with rising temperature and passes a maximum, followed by a decrease. The thermostability of polyphenol oxidase activity was studied using a particular pH of 7.0 at different temperatures of 25, 30, and 35 °C for various incubation times (0, 1, 3, and 5 h) (Table 6 and Figure 6). It was observed that the polyphenol oxidase activity was relatively stable at 30 °C until 5 h incubation. The polyphenol oxidase activities decreased by about 50 % at 25 °C for 5 h of incubation. It was interesting to find that the stability of polyphenol oxidase activity was relatively low at 35°C, as it decreased by about 73% of original activity for 5h of incubation.

Table 6. Relationship between Relative Activity of Polyphenol Oxidase Enzyme and Incubation Time at Different Temperatures

Temperature (°C)	Incubation time (h)	Polyphenol oxidase activity (10^{-3} EU)	Relative activity (%)
25	0	0.28	100
	1	0.24	84.72
	3	0.19	68.60
	5	0.14	49.64
30	0	0.33	100
	1	0.30	90.53
	3	0.26	77.64
	5	0.22	67.77
35	0	0.26	100
	1	0.18	69.36
	3	0.13	51.28
	5	0.07	26.92

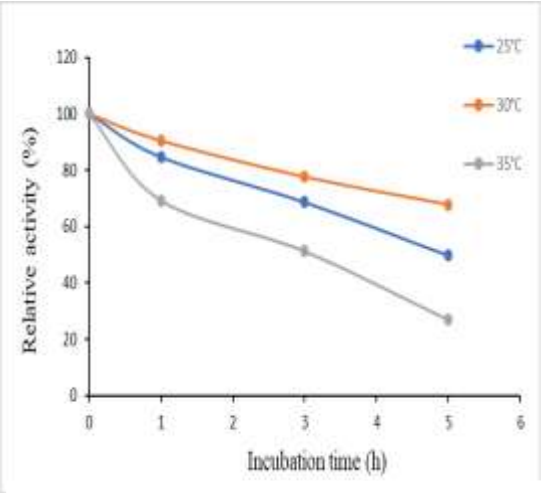

Figure 6. Plot of relative activity of polyphenol oxidase *vs* incubation time at different temperature

Reaction Time on Polyphenol Oxidase-catalyzed Reaction

Reaction time is also a major factor in enzyme activity. The significance of the reaction time is created by the different enzymes that record the starting time (Das and Prasad, 2010). In this work, the action of the polyphenol oxidase on catechol substrate was studied in phosphate buffer pH (7.0). The amount of orthoquinone product as a function of reaction times of 1, 3, 6, 9, 12, 15, 18, 21, and 24 min was determined at 420 nm by the UV-visible spectroscopic method (Table 7 and Figure 7). The figure shows the plot of the velocity of the polyphenol oxidase reaction as a function of reaction time. At the beginning of the reaction (during 5 min), the reaction is very fast. Then, velocity decreased steadily. Therefore, in sequence studies, the reaction time of 3 min was used for the initial velocity measured in enzyme kinetics.

Table 7. Relationship between Reaction Time and Different Velocity of Polyphenol Oxidase-catalyzed Reaction

No.	Reaction Time (min)	Velocity (10^5 M min^{-1})
1	1	1.27
2	3	0.75
3	6	0.51
4	9	0.39
5	12	0.33
6	15	0.28
7	18	0.25
8	21	0.22
9	24	0.19

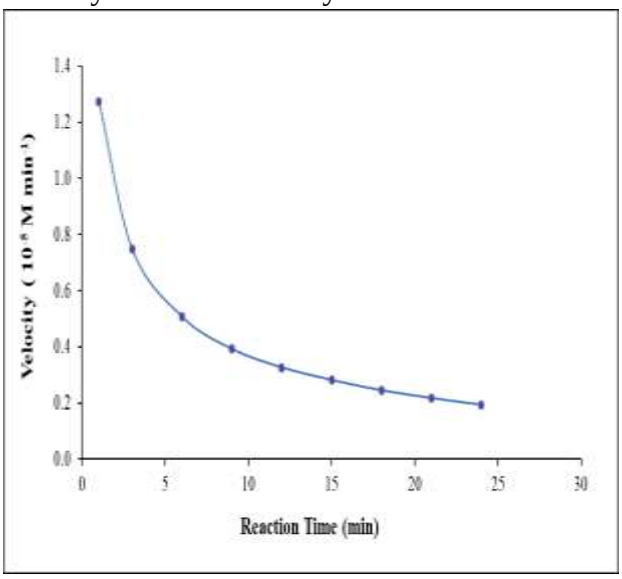

Figure 7. Plot of different velocity of polyphenol oxidase-catalyzed reaction as a function of reaction time

Conclusion

The ammonium sulphate precipitation method and gel filtration chromatography method (Sephadex G-100) were used to extract purified polyphenol oxidase from *Musa acuminata* Simmonds peels. Polyphenol oxidase activity was determined by a spectrophotometric method using catechol as a substrate at 420 nm. The specific activity and relative purity of the enzyme were increased by about 3.52 folds from the crude extract to the final purification step. The optimum pH of the polyphenol oxidase enzyme was found to be 7.0 in a potassium phosphate buffer and the optimum temperature was 30°C. At a pH value of 7.0, the polyphenol oxidase activity was relatively stable, whereas the polyphenol oxidase activity decreased by about 60 % and 56 % of original activity at 6.5 and 7.5, respectively, for 5 h incubation. At 25 and 35°C, polyphenol oxidase activities decreased by about 50 % and 73 % of its original activity, respectively, for 5 h of incubation. The activation energy (Ea) of the polyphenol oxidase-catalyzed reaction was found to be 2.404 kcal mol-1.

Acknowledgements

The authors would like to thank the Department of Higher Education, Ministry of Education, Yangon, Myanmar. We would like to express our sincere thanks to Dr Tin Maung Tun (Rector) and Dr Khin Chit Chit, Dr Cho Cho, and Dr Thidar Aye (Pro-Rectors), University of Yangon. Our warmest thanks are also extended to Professor Dr Ni Ni Than, Head of the Department of Chemistry, University of Yangon, for her kind encouragement, permission to submit this paper and many helpful suggestions.

References

Atkins, P. W. (1994). *Physical Chemistry*. New York: 5th Ed., Oxford University Press, pp. 899-910

Aziz, G. M., and A. J. R. AL-Sa'ady. (2016). "Extraction conditions of Polyphenol Oxidase from Banana Peel". *Baghdad Science Journal*, vol. 13 (3), pp. 251 - 263

Aziz, G. M., A. J. Al-Sa'ady, and D. S. Bedan. (2018). "Characterization and Immobilization of Purified Polyphenol Oxidase Extracted from Banana Peel". *Iraqi Journal of Biotechnology*, vol. 17 (2), pp. 13-22

Campbell, P. N., and A. D. Smith. (2000). *Biochemistry Illustrated*. London: 4th Ed., Churchill Livingstone Harcourt Publisher Ltd., ppt. 75-80

Chaisakdanugull, C, and C. Theerakulkait. (2009). "Partial Purification and characterization of Banana [Musa (AAA Group) 'Gros Michel']". *Internal Journal of Food Science and Technology*, vol. 44, pp. 840-846

Das, G. and M.P Prasad. (2010). "Isolation, Purification and Mass Production of Protease Enzyme from *Bacillus subtilis*". *International Research Journals of Microbiology*, vol. 1, pp. 026-031

Hendrickson, C.H., L.C. Byrd, and N.W Hunter. (2007) *A Laboratory Manual for General, Organic, and Biochemistry*, New York: 6th Ed., Ma Graw Hill Science/Engineering/Math

Jaenicke, R. and G. Bohm. (1998). "The Stability of Proteins in Extreme Environments", *Curr. Opin. Struct. Biol,* vol. 8 (6), pp. 738-748

Karakus, E. and S. Pekyardimci. (2009). "Purification and Biochemical Characterization of Polyphenol Oxidase from Alanya Banana (Musa caritalicevendishi)". *Asian Journal of Chemistry*, vol. 4, pp. 3138-3150

Sawhney, S. K., and R.Singh. (2000). Introductory Practical Biochemistry. New Delhi: Narosa Publishing House, pp. 88-96

Tin Tin Myo (2009). Isolation, Immobilization, and *Application of Polyphenol Oxidase from Avocado* (*Persea Americana Mill*.). Yangon: PhD Dissertation, Chemistry Department, Yangon University

SYNTHESIS AND CHARACTERIZATION OF Cu- DOPED TIO_2 NANOPARTICLES BY SOL - GEL METHOD

Hay Mar Oo[1], Hlaing Hlaing Oo[2], Cho Cho[3]

Abstract

The study was designed to study the effect of copper doping of TiO_2 with three different copper concentrations and calcined at 500 to 800 °C for 2 hours on the anatase-rutile phase transition and composition. The prepared powder samples were characterized by X-ray Diffraction (XRD), Energy Dispersive X- ray Fluorescence (EDXRF), Scanning Electron Microscopy-Energy Dispersive X-ray Spectroscopy (SEM-EDX). The XRD results suggested that the pure TiO_2 powder calcined at 500 °C was in 100 % anatase phase, whereas these materials transformed the mixing of a few anatase phases and mainly rutile phases at 600 °C. Therefore, the phase transition temperature of TiO_2 in this preparation method was 600 °C. The average crystallite sizes of prepared TiO_2 materials by XRD analysis were in the range of 25.50 to 96.39 nm. The average crystallite sizes increased with increasing calcined temperature. The associated work of this research is the addition of $CuSO_4$ to the crystal structure of TiO_2 synthesized by the sol-gel method using titanium(IV) isopropoxide, isopropanol, and copper(II) sulphate, and calcined at 500 to 800 °C. The XRD results of prepared Cu-doped TiO_2 materials described the anatase phase at 500°C and 600 °C, and the mixing of a few anatase phase and mainly rutile phase for Cu-doped TiO_2 nanoparticles at 700 °C. Therefore, the phase transition temperature of Cu-doped TiO_2 nanoparticles was 700 °C. The synthesized Cu-doped TiO_2 materials were fully transformed to the rutile phase at 800 °C. The average crystallite size of Cu-doped TiO_2 materials was in the range of 25.67 to 45.49 nm. The XRD study revealed that all the prepared samples have tetragonal crystal structures that were not changed through the doping process.

Keywords: TiO_2 nanoparticles, Cu-doped TiO_2 nanoparticles, sol-gel method, phase transition

Introduction

TiO_2 has become one of the most important semiconductor materials in daily life. Titanium dioxide was first commercially used during the 20th century for applications that include pigments in paint, UV blockers, batteries and food coloring (Byrne *et al.*, 2019). Titanium dioxide in comparison with other semiconductor catalysts, has many advantages, such as suitable optical and electron properties, chemical stability, corrosion resistance and non-toxicity. Titanium dioxide has been widely used as a catalyst under UV irradiation and was considered the best choice among several other metal oxides (Ahmed, 2015). These include ease of preparation, strong oxidizing ability, long term stability, nontoxicity, high refractive index, high dielectric constant and low cost (Fisher *et al.*, 2013). TiO_2 is naturally present in three main phases: anatase (tetragonal, a= b= 3.785 Å, c= 9.54 Å), brookite (orthorhombic, a= 5.143 Å, b= 5.456 Å, c= 9.182 Å) and rutile (tetragonal, a=b= 4.593 Å, c= 2.959 Å). The thermodynamically metastable phases, anatase and brookite, transition irrevocably into the stable rutile phase at high temperatures (Hanaor and Sorrell, 2011).

Recently, copper has been increasingly investigated as a dopant for titania (Ahmed, 2015). Copper has been previously investigated as a potential dopant in TiO_2 but to date, a detailed systematic analysis of the effect of Cu doping on the phase stability of TiO_2 is lacking (Yoong *et al.*, 2009). It is one of the best candidate metal dopants for TiO_2 surfaces, because of its relative abundance, high electronic conductivity and low cost as compared to noble metals such as Ag and

[1] Department of Chemistry, University of Yangon
[2] Department of Chemistry, West Yangon University
[3] University of Yangon

Cu is also a metallic element essential to human health and is considered a low toxicity metal to humans.

In this research, the sol-gel method was chosen for the preparation of pure TiO_2 and Cu-doped TiO_2 nanoparticles, because this is the easiest method that can be performed at various calcination temperatures. In the present work, Cu-doped TiO_2 nanoparticles were prepared with titanium(IV) isopropoxide as a precursor, three different copper concentrations, and calcined at 500 to 800ºC.

Materials and Methods

Sample collection

Titanium(IV) isopropoxide and isopropanol were purchased from Academy Chemical Group at 27th street, Pabedan Township, Yangon. The apparatus consists of conventional labware, glassware and modern equipment. Some of the instruments used in the experiments are E-Mettler balance (210 ± 0.1 mg) (LA – 310 S), magnetic stirrer (Bibby), muffle furnace (Range 100-1100 ºC Gallenkamp, England) and thermal control status oven (H 053, 240 V, England).

Preparation of TiO_2 and Cu-Doped TiO_2 Nanoparticles

TiO_2 nanoparticles were synthesized by using the sol-gel method, which involves the hydrolysis and condensation of titanium (IV) isopropoxide. Briefly, 46.16 mL of titanium isopropoxide was added to 200 mL of isopropanol. This solution was stirred for 15 min. To this solution, 200 mL of deionized water was added. This mixture was stirred for another 30 min. The resulting gel was dried in the oven set at 100 ℃ for 12 h. The resulting powder was annealed at 500 °C, 600 °C, 700 °C and 800 °C at a ramp rate of 10 °C/min and held at the target temperature for 2 h. For a 2% copper sample, 45.24 mL of titanium (IV) isopropoxide was added to 200 mL of isopropanol and stirred for 15 min (Solution A). After that, 0.8705 g of copper (II) sulphate ($CuSO_4$) was added to 200 mL of deionized water, which was stirred for 15 min (Solution B). Solution B was added to Solution A and this was stirred for 30 min. The resulting gel was dried in the oven at 100 °C for 12 h. The resulting powder was annealed at 500 °C, 600 °C, 700 °C and 800 °C at a ramp rate of 10 °C/min and held for 2 h. This method was repeated for the 4% and 8% copper samples by altering the amounts of titanium(IV) isopropoxide and $CuSO_4$ (4%–44.32 mL and 1.7375 g; 8%–42.47 mL and 3.5075 g).

Characterization of TiO_2 and Cu-doped TiO_2 materials

The prepared TiO_2 and Cu-doped TiO_2 materials were characterized by X-ray Diffraction (XRD) using a Rigaku X-ray Diffractometer (RINI 2000/PC software, Cat.NO.9240 J101, Japan) at Universities' Research Center, Yangon, Myanmar was used. The morphology and qualitative elemental composition of prepared samples were carried out by using Scanning electron microscope with energy dispersive X- ray (SEM-EDX), EVO-18 Germany at University Research Center, Magway, Myanmar. Qualitative elemental composition of prepared samples was detected by Energy Dispersive X- ray Fluorescence (EDXRF) technique using EDX 7000, Japan at Department of Chemistry, Monywa University, Monywa, Myanmar.

Results and Discussion

Characterization of Prepared TiO_2 and Cu-doped TiO_2 materials

The pure TiO_2 and Cu-doped TiO_2 materials were synthesized from titanium(IV) isopropoxide, $Ti(OC_3H_7)_4$ in iso-propanol ($CH_3CHOHCH_3$), used as solvent. Anhydrous $CuSO_4$ was used as the precursor for Cu doping in TiO_2 materials.

Synthesized TiO_2 and Cu doped TiO_2 materials by XRD Analysis

The effect of copper doping through TiO_2 crystal structure on the anatase to rutile phase transition temperature was analysed by X-ray Diffraction technique. The recorded XRD diffraction patterns for synthesized TiO_2 are shown in Figure 1. XRD patterns of prepared TiO_2 materials calcined at 500 °C (Figure 1(a)) clearly show the identical Miller indices of (101), (103), (004), (112), (200), (105), (211), and (204) with the standard card database, and pure anatase phase (Card number 202243). The standard card data also confirmed the diffraction peaks at the 2θ values of 25.48° represented Miller indices (101) and 48.18 for (200) were major peaks for the anatase phase of TiO_2.

The calcined temperatures of TiO_2 materials at 600 °C and 700 °C showed the diffraction peak with Miller indices of (110), (101), (200), (111), (210), (211), (220), (002), (310), (221), and (310). The strong intensity peak at a 2θ value of 27.4 with the Miller index (110) proved the transformation of the rutile phase introduced at this temperature. The recorded data were identical with the standard card and it indicated the rutile phase of prepared TiO_2 materials. Moreover, the small additional diffraction peak of the anatase phase at a 2θ value approximately 25 ° existed at calcined temperature of 600 °C (Figure 1(b)). It can be suggested that the phase transformation of anatase phase to the rutile phase co-existed at this calcined temperature. The calcined temperatures of 700 °C (Figure 1(c)) and 800 °C (Figure 1(d)) clearly showed the pure rutile phase of prepared TiO_2 materials. Therefore, the calcined temperature at 600 °C is the phase transition temperature. The main diffraction peaks with Miller indices of the anatase and rutile were (101) and (110), respectively.

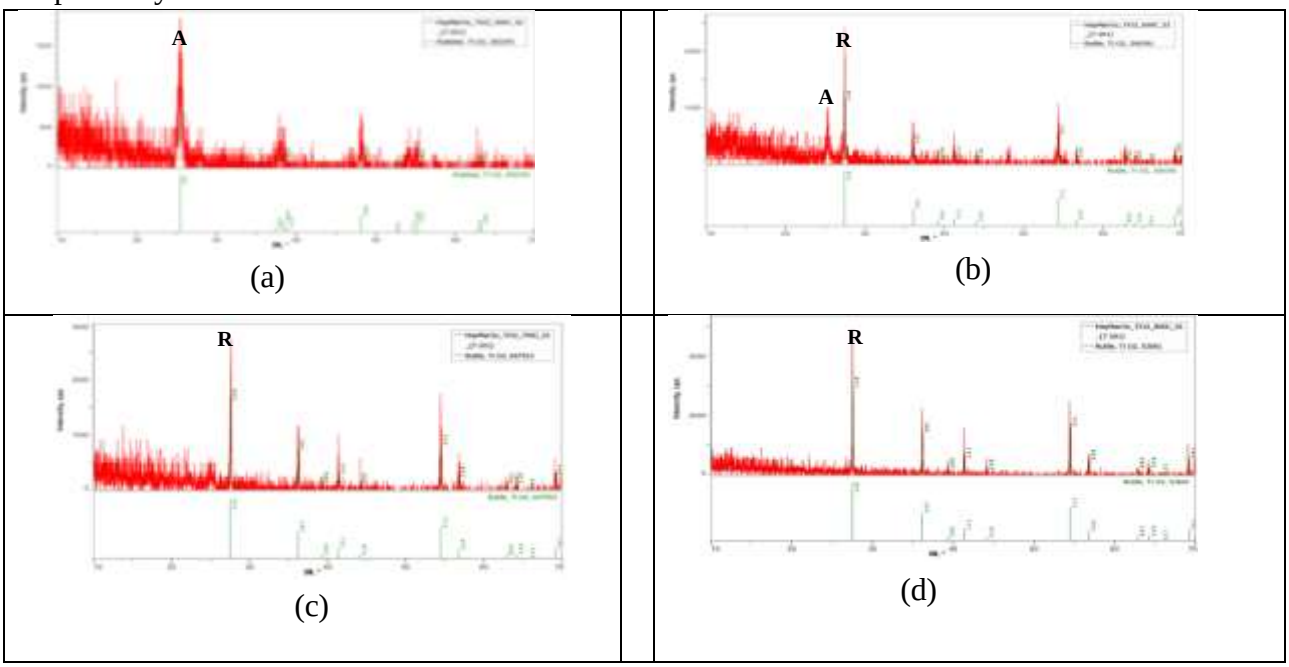

Figure 1. XRD patterns of prepared TiO_2 materials calcined at (a) 500 ºC, (b) 600 ºC and (c) 700 ºC and (d) 800ºC (A: anatase and R: rutile)

The crystallite sizes of prepared TiO_2 and 2%, 4%, and 8% Cu-doped TiO_2 materials calcined at four different temperatures (500 °C, 600 °C, 700 °C, and 800 °C) were identified by X-ray diffraction. The simplest and most widely used method for estimating the average crystallite size is from the full width at half maximum (FWHM) of a diffraction peak using the Scherrer equation, $d = K\lambda / \beta \cos \theta$, where d is the crystallite size, λ is the diffraction wavelength, β is the corrected FWHM, θ is the diffraction angle, and K is a constant close to unity. The crystallite sizes, lattice parameters, and crystal phases of prepared TiO_2 materials were calculated by this method as shown in Table 1. The average crystallite sizes of the anatase phase of TiO_2 materials were in the range of 25.50 to 94.50 nm, with the crystal structure being tetragonal in all prepared TiO_2 materials. The average crystallite sizes of prepared TiO_2 materials were within the range of nanoparticles from 1 to 100 nm. Thus, the prepared TiO_2 materials can be confirmed as TiO_2 nanoparticles.

Table 1. XRD Characterization Data of Prepared pureTiO_2 Materials at Different Calcined Temperatures

Calcined temperature	Average crystallite size (nm)		Lattice parameters (Axial length)			Crystal phase
(°C)	XRD	Calculated	a / Å	b / Å	c/ Å	
500	25.50	25.67	3.7873	3.7873	9.5079	Anatase
600	35.60	35.42	3.7873	3.7873	9.5079	Anatase & Rutile
700	93.75	96.39	4.5805	4.5805	2.9721	Rutile
800	94.80	94.50	4.5782	4.5782	2.9536	Rutile

The XRD patterns of 2%, 4%, and 8% copper-doped TiO_2 materials were also described in Figures 2 to 4 and Tables 2 to 4. The standard card data from the XRD library confirmed the XRD diffraction peaks of copper-doped TiO_2 materials (2%, 4%, and 8%) calcined at 500 °C and 600 °C; the 2θ values of 25.4° represented Miller indices (101), 37.8° for (004), and 48.06° for (200) were major peaks for the anatase phase of TiO_2. The additional diffraction peaks of a copper crystal doped through TiO_2 materials showed 2θ value of 51°, which indicated the (220) plane for 2% Cu-doped TiO_2 and 2θ value of 43.5°, which indicated the (111) plane for 8% Cu-doped TiO_2. As a result, the intensity ratio of the copper dopant peak is lower in comparison with the host TiO_2 materials.

The XRD pattern of Cu-TiO_2 materials calcined at 700 °C showed that the diffraction peaks at the 2θ values of 25.4° represented diffraction peaks with Miller indices (101); diffraction peaks of 27.50° for (110), 36.70° for (103), 37.8° for (004), 48.06° for (200), 54.16° for (105) and 55° for (211) are major diffraction peaks for the anatase phase of TiO_2 materials for prepared 2%, and 4%. The XRD patterns showed the mixing of a few anatase phases and mainly rutile phases for 8% Cu-doped TiO_2 materials calcined at 700 °C. The XRD diffraction peaks of the copper crystal phase at 43.5° indicated the (111) plane of Cu for 8% Cu-doped TiO_2 materials calcined at 700 °C. At 700 °C, XRD results showed the mixing of the anatase phase and the rutile phase for Cu-TiO_2. Therefore, the phase transition temperature for Cu-doped TiO_2 was 700°C.

The XRD data of synthesized Cu-TiO_2 materials calcined at 800 °C clearly showed that the diffraction peaks at the 2θ values of approximately 27.50° represented Miller indices (110), 36.7° for (103), 37.8° for (004), 48.06° for (200), 54.16° for (105) and 55° for (211), which are major diffraction peaks for the rutile phase of TiO_2 materials. The XRD diffraction peaks of copper

crystal phase at 42.25° and 48.50° indicated the (200) and (202) planes of a metallic CuO plane, and 43.5° indicated the (111) plane of copper doping. Therefore, the pure rutile phases of Cu-TiO_2 materials with tetragonal crystal structures were obtained at calcined temperatures of 800 °C. According to the reported literature, the XRD patterns of anatase phases have a main diffraction peaks at 2θ value of 25.2° corresponding to the (101) plane while the main diffractions of rutile phases are at a 2θ values of 27.4° (110 plane) and 30.8° (121 plane), respectively (Sarteep *et al.*, 2016). The current research data on the synthesized Cu-TiO_2 materials were in good agreement with the reported literatures.

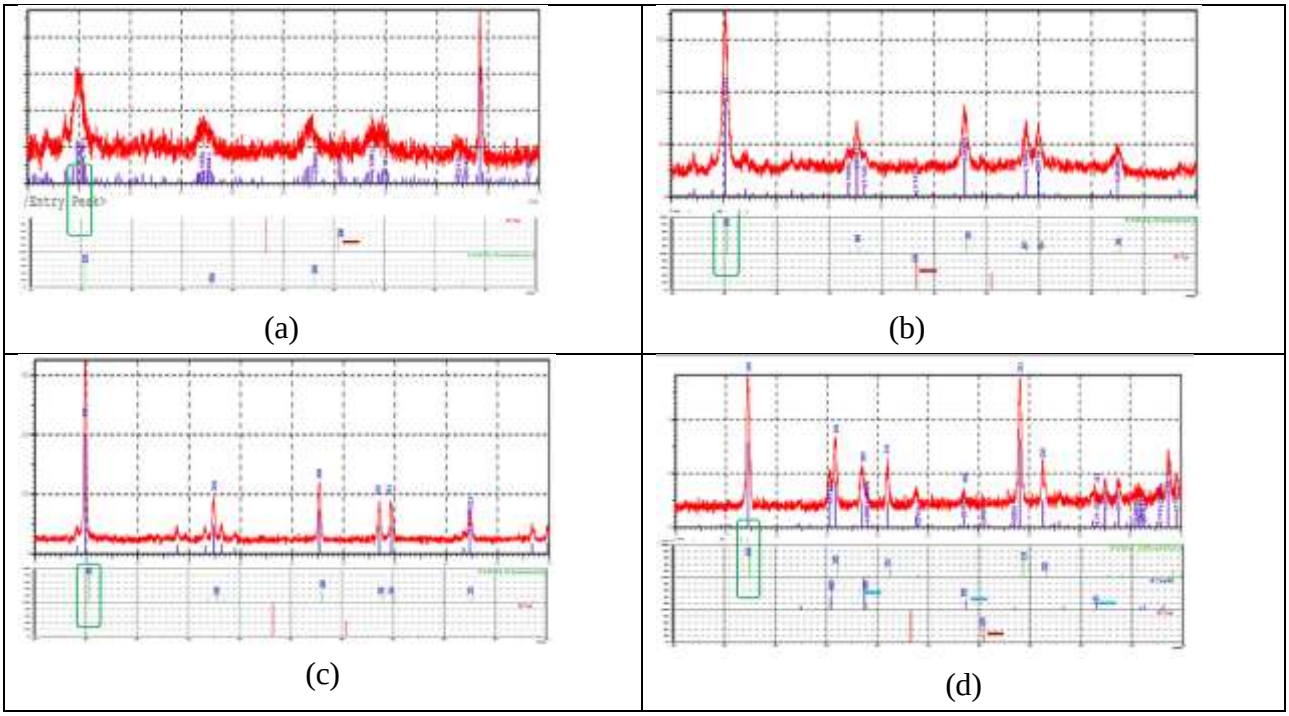

Figure 2. XRD patterns of prepared 2%Cu-TiO_2 materials calcined at (a) 500ºC, (b)600 ºC and (c) 700 ºC and (d) 800ºC

Table 2. XRD Characterization Data of Prepared 2% Cu-TiO_2 Materials at Different Calcined Temperatures

Calcined temperature (°C)	Average crystallite size (nm)		Lattice parameters (Axial length)			Crystal phase
	XRD	Calculated	a / Å	b / Å	c/ Å	
500	22.50	23.56	3.7850	3.7850	9.547	Anatase
600	25.60	25.78	3.7723	3.7723	9.5260	Anatase
700	33.75	34.17	3.7807	3.7807	9.5039	Anatase
800	40.80	40.37	4.579	4.579	2.9566	Rutile

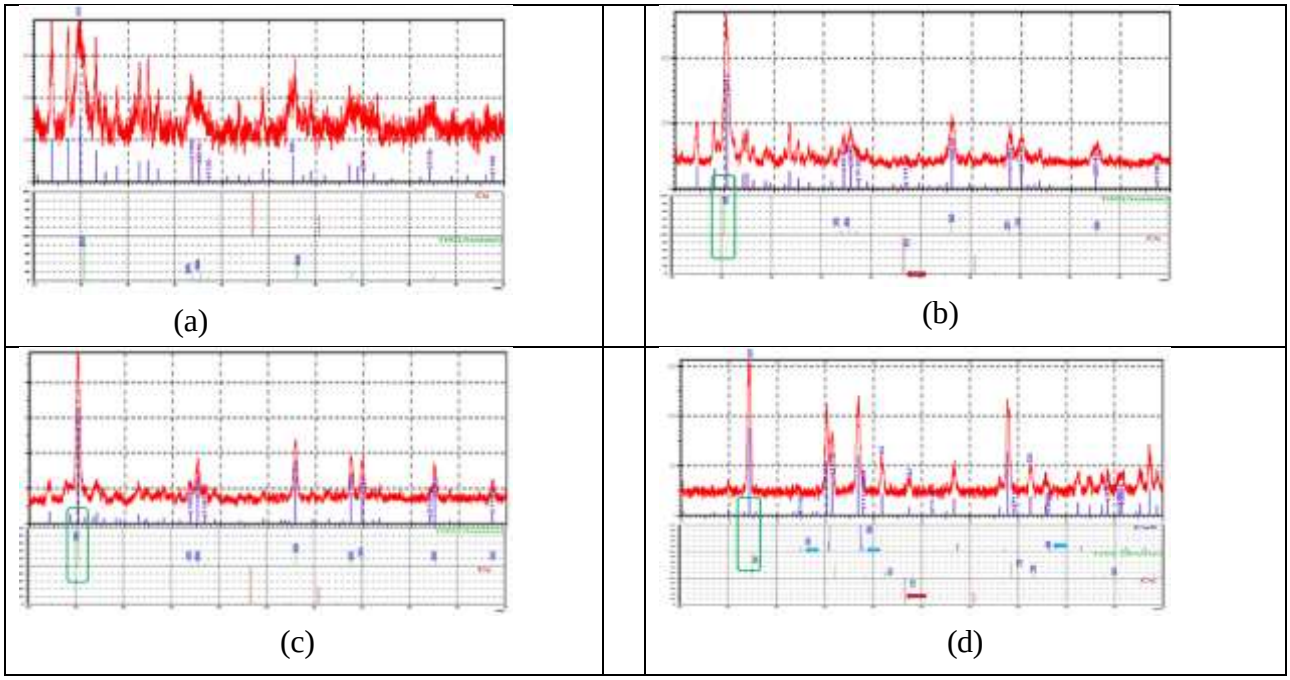

Figure 3. XRD patterns of prepared 4%Cu-TiO_2 materials calcined at (a) 500ºC, (b)600 ºC and (c) 700 ºC and (d) 800ºC

Table 3. XRD Characterization Data of Prepared 4% Cu-TiO_2 Materials at Different Calcined Temperatures

Calcined temperature (°C)	Average crystallite size (nm)		Lattice parameters (Axial length)			Crystal phase
	XRD	Calculated	a / Å	b / Å	c/ Å	
500	28.40	27.71	3.7829	3.7829	9.2569	Anatase
600	32.17	32.19	3.7760	3.7760	9.4860	Anatase
700	41.10	40.81	3.7845	3.7845	9.2559	Anatase
800	46.30	45.49	4.5746	4.5746	2.9478	Rutile

The average crystallite sizes of Cu-TiO_2 materials were in the range of 25.67 to 45.49 nm with a crystal structure of tetragonal in all prepared copper-doped TiO_2 materials, and it can also be proved that the prepared copper-doped TiO_2 materials can be confirmed as Cu-TiO_2 nanoparticles. According to the XRD data, the copper-doping process does not disturb the TiO_2 crystal network due to its transformation from anatase to rutile phase, indicating that the metal dopant is merely placed on the surface of the crystals without being covalently anchored into the crystal lattice (Nainani *et al*., 2012).

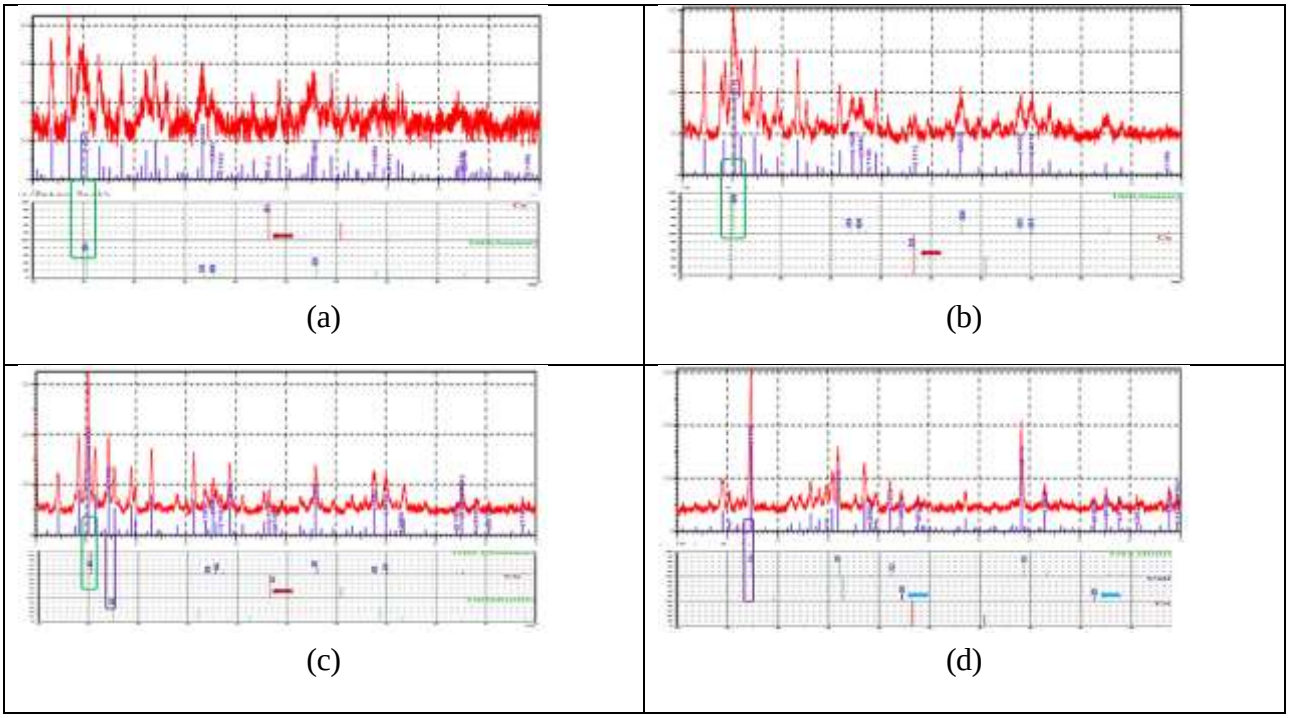

Figure 4. XRD patterns of prepared 8%Cu-TiO_2 materials calcined at (a) 500ºC, (b)600 ºC and (c) 700 ºC and (d) 800ºC

Table 4. XRD Characterization Data of Prepared 8% Cu-TiO_2 Materials at Different Calcined Temperatures

Calcined temperature (°C)	Average crystallite size (nm)		Lattice parameters (Axial length)			Crystal phase
	XRD	Calculated	a / Å	b / Å	c/ Å	
500	24.75	25.41	3.785	3.7850	9.547	Anatase
600	26.87	29.79	3.7380	3.7380	9.4462	Anatase
700	35.90	38.27	3.7845	3.7845	9.2559	Anatase & Rutile
800	42.70	42.15	4.5898	4.5898	2.9598	Rutile

Morphology of Synthesized TiO_2 and Cu-doped TiO_2 by SEM

The surface morphologies of TiO_2 and Cu-doped TiO_2 nanoparticles, calcined at 700 ºC and 800 ºC were investigated by SEM (Figure 5). SEM images of synthesized materials showed that all samples were polycrystalline and highly agglomerated. The agglomerations of doped materials seemed to be excessive compared to pure TiO_2.The copper doped TiO_2 materials consisted of finer particles but were different from TiO_2 materials. The distribution of Cu on the surface of TiO_2 materials is not uniform; there are irregularly shaped particles that are the aggregation of tiny crystals. Most of the particles were agglomerated and of irregular shape; some were tetragonal. The pure TiO_2 materials were large particles, and the copper-doped TiO_2 materials had a small and homogeneous distribution. The crystallite sizes of Cu doped TiO_2 nanoparticles were smaller than those of pure TiO_2 nanoparticles, which is in good agreement with the results of SEM screening of TiO_2 nanoparticles and copper-doped TiO_2 nanoparticles.

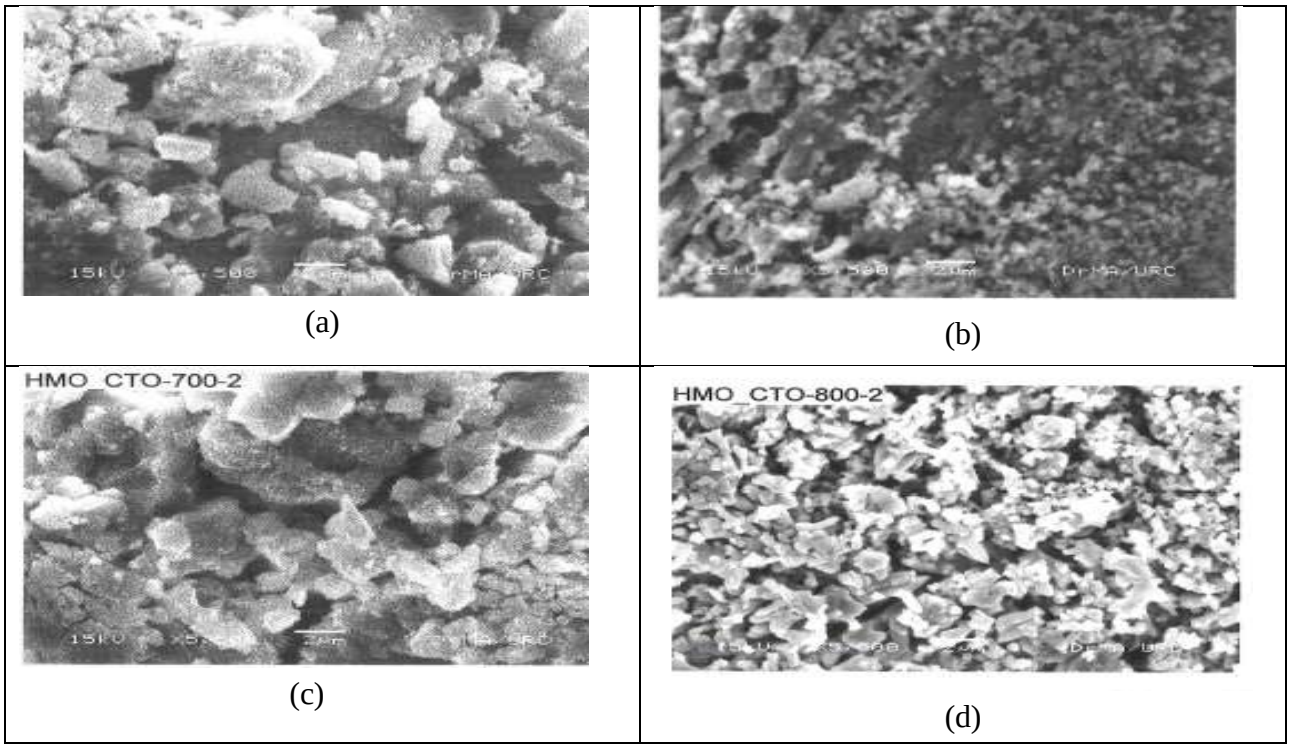

Figure 5. SEM images of (a) pure TiO_2 material calcined at 700 °C; (b) pure TiO_2 material calcined at 800 °C; (c) Cu- TiO_2 material calcined at 700 °C, and (d) Cu- TiO_2 material calcined at 800 °C

Evaluation of Elemental Composition by SEM-EDX and EDXRF

The elemental compositions of synthesized TiO_2 and Cu-doped TiO_2 materials were characterized by SEM-EDX and EDXRF techniques. The elemental compositions of TiO_2 and Cu-doped TiO_2 are shown in Figures 6 (a) and (b) and Table 5. According to the EDX results, the weight percents of Ti in TiO_2 and Cu-TiO_2 were 99.81 % and 63.92 %, respectively, and Cu in Cu-TiO_2 was 36.08 % at a calcination temperature of 800 °C. The relative abundance of elements and EDXRF spectra of Cu-TiO_2 are presented in Table 6 and Figure 7. From EDXRF analysis, the relative abundances of TiO_2 and CuO were 68.92% and 30.06 %, respectively. Therefore, the EDXRF spectrum confirmed the presence of copper dopant in Cu-TiO_2.

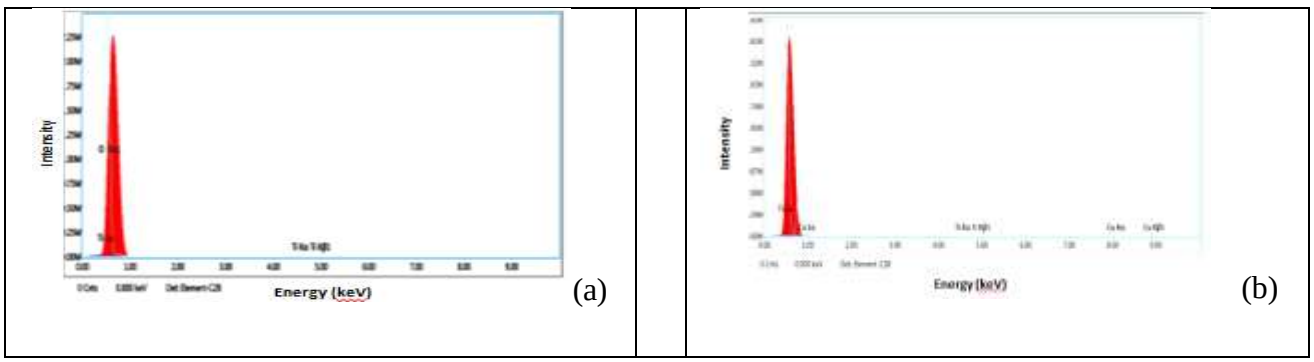

Figure 6. EDX spectrum of prepared (a) pure TiO_2 and (b) Cu-TiO_2 nanoparticles calcined at 800ºC

Table 5. EDX data of Prepared TiO_2 and Cu-Doped TiO_2 Nanoparticles calcined at 800 ºC

Element	Weight (%)	
	TiO_2	Cu-TiO_2
Cu	-	36.08
Ti	99.81	63.92

Table 6. Relative Abundance of the Elements of Cu-Doped TiO_2 Nanoparticles by EDXRF at 800 ºC

Elements in oxide form	Relative Abundance(%)
TiO_2	68.92
CuO	30.06
SiO_2	0.83
CaO	0.09
NiO	0.07
Rb_2O	0.01

Figure 7. EDXRF spectrum of prepared Cu Doped TiO_2 nanoparticles calcined at 800 ºC

Conclusion

The Cu-doped TiO_2 nanoparticles were successfully synthesized by sol-gel method and the effect of copper doping on TiO_2 was examined at different temperatures (500 ºC to 800 ºC). The pure TiO_2 nanoparticles calcined at 700 ºC showed 100 % rutile phase, and the Cu-TiO_2 nanoparticles showed pure rutile phase at 800 ºC. The tetragonal crystal network of TiO_2 did not change due to the copper doping process. Moreover, XRD analysis showed that the phase transformation temperature of pure TiO_2 was 600 ºC and that of Cu-TiO_2 nanoparticles was approximately 700 ºC. According to the XRD data, the average crystallite sizes of Cu-TiO_2 nanoparticles was smaller than that of pure TiO_2 nanoparticles. The surface morphology of Cu-TiO_2 nanoparticles showed that the majority of particles were agglomerated and irregular in shape; some were tetragonal in shape. The EDX spectrum confirmed that Cu ions were successfully doped into the TiO_2 host structure.

Acknowledgements

The authors would like to express profound gratitude to the Department of Higher Education, Ministry of Higher Education, Yangon, Myanmar, for providing the opportunity to do this research and Myanmar Academy of Arts and Science for allowing to present this paper.

References

Ahmed, H. A. R. (2015)."Preparation and Characterization of Copper-Doped and Silver-Doped Titanium Dioxide Nano-Catalysts for Photocatalytic Applications". Thesis. United Arab Emirates: Department of Mechanical Engineering, United Arab Emirates University, P. 163

Byrne, C., L. Moran, D. Hermosilla, N. Merayo, A. Blanco, S. Rhatigan, S. Hinder, P. Ganguly, M. Nolan, and S.C. Pillai. (2019). "Effect of Cu Doping on the Anatase to Rutile Phase Transition in TiO_2 Photocatalysts: Theory and Experiments". *Applied Catalysis B: Environmental,* vol.244, pp. 266-276

Fisher, M. B., D. A. Keane, S.J.M Guigan P. Fernandez-Ibanez, J. Colreavy, S.J.Hinder, K.G.. McGuigan, and S. C. Pillai. (2013). "Nitrogen and Copper Doped Solar Light Active TiO_2 Photocatalysts for Water Decontamination". *Applied Catalysis B: Environmental*, vol.130-131, pp. 8- 13

Hanaor, D. A., and C. C. Sorrell. (2011). "Review of the Anatase to Rutile Phase Transformation". *Journal of Mater. Sci*, vol.46(4), pp.855-874

Nainani, R., P. Thakur, and M. Chaskar. (2012). " Synthesis of Silver Doped TiO_2 Nanoparticles for the Improved Photocatalytic Degradation of Methyl Orange", *Journal of Materials Science and Engineering*, vol. B 2 (1), pp.52-58

Sarteep, Z., A. E. Pirbazari, and M. A. Aroon. (2016). "Silver Doped TiO_2 Nanoparticles: Preparation, Characterization and Efficient Degradation of 2, 4-dichlorophenol Under Visible Light", *J. Water Environ. Nanotechnol*, vol.1(2), pp.135-144

Yoong, L., F. K. Chong, and B. K. Dutta. (2009). "Development of Copper Doped TiO_2 Photocatalyst for Hydrogen Production under Visible Light". *Energy*, vol. 34, pp.1652-1661

STUDY ON PHYTOCHEMICAL CONSTITUENTS AND SOME BIOLOGICAL ACTIVITIES OF THE ROOT OF *EURYCOMA LONGIFOLIA* JACK

Cho Cho Win[1], Khin Chaw Win[2], Myint Myint Khine[3], Ni Ni Than[4]

Abstract

Eurycoma longifolia Jack is a plant species that belongs to the Simaroubaceae family, and it is also known locally as Bittu Bark in Myanmar, Piak and Tung Saw in Thailand, and Tongkat Ali in Malaysia. The objective of this study was to evaluate the phytochemical constituents and some biological activities of root of *E. longifolia*. The phytochemical constituents were investigated by the test tube and TLC profiling methods. Some biological activities such as antimicrobial, antioxidant, and cytotoxicity activities were determined by using the Agar Well Diffusion method, DPPH assay and Brine shrimp lethality bioassay**.** The antioxidant activity of ethanol extract (IC_{50} = 204.4 µg/mL) was shown to be more potent than watery extract (IC_{50} = 765.1 µg/mL) of *E. longifolia* root. The ethyl acetate extract of the sample was found to have more potent antimicrobial activity against all eight tested microorganisms in the inhibition zone diameter range (24 -32 mm) than those of ethanol, methanol, and watery extracts. Moreover, the cytotoxic effect of ethanol extract (LC_{50} = 233.35 µg/mL), which showed substantial toxicity was slightly more toxic than the positive control of standard potassium dichromate (LC_{50} = 244.46 µg/mL).

Keywords: *Eurycoma longifolia* Jack, antioxidant activity, antimicrobial activity, cytotoxicity

Introduction

Traditional medicine has employed medicinal plants to treat a variety of ailments. However, using these herbs improperly can have negative side effects. Therefore, it is necessary to conduct scientific research to investigate the pharmacological characteristics of diverse plants. One of the most well-liked medicinal herbs in Southeast Asia, *E. longifolia*, also known as Tongkat ali in Malaysia and locally, Bittu Bark in Myanmar, was the subject of this study. It is a member of the family Simaroubaceae. It is a tall, slender tree that resembles a shrub and grows in sandy soil. It has pinnately shaped compound leaves that are green in colour. The leaves have smooth edges and are opposite or subopposite, lanceolate to ovate-lanceolate. The blooms are small, unisexual, reddish, and tightly packed. When ripe, the ovoid fruits turn a dark reddish brown colour (Keng, 1978). More practical formulations, including additives blended with tea and coffee, have recently been available. Its main constituents include terpenoids, alkaloids, and quassinoids. Pharmacological testing on *E. longifolia* has demonstrated that it has anti-malarial, anticancer, anti-inflammatory, and other properties (Shaheed *et al*., 2016).

The imbalance between reactive oxygen and nitrogen RON species synthesis and antioxidant defence leads to oxidative stress. Oxidative stress is linked to ageing and a number of illnesses, including cancer and chronic obstructive pulmonary disease (Hassan, 2015). The main goal of this study is to identify some biological processes, such as antioxidants related to lowering oxidative stress and antimicrobial activity to treat infectious disorders and food poisoning caused on by consuming foods infected by pathogenic bacteria.

[1] Department of Chemistry, University of Yangon
[2] Department of Chemistry, Yangon University of Distance Education
[3] Pathein University
[4] Department of Chemistry, University of Yangon

Figure 1. Photographs of plant and roots of ***Eurycoma longifolia*** **Jack**

Materials and Methods

Collection of Sample

The sample was collected from Dawei Township, Tanintharyi Region, Myanmar in October, 2021. Then, the sample was authenticated at the Department of Botany, University of Yangon. The collected sample was washed with water and air dried as shown in Figure 1. The dried roots were then ground into a powder using a grinding machine. The powdered sample was stored in an air-tight container to prevent moisture changes and other contaminations.

Chemicals

Methanol, ethanol, ethyl acetate, 2,2-diphenyl-1-picryhydrazyl (DPPH), potassium dichromate, sodium hydroxide, caffeine, distilled water, Trypticase soy broth from Difco U.S.A, Muller Hinton agar (Hi-Media) and triple sugar iron from Becton, U.S.A,

Instruments

Quartz cuvette (4 mL), UV-visible spectrophotometer (UV-7504), a shaker, an autoclave (Tomy Seiko Co., Ltd, Tokyo, Japan), petri dish, spirit burner, polyethylene plastic bag, a refrigerator and an incubator

Preparation of Extracts

About 50 g of dried powdered samples of roots of ***Eurycoma longifolia*** was extracted by using appropriate solvents (EA, EtOH and MeOH) and sonicating the samples three times in 1000 mL of each solvent for 1 h. The filtrate was concentrated in a rotatory evaporator to obtain the extracts.

Preparation of Watery Extract

A watery extract of the dried powdered sample was obtained by boiling 20 g of sample with 300 mL of distilled water for about 30 min on a hot plate, and it was filtered. Then, the filtrate was concentrated by evaporation on a hot plate.

Preliminary Phytochemical Tests

Preliminary phytochemical tests were performed by using a reported method. A preliminary phytochemical investigation was used to classify phytoconstituents embedded in the samples, through a reported method (M-Tin Wa, 1972; Trease and Evans, 1980; Shriner *et al*., 1980).

Phytochemical Investigation by TLC Profiling

A sample was prepared by diluting the crude extract of methanol and then applying usually 1-10 μL volumes to the origins of a TLC plate, 2 cm above its bottom, using capillary tubes. After

the application of the sample on the plate, the plates were kept in a TLC glass chamber (solvent saturated). And then, the mobile phase was allowed to move through the adsorbent phase up to the plate. TLC was performed for the presence of alkaloids, coumarins, phenols, steroids, and terpenoids.

In Vitro Antioxidant Activity by DPPH Free Radical Scavenging Assay

Preparation of DPPH solution

DPPH (4.732 mg) was completely dissolved in ethanol (100 mL). The prepared solution was placed in the brown reagent bottle and was stored in the refrigerator for no more than 24 h.

Determination of antioxidant activity

Using a DPPH radical scavenging test, the antioxidant activity of ethanol and watery extracts was evaluated (Marinova and Batchvaro, 2011). First, a stock solution was made by mixing 20 mg of each extract with 20 mL of ethanol. After that, this stock solution was serially diluted at five different concentrations (1000, 500, 250, 125, and 62.5 µg/mL). An oxidant was a solution of 4 mg of DPPH in 100 mL of ethanol. Ascorbic acid, which possesses strong antioxidant properties, was used as a positive control. After that, 1.5 mL of the tested sample solution and 1.5 mL of the DPPH solution were combined and incubated for 30 min. Then, the absorbance was measured spectrophotometrically at 517 nm in triplicate. The following equation was used to determine the amount of inhibition of the DPPH free radical:

$$\% \text{ RSA} = \frac{A_{DPPH} - (A_{\text{sample}} - A_{\text{blank}})}{A_{DPPH}} \times 100$$

Where, % RSA = % radical scavenging activity
A_{DPPH} = absorbance of DPPH in EtOH solution
A_{sample} = absorbance of sample and DPPH solution
A_{blank} = absorbance of sample and EtOH solution

Screening of Antimicrobial Activity of the Sample by Agar Well Diffusion Method

By using the agar well diffusion method, the antimicrobial activity of four crude extracts from the roots of *E. longifolia* Jack was assessed against eight strains of microorganisms, including *Agrobacterium tumefaciens*, *Bacillus pumilus*, *Bacillus subtilis*, *Staphylococcus aureus*, *Pseudomonas fluorescens*, *Micrococcus luteus*, C*andida albicans*, and *Escherichia coli* at Chemistry Department Pathein University's.

Determination of Antimicrobial Activity by Agar Well Diffusion Method

The Agar Well Diffusion method was used for antimicrobial evaluation. Firstly, the tested microorganisms were inoculated in Muller Hinton Broth at 37 °C for overnight. On the next day, the overnight broth culture was diluted with normal saline. Muller Hinton agar plates were prepared and sterilized by autoclaving at 121°C for 15 min. The broth inoculums were evenly spread out with sterile cotton swabs on the agar plates to obtain the uniform inoculum. After the plates were inoculated, 8 mm diameter wells were made on the agar medium by using a sterile cork. The wells were then filled with the respective extract solutions with the concentration (100 mg per 1 mL). The antimicrobial agent diffuses in the agar medium and inhibits the growth of the microbial strain tested. Plates were incubated for 24 h to allow diffusion through the agar medium to form zones of inhibition (Perez, *et al*, 1990).

Determination of Cytotoxicity Activity

Sample solutions and solutions of standard potassium dichromate and caffeine were made up at various concentrations between 50 and 800 µg/mL. Separate clean vials were filled with sample solutions corresponding to 50, 100, 200, 400, and 800 µg/mL. Each vial was filled with a mixture of 9 mL of artificial seawater and 1 mL of a sample at various concentrations. Ten live brine shrimp nauplii were put into each vial by using a Pasteur pipette. For control solutions, a similar procedure was used. All vials were incubated for 24 h at room temperature with light. In control and test vials, the number of shrimp that survived was counted, and median lethal concentrations (LC_{50}) were computed using the Microsoft Excel programme (Meyer *et al*., 1982).

Results and Discussion

Phytochemical Constituents of *E. longifolia* Jack Root

The phytochemical screening of *E. longifolia* was preliminarily done by the test tube methods. Alkaloids, α-amino acids, carbohydrates, glycosides, organic acids, phenolic compounds, reducing sugars, saponins, starch, steroids, flavonoids, and terpenoids were found in the root of *E. longifolia*, whereas tannins, and cyanogenic glycosides were absent. From TLC profiling of methanol extract, the classes of phytochemical constituents, such as alkaloids, terpenoids, steroids, phenolic compounds, and coumarins, are found to be present.

***In vitro* Antioxidant Activity of Crude Extracts from Root of *E. longifolia* Jack by DPPH Free Radical Scavenging Activity**

Antioxidant activity of ethanol and watery extracts from root of *E. longifolia* was evaluated by DPPH free radical scavenging activity. This activity was used to determine antioxidant activity based on the scavenging activity from the donation of hydrogen or radicals by using stable DPPH in the absorbance at 517 nm. In this study, the IC_{50} values of ethanol and watery extracts were 204.4 μgmL^{-1} and 765.1 μgmL^{-1} while ascorbic acid showed 4.4 μgmL^{-1}. Among the two extracts, the ethanol extract showed higher antioxidant activity than the water extract. The results, showed antioxidant activity in order to reduce oxidative stress in the body based on these relationships. These results are shown in Tables 1and 2 and Figures 2 and 3.

Table 1. Average % Radical Scavenging Activity and IC_{50} Values of Crud Extracts from the Root of *E. longifolia* Jack

Extracts	% RSA ± SD at Different Concentration (µg/mL)					IC_{50} (µg/mL)
	62.5	125	250	500	1000	
(Ethanol extract)	33.23± 3.39	39.82± 1.82	55.83± 1.12	70.50± 0.38	91.42± 1.47	204.4
(Watery extract)	31.58± 0.15	33.38± 0.26	37.87± 0.62	44.90± 1.26	54.49± 2.96	765.1

Table 2. % RSA (Radical Scavenging Activity) of Standard Ascorbic Acid

Sample	% RSA ± SD at Different Concentration (µg/mL)					IC_{50} (µg/mL)
	1.25	2.5	5	10	20	
Ascorbic acid	23.67± 1.26	27.39± 0.15	55.4± 0.82	87.43± 1.38	96.16 ± 0.00	4.4

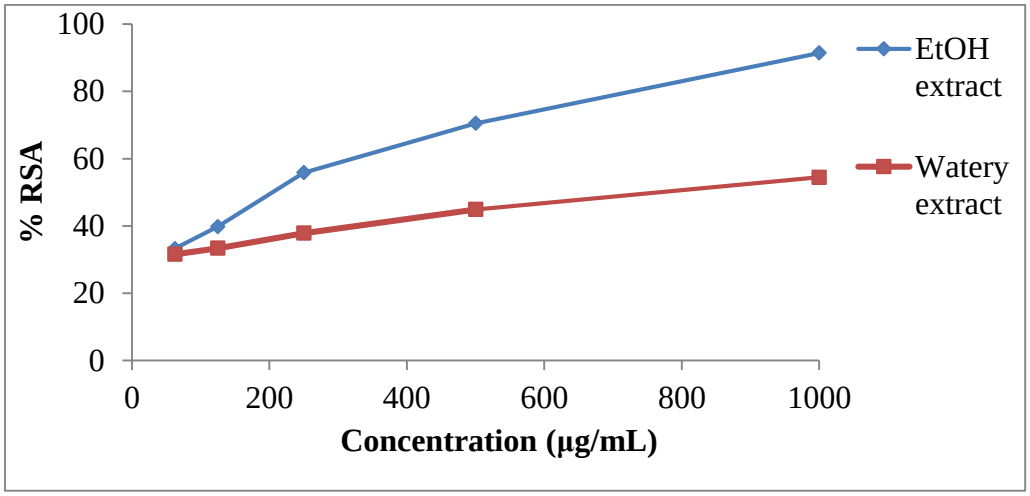

Figure 2. DPPH free radical scavenging activities of crude extracts of *E. longifolia* Jack at different concentrations

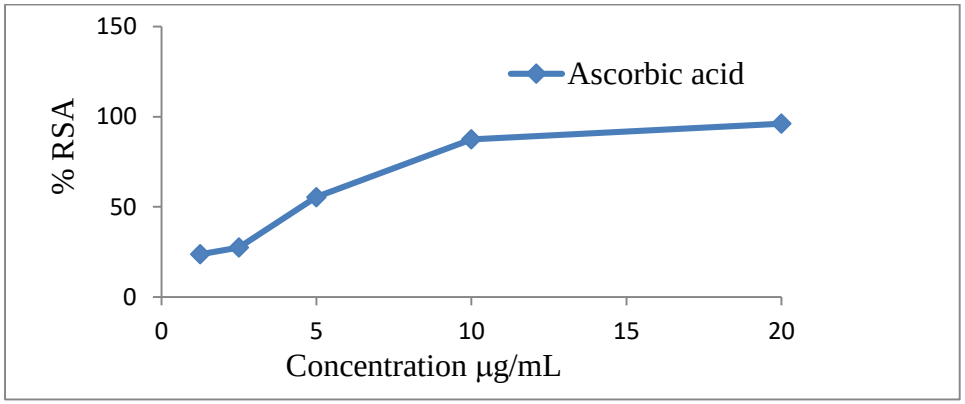

Figure 3. DPPH free radical scavenging activities of standard ascorbic acid

Antimicrobial Activity of Crude Extracts of *E. longifolia* Jack Root

The diameter of the inhibition zone including the well diameter (8 mm) was measured to determine the antimicrobial activity. In this study, three Gram negative bacteria (*A. tumefacies, P. fluorescens, and E. coli*), four Gram positive bacteria (*B. subtilis, B. pumilus, M. luteus, and S. aureus*), and the fungus *C. albicans* were evaluated against four extracts (EtOAc, EtOH, MeOH, and aqueous) of *E. longifolia* Jack. The activity of the examined microorganisms increased with increasing inhibition zone diameter. The results showed that all of the extracts had potent antimicrobial activity, with inhibition zone diameter varying from 18 to 32 mm on all tested microorganisms. On five of the tested microorganisms (*A. tumefacies*, *B. pumilus*, *B. subtilis*, *C. albicans*, *S. aureus*), the activity of the EtOAc extract was more potent than the positive controls (chloramphenicol and nystatin), comparable to two of the tested microorganisms (*E. coli*, *M.luteus*) and less potent than one of the tested microorganisms (*P. fluorescens*). On the seven tested bacteria, the ethanol and methanol extracts of *E. longifolia* Jack root showed the maximum activity, while

the watery extract displayed the highest activity on four selected microorganisms. These results are shown in Figures 4 and 5, and Table 3.

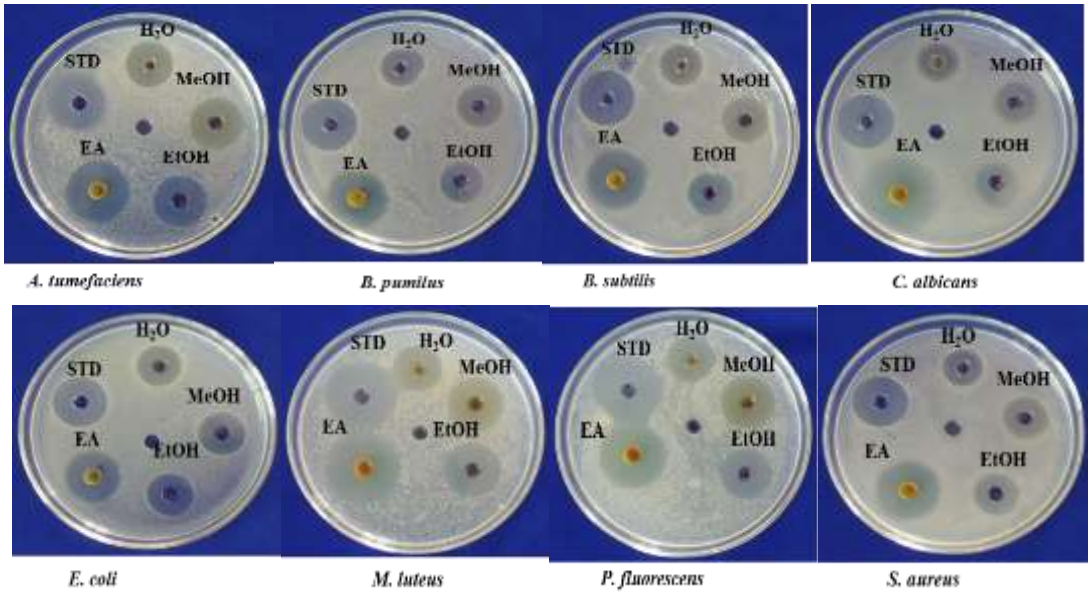

Figure 4. Screening of antimicrobial activities of the root of *E. longifolia* Jack

Table 3. Inhibition Zone Diameter of the Root of *E.longifolia* Jack Against Eight Different Microorganisms

Extracts	Inhibition Zone Diameter (mm) against eight microorganisms							
	A. tumefacies	***B. pumilus***	***B. subtilis***	***C. albicans***	***E. coli***	***M. luteus***	***P. fluorescens***	***S. aureus***
Watery	21(+++)	18(++)	19(++)	19(++)	21(+++)	21(+++)	20(+++)	19(++)
MeOH	23(+++)	21(+++)	21(+++)	19(++)	21(+++)	24(+++)	24(+++)	20(+++)
EtOH	24(+++)	20(+++)	21(+++)	19(++)	21(+++)	25(+++)	22(+++)	20(+++)
EtOAc	27(+++)	26(+++)	26(+++)	32(+++)	24(+++)	30(+++)	29(+++)	26(+++)
*STD	25(+++)	25(+++)	25(+++)	-	24(+++)	30(+++)	31(+++)	24(+++)
**STD				24(+++)				

Diameter of agar well = 8 mm
(-) no activity
(+) 9 mm ~ 14 mm, Low activity
(++) 15 mm ~ 19 mm, medium activity
(+++) 20 mm above, high activity

***STD = chloramphenicol for bacteria**
****STD = nystatin for fungus**

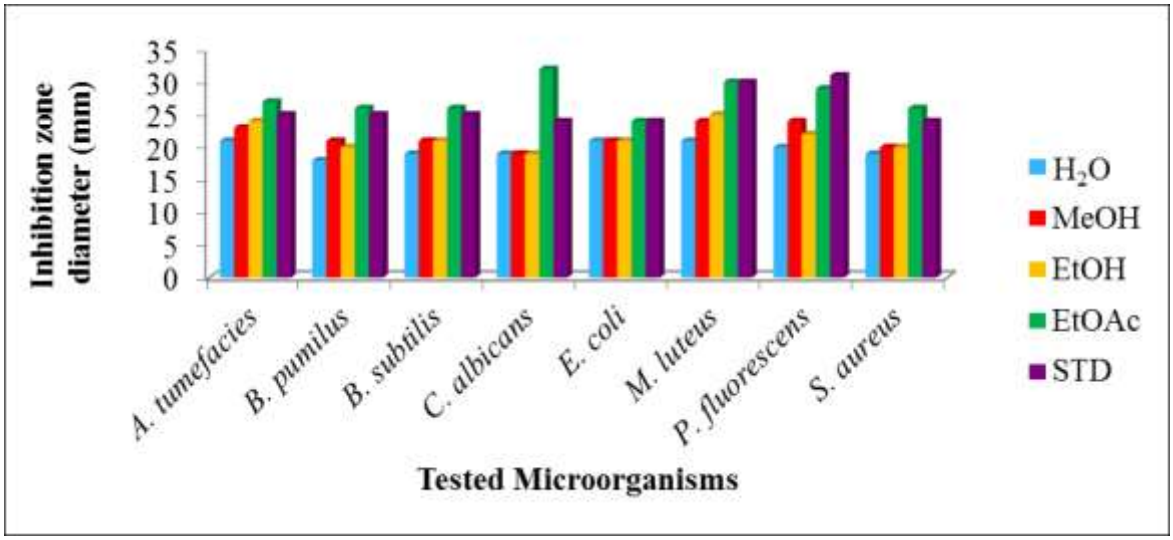

Figure 5. Inhibition zone diameters for crude extracts of root of *E. longifolia* Jack

Investigation of Cytotoxicity Activity of the Root of *E. longifolia* Jack by Brine Shrimp Lethality Bioassay

By using a brine shrimp lethality test, the cytotoxicity of ethanol and watery extract of the root of *E. longifolia* Jack was evaluated. The ethanol extract of the root of *E. longifolia* Jack was found to be an LC_{50} value of 233.35 µg/mL, while the watery extract was a value of 254.42 µg/mL. In comparison to the two extracts, the ethanol extract showed greater toxicity. The LC_{50} value of the ethanol extract was 233.35 µg/mL, which was significantly more toxic than the positive control of standard potassium dichromate (244.46 g µg/mL), which also showed substantial toxicity. These results are shown in Table 4 and Figure 6.

Table 4. Results of Cytotoxicity on Ethanol and Watery Extracts of Roots of *E.longifolia* Jack (Myanmar)

Sample	Death % of Brine Shrimp in Various Concentrations (µg/mL)					
	50	**100**	**200**	**400**	**800**	**LC_{50}**
EtOH	6.67 ±0.57	23.33 ±0.57	43.33 ±0.57	83.33 ±0.57	100 ±0.00	233.35
Watery	13.33 ±1.15	23.33 ±0.57	33.33 ±0.57	70.00 ±1.00	96.67 ±0.57	254.42
*$K_2Cr_2O_7$	23.33 ±0.57	33.33 ±0.57	43.33 ±0.57	73.33 ±1.15	96.67 ±0.57	244.46
**Caffeine	0.00	0.00	6.67±0.82	16.67±0.94	30±0.47	>1000

*positive control = $K_2Cr_2O_7$ ** negative control = Caffeine

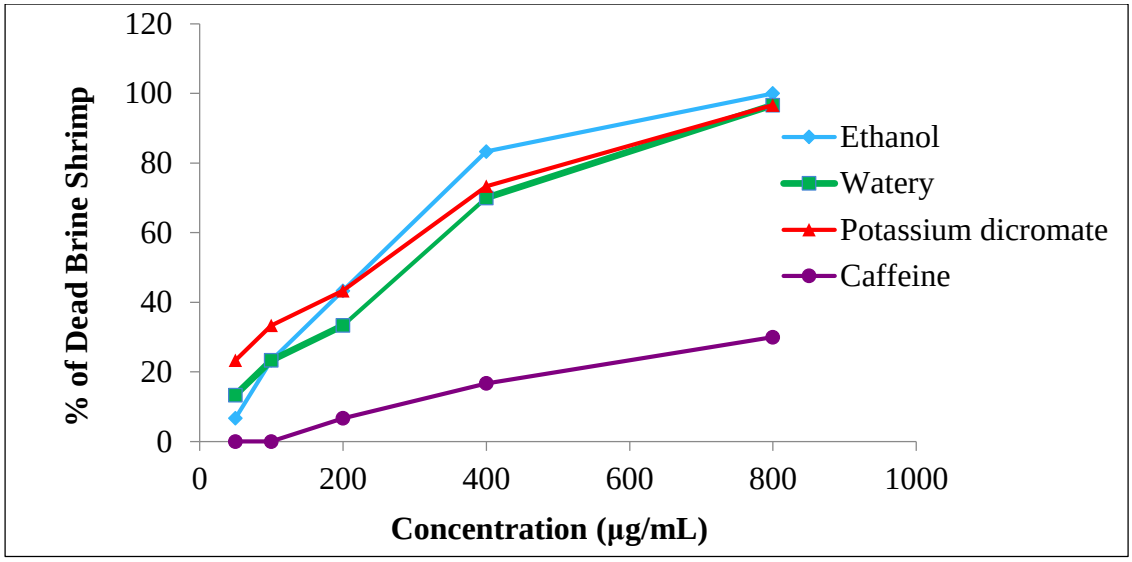

Figure 6. Cytotoxic activity of *E. longifolia* Jack root

Conclusion

From the overall assessment of the chemical investigation into the root of *E. longifolia*, the following inferences could be concluded. The preliminary phytochemical tests revealed the presence of alkaloids, α-amino acid, carbohydrate, glycoside, organic acid, phenolic compounds, saponin, starch, steroid, flavonoids and terpenoids, but the absence of cyanogenic glycoside, and tannins in the root of ***E. longifolia*** Jack. From the DPPH radical scavenging assay, the ethanol extracts (91.42 ± 1.47) µg/mL showed higher antioxidant activity than watery extract (54.49 ± 2.96) µg/mL on the concentration of 1000 µg/mL. And then**,** all of the extracts showed potent antimicrobial activity, with inhibition zone diameters ranging from 18 to 32 mm on the all tested microorganisms. Among these extracts, EtOAc extract exhibited higher potency than positive control (chloramphenicol, nystatin) on five tested microorganisms, similar to two tested microorganisms and weaker than one tested microorganism. These results suggest that ethyl acetate fraction would be potential to be used for isolation of bioactive constituents. Moreover, the present study on cytotoxic activity also indicated that the LC_{50} values of ethanol (233.35 µg/mL) and watery extract (254.42 µg/mL) were significantly cytotoxic in comparison with positive control standard potassium dichromate solution (244.46 µg/mL). Thus, the extracts of this plant will be reliable for the treatment of numerous antioxidant - related diseases and many other diseases because of its cytotoxicity activity. According to these findings, the extracts of *E. longifolia* Jack root (Myanmar) will be effective in the treatments of a variety of disorders including bacterial infections, inflammation and cancers**.**

Acknowledgements

The authors gratefully acknowledge the Department of Higher Education (Lower Myanmar), the Ministry of Education, Myanmar, and the Myanmar Academy of Arts and Sciences for providing the opportunity to read this paper.

References

Hassan, W. N. A. W., R. M. Zulkifli, F. Ahmad, and M. A. C. Yunus. (2015). "Antioxidant and Tyrosinase Inhibition Activities of *Eurycoma longifolia* and *Swietenia macrophylla*". *Journal of Applied Pharmaceutical Science*, vol. 5 (8), pp. 6-10

Keng, H. (1978). *Orders and Families of Malayan Seed Plants*. Singapore: Singapore University Press

Marinova, G., and V. Batchvarov. (2011). "Evaluation of the Methods for Determination of the Free Radical Scavanging Activity by DPPH". *Bulgarian Journal of Agricultural Science*, vol. 17(1), pp. 11-24

Meyer, B., N. Ferrigni, J. Putnam, L. Jacobsen, D. Nichols, and J. Melaughlin. (1982). Brineshrimp: A Convenient General Bioassay for Active Plant Constituents. *Planta Med*. vol. 45, pp. 31- 34

M-Tin Wa. (1972). "Phytochemical Screening, Methods and Procedures". *Phytochemical Bulletin of Botanical Society of America*, vol. 5(3), pp. 4-10

Perez, C., M. Paul, and P. Bazerque. (1990). "Antibiotic Assay by Agar Well Diffusion Method". *Alta BioMed Group Experiences*, vol. 15, pp. 113-115

Shaheed, U. R., C. Kevin, and H. Y. Hye. (2016). "Review on Traditional Herbal Medicine, *Eurycoma Longifolia* Jack (Tongkat ali): Its Traditional and Uses, Chemistry, Evidence-Based Parmacology and Toxicology". *Molecules*, vol.21(331), pp. 1-31

Shriner, R.L., R.C. Fuson, D.Y. Curtin and T.C. Morrill. (1980). *The Systematic Identification of Organic Compounds*. A Laboratory Manual, New York, John Wiley and Sons

Trease, G.E., and W.C. Evans. (1980). *Pharmacognosy*. London: 1st Ed., Spottiswoode Ballantyne and Co Ltd., pp. 108, 529

SYNTHESIS AND CHARACTERIZATION OF ZINC SULPHIDE QUANTUM DOTS

Aye Mya Phyu [1], Yi Yi Myint [2]

Abstract

Zinc sulphide quantum dots (QDs) have been synthesized by the hydrothermal method. In this method, zinc acetate $Zn(CH_3CO_2)_2$ and sodium sulphide nonahydrate $Na_2S.9H_2O$ were used as starting materials. Glacial acetic acid was used to adjust the selected pH values of the system (pH=4, 5, and 6), and ammonia solution was used to obtain the pH values of the system (pH=8, 9, and 10). The synthesized ZnS QDs were characterized by using X-ray Diffraction Analysis (XRD), Fourier Transform Infrared Spectroscopy (FT IR), and UV-Visible Spectroscopy. The crystallite size range (8-13 nm) of the synthesized ZnS QDS was determined from the results of the XRD patterns by using Debye-Scherrer's equation. From the FT IR spectrum, a metal-sulphur bond (Zn-S) was found at 639 cm^{-1}. UV/Vis spectra indicated the absorption wavelengths of ZnS QDs at 270 nm.

Keywords: Quantum dots, hydrothermal method, zinc sulphide, Debye-Scherrer's equation

Introduction

Quantum dots are small, fluorescent nanocrystals that are < 10 nm in diameter (Suri *et al*., 2013). Quantum dots are generally constructed from elements of Groups II (e.g., Zn, Cd), -IV (e.g., Se, S), III-V, and IV-VI of the periodic table (Pawar *et al*., 2018). Quantum dots are semiconductor nanocrystals resistant to chemical degradation, high thermal stability, and optical properties (high brightness) (Grigore *et al*.,2017). Semiconductor nanocrystals of ZnS have been extensively studied for their quantum confinement effect, dielectric confinement effect, and unique size-dependent photoemission properties (Jothi *et al*., 2013). ZnS nanoparticles have attracted great interest because of their potential applications in field effect transistors, light emitting diodes, photocatalysis, solar cells, and biological sensors (Xue *et al*., 2011). The semiconducting quantum dots (QDs) have full access to the whole solar spectrum (Baruach *et al*., 2019). For ZnS nanoparticles, the band gap increases with the decrease in particle size, which results in a blue shift of the absorption oneset (Xue *et al*., 2011). Hydrothermal methods have been reported for the synthesis of QDS with small crystal size, a narrow distribution, good crystallinity, and high photoluminescence intensity (Bodo and Singha, 2016).

ZnS is highly suitable as a window layer in hetero-junction photovoltaic solar cells because the wide band gap decreases the window absorption loss and improves the short circuit current of the cell (Jothi *et al*., 2013). ZnS is a polymorphous material that exits in two crystalline forms, namely zinc blend (sphalerite) and Wurtzite. In both forms, the co-ordination geometry is at the Zn and S tetradedrals. Zinc blend has a more stable cubic form (fcc), whereas wurtzite has a hexagonal form (hcp). ZnS exhibits a large band gap of approximately 3.54 eV and 3.91 eV for zinc blend and wurtzite, respectively. Zinc blend has four asymmetric units in its unit cell, where wurtzite has 2. Nano ZnS possess anomalous physical and chemical properties such as an enhanced surface to volume ratio, the quantum size effect, the surface to volume effect, the macroscopic quantum tunnelling effect, more optical absorption, chemical activity and thermal resistance, catalysis, and a low melting point (Kaur *et al*., 2016).

[1] Department of Chemistry, Meiktila University
[2] Department of Educational Research, Planning and Training, Yangon

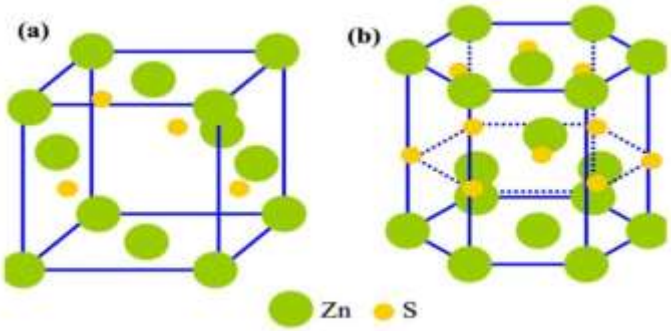

Figure 1. Crystalline structure of ZnS (a) cubic sphalerite and (b) hexagonal wurtzite (Kaur *et al.,* 2016)

Materials and Methods

Preparation of Zinc Sulphide Quantum Dots (ZnSQDs) by Hydrothermal Method

Firstly, 0.22 g of zinc acetate was dissolved in 120 mL of distilled water to get solution A. 0.4 g of sodium sulphide nonahydrate was dissolved in 20 mL of distilled water to obtain solution B. Solution A and solution B were mixed. Then glacial acetic acid solution was used to adjust the selected pH values of the system (pH = 4, 5, 6), and ammonia solution was used to obtain the pH values of the system (pH = 8, 9, 10).

The resultant solution was sonicated in the ultrasonic bath for 30 minutes. After sonication, the solution was transferred into a Teflon vessel, and then the vessel was put into a stainless steel tank to perform the hydrothermal treatment, which was placed in a vacuum oven at 140 °C for 24 h. Then it was cooled to room temperature. After cooling, the collected precipitates were washed several times with distilled water and ethanol until a neutral solution was obtained. And then it was allowed to stand for precipitation. The precipitates obtained were poured into the Petri dish and dried at room temperature for three days. Then the dried powder was placed in crucibles, and it was carried out under vacuum at 50 °C for 10 h.

In this way, 0.10410 g of dried sample (ZnS 8) of pH 8, 0.1145 g of dried sample (ZnS 9) of pH 9, 0.12183 g of dried sample (ZnS 10) of pH 10, 0.11028 g of dried sample (ZnS 4) of pH 4, 0.08351 g of dried sample (ZnS 5) of pH 5, and 0.11620 g of dried sample (ZnS 6) of pH 6 were obtained. The dried samples were used for further characterization.

Characterization of Prepared Zinc Sulphide Quantum Dots Powder by XRD, FT IR, and UV-Visible Analysis

XRD analysis

Powder x-ray diffraction (XRD) patterns were obtained by using a Rigaku Multiplex 2 kW, x-ray diffractometer with Cu-K_α radiation of wavelength 1.54056 Å.

FT IR analysis

The sample using (1% KBr) was first inserted separately in the sample holder (cassette). The KBr sample was then pressed into solid discs. Then, using air as a reference, each pellet was analyzed using a Perkin Elmer 1600 Fourier Transform Infrared Spectrometer (FT-IR) with a scan speed of 16 scans/sec from 400 to 4000 cm^{-1}. It was used to identify the functional groups present in the sample.

UV-Visible analysis

The samples were examined by a UV-Visible spectrophotometer for the absorption spectrum (λ_{max}).

Results and Discussion

Yield percent of ZnS quantum dots

Table 1 shows the yield percents of the prepared zinc sulphide quantum dots. The percent yield was calculated by using the formula,

$$\text{Yield (\%)} = \frac{\text{Actual Yield}}{\text{Theoretical Yield}} \times 100$$

Higher yield percentages were obtained at higher pH values. In this study, the highest yield percent of 99 was obtained using pH 10.

Table 1. Percent Yield of Zinc Sulphide Quantum Dots (Based on amount of zinc acetate)

No.	Nanoparticle (QDs)	Yield (%)
1	ZnS 4	85 %
2	ZnS 5	68 %
3	ZnS 6	85 %
4	ZnS 8	85 %
5	ZnS 9	85 %
6	ZnS 10	99 %

X-ray analysis

From X-ray analysis, XRD patterns and their respective data for ZnS quantum dots are shown in Figure 2 and Table 2 for ZnS 4, Figure 3 and Table 3 for ZnS 5, Figure 4 and Table 4 for ZnS 6, Figure 5 and Table 5 for ZnS 8, Figure 6 and Table 6 for ZnS 9, and Figure 7 and Table 7 for ZnS 10.

In each XRD pattern, the most intense peak was found along the plane (111), with the d-spacing about 3.16 Å at a 2θ value of 28°, indicating the orientation of the majority of the nano-crystallites along this axis. Other prominent peaks were found for the plane (220), with the d-spacing 1.92 Å at a 2θ value of 47° and the plane (311), with the d-spacing 1.64 Å at a 2θ value of 56°. All the peaks are well matched with the standard peaks from the library. It is also noticed that there are either no extra or any impurity phases evident in ZnS samples, indicating that the prepared samples are single-phase with high purity.

The broadened peaks indicated the smaller particle size of the sample. The average crystallite sizes of the quantum dots are calculated by Debye Scherrer's formula, $D = \frac{K\lambda}{\beta \cos\theta}$, where D is the average crystallite size in nm, K is proportionally constant, λ is the wavelength of incident x ray (1.54056 Å), β is the full width at halt maximum (FWHM), and θ is the Bragg angle. The average crystallite sizes were calculated to be 8.65 nm for ZnS 4, 8.30 nm for ZnS 5, 7.9 nm for ZnS 6, 9.10 nm for ZnS 8, 8.30 nm for ZnS 9, and 12.40 nm for ZnS 10.

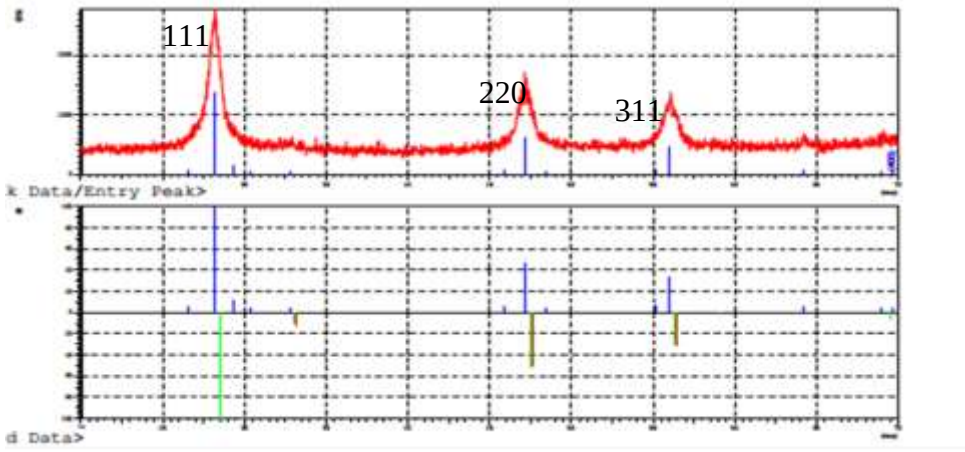

Figure 2. XRD diffraction pattern of prepared ZnS 4

Table 2. X-ray Diffraction Peaks Data of Prepared ZnS 4

No.	2θ (°)	d (Å)	FWHM (°)	Crystallite size (Å)	Crystallite size (nm)	Miller indices (h k l)
1	28.1826	3.16387	0.90360	90.6	9.06	111
2	47.1609	1.92558	1.04930	82.5	8.25	220
3	56.0257	1.64009	1.04000	86.4	8.64	311

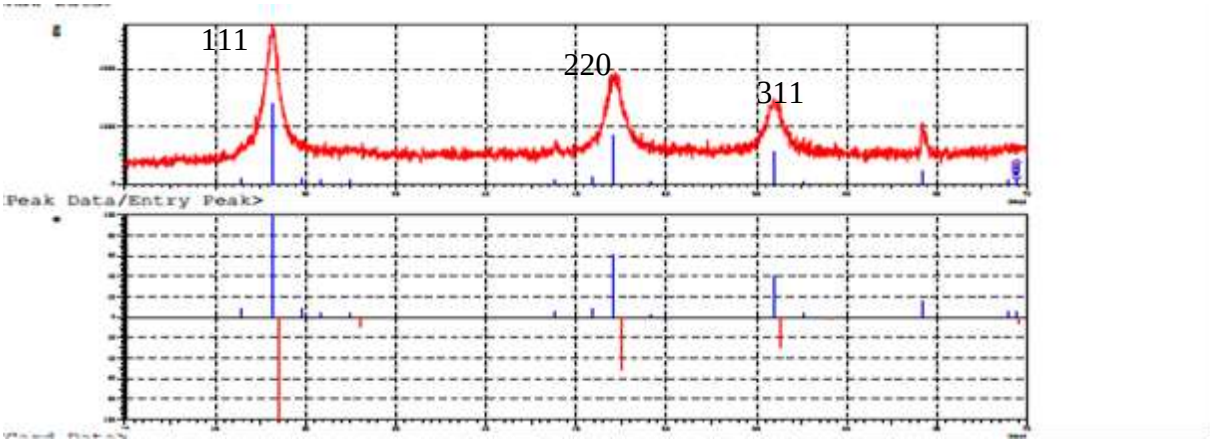

Figure 3. X-ray diffraction pattern of prepared ZnS 5

Table 3. X-ray Diffraction Peaks Data of Prepared ZnS 5

No.	2θ (°)	d (Å)	FWHM (°)	Crystallite size (Å)	Crystallite size (nm)	Miller indices (h k l)
1	28.1528	3.16715	0.96600	84.7	8.47	111
2	47.1163	1.92729	1.08000	80.0	8.00	220
3	55.9533	1.64204	1.06500	84.4	8.44	311

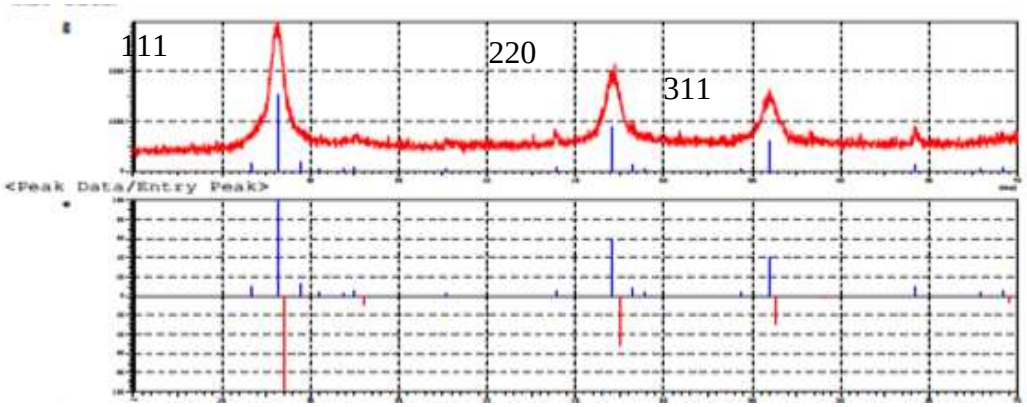

Figure 4. X-ray diffraction pattern of prepared ZnS 6

Table 4. X-ray Diffraction Peaks Data of Prepared ZnS 6

No.	2θ (°)	d (Å)	FWHM (°)	Crystallite size (Å)	Crystallite size (nm)	Miller indices (h k l)
1	28.1351	3.16910	0.95350	85.8	8.58	111
2	47.0996	1.92794	1.02000	69.7	6.97	220
3	47.0996	1.64177	1.06500	84.4	8.44	311

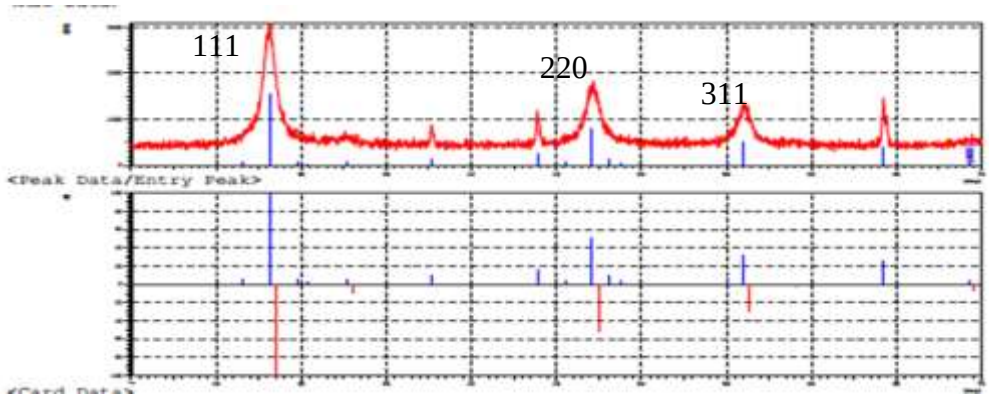

Figure 5. X-ray diffraction pattern of prepared ZnS 8

Table 5. X-ray Diffraction Peaks Data of Prepared ZnS 8

No.	2θ (°)	d (Å)	FWHM (°)	Crystallite size (Å)	Crystallite size (nm)	Miller indices (h k l)
1	28.1411	3.16844	0.90460	90.50	9.05	111
2	47.1196	1.92717	0.99000	87.50	8.75	220
3	56.0123	1.64045	0.94670	95.01	9.50	311

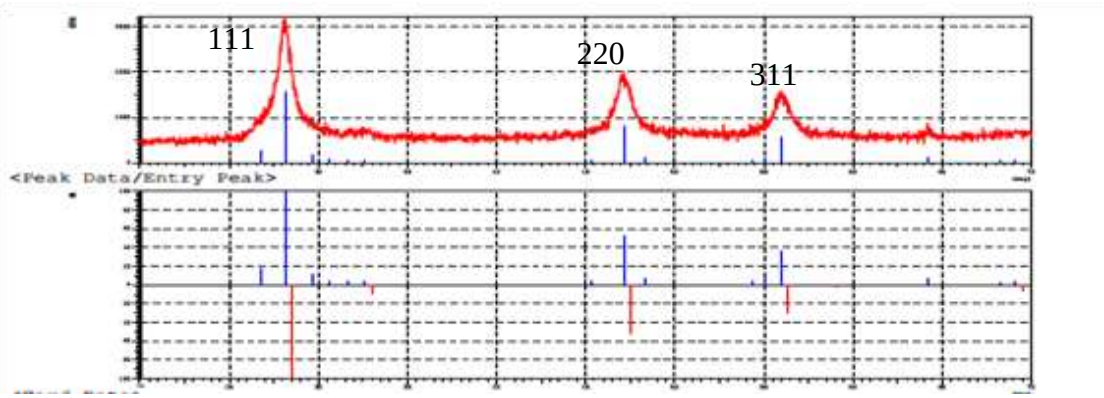

Figure 6. X-ray diffraction pattern of prepared ZnS 9

Table 6. X-ray Diffraction Peaks Data of Prepared ZnS 9

No.	2θ (°)	d (Å)	FWHM (°)	Crystallite size (Å)	Crystallite size (nm)	Miller indices (h k l)
1	28.1302	3.16964	1.00280	81.6	8.16	111
2	47.1296	1.92678	1.08000	80.1	8.01	220
3	55.9883	1.64110	1.02500	87.7	8.77	311

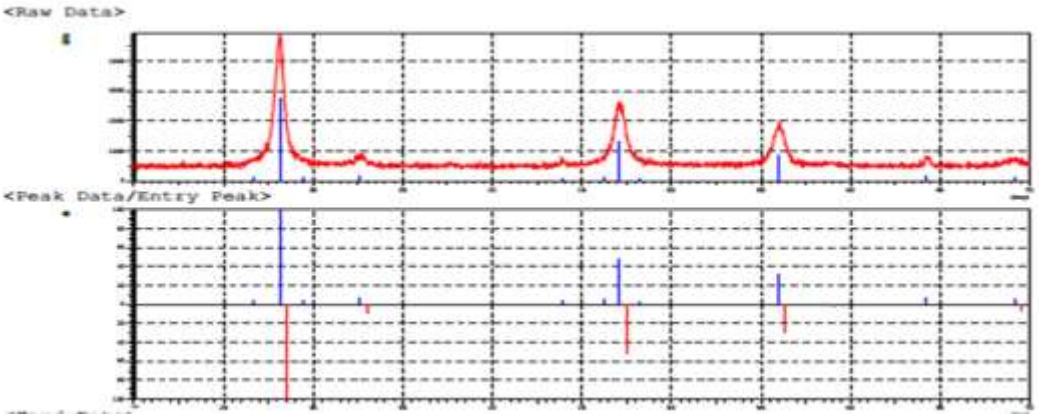

Figure 7. XRD diffraction pattern of prepared ZnS 10

Table 7. X-ray XRD Diffraction Peaks Data of Prepared ZnS 10

No.	2θ (°)	d (Å)	FWHM (°)	Crystallite size (Å)	Crystallite size (nm)	Miller indices (h k l)
1	28.1215	3.17060	0.61610	132.8	13.28	111
2	47.1024	1.92783	0.73430	117.9	11.79	220
3	55.9760	1.64143	0.73460	122.4	12.24	311

According to Table 8, the axial lengths a, b, and c are equal, and the angles, α, β and γ are 90°. Therefore, the crystalline structure of the synthesized zinc sulphide quantum dots is cubic. Since Miller indices are all odd and all even, it is face-centred cubic (fcc). The XRD results of the synthesized zinc sulphide quantum dots are consistent with the crystallite size and structure of zinc sulphide quantum dots.

Table 8. Lattice Parameters of Zinc Sulphide Quantum Dots for All Selected pH(s)

Phase name	a, Å	b, Å	c, Å	α, °	β, °	γ, °
Zinc sulphide	5.40600	5.40600	5.400600	90.000	90.000	90.000

FT IR analysis

FTIR is an analytical technique used to identify information about the chemical bonding in a material. The infrared absorption spectra (FTIR) of the ZnS quantum dots were recorded in the range of 400–4000 cm^{-1}, and the spectra are shown in Figures 8, 9, 10, and 11 with the spectral data described in Table 9. Spectrum analysis of the ZnS shows the presence of a broad and intense band at around 3330 cm^{-1}, which is attributed to the O-H stretching vibration (Silverstein *et al.*,2005). The presence of a band around 1627 cm^{-1} may correspond to the O–H bending vibration. The presence of these bands indicates the existence of water on the surface of ZnS samples. The absorption at 1086 cm^{-1} indicates the C-O stretching vibration. The prominent peak at 639 cm^{-1} indicates the Zn-S (metal-sulphur bond) (Zhao *et al*., 2007). The strong absorption bands in the range of 450–650 cm^{-1} are related to the vibrational characteristics of ZnS (Liu *et al*., 2017).

Figure 8. FT IR spectrum of prepared ZnS 4

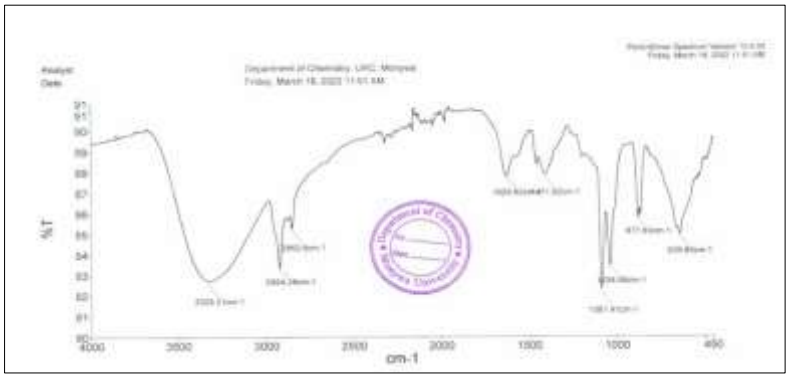

Figure 9. FT IR spectrum of prepared ZnS 5

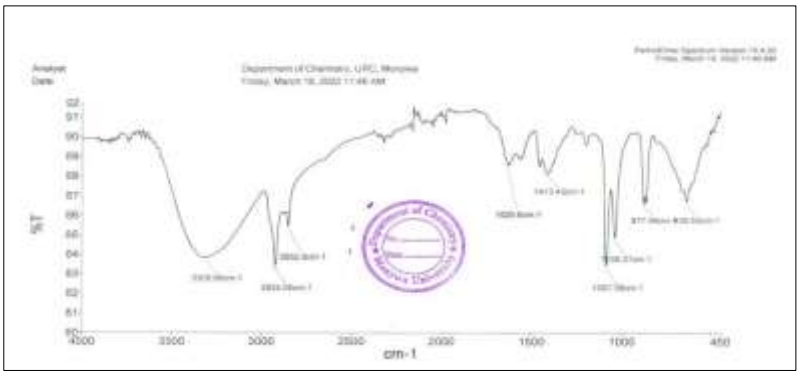

Figure 10. FT IR spectrum of prepared ZnS 6

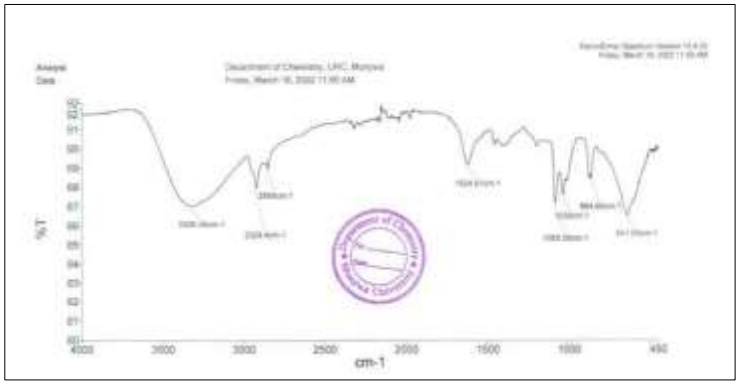

Figure 11. FT IR spectrum of prepared ZnS 9

Table 9. FT IR Assignments of Prepared ZnS Quantum Dots

	Observed frequency(cm^{-1})				**Assignment**	**Literature frequency(cm^{-1})***
	ZnO 4	**ZnO 5**	**ZnO 6**	**ZnO 9**		
1	3334	3328	3308	3326	-OH stretching vibration	3550-3200
2	1627	1629	1629	1624	-OH bending vibration	1666-1586
3	1086	1087	1087	1085	C-O stretching vibration	1200-1000
4	639	639	639	639	Zn-S metal sulphide band	650-450

*Silverstein *et al*., 2005; Frost *et al*., 2002; Liu *et al*., 2017

UV-visible analysis

The optical properties of ZnS quantum dots were determined from absorption measurements in the range of 200-600 nm. The absorption corresponds to electron excitation from the valence band to the conduction band. The plots of optical absorbance versus wavelength for prepared ZnS quantum dots are shown in Figures 12, 13, 14, 15, 16, and 17 for ZnS 4, ZnS 5, ZnS 6, ZnS 8, ZnS 9, and ZnS 10, respectively. In each absorption spectrum, the strongest absorption peak of the prepared ZnS sample appears at around 270 nm. UV/ Vis spectra indicate the absorption

wavelengths of ZnS 4, ZnS 5, ZnS 6, ZnS 8, and ZnS 10 are the same at 270 nm, and ZnS 9 is 260 nm. ZnS has good absorption for light in the wavelength range of 220-350 nm (Gadalla *et al.*, 2018).

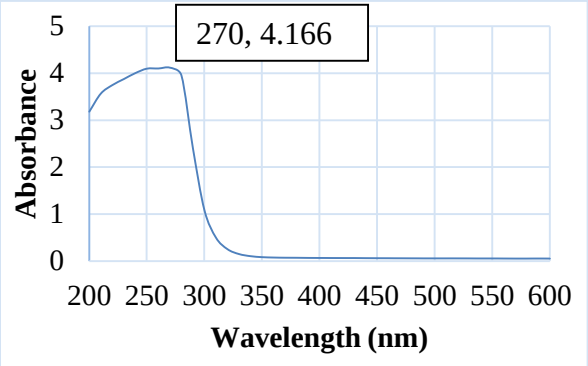

Figure 12. UV-visible spectrum of ZnS 4

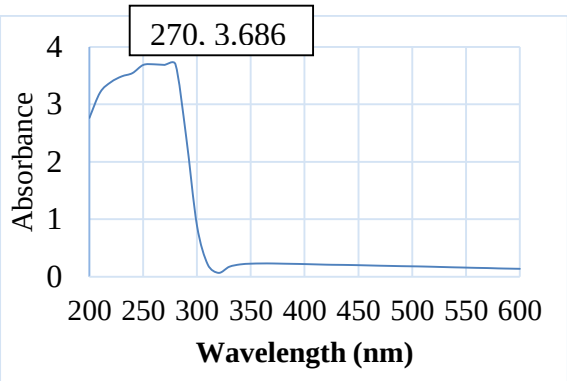

Figure 13. UV-visible spectrum of ZnS 5

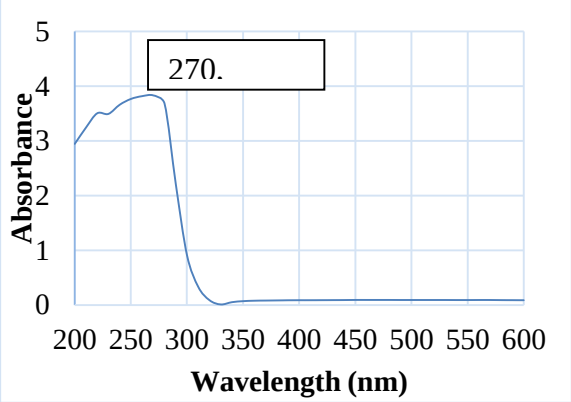

Figure 14. UV-visible spectrum of ZnS 6

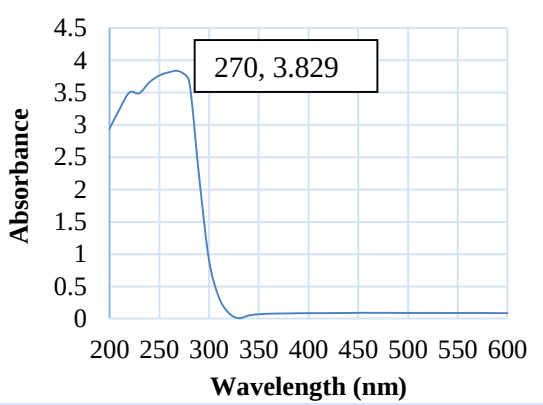

Figure 15. UV-visible spectrum of ZnS 8

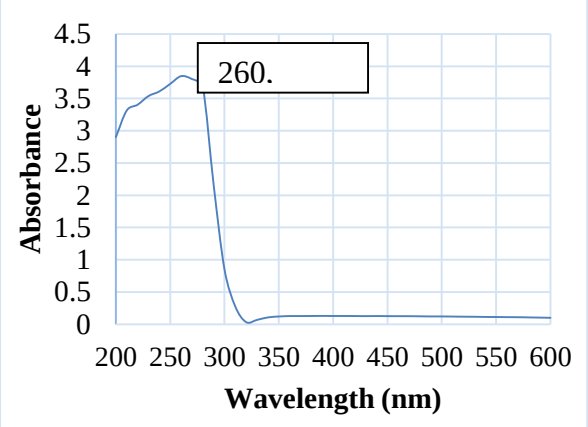

Figure 16. UV-visible spectrum of ZnS 9

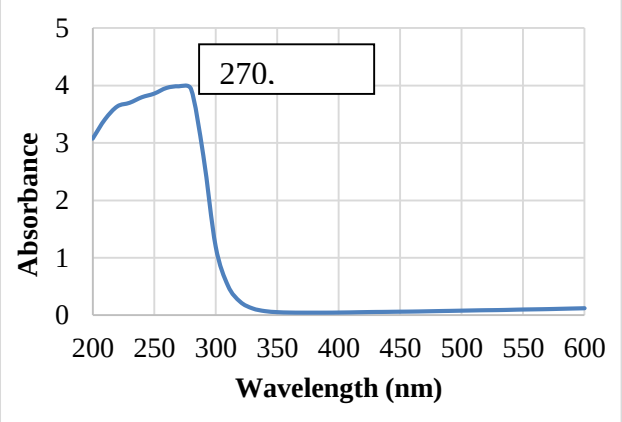

Figure 17. UV-visible spectrum of ZnS 10

Conclusion

In this research work, zinc sulphide quantum dots were synthesized by the hydrothermal method using zinc acetate and sodium sulphide nonahydrate as starting materials. The yield percents were found to be 68% of ZnS 5, 85 % of ZnS 4, Zn 6, ZnS 8, ZnS 9, and 99 % of ZnS 10 based on zinc acetate. By X-Ray Diffraction (XRD) analysis, zinc sulphide quantum dots were indexed as face-centred cubic, and the average crystallite sizes were observed in the range

of 7.9 to 12.4 nm. FT IR spectra of all zinc sulphide quantum dots showed a strong peak at 639 cm^{-1}. UV/Vis spectra indicated the absorption wavelengths of ZnS 4, ZnS 5, ZnS 6, ZnS 8, and ZnS 10 were the same at 270 nm, and ZnS 9 was at 260 nm. In an acidic medium, the higher the pH values, the smaller the crystallite sizes observed. So as to regard all the pH values used in acidic conditions, the crystallite sizes are inclusive of quantum dot sizes. In an alkaline medium, the crystallite size at pH 10 deviates from quantum dot sizes.

Acknowledgements

The authors would like to thank the Department of Higher Education, Ministry of Education, Yangon, Myanmar, for allowing us to carry out this research programme. Thanks are also extended to the Myanmar Academy of Arts and Science and Professor Dr Thandar Aung, Head of the Department of Chemistry, Meiktila University, for allowing us to carry out this research programme.

References

Baruah, J. M., S. Kalita, and J. Narayan. (2019). "Green Chemistry Synthesis of Biocompatible ZnS Quantum Dots (QDs): Their Application as Potential Thin Films and Antibacterial Agent". *International Nano Letters*, vol.9, pp.149-159

Bodo, B., and R. Singha. (2016). "Structural and Optical Properties of ZnS Quantum Dots Synthesized by CBD Method". *International Journal of Scientific and Research Publications*, vol. 6 (8), pp.461-465

Frost, R.L., P.A. Williams, W. Martens, and T. Kloprogge. (2002). "Raman and Infrared Spectroscopic Study of the Vivianite-group Phosphates Vivianite, Baricite and Bobierrite". *Mineralogical Magazine*, vol. 66 (6), pp.1063-1073

Gadalla, A., M.S. Abd el-Sadekb, and R. Hamood. (2018). "Synthesis, Structural and Optical Characterization of CdS and ZnS Quantum Dots". *Chalcogenide Letters*, vol. 15 (5), pp. 281 - 291

Grigore, M. E., A.M. Holban, and and A. M. Grumezescu. (2017). *Nanotherapeutics in the Management of Infections and Cancer*. In Nanobiomaterials Science, Development and Evaluation. Razavi,M., and A. Thakor (Editors). Amsterdam: Elsevier, pp.163-189

Jothi, N.S.N, A.G. Joshi, R.J. Vijay, A. Muthuvinayagam, and P. Sagayaraj. (2013). "Investigation on One-pot Hydrotherml Synthesis, Structural and Optical Properties of ZnS Quantum Dots". *Materials Chemistry and Physics*, vol. 138, pp.186-191

Kaur, N., S. Kaur, J. Singh and M. Rawat. (2016). "A Review on Zinc Sulphide Nanoparticles: From Synthesis, Properties to Applications". *Journal of Bioelectronics and Nanotechnology*, vol. 1(1), pp.1-5

Liu, L.N., J.G. Dai, T.J. Zhao, S.Y.Guo, D.S.Hou, P. Zhang, J. Shang, S. Wang, and S. Han.(2017). "A Novel Zn(II) Dithiocarbamate/ZnS Nanocomposite for Highly Efficient Cr^{6+} Removal from Aqueous Solutions". *RSC Adv.* vol. **7**, pp.35075–35085

Pawar, R.S.,P.G.Upadhaya, and V.B. Patravale. (2018). *Quantum Dots*: Novel *Realm in Biomedical and Pharmaceutical Industry*. In Handbook of Nanomaterials for Industrial Applications. C.M.Hussain (Editor). Amsterdam, Elsevier, pp.621-637

Silverstein, R.M., F.X. Webster, and D.J. Kiemle. (2005). *Spectrometric Identification of Organic Compounds*. New York: 7th edition, John Wiley and Sons, pp.88-89

Suri, S., G. Raun, J. Winter, and C. E. Schmidt. (2013). *Microparticles and Nanoparticles*. In Biomaterial Science. Ratner, B.D., A.S. Hoffman, F.G. Schoen, and J.E.Lemons (Editors). London: 3rd edition, Academic Press

Xue, L., C. Shen, M. Zheng, H. Lu, N. Li, G. Ji, L. Pan and J. Cao. (2011). "Hydrothermal Synthesis of Graphene-ZnS Quantum Dot Nanocomposites". *Materials Letters*, vol. 65, pp. 198-200

Zhao, Y., F. Wang, Q. Fu, W. Shi. (2007). "Synthesis and Characterization of ZnS/hyperbranched Polyester Nanocomposite and its Optical Properties". *Polymer*, vol.48, pp.2853–2859

STUDY ON THE REMOVAL OF LEAD IONS BY PREPARED CELLULOSE ACETATE-RICE HUSK COMPOSITE FILMS

Ei Ei Mon,[1] Ei Ei Hlaing[2], Hnin Hnin Than[3]

Abstract

This research was aimed to study the characterization and adsorption properties of prepared cellulose acetate-rice husk composite films. Rice husk (Zeyar) was collected from a local rice mill in Hlegu Township, Yangon Region, Myanmar. The characterizations of prepared cellulose acetate and rice husk were determined according to physicochemical properties such as pH, moisture content, and bulk density. The polymer composite films were prepared by using cellulose acetate (CA), rice husk (RH), and glutaraldehyde as a cross-linker. The prepared CA-RH composite films were characterized by conventional methods such as swelling and modern techniques such as EDXRF and SEM. For the removal of lead ions by CA-RH composite films, the effects of various parameters such as pH, initial concentration, contact time, and dosage were investigated by batch method. The adsorption capacity decreased with the increase in the initial concentration of lead ions in the solution. In conclusion, CA-RH composite films should be used as an effective adsorbent for the removal of heavy metal ions from industrial wastewater.

Keywords: Cellulose acetate, rice husk, composite film, heavy metal ions, sorption

Introduction

Cellulose acetate membrane (CAM) is one of the good sorbents since it is low-cost and renewable (Hui *et al*., 2006). Moreover, CAM has a comparatively high modulus, tensile strength, and adequate flexural and is a microdispersion sorbent, which enhances its capability to adsorb heavy metals (Tian *et al*., 2011), as CAM is grafted with functional groups such as –$OCOCH_3$ and –OH groups, so that CAM can bond with heavy metal ions through surface complexation mechanisms (Kamaruzaman *et al*., 2017). Cellulose is a polymer of glucose molecules. In turn, glucose, which is the primary source of energy for living cells, whether it is ingested (as in animals) or synthesized (as in plants), is a six-carbon molecule that includes a hexagonal ring. One of the six carbons lies above the ring and is attached to a hydroxyl group; two of the carbons within the ring itself are also attached to a hydroxyl group. These three -OH groups can readily react with other molecules to form hydrogen bonds. The hydrogen atom of the hydroxyl group, which is attached to the oxygen that is also attached to carbon on the other side, can be readily displaced by certain molecules that then take that hydrogen's spot in the parent glucose construct. One of these molecules is acetate. Acetate, the form of acetic acid that has lost its acidic hydrogen, is a two-carbon compound often written CH_3COO^-. Cellulose acetate, as the term is commonly used, actually refers to cellulose diacetate, in which two of the three available hydroxyl groups in each glucose monomer have been replaced by acetate. Cellulose acetate is the most important cellulose ester (Puls *et al*., 2011).

Rice husk is a by-product of rice production during milling which can be used in agriculture activity in Asia and particularly Myanmar (Mahvi *et al*., 2005). The quantity of rice husk depends on the kinds of paddy, grain type, soil and climatic condition in which the paddy is cultivated, and type of rice mill used (Farook and Ismail, 2005). The production of rice, one of the major food crops in the world, generates one of the major wastes of the world, namely, rice husks (RHs). The abundant, cheap, regenerable RHs naturally have high contents of silica and the silica, has a high reactivity (xiong *et al*., 2009).

[1] Department of Chemistry, Dagon University
[2] Department of Chemistry, Hinthada University
[3] Department of Chemistry, Dagon University

Heavy metals such as cadmium, lead, zinc, nickel, copper, and chromium (III) or their compounds have been extensively used by various metal-finishing, mining, and chemical industries. This has led to a sharp increase in the contamination of water. Because of their toxicity, the presence of any of these metals in excessive quantities will interfere with many beneficial uses of the water (Srivastava and Majumder, 2008). The maximum limit under the standard is 0.02 mg L^{-1} for Cd, 0.50 mg L^{-1} for Pb, and 1.0 mg L^{-1} each for Zn, Ni, Cu, and Cr (III). Despite their potential toxicity, many of these metals are still widely used (Hamidi *et al*., 2008).

Lead is a gray-white, soft metal with a low melting point, a high resistance to corrosion, and poor electrical conducting capabilities. It is highly toxic. In addition to its highly concentrated ores, lead is naturally available in all environmental media in small concentrations. Lead is one of the industrial pollutants that may enter the ecosystem through soil, air, and water. Inorganic lead causes disturbances in the center nervous system by changing the characteristics of the early organism. According to the WHO, the maximum permissible limit (MPL) of lead in drinking water is 0.1 mg L^{-1}. Hence, the appropriate treatment of industrial wastewater, which releases lead into aquatic and terrestrial systems, is very important. At present, different methods have been utilized to remove heavy metals from the contaminated wastewater, such as filtration, adsorption, chemical precipitation, ion exchange, membrane separation methods, and electro-remediation methods (Naeema and Kandi, 2014). The aim of the research is to study the characterization and adsorption properties of prepared cellulose acetate-rice husk composite films.

Materials and Methods

Sampling

Rice husk from the species Zeyar was collected from a local rice mill in Hlegu Township, Yangon Region. A cellulose acetate was purchased from Academy Chemical Group in 28th Street, Pabedan Township, Yangon Region.

Preparation of Cellulose Acetate-Rice Husk Composite Films

The casting solution used in this work consisted of a mixture of cellulose acetate and rice husk. A cellulose acetate solution of (5 % w/v) was prepared by dissolving 5 g of cellulose acetate in 100 mL of formic acid using a magnetic stirrer for 5 h to get a clear, homogeneous casting solution. The solution was then added to rice husk powder in various ratios and stirred with a magnetic stirrer. A cellulose acetate-rice husk solution was then added with different weights of rice husk and 0.1 % v/v glutaraldehyde as a cross-linker. The polymer solutions were kept for sufficient time to remove any bubble formation and were cast onto a cleaned and dried glue tray at room temperature. Trays were left for about 5 days to obtain cellulose acetate-rice husk (CA-RH) composite films. The films after drying were easily removed from the glue tray and immersed in a 1 M NaOH solution to remove residual materials, then washed with distilled water several times to remove alkali and unreacted materials, and finally dried in the air at room temperature. Then, the various cellulose acetate-rice husk composite films were obtained.

Removal of Lead (II) Ions from Aqueous Solution

A stock solution containing 200 mg L^{-1} lead (II) nitrate was prepared. Working solutions were prepared from the stock solution by dilute appropriate aliquots with distilled water. Each 100 mL of this solution was mixed with 2 cm × 2 cm of prepared composite films in the flask. The flask was placed in an electric shaker at room temperature and shaken for 1 h. The sample was allowed to stand to settle out the solid particles, and the residual lead (II) ion solution was taken out and then diluted to a certain volume. It was followed by complexometric titration using EDTA and the

xylenol orange indicator (Vogel, 1961). The effect of PH, contact time, dosage on the removal of Pb (II) ions by cellulose acetate-rice husk (CA-RH 4) composite film were investigated.

Characterization of Prepared Cellulose Acetate-Rice Husk Composite Film before and after Adsorption of Lead (II) Ions

The prepared cellulose acetate-rice husk composite films before and after adsorption of lead (II) ions were examined by SEM for a visual inspection of surface morphological porosity. The procedure of EDXRF procedure was done according to the recommended standard procedure as reported in the catalogue.

Application of Prepared Cellulose Acetate-Rice Husk Composite Film in the Treatment of Lead (II) Ions in Industrial Waste Water

The industrial wastewater sample was collected from the industrial zone of Thingangyun Township. The prepared cellulose acetate-rice husk composite film (2 cm × 2 cm) was suspended in 100 mL of industrial wastewater at pH 5. The sample was equilibrated in an electric shaker for 1 h at ambient temperature.

After 1 h shaking, the sample was allowed to stand to settle out the solid particles. The residue was then separated by filtration. The content of lead ions in decanted wastewater was determined by an atomic absorption spectrophotometer.

Results and Discussion

Cellulose Acetate-Rice Husk Composite Films

Cellulose acetate–rice husk composite films were prepared by solution-casting from cellulose acetate and rice husk at various compositional ratios. Figure 1 shows the cellulose acetate-rice husk composite films, which consist of a mixture of cellulose acetate (5% w/v), various weight percents of rice husk, and glutaraldehyde (0.1% v/v) as a cross-linker. The cellulose acetate-rice husk composite films were prepared by casting, evaporation, and annealing. The films differ in their preparation processes in accordance with the various amounts of rice husk content. The prepared CA-RH 4 composite film was chosen for the removal of lead ions from aqueous solutions.

CA-RH 1 **CA-RH 2** **CA-RH 3** **CA-RH 4** **CA-RH 5**

CA-RH-1 = Cellulose acetate-rice husk film (5:0.2 % w/w in 100 mL of formic acid)
CA-RH-2 = Cellulose acetate-rice husk film (5:0.4 % w/w in 100 mL of formic acid)
CA-RH-3 = Cellulose acetate-rice husk film (5:0.6 % w/w in 100 mL of formic acid)
CA-RH-4 = Cellulose acetate-rice husk film (5:0.8 % w/w in 100 mL of formic acid)
CA-RH-5 = Cellulose acetate-rice husk film (5:1.0 % w/w in 100 mL of formic acid)

Figure 1. Cellulose acetate-rice husk composite films

Removal of Lead (II) ions by Cellulose Acetate-Rice Husk Composite Films

The pH of an aqueous solution is an important parameter in the adsorption of Pb(II) ions from the aqueous solution onto the adsorbent. Figure 2 illustrates that the effect of pH obviously influences the adsorption of the Pb (II) ions from an aqueous solution by the CA-RH 4 composite film. The removal of the Pb (II) ion increased with increasing pH, and the maximum adsorption capacity was observed at pH 5.

Figure 3 represents the maximum adsorption that was reached at 20 min for the removal of Pb(II) ions. After the maximum contact time has been reached, the percent removal becomes independent of time due to the decrease in the number of adsorption sites.

The effects of the amount of cellulose acetate-rice husk composite films in the range of 0.065 g (4 cm^2), 0.118 g (9 cm^2), 0.158 g (16 cm^2), 0.225 g (25 cm^2), and 0.297 g (36 cm^2) on the removal of Pb(II) ions from a constant initial concentration of 200 mg L^{-1} at pH 5 were investigated. According to Figure 4, it can be seen that as the amount of cellulose acetate-rice husk composite films increases, the percent removal of Pb(II) ions increases. It can be observed that 96.5% of Pb(II) ions can be removed with 0.297 g (36 cm^2) of CA-RH 4 composite film in an initial concentration of 200 mg L^{-1} of Pb (II) ions at pH 5.

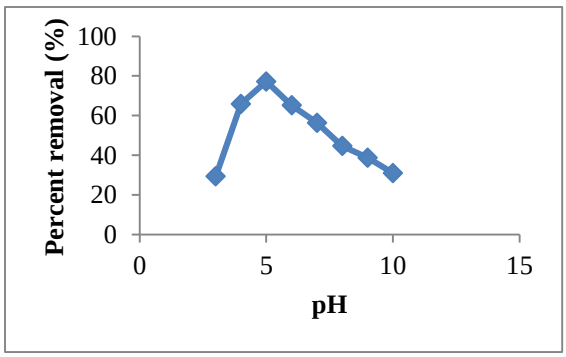

Figure 2. Effect of pH on the removal of Pb(II) ions by cellulose acetate-rice husk (CA-RH 4) composite film

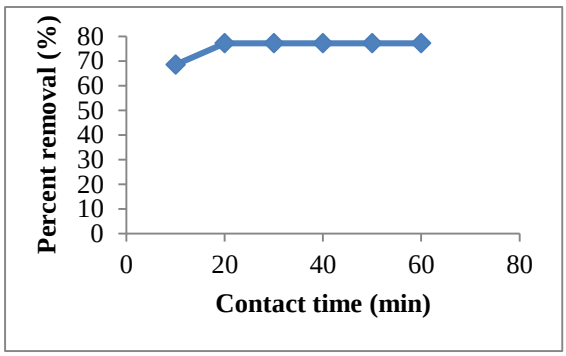

Figure 3. Effect of contact time on the removal of Pb(II) ions by cellulose acetate-rice husk (CA-RH 4) composite film

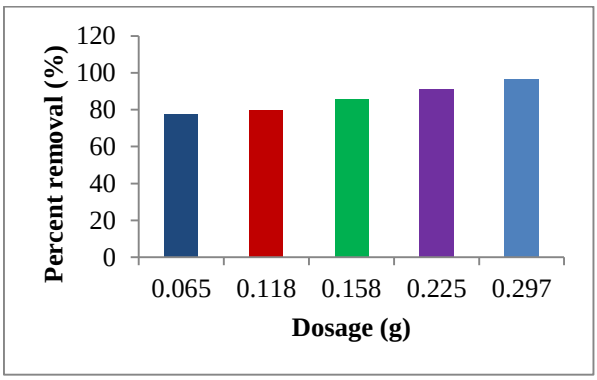

Figure 4. Effect of dosage on the removal of Pb(II) ions by cellulose acetate-rice husk (CA-RH4) composite film

Characterization by SEM Analysis

Figure 5 shows the surface morphology of the cellulose acetate-rice husk (CA-RH 4) composite film. The morphological features of the cellulose acetate-rice husk composite film, including the striated nature of the film, may be responsible for the enhanced specific sorption properties. Figure 6 shows the surface morphology of the Pb(II) ions loaded on the cellulose

acetate-rice husk (CA-RH 4) composite film. It can be clearly seen that Pb(II) ions were sorbed in the voids of the composite films, suggesting that a large cluster of Pb(II) ions has been sorbed and precipitated onto the surface of composite films. A less rugged surface is observed, which can be due to the difference in the coordination sphere of Pb(II) ions.

Characterization by EDXRF analysis

Figure 7 shows the EDXRF spectrum of the cellulose acetate–rice husk composite film. The spectrum indicated that silica (ca. 80.454 %) is the major constituent in the film. It is a semi quantitative value measured on a matrix basis. The presence of Pb(II) ions sorbed on the cellulose acetate-rice husk composite film is shown by the EDXRF spectrum represented in Figure 8. The measurements made and values therein are more semiquantitative and on a matrix basis. It can be observed that each spectrum indicates that the relevant Pb(II) ions were sorbed on the composite films. An interesting observation is the alternation of spectra after Si(II) ions have been replaced by Pb(II) ions. It can be inferred from the pronounced peaks that each spectrum had represented. Figure 8 bears out the fact that from a mixture of Pb(II) ions was sorbed by the composite films.

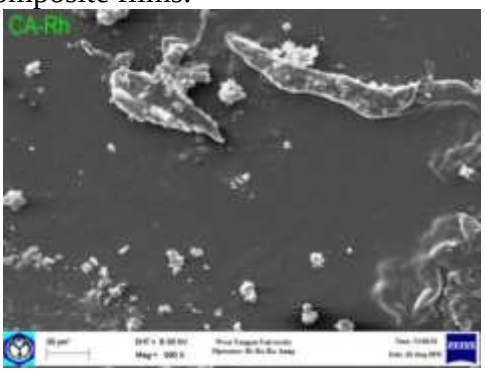

Figure 5. SEM micrograph of cellulose acetate-rice husk (CA- RH 4) composite film

Figure 6. SEM micrographs of cellulose acetate-rice husk (CA-RH 4) composite film after lead adsorption

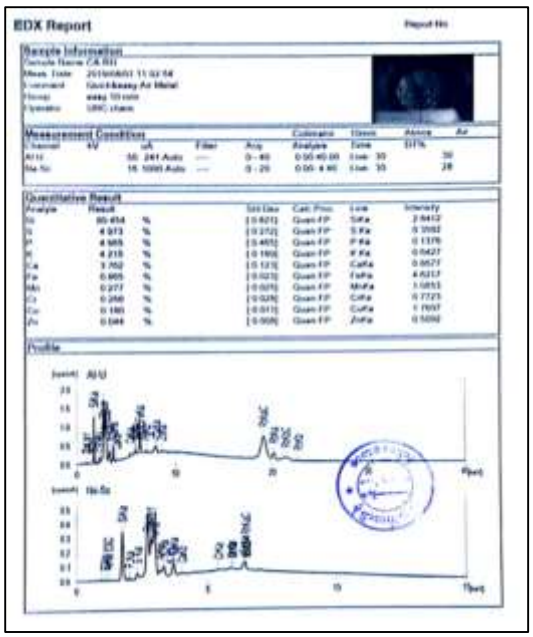

Figure 7. EDXRF spectrum of cellulose acetate-rice husk (CA-RH 4) composite film.

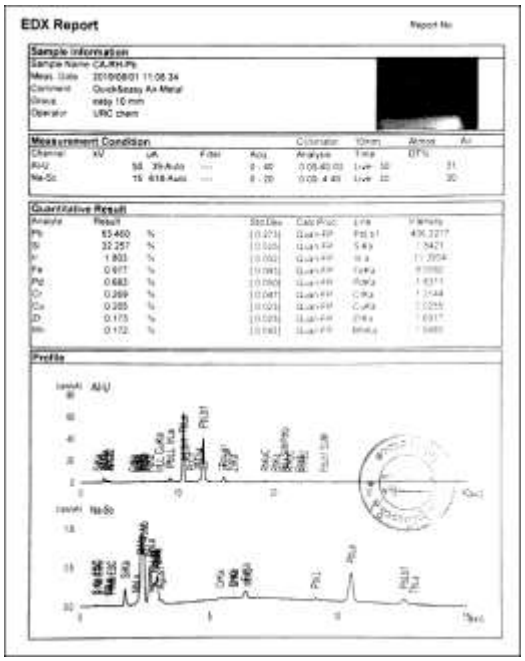

Figure 8. EDXRF spectrum of cellulose acetate-rice husk (CA-RH 4 composite film after lead adsorption

AAS Analysis of Lead from Wastewater Treatment

The Lead(II) ion concentrations in industrial wastewater sample were determined by an atomic absorption spectrophotometer. The Lead(II) ion concentration was found to be 5.66 mg L^{-1} in industrial wastewater. It can be seen that the Lead(II) ion in wastewater sample was reduced significantly by the cellulose acetate-rice husk composite film. The results are shown in Table 1. On examination of the resulting data, removal efficiency was 87.6 %. The process of removing Lead(II) ions from wastewater sample by cellulose acetate-rice husk composite film can be used for the effective treatment of industrial effluents.

Table 1. Lead Removal Efficiency in Battery Wastewater by using Cellulose Acetate-Rice Husk (CA-RH-4) Composite Film

Metal Ions	Before treatment (mg L^{-1})	After treatment (mg L^{-1})	Removal efficiency (%)
Pb	5.66	0.7018	87.6

Conclusion

In the research, the ability of a cellulose acetate-rice husk composite film to adsorb Pb(II) ions from aqueous solutions has been explored. The maximum adsorption capacity of the Pb(II) ions by the cellulose acetate-rice husk composite film was about pH5. The percent removal increased with decreasing initial concentrations of Pb(II) ions. It was observed that 77.2 % of Pb(II) ions was removed with a dosage of 0.065 g of cellulose acetate-rice husk composite film in 100 mL of 200 mg L^{-1} Pb(II) ion solutions. The data obtained from all experiments for the removal of Pb(II) ions from aqueous solutions showed that with increasing, contact time, the removal percent also increased. After 20 min, the removal of Lead(II) ions became independent of time. As the amount of sorbent increased, the percent removal increased was 96.5 % of Pb(II) ions was removed with a dosage of 0.297 g (36 cm^2) of cellulose acetate-rice husk composite film in an initial concentration of 200 mg L^{-1} of Pb(II) ions. The lead concentration of 5.66 mg L^{-1} was found in industrial wastewater, which was removed by using cellulose acetate-rice husk composite film. On examination of the resulting data, 87.6% removal efficiency was observed. The cellulose acetate-rice husk composite film can be used as an effective and efficient sorbent for the treatment of industrial effluents. Therefore, cellulose acetate-rice husk composite film should be used as an ecofriendly and environmental-friendly adsorbent material for wastewater treatment.

Acknowledgement

The authors would like to express their profound gratitude to the Myanmar Academy of Arts and Science for giving permission to submit this paper and to Professor and Head Dr. Daw Hnin Hnin Than, Department of Chemistry, Dagon University, for her kind encouragement.

References

Farook, A., and M. Ismail. (2005). "Production and Characterization of Rice Husk Ash as A Source of Pure Silica". *J. Am. Oil Chem. Soc.*, vol.77, pp.437-440

Hamidi, A. A., M. N. Adlan, and K. S. Ariffin. (2008). "Heavy Metals (Cd, Pb, Zn, Ni, Cu and Cr (III)) Removal from Water in Malaysia: Post Treatment by High Quality Limestone". *Bioresource Technology*, vol.99, pp.1578-1583

Hui, Y. Z., X. G. Chen, C. S. Liu, X. H. Meng, and L. J. Yu. (2006). "Cellulose Acetate/ Chitosan Multimicrospheres Preparation and Ranitidine Hydrochloride Release in Vitro". *Drug Delivery*, vol.13, pp.261-267

Kamaruzaman, S., N. I. F. Aris, N. Yahaya, L. S. Hong, and M. R. Razak. (2017). "Removal of Cu (II) and Cd (II) Ions from Environmental Water Samples by using Cellulose Acetate Membrane". *Journal of* Environmental *Analytical Chemistry*, vol.4, pp.2380-2391

Mahvi, A. H., N. Alavi, and A. Maleki. (2005). "Application of Rice Husk and its Ash in Cadmium Removal from Aqueous Solution". *Journal of biological sciences*, vol.8 (5), 721-725

Naeema H., and Y. Kandi. (2014). "Removal of Lead (II) from Waste Water by Adsorption". *Journal of Current Microbiology and Applied Science*, vol.3 (4), pp.207-228

Puls,J., S. A. Wilson, and D. Holter. (2011). "Degradation of Cellulose Acetate-Based Materials: A Review". *J. Polym. Environment*, vol.19, pp. 152-165

Srivastava N. K., and C. B. Majumder. (2008). "Novel Biofiltration Methods for the Treatment of Heavy Metals from Industrial Wastewater". *Journal of Hazardous Materials*, vol. pp.151, 1-8

Tian, Y., M. Wu, R. Liu, Y. Li, and D. Wang, J.Tan, R.Wu, and Y.Haung. (2011). "Electrosperm Membrane of Cellulose Acetate for Heavy Metal Ions Adsorption in Water Treatment". *Carbohydrate Polymers*, vol. 83, pp.743-748

Vogel, A. I. (1961). "*A Text Book of Quantitative Inorganic Analysis*" London: 3rd Ed, Longmans, Green & Co. Ltd.,

Xiong,L., E. H. Sekiya, P.Sujaridworakun, S.Wada, and K.Saito. (2009). "Burning Temperature Dependence of Rice Husk Ashes in Structure and Property". *Journal of Metals, Materials and Minerals*, vol.19, pp.95-99

ISOLATION AND CHARACTERIZATION OF A BIOACTIVE COMPOUND AND SCREENING OF ANTIMICROBIAL AND ANTIOXIDANT ACTIVITIES OF *STEPHANIA VENOSA* (BL.) SPRENG (TAUNG-KYA) TUBER

Mi Aye Aye Aung[1], Kay Khine Nyunt[2], Myint Myint Khine[3], Ni Ni Than[4]

Abstract

Stephania venosa (Bl.) Spreng (Taung-kya), belonging to the family Menispermaceae and is a rich source of alkaloids commonly found as herbaceous perennial vine with a large tuber. The aim of the research includes preliminary phytochemical investigations, isolation and identification of bioactive chemical constituent and *in vitro* antimicrobial and antioxidant activities of different crude extracts from the tuber of *S. venosa*. The preliminary phytochemical screening revealed the presence of alkaloids, α-amino acid, carbohydrates, glycosides, flavonoids, organic acids, phenolic compounds, reducing sugars, steroids, saponins and tannins in the samples by using the standard methods. The air-dried powder plant sample was subjected to cold percolation with 80 % methanol and fractionation with petroleum ether only, petroleum ether and ethyl acetate, ethyl acetate only, and ethyl acetate and methanol. The isolated compound (0.03 g, 0.06%) was separated from ethyl acetate fraction by using silica gel column chromatographic separation method. It was identified by using modern spectroscopic methods such as UV-visible, FT IR, ^{1}H NMR, ^{13}C NMR and mass spectrometry and also by comparing with the reported data. The antimicrobial activity of different crude extracts (PE, EtOAc, EtOH, MeOH and Watery) from tuber of *S. venosa* was tested by the agar well diffusion method. Ethyl acetate extract has the most potent antimicrobial activity (the inhibition zone diameter range between 17 to 22 mm) against tested microorganisms except as *Bacillus pumilus.* The antioxidant activity was investigated by using DPPH free radical scavenging assay method. The IC_{50} values of watery and ethanol extracts were found to be 173.61 and 134.93 μg/mL, respectively. The IC_{50} value of isolated compound was also observed as 24.43 μg/mL. Therefore, the isolated compound possesses higher potent antioxidant activity than the extracts.

Keywords: *Stephania venosa* (Bl.) Spreng, bioactive compound, antimicrobial activity, antioxidant activity

Introduction

Nowadays, the use of traditional medicine has greatly increased in Myanmar and all over the world. Depression and anxiety disorders are the most common mental illnesses in humans (Wong and Licinio, 2002). According to the World Health Organization (WHO), the majority of medicinal plants in disease management have established their use in the primary health care delivery system. *Stephania venosa* (Bl.) Spreng is a herbaceous perennial vine growing to around four metres tall with a large tuber on the ground. It is widely distributed in eastern, southern Asia, and Australia. Its leaves are spirally arranged on the stem with the leaf petiole attached near the centre of the leaf. It is a plant rich in alkaloids. Its tubers have been used in traditional medicine such as nerve tonics, aphrodisiacs and appetizers. Moreover, it is also used for the treatment of asthma, hyperglycemia, microbial infections, and cancer. *S. venosa* leaves have been used to treat ringworm, tinea versicolor, chronic cancer, and acne. It has been reported to have a range of biological effects (Moongkarndi *et al*., 2004). The biological compounds that belong to secondary metabolites include phenolic compounds, steroids, flavonoids, and alkaloids.

The phytochemical screening from the tuber of the plant showed the presence of a wide variety of isoquinoline and aporphine alkaloids with different structural types including

[1] Department of Chemistry, University of Yangon
[2] Department of Chemistry, Dagon University
[3] Pa-thein University
[4] Department of Chemistry, University of Yangon

tetrahydropalmatine, crebanine, *O*-methylbulbocapnine and *N*-methyltetrahydropalmatine. *S. venosa* contains pharmacological activities such as cytoxic, antimicrobial, anti-inflammatory, antihyperglycemic, anti-acetylcholinesterase, antitubercular, antioxidant and antiprotozoal activities (Ingkaninan *et al*., 2006; soares *et al*., 1997).

The aim of the present work is to an isolate alkaloid and to screen the antimicrobial and antioxidant activities of the tuber of *S. venosa.*

Scientific classification of *Stephania venosa* (Bl.) Spreng

Family : Menispermaceae

Botanical name : *Stephania venosa* (Bl.) Spreng

Myanmar name : Taung-kya

Part used : Tuber

Tuber

Figure 1. The photograph of tuber of *Stephania venosa* (Bl.) Spreng

Materials and Methods

Collection and Identification of Plant Samples

The tuber of *S. venosa* was collected from Than-Hlwin Township, Yangon Region, Myanmar, in June, 2019. The plant was identified at the Department of Botany, Hpa-an University.

Preliminary Phytochemical Tests on the Tuber of *S. venosa*

The tuber of *S. venosa* (Taung-kya) was screened for the presence or absence of bioactive constituents such as alkaloids, α-amino acid, carbohydrates, glycosides, flavonoids, organic acids, phenolic compounds, reducing sugars, steroids, saponins and tannins (Harborne, 1984).

Extraction and Isolation from the Tuber of *S. venosa*

The air-dried powder of *S. venosa* tuber (1000 g) was macerated with 80 % methanol (5L) for one week at room temperature. Then, the filtrate was filtered through Whatman no.1 filter paper. The extraction was performed three times as the same procedure mentioned above. Total filtrate was concentrated under reduced pressure by using rotary evaporator to provide the methanol crude extract (50 g). The 50 g of methanol extract was subjected to column chromatographic separation over silica gel (200 g, 70-230 mesh) using petroleum ether: ethyl acetate solvent system with increasing polarity to give four fractions. The ethyl acetate fraction (Fraction-III) was rechromatographed over silica gel with solvents increasing order of polarity using pure petroleum ether, petroleum ether: ethyl acetate, pure ethyl acetate and ethyl acetate: methanol. A white crystalline compound was obtained from (PE: EtOAc, 5:1) fraction and the yield percent is 30 mg (0.06 %) based on the methanol extract (50 g).

Identification of The Isolated Compound

The isolated compound from *S. venosa* was identified by TLC, UV-visible, FT IR, ^{1}H NMR, ^{13}C NMR and MS from the Institute of Chemistry, Vietnam Academy of Science and Technology, Hanoi.

The ^{1}H and ^{13}C NMR of compound was recorded on an Advance NEO NMR spectrometer, and the chemical shifts were expressed in the δ (ppm) scale with TMS as an internal standard. The mass spectrum was recorded on an LC-MSD-Trap-SL Print mass spectrometer.

Screening of Antimicrobial Activity of *S. venosa*

In vitro, antimicrobial assay of the petroleum ether, ethyl acetate, ethanol, methanol and watery extracts from tuber of *S. venosa* was performed at Department of Chemistry, Pa-thein University. The tested eight microorganisms such as *Escheerichia coli, Candida albicans, Bacillus subtilis, Staphylococcus aureus, Pseudomonas fluorescens, Agrobacteriumb tumefaciens, Bacillus pumilus and Micrococcus luteus.* The antimicrobial activity was determined by the agar well diffusion method (Selvamohan *et al*., 2012).

In vtro Antioxidant Activity by DPPH Free Radical Scavenging Assay

The effect on DPPH free radical scavenging activity of Taung-kya was determined by a UV-visible spectrophotometric method according to the procedure described by (Marinova and Batchvarov, 2011). The control solution was prepared by mixing 1.5 mL of 180 µM DPPH solution with 1.5 mL of ethanol using a shaker. The sample solution was also prepared by mixing thoroughly 1.5 mL of 180 µM DPPH solution and 1.5 mL of test sample solution with concentration (1000 - 62.5 µg/mL). The mixed solutions were allowed to stand at room temperature for 30 min. After 30 min, the absorbance of each sample solution was measured at 517 nm by using UV-visible spectrophotometer. The percent radical scavenging activity was calculated by the following equation.

$$\% \text{ RSA} = \frac{A_{control} - (A_{sample} - A_{blank})}{A_{control}} \times 100$$

Where % RSA = % radical scavenging activity

$A_{control}$ = absorbance of DPPH in EtOH solution

A_{Sample} = absorbance of sample and DPPH solution

A_{blank} = absorbance of sample and EtOH solution

The experimental results were performed in triplicate. The data were recorded as mean ± standard deviation.

Results and Discussion

Preliminary Phytochemical Investigation for *S. venosa*

The phytochemical tests revealed the presence of secondary metabolites including alkaloids, α-amino acids, carbohydrates, glycosides, flavonoids, phenolic compounds, reducing sugars, steroids, saponins, and tannins in the tuber of *S. venosa*. The preliminary phytochemical results are shown in Table 1.

Table 1. Results of Preliminary Phytochemical Tests on the Tuber of *S. venosa*

(+) = presence (-) = absence (ppt) = precipitation

No.	Test	Extracts	Test Reagent	Observation	Remark
1	Alkaloids	1% HCl	(i)Wagner's reagent	bown ppt	+
			(ii)Dragendorff's reagent	orange ppt	+
			(iii) Mayer's reagent	white ppt	+
			(iv) sodium picrate	yellow ppt	+
2	α-Amino acids	H_2O	ninhydrin	purple colour	+
3	Carbohydrates	H_2O	10 % α-naphthol and conc:H_2SO_4	red ring	+
4	Cyanogenic glycosides	H_2O	sodium picrate solution	no colour	-
5	Flavonoids	EtOH	Mg ribbon & conc: HCl	pink colour	+
6	Glycosides	H_2O	10 % lead acetate	white ppt	+
7	Phenolic compounds	EtOH	1 % $FeCl_3$	reddish-brown ppt	+
8	Reducing sugars	H_2O	Benedict's solution	brick red ppt	+
9	Saponins	H_2O	distilled water	frothing	+
10	Starch	H_2O	iodine solution	no blue colour	-
11	Steroids	PE	acetic anhydride and conc:H_2SO_4	greenish brown colour	+
12	Tannins	EtOH	ferrous sulphate	reddish-brown ppt	+
13	Terpenoids	$CHCl_3$	acetic anhydride and conc:H_2SO_4	no colour	-

(+) = presence (-) = absence (ppt) = precipitation

Characterization of an Isolated Compound from the Tuber of *S. venosa*

A compound was isolated from ethyl acetate fraction of *S. venosa* tuber by the column chromatographic separation technique. The isolated compound was obtained as a white crystal after recrystallization in methanol. The R_f value of compound was found to be 0.57 (PE:EtOAc, 1:1 v/v) and it is soluble in ethyl acetate and methanol solvent. It is provided in orange colour with Dragendorff 's reagent by checking on TLC. The UV-visible and FT IR spectra of the isolated compound in methanol are shown in Figure 2. The wavelength of maximum absorption was observed at 282 nm and it may be due to the ($\pi \rightarrow \pi^*$) transition of C=C. The FT IR spectral data and band assignments are described in Table 2. The FT IR spectral data revealed the presence of =C-H stretching vibration (3050 and 3020 cm^{-1}), an aromatic ring (1635, 1611, and 1513 cm^{-1}), an ether linkage (1137, 1078, and 1050 cm^{-1}), and *o*-disubstituted benzene (785 cm^{1}). In addition, the structure of compound was identified by ^{1}H NMR, ^{13}C NMR, and ESI MS (Figures 3, 4 and 5). In the 600 MHz ^{1}H NMR spectrum of the isolated compound, the signals were observed at δ 6.89 ppm for H-1, δ 6.73 ppm for H-4, δ 6.92 ppm for H-11 and δ 6.96 ppm for H-12 exhibited on the aromatic ring and the methylene proton H-8 showed a pair doublet at δ 4.22 and δ 3.53 ppm. The four methoxy groups were observed at δ 3.85 ppm H-2, δ 3.86 ppm H-3, δ 3.84 ppm H-9 and δ 3.83 ppm H-10 displayed on the aromatic ring. Additionally, the aliphatic signals were assigned at δ 3.11 and δ 2.66 ppm (5a, b) and δ 3.23 and δ 2.76 ppm (6a, b) due to CH_2-CH_2 spin system.

In 150 MHz ^{13}C NMR spectrum of a compound, the spectrum indicated the presence of twenty-one carbon signals. Including, the four methoxy carbons were found to be at δ 56.72, δ 56.42, δ 60.80 and δ 56.37 ppm for carbon position (2, 3, 9 and 10). Furthermore, the downfield shift of the ^{13}C NMR signal of CH (δ 60.56 ppm C-13a) and CH_2 (δ 52.68 ppm C-6) and (δ 54.85 ppm C-8) groups indicated these carbon atoms were adjacent to the nitrogen atom. Moreover, the eight quaternary carbon were found at δ 149.30 ppm for C-2, δ 149.16 ppm for C-3, δ 127.83 ppm for C-4a, δ 128.70 ppm for C-8a, δ 146.28 ppm for C-9, δ 151.76 ppm for C-10, δ 128.89

ppm for C-12a and δ 130.70 ppm for C-13b (Table 3). According to the ^{1}H NMR and ^{13}C NMR results, the isolated compound was identified as tetrahydropalmatine (Joanne *et al*., 2003). The MS spectrum, the molecular weight of compound was confirmed by the MS spectrum, which shows an *m/z* value of $[M + H]^{+}$ at 356.0. Finally, the structure of the isolated compound was assigned as tetrahydropalmatine.

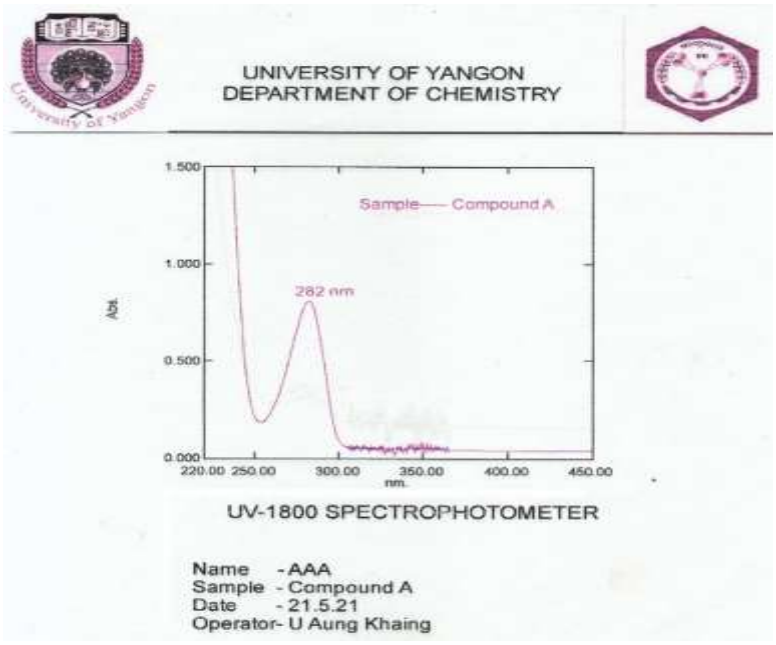

(a)

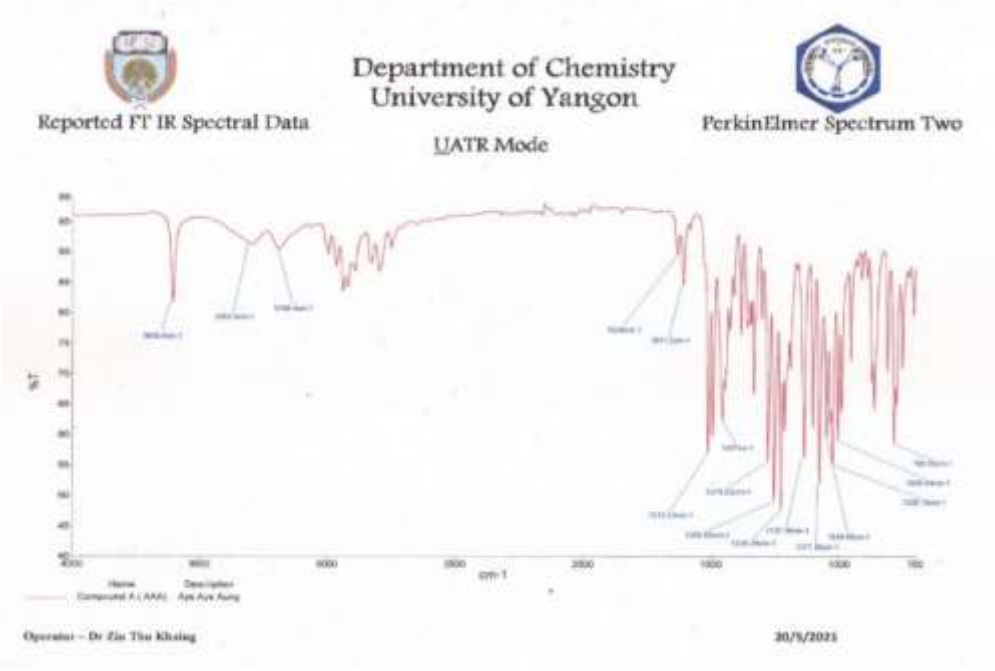

(b)

Figure 2. (a) UV and (b) FT IR spectra of the isolated compound from *S. venosa*

Table 2. FT IR Spectral Data and Band Assignment of the Isolated Compound

Wavenumber (cm^{-1})	Assignments
3050 and 3020	=C-H stretching vibration
2970 and 2890	C-H asymmetric stretching vibration
2850	C-H symmetric stretching vibration
1635, 1611 and 1513	C=C stretching vibration in aromatic ring
1457	C-H bending vibration
1279, 1255 and 1228	C-N aliphatic stretching vibration
1137 ,1078 and 1050	C-O-C stretching vibration
1026 and 1005	C-C ring stretching vibration
785	C-H out of plane bending vibration

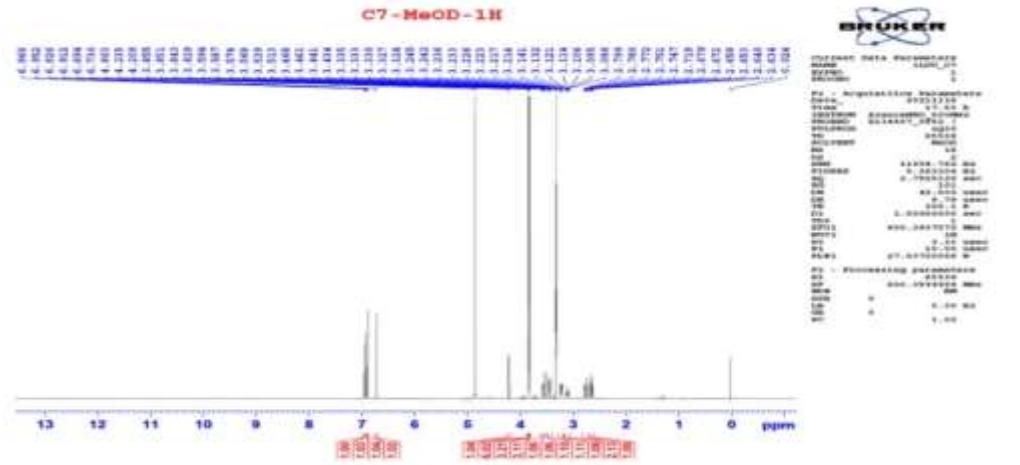

(a)

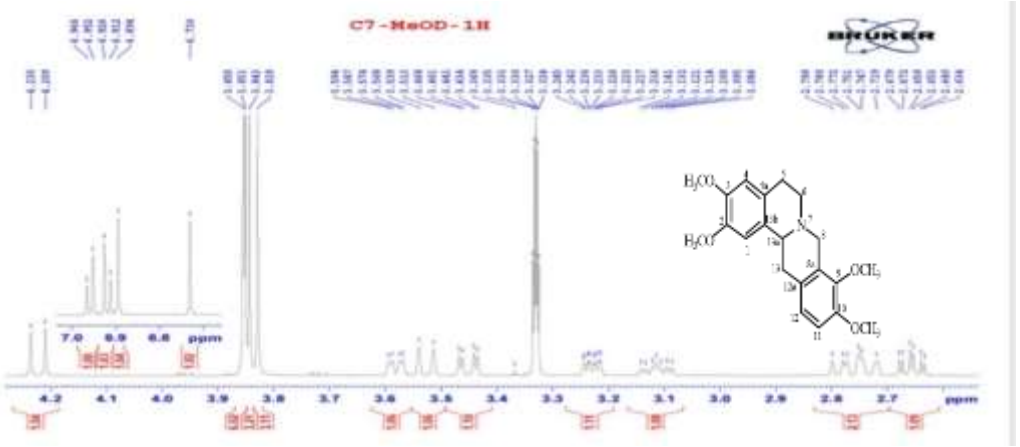

(b)

Figure 3. (a) and (b) ^{1}H NMR spectra (600 MHz, MeOD) of the isolated compound

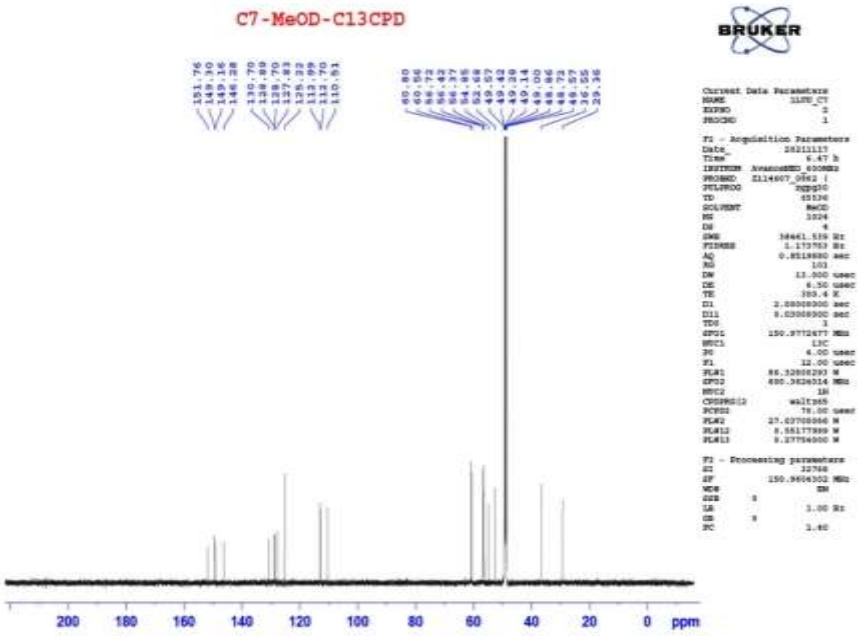

(a)

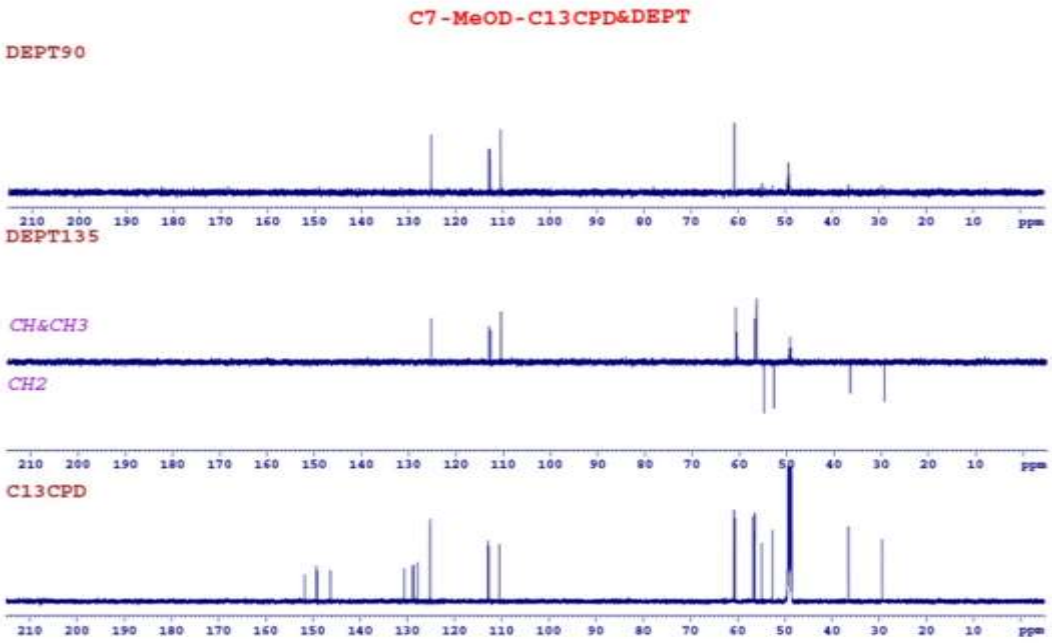

(b)

Figure 4. (a) ^{13}C NMR and (b) ^{13}C NMR (DEPT) spectra (150 MHz, MeOD) of the isolated compound

Table 3. ^{1}H NMR and ^{13}C NMR Spectra Data of the Isolated Compound

Position	Isolated compound		Literature * $CDCl_3$	
	δ_H (J Hz)	**δ_C (DEPT)**	**δ_H (J Hz)**	**δ_C (DEPT)**
1	6.89 (s)	110.51 (CH)	6.73 (s)	108.59 (CH)
2	-	149.30 (C)	-	147.48 (C)
3	-	149.16 (C)	-	147.42 (C)
4	6.73 (s)	112.99 (CH)	6.62 (s)	111.33 (CH)
4a	-	127.83 (C)	-	126.76 (C)
5	(a) 3.11 (obsc) (b) 2.66 (obsc)	29.36 (CH_2)	(a) 3.13 (obsc) (b) 2.66 (obsc)	29.06 (CH_2)
6	(a) 3.23 (obsc) (b) 2.66 (obsc)	52.68 (CH_2)	(a) 3.21 (obsc) (b) 2.66 (obsc)	51.48 (CH_2)
8	(a) 4.22 (d,15.60) (b) 3.53 (d,15.60)	54.85 CH_2)	(a) 4.24 (d, 15.63) (b) 3.54 (d, 15.63)	53.96 (CH_2)
8a	-	128.70 (C)	-	127.07 (C)
9	-	146.28 (C)	-	145.06 (C)
10	-	151.76 (C)	-	150.24 (C)
11	6.92d, 8.40)	112.70 (CH)	6.79 (d,8.38)	110.94 (CH)
12	6.96 (d, 8.40)	125.22 (CH)	6.88 (d,8.38)	123.82 (CH)
12a	-	128.89 (C)	-	128.61 (C)
13	(a)3.45(dd, 16.20, 4.20) (b)2.76 (obsc)	36.55 (CH_2)	(a) 3.27 (dd,15.76, 3.65) (b) 2.83(dd,15.76, 11.49)	36.28 (CH2)
13a	3.58 (obsc)	60.56 (CH)	3.54 (obsc)	59.29 (CH)
13b	-	130.70 (C)	-	129.66 (C)
2-OCH_3	3.85 (s)	56.72 (CH_3)	3.87 (s)	56.05 (CH_3)
3-OCH_3	3.86 (s)	56.42 (CH_3)	3.89 (s)	55.84 (CH_3)
9-OCH_3	3.84 (s)	60.80 (CH_3)	3.85 (s)	60.14 (CH_3)
10-OCH_3	3.83 (s)	56.37 (CH_3)	3.84 (s)	55.81 (CH_3)

*(Joanne *et al*., 2003). obsc = obscure

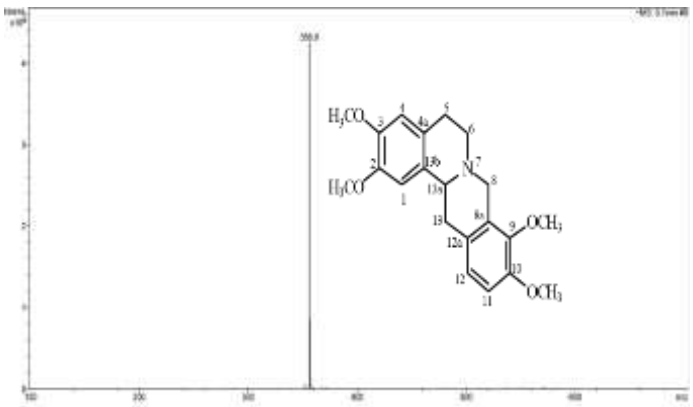

Figure 5. ESI Mass Spectrum of the isolated compound (*m/z* of +MS=356)

Screening of Antimicrobial Activity of Crude Extracts and the Isolated Compound

The present study was aimed to evaluate the potency of petroleum ether, ethyl acetate, ethanol, methanol, and watery extracts from the tuber of *S. venosa* against eight different strain of microorganisms such as *Escheerichia coli, Candida albicans, Bacillus subtilis, Staphylococcus aureus, Pseudomonas fluorescens, Agrobacteriumb tumefaciens, Bacillus pumilus, and Micrococcus luteus* by using agar well diffusion method. The measurable zone diameter, including the well diameter, shows the degree of antimicrobial activity. The agar well diameter is 10 mm. The greater zone diameter indicates the higher potency of the antimicrobial activity. According to the results shown in Table 4 and Figure 6, the petroleum ether, ethyl acetate, ethanol, methanol, and watery extracts showed antimicrobial activity against all tested microorganisms (12 mm to 22 mm). Among these extracts, the ethyl acetate extract (17 mm to 22 mm) showed higher inhibition zone diameter than the other extracts, except for *Bacillus pumilus*. Therefore, the ethyl acetate extract may be traditionally used for treating antimicrobial infections.

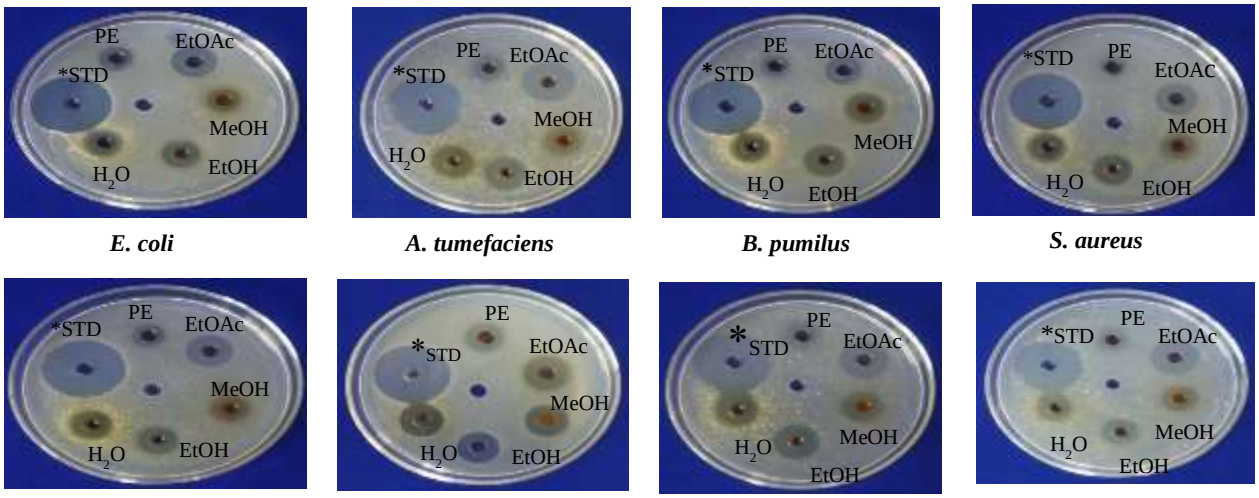

*STD = Chloramphenicol for bacteria, *STD = Nystatin for fungus

Figure 6. Antimicrobial activity of various extracts from tuber of *S. venosa*

Table 4. Antimicrobial Activity Results of *S. venosa*

Microorganisms	Inhibition Zone Diameter (mm)					
	PE extract	EtOAc extract	EtOH extract	MeOH extract	H_2O extract	*STD
E. coli	14	19	16	15	13	32
C. albicans	16	20	20	20	20	33
B. subtilis	14	19	17	16	15	33
S. aureus	12	19	18	14	14	32
P. fluorescens	13	21	17	16	15	30
A. tumefaciens	12	22	19	18	18	30
B. pumilus	13	17	20	20	13	33
M. luteus	12	21	20	18	17	33

Agar well diameter = 10 mm (1µg/mL)
10 mm – 14 mm = (+) low activity
15 mm – 19 mm = (++) medium activity
20 mm and above = (+++) very high activity

Antioxidant Activity of Crude Extracts of *S. venosa*

The antioxidant activity was determined in terms of hydrogen donating or radical scavenging ability in the present of the stable free radical (DPPH) using spectrophotometric method. *In vitro* antioxidant activity of the 95% ethanol, watery extracts, and a compound from the tuber of *S. venosa* and the standard ascorbic acid were determined by using free radical scavenging DPPH assay. In this study, the various concentration (15.625, 31.25, 62.5, 125, 250, and 500 µg/mL) of ethanol and watery extracts and six different concentration (3.125, 6.25, 12.5, 25, 50 and 100 µg/mL) of an isolated compound were used. An increase in radical scavenging activity evaluates a decrease in absorbance. The radical scavenging activities of the different crude extracts and a compound were expressed in % RSA and IC_{50} (50% inhibitory concentration). The absorbance of these solutions was measured at 517 nm by using a UV spectrophotometer. These results are shown in Tables (5 and 6) and Figures (7 and 8). According to the results, the IC_{50} values of ethanol, watery extracts and a compound were found to be 134.93, 173.61, and 24.43 µg/mL. Therefore, the lower the IC_{50} value exhibits the higher the antioxidant activity in the sample. The antioxidant activity was found to be lower than that of standard ascorbic acid (2.83 µg/mL).

Table 5. Antioxidant Activity of Crute Extracts *S. venosa tuber*

Samples	% RSA (mean ± SD) in different concentrations						IC_{50} (µg/mL)
	15.625	31.25	62.5	125	250	500	
Ethanol	16.62 ± 0.008	29.31 ± 0.026	32.48 ± 0.017	46.44 ± 0.025	91.24 ± 0.005	98.09 ± 0.016	134.93
Watery	20.55 ± 0.005	25.85 ± 0.029	30.96 ± 0.030	42.54 ± 0.001	61.13 ± 0.000	82.58 ± 0.009	173.61

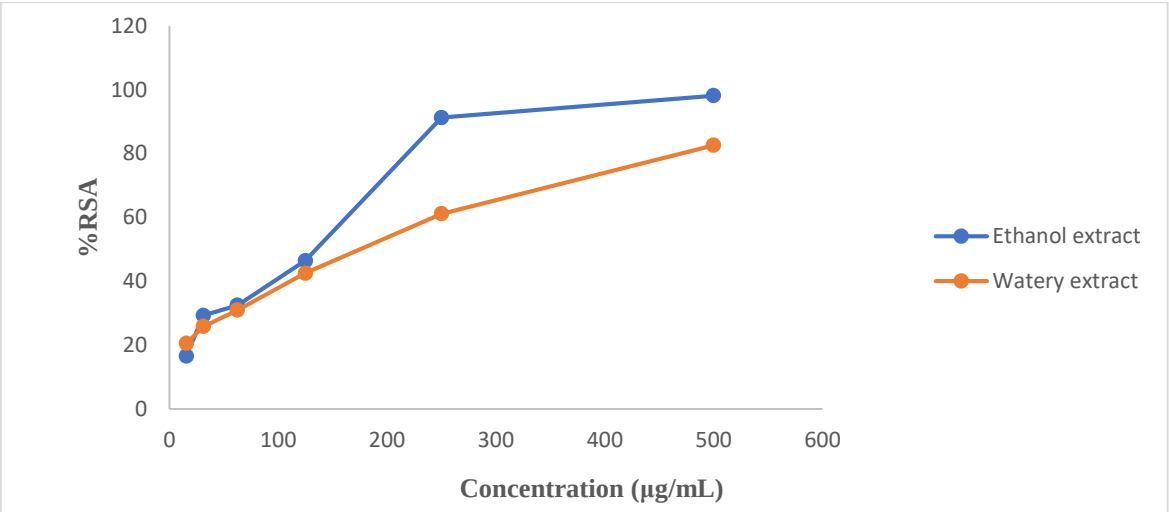

Figure 7. % RSA of ethanol and watery extracts of *S. venosa versus concentration*

Table 6. Antioxidant Activities of Isolated Compound and Standard Ascorbic Acid

Samples	% RSA (mean ± SD) in different concentrations (µg/mL)						IC_{50} (µg/mL)
	1.5625	3.125	6.25	12.5	25	50	
Compound	31.57 ± 0.063	45.48 ± 0.009	47.39 ± 0.041	48.95 ± 0.004	50.57 ± 0.003	52.02 ± 0.001	24.43
Ascorbic acid	33.03 ± 0.040	53.94 ± 0.095	90.48 ± 0.017	94.16 ± 0.000	96.94 ± 0.000	96.76 ± 0.000	2.83

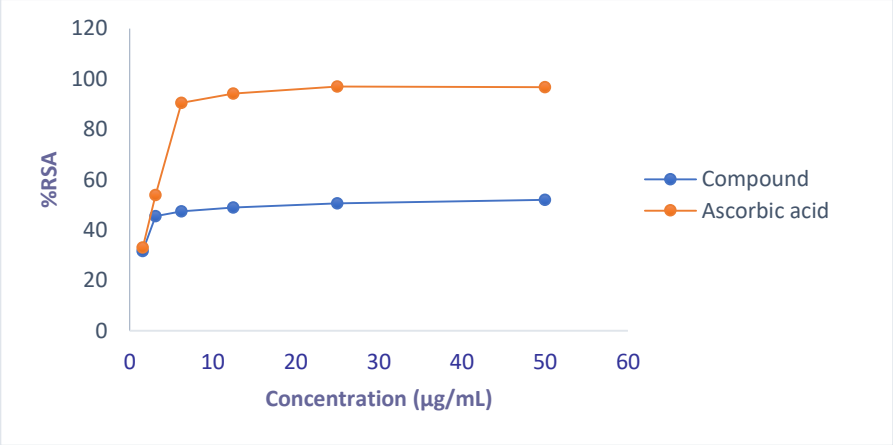

Figure 8. % RSA of isolated compound and standard ascorbic acid versus concentration

Conclusion

The overall assessments of the research work include preliminary phytochemical investigations, isolation, and identification of a bioactive compound, *in vitro* antimicrobial and antioxidant activities from the tuber of *S. venosa*. The important bioactive molecules of the sample were explored with preliminary phytochemical screening and reported to consist of alkaloids, α-amino acid, carbohydrates, glycosides, flavonoids, organic acids, phenolic compounds, reducing sugars, steroids, saponins, and tannins. The isolated compound (0.06 % yield and white crystal) was separated from the ethyl acetate extract by using a thin layer and column chromatographic separation techniques. The isolated compound was identified by the modern spectroscopic methods such as TLC, UV-visible, FT IR, ^{1}H NMR, ^{13}C NMR, and MS. According to the results, the isolated compound would be deduced as an alkaloids compound: tetrahydropalmatine ($C_{21}H_{25}NO_4$, R_f = 0.57). The different crude extracts such as ethyl acetate, ethanol, methanol, and watery extracts exhibited the significant antimicrobial activity by the agar well diffusion method. The ethyl acetate extract has the most potent antimicrobial activity than the other extracts, except for *B. pumilus* against test microorganisms. The antioxidant activity of the crude extracts and the isolated compound was determined by DPPH assay method. According to the results, the ethanol extract (IC_{50} value =134.93 µg/mL) indicated antimicrobial activity than the watery extract (IC_{50} value =173.61 µg/mL). Furthermore, the isolated compound also showed higher antioxidant activity (IC_{50} value =24.43 µg/mL) than the extracts. Alkaloids are bioactive compounds and it can be used for therapeutic agents in several ailments. Therefore, *S. venosa* is a very popular medicinal plant in traditional medicine.

Acknowledgements

The authors would like to thank the Department of Higher Education, Ministry of Education, Myanmar, for the permission of doing this research and Myanmar Academy of Arts and Sciences for allowing the writing of this paper.

References

Harborne, J. B. (1984). *Phytochemical Methods A Guide to Modern Techniques of Plant Analysis.* New York*:* 2nd Ed., Chapman and Hall, 120-160

Joanne, T. B., P. A. S. Donald, H. L. K. Colin, A. B. Karl, and K. William. (2003). "Characterization of Alkaloids from some *Australian Stephania* (Menispermaceae) Species". *Phytochemistry*, 63, pp 711-720

Marinova, G. and V. Batchvarov. (2011)." Evaluation of the Methods for Determination of the Free Radical Scavenging Activity by DPPH ". *Bulgarian Journal of Agricultural Science*, 17, pp11-24

Selvamohan, T., V. Ramadas, and S, S, S, Kishore. (2012)**.** "Antimicrobial Activity of Selected Medicinal Plants Against Some Selected Human Pathogenic Bacteria". *Advances in Applied Science Research*, vol.3(5), pp3374-3381

Soares, J. R., Dins, T. C.P. A Cunha, and L. M. Ameida. (1997). "Antioxidant Activity of some Extracts of Thymus zygis.". *Free Radical Research Journal*, vol.26, pp 469-478

Moongkarndi, P., N., Kosem, O., Luanratana, S., Jongsomboonkusol, and N., Pongpon. (2004). "The Antiproliferative activity of Thai Medicinal Plant Extracts On Human Breast Adenocarcinoma Cell Line". *Fitoterapia*, vol.75, pp.375-377

Ingkaninan, K., P. Phengpa, S. Yuenyongsawad, and N. Khorana. (2006). "Acetylcholinesterase inhibitors from *Stephania venosa* tuber". *J. Pharmacy Pharmacol*., vol.58, pp.695-700

Wong, M. L., and J. Licinio. (2001). Research and Treatment Approaches to Depression. *Nat. Rev. Neurosci*., vol.2, pp.343-351

INVESTIGATION OF SOME BIOLOGICAL ACTIVITIES AND ISOLATION OF PHYTOCONSTITUENTS FROM THE LEAVES OF *DREGEA VOLUBILIS* (L. F.) (GWAY-TAUK)

Nan Wa Thone Oo[1], Prema[2], Ni Ni Than[3]

Abstract

The study aims to investigate some biological activities and the isolation of phytoconstituents from the leaves of *Dregea volubilis* (L. f.). *Dregea volubilis* belongs to the Apocynaceae family, and it is locally known as "Gway-tauk" in Myanmar. In our experiments, six compounds (**1-6**) were isolated from the EtOAc extract of Gway-tauk leaves, and they were characterized by some physico-chemical tests, R_f values on TLC, and modern spectroscopic methods such as UV and FT IR. The antimicrobial activity of EtOH extract showed moderate activity with the inhibition zone diameter range between 10~15 mm against eight tested microorganisms. Then, EtOH and watery extracts were found to have no cytotoxic effect on brine shrimp up to the maximum dose of 1000 µg/mL. Moreover, the watery extract (bitterness value, 320) of Gway-tauk leaves was less bitter than standard quinine hydrochloride R (bitterness value, 2000). In the α-amylase inhibitory activity, the IC_{50} values of ethanol and watery extracts were observed to be 3.64 and 2.67 µg/mL. The antioxidant activity of ethanol (IC_{50}: 3.54 µg/mL) and watery (IC_{50}: 5.11 µg/mL) extracts of Gway-tauk leaves possessed potent antioxidant activity, as well as positive control ascorbic acid (IC_{50}: 2.60 µg/mL).

Keywords: *Dregea volubilis*, antimicrobial activity, cytotoxicity, bitterness value, α-amylase inhibitory activity, antioxidant activity

Introduction

Herbal medicines are traditionally used for the treatment of various illnesses. Hence, medicinal plants have been receiving great attention worldwide from researchers because of their safe utility. Medicinal plants that provide a large group of economically important plants provide the basic raw materials for indigenous pharmaceuticals (Natarajan *et al*., 2013). Myanmar is the second-largest country in Southeast Asia, and about half of the land area is covered with forest. Myanmar has been using herbal remedies for medicinal purposes due to the rich diversity of medicinal plants in various climate change zones. Approximately 11,800 species belonging to 273 families of plants have been recorded in the Myanmar flora. Several of these plant species are used in traditional cosmetics and/or folk medicine. However, most of the scientific evidence for the bioactivities of these medicinal plants and phytochemical constituents is still behind the scenes. The plant *D. volubilis* is a large, woody, twining perennial shrub of the Apocynaceae family. It is a stocky, smooth, frosted, woody vine (Karthika *et al*., 2012). The leaves are ovate, 7.5 to 15 cm long, 5 to 10 cm wide, rather leathery, rounded, or pointed at the base. The flowers are green in clusters, about 1 cm wide. The fruits are usually double, broadly lanceolate, 7.5 to 10 cm long, plump, longitudinally ribbed, and velvety until ripe (Barathamma *et al*., 2015). The plant is found in Southeast Asia, including India, Sri Lanka, Indonesia, Bangladesh, Cambodia, Vietnam, Malaysia, and the Philippines, Thailand, China, and Myanmar. It is widely used to treat eye infections, tumors, asthma, skin diseases, rheumatic pain, cough, fever, severe colds, dyspepsia, urinary tract infections, and hemorrhoids (Pandikumar *et al*., 2007; Biju, 2007; Rajadurai *et al*., 2009). Recently, numerous studies have suggested that the extract from *D. volubilis* leaf specimens has many biological activities. However, scientific evidence from this sample has not been reported yet in Myanmar. Therefore, in this present study, *D. volubilis* (Gway-tauk) leaves have been chosen to investigate some biological activities and isolate phytoconstituents.

[1] Department of Chemistry, East Yangon University, Myanmar
[2] Department of Chemistry, University of Yangon, Myanmar
[3] Department of Chemistry, University of Yangon, Myanmar

Materials and Methods

Plant Material

Dregea volubilis leaves were collected from Mawlamyine Township, Mon State, in November 2021. After collection, the sample was confirmed at the Department of Botany, University of Yangon. The fresh leaves were cleaned by washing them with water and air-drying at room temperature. The dried leaves were cut into small pieces and ground into powder by using a grinding machine. The powdered sample was stored in an airtight container to prevent contamination and kept for the isolation of organic compounds and screening biological activities.

Materials, Equipments, and Instruments

Ascorbic acid, acarbose (standard) and α-amylase enzyme (from human saliva),agar, caffeine , DPPH (2,2-diphenyl-1-picrylhydrazyl), distilled water, ethyl acetate, 95 % ethanol, glucose, peptone, yeast, 0.1 M hydrochloric acid, 1 mM iodine solution, petroleum ether PE (b.pt 60 –80 °C), 0.02 M phosphate buffer solution, potassium dichromate ($K_2Cr_2O_7$), purified drinking water, 0.5% starch solution, quinine hydrochloride R, sodium chloride (NaCl)

Air pump, automatic high-speed autoclave (Model S-90 N, Tomy Seiko Co., Ltd., chambers, clean bench (Hitachi Ltd., Japan), hot plate, hot oven (Modern, GM-10 E (DRWG, No.9 B-815051)), a refrigerator and incubator box (Sanyo Co., Ltd.), quartz cuvette (4 mL) and UV-visible spectrophotometer (GENESYS 10 S UV-VIS, China), water bath (Yamoto Model BT-18 No. 157)

Preparation of Crude Extracts

Air-dried powdered leaves of *Dregea volubilis* (L. f.) Benth ex Hook. f. (Gway-tauk) (400 g) was extracted with ethanol (2 L) by sonication (1 h × 6 times) and filtered. The filtrate was evaporated to get a crude extract. The crude ethanol extract was partitioned with PE (800 mL) and water (50 mL) by using a separatory funnel. When the solvent was removed, a PE extract was obtained. Then, the aqueous layer was partitioned with EtOAc (800 mL), resulting in EtOAc and H_2O extracts.

Isolation of Organic Compounds from Gway-tauk Leaves

Organic compounds were separated from the crude extract by the column chromatographic method. Silica gel (200 g) was used as an adsorbent and a PE: EtOAc mixture was used as eluent with different solvents in ratios from non-polar to polar. A total of 15 fractions were obtained. Each individual fraction was checked by TLC using 5 % H_2SO_4 as the visualization agent. The fractions with the same R_f values were combined, and nine combined fractions were obtained. Among them, Fraction F-2 was chromatographed by normal-phase silica gel open column chromatography with PE: EtOAc (19:1, v/v) as a solvent system, to obtain compound **1** (20 mg, 0.005%) and compound **2** (50 mg, 0.013%). The fractions F-3, F-5, and F-6 were purified by silica gel open column PE: EtOAc (9:1, 1:2, and 1:5, v/v) to obtain compound **3** (40 mg, 0.01%), compound **4** (15 mg, 0.004%) and compound **5** (16 mg, 0.004%). Compound **6** (60 mg, 0.015%) was obtained from the fraction by silica gel column chromatography, using EtOAc: MeOH (90:1, v/v) as a solvent system.

Antimicrobial Activity of Various Crude Extracts of *Dregea volubilis* (L. f.) Benth ex Hook. f. (Gway-tauk) Leaves by Agar Well Diffusion

The antimicrobial activity of PE, EtOAc, EtOH, and H_2O from leaves of Gway-tauk were determined against eight strains of microorganisms such as *Agrobacterium tumefaciens*, *Bacillus pumilus*, *Bacillus subtilis*, *Candida albicans*, *Escherichia coli*, *Micrococcus luteus*, *Pseudomonas fluorescens*, and *Staphylococcus aureus* by employing Agar well diffusion method. In this antibacterial activity assay, the nutrient agar (20-25 mL) was boiled, poured into the test tube, sealed with cotton, and autoclaved at 121 °C for 15 min (Finegold, 1978). After autoclaving, the tubes were cooled to 30-35 °C and poured into sterilized petri dishes, and 0.1-0.2 mL of test organisms were also added to them (Cruickshank, 1960). They were allowed to settle the agar for 2-3 h. After the agar was set, 8 mm agar wells were made using the agar well cutter. Thereafter, about 0.2 mL of the sample, namely the PE, EtOAc, EtOH, and H_2O solutions of Gway-tauk leaves, was added to each well and incubated at 37 °C for 24 h. The zone of inhibition that appeared around the agar well indicated the presence of antimicrobial activity.

Determination of Cytotoxicity of Ethanol and Watery Extracts of Gway-tauk Leaves

Crude extracts of Gway-tauk leaves were investigated by brine shrimp lethality bioassay according to the procedure described by Mayer *et al*. (1982). The brine shrimp was used in this study for cytotoxicity bioassay (Ali *et al*., 2013). Artemia cysts (0.1 g) were added to the 300 mL separating funnel of artificial sea water. Each extract and standard (5 mg) were dissolved in (5 mL) of distilled water to obtain a stock solution (1000 µg/mL) from that the concentrations of each solution (1000, 100, 10, and 1 µg/mL) were prepared bytenfold diluted with distilled water. After that, artificial seawater (9 mL) and (1 mL) of various concentrations of samples and standard solutions were added to each chamber. Live brine shrimp (10 nauplii) were then removed with a Pasteur pipette and added to each chamber. They were incubated at RT for about 24 hours. After 24 hours, the number of dead or surviving *Artemia* was counted, and the 50 % lethal dose (LD_{50}) was calculated by a linear regressive Excel programme (Sahgal *et al*., 2010). The control solution was prepared by using distilled water in place of the sample solution.

Determination of Bitterness Values

Bitters are medicinal plant materials that have a strong bitter taste. The bitter properties of plant material are determined by comparing the threshold bitter concentration of an extract of materials with that of dilute solution of quinine hydrochloride R. The bitterness value is expressed in units equivalent to the bitterness of a solution containing 1 g of quinine hydrochloride R in 2000 mL (WHO, 1998).

$$\text{Bitterness value} = \frac{2000 \times C}{A \times B}$$

Where,

A = concentration of stock solution (C_s) mg/mL

B = volume of (V_s) mL tube with threshold bitterness concentration

C = quantity of quinine hydrochloride (in mg) tube with threshold bitter Concentration

Determination of *α*-Amylase Inhibition Potency

Alpha amylase is an enzyme that hydrolyzes the alpha-bonds of large alpha linked polysaccharides such as glycogen and starch to yield glucose and maltose. Alpha amylase inhibitory activity was based on the starch iodine method that was originally developed and later employed by others for determination of amylase activity in plant extracts with some modifications (Yang *et al*., 2012). In the *α*-amylase assay, the starch-iodine method was used. The percent inhibition of each sample solution was calculated using the following formula.

$$\% \text{ Inhibition} = \frac{A_{control} - A_{sample}}{A_{control}} \times 100$$

Where,

$A_{control}$ = the absorbance of the control solution

A_{sample} = the absorbance of sample solution

Determination of Antioxidant Activity by DPPH Free Radical Scavenging Assay

The antioxidant activity of 70 % ethanol and watery extracts was measured by the DPPH Free Radical Scavenging Assay (Lee *et al*., 2002). The active free radical scavenging of DPPH (2,2-diphenyl,1-picrylhydrazyl) was determined by a spectrophotometric method. The following equation was used to calculate the percentage inhibition of each plant material: IC_{50} values (half-maximal inhibitory concentration) were calculated using the linear regressive Excel programme.

$$\% \text{ Inhibition} = \frac{A_{control} - A_{sample}}{A_{control}} \times 100$$

Where,

$A_{control}$ = the absorbance of control solution

A_{sample} = the absorbance of tested sample solution

Results and Discussion

Identification of Isolated Compounds from Gway-tauk Leaves

The six isolated compounds (1-6) from the EtOAc extract of the leaves of Gway-tauk were identified by chemical tests, TLC, UV and FT IR spectroscopy.

Identification of isolated compound 1

Compound **1** (0.005 % yield) was isolated as a colourless needle crystal from an EtOAc extract of the leaves of Gway-tauk. It is soluble in PE, $CHCl_3$, EtOAc, and acetone, but MeOH, EtOH, and H_2O are insoluble. It is UV active and the R_f value was found to be 0.71 in PE: EtOAc (19:1 v/v). Compound **1** was classified as steroid compound. Because the reaction with the Libermann-Burchard test produced green coloration, compound 1 was classified as a steroid compound. The presence of C=C resulted a yellow spot on the TLC chromatogram with iodine vapour as shown in (Figure 1(a)). It also provided a yellow colour on TLC when treated with 5 % H_2SO_4 followed by heating. The UV spectrum of compound **1** in MeOH is shown in (Figure 1 (b)). According to the UV spectrum, the main absorption bands were found at 239 and 272 nm. Therefore, compound **1** contained a double bond conjugation. The functional groups present in compound **1** were also examined by FT IR spectroscopy. The presence of =C-H stretching and bending of the alkene group appears at 3100 cm^{-1} and 995 cm^{-1}. The bands at 1742 cm^{-1} indicated

the stretching vibration of C=O in the carbonyl group. The characteristic bands at 2918 and 2850, 1442 and 1388, 1170, and 1152 cm^{-1} also indicated the presence of C-H stretching of asym and sym CH_2 and CH_3 groups, C-H bending of methylene and methyl groups, and C-O stretching of the cyclic O group (Figure 1(c)). All of the above results, such as R_f value, chemical properties, and UV and FT IR spectral data of compound **1,** may be considered as steroid compounds containing ester groups.

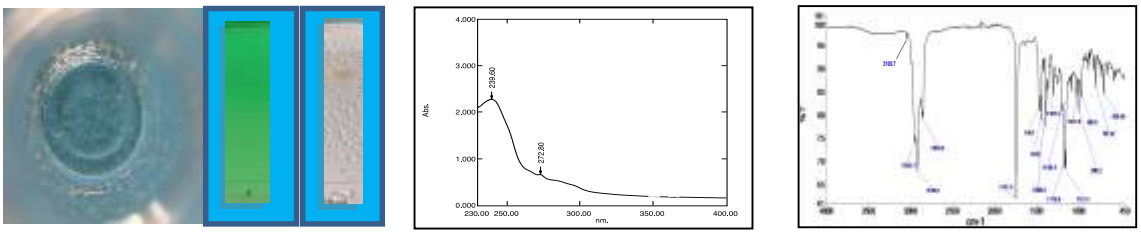

(a) **(b)** **(c)**

Figure 1. (a) TLC of isolated compound 1

(b) UV spectrum of isolated compound 1 in MeOH

(c) FT IR spectrum of isolated compound 1

Identification of isolated compound 2

Compound 2 (0.013 %) was isolated from an EtOAc extract of Gway-tauk leaves as a white, amorphous substance. It is soluble in PE, $CHCl_3$, and EtOAc but insoluble in acetone, MeOH, EtOH, and H_2O. It is UV inactive, and the R_f value was found to be 0.36 in PE: EtOAc (19:1 v/v). Compound **2** was classified as an organic acid since the reaction with bromocresol green gave a yellow coloration (Figure 2(a)). It also provided a pink colour to TLC when treated with 5 % H_2SO_4 followed by heating. The functional groups present in compound **2** were also studied by FT IR spectroscopy as shown in Figure 2 (b). The presence of O-H stretching in the alcoholic group was also confirmed by the appearance of a peak at 3450 cm^{-1}. The bands at 1713 cm^{-1} showed stretching vibrations of C=O in the carbonyl group. The characteristic bands at 2918 and 2850, 1463, 1377, 1367, 1059 and 1038 cm^{-1} also showed the presence of C-H stretching and bending of CH_2 and CH_3 groups, C-H bending of the methylene and methyl groups, O-H bending of the alcoholic group and C-O stretching of the cyclic-O group. All of the above-mentioned results obtained from R_f value, physico-chemical characterization, and modern spectroscopic techniques such as FT IR spectral data, indicate that the compound **2** may be considered an organic acid compound.

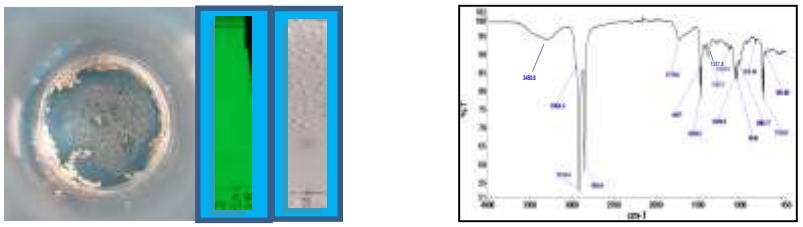

(a) **(b)**

Figure 2. (a) TLC of isolated compound 2

(b) FT IR spectrum of isolated compound 2

Identification of isolated compound 3

Compound 3 was isolated as a colourless needle crystal from an EtOAc extract of Gway-tauk leaves (0.01 % yield). The melting point is 138-140 ºC. The FT IR spectral data of compound **3** were found to be 3645, 2932, 2850, 1645, 1463, 1377, 1367, 1052 and 959 cm^{-1} (Patra *et al*., 2010). The compound **3** was found to be similar to those of reported *β*–sitosterol. So, the compound **3** was assigned as *β*-sitosterol and its chemical structure is shown in Figures 3 (a, b, c).

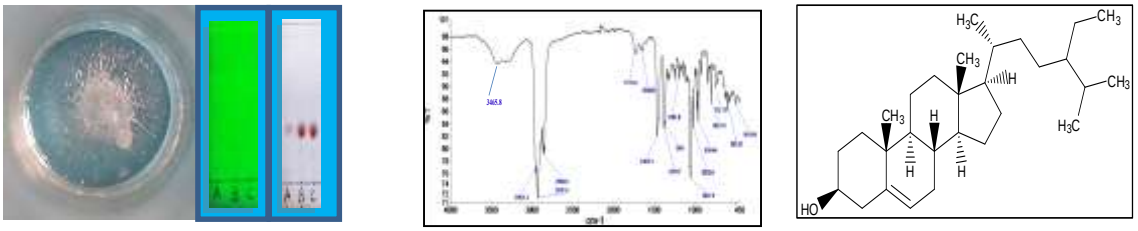

(a) **(b)** **(c)**

Figure 3. (a) Image of morphology and TLC of isolated compound 3
(b) FT IR spectrum of isolated compound 3
(c) Chemical structure *β*-sitosterol ($C_{29}H_{50}O$)

Identification of isolated compound 4

Compound **4** (0.004% yield) was isolated as a colourless crystal from an EtOAc extract of the leaves of Gway-tauk. It is soluble in PE, $CHCl_3$, EtOAc, and acetone but insoluble in MeOH, EtOH, and H_2O. It is UV inactive, and the R_f value was found to be 0.51 in PE: EtOAc (1:2 v/v). Compound **4** was classified as an organic acid compound since the reaction with bromocresol green gave yellow coloration. It also provided a cherry red colour on TLC when treated with 5 % H_2SO_4, followed by heating (Figure 4(a)). From the spectrum, the presence of O-H stretching of the alcoholic group could also be confirmed, with the peak appearing at 3319 cm^{-1}. The bands at 1703 cm^{-1} indicated the stretching vibration of C=O in the carbonyl group. The characteristic bands at 2932 and 2850, 1463 and 1377, and 1052 cm^{-1} also indicated the presence of C-H stretching of asym and sym CH_2 and CH_3 groups, C-H bending of methylene and methyl groups, and C-O stretching of the cyclic O group. With all of the above data obtained from the R_f value, physico-chemical data, and FT IR spectral data, compound **4** may be considered an organic acid compound (Figure 4(b)).

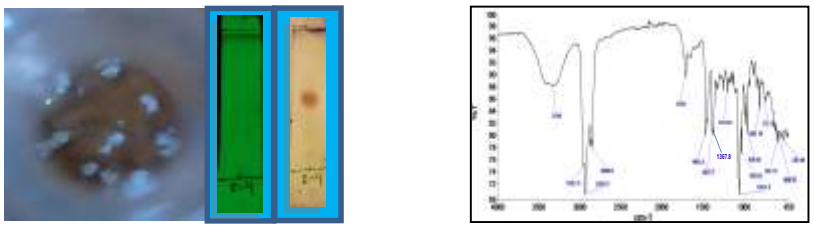

(a) **(b)**

Figure 4. (a) TLC of isolated compound 4
(b) FT IR spectrum of isolated compound 4

Identification of isolated compound 5

Compound **5** (0.004 % yield) was isolated as a white amorphous compound from an EtOAc extract of the leaves of Gway-tauk. It is soluble in $CHCl_3$, EtOAc, acetone, MeOH, and EtOH but insoluble in H_2O. It is partially dissolved in PE. It is UV active, and the R_f value was found to be 0.27 in PE: EtOAc (1:9 v/v). Compound **5** was classified as an organic acid compound since the reaction with bromocresol green gave it a green coloration. It was classified as terpenoids compound since the reaction with Libermann-Burchard test gave red colouration. It also provided a pink colour to TLC when treated with 5 % H_2SO_4 followed by heating. And then, it was given a blue colour on TLC when treated with vanillin followed by heating (Figure 5(a)). The UV spectrum (Figure 5 (b)), of compound **5** revealed the absorption maxima (λ_{max}) at 216 nm and 257 nm in MeOH indicating the presence of a conjugated double bond group due to $\pi \rightarrow \pi^*$ transition. Compound **5** is illustrated in (Figure 5 (c)). The broad band ranging between 3550~2500 cm^{-1} indicated a carboxylic acid –COOH group and a –OH stretching vibration. The absorption band which appeared at 3358 cm^{-1} showed the presence of an alcoholic group. The band at 1728 cm^{-1} referred to α, β-unsaturated carbonyl group and at 1645 cm^{-1} and 1452 cm^{-1} indicated the presence of C=C group of aromatic rings. In addition, the absorption bands at 1370 cm^{-1} are appeared due to O-H bending vibration and the absorption bands at 1234 cm^{-1}, 1166 cm^{-1} and 1056 cm^{-1} due to C-O stretching vibration of the alcoholic group. All of the above data obtained from R_f value, physico-chemical and UV and FT IR spectral data, compound **5** may be considered as terpenoid compound containing acid group.

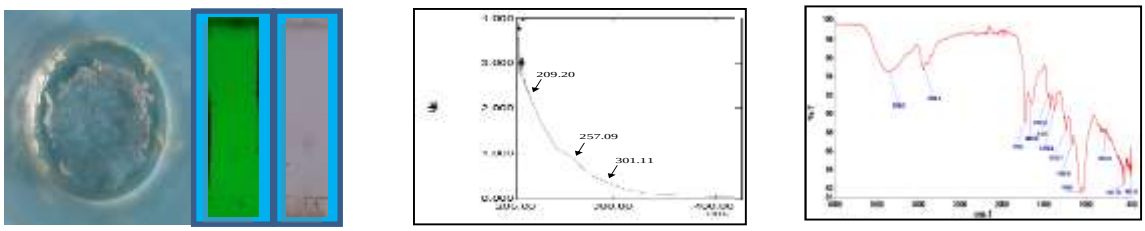

(a) **(b)** **(c)**

Figure 5. (a) TLC of isolated compound 5
(b) UV spectrum of isolated compound 5 in MeOH
(c) FT IR spectrum of isolated compound 5

Identification of isolated compound 6

Compound **6** (0.015 % yield) was isolated as a colorless crystal from an EtOAc extract of the leaves of Gway-tauk. It is soluble in EtOAc, $CHCl_3$, and MeOH but insoluble in PE, acetone, and EtOH. It is partially dissolved in H_2O. It is UV inactive and the R_f value was found to be 0.48 in EtOAc: MeOH (90:1 v/v). Compound **6** was classified as a glycoside compound since the reaction with 10 % lead acetate solution gave white precipitation. It also provided a blue colour on TLC when treated with vanillin followed by heating (Figure 6(a)). The functional groups present in compound **6** were also studied by FT IR spectroscopy. FT IR spectrum (KBr, ν_{max} cm^{-1}) of isolated compound **6** is illustrated in Figure 6 (b). The presence of O-H stretching and bending in the alcoholic group could be confirmed by with the peaks appearing at 3397 and 1377 cm^{-1}. The bands at 1703 cm^{-1}, suggested the stretching vibration of C=O in carbonyl group. The characteristic bands at 2932, 2850, 1463, 1191, 1052, and 1023 cm^{-1} also showed the presence of C-H stretching and bending in the CH_2 group and C-O stretching of the alcoholic group. All of the above results obtained from R_f value, physico-chemical characterization, and modern spectroscopic techniques such as FT IR spectral data suggest that the compound **6** may be considered a glycoside compound containing an ester group.

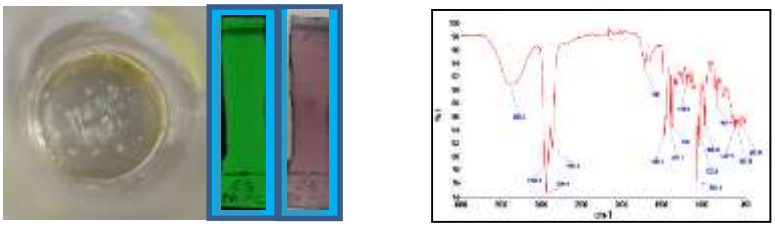

(a) **(b)**

Figure 6. (a) TLC of isolated compound 6
(b) FT IR spectrum of isolated compound 6

Antimicrobial Activity of Various Crude Extracts of *Dregea volubilis*

The antimicrobial activities of various crude extracts of *D. volubilis* (Gway-tauk) leaves such as PE, EtOAc, EtOH, and H_2O were investigated by the agar well diffusion method. From the results, it was found that EtOH extract possessed moderate activity with the inhibition zone 10-15 mm against all tested microorganisms. EtOAc and H_2O extracts exhibited the inhibition zone diameters in the range of 10-14 mm against the six tested microorganisms. Except for the other six microorganisms, PE extract showed antimicrobial activity with inhibition zone diameters of 9 mm against two microorganisms, *B. subtilis* and *C. albicans*. The observed data are summarized in Table 1.

Table 1. Inhibition Zone Diameter of Various Crude Extracts from Leaves of Gway-tauk by Agar Well Diffusion Method

No.	Microorganisms	Diameter of inhibition zone (mm) in various crude extracts				
		PE	EtOAc	EtOH	H_2O	STD
1	*A. tumefaciens*	-	14	10	-	18
2	*B. pumilus*	-	12	10	12	17
3	*B. subtilis*	9	12	13	11	17
4	*C. albicans*	9	12	14	10	15
5	*E. coli*	-	12	15	10	18
6	*M. luteus*	-	-	10	11	17
7	*P. fluorescens*	-	13	12	-	19
8	*S. aureus*	-	-	10	11	17

Diameter of agar well = 8 mm 15 mm - 19 mm activity = (++) Medium
10 mm - 14 mm activity = (+) Low 20 mm above activity = (+++) High

Cytotoxicity of Ethanol and Watery Extracts of Gway-tauk Leaves

According to the results, the cytotoxicity of ethanol and watery extracts from *D. volubilis* (Gway-tauk) leaves was evaluated by brine shrimp lethality bioassay. The ten of *Artemia salina* are used in each chamber. The LD_{50} values of both ethanol and watery extracts were found to be > 1000 g/mL. It means that the Gway-tauk leaves have no cytotoxic activity. Standard caffeine showed no cytotoxicity up to a concentration of100 g/mL, whereas the cytotoxicity of standard $K_2Cr_2O_7$ was LD_{50} - 43.75 g/mL. The results are shown in Table 2.

Table 2. Cytotoxicity of Ethanol and Watery Extracts of Leaves of Gway-tauk and Standard on *Artemia salina* (Brine Shrimp)

No.	Tested samples	Dead % by using different concentration (µg/mL) of samples (Mean ± SEM)				LD_{50} (µg/mL)
		1	10	100	1000	
1	Watery extract	17 ± 0.99	23 ± 0.38	30 ± 0.65	40 ± 0.00	>1000
2	EtOH extract	25 ± 1.00	40 ± 0.00	43 ± 1.15	47 ± 0.58	>1000
3	*Caffeine	0 ± 0.00	23 ± 0.00	30 ± 0.00	40 ± 0.00	>1000
4	*$K_2Cr_2O_7$	7 ± 1.00	20 ± 0.00	100 ± 0.00	100 ± 0.00	43.75

*Used as cytotoxic standard

The Bitterness Values of Gway-tauk Leaves

The bitter properties of plant substances are determined by comparing the threshold bitter concentration of an extract with that of standard standard quinine hydrochloride. The watery extract of Gway-tauk gives a bitter sensation (320). The tested sample was found to be less bitter than standard quinine hydrochloride (2000).

α-Amylase Enzyme Inhibition Activity of Ethanol and Watery Extracts of Gway-tauk Leaves

The *α*-amylase inhibitory activities of ethanol and watery extracts of Gway-tauk leaves were investigated by the starch- iodine method. The percentage inhibition of ethanol and watery extracts was studied at concentrations of (125, 62.5, 31.25, 15.62, 7.81, 3.92 and 1.95 µg/mL), respectively. The percent inhibition of *α*-amylase activity of watery extract (IC_{50} - 2.67 µg/mL) is more potent than that of ethanol extract (IC_{50}- 3.64 µg/mL). These two extracts exhibited higher activity than standard acarbose (IC_{50} = 3.91 µg/mL). These observations are detailed in Figure 7 and Table 3.

Table 3. *α*-Amylase Inhibition % and IC_{50} of the Crude Extracts of Gway-tauk Leaves and Standard (Acarbose)

No.	Tested samples	% Inhibition in different concentrations (µg/mL)							IC_{50} (µg/mL)
		1.95	3.91	7.81	15.62	31.25	62.5	125	
1	Watery extract	47.4 ± 0.48	54.28 ± 0.71	56.83 ± 0.48	58.19 ± 0.22	61.73 ± 0.12	63.42 ± 0.13	65.54 ± 0.32	2.67
2	EtOH extract	46.69 ± 0.34	50.57 ± 0.19	52.57 ± 0.46	56.66 ± 0.22	58.79 ± 0.13	62.97 ± 0.17	64.97 ± 0.54	3.64
3	*Acarbose	42.99 ± 0.19	49.99 ± 0.25	59.58 ± 0.66	63.91 ± 0.20	66.51 ± 0.37	68.40 ± 0.21	69.78 ± 0.39	3.91

*Used as standard

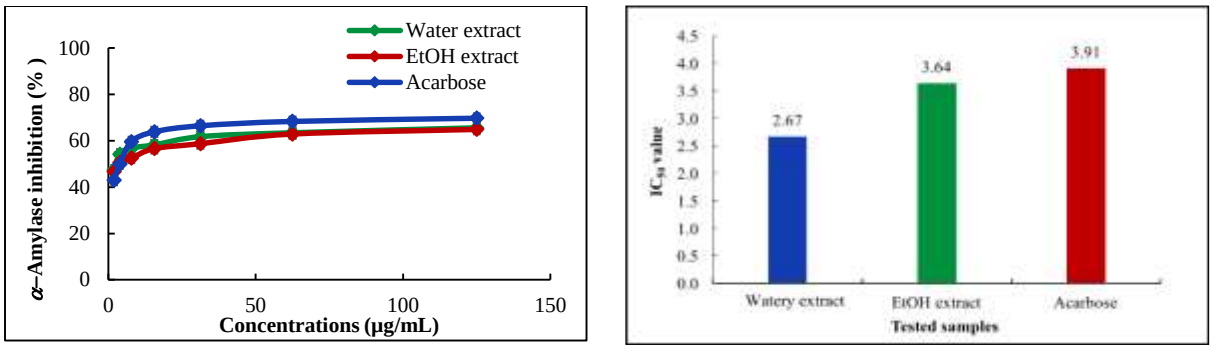

(a) **(b)**

Figure 7. (a) *α*-Amylase inhibition % of Gway-tauk leaves

(b) A bar graph of IC_{50} value of antidiabetic activity of crude extracts of Gway-tayk leaves

Antioxidant Activity of Ethanol and Watery Extracts of Gway-tauk Leaves

The antioxidant activity of ethanol and watery extracts of *D. volubilis* (Gway-tauk) leaves was evaluated by a DPPH (2,2-diphenyl-1-picrylhydrazyl) radical scavenger test. Ethanol extract (IC_{50} - 3.54 µg/mL) was found to be more potent than watery extract (IC_{50} - 5.11 µg/mL). Their antioxidant activity was compared with that of standard ascorbic acid (IC_{50} = 2.60 µg/mL). Since the lower the µg/mL values, the higher the antioxidant activity of the sample, an ethanol extract of Gway-tauk leaves possessed higher antioxidant activity than a watery extract. Ethanol extract of Gway-tauk leaves was found to be less effective than standard ascorbic acid (IC_{50} = 2.60 µg/mL). The results are shown in Table 4 and Figure 8.

Table 4. %RSA and IC_{50} Values of Crude Extracts of Gway-tauk Leaves and Standard (Ascorbic acid)

No.	Tested samples	% RSA ± SD of different concentrations (µg/mL)							IC_{50} (µg/mL)
		1.95	3.91	7.81	15.63	31.25	62.5	125	
1	Watery extract	42.22 ± 0.19	46.93 ± 0.33	56.90 ± 0.38	63.91 ± 0.31	66.00 ± 0.47	73.22 ± 0.57	82.02 ± 0.38	5.11
2	EtOH extract	45.52 ± 0.14	51.02 ± 0.69	59.20 ± 0.70	65.46 ± 0.45	69.38 ± 0.58	74.55 ± 0.62	77.01 ± 0.69	3.54
3	*Ascorbic acid	45.89 ± 0.31	58.20 ± 0.51	61.58 ± 0.25	70.76 ± 0.26	77.89 ± 0.51	85.19 ± 0.07	89.19 ± 0.07	2.60

*Used as standard

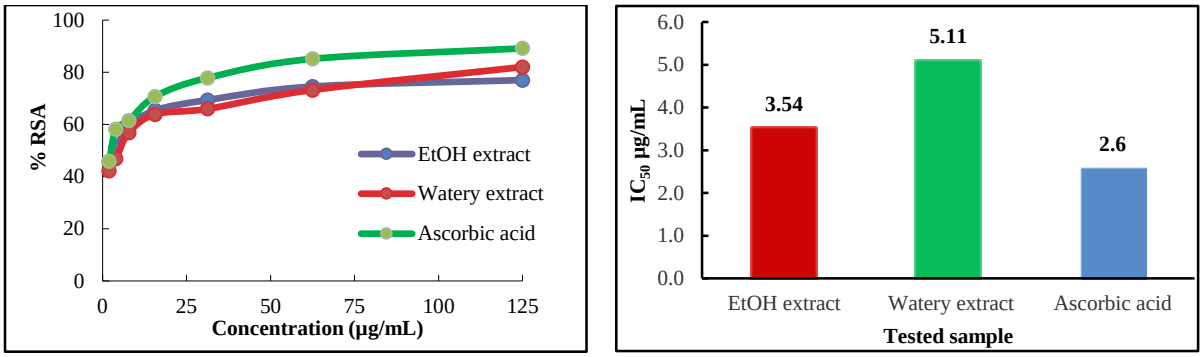

(a) **(b)**

Figure 8. (a) Radical scavenging activity of different concentrations of crude extracts of Gway-tauk leaves

(b) A bar graph of IC_{50} values of crude extracts of Gway-tauk leaves and standard ascorbic acid

Conclusion

The column chromatographic method was used to isolate chemical constituents from an EtOAc extract of Gway-tauk leaves, which were then characterised by physio-chemical property tests and modern spectroscopic techniques such as UV and FT IR. Compound **1** was a steroid compound (0.005%, colourless needle crystal), compound **2** was an organic acid compound (0.013%, white amorphous), compound **3** was *β*-sitosterol (0.01%, colourless needle crystal), compound **4** was an organic acid compound (0.004%, colourless crystal), compound **5** was a terpenic acid compound (0.004%, white amorphous), and compound **6** was a glycoside compound (0.015%, colourless crystal). From the results of antimicrobial activity, it was found that EtOH extract showed the highest level of inhibition zone diameters in the range of 10-15 mm against all tested microorganisms. According to the observed cytotoxicity results, ethanol and watery extracts had no cytotoxic effect on the brine shrimp at a 1000 µg/mL concentration. The bitterness value of the watery extract of Gway-tauk leaves was lower. The *α*-amylase inhibitory activity of ethanol and watery extracts of Gway-tauk leaves was evaluated by the starch-iodine method. The IC_{50} values of ethanol and watery extracts were observed to be 3.64 and 2.67 µg/mL. Both extracts were more potent than standard acarbose (3.91 µg/mL). Furthermore, an ethanol extract (IC_{50} =3.54µg/mL) of Gway-tauk leaves was more potent than a watery extract (IC_{50} = 5.11 µg/mL) in antioxidant activity.

Acknowledgements

The authors would like to express our gratitude to the Department of Higher Education, Ministry of Education, Myanmar, for their permission to do this research and also to the Myanmar Academy of Arts and Sciences for allowing to read this paper.

References

Ali, N., U. Aleem, S. W. A. Shah, I. Shah, M. Junaid, G. Ahmed, W. Ali, and M. Ghias. (2013). "Acute Toxicity, Brine Shrimp Cytotoxicity, Anthelmintic and Relaxant Potentials of Fruits of *Rubus Frurticosis* Agg". *BioMed Central Complementary and Alternative Medicine*, vol. 13, p. 138

Bharathamma, G., and G. Sudarsanam. (2015). "Phytochemical Investigation of Aqueous Fruit Extracts of *Dregea volubilis* Benth". *Indian Journal of Plant Sciences*, vol. 9**,** pp. 11-15

Biju, P. G., V. G. Devi, Y. Lija, and A. Abraham. (2007). "Protection Against Selenite Cataract in Rat Lens by Drevogenin D, a Triterpenoid Aglycone from *Dregea volubilis*". *Journal of Medical Food*, vol. 10 (2), pp. 308-315

Cruickshank, R. (1975). *Handbook of Bacteriology*. London: 11th Edition, E. and S. Livingstone Ltd., pp. 980

Finegold, S. M., W. J. Mortin, and E. G. Scott. (1978). *Diagnostic Microbiology*. London: The C. V. Mosby Co., pp. 124-131

Karthika, K. S., and K. S. Sanjaya. (2012). "A Pharmacognostic Evaluation on *Dregea volubilis* Benth". *International Journal of Pharmacy*, vol. 7 (3), pp. 319-336

Lee, E. L., V. I. Volkov, M. W. Byun, and C. H. Lee. (2002). "Detection of Free Radicals in Gamma-Irradiated Soybean Paste and Model System by Electron Spin Resonance Spectroscopy". *Journal of Radiation Physics and Chemistry*, vol. 64, pp. 61-66

Mayer, B. N., N. R. Ferrigni, J. E. Putnam, L. B. Jacobsen, D. E. Nichols , and J. L. Mclaughlin. (1982). "Brine Shrimp: A Constituents". *Journal of Medical Plant Research*, vol. 45, pp. 31-35

Natarajan, V., and A. S. A. G. Dhas. (2013). "Phytochemical Composition and in *Vitro* Antimicrobial, Antioxidant Activities of Ethanolic Extracts of *Dregea volubilis* Benth". *Journal of Advances in Biological Research*, vol. 7 (3), pp. 81–88

Pandikumar, P., M. Ayyanar, and S. Ignacimuthu. (2007). "Medicinal Plants Used by Malasar Tribes of Coimbatore District, Tamil Nadu". *Indian Journal of Traditional Knowledge*, vol. 6, pp. 579-582

Patra, A., S. Jha, P. N. Murthy, M. Ghosh, and A. Sharone. (2010), "Isolation and Characterization of *β*-sitosterol from the Leaves of *Hygrophila spinosa* T. Anders", *International Journal of Pharmaceutical Sciences and Research (IJPSR)*, vol. 1 (2), pp. 95-100

Rajadurai M, V. G. Vidhya, and M. Ramya and A. Bhaskar. (2009). "Ethno-Medicinal Plants Used by the Traditional Healers of Pacchamalai Hills, Tamil Nadu, India". *Journal of Ethanobiol Ethanomed*, vol. 3, pp. 39-41

Sahgal, G., S. Ramanathan, S. Sasidharan, M. N. Mordi, S. Ismail, and S. M. Mansor. (2010). "Brine Shrimp Lethality and Acute Oral Toxicity Studies on *Swietenia Mahagoni* (Linn.) Jacq Seed Methanolic Extract". *Journal of Pharmacognosy Research*, vol. 2, pp. 215-220

WHO (1998). "Quality Control Method for Medicinal Plant Materials, In; Determination of Extractable Matter and Determination of Bitterness Value". *Geneva*. vol. 30, p. 80

Yang, X. W., M. Z. Huang, Y. S. Jin, L. N. Sun, Y. Song, and H. S. Chen. (2012). "Phenolic from Bidens Bipinnata and their Amylase Inhibitory Properties". *Journal of Fitoterapia*, vol. 83 (7), pp. 1169-1175

EXTRACTION AND CHARACTERIZATION OF ESSENTIAL OIL EXTRACTED FROM THE BULBS OF *ALLIUM SATIVUM* LINN. (GARLIC)

Yatanar Aye Thant[1], Hnin Hnin Than[2]

Abstract

Garlic, a member of the Alliaceae family has been used for thousands of years as a food additive, spice, and medicine. Garlic extract has been shown to reduce serum cholesterol levels and increase blood coagulation time. Alkaloids, α- amino acids, carbohydrates, glycosides, phenolic compounds, reducing sugars, saponins, tannin, hydrolysable tannin, flavonoids, steroids are present in garlic bulbs, but starch is not. From the study of the elemental analysis by EDXRF (Energy Dispersive X-Ray Fluorescence), the essential metal potassium (1.321 %), sulphur (1.176%), calcium (0.081%), and iron (0.006%) were found in the garlic. The toxic heavy metals such as arsenic (As), cadmium (Cd), mercury (Hg), and lead (Pb) were not detected in the bulb sample. The essential oil was isolated from *Allium sativum* L. (garlic) by steam distillation. The mixture of essential oil with water was separated with *n*-hexane. The antioxidant activity of extracted essential oil, ethanol and watery extracts was screened by the DPPH free radical scavenging assay method. The IC_{50} value of extracted essential oil was found to be 514.79 µg/mL, while the 95 % ethanol and watery extracts were 55.70 µg/mL and 147.55 µg/mL. So, 95% ethanol has the most potent antioxidant activity. The organic constituents in the extracted essential oil of garlic were investigated at the Department of Research and Innovation National Laboratory (DRI), Yangon. Seven compounds (methyl-1-propenyl disulfide, diallyl disulphide, 2-vinyl-1, 3-dithiane, 3-vinyl-1, 2-dithicyclohex-4-ene, 3-vinyl-1, 2-dithicyclohex-5-ene, di-2-propenyl trisulphide and di-2-propenyl tetrasulfide) were detected in the essential oil of garlic. So, from all of these experimental data, it can be inferred that *Allium sativum* L. (garlic) can be useful for medicinal purposes.

Keywords: *Allium sativum* Linn., DPPH, steam distillation method, GC-MS, EDXRF

Introduction

Garlic is one of those plants that has been used for centuries to fight infectious diseases. Botanically, garlic is known as *Allium sativum* and is a member of Alliaceae family. Garlic is closely related to the onion, shallot, leek, chive, and rakkyo (Ali and Mohsen, 2014).

Garlic is native to Central Asia, from where its cultivation has spread to Southwest Asia and the Mediterranean region. Today, garlic is cultivated in regions with a moderate or subtropical climate all over the world (Al-Snafi, 2013).

Garlic extract has been shown to reduce serum cholesterol levels and increase blood coagulation time (Singh *et al*., 2001). So, garlic is a natural health promoter and a wonder drug available from Mother Nature. Moreover, garlic possesses anticancer, antiviral, antioxidant, and anti-inflammatory properties. The parts of the plant used medicinally include fresh bulbs, dried bulbs and oil extracted from the garlic. So, garlic is the super food to maintain health, and it has been used as a medicinal plant since ancient times, and it is still used in folk medicine all over the world (Sethi *et al.*, 2014). Garlic essential oil is obtained through steam distillation of garlic.

Antioxidant compounds in food are found to have a health-protecting factor. Antioxidants are whole grains, fruits, and vegetables. In this study, the DPPH assay was a rapid, easy and economical method to measure antioxidant activity of the sample, which could be viewed by the naked eye (Rahman *et al*., 2012).

[1] Department of Chemistry, Dagon University
[2] Head of Department of Chemistry, Dagon University

Gas chromatography-mass chromatography (GC-MS) is a method that combines features of gas-liquid chromatography and mass spectrometry to identify different substances within a test sample (Silverstein, 1998). GC-MS has long been the method of choice for identifying volatile compounds in complex mixtures (Karasek, 1988). For the identification of organic constituents in the extracted essential oil of garlic, a GC-MS spectrometer was used to analyse the molecular weight and molecular structure of organic compounds. Mineral elements play an important role in the health and disease of humans and animals. The functions of minerals in humans and animals are interrelated. Deficiencies in trace elements have been implicated in various health problems.

Material and Methods

Sampling

The fresh bulbs of *Allium sativum* L. (garlic) were collected from Pakokku Township, Magway Region (Figure 1).

The sample's fresh bulbs were washed, sliced with a knife, and dried in the shade for 7 days. The dried samples were crushed into fine powder using a blender and stored in an airtight container to prevent moisture changes and other contaminations.

Botanical Aspects

Botanical name	: *Allium sativum* L.
Genus	: *Allium*
Species	: *Sativum*
Family	: Amaryllidaceae
English name	: Garlic
Myanmar name	: Kyat-Thon- Phyu

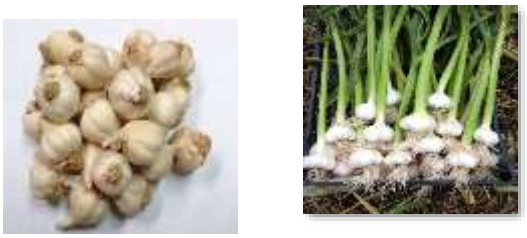

Figure 1. Photographs of *Allium sativum* Linn. (garlic)

Phytochemical Investigation of the Bulbs of *Allium sativum* L. (Garlic)

Phytochemical tests for *Allium sativum* L. (garlic) were carried out according to the test tube method to investigate the presence or absence of phytochemical constituents such as alkaloids, α-amino acids, carbohydrates, glycosides, phenolic compounds, reducing sugars, saponins, tannins, hydrolysable tannins, flavonoids, steroids, and starch. The results are shown in Table 1.

Determination of Qualitative Elemental Analysis of *Allium sativum* L. (Garlic) Bulbs by EDXRF Technique

Some elements were present in dried powder sample; qualitative elemental analysis was performed by the EDXRF (Energy Dispersive X-Ray Fluorescence) method at the Physics Department, Maubin University. The results are shown in Figures 2 and 3.

Screening of Antioxidant Activity of Extracted Essential Oil and Crude Extracts of *Allium sativum* L. (Garlic) by DPPH free Radical Scavenging Assay Method

A DPPH (1,1-diphenyl-2-picrylhydrazyl) radical scavenging assay was chosen to assess the antioxidant activities of extracted essential oil, ethanol and watery extracts of sample. This assay has been widely used to evaluate the free radical scavenging effectiveness of various flavonoids and polyphenols in food systems. The results are shown in Table 2 and Figures 4 and 5.

Extraction of Essential Oil from the Bulbs of *Allium sativum* L. (Garlic) by Steam Distillation Method

A round-bottomed flask was filled with freshly prepared garlic bulb paste (100 g) and 500 mL of distilled water. The flask was fitted with a steam distillation set. When the flask was heated on the heating mantel for about 4 h, the condensed mixture of oil and water separated out and was collected in the receiver flask. From this mixture, the essential oil was isolated in the separation funnel by using n-hexane. The resulting solution was dried over anhydrous sodium sulphate and filtered to get the essential oil.

Identification of Organic Compounds Present in Extracted Essential Oil of *Allium sativum* L. (Garlic) Bulbs by GC-MS Spectroscopic Method

In order to determine the organic constituents in the extracted essential oil of garlic, the GC-MS method was performed at the Department of Research and Innovation National Laboratory (DRI), Yangon. The results are shown in Figures 6 – 12.

Results and Discussion

Preliminary Phytochemical Tests of *Allium sativum* L. (Garlic)

Garlic bulbs were found to contain alkaloids, α- amino acids, carbohydrates, glycosides, phenolic compounds, reducing sugars, saponins, tannins, flavonoids, steroids, hydrolysable tannins, and no starch (Table 1).

Qualitative Elemental Analysis of *Allium sativum* L. (Garlic) by Energy Dispersive X-ray Fluorescence (ED XRF) Technique

X-ray spectrometer permits simultaneous analysis of light elements and heavy metals (Griken *et al*., 1986). In this research work, the relative abundance of elements present in the bulbs of *Allium sativum* L. (garlic) was determined by an ED XRF spectrometer. The ED XRF spectrum is shown in Figures 2 and 3. It can be seen that mineral elements such as K (1.321%), S (1.176%), P (0.387%), Ca (0.081%), Fe (0.006%), Zn (0.004%),Cu(0.003 %), Mn (0.001%),Ni(0.001%), and Sr (0.001%) are present in the sample bulbs. It was found that there is no contamination with toxic metals such as Cd, As, Pb, and Hg.

Screening of Antioxidant Activity of Extracted Essential Oil and Crude Extracts by DPPH Free Radical Scavenging Assay Method

The antioxidant activity was studied on essential oil and crude extracts (95% EtOH and H_2O) of the bulbs of *Allium sativum* L. (garlic) by using a DPPH free radical scavenging assay method. DPPH (1,1-diphenyl-2-picryl-hydrazyl) method is based on changing colour to reduce free radical DPPH in essential oil and crude extracts (95% EtOH and H_2O) of various concentrations. The antioxidant activities were expressed as a 50% oxidative inhibitory concentration (IC_{50}).

In the determination of antioxidant activity, the values of essential oil, 95 % EtOH, and H_2O extracts were found to be 514.79, 55.70, and 147.55 µg/mL respectively. The antioxidant activity of 95% ethanol extract is more potent than the H_2O extract (Table 2, Figures 4 and 5).

Extraction of Essential Oil from the Bulbs of *Allium sativum* L. (Garlic) by Steam Distillation Method

The essential oil of the bulbs of *Allium sativum* L. (garlic) was extracted by steam distillation. The yield percent of essential oil was 21.3 %.

Table 1. Results of Phytochemical Investigation of the Bulbs of *Allium sativum* L. (Garlic)

No.	Tests	Extract	Test reagents	Observation	Results
			(i) Dragendorff's reagent	orange ppt	+
1.	Alkaloids	1 % HCl	(ii) Mayer's reagent	white ppt	+
			(iii)Wagner's reagent	reddish brown ppt	+
2.	α -amino acids	H_2O	Ninhydrin reagent	purple spot	+
3.	Carbohydrates	H_2O	10 % α-Naphthol and conc:H_2SO_4	violet ring	+
4.	Glycosides	H_2O	10 % lead acetate	white ppt	+
5.	Phenolic compounds	H_2O	10 % ferric chloride	deep blue colour	+
6.	Reducing sugars	H_2O	Benedict's solution	green colour	+
7.	Saponins	H_2O	Distilled water	frothing	+
8.	Starch	H_2O	1 % Iodine solution	no deep blue colour	-
9.	Tannin	H_2O	1 % Gelatin sol^n: and 5 % $FeCl_3$	white ppt	+
10.	Hydrolysable Tannin	H_2O	10 % NaOH	emulsion on shaking	+
11.	Flavonoids	95 % EtOH	Mg ribbon and conc: HCl	pink colouration	+
12.	Steroids	MeOH	$CHCl_3$ and conc:H_2SO_4	red colour	+

(+) present, (-) absent, ppt = precipitate

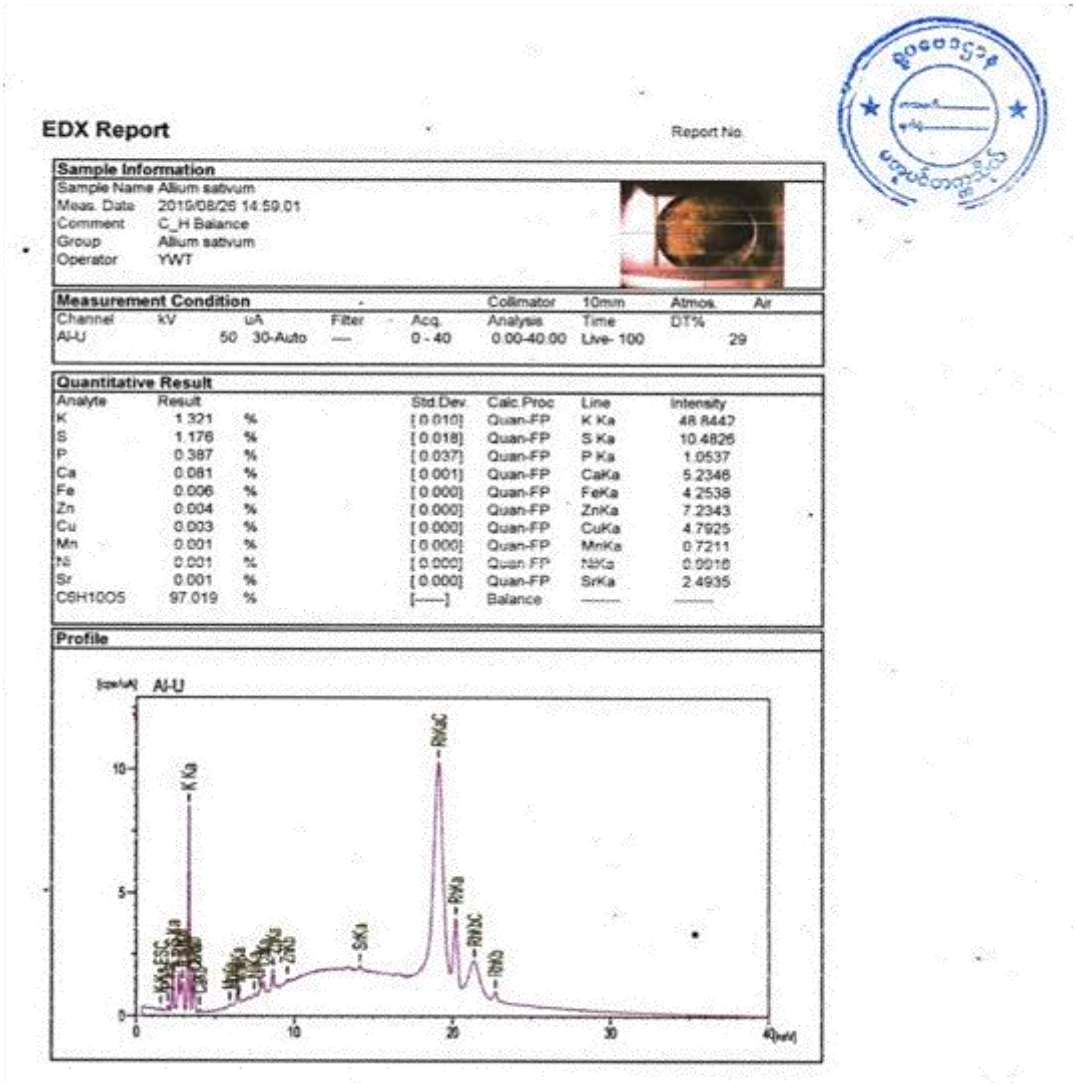

EDX Report

Report No.

Sample Information

Sample Name	Allium sativum
Meas. Date	2019/08/26 14:59:01
Comment	C_H Balance
Group	Allium sativum
Operator	YWT

Measurement Condition

Channel	kV	uA	Filter	Acq.	Collimator	10mm	Atmos.	Air
					Analysis Time	Live- 100	DT%	
Al-U	50	30-Auto	---	0 - 40	0.00-40.00		29	

Quantitative Result

Analyte	Result		Std.Dev.	Calc.Proc	Line	Intensity
K	1.321	%	[0.010]	Quan-FP	K Ka	48.8442
S	1.176	%	[0.018]	Quan-FP	S Ka	10.4826
P	0.387	%	[0.037]	Quan-FP	P Ka	1.0537
Ca	0.081	%	[0.001]	Quan-FP	CaKa	5.2346
Fe	0.006	%	[0.000]	Quan-FP	FeKa	4.2538
Zn	0.004	%	[0.000]	Quan-FP	ZnKa	7.2343
Cu	0.003	%	[0.000]	Quan-FP	CuKa	4.7925
Mn	0.001	%	[0.000]	Quan-FP	MnKa	0.7211
Ni	0.001	%	[0.000]	Quan-FP	NiKa	0.0016
Sr	0.001	%	[0.000]	Quan-FP	SrKa	2.4935
C9H10O5	97.019	%	[----]	Balance	------	------

Profile

Figure 2. ED XRF spectrum of the bulbs of *Allium sativum* L. (garlic)

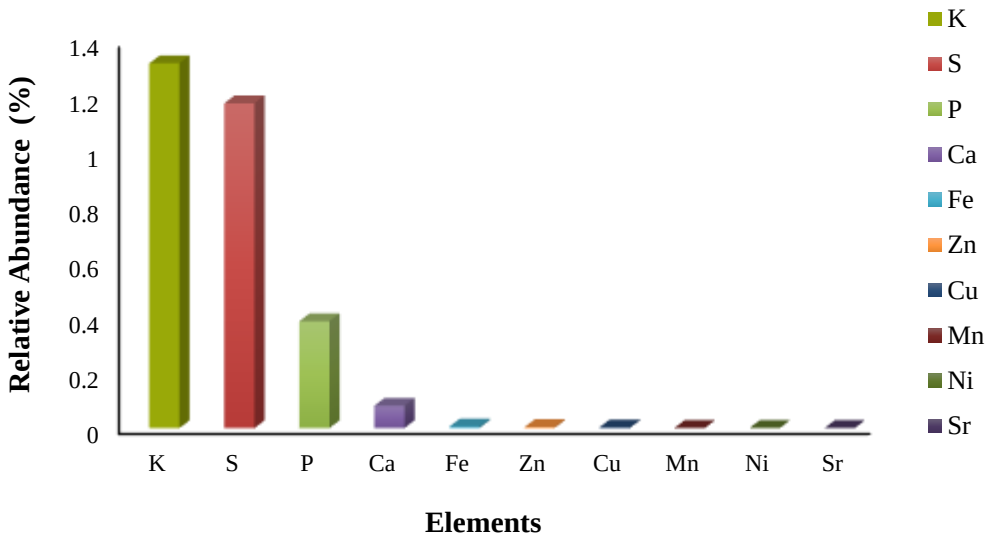

Figure 3. The bar graph of relative abundance of elements in the *Allium sativum* L. (garlic) by ED XRF

Table 2. Percent RSA and IC_{50} Value of Essential Oil and Crude Extracts (95 % EtOH and H_2O) from the Bulbs of *Allium Sativum* L. (Garlic) and Standard DPPH in Various Concentrations

Extracts	Percent RSA ± SD of different concentrations of extracts (%)							IC_{50}
	12.5	25.0	50.0	100.0	200.0	400.0	800.0	(µg/mL)
Watery	37.77 ± 0.009	39.29 ± 0.004	43.68 ± 0.003	47.53 ± 0.004	52.88 ± 0.005	65.66 ± 0.010	78.22 ± 0.015	147.55
95% Ethanol	30.82 ± 0.004	37.95 ± 0.002	47.81 ± 0.001	67.40 ± 0.006	92.74 ± 0.004	94.79 ± 0.004	102.34 ± 0.007	55.70
Essential oil	30.39 ± 0	31.22 ± 0.0007	32.53 ± 0.0014	35.39 ± 0.0042	37.30 ± 0.0007	45.411 ± 0.0148	77.82 ± 0.0153	514.79
DPPH (Std.)	49.23 ± 0.002	59.36 ± 0.006	71.63 ± 0.002	86.20 ± 0.000	97.24 ± 0.001	98.47 ± 0.000	99.06 ± 0.003	13.46

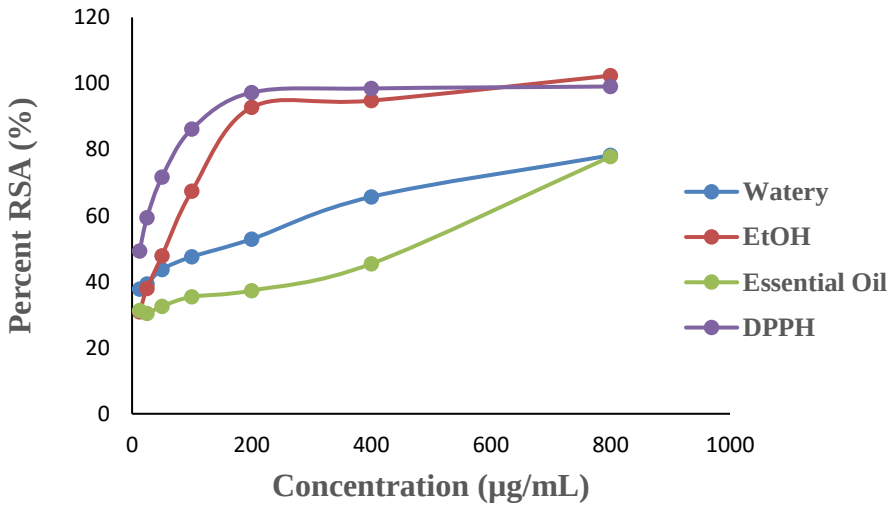

Figure 4. Plot of percent radical scanvenging activity (% RSA) vs. concentration (µg/mL) of extracted essential oil and crude extracts of *Allium sativum* L. (garlic) and standard DPPH

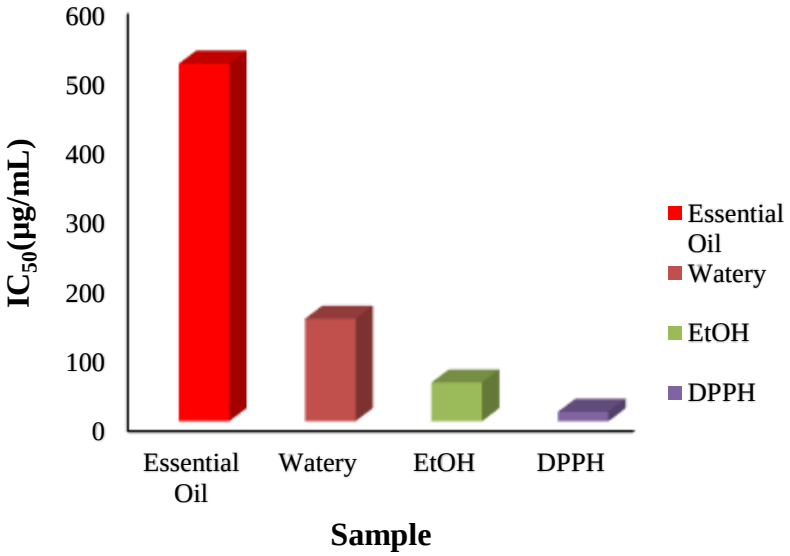

Figure 5. The bar graph of IC_{50} values of extracted essential oil and crude extracts of the bulbs of *Allium sativum* L. (garlic)

Identification of Organic Compounds in Essential Oil of *Allium sativum* L. (Garlic) by GC-MS Spectroscopic Method

Gas chromatography-mass spectrometry (GC-MS) is the most important tool for the identification of unknown organic compounds, both by matching spectra with reference spectra and by a priori spectral interpretation. According to the GC-MS chromatogram, the peak appears at the retention time of 6.60 min with 100 % abundance. At this retention time of 2.925 min, the GC-MS spectra (Figure 6) show the molecular ion peak at *m/z* 120, indicating the molecular weight of the compound is 120 and the molecular formula is $C_4H_8S_2$, and so this compound is methyl-1-propenyl disulphide. At this retention time, 4.728 min, the GC-MS spectra (Figure 7) show the molecular ion peak at *m/z* 146, indicating the molecular weight of the compound is 146 and the molecular formula is $C_6H_{10}S_2$, and so this compound is diallyl disulphide. At this retention time of 4.736 min, the GC-MS spectra (Figure 8) show the molecular ion peak at *m/z* 146, indicating the molecular weight of the compound is 146 and the molecular formula is $C_6H_{10}S_2$, and so it is 2-vinyl-1,3-dithiane. At this retention time of 6.254 min, the GC-MS spectra (Figure 9) show the molecular ion peak at *m/z* 144, indicating the molecular weight of the compound is 144 and the molecular formula is $C_6H_8S_2$, and so it is 3-vinyl-1,2-dithiacyclohex-4-ene. At this retention time of 6.596 min, the GC-MS spectra (Figure 10) show the molecular ion peak at *m/z* 144, indicating the molecular weight of the compound is 144 and the molecular formula is $C_4H_8S_2$, and so it is 3-vinyl-1,2-dithiacyclohex-5-ene. At this retention time of 7.700 min, the GC-MS spectra (Figure 11) show the molecular ion peak at *m/z* 178, indicating the molecular weight of the compound is 178 and the molecular formula is $C_6H_{10}S_3$; and so, it is di-2-propenyl trisulphide. At this retention time of 10.772 min, the GC-MS spectra (Figure 12) show the molecular ion peak at *m/z* 210, indicating the molecular formula is $C_6H_{10}S_4$, and so it is di-2-propenyl tetrasulphide.

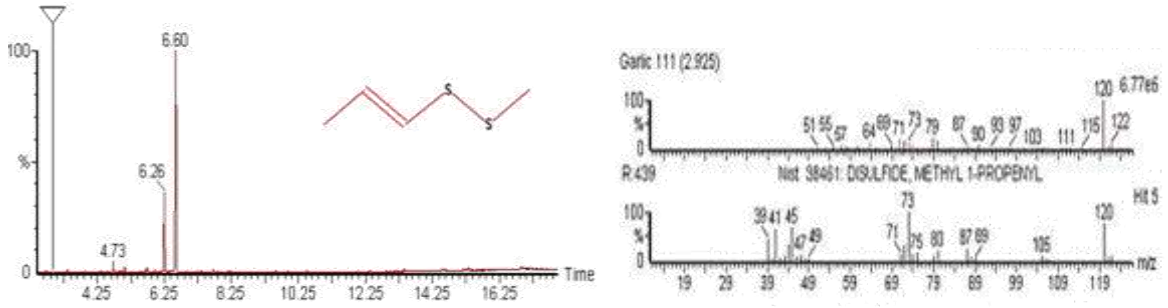

Figure 6. Gas chromatogram and mass spectra of methyl-1-propenyl disulphide

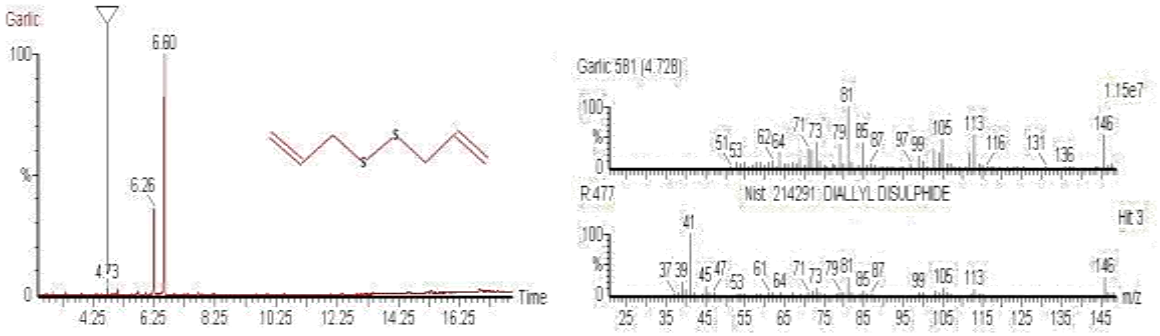

Figure 7. Gas chromatogram and mass spectra of diallyl disulphide

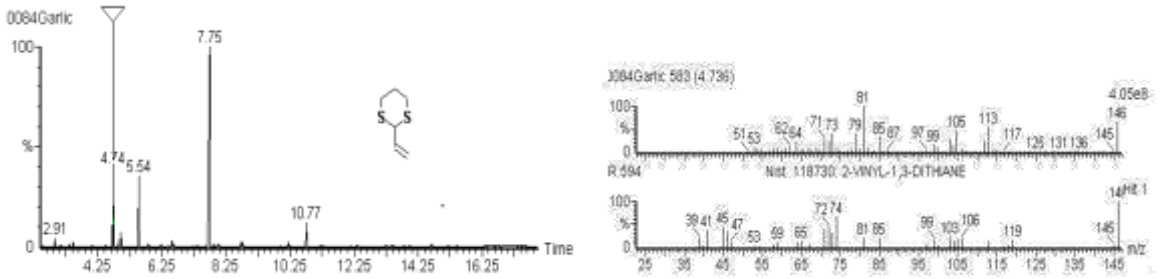

Figure 8. Gas chromatogram and mass spectra of 2-vinyl-1, 3-dithiane

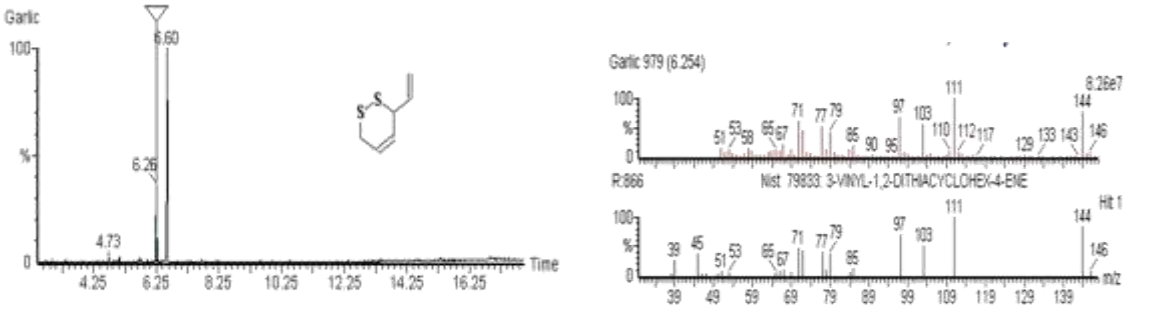

Figure 9. Gas chromatogram and mass spectra of 3-vinyl-1,2-dithiacyclohex-4-ene

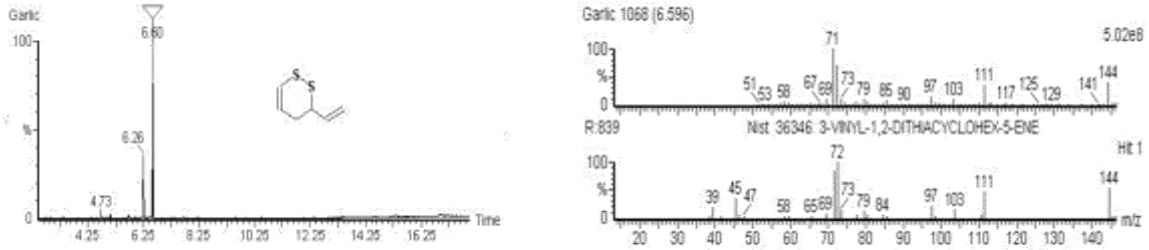

Figure 10. Gas chromatogram and mass spectra of 3-vinyl-1,2-dithiacyclohex-5-ene

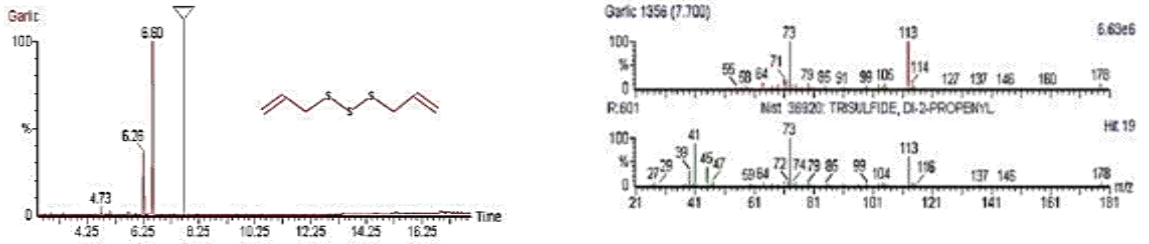

Figure 11. Gas chromatogram and mass spectra of di-2-propenyl trisulphide

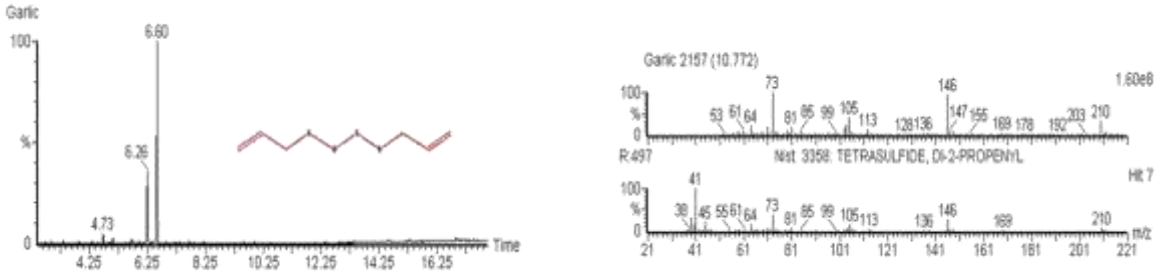

Figure 12. Gas chromatogram and mass spectra of di-2-propenyl tetrasulphide

Conclusion

The bulbs of garlic were chosen to be studied in the present work because these bulbs have many biological activities. Alkaloids, α- amino acids, carbohydrates, glycosides, phenolic compounds, reducing sugars, saponins, tannins, hydrolysable tannins, flavonoids, and steroids are present in garlic bulbs, but starch is not. From the study of the elemental analysis of the *Allium sativum* L. (garlic) bulbs, the essential metals potassium (1.321%), sulphur (1.176%), calcium (0.081%), and iron (0.006%) were found in the garlic sample. The toxic heavy metals such as arsenic (As), cadmium (Cd), mercury (Hg), and lead (Pb) were not detected in the bulb sample. The essential oil (21.3% yield) was extracted from *Allium sativum* L. (garlic) by steam distillation. The antioxidant activity of extracted essential oil, ethanol extract, and watery extract was screened by the DPPH free radical scavenging assay method. The IC_{50} value of extracted essential oil was found to be 514.79 µg/mL, 95% EtOH extract was 55.70 µg/mL and watery extract was 147.55 µg/mL. So, 95% EtOH has the most potent antioxidant activity. Seven sulphur containing compounds were detected in garlic essential oil by GC-MS analysis: methyl-1-propenyl disulphide, diallyl disulphide, 2-vinyl-1, 3-dithiane, 3-vinyl-1, 2-dithicyclohex-4-ene, 3-vinyl-1, 2-dithicyclohex-5-ene, di-2-propenyl trisulphide, and di-2-propenyl tetrasulphide. Therefore, it may be deduced from all of these experimental results that *Allium sativum* L. (garlic) has Therefore, it may be deduced from all of these experimental results that Allium sativum L. (garlic) has medicinal value.

Acknowledgements

The authors would like to thank the Myanmar Academy of Arts and Science for allowing to present this paper.

References

Ali, R., and S. N. Mohsen. (2014). "Phytochemical Characteristics of Garlic (*Allium sativum* L.) Oil: Effect of Extraction Procedure". *International Journal of Nutrition and Food Sciences*, vol. 3 (6-1), pp. 1-5

Al-Snafi, A. E. (2013). "Pharmacological Effect of *Allium* Species Grown In Iraq. An Overview". *International Journal of Pharmaceuticals and Health Care Research,* vol. 01 **(**04), pp. 132-147

Karasek, F. W., and E. C. Ray. (1988). *Basic Gas Chromatography-Mass Spectrometry: Principles & Techniques*. Amsterdam: 1st Edition, Elsevier Science

Rahman, M. M., V. Fazlic, and W. N. Saad. (2012). "Antioxidant Properties of Raw Garlic (*Allium sativum* L.) Extract". *International Food Research Journal*, vol. 19 (2), pp. 589-591

Sethi, N., S. Kaura, N. Dilbaghi, M. Parle, and M. Pal. (2014). "Garlic A Pungent Wonder from Nature", *International Research Journal of Pharmacy*, vol. 5 (7), pp. 523-529

Silverstein, R. M., and F. X. Webster (1998). *Spectrometric Identification of Organic Compounds*. New York: 6th Edition, John Wiley & Sons, Inc; pp.71-125

Singh, U. P., B. Prithiviraj, B. K. Sarma, S. Mandavi, and A. B. Ray. (2001). "Role of Garlic (*Allium sativum* L.) in Human and Plant Diseases". *Indian Journal of Experimental Biology*, vol. 39, pp. 310-322

INVESTIGATION OF ANTIMICROBIAL ACTIVITY, ALPHA-AMYLASE INHIBITION ACTIVITY AND CYTOTOXIC ACTIVITY OF RHIZOME OF *BERGENIA CILIATA* (HAW) STERNB. (NATSEI GAMON)

Yamone Pyae Pyae Thinn[1], Khin Chaw Win[2], Hnin Hnin Than[3]

Abstract

This research aims to investigate some biological activities such as antimicrobial activity, α-amylase inhibition activity, and cytotoxic activity of the rhizome of Natsei gamon. The rhizome of Natsei gamon was collected from Lungpi Village, Falam Township, Chin State, Myanmar, in February 2019. In the present work, antimicrobial activity, α-amylase inhibition activity, and cytotoxicity have been determined. According to the results of antimicrobial activity, methanol and chloroform extracts of Natsei gamon did not show any antimicrobial activity against all of the microorganisms tested. But petroleum ether extract exhibited activity against six microorganisms, such as *Bacillus subtilis, Staphylococcus aureus, Pseudomonas aeruginosa, Bacillus pumilus, Candida albicans*, and *Escherichia coli* with an inhibition zone diameter range of 13-15 mm. Ethyl acetate and ethanol extracts significantly inhibited only *Pseudomonas aeruginosa*, with an inhibition zone diameter of 20 mm. The α-amylase inhibition activity of ethanol and watery extracts of rhizome of Natsei gamon was determined by α-amylase inhibition assay or DNS reagent method. These two crude extracts were found to possess α-amylase inhibition activity. The ethanol extract (IC_{50} = 0.78 μg/mL) was found to have higher potency than that of watery extracts (IC_{50} = 0.85 μg/mL) in α- amylase inhibition activity. The cytotoxicity of watery and ethanol extracts of the rhizome of Natsei gamon is free from cytotoxic effect until a concentration of 1000 μg/mL.

Keywords: *Bergenia ciliata* (Haw.) Sternb., antimicrobial activity, α-amylase inhibition activity, cytotoxic activity

Introduction

The plants of the *Bergenia ciliata* (Haw.) Sternb. family belong to Saxifragaceae, a kind of perennial herb containing rich medicinal ingredients and having high application values. They are growing in India, Pakistan, China and Myanmar. It is a very important medicinal plant, widely applied in many fields (Guo *et al*., 2004). The plant of *Bergenia* has a height range of 10 to 80 cm, with short internodes. This is a kind of perennial herb, containing rich medicinal ingredients and having high application values. Its underground rhizomes grow creepingly, with radical branches. As a medicinal plant, *B. ciliata* (Haw.) Sternb. is being widely used for such things as cough, stopping bleeding, kidney stones, heart disease, pulmonary infection (especially asthma disease), menstrual disorder, stomach disorder, cold, and fever (Madiha *et al*., 2016).

People and other living organisms need certain nutrients to survive. Microorganisms are available naturally in the surrounding environment; they can easily reach food during harvesting, slaughtering, processing, and packaging (Hatab *et al*., 2016). Microbes are tiny living things that are found all around us and are too small to be seen by the naked eye. Microorganisms include bacteria, protozoa, algae, and fungi. In the present work, the antimicrobial activity of six crude extracts as petroleum ether, ethyl acetate, ethanol, methanol, chloroform, and water from the rhizome of Natsei gamon was determined against six strains of microorganisms such as *Bacillus subtilis, Staphylococcus aureus, Pseudomonas aeruginosa, Bacillus pumilus, Candida albicans, and Escherichia coli* by employing the agar well diffusion method.

α-amylase (α-1,4 glucan-4-glucanohydrolase) is an endoglycosidase,which hydrolyses starch and related α-1,4-linked glycosyl polysaccharides. It is the major form of α-amylase found

[1] Department of Chemistry, Dagon University
[2] Department of Chemistry, Yangon University of Distance Education
[3] Head of Department of Chemistry, Dagon University

in human and other mammals (Garrison *et al*., 1986). The saliva in your mouth contains amylase, which is another starch digesting enzyme. Breaking down starch molecules into small glucose molecules, enables them to pass gut wall and into the bloodstream as an energy supply for the body's cells. The enzyme amylase is the biological catalyst for this reaction (Elsnoussi *et al.*, 2012). The inhibition of their activity in the digestive tract of humans is considered an effective tool to control diabetes (Hara and Honda, 1990).

Cytotoxicity studies are a useful initial step in determining the potential toxicity of a test substance, including plant extracts or biologically active compounds isolated from plants. Minimal to no toxicity is essential for the successful development of a pharmaceutical or cosmetic preparation, and in this regard, cellular toxicity studies play a crucial role (Tulay, 2018). In this study, the cytotoxicity of water and ethanol extracts of the rhizome of Natsei gamon was evaluated by a brine shrimp cytotoxicity bioassay.

Materials and Methods

Collection and Preparation of the sample

The rhizomes of Natsei gamon were collected from Lungpi Village, Falam Township, Chin State in February 2019. Then, the sample was identified at the Department of Botany, University of Yangon.

The fresh rhizomes were cleaned by washing with water and air-drying at room temperature for 2 weeks. The dried rhizomes were cut into small pieces and were ground into powder by using a grinding machine. The dried powdered samples were stored in an airtight container to prevent moisture changes and other contaminations. The dried powdered samples were used to investigate for their chemical and biological activities.

Preliminary Phytochemical Investigation of Rhizome of Natsei Gamon

Phytochemical investigation of rhizome of Natsei gamon was carried out according to the reported methods. In the present work, the plant sample tested alkaloids, α-amino acids, carbohydrates, flavonoids, cyanogenic glycosides, glycosides, phenolic compounds, organic acids, reducing sugars, saponins, starch, steroids, tannins and terpenoids (M-Tin Wa, 1972). The presence of these phytochemicals makes the plant useful for treating different ailments and have a potential of providing useful drugs of human use.

Determination of Nutritional Values

Nutritional values such as moisture content, ash content, fat content, fibre content, protein content, and energy value of the selected sample were determined by AOAC method (AOAC, 2000). Total carbohydrate content was determined by phenol-sulphuric acid method (Neeru *et al.*, 2015). The results were expressed as milligrammes of glucose, and then the percentage carbohydrate content was also calculated from the above results.

$$\text{percent of total carbohydrate} = \frac{\text{mg of glucose}}{\text{volume of test sample}} \times 100$$

Determination of Antimicrobial Activity of Crude Extracts of Rhizome of Natsei Gamon by Agar Well Diffusion Method

The powder of Natsei gamon rhizome was mixed with each of PE, EtOAc, EtOH, $CHCl_3$, MeOH, and H_2O to prepare six crude extracts for about 5 h, and this solution was evaporated on a water bath. The antimicrobial activity of these six crude extracts was screened by the agar-well diffusion method.

Crude extract (0.5 g), peptone (0.5 g), and sodium chloride (0.25 g) were mixed with distilled water and made up to 100 mL with distilled water. The pH of this solution was adjusted to 7.2 with a 0.1 M sodium hydroxide solution, and 1.5 g of agar was added.

Nutrient agar was prepared according to the method described by Mar Mar Nyein *et al.*, (1991). Briefly, nutrient agar was boiled, and 20-25 mL of the medium was poured into a test tube and plugged with cotton wool, and autoclaved at 121 ºC for 15 min. Then the suspension was also added to the dishes. After allowing the agar to set for 30 min, a 10 mm agar plate well was made with using a sterile cork border. Following that, 0.1 mL of sample was added to the agar-well and incubated at 37 ºC for 24 h. The zone of inhibition diameter was used to determine the extent of antimicrobial activity. The results are described in Figures 2 and 3, and Table 3.

Determination of α-Amylase Inhibition Activity of Crude Extracts of Rhizome of Natsei gamon by DNS Reagent Method

The α-amylase inhibition activity of ethanol and watery extracts of rhizomes of Natsei gamon was determined by using a UV-visible spectrophotometer. In a test tube, 500 µL of extract solution was added and followed by 500 µL of 0.02 M sodium phosphate buffer (pH 6.9) containing α-amylase solution (2 mg/mL). The contents of test tubes were pre-incubated at 25℃ for 15 min, after which 500 µL of a 1% starch solution with buffer (pH 6.9) was added at timed intervals. The reaction mixture was incubated at 50℃ for 20 min. The reaction was terminated by adding 1000 µL of dinitrosalicylic acid (DNS) reagent and further incubating in boiling water for 5 min, then cooling to room temperature. The contents of each test tubes were diluted with 5 mL distilled water, and the absorbance was measured at 540 nm in a spectrophotometer. A control was prepared using the same procedure but without extract. The α-amylase inhibitory activity was calculated by the following equation.

$$\% \text{ inhibition} = [\, A_{control} - (A_{sample} - A_{blank}) / A_{control} \times 100]$$

Where, % Inhibition = % α-amylase inhibition

A_{sample} = Absorbance of the sample +enzyme solution+ DNSA solution

B_{blank} = Absorbance of blank (sample + DNSA solution)

$A_{control}$ = Absorbance of control (without sample)

The α-amylase power (IC_{50}) is expressed as the test substance's concentration (µg/ mL) that results in a 50 % reduction of the initial absorbance of DNS solution and that allows to determine the concentration. IC_{50} (50 % inhibition concentration) values were calculated using the linear regression Excel programme. IC_{50} values of crude extracts of the rhizome of Natsei gamon are shown in Figure 4 and Tables 4 and 5.

Determination of Cytotoxicity by Brine Shrimp Lethality Bioassay of Rhizome of Natsei Gamon

The brine shrimp (*Artemia salina*) was used in this study for cytotoxicity bioassays. Brine shrimp eggs were purchased from a pet shop in Baho Road, Hlaing Township, Yangon Division. Brine shrimp eggs (ca. 0.25 g) were added to the beaker, along with 500 mL of sea water. The beaker was placed near a lamp. Light is essential to hatching. Brine shrimp eggs also required a constant supply of oxygen and a 24-h incubation period at room temperature (Ahmed *et al*., 2010).

Each chamber of the ice tray was filled with artificial sea water (9 mL), different concentrations of samples, and standard solutions. Alive brine shrimp (10 nauplii) were taken with a Pasteur pipette and placed into each chamber. They were incubated at room temperature for about 24 h. The number of dead or alive brine shrimp was counted after 24 h, and 50% of the lethal dose (LD_{50}) was calculated (Sahagal *et al*., 2010). The results are shown in Table 6.

Results and Discussion

Preliminary Phytochemical Investigation of Rhizome of Natsei Gamon

The phytochemical constituents of Natsei gamon rhizomes were investigated by the test tube method.

The phytochemical tests revealed that the sample contained alkaloids, α-amino acids, carbohydrates, flavonoids, glycosides, phenolic compounds, organic acids, reducing sugars, saponins, starch, steroids, tannins and terpenoids. However, cyanogenic glycosides were not detected in the rhizome of Natsei gamon. The results are summarized in Table 1.

Table 1. Phytochemical Results of Rhizome of Natsei Gamon

No	Test	Extract	Test Reagent	Observation	Results
1	Alkaloids	1 % HCl	Dragendroff's reagent Mayer's reagent Wagner's reagent Sodium picrate solution	Orange ppt White ppt Reddish brown ppt Yellow ppt	+ + + +
2	α- amino acids	H_2O	Ninhydrin reagent	Purple spot	+
3	Carbohydrates	H_2O	10 % α- naphthol, conc:H_2SO_4	Pink ring	+
4	Cyanogenic glycosides	H_2O	Sodium picrate solution	No brick red colour	-
5	Flavonoids	EtOH	Mg turning, conc: HCl	Orange colour	+
6	Glycosides	H_2O	10 % Lead acetate solution	White ppt	+
7	Organic acids	EtOH	Bromocresol green indicator	Blue colour	+
8	Phenolic compounds	EtOH	1 % $FeCl_3$ solution	Dark blue colour	+
9	Reducing sugars	H_2O	Benedict's solution	Green colour	+
10	Saponins	H_2O	Distilled water	Frothing	+
11	Starch	H_2O	1 % Iodine solution	Brown colour	+
12	Steroids	$CHCl_3$	Acetic anhydride, conc: H_2SO_4	Green colour	+
13	Tannins	H_2O	1 % Gelatin	White ppt colour	+
14	Terpenoids	$CHCl_3$	Acetic anhydride, conc: H_2SO_4	Pink colour	+

(+) = presence, (-) = absence, (ppt) = precipitate

Nutritional Values of Rhizome of Natsei gamon

The rhizome of Natsei gamon contains moisture (1.39 %), ash (5.56 %), fat (1 %), fibre (8.01 %), protein (3.66 %), carbohydrate (46.06 %), and energy values of 207.88 kilocalories in 100 g of sample.

The relatively high moisture content of the plant indicates a possible reduction in plant shelf life. The higher the ash content, the better the quality. Low-fat foods are known to reduce chlorosterol. Higher-fibre foods cause intestinal irritation and lower bioavailability. The protein content of these rhizomes, even though it appears to be low, has many medicinal properties.

The presence of important nutrients like fats, fibre, proteins, and carbohydrates, and the physical properties such as moisture and ash indicate that the selected rhizome sample could be used as a nutritionally valuable and healthy ingredient to improve traditional medicinal formulations and to treat many diseases, according to the findings. The results are shown in Table 2.

Table 2. Nutritional Values of Rhizome of Natsei Gamon

No	Nutrients	Contents %
1	Moisture	1.39
2	Ash	5.56
3	Fat	1.00
4	Fibre	8.01
5	Protein	3.66
6	Total Carbohydrate	46.06
7	Energy Value (kcal/100 g)	207.88

Antimicrobial Activity of Crude Extracts of Natsei Gamon against Six Microorganisms

Investigation of the antimicrobial activity of six crude extracts, such as PE, EtOAc, EtOH, $CHCl_3$, MeOH, and H_2O, from the rhizome of the Natsei gamon sample was done by the agar well discussion method according to the procedure presented. In this investigation, these extracts were tested on six harmful microorganisms, including *Bacillus subtilis, Staphylococcus aureus, Pseudomonas aeruginosa, Bacillus pumilus, Candida albicans,* and *Escherichia coli.* The diameter of the agar well was 10 mm. When comparing different antimicrobial agents to known concentrations, the inhibitory zone diameter is taken as a measure of antimicrobial activity (Figure 1). The larger the diameter, the higher the antimicrobial activity of the test agents.

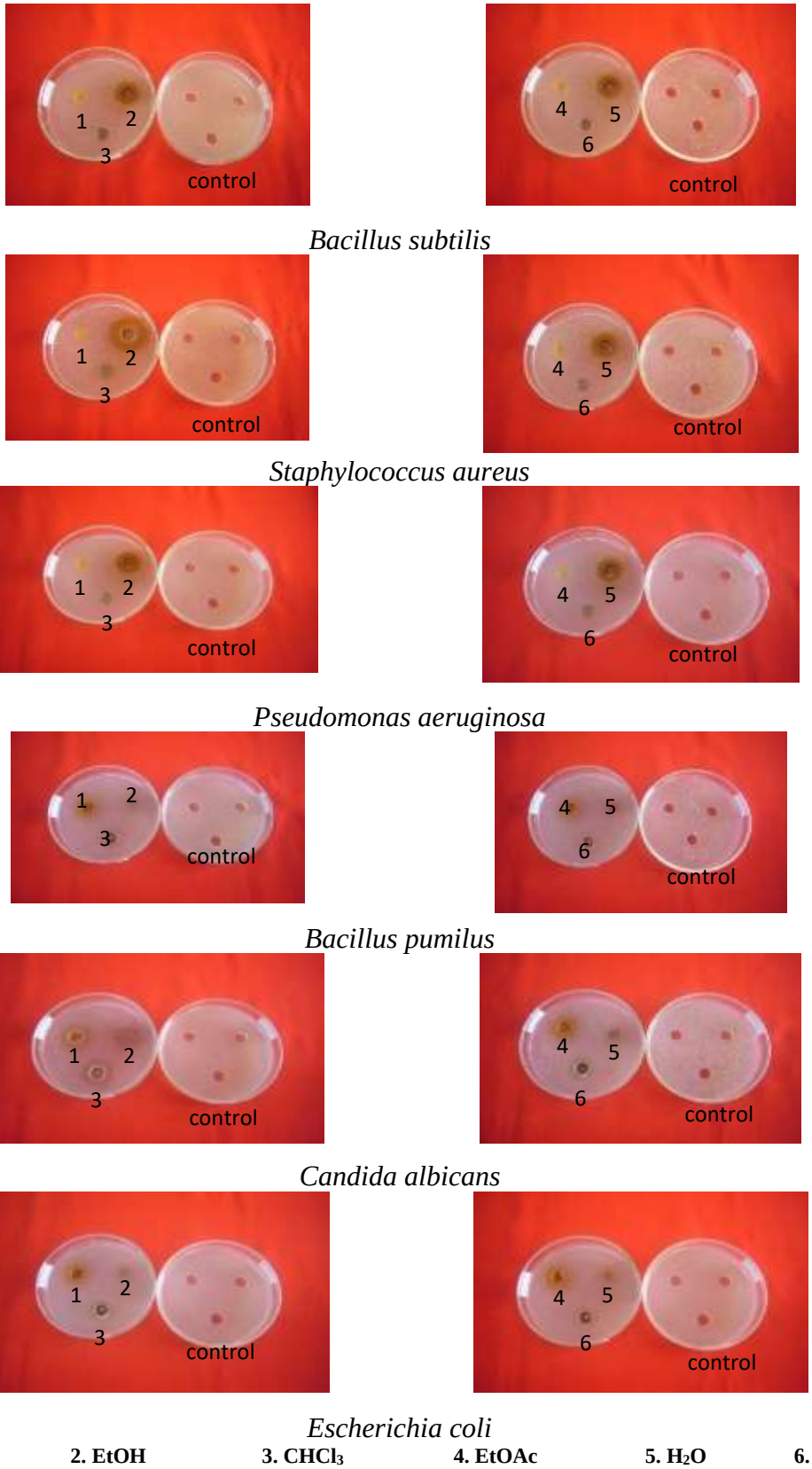

1. PE **2. EtOH** **3. $CHCl_3$** **4. EtOAc** **5. H_2O** **6. MeOH**

Figure 1. Effect of different crude extracts from rhizome of Natsei gamon on six microorganisms

According to the results of antimicrobial activity, petroleum ether extract showed all strains of microorganisms with the inhibition zone diameter range of 13-15 mm. Watery, ethyl acetate, and ethanol extracts of the sample inhibited only one microorganism *Pseudomonas*

aeruginosa, with an inhibition zone diameter of 15-20 mm. Ethyl acetate and ethanol extracts significantly inhibited only *Pseudomonas aeruginosa*, with an inhibition zone diameter of 20 mm. The results are shown in Figure 2 and Table 3.

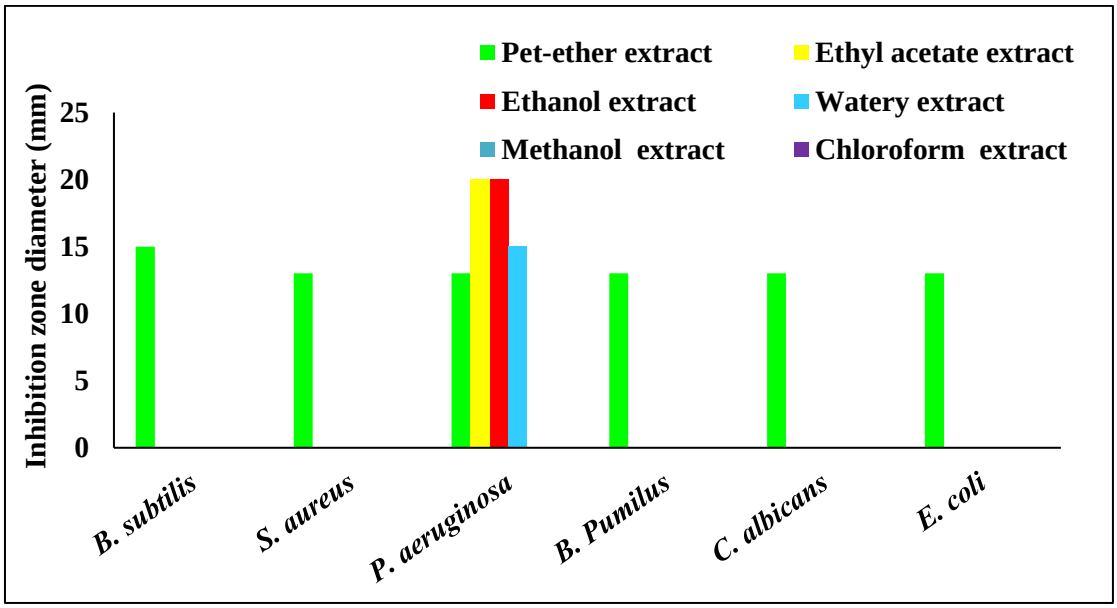

Figure 2. Inhibition zone diameters of crude extracts of rhizome of Natsei gamon against six microorganisms

Table 3. Antimicrobial Activity of Crude Extracts of Rhizome of Natsei Gamon Against Six Microorganisms

Microorganism	Inhibition zone diameter of extracts(mm)					
	PE	EtOAc	**EtOH**	**MeOH**	**$CHCl_3$**	**H_2O**
B.subtilis	15	-	-	-	-	-
S.aureus	13	-	-	-	-	-
P.aeruginosa	13	20	20	-	-	15
B. Pumilus	13	-	-	-	-	-
C. albicans	13	-	-	-	-	-
E.coli	13	-	-	-	-	-

Diameter of agar well = 10mm
10mm ~ 14 mm = (+)
15mm ~ 19mm = (++)
20 mm above = (+++)
No activity = (-)
Susceptible ≥ 21 = (+++)
Intermediate 17.20 = (+++)
Resistant ≤ 16 = (+)

α-Amylase Inhibition Activity of Crude Extracts of Natsei Gamon

The α-amylase inhibition activity of a crude extracts of the rhizome of Natsei gamon was measured by using DNS reagent method. In this study, *in vitro* α-amylase inhibitory activities of ethanol and water extracts from rhizomes of Natsei gamon were investigated. The percent inhibition of the α-amylase by ethanol and water extracts was studied in concentrations of (10, 5,

2.5, 1.25, 0.625 and 0.312 µg/mL) respectively. The percent inhibition of the sample on α-amylase enzyme activity increased with the increasing concentration.

From the percent inhibition, the respective IC_{50} values for the water and ethanol extracts were calculated. The ethanol and water extracts of the rhizome of Natsei gamon were investigated for *in vitro* α-amylase inhibition, and their activity was compared with that of the standard anti-diabetic drug, acarbose. The IC_{50} values of water and ethanol extracts of Natsei gamon were observed to be 0.85 µg/mL and 0.78 µg/mL respectively. These two extracts posses α-amylase inhibition activity. But these two extracts showed lower potent of α-amylase inhibition activity than the standard drug acarbose (IC_{50}= 0.59 µg/mL). These observations are illustrated with a bar graph diagram in Figure 3 and Tables 4 and 5.

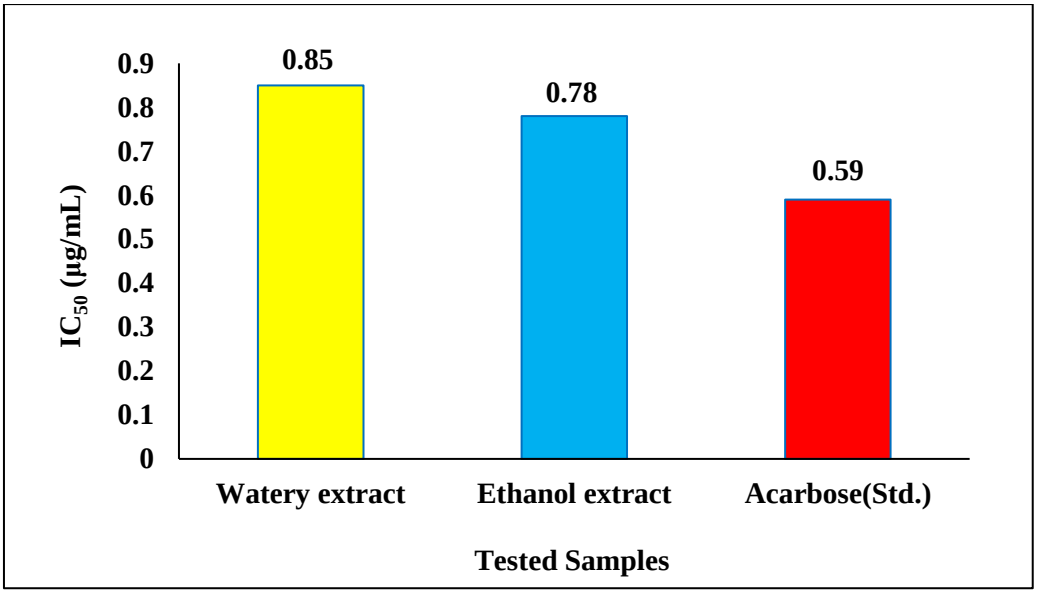

Figure 3. Comparison of IC_{50} values of watery and ethanol extracts from rhizome of Natsei gamon with standard acarbose

Table 4. α-Amylase Enzyme Inhibitions Activity of Ethanol and Watery Extracts of Rhizome of Natsei Gamon and Standard Acarbose

Sample	% Inhibition (Mean ± SD) In Different Concentration (µg/mL)					
	0.312	0.625	1.25	2.5	5	10
Water (extract)	48.83 ± 0.000	49.08 ± 0.001	51.56 ± 0.001	53.33 ± 0.001	56.61 ± 0.005	57.13 ± 0.002
Ethanol (extract)	40.19 ± 0.006	48.83 ± 0.000	53.52 ± 0.004	54.15 ± 0.000	56.67 ± 0.002	58.19 ± 0.002
Acarbose (Std.)	49.54 ± 0.000	50.04 ± 0.002	51.96 ± 0.003	52.27 ± 0.001	54.75 ± 0.001	58.15 ± 0.000

Table 5. IC_{50} Values of Crude Extracts from Rhizome of Natsei gamon and Standard Acarbose

Sample	IC_{50} (µg / mL)
Watery Extract	0.85
Ethanol Extract	0.78
Acarbose (Std.)	0.59

Cytotoxicity of Crude Extracts of Natsei Gamon by Brine Shrimp Assay

The cytotoxicity of watery and ethanol extracts of the rhizome of Natsei gamon was evaluated by a brine shrimp cytotoxicity bioassay. Ten brine shrimp (*Artemia salina*) are used for each chamber. The cytotoxicity effect was expressed as LD_{50} values (50 % lethal doses). In this bioassay, potassium dichromate and caffeine were used as cytotoxic standards.

According to these results, the LD_{50} values of water and ethanol extracts of the rhizome of Natsei gamon and standard caffeine did not show any cytotoxicity until 1000 µg/mL concentration, whereas the LD_{50} values of standard potassium dichromate were found to have a cytotoxic effect at less than 1 µg/mL of concentration. These results are shown in Table 6.

Table 6. Cytotoxicity Effect of Ethanol and Watery Crude Extracts of Rhizome of Natsei Gamon with Standard Caffeine and Potassium Dichromate

Sample	% of dead brine shrimp (Mean±SD) in various concentration (µg/mL)				LD_{50} (µg/mL)
	1	10	100	1000	
Ethanol Extract	6.66 ± 0.577	26.66 ± 0.577	36.66 ± 0.577	46.66 ± 0.577	>1000
Watery Extract	10.00 ± 1	20.00 ± 1	40.00 ± 1	46.66 ± 0.577	>1000
*Caffeine	0 ± 0	0 ± 0	26.66 ± 0.577	36.66 ± 0.577	>1000
*$K_2Cr_2O_7$	63.33 ± 0.577	66.66 ± 0.577	76.66 ± 1.154	100 ± 0	<1

* Used as cytotoxic standard

Conclusion

From the overall assessments of a chemical and biological investigation of the rhizome of Natsei gamon, the following inferences could be deduced.

In the preliminary photochemical investigation, it was found that alkaloids, α-amino acids, carbohydrates, flavonoids, glycosides, organic acids, steroids, phenolic compounds, reducing sugars, saponins, starch, tannins and terpenoids were present in the sample. The plant is reported to contain numerous phytochemical medicinal properties.

The nutritional values are 1.39% of moisture, 5.56% of ash, 3.66% of proteins, 1% of fats, 8.01% of fibre, 46.06 % of carbohydrates, and 207.88 (kcal/100g) of energy value were determined in the rhizome of Natsei gamon. The plants are rich sources of fibre and carbohydrates.

According to the results of antimicrobial activity, petroleum ether extract showed the all strains of microorganisms with the inhibition zone diameters range of 13-15 mm. Ethyl acetate, and ethanol extracts of the sample significantly inhibited only *Pseudomonas aeruginosa* with zone diameter of 20 mm. Watery extract inhibited only *Pseudomonas aeruginosa* with–an inhibition zone diameter of 15 mm.

The α-amylase inhibition activity of ethanol and water extracts of the rhizome of Natsei gamon was evaluated by the DNS reagent method. The α-amylase activity of ethanol extracts (IC_{50} = 0.78 μg/mL) is higher than watery extracts (IC_{50} = 0.85 μg/mL). α-amylase inhibition activity of both extracts was found to be lower potency than that of standard acarbose (drug) (IC_{50} = 0.59 μg/mL). From this observation, ethanol extract showed higher potency of antioxidant and α-amylase inhibition activities than watery extract of the rhizome of Natsei gamon.

From this research, watery and ethanol extracts are free from cytotoxic effects until 1000 μg/mL concentration. Therefore, these crude extracts of rhizome of Natsei gamon were evaluated for their non-cytotoxic effect.

Therefore, this research programme may contribute to the scientific development of Myanmar traditional medicine, especially in the areas concerned with α-amylase inhibition properties (antidiabetic disease), oxidative stress, non-toxics and the bacterial infections.

Acknowledgements

The authors would like to thank the Myanmar Academy of Arts and Science for allowing to present this paper.

References

A. O. A. C. (2000). *Official Methods of Analysis, Association of Official Analytical Chemists.* Washington D.C: 17th Ed., 526

Ahmed, Y., H. Sohrab, S. M. Al-Reza, F. S. Tareq, C. M. Hasan, and M. A. Sattar. (2010). "Antimicrobial and Cytotoxicity Constituents from Leaves of *Bergenia ciliata.*" *Food Chem Toxi*., vol.48, pp.549-552

Elsnoussi, A. H. M., S. A. J. Mohammad, A. F. Lee, S. Amirin, C. H. Sue, T. C. Soo, A. Z. Mohd, and Y. F. Mun. (2012). "Potent α-glucosidase and α-amylase Inhibitory Activities of Standardized 50% Ethanolic Extracts and Anti-Diabetic Mechanism". *BMC. Complementary & Med*., vol.12, p.176

Garrison, R. (1986). "Amylase". *Emerg. Med. Clin. North. Am*., vol.4 (2), pp. 27-315

Guo, H. Y., K. K. Song, and Q. X. Chen. (2004). "The Synthesis of Two Arbutin Derivatives and Inhibitory Effect of them on Tyrosinase". *J. Xi. Univ. Nat. Sci*., vol.43, pp.1-4

Hara, Y., and M. Honda. (1990). "The Inhibition of α-amylase by Tea Polyphenols". *Argic. Biol. Chem*., vol.54, pp.939-945

Hatab, S., R. Athanasio, R. Holley, A. R. Gonzalez, and C. B. Narvaez. (2016). "Survival and Reduction of Shiga toxin-producing *E.coli* in a Fresh cold- Pressed Juice Treated with Antimicrobial Plant Extracts". *J. food. Sci*., vol.81, pp.987-995

Madiha, A., R. P. Abdul, H. Ihsan-ul, B. Gulnaz, M. Kehkashan, R. U. Tofeeq, Z. Muhammad, and M. Bushra. (2016). "Antioxidant, Anticancer and Antibacterial Potential of Zakhm-e-hayat Rhizomes Crude Extracts and Fractions". *Pak. J. Pharm. Sci*., vol.29(3), pp.895-902

Mar Mar Nyein, Chit Maung, Mya Bwin, and S. J. Tha. (1991). "*In vitro* Testing of various Indigenus Plant Extracts on Human Pathogenic Bacteria". *Myanmar Hlth. Sci. Res. J.*, vol.3, pp. 89-99

M-Tin Wa. (1972). "Screening Methods and Procedures". *Phytoche. Bull. Bot.Soci. Ameri.*, vol.5, pp.4-10

Neeru, A., K. M. Divya, and R. Khushboo. (2015). "Estimation of Total Carbohydrate Present in Dry Fruits". *J. Env. Sci. Toxi. & Food. Tech*., vol.1(6), pp.24-27

Rammohan, S., M. Z. Asmawi, and S. Amirin. (2008). "*In vitro* α-Glucosidase and α-Amylase Enzyme Inhibitory Effects". *Depart. Pharma. Malay*., vol 55(2), pp.391-398

Sahagal, G., S. Ramanathan, S. Sasidharan, S. M. S. Mordic, and S. Ismailu. (2010). "A Cute Oral Toxicity Studies on *Bergenia ciliata* (Haw). Sternb. Methanolic Extract". *Pharmaco Res*.,vol 2, pp.215-220

Tulay, A. C. (2018). "Introductory Chapter: Cytotoxicity". *Depart. Bio. Intech*., vol .10, pp.244-772

LUPANE TRITERPENOIDS FROM THE ROOTS OF *DIOSPYROS EHRETIOIDES* Wall. AND EVALUATION OF SOME BIOLOGICAL ACTIVITIES

Mya Mu Aye*

Abstract

In this research, the roots of *Diospyros ehretioides* from Tetma Village, Nyaung U Township, Mandalay Region were selected to investigate some chemical constituents and some biological activities such as acute toxicity and antimicrobial activities. Four known lupane triterpenoids, lupeol, betulin, betulinaldehyde, and betulinic acid were isolated from the roots of *Diospyros ehretioides* by column chromatography. The structures of these isolated compounds were identified by extensive spectroscopic analyses such as UV, IR, ^{1}H and ^{13}C NMR, DQF-COSY, HMQC, and HMBC spectra and comparison with the literature data. The acute toxicity of the ethanol extract of the roots evaluated by Organization for Economic Cooperation and Development (OECD) 425 guideline revealed no toxic effects and lethality at a dose of 5000 mg/kg (LD_{50}>5000 mg/kg). Moreover, the antimicrobial activity of crude extracts (ethanol, DCM and hexane) of *Diospyros ehretioides* root was evaluated against five pathogenic microorganisms by agar well diffusion method. Except for *E. faecalis*, all crude root extracts inhibited four microorganisms, with the inhibition zone diameters ranging from 10 to 15 mm, respectively.

Keywords: Lupane triterpenoids, *Diospyros ehretioides*, antimicrobial activities, acute toxicity

Introduction

Triterpenes comprise one of the most interesting groups of natural products due to their diverse structural features as well as biological and pharmacological activities (Hanson, 2003; Parmar *et al*., 2013). They are abundantly present in plants in the form of free aglycones and, more rarely, as glycoconjugates (Chappell, 1995). In many Asian countries, herbal products containing triterpenes are widely described to prevent or to treat a variety of diseases by traditional healers (Xu *et al*., 2004). They proved to have antibacterial, antiviral, antifungal, antioxidant and anti-inflammatory properties, as well as anticancer activity. Lupeol, the most common triterpenoid, has previously demonstrated to exhibit interesting therapeutic properties such as antimalarial, anti-inflammatory and antitumor activities (Alves *et al*., 1997).

Diospyros (family Ebenaceae) is a large genus of over 700 species of deciduous and evergreen trees and shrubs, which are distributed in both the hemispheres. However, the majority of the species are native to tropical and subtropical regions including Myanmar. *Diospyros ehretioides* grows abundantly in Cambodia, India, Thailand, and Myanmar (Chopra *et al*., 1965), where is known with the common names of Aukchinsa, Bok-pin, and Thipok (Kress *et al*., 2003). In herbal medicine a decoction of *Diospyros ehretioides* roots is used as an emetic and against diarrhea, whereas a bark decoction is used as an antidiuretic. In previous chemical studies, palmarumycins JC1 and JC2, isodiospyrin and isodiospyrol A were isolated from the fruits of *Diospyros ehretioides*. Palmarumycin JC2 and isodiospyrol A possess antimalarial, antifungal, antimycobacterial, and cytotoxic activities (Prajoubklang, 2005).

The isolation and identification of four lupane triterpenoids, lupeol (1), betulin (2), betulinaldehyde (3), and betulinic acid (4) from the ethanolic extract of the roots of *Diospyros ehretioides* are studied in this research.

* Department of Chemistry, Shwebo University

Materials and Methods

Plant Material

The roots of *Diospyros ehretioides* were collected in July 2012 from Tetma Village, Nyaung U Township, Mandalay Region, Myanmar and the species were identified by U Aung Kyaw Oo, Associate Professor (Rtd.), Department of Botany, Meiktila University. A voucher specimen of this plant (N-12) has been deposited at the Department of Chemistry, University of Mandalay.

General Experimental Procedure

Melting points were measured on Fisher-Johns melting apparatus. Optical rotation was measured with a Perkin Elmer 241 polarimeter, *c* in g/mL. Infrared spectra were recorded on NaCl disks on an FT-IR Perkin Elmer Paragon 100 PC spectrometer or KBr disks on a Shimadzu FT-IR spectrometer; ν in cm^{-1}. NMR experiments were performed on a Bruker AV 300 spectrometer, at 200 MHz (^1H) and 600 MHz (^1H) and 150 MHz (^{13}C) with TMS. NMR chemical shifts (δ) were reported in ppm and solvent peaks were used as internal standards. The coupling constant (*J*) values were reported in Hertz (Hz). The multiplicity of each carbon atom was determined by DEPT spectrum. DQF-COSY, HMQC, and HMBC spectra were recorded using standard pulse sequences. NMR spectra were recorded in $CDCl_3$, Sigma-Aldrich. ESIMS data were recorded on a Thermo TSQ mass spectrometer, by flow injection analysis (FIA), with an electron spray ionization source (ESI). For silica gel and reversed phase column chromatography, Merck Kieselgel 60 (40-63 μm) and Merck Li Chroprep RP-18 (25-40 μm) were employed, respectively; for direct phase and reversed phase TLC, (20 x 20 cm) silica gel 60 (GF_{254}, Merck) or RP-18 (F_{254S}, Merck), aluminium-supported plates were used. Compounds were visualized under UV light (254 and 366 nm) and, additionally, they were stained by exposure to a 0.5% solution of vanillin in H_2SO_4-EtOH (4:1), followed by gentle heating at 100 ˚C. Reagent grade solvents were purchased from Aldrich.

Extraction of *Diospyros ehretioides*

Dry powdered root of *Diospyros ehretioides* (1.0 kg) was percolated with 95% ethanol (3 L) for two weeks at room temperature. The filtrates were concentrated by a rotary evaporator to give 23.6 g of extract. The extract was partitioned between water and EtOAc. Each filtrate was evaporated to dryness under reduced pressure at 40 ˚C to yield EtOAc (4.0 g), and aqueous extracts (19.0 g). The ethyl acetate extract was further partitioned between *n*-hexane and acetonitrile. Each layer was evaporated to dryness under reduced pressure at 40 ˚C to yield residue A (1.8 g) and residue B (2.1 g) from the hexane and the acetonitrile fractions, respectively.

Isolation and Purification of Lupane Triterpenoids from the Hexane Fraction of *Diospyros ehretioides*

Residue A (1.8 g) was separated by column chromatography on silica gel 60. Elution with a *n*-hexane-EtOAc gradient gave 200 fractions, approximately 8 mL each. The fractions were combined on the basis of their TLC profiles, to give thirteen main fractions (fractions I-XIII). Fraction I (253.5 mg) was further chromatographed on a silica gel 60 column. Elution with 100% CH_2Cl_2 gave three combined fractions, I-A/C. The combined fraction, I-A (275.5 mg) displayed one main purple spoton TLC by applying vanillin spraying agent. This fraction was further crystallized from MeOH to yield 228.0 mg of lupeol (**1**) as colorless needles. Fraction IV (147.3 mg) was separated by column chromatography over a RP-18 column. Elution with 100% MeOH afforded five main fractions, IV-A/E. The fraction IV-B yielded 4.8 mg of betulinaldehyde (**3**) as colorless crystalline needles, which was detected on a TLC plate as a purple spot by the vanillin spraying reagent. Fraction VII (46.9 mg) was separated on a RP-18 column. Elution with

a MeOH-H_2O gradient yielded three main fractions, VII-A/C. The fraction VII-C (40.8 mg) was further purified by silica gel 60 column chromatography. Elution with a gradient of CH_2Cl_2-EtOAc gave 26.3 mg of betulin (**2**) as a colorless solid. Fraction XIII (94.2 mg) was separated on a RP-18 column. Elution with a gradient of MeOH-H_2O yielded 40 fractions of approximately 8 mL each, which were then combined according to their TLC profiles to give four main fractions, XIII-A/D. The fraction XIII-A (10.6 mg) was further purified on a silica gel 60 column eluted with a gradient of CH_2Cl_2-EtOAc to yield 6.0 mg of betulinic acid (**4**) as a colorless solid.

Some physicochemical properties such as melting points and optical rotation of these isolated compounds were determined. The structures of these isolated compounds were identified by using FT IR and modern NMR spectroscopic techniques such as ^{1}H NMR, ^{13}C NMR, and ESIMS Mass spectroscopies, and by comparing with the reported data. The NMR and Mass spectra of the isolated compounds were measured at Department of Pharmaceutical Science, Faculty of Pharmacy, Meijo University, Nagoya, Japan and Dipartimento di Chimica and CEMEC, Università di Pavia, Pavia, Italy.

Acute Toxicity Study on Albino Mice Model

The oral acute toxicity study of the ethanol extract of *Diospyros ehretioides* roots was carried out using the "Up-and-Down" method for testing in mice at single doses of 175, 550, 1750 and 5000 mg/kg in accordance with the OECD guideline no. 425 (OECD, 2008). It was determined at Biochemistry Research Division, Department of Medical Research (Pyin Oo Lwin Branch). Male albino mice were used for each dose level in the study. According to the test description, total number of 7 adult male albino mice, weighing (25-40 g) were selected and divided into five groups. Group (IV) contained three animals except groups (I-III). An animal was picked at a time, weighed and dosed with the equivalent volume of extract dissolved in distilled water. The extract was administered orally using feeding nozzle. Group (I), (II) and (III) mice were administered with extracts of sample 175 mg/kg, 550 mg/kg and 1750 mg/kg body weight per dose. Group (IV) mice were giving orally with extract of sample 5000 mg/kg body weight per dose. Group (V) mice performed as a control group. Each was then observed every 15 min in the first 4 h after dosing, every 30 min for 6 h and daily for 48 h according to the specifications of the OECD. The body weight of the mice was measured on day 1, 7, and 14. The mice were monitored for a total of 14 days for a possible long-term lethal outcome.

Preparation of Crude Extracts from Roots of *Diospyros ehretioides*

Dried powdered roots of *Diospyros ehretioides* (100 g) were percolated in 300 mL of ethanol for one week and filtered. This procedure was repeated for three times. Then the filtrate was concentrated to dryness by a vacuum rotatory evaporator to provide respective ethanol crude extract. Similarly, dichloromethane and hexane extracts of each dried roots powdered were prepared according to the above procedure.

Evaluation of Antimicrobial Activity by Agar Well Diffusion Method

The Agar-well diffusion method was used for evaluating antimicrobial activity of the ethanol, dichloromethane and hexane extract of *Diospyros ehretioides* roots. Gram negative bacteria (*Escherichia coli*), three-gram positive bacteria (*Staphylococcus aureus, Enterococcus faecalis* and *Bacillus cereus*), and one strain of fungus (*Candida albicans*) were used as test microorganisms and antibiotic, chloramphenicol was used as a standard. After overnight incubation at 27 ˚C, the diameters of inhibition zone including agar well were measured. In the antimicrobial test with the root extracts, the greater the inhibition zones for the test microorganisms, the better the antimicrobial activity of the extracts.

Results and Discussion

Structure Elucidation of Lupane Type Triterpenoid Compounds

Chromatographic separation of the hexane fraction from an ethanolic extract of the roots of *Diospyros ehretioides* afforded four lupane type triterpenoids (**1-4**) (Figure 1).

Compound **1** was obtained as colorless crystalline needles, mp 213-215˚C, $[\alpha]_{20}^{D}$ = +23.87 (*c* 0.009, CH_2Cl_2). It exhibited the molecular formula $C_{30}H_{50}O$ from the molecular ion peak at *m/z* 426. The IR spectrum showed the absorption bands for hydroxyl group at 3344 cm^{-1} and double bond at 1642 cm^{-1}. The ^{1}H NMR spectrum of compound **1** exhibited the characteristic signals of a lupane type triterpenoid, which included six methyl groups attached to quaternary carbons [δ 0.97 (Me-23), 0.79 (Me-24), 0.83 (Me-25), 1.03 (Me-26), 0.94 (Me-27), 0.80 (Me-28), respectively] and one vinyl methyl group at δ 1.68 (Me-30). The multiplet of one proton at δ 2.37, assignable to 19β-H, is characteristics of lupeol. The H-3 proton, geminal to an OH group, showed a double doublet at δ 3.19 while a pair of doublets at δ 4.69 and δ 4.57 (1H, each) was indicative of the olefinic protons H-29a and H-29b.

The structural assignment of compound **1** was further identified by its ^{13}C NMR and DEPT spectral data which showed 30 carbon signals as seven methyl groups at [δ_C 28.0 (C-23), δ_C 15.4 (C-24), δ_C 15.9 (C-25), δ_C 16.1 (C-26), δ_C 14.6 (C-27), δ_C 18 (C-28) and δ_C 19.8 (C-30)], a secondary hydroxyl bearing carbon at δ_C 79.0 (C-3) and an exomethylene carbon at δ_C 109.3 (C-29), sp^2 quaternary carbon at δ_C 150.9 (C-20), in addition to ten sp^3 methylene carbons, sp^3 five methine carbons and five quaternary carbons.

The shielding of C-23 (δ_C 28.0) methyl of compound **1** could be due to the influence of the adjacent C-3 hydroxyl group. The position of the hydroxyl group at C-3 was assigned by an HMBC spectrum in which the oxymethine proton at δ 3.19 (H-3) showed correlations with δ_C 38.7 (C-1), δ_C 38.8 (C-4), δ_C 27.4 (C-2) and δ_C 15.4 (C-24). The position of a methine proton at C-19 was determined from HMBC correlation of δ 2.37 (H-19) with δ_C 48.3 (C-18), δ_C 38.1 (C-13), δ_C 29.9 (C-21), δ_C 19.8 (C-30) and δ_C 150.9 (C-20). HMBC correlations of compound **1** is shown in Figure 2. Thus, on the basic of spectroscopic data and comparison with the previous report (Suryati *et al*., 2011), the structure of compound **1** was identified as lupeol. (Table 1)

Compound **2** was isolated as colorless solid, mp 248-252 ˚C, $[\alpha]_{20}^{D}$ = + 14.17 (*c* 0.002, CH_2Cl_2). The IR spectrum showed absorption bands of a hydroxyl group at 3381 cm^{-1} and a double bond at 1645 cm^{-1}. The molecular formula $C_{30}H_{50}O_2$ was determined from the peak at *m/z* 465.42 $[C_{30}H_{50}O_2+Na]^+$ in the ESIMS spectrum. As compound **1,** compound **2** was revealed as a purple spot on TLC plates sprayed by the sulpho-vanillin reagent. The ^{1}H NMR spectrum of compound **2** was very similar to that of compound **1**. It included a double of doublets resonating at δ 3.18, which was characteristic of αH-3, and two doublets of geminal protons at δ 4.58 and δ 4.69 attributable to 2H-29. These signals together with the methyl singlet at δ 1.68 suggested that compound **2** was a lupeol-type triterpenoid. AB system was observed at δ 3.79 and δ 3.33 (1H each), assigned to an oxymethylene group, replaced the signal of Me-28 (δ 0.80) in the ^{1}H NMR spectrum of lupeol (**1)**.

The ^{13}C NMR spectrum established compound **2** as a lupeol type triterpene derivative. The characteristics of sp^2 carbon comprising the double bond was observed at δ_C 109.7 (C-29). Oxygenated carbon shifts for C-3 and C-28 were observed at δ_C 78.9 and δ_C 60.6, respectively. The ^{13}C NMR and DEPT spectral data revealed that compound **2** with six sp^3 methyl carbons, totally thirty carbon atoms which is equivalent to the total number of carbon atoms in triterpenoid. The position of the hydroxyl group at C-3 was determined by an HMBC spectrum in which the carbinol methine proton at δ 3.18 (H-3) showed correlations with δ_C 27.4 (C-2) and δ_C 15.4 (C-24). The position of a methine proton at C-19 was determined from HMBC

correlations of δ 2.38 (H-19) with δ_C 47.8 (C-18), δ_C 29.8 (C-21), δ_C 109.7 (C-29) and δ_C 150.5 (C-20). Moreover, the oxymethylene protons signals at δ 3.33 and δ 3.79 (H-28) showed long-range correlations with δ_C 29.2 (C-16), δ_C 47.8 (C-17) and δ_C 33.9 (C-22). The long-range HMBC correlations of compound **2** is shown in Figure 3. Based on these data and comparison with the literature (Ayotollahi *et al*., 2011; Tijjani *et al*., 2012) compound **2** was assigned the known structure, 20(29)-lupene-3,28-diol, which is commonly known as the triterpenoid diol betulin. (Table 1)

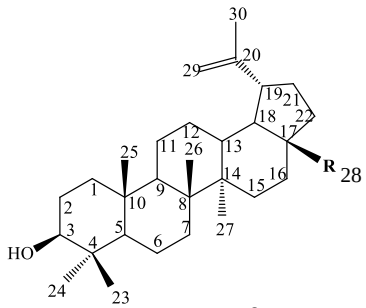

(**1**) R = $-CH_3$ (**2**) R = $-CH_2OH$

(**3**) R = $-CHO$ (**4**) R = $-COOH$

Figure 1. Structures of lupane triterpenoids 1-4 isolated from *Diospyros ehretioides*

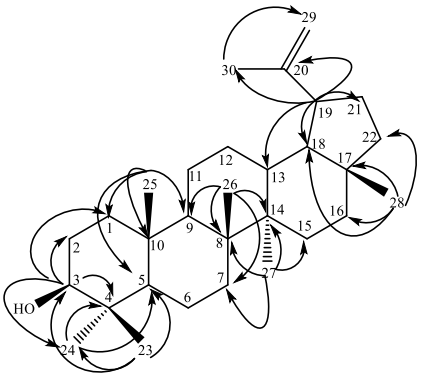

Figure 2. HMBC correlations of compound 1

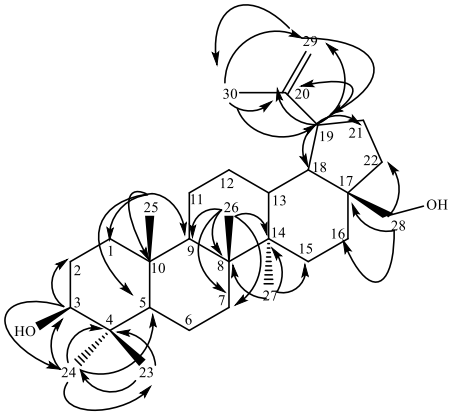

Figure 3. HMBC correlations of compound 2

Compound **3** was isolated as colorless crystalline needles from MeOH, mp. 186-189 ˚C, $[\alpha]_{20}^{D}$ = +17.49 (*c* 0.002, CH_2Cl_2). The mass spectrum exhibited an $[M+H]^+$ peak at m/z 441.42 corresponding to $C_{30}H_{48}O_2$. The IR spectrum showed the absorption at 3372 cm^{-1} (hydroxyl group), 1715 cm^{-1} (aldehyde carbonyl) and 1645 cm^{-1} (double bond). The ^1H NMR spectrum of compound **3** was very similar to those of **1**. It showed five methyl singlets at δ 0.96 (Me-23), 0.75 (Me-24), 0.82 (Me-25), 0.91 (Me-26), 0.97 (Me-27), respectively, one vinyl methyl at δ 1.69 (Me-30) and the signal of an aldehydic proton at δ 9.68 (H-28). The signal of the methine proton H-19 resonated at δ 2.85, and was downfield shifted with respect to the corresponding

signal of compound **1** (δ 2.37 ppm). This finding indicated the presence of a carbonyl group at C-28. The secondary carbinol at C-3 showed a multiplet at δ 3.17 while a pair of broad singlets at δ 4.75 and δ 4.63 was assigned to the olefinic protons H-29a and H-29b. These data indicated that compound **3** had the structure of a pentacyclic lupeol-type triterpenoid with an aldehyde group attached to C-17. The aldehydic proton was also confirmed by the FT IR spectrum. In FT IR spectrum, the aldehydic C-H stretching band was observed at 2704 cm^{-1}. Comparison of the spectroscopic data and physical data of compound **3** with the literature (Haque *et al*., 2013; Tung *et al*., 2010) confirmed its identity as with betulinaldehyde. (Table 2)

Compound **4** was isolated as a colorless solid by crystallization from MeOH, mp. 282-285 ˚C, $[\alpha]_{20}^{D}$ = + 13.33 (c 0.0006, CH_2Cl_2). It gave a red spot on a silica gel TLC plate sprayed by the sulpho-vanillin reagent. The IR spectrum showed absorption bands for hydroxyl and carboxylic groups at 3652 and 1688 cm^{-1}, respectively. The ESIMS spectrum displayed a $[M-H]^-$ negative peak at m/z 455.46, which indicated the molecular formula $C_{30}H_{48}O_3$. The ^1H NMR spectrum was typical of lupane-type compounds. In fact, it displayed signals attributable to an exomethylene group at δ 4.61 and δ 4.74 (1H each, broad singlets), which together with an allylic methyl at δ 1.69 indicated the presence of an isopropenyl unit. The double doublet at δ 3.19 could be assigned to αH-3 bound to an oxygenated carbon. In addition, a multiplet at δ 3.01 was assigned to βH-19 and five singlets of methyl groups resonated at δ 0.75 (Me-24), 0.82 (Me-25), 0.93 (Me-26), 0.96 (Me-23), and 0.97 (Me-27). The downfield-shift of the signal assigned to βH-19 (δ 3.01), compared with the corresponding proton of lupeol (**1**) (δ 2.37), indicated the presence of a β-COOH attached to C-17. Based on these data and comparison with the literature (Haque *et al*., 2013; Lee *et al*., 2005), compound **4** was identified as betulinic acid. (Table 2)

Physicochemical and spectroscopic data of compounds **1**-**4** are reported as below:

Lupeol (**1**)- Colorless crystalline needles; $[\alpha]_{20}^{D}$ = +23.87 (*c* 0.009, CH_2Cl_2); mp. 213-215 ˚C; ESIMS: $[M+Na]^+$ *m/z* 449 for $C_{30}H_{50}O$+Na; IR (KBr) ν = 3344.7, 3069.8, 2946.4, 2866.3, 1642.4, 1456.3, 1382.0, 1038.7, 882.5 cm^{-1}; the ^1H NMR and ^{13}C NMR spectral data are reported in Table 1.

Betulin (**2**)- Colorless solid; $[\alpha]_{20}^{D}$= +14.17 (*c* 0.002, CH_2Cl_2); mp. 248-252 ˚C; ESIMS: $[M+Na]^+$ *m/z* 465 for $C_{30}H_{50}O_2$+Na; IR (KBr) ν = 3381.3, 2936.7, 2870.2, 1645.3, 1541.2, 1457.3, 1030.9, 882.5 cm^{-1}; the ^1H NMR and ^{13}C NMR spectral data are reported in Table 1.

Betulinaldehyde (**3**)- Colorless crystalline needles; $[\alpha]_{20}^{D}$= +17.49 (*c* 0.002, CH_2Cl_2); mp. 186-189 ˚C; ESIMS: $[M+H]^+$ *m/z* 441.42 for $C_{30}H_{48}O_2$+H; IR (NaCl) ν = 3372.4, 2704.0, 1715.8, 1645.0 cm^{-1}; the ^1H NMR spectral data are reported in Table 2.

Betulinic acid (**4**)- Colorless solid; $[\alpha]_{20}^{D}$= +13.33 (*c* 0.0006, CH_2Cl_2); mp. 283-285 ˚C; ESIMS: $[M-H]^-$ *m/z* 455.46 for $C_{30}H_{48}O_3-H$; IR (KBr) ν = 3652.3, 2926.1, 2862.5, 1688.7, 1455.3, 1039.7, 892.2 cm^{-1}; the ^1H NMR spectral data are reported in Table 2.

Table 1. The Comparison of ^{13}C NMR Data and ^{1}H NMR Data of Compound 1, 2 and Lupeol and Betulin

Position	δ_C [ppm]		δ_H [ppm] (mult, J in Hz)		δ_C [ppm]		δ_H [ppm] (mult, J in Hz)	
	1[a]	**Lupeol[b]**	**1[a]**	**Lupeol[b]**	**2[a]**	**Betulin[b]**	**2[a]**	**Betulin[b]**
1	38.7	38.9	0.91, 1.67		38.7	38.9	0.91, 1.67	
2	27.4	24.6	1.68, 1.56	1.62, *m*	27.4	27.5	1.61, 1.57	
3	79.0	79.2	3.19, *dd* (11.5, 4.8)	3.18, *t*	78.9	79.2	3.18, *dd* (11.0, 5.3)	3.18, *dd* (11.2, 5.2)
4	38.8	39.0			38.9	38.8		
5	55.3	55.5	0.68	0.67, *t*	55.3	55.4	0.68	
6	18.3	18.5	1.36, 1.52		18.3	18.4	1.41, 1.53	
7	34.3	34.4	1.39		34.3	34.3	1.40	
8	40.9	41.0			40.9	41.0		
9	50.5	50.6	1.27	1.25, *t*	50.4	50.5	1.27	
10	37.2	37.3			37.2	37.4		
11	20.9	21.1	1.22, 1.41		20.8	20.9	1.19, 1.42	
12	25.2	25.3	1.07, 1.68		25.2	25.3	1.03, 1.68	
13	38.1	38.2	1.66		37.3	37.2	1.65	
14	42.4	43.0			42.7	42.8		
15	27.5	27.7	1.02, 1.59		27.1	27.1	1.05, 1.70	
16	35.6	35.8	1.37, 1.47		29.2	29.2	1.25	
17	43.0	43.2			47.8	47.9		
18	48.3	48.5	1.36	1.35, *dd*	47.8	47.9	1.58	
19	47.9	48.2	2.37, *m*	2.38, *m*	48.8	48.8	2.38	
20	150.9	151.2			150.5	150.6		
21	29.9	30.0	1.33, 1.92		29.8	29.8	1.42	
22	40.0	40.2	1.20, 1.38		33.9	34.1	1.03, 1.86	
23	28.0	28.2	0.97, *s*	0.96, *s*	27.9	28.1	0.97, *s*	0.96, *s*
24	15.4	15.6	0.79, *s*	0.75, *s*	15.4	15.4	0.77, *s*	0.75, *s*
25	15.9	16.2	0.83, *s*	0.82, *s*	16.1	16.2	0.83, *s*	0.80, *s*
26	16.1	16.3	1.03, *s*	1.02, *s*	15.9	16.1	1.03, *s*	0.97, *s*
27	14.6	14.7	0.94, *s*	0.95, *s*	14.8	14.8	0.98, *s*	0.99, *s*
28	18.0	18.1	0.80, *s*	0.78, *s*	60.6	60.6	3.33, *d* (10.8) 3.79, *d* (10.8)	3.33, *d* (11.0) 3.79, *d* (11.0)
29a	109.3	109.5	4.69, *d* (2.3)	4.68, *d*	109.7	109.8	4.69, *d* (2.1)	4.70, *d*
29b			4.57, *d* (2.3)	4.56, *d*			4.58, *d* (2.1)	4.58, *d*
30	19.8	19.5	1.68, *s*	1.67, *s*	19.1	19.2	1.68, *s*	1.67, *s*

[a]The ^{1}H NMR data were measured in $CDCl_3$ at 600 MHz and ^{13}C NMR at 150 MHz

[b]The ^{1}H NMR data were measured in $CDCl_3$ at 500 MHz and ^{13}C NMR at 125 MHz

Table 2. ^{1}H NMR Spectroscopic Data (δ in ppm, J in Hz) for Compounds 3 and 4, Betulinaldehyde and Betulinic Acid

Position	3	Betulinaldehyde*	4	Betulinic acid**
	δ_H (mult)[c]	δ_H (mult, J in Hz)[d]	δ_H (mult)[c]	δ_H (mult, J in Hz)[d]
3	3.17, dd (11.3, 4.7)	3.12, dd (11.2, 4.8)	3.19, dd	3.16, dd (10.8, 5.4)
19	2.85, m	2.80, m	3.01, dt (10.3, 4.5)	2.97, dt (10.4, 4.8)
23	0.96, s	0.84, s	0.96, s	0.80, s
24	0.75, s	0.68, s	0.75, s	0.73, s
25	0.82, s	0.75, s	0.82, s	0.91, s
26	0.91, s	0.90, s	0.93, s	0.94, s
27	0.97, s	0.89, s	0.97, s	0.95, s
28	9.68, s	9.60, s		
29a	4.75, brs	4.68, brs	4.74, brs	4.71, brs
29b	4.63, brs	4.56, brs	4.61, brs	4.58, brs
30	1.69, s	1.63, s	1.69, s	1.67, s

*(Tung *et al*., 2010) **(Lee *et al*., 2005)
[c]The ^{1}H NMR data were measured in $CDCl_3$ at 200 MHz
[d]The ^{1}H NMR data were measured in $CDCl_3$ at 400 MHz

Effect of Ethanol Extracts on Acute Toxicity

The acute toxicity test by the Up and Down method at an oral limit doses of 175, 550, 1750 and 5000 mg/kg of the ethanol extract of *Diospyros ehretioides* roots caused no death in the mice. No lethal effects were noted throughout the short and long-term observation periods (Table 3). No toxicity signs were observed in the mice throughout the 14 days study period. The acute toxicity study did not show any toxicity signs and symptoms at 175, 550, 1750 and 5000 mg/kg. No morbidity or mortality was observed in the treated groups at 175-5000 mg/kg doses during the acute toxicity study. Even with the doses up to 5000 mg/kg body weight administration, there is no lethality after 14 days. As a result, the oral doses of the extract could be greater than 5000 mg/kg body weight.

Table 3. Acute Toxicity of the Ethanol Extract of the *Diospyros ehretioides* Root Based on Daily Body Weight

Test	Groups	Dosage of Extract (mg/kg)	Sex	Marking	Body weight (g)			Mortality
					1st day	7th day	14th day	
1	I	175	Male	Back	30	30	27	Nil
2	II	550	Male	Head	37	35	34	Nil
3	III	1750	Male	L-leg	25	20	21	Nil
4	IV	5000	Male	Tail R-leg	34	32	33	Nil
5	IV	5000	Male	Head Back	30	29	27	Nil
6	IV	5000	Male	Head R-leg L-leg	31	30	31	Nil
7	V (control)	-	Male					Nil

Nil = no lethality of the albino mice

Antimicrobial Activity of Root Extracts

The roots of *Diospyros ehretioides* were extracted with ethanol, dichloromethane DCM and hexane respectively. The inhibitory effect of root extracts was tested against five pathogenic microorganisms by Agar well diffusion method. The result in different extents of inhibition is shown in Table 4 and Figure 4. Antimicrobial activity of the all crude extracts showed against four microorganisms: *Escheichia coli*, *Staphylococcus aureus*, *Bacillus cereus* and *Candida albicans* with the range of inhibition zone diameter between (10~15 mm). The DCM extract of *Diospyros ehretioides* exhibited low antimicrobial activity against all tested strains except *Enterococcus faecalis*. Ethanol extract of the sample responds medium activities on fungus stain, *Candia albicans*. The *Enterococcus faecalis* strain did not inhibit against the ethanol, DCM and hexane extracts of *Diospyros ehretioides*.

(a) **(b)** **(c)** **(d)** **(e)**

(a) *Escheichia coli* (b) *Enterococcus faecalis* (c) *Staphylococcus aureus*
(d) *Bacillus cereus* (e) *Candida albicans*

Figure 4. Inhibition Zone Diameters of the crude extracts of *Diospyros ehretioides* roots tested with five microorganisms

Table 4. Antimicrobial Activity of the Extracts of *Diospyros ehretioides* Root by Agar Well Diffusion Method

No	Test Microrganisms	Inhibition Zone Diameters (mm)			
		EtOH Extract	DCM Extract	Hexane Extract	Chloramphenicol
1	*E. coli*	12	10	10	26
2	*E. faecalis*	0	0	0	30
3	*S. aureus*	11	12	10	32
4	*B. cereus*	13	13	11	24
5	*C. albicans*	15	12	10	27

Agar well = 8 mm, 9mm ~ 14 mm = (+) low activity, 15 mm ~ 19 mm = (++) medium activity,
20 mm and above = (+++) high activity, Std. = Chloramphenicol

Conclusion

Medicinal plants used in folk medicine still represent an interesting source for the development of different products with various useful properties. In this chemical investigation of the constituents of *Diospyros ehretioides* roots, the lupane triterpenoids lupeol (**1**), betulin (**2**), betulinaldehyde (**3**), and betulinic acid (**4**) have been isolated and identified by modern NMR spectroscopic techniques. It is worth noting that with a content of 228 μg/g dry roots, the ethanolic extract of *Diospyros ehretioides* roots represents one of the richest known sources of the anticancer and anti-inflammatory triterpenoid lupeol (Saleem, 2009). In addition, betulinic acid (**4**), which is also present in the extract, has antiretroviral, antimalarial, and anti-inflammatory properties, as well as potential anticancer activity, as topoisomerase inhibitor. In the study of acute toxicity by OECD-425 guideline, no toxic sign and no death were recorded at the dose of 5000 mg/kg of ethanol extract. Therefore, the test sample showed free from acute

toxic effect up to the dose of 5000 mg/kg and can be considered relatively safe. The antimicrobial activities of the extracts determined by Agar well diffusion method on five pathogenic microorganisms. Ethanol extract, DCM extract and hexane extract respond low activities on four tested organisms such as *Escherichia coli*, *Staphylococcus aureus, Bacillus cereus* and *Candida albicans* and no activity on *Entrococcus faecalis.* Due to the content of bioactive compounds, the roots of *Diospyros ehretioides* have great potential for producing healthy products. Moreover, the use of the roots in herbal medicine appears to be supported by scientific evidence.

Acknowledgements

This work was financially supported by the European Commission, ERASMUS MUNDUS Action-2 program-PANACEA, Universite Montpellier 2, France/Università di Pavia, Italy. The author acknowledges Dr Myo Myo, Rector, Shwebo University for her permission to submit the paper and also thanks to Professor and Head Dr Thi Thi Aung and Professor Dr Mya Theingi, Department of Chemistry, Shwebo University. Special thanks are also to Associate Professor Dr Yoshiaki Takaya, Department of Pharmaceutical Science, Faculty of Pharmacy, Meijo University, Nagoya, Japan for NMR measurements. Special mention to Dr Andrea Gandini, Department of Organic Chemistry (Lab B2), Università di Pavia, Italy for his help and MS spectroscopic measurements.

References

Alves, D. S., J. V. Soares, and S. Amaral. (1997). "Biomass of Primary and Secondary Vegetation in Rondônia, Western Brazilian Amazon". *Global Change Biology*, vol. 3 (5), pp. 451-462

Ayotollahi, A. M., M. Ghanadian, S. Afasharypour, O. M. Abdellac, M. Mirzai, and A. Gholamreza. (2011). "Pentacyclic Triterpenes in *Euphorbia microsciadi*a with their T-cell Proliferation Activity". *Iran J of Pharm Res.*, vol. 10 (2), pp. 287-294

Chappell, J. (1995). "Biochemistry and Molecular Biology of the Isoprenoid Biosynthetic Pathway in Plants". *Annu. Rev. Plant. Physiol. Plant Mol. Biol*., vol. 46, pp. 521-547

Chopra, R. N., R. L. Badhwar, and S. Ghosh. (1965). *Poisonous Plants of India*. Indian Council of Agricultural Research, New Delhi

Hanson, J. R. (2003). *Natural Products: The Secondary Metabolites*. The Royal Society of Chemistry, Cambridge, UK: pp. 112-121

Haque, A., M. M. Ali Siddiqi, A. M. Sarwaruddin Chowdhury, and C. M. Hasan. (2013). "Isolation of Betulinic Acid and 2,3-Dihydroxyolean-12-en-28-oic Acid from the Leaves of *Callistemon linearis*". *Dhaka Univ. J. Sci*., vol. 61 (2), pp. 211-212

Kress, W. J., A. D. Robert, and F. Ellen. (2003). *A Check List of the Trees, Shrubs, Herbs, and Climbers of Myanmar*. SMITHSONIAN INSTITUTION, Contributions from the Unites States National Herbarium, vol. 45, pp. 1-590

Lee, T. H., J. L. Chiou, C. K. Lee, and Y. H. Kuo. (2005). "Separation and Determination of Chemical Constituents in the Roots of *Rhus javanica* L.var. *roxburyhiana*". *J. Chin. Chem. Soc*., vol. 52 (4), pp. 833-841

Organization for Economic Cooperation and Development. (2008). *Acute Oral Toxicity: Up and Down Procedure, Guideline for the Testing of Chemicals 425 OECD*. Paris: pp. 1-2

Parmar, S. K., T. P. Sharma, V. B. Airao, and R. Bhatt. (2013). "Neuropharmacological Effects of Triterpenoids". *Phytopharacology*, vol. 4 (2), pp. 354-372

Prajoubklang, A., B. Sirittunyalug, and P. Charoenchai. (2005). "Bioactive Deoxypreussomerins and Dimeric Naphthoquinones from *Diospyros ehretioides* Fruits: Deoxypreussomerins May Not Be Plant Metabolites but May Be from Fungal Epiphytes or Endophytes". *Chemistry & Biodiversit*y, vol. 2 (10), pp. 1358-1367

Saleem, M. (2009). "Lupeol, A Novel Anti-inflammatory and Anti-cancer Dietary Triterpene". *Cancer Lett.*, vol. 285 (2), pp. 109-115

Suryati, H., M. N. Nurdin, M. N. Dachriyanus, and Hj. Lajis. (2011). "Structure Elucidation of Antibacterial Compound from *Ficus deltoidea* Jack Leaves". *Indo. J. Chem*., vol. 11 (1), pp. 67-70

Tijjani, A., I. G. Ndukue, and R. G. Ayo. (2012). "Isolation and Characterization of Lup-20(29)-ene-3, 28-diol (Betulin) from the Stem Bark of *Adenium obesum* (Apocynaceae)". *Trop J Pharm Res*., vol. 11 (2), pp. 259-262

Tung, N. H., H. J. Kwon, J. H. Kim, J. C. Ra, J. A. Kim, and Y. H. Kim. (2010). "An Anti-influenza Component of the Bark of *Alnus japonica*". *Arch. Pharm. Res*., vol. 33 (3), pp. 363-367

Xu, R., G. C. Fazio, and S. P. T. Matsuda. (2004). "On the Origins of Triterpenoid Skeletal Diversity". *Phytochemistry*, vol. 65 (3), pp. 261-291

THE CHEMICAL AND SPECTRAL ANALYSES OF THE PREPARED CELLULOSE ACETATES FROM WHEAT STRAW POWDER AND SAWDUST POWDER

Yi Yi Lwin[1], Thida Kyaw[2], Yi Yi Myint[3]

Abstract

In this research, the preparation of cellulose powders from the wheat straw powder and sawdust powder by dewaxing and pulping processes, the preparation of cellulose acetates by the sonification process, and the identification of prepared cellulose acetates by chemical and spectral analyses were carried out. The cellulose acetates were prepared by the optimized acetylation of respective celluloses with an acetic acid-acetic anhydride-toluene solvent mixture using perchloric acid as a catalyst increasing the reaction rate for 1, 2, 3, and 4 h of sonication. The acetylation procedure was modulated by an ultrasonic cleaner. Then, the prepared cellulose acetates (WSCAs and SDCAs) from wheat straw powder and sawdust powder had been identified by chemical (acid-base titration) and spectral (FT IR, XRD, NMR) analyses for the degree of substitution of acetyl groups on the corresponding prepared cellulose acetates. From the titration data, FTIR spectral data and XRD spectral data, the optimum acetylation by 1 h sonication, which provides the highest degree of substitution and the highest yield percent, had been selected. Then WSCA-1 and SDCA-1 obtained by selected acetylation were further identified by ^{1}H and ^{13}C NMR (Nuclear Magnetic Resonance) spectroscopic methods.

Keywords: acetylation, sonication processes**,** acid-base titration, FT IR, XRD, NMR

Introduction

Cellulose acetate is a well-known industrial product that finds many commercial applications (Edgar *et al.*, 2001). It is used as a film base in photography, as a component in some coatings, and as a frame material for eyeglasses, as a synthetic fiber in the manufacture of cigarette filters and playing cards, as a fiber in textiles because of its relatively low cost, draping quality, softness, comfort, luster, and natural feel, as a substrate for motion picture camera film, as an ingredient in sheet and molded objects **(**Morgan, 2013). Cellulose acetate is typically made from wood pulp (cellulose) through reaction with acetic acid and acetic anhydride in the presence of sulphuric acid as a catalyst. Cellulose triacetate, (triacetate, CTA or TAC) is significantly more heat resistant than cellulose diacetate (Lindsey, 2010). In recent years, there has been strong emphasized to develop new cellulose-based materials because of the biodegradability and renewable aspects of these materials. Cellulose is an organic compound with the formula $(C_6H_{10}O_5)_n$, a polysaccharide consisting of a linear chain of several hundred to many thousands of β (1-4) linked D-glucose units. Cellulose can be produced from sources of lignocellulosic materials such as corn stalks, wheat straw, rice straw, agricultural by products such as corn fiber, rice hulls etc. **(**Crawford,1981; Updegraff, 1969).

The aim of this research is to prepare cellulose acetates by time-limit sonication processes, and then analyze the prepared cellulose acetates by chemical (acid-base titration) method, spectral (FT IR, XRD, ^{1}H and ^{13}C NMR) analyses for the determination of the degree of substitutions, crystallinity indices and average crystallite sizes. The cellulose acetates have been used to fabricate the cellulose acetate membranes which would be applied in clinical sense such as the separation of hemoglobin variants by electrophoresis and in wastewater treatment such as removal of toxic materials (Yi Yi Lwin, 2020).

[1] Department of Chemistry, Myingyan University
[2] Department of Chemistry, Mandalar University
[3] Department of Chemistry, University of Mandalay

NMR characterization of cellulose acetate and chemical shift assignments

Hiroyuki, Hisaho, and Shimizu (2015) investigated the cellulose acetates (CA) with degrees of substitution (DS) ranging from 2.90 to 0.92 by two-dimensional NMR spectroscopy. From the NMR spectroscopic analysis, the ^{1}H and ^{13}C NMR chemical shifts of the eight anhydroglucose units (AGUs) that contain CA are: 2,3,6-tri-, 2,3-di-, 2,6-di-, 3,6-di, 2-mono-, 3-mono-, 6-mono-, and unacetylated AGUs.

Materials and Methods

Sample Collection and Sample Preparation (Sampling)

The agricultural byproducts such as wheat straw and sawdust were collected from Myingyan Township, Myingyan District, Mandalay Region.

Wheat straw and sawdust raw materials were cut into small pieces, rinsed with water, and dried. The dried pieces were blended and sieved with a 120-mm mesh. After that, the powder dusts were sieved again with a 150-mm mesh. Then the sampling powders were collected to be used for cellulose isolation.

Preparation of Celluloses

In the preparation of cellulose, the powders were firstly dewaxed (removing pectin) by toluene-ethanol (2:1, v/v) and then pulping process was made by alkaline hydrolysis of dewaxed powders for 9 h refluxing with 15 % NaOH (removing lignin), and by bleaching (removing non-cellulosic coloring materials) (Yi Yi Lwin *et al.*,2020). The yield percent of prepared wheat straw and sawdust celluloses were calculated.

Preparation of Cellulose Acetate

Wheat straw and sawdust cellulose acetates were prepared by acetylation of the respective celluloses conducted with acetic acid- acetic anhydride-toluene solvent mixture in the presence of perchloric acid as a catalyst for 1, 2, 3 and 4 h sonication using ultrasonic cleaner.

Acetylation of wheat straw and sawdust celluloses by 1, 2, 3 and 4 h sonication

5 mL glacial acetic acid, 0.5 mL perchloric acid, and 10 mL of toluene were mixed and allowed to stand for 30 min. Then 1g of wheat straw cellulose was added and shaken thoroughly for 10 min. Then, 5 mL of acetic anhydride was added and shaken again for 30 min. In addition, 15 mL of acetic acid was added and the suspended solution was incubated in an ultrasonic cleaner under operating temperature of 80◦C for 1 h. Then the suspension was poured into the beaker containing 150 mL distilled water. Finally, cellulose acetate suspension was centrifuged, dried and weighed. The same procedure was performed under the operating temperature of 80°C for 2, 3 and 4 h sonication.

The above same procedures were also performed with the sawdust cellulose. The resultant cellulose acetates are shown in Figures 1 and 2. The yield percent of wheat straw cellulose acetates (WSCA-1, 2, 3 and 4) and sawdust cellulose acetates (SDCA-1, 2, 3 and 4) were calculated.

(a) (b) (c) (d) (e)

Figure 1. (a) Prepared WSC (b) WSCA-1, (c) WSCA-2, (d) WSCA-3 (e)WSCA-4

(a) (b) (c) (d) (e)

Figure 2. (a) Prepared SDC (b) SDCA-1, (c) SDCA-2, (d) SDCA-3, (e) SDCA-4

Determination of Degree of Substitution of Acetyl Groups in Prepared Cellulose Acetates

Acid-base titration

The degree of substitution (DS) is the average value of acetyl groups which replace the hydroxyl groups in the AGU units. The titrations were performed for the determination of DS. A 5.00 mL of NaOH (0.25 M) and 5 mL of ethanol were added to about 0.1 g cellulose acetate. Then, this mixture was left to stand for 24 h. After that, 10.00 mL of HCl (0.25 M) was added to the system. Next, the mixture was titrated with a standard (0.25 M) NaOH solution, using phenolphthalein indicator. This procedure was repeated in triplicate. The following equation was used to determine the percentage of acetyl groups (Kelly *et al*., 1989).

$$\text{Acetyl Group (\%)} = \frac{([(Vb_i + Vb_t)\mu_b - (V_a)\,\mu_a]\,43)}{m_{CA}} \times 100$$

(%) = percentage of acetyl groups
Vb_i = volume of NaOH added to the system
Vb_t = volume of NaOH spent in the titration
μ_b = concentration of NaOH
V_a = volume of HCl added to the system
μ_a = concentration of HCl
43 = molar weight of acetyl group
m_{CA} = weight of cellulose acetate sample

$$\text{Degree of substitution (D.S)} = \frac{[162\ \text{AG (\%)}]}{[43 \times 100 - 42\ \text{AG (\%)}]}$$

162 = the molecular weight of anhydroglucose unit (Badejo *et al.*, 2018)

FT IR spectroscopic analysis

The functional groups of prepared cellulose and cellulose acetates were identified by FTIR spectrometer and measured at the Department of Chemistry, University of Mandalay. From these spectral data, the degree of substitutions (DS) of acetyl groups in the prepared cellulose acetates were determined by the ratio of the peak area of carbonyl peak and that of hydroxyl peak (Cheng, *et al*., 2010).

Degree of Substitutions (DS) = $A_{C=O} / A_{OH}$

$A_{C=O}$ = peak area of carbonyl groups in ester, A_{OH} = peak area of OH groups

Determination of Crystallinity Indices and Average Crystallite Sizes of Prepared Cellulose Acetates by XRD (X-ray diffraction)

The prepared cellulose acetates were identified by XRD and measured at URC, University of Yangon. From the resulting XRD data, the average crystallite sizes and crystallinity indices and the crystallite sizes (D_{hkl}) for all cellulose acetates could be calculated according to the following relations (Regiani *et al.,* 1999).

$I_{CA} = 1 - I_{min} / I_{max}$

I_{CA} = the crystallinity index of CA

I_{min} = the intensity minimum between ° of 2θ

Debye Scherrer equation

$D_{hkl} = k\lambda / \beta_{hkl} \cos\theta$

hkl = the average dimension of the crystallites, (lattice planes)

D_{hkl} = the size of the crystallite

k = the Scherrer constant (0.84 or 0.9)

λ = the wavelength of the x-ray diffraction (0.154056 nm)

θ = the Bragg angle (reflection angle) for the crystal planes (hkl) (He, *et al.*, 2008)

Isolation of Pure WSCA and SDCA compounds from prepared crude WSCA-1 and SDCA-1 by Column Chromatography

The selected wheat straw and sawdust cellulose acetates **(WSCA-1 and SDCA-1)** obtained by acetylation with 1 h sonication had been purified by isolation with column chromatography for further investigation. (Figure 3) The results are shown in Table 1.

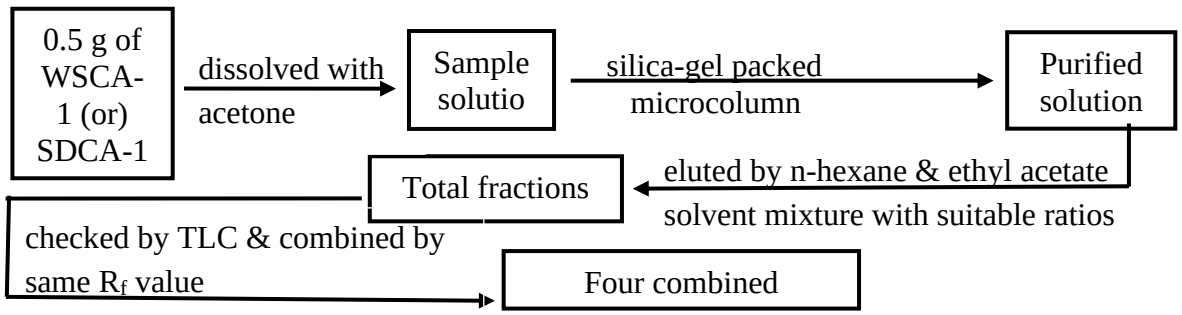

Figure 3. Flow diagram for isolation of pure WSCA and SDCA compounds from prepared crude cellulose acetates by column chromatography

Table 1. Combination of Fractions with Same R_f Values Checked by TLC (Thin Layer Chromatographic) Plates

Sample	Combining fractions	R_f values	Fraction with same R_f values	Sample	Combining fractions	R_f values	Fraction with same R_f values
WSCA-1	2 to 10	0.86	I	SDCA-1	3 to 8	0.86	I
	11 to 14	0.82	II		10 to 16	0.82	II
	17 to 29	0.62	III		19 to 27	0.62	III
	33 to 47	0.55	IV		30 to 38	0.55	IV

The resultant fractions of pure WSCA-1 and SDCA-1 compounds were analyzed by NMR spectroscopy at the Department Centre of Ningxia Organic Synthesis and Engineering Technology, Institute of Ningxia Academy of Agriculture and Forestry Sciences, Yinchuan, Ningxia, China. The resultant NMR spectra had been assigned and characterized by ^{1}H and ^{13}C NMR to determine the degree of substitution of acetyl groups on the prepared wheat straw and sawdust cellulose acetates.

Results and Discussions

Preparation of Cellulose

The celluloses were prepared from wheat straw and sawdust powders by dewaxing process with (2:1 v/v) toluene/ethanol mixture and by pulping process for 9-h refluxing with 15% NaOH. The yield percentages of dewaxed powder and cellulose in each process are shown in Tables 2 and 3.

Table 2. Yield (%) of Dewaxed Wheat Straw and Sawdust Powders by Extraction with (2:1 v/v) Toluene/Ethanol Mixture

No.	Type of sample powder	Weight of powder (g) (Before dewaxing)	Weight of powder (g) (After dewaxing)	Yield (%) of Dewaxed powder	Yield (%) of Pectin
1.	Wheat straw	100.00	96.04	**96.04**	**3.96**
2.	Sawdust	100.00	98.36	**98.36**	**1.64**

From the results of dewaxing process after removal of pectin, there is a higher composition of pectin (3.96%) in wheat straw powder which is one of the main constituents of plant than that (1.64%) in sawdust powder.

Table 3. Yield (%) of Wheat Straw and Sawdust Celluloses after Refluxing with 15% NaOH

No.	Type of sample powder	Weight of powder (g) (Before refluxing)	Weight of powder (g) (After refluxing)	Yield (%) of cellulose
1.	Wheat straw	10.00	3.43	**34.30**
2.	Sawdust	10.00	5.87	**58.70**

After removal of lignin**,** the wheat straw powder was found to contain 34.30 % cellulose and sawdust powder contained 58.70 % cellulose.

Preparation of Cellulose Acetate

Cellulose acetates were prepared by acetylation with various time limit sonication processes. The results are shown in Table 4.

Table 4. Yield (%) of (WSCA-1, -2, -3 & -4) and (SDCA-1, -2, -3 & -4) by Acetylation with 1, 2, 3 & 4 h Sonication Processes

No.	Types of CA	Weight of Cellulose (g) (before acetylation)	Weight of Cellulose Acetate (g) (after acetylation)	Yield (%) of cellulose acetate
1.	WSCA-1	1.0000	0.5324	**53.24**
2.	WSCA-2	1.0000	0.4948	49.48
3.	WSCA-3	1.0000	0.4865	48.65
4.	WSCA-4	1.0000	0.4588	45.88
1.	SDCA-1	1.0000	0.5761	**57.61**
2.	SDCA-2	1.0000	0.5527	55.27
3.	SDCA-3	1.0000	0.5443	54.43
4.	SDCA-4	1.0000	0.5298	52.98

The yield percents of 53.24% of WSCA-1 and 57.61% of SDCA-1 were obtained under the optimum condition (acetylation with acetic acid-acetic anhydride-toluene by 1-h sonication which gives the highest yield percent and higher degree of acetylation). Then, pure cellulose acetate compounds were separated by column chromatography. The fractions of pure WSCA-1 and SDCA-1 compounds had been isolated by n-hexane-ethyl acetate solvent system and were analyzed by ^{1}H and ^{13}C NMR spectroscopy.

Degree of Substitution of WSCA-1, -2, -3 &-4 and SDCA-1, -2, -3 & -4 by Acid-Base Titration

The prepared WSCAs and SDCAs were identified by the degree of substitution of acetyl groups in the prepared cellulose acetates. The results are shown in Table 5.

Table 5. Degree of Substitution of WSCA-1, -2, -3 & -4 and SDCA-1, -2, -3 & -4 by Acid-Base Titration

Types of CA sample	Weight of sample (mg)	Vol. of NaOH added, V_i(mL)	Vol. of NaOH Spent, V_t(mL)	Conc. of NaOH (μ_b)(M)	Vol. of HCl added (V_a)(mL)	Conc. of HCl (μ_a)(M)	AG (%)	Degree of substitution
WSCA-1	100.00	5.00	9.20	0.25	10.00	0.25	44.15	**3.04**
WSCA-2	100.00	5.00	8.80	0.25	10.00	0.25	40.85	2.56
WSCA-3	100.00	5.00	8.60	0.25	10.00	0.25	38.70	2.34
WSCA-4	100.00	5.00	8.40	0.25	10.00	0.25	36.55	2.14
SDCA-1	100.00	5.00	9.00	0.25	10.00	0.25	36.55	**2.79**
SDCA-2	100.00	5.00	7.90	0.25	10.00	0.25	26.90	1.69
SDCA-3	100.00	5.00	7.60	0.25	10.00	0.25	27.95	1.76
SDCA-4	100.00	5.00	7.20	0.25	10.00	0.25	23.65	1.45

From the results of titration, three acetyl groups substituted in anhydroglucose unit (AGU) of WSCA-1(3.04) and SDCA-1(2.79) compounds were calculated. So, these compounds could be expected to be **triacetate** and the other acetates could be assumed to be diacetates.

Degree of substitution of WSCA-1, -2, -3 & -4 and SDCA-1, -2, -3 & -4 by FTIR Spectroscopy

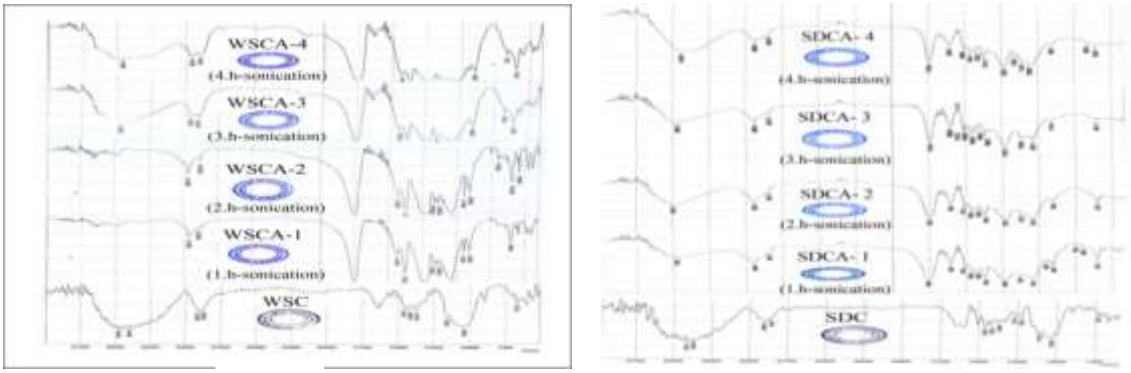

(a) **(b)**

Figures 4 (a) FTIR spectra of WSC and WSCA-1, 2, 3 & 4

(b) FTIR spectra of SDC and SDCA-1, 2, 3 & 4

According to the above Figures 4(a) and (b), there are no OH- stretching bands in WSCA-1. But all SDCA spectra show OH- stretching bands. The intensity of OH- stretching band were decreased gradually in the order of SDCA-1 > SDCA-2 > SDCA-3 > SDCA-4. So, acetylation with 1 h sonication seems to occur complete acetylation. Hence, the optimum time-limit is 1 h sonication. From these FTIR spectra, the peak areas of OH-peaks and the peak areas of C=O peaks had been calculated and the degree of substitutions of corresponding CAs had been calculated based on the values of peak areas according to Kelly., *et al* (1989).

Table 6. The Degree of Substitutions of Prepared WSCA-1, 2, 3 & 4 and SDCA-1, 2, 3 & 4 by 1, 2, 3 & 4 h Sonication Processes

No.	Types of sample	$A_{C=O}$	A_{OH}	Degree of Substitution	No.	Types of sample	$A_{C=O}$	A_{OH}	Degree of Substitution
1.	WSCA-1	14400	4800	**3.00**	1.	SDCA-1	16700	5600	**2.98**
2.	WSCA-2	14250	4875	2.92	2.	SDCA-2	19000	9800	1.94
3.	WSCA-3	17500	9625	1.82	3.	SDCA-3	22000	13700	1.61
4.	WSCA-4	15000	9000	1.67	4.	SDCA-4	17100	11250	1.52

$A_{C=O}$ = peak area of carbonyl groups in ester, A_{OH} = peak area of OH groups

According to Table 6, the degree of substitution, 3.00 indicates that WSCA-1 would be triacetate and those of the others indicate that WSCA-2, -3, -4 were assumed to be diacetates. Then, the degree of substitution, 2.98 indicates that SDCA-1 would be triacetate and those of the others indicate that SDCA-2, -3, -4 were assumed to be diacetates.

Crystallinity Indices and Average Crystallite Sizes of Prepared WSC & WSCA-1.2, 3, &4, and SDC & SDCA-1, 2, 3& 4 by XRD

The following XRD diffractograms show the isolated WSC, SDC by alkaline hydrolysis (refluxed with % NaOH for 9-hours), (WSCA-1, 2, 3 & 4) and (SDCA-1, 2, 3 & 4) acetylated by 1, 2, 3 & 4 h sonication (Figures 5 and 6)**.**

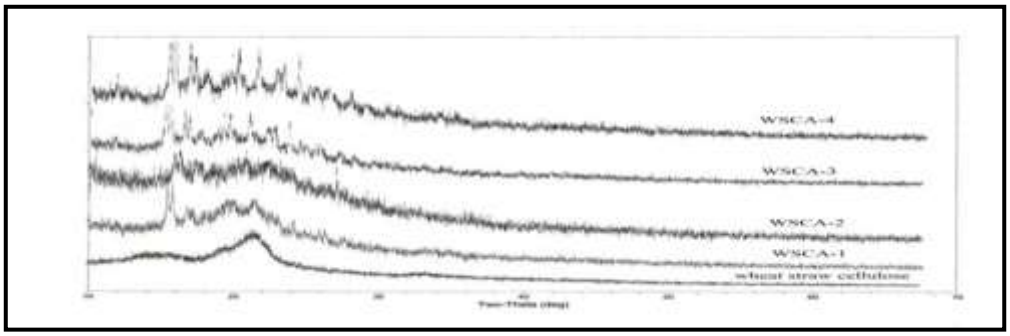

Figure 5. X-ray diffractograms of WSC and WSCA -1, 2, 3, and 4

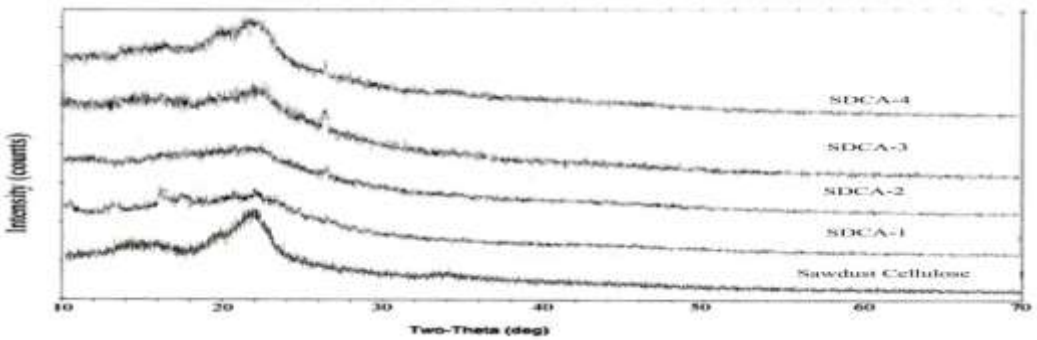

Figure 6. X-ray diffractograms of SDC, SDCA-1, 2, 3, and 4

In X-ray diffractogram of WSC, a sharp diffraction peaks at 17°.18°, 20°, and 21°(2θ) in WSC and SDC indicate the presence of cellulose. Diffractogram shows lower peak intensities at 20°(2θ) in WSCA-1, 2, 3 & 4 and at 17°, 18° (2θ) in SDCA-1, 2, 3 & 4 whereas sharp peaks at 17°, 18° (2θ) and broader peaks at 20°(2θ) in WSCA-1, 2, 3 & 4 and lower and broader peak intensities at 17°, 18° (2θ) in SDCA-1, 2, 3 & 4. The sharp peaks observed are due to their crystalline nature. The lower peak intensities indicate that the complete removal of non-cellulose due to alkaline hydrolysis and acetylation occur (Bledzki *et al.*, 1999). The crystallinity index of WSC and SDC was only one value, 0.65. The crystallinity indices decrease gradually from WSCA-1, 2, 3, & 4 and SDCA-1, 2, 3, & 4 but the particle sizes increase, in WSCA-1.2.3 & 4 and in SDCA-1, 2, 3, & 4 which were calculated by Debye Scherrer equation from the data of diffraction peaks (Table 7). The higher crystallinity indices indicate the greater elimination of both lignin and hemicelluloses which are amorphous substances (Fu and Lucia, 2003). So, it could be assumed that pure WSCA-1 and SDCA-1 were assumed to be triacetates which were completely substituted by three hydroxyl groups of cellulose monomers with three acetyl groups.

Table 7. Crystallinity Indices and Average Crystallite Sizes of Prepared WSC, WSCA-1, 2, 3 & 4 and SDC, SDCA-1, 2, 3 & 4

No.	Types of sample	I_{max}	I_{min}	I_c	Average crystallite sizes (nm)
1	WS Cellulose	21.971	14.370	**0.65**	**13.94**
2.	WSCA-1	21.682	17.441	0.80	21.41
3.	WSCA-2	21.472	17.556	0.80	21.63
4.	WSCA-3	22.770	17.420	0.77	26.26
5.	WSCA-4	22.941	17.501	0.76	29.12
6.	SD Cellulose	21.978	14.287	**0.65**	**21.42**
7.	SDCA-1	22.322	17.347	**0.78**	18.85
8.	SDCA-2	22.382	17.230	0.77	22.06
9.	SDCA-3	22.681	17.420	0.76	22.67
10.	SDCA-4	22.683	17.085	0.75	23.32

The Identification of WSCA-1 and SDCA-1 by NMR Spectroscopy with the Calculation of the Degree of Substitution

The following figures 7 and 8 indicates the ^{1}H NMR spectra of WSCA-1 and SDCA-1.

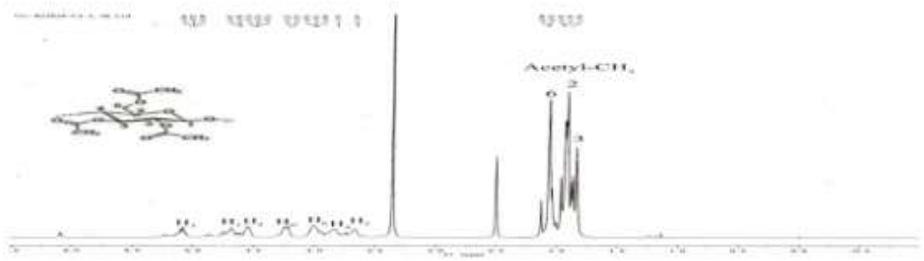

Figure 7. ^{1}H NMR spectrum of wheat straw cellulose acetate (WSCA-1)

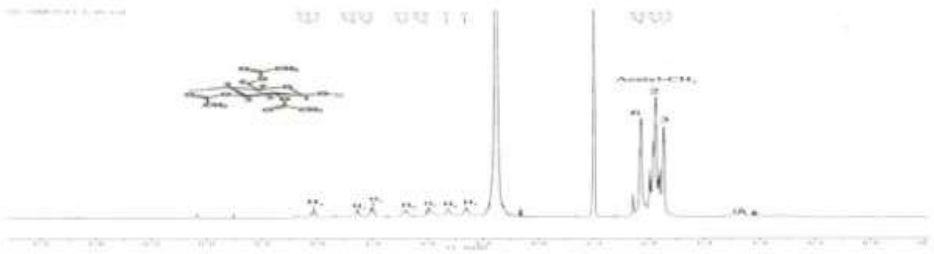

Figure 8. ^{1}H NMR spectrum of sawdust cellulose acetate (SDCA-1)

The following Tables 8 and 9 show ^{1}H NMR spectral data for WSCA-1 and SDCA-1.

Table 8. Chemical Shifts of ^{1}H NMR Signals for AGU Protons of WSCA-1 and SDCA-1 Compounds

Signals of AGU protons	Chemical shifts of WSCA-1 δ (ppm)	Chemical shifts of SDCA-1 δ (ppm)	Reference chemical shift * (δ) values
H-1	4.68	4.68	**4.70**
H-2	4.55	4.54	**4.61**
H-3	5.09	5.06	**4.97**
H-4	3.84	3.83	**3.72**
H-5	3.69	3.67	**3.68**
H-6	4.24	4.24	**4.30**
H-6′	4.00	4.02	**4.04**

AGU = Anhydroglucose unit (monomer of cellulose acetate)
***** Hiroyuki. *et al*., (2015)

Table 9. Chemical Shifts of ^{1}H NMR Signals for Acetyl Methyl Protons of C-6, C-2, C-3 of AGU of WSCA-1 and SDCA-1

Type of cellulose acetate	δ (ppm) of Acetyl-CH_3 protons		
	Me-6	**Me.2**	**Me-3**
WSCA-1	1.96	1.95	1.96
SDCA-1	1.91	1.86	1.89

Typical resonance characteristic of CH_3 groups at 2.2 to 1.5 ppm was reported by Hiroyuki *et al*., (2015). According to the Tables (8) and (9), ^{1}H NMR spectrum showed the peaks for 6 acetyl methyl protons at C-6 of AGU unit of WSCA and SDCA had the chemical shift values of 1.96 δ (ppm) and 1.91 δ (ppm), at C-2 had 1.95 δ(ppm) and 1.86 δ (ppm), at C-3 had 1.96 δ (ppm) and 1.89 δ (ppm). The signals for AGU protons are found in the range from 3.66 to 5.09 δ (ppm). These NMR signals confirm that the prepared WSCA-1 and SDCA compounds constitute the existence of acetyl methyl protons at carbon no. 6, 2 and 3 of AGU and that of each single proton on the AGU ring carbons.

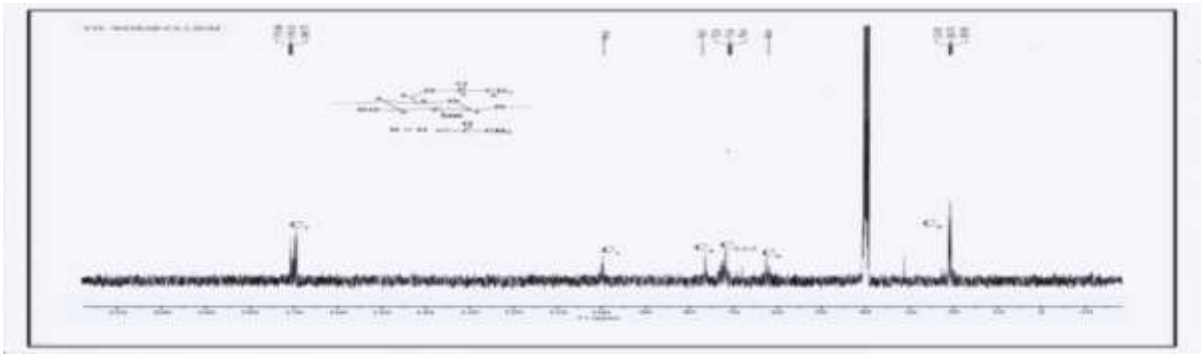

Figure 9 ^{13}C NMR spectrum of wheat straw cellulose acetate (WSCA-1)

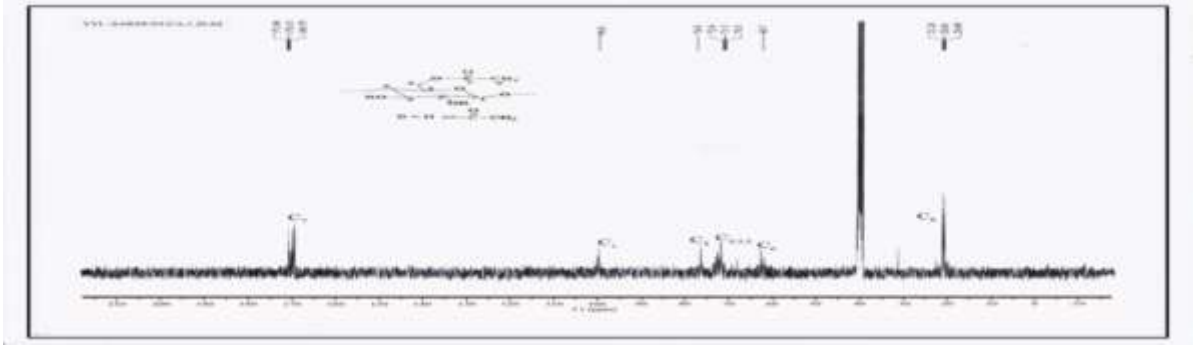

Figure 10. ^{13}C NMR spectrum of sawdust cellulose acetate (SDCA-1)

The above ^{1}H-decoupled ^{13}C NMR spectra indicate that the peaks for carbon number (1) to (5) on the ring carbons and carbon number (6) outside of the AGU ring compound and resonates at the respective chemical shifts. The complete acetylation occurs on carbon numbers 6, 2, and 3 by indicating the chemical shifts of about 21.0, 20.7, and 20.5 δ(ppm) for acetyl methyl carbons and also about 169.4, 170.1, and 171.1 δ(ppm) for acetyl carbonyl carbons at carbon number 6, 2 and 3 in WSCA-1 and the chemical shifts of about 21.2, 20.8, and 20.1 δ(ppm) for acetyl methyl carbons and 169.8, 170.1 and 171.1 δ(ppm) for acetyl carbonyl carbons on 6, 2, and 3 ring carbon atoms of AGU in SDCA-1 (Figures 9 and 10) The following Table 10 shows the signals for carbons in anhydroglucose unit and acetyl carbonyl carbons for each ^{13}C NMR spectrum in comparison with reference data.

Table 10. Chemical Shifts of ^{13}C NMR Signals for Ring Carbons with Their Substitutions of Acetyl Carbonyl Carbons (C-6, C-2, C-3) of AGU of WSCA-1 and SDCA-1

Signals of AGU carbons	Chemical shifts of WSCA-1, δ (ppm)	Chemical shifts of SDCA-1, δ (ppm)	Reference chemical shift*, (δ) ppm
C-1	99.8	99.9	**98.9**
C-2	70.4	70.3	**71.1**
C-3	71.8	71.5	**71.8**
C-4	76.5	76.8	**75.2**
C-5	72.8	72.6	**72.0**
C-6	60.4	60.7	**61.4**

*Hiroyuki et al., (2015)

Table 11. Chemical Shifts of ^{13}C NMR Signals for Acetyl Methyl Carbons and Carbonyl Carbons (C-6, C-2, C-3) of AGUs of WSCA-1 and SDCA-1

	Substituted position	Chemical shifts of acetyl methyl carbons δ (ppm)	Chemical shifts of carbonyl carbons δ (ppm)
WSCA-1	**C-6**	**21.0**	**169.4**
	C-2	**20.7**	**170.1**
	C-3	**20.5**	**171.0**
SDCA-1	**C-6**	**21.2**	**169.8**
	C-2	**20.8**	**170.1**
	C-3	**20.1**	**171.1**

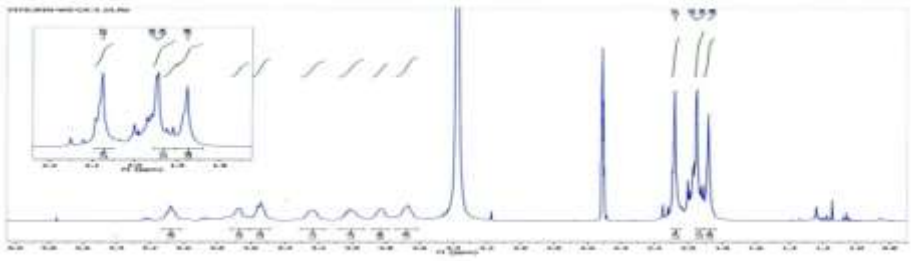

Figure 11 ^{1}H NMR spectrum showing the intensities of proton peaks of WSCA-1

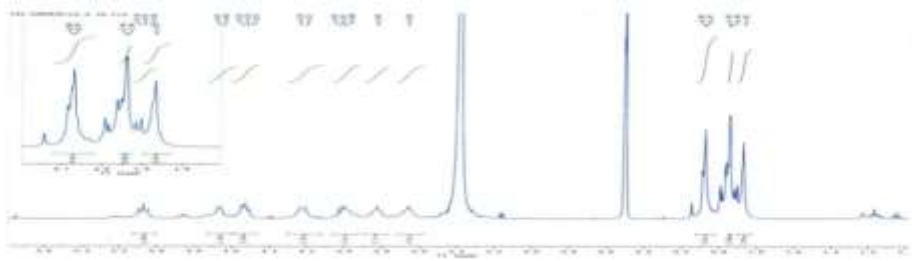

Figure 12. ^{1}H NMR spectrum showing the intensities of proton peaks of SDCA-1

In ^{1}H NMR spectrum of WSCA-1, the intensities for C-6, C-2, C-3 acetyl methyl protons were 2.74, 3.17, 2.66 and 3.41, 2.26, 2.45 in SDCA-1 spectrum. These had been confirmed that three protons of acetyl groups were attached to each acetyl methyl carbons. (Figures 11 and 12). The intensities for the ring protons were 1.38 attached at C-5, 0.96 at C-4, 1.26 at C-2, 1.01 at C-1 and 1.00 at C-3, 1.24 at C-6, 1.11 at C$^{/}$-6, outside of the AGU ring in WSCA-1. In SDCA-1, the intensities for the ring protons were 1.21 attached at C-5, 1.11 at C-4, 1.24 at C-2, 1.16 at C-1, 1.00 at C-3, and 1.31 at C-6, 1.27 at C$^{/}$-6, outside of the AGU ring. These data had been concluded that only one proton attached to each corresponding carbon in each cellulose acetate.

According to Cheng *et al.* (2010), the degree of substitution (DS) was calculated from the spectral intensities. The area of acetyl proton can be calculated by two-sides region between 1.9 to 2.2 ppm corresponds to three acetyl protons, the area of (AGU) ring protons can be calculated from two-sides region between 3.6 to 5.2 ppm corresponds to the seven (AGU) protons. The ratio of 1/3 of area of the acetyl protons to 1/7 of the area of the (AGU) protons gave the degree of substitution (DS). From the above ^{1}H NMR spectral data, the DS value of WSCA-1and SDCA-1 are listed in the following Table 12.

Table 12. Degree of Substitution Values for WSCA-1 and SDCA-1

Types of CA	Area of acetyl protons (cm^2)	1/3 of Area of Acetyl protons (cm^2)	Area of AGU ring protons (cm^2)	1/7 of Area of AGU ring protons (cm^2)	Degree of substitution (DS)
WSCA-1	9.46	3.16	7.41	1.06	2.98
SDCA-1	8.58	2.86	6.95	0.99	2.88

According to the values of DS obtained from calculations of titration data, FTIR, XRD and ^{1} H NMR and ^{13}C NMR spectral data, the prepared WSCA-1 and SDCA-1 were assumed to be triacetates.

Conclusion

In this research, the cellulose acetates were prepared according to the optimized acetylation method which provides the highest substitution of acetyl groups and the highest yield percent by four different time-limit sonication processes. Then the chemical and spectral analyses of prepared WSCAs and SDCAs were performed by acid-base titration, FT IR, XRD and NMR for the determination of the degree of substitution. From the titrimetric data, the optimized WSCA-1 has the DS values 3.04 and SDCA-1 has 2.79. So, these compounds can be regarded as cellulose triacetates. From the calculations by FT IR spectral data the value of DS for WSCA-1 is 3.00 and that for SDCA-1 is 2.98 that have confirmed that the prepared compounds are triacetates. Moreover, XRD informs that increasing crystallinity indices of acetates indicate the conversion of amorphous to crystalline nature and celluloses are completely converted to cellulose acetates. Then, the average crystallite sizes of these compounds are in the range of nanoparticle-size which are applied in the fabrication of cellulose acetate membrane. These WSCAs and SDCAs had been further identified by NMR spectroscopy. According to the ^{1}H NMR and ^{13}C NMR spectral data and the intensities of ^{1}H NMR spectral data, and the calculation of the values of DS (2.98. 2.88), the prepared WSCA and SDCA were found to be triacetates. In the sense of this research, agriculture byproducts and wastes can be made as the effective and valuable acetylated cellulose products for social needs. This paper reports the interested area for the fabrication of low-cost cellulose acetate based-products, cellulose acetate membrane which would be applied in the separation of hemoglobin variants by electrophoresis as a separating sheet or in wastewater treatment as the filtration membrane.

Acknowledgements

The authors would like to express their profound gratitude to the Ministry of Education, Department of Higher Education, Yangon, for provision of opportunity to do this research and Myanmar Academy of Arts and Science for allowing to present this paper.

References

Badejo O., N. A. Aderanti, A. A. Babarinde, and A. Ibikunle. (2018). "The Functional Properties of Cellulose of Wheat Offal (*Triticum aestivum*) on Acetylation", *International Journal of Scientific & Engineering Research,* vol. 9 (3), pp- 338-346

Bledzki, A. K, and J. Gassan. (1999). "Composites Reinforced with Cellulose Based Fibers". *Progress Polymer Science*, vol. 24, pp. 221-274.

Cheng, H., N, K. M. Dowd, G.W. Selling, and A. Biswas. (2010). "Synthesis of Cellulose Acetate from Cotton Byproducts," *Journal of Carbohydrate Polymers*, vol. 80, pp. 449- 452

Crawford, R. L. (1981). "Lignin Biodegradation and Transformation" New York: John Wiley and Sons. ISBN 0-471-05743-6.

Edgar, K. J., C. M. Buchanan, J. S. Debenhanm, P. A. Rudquist, B. D Seiler, M.C., Shelton, and D,Tindall. (2001). "Advance in Cellulose Ester Performance and Application". *Progress in Polymer Science*, vol. 26 (9), pp. 1605-1688

Fu, S., and L.A. Lucia. (2003). "Investigation of the Chemical Basis for Inefficient Lignin Removal in Softwood Kraft during Oxygen Delignification," *Industrial & Engineering Chemistry Research*, vol. 42, pp. 4269-4276

He, J., S., Cui, and S.Y. Wang. (2008). "Preparation and Crystalline Analysis of High-Grade Bamboo Dissolving Pulp for Cellulose Acetate," *Journal of Applied Polymer Science*, vol.107, pp.1029-1038

Hiroyuki, K., H. Hisaho, and S. Yuuichi. (2015). "NMR Characterization of Cellulose Acetate: Chemical Shift Assignments, Substituent Effects, and Chemical Shift Additivity" *Carbohydrate Polymers*, vol. 118, pp. 91-100

Kelly, S. S., A. C. Puleo, and D. R. Paul. (1989). "The Effect of Degree of Acetylation on Gas Sorption and Transport Behavior in Cellulose Acetate." *Journal of Marine Science*. vol. 47, pp. 301-332

Lindsey, B. (2010). "Eastman to Boost Cellulose Triacetate Capacity at King Sport" *HIS Chemical week* November 1, 2010.

Morgan, E. (2013). "Frame Material". All About Vision. Com. Retrieved 2013-08-07.

Regiani, A. M., E. Frollini, G. A. Marson, G. M. Arantes, and O. A. Elseoud. (1999). "Aspects of Acylation of Cellulose under Homogeneous Solution Conditions," *Journal of Polymer Science, Part A*: *Polymer Chemistry* vol. **37**, pp. 1357-1363

Updegraff, D.M. (1969) "Semi-micro-Determination of Cellulose in Biological Materials". *Analytical Biochemistry*. vol.32 (3): pp. 420-424.

Yi Yi Lwin, Thida Kyaw, and Yi Yi Myint. (2020). "Determination on the Optimum Condition for the Preparation of Cellulose Acetates from Maize Straw Powder, Wheat Straw Powder and Sawdust Powder". *Journal of Myanmar Academy of Arts and Science.* vol. 18, (1A), July, pp. 341-348.

Yi Yi Lwin. (2020). *Investigation on the Preparation, Identification and Application of Nanocellulose Acetates from Maize Straw Powder, Wheat Straw Powder and Sawdust (Asia Woody Plant) Powder*, PhD Dissertation, Chemistry Department, Mandalay University.

IDENTIFICATION OF APIGENIN AND LUTEOLIN ISOLATED FROM THE AERIAL PARTS OF *BACOPA MONNIERI* (L.) WETTST *IN VITRO* EVALUATION OF *α*-AMYLASE AND *α*-GLUCOSIDASE INHIBITION ACTIVITY

Aye Aye Thant[1], Yi Yi Win[2], Myint Myint Khine[3], Ni Ni Than[4]

Abstract

The present research deals with the analysis to isolate organic compounds and examine antidiabetic activity from the aerial parts of the Bacopa monnieri (Byone-hmwe) plant collected from the Twantay Township, Yangon Region. By column and thin layer chromatography, apigenin (AAT-2) and luteolin (AAT-3) were isolated from the active ethyl acetate fraction and identified by using UV, FT IR, 1HNMR, and NMR spectroscopic methods. The spectrophotometric method was used to determine the antidiabetic activity of a drug using metformin, an oral hypoglycemic agent, as a positive control for the inhibition effect on α-amylase and α-glucosidase enzymes. The α-amylase inhibitory effect (IC_{50}= 54.09 μg/mL,78.14 μg/mL) and *α*-glucosidase inhibitory effect (IC_{50} = 62 μg/mL, 91.66 μg/mL) were observed in ethanol and watery extracts. Furthermore, apigenin and luteolin inhibited α-amylase (IC_{50}= 1.049 μg/mL, 0.75 μg/mL) and α-glucosidase (IC_{50} = 0.558 μg/mL, 0.507 μg/mL), which was comparable with the standard drug metformin (IC_{50} = 0.497 μg/mL). The percentage of enzyme inhibition of isolated luteolin was nearly the same as that of standard metformin.

Keywords: *Bacopa monnieri*, *α*-amylase inhibition, *α*-glucosidase inhibition, apigenin, luteolin

Introduction

Bacopa monnieri, an important medicinal plant of the family Scrophulariaceae is used in the traditional medicine to treat various nervous disorders and to promote memory and intellect. Some important medicinal uses of the plant *B. monnieri* are the treatment of different diseases and its traditional formulation (Lal and Baraik, 2019). Flavonoids are a major group of polyphenolic compounds that have been reported to possess inhibitory activity against α-glucosidase (Williams, 2013). In relation to their structure, the number and position of their hydroxyl groups in the molecule are determining factors for enzyme inhibition. The inhibitory activity increased considerably with an increase in the number of hydroxyl groups on the B ring. Animal experiments revealed that ethanol extracts of *B. monnieri* have a positive effect on haemoglobin glycosylation *in vivo*, anti-oxidant potential, and *in vitro* peripheral glucose utilization. Bacoside, a triterpenoid isolated from the plant extract, has been found to increase glycogen content in the liver of diabetic rats and peripheral glucose utilization in the diaphragm (Ghosh *et al*., 2011). The current study aims to isolate and identify the two flavones, apigenin (AAT-2) and luteolin (AAT-3), from *B. monnieri's* aerial parts and to determine their antidiabetic activity.

Botanical Aspect of *Bacopa monnieri* (L.) Wettst (Byone-hmwe)

Family: Plantaginaceae
Botanical name: *Bacopa monnieri* (L.) Wettst.
Myanmar name: Byone-hmwe
Part used: the aerial parts

Figure 1. *Bacopa monnieri*

[1] Department of Chemistry, University of Yangon,
[2] Department of Chemistry, Hpan-an University
[3] Myingyan University
[4] Department of Chemistry, University of Yangon

Materials and Methods

Plant Material

The sample was collected from Twantay Township, Yangon Region, in July 2019 and identified as *Bacopa monnieri* (L) Wettest, by the authorized botanist at the Department of Botany, University of Yangon. The sample was dried under the shade for a week, cut into very small pieces, and then ground into a purely fine powder using an electric grinder. The powdered sample was stored in airtight containers.

Extraction and Isolation of Pure Compounds (AAT-2 and AAT-3)

Dried powder (1000 g) of aerial parts of *B. monnieri* was extracted with 95% ethanol. After evaporation of the solvent, the resulting crude extract was successively partitioned between organic solvents (petroleum ether, ethyl acetate) and water. The ethyl acetate crude extract (11 g) was chromatographically separated on silica gel 60 (70-230 mesh, Merck) with a petroleum ether and ethyl acetate mixture used as an eluent, varying solvent ratios from non-polar to polar. Each and every fraction was checked with TLC and a UV detector. The fractions with the same R_f values were combined, and six combined fractions were obtained. Among them, the combined fraction (V) was rechromatographed by using the same adsorbent and eluent as mentioned in the previous column. Pure pale-yellow and yellow crystals were obtained and checked on TLC for purity. It gave one spot on TLC (R_f = 0.5) and (R_f = 0.4) with pet-ether: ethyl acetate (1:1) (v/v). The weight of the isolated compounds (AAT-2) was 50 mg and (AAT-3) was 30 mg, and their yield percents were found to be 1.25% and 0.75% based on the ethyl acetate crude extract, respectively. The FT IR and UV-vis spectra were measured at the Department of Chemistry, University of Yangon and ^{1}H NMR and ^{13}C NMR were measured at the Division of Natural Product Chemistry, Institute of Natural Medicine, and University of Toyama, Japan.

Screening of *In vitro* Antidiabetic Activity

In diabetes, the body cannot produce enough insulin or uses insulin, and it is diagnosed by observing raised levels of glucose in the blood (Khadayat et al., 2020). One of the therapeutic approaches to controlling postprandial hyperglycemia in T2DM is to inhibit the digestion of dietary carbohydrates. Pancreatic α-amylase (E.C.3.2.1.1) is a key enzyme that breaks down dietary carbohydrates such as starch into simple monosaccharides in the digestive system. These are further degraded by α-glucosidases to glucose, which, on absorption, enters the bloodstream. Therefore, inhibiting the α-amylase and α-glucosidase enzymes, for example, can suppress carbohydrate digestion, delay glucose uptake, and, as a result, lower blood sugar levels.

Determination of *α*-Amylase Inhibition Activity

The α-amylase enzyme inhibition potential was assessed using a 3, 5-dinitrosalicylic acid (DNSA) assay (Kajaria *et al*., 2013). The reaction mixture contained 1mL of phosphate buffer (0.04 M, pH = 6.9), 1 mL of α–amylase: 1 U/mL, and 1 mL of varying concentrations of ethanol and watery extracts. Apigenin (AAT-2) and luteolin (AAT-3) were preincubated at 37 ℃ for 20 min. Next, 0.4 mL of 1% soluble starch (0.004 M phosphate buffer pH 6.9) was added as a substrate and incubated at 37℃ for 30 min; 0.6 mL of the 3, 5-dinitrosalicylic acid (DNS) reagent was then added and boiled for 20 min. The absorbance of the resulting mixture was assessed at 540 nm using a UV spectrophotometer. Metformin, a well-known α-amylase inhibitor, is an excellence standard in a wide range of concentrations. Samples without plant extracts were used controls, as the blank solution (without amylase) and each test was carried out in triplicate. The outcome was expressed as percentage inhibition, which was calculated using the following equation.

$$\% \text{ Inhibition} = \frac{C-(A-B)}{C} \times 100$$

Where A= absorbance of the sample

B = absorbance of blank (without amylase)

C = absorbance of the control (without test sample)

Standard deviation (SD) and 50% inhibition concentration (IC_{50}) values were calculated by the linear regression programme.

Determination of *In vitro α*-Glucosidase Inhibitory Assay

The effect of the plant extracts on *α*-glucosidase activity was determined according to the method described by Kim *et al*., 2011. The substrate solution, *p*-nitrophenyl glucopyranoside (PNPG), was prepared in 0.04 M phosphate buffer, at pH 6.9. 1 mL of *α*-glucosidase (0.5 U/mL) was preincubated at 37 ℃ for 20 min with 1 mL of the ethanol and water extracts and isolated compounds; apigenin (AAT-2) and luteolin (AAT-3). Then 0.5 mL of 0.003 M (PNPG) as a substrate dissolved in 0.04M phosphate buffer (pH 6.9) was added to start the reaction. The reaction mixture was then incubated at 37 ºC for 20 min and stopped by adding 1 mL of 0.1 M Na_2CO_3. The *α*-glucosidase activity was determined by measuring the yellow-coloured *p*-nitrophenol released from PNPG at 405 nm using a UV spectrophotometer. Samples without plant extracts were used as controls and as the blank solutions (without amylase) and each test was carried out in triplicate. The outcome was expressed as percentage inhibition, which was calculated using the following equation.

$$\% \text{ Inhibition} = \frac{C-(A-B)}{C} \quad 100$$

Where, A = absorbance of the sample

B = absorbance of blank (without amylase)

C = absorbance of the control (without test sample)

Standard deviation (SD) and 50% inhibition concentration (IC_{50}) values were calculated by the linear regression programme.

Results and Discussion

The *α*-amylase is found in saliva and pancreatic juice, which hydrolyzes alpha-linked polysaccharides' alpha bonds like in starch and glycogen, resulting in glucose and maltose that can quickly enter the bloodstream. It is the primary amylase type present in humans and other mammals. Inhibition of *α*-amylase delays the digestion process by hampering the breakdown of starch in the intestine and, hence, can be utilized as an effective strategy for regulating hyperglycemic conditions (Oyedemi *et al.*, 2017). The plant extract showed potent inhibition of α-amylase activity. The active components in the extract compete with the substrate for binding to the active site of the enzyme, preventing the breakdown of the oligosaccharide to disaccharides. This demonstrates that the inhibition percentage increases with the concentration of the extract increased. The highest percent of α-amylase inhibition and the lowest IC_{50} value inhibitors of α-glucosidase delay the breakdown of carbohydrates in the small intestine and diminish the postprandial blood glucose excursion in a person suffering from diabetes (Ogunwande *et al*., 2007). The plant extract exhibited potent inhibition of α-glucosidase activity such that the active components in the extract do not compete with the substrate for binding to a separate site on the enzyme to retard the conversion of disaccharides to monosaccharides (Mogale *et al*., 2011).

The present finding reveals that *B. monnieri'*s aerial parts efficiently inhibit the *α*-amylase and α-glucosidase enzymes. The enzyme inhibition activity of ethanol and watery extracts, and isolated compounds; apigenin (AAT-2), and luteolin (AAT-3) was evaluated by a UV spectroscopic method. From the mean absorbance values, the α-amylase and α-glucosidase inhibition of ethanol extract (IC_{50} = 54.09 µg/mL) and (IC_{50} = 62.5µg/mL) had more inhibitory potential than watery extract (IC_{50} = 78.14 µg/mL) and (IC_{50} = 91.66 µg/mL) as shown in Tables 1, and 2, and Figures 2 and 3. In contrast, the isolated compound, luteolin (IC_{50} = 0.558 µg/mL) more effectively inhibited enzyme activity than apigenin (IC_{50}=1.049 µg/mL), respectively (Table 3, Figure 4). In these assay methods, metformin was used as the positive control. In comparison to metformin, luteolin had the highest anti-diabetic activity, followed by ethanol and watery extracts, as well as apigenin (Table 4, Figure 5).

Table 1. IC_{50} Values of *α*-Amylase Inhibitory Activity of Crude Extracts of the Aerial Parts of *B. monnieri*

Samples	**% Inhibition in Different Concentrations (µg/mL)**						**IC_{50} (µg/mL)**
	31.25	**62.5**	**125**	**250**	**500**	**1000**	
Ethanol extract	33.89 ± 0.01	55.93 ± 0.57	62.71 ± 0.42	71.18 ± 0.33	88.13 ± 1.12	94.91 ± 0.98	54.09
Watery extract	27.11± 1.10	44.89 ± 0.02	65.30 ± 0.56	77.55 ± 0.66	83.69 ± 1.40	95.91 ± 0.46	78.14
*Standard metformin	46.93 ± 0.26	63.26 ± 0.02	77.55 ± 0.03	79.59 ± 0.37	85.71 ± 0.48	96.37 ± 1.98	45.31

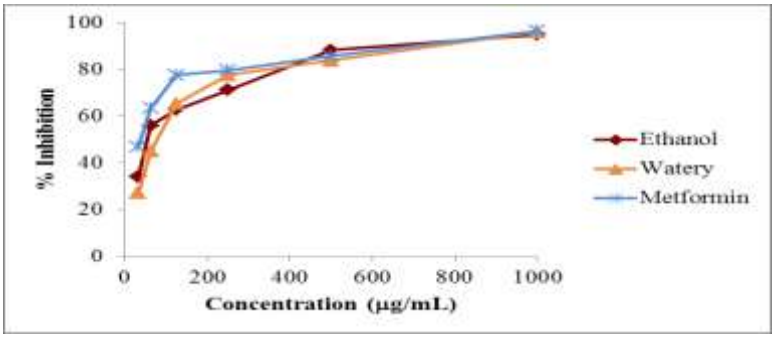

Figure 2. A plot of α-amylase inhibition activity versus concentrations of crude extracts of the aerial parts of *B. monnieri*

Table 2. IC_{50} Values of α-Glucosidase Inhibitory Activity of Crude Extracts of the Aerial Parts of *B. monnieri*

Sample	% Inhibition in Different Concentrations (µg/mL)						IC_{50} (µg/mL)
	31.25	62.5	125	250	500	1000	
Ethanol extract	36.20 ± 1.03	50.00± 0.92	67.24 ± 0.48	75.86 ± 1.11	82.75 ± 1.40	94.82 ± 0.40	62.50
Watery extract	29.31± 0.48	37.93 ± 0.90	63.79 ± 0.25	70.68 ± 1.50	79.31 ± 0.87	89.65 ± 1.21	91.66
*Standard metformin	41..37 ± 0.08	55.17 ± 0.73	62.06 ± 0.21	77.41± 1.07	86.2 ± 1.33	93.1 ± 0.40	50.79

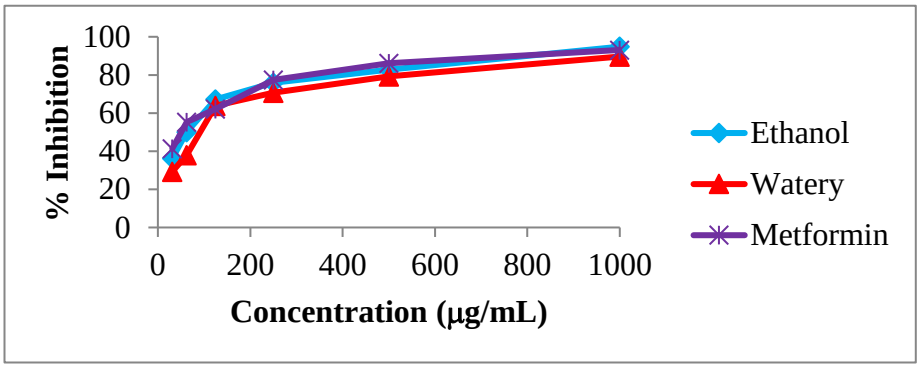

Figure 3. A plot of α-glucosidase inhibition activity versus concentrations of crude extracts of the aerial parts of *B. monnieri*

Table 3. IC_{50} Values of α- Amylase Inhibitory Activity of Isolated Compounds AAT-2 and AAT-3 of the Aerial Parts of *B. monnieri*

Samples	% Inhibition in Different Concentrations (µg/mL)						IC_{50} (µg/mL)
	0.3125	0.625	1.25	2.5	5	10	
AAT-2	24.56± 0.11	36.84± 0.28	52.63± 0.56	63.15± 0.93	80.70± 0.21	92.98± 2.73	1.049
AAT-3	40.35± 0.69	52.67± 0.56	63.15± 0.48	78.94± 0.32	89.47± 0.15	94.73± 1.73	0.558
*Standard metformin	36.59± 1.53	57.89± 0.31	64.91± 0.48	77.19± 0.81	85.96± 0.82	96.49± 0.73	0.497

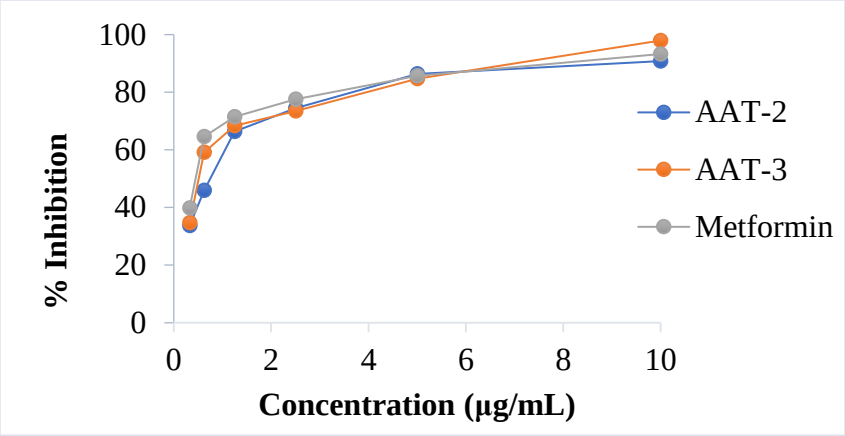

Figure 4. A plot of α-amylase inhibition activity versus concentrations of crude extracts of the aerial parts of *B. monnieri*

Table 4. IC_{50} Values of α-glucosidase Inhibitory Activity of Isolated compounds AAT-2 and AAT-3 of the Aerial Parts of *B. monnieri*

Sample	% Inhibition in Different Concentrations (µg/mL)						IC_{50} (µg/mL)
	0.3125	0.625	1.25	2.5	5	10	
AAT-2	33.67± 1.03	45.91± 0.48	66.32± 0.90	74.48± 0.87	86.33± 1.07	90.81± 1.33	0.750
AAT-3	34.69± 0.92	59.18± 1.01	68.36± 0.87	73.46± 0.48	84.69± 1.41	97.95± 1.11	0.508
*Standard metformin	39.82± 1.21	64.60± 0.73	71.42± 1.02	77.55± 1.41	85.71± 0.25	93.27± 1.50	0.441

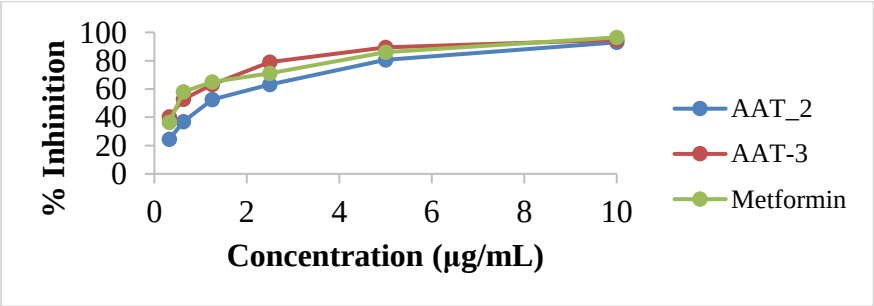

Figure 5. A plot of α-glucosidase inhibition activity versus concentrations of isolated compounds of the aerial parts of *B. monnieri*

Structure Elucidation of Antidiabetic Active Isolated Compound (AAT-2)

The compound AAT-2 was isolated from an ethyl acetate extract of *B. monnieri*. It was obtained as pale-yellow crystals by using PE: EA = 1:1; the R_f value is 0.5. It may be a flavonoid compound because it gave off a red colour when treated with Mg/HCl and a brown colour when reacted with 10% $FeCl_3$.The UV-vis spectra of AAT-2 showed the flavonoid bands II and I in methanol at 268 nm and 336 nm respectively. This absorption band is in agreement with a flavone (band II, 210-280 and band I, 310-350 nm). The UV spectrum in NaOH exhibited a 57 nm

bathochromic shift of the main absorption (band I) with increasing intensity. That indicated the presence of free 4' and 7 hydroxy groups. A 7 nm bathochromic shift of band II in the presence of NaOAc in MeOH also indicated that AAT-2 possessed a 7 hydroxy group and the UV-vis spectrum in $AlCl_3$/HCl produced a 45 nm bathochromic shift of band I, suggesting the presence of 5 hydroxy group. No hypochromic shift was observed in band I of the $AlCl_3$ spectrum, indicating the absence of *ortho*-dihydroxy groups. The UV-vis spectral properties in various shift reagents of AAT-2 were found to be identical to those of the 5, 7, and 4′trihydroxy flavone (Ei Shoubaky *et al.*, 2016).

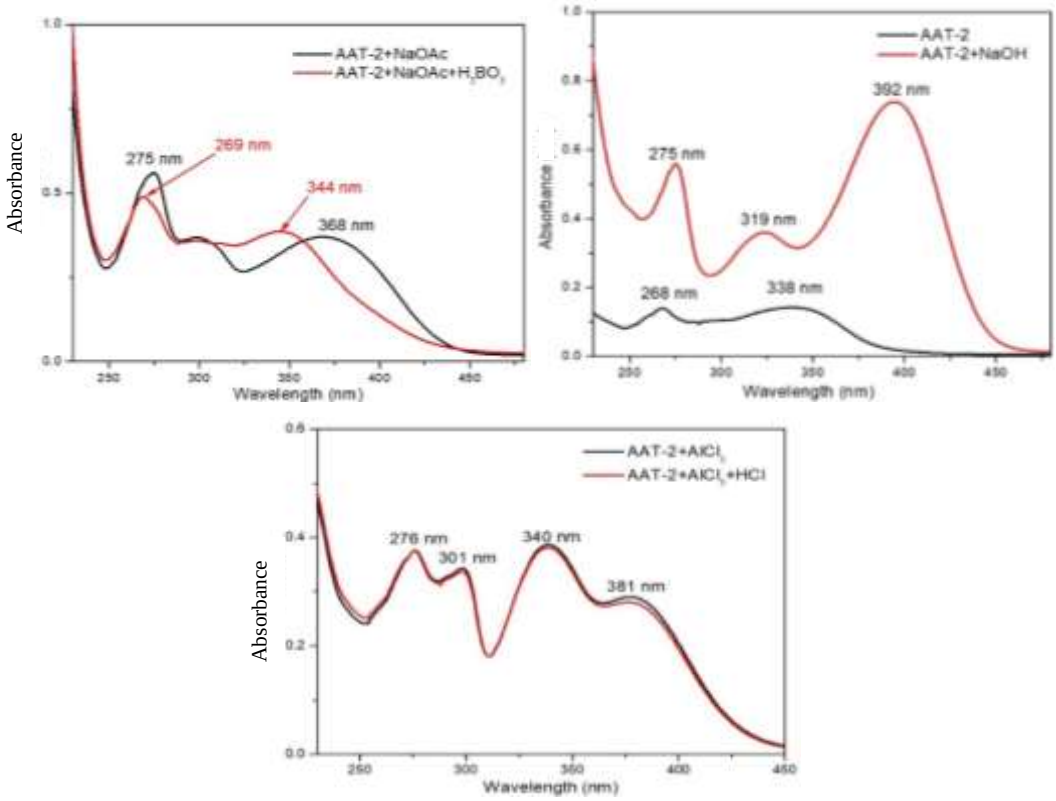

Figure 6. UV spectra of an isolated compound Apigenin (AAT-2) by using shift reagents

In the FT IR spectrum of compound AAT-2, the strong and broad absorption band that appeared at 3274 cm^{-1} indicated the presence of a hydroxyl group. The strong band at 1650 cm^{-1} was due to the C=O stretching vibration of a carbonyl group. The C=C stretching vibration showed at 1604, 1555, and 1495 cm^{-1}. Moreover, asymmetric and symmetric stretching vibration (C-O-C) was described at 1267 cm^{-1} (Figure 7).

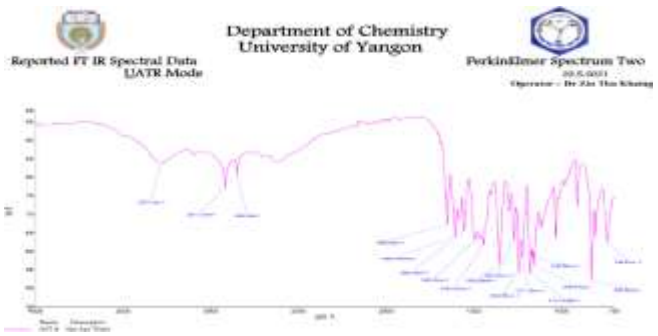

Apigenin (pale yellow crystals)

10% $FeCl_3$

Figure 7. FT IR spectrum of an isolated compound apigenin (AAT-2)

The ^{1}H NMR spectrum of compound AAT-2 (Figure 8) contained 15 protons. The ^{1}H NMR was taken in the deuterated dimethyl sulphoxide, and the proton at positions 2' and 6' due to symmetry appeared as a doublet at 7.091 ppm, and the proton at positions 3' and 5' at 6.091 ppm, upfield due to the neighbouring electron-donating hydroxyl group. The single olefinic proton of the H-3 singlet and two meta-coupled aromatic protons at H-8 and H-6 gave doublet signals at 5.64 and 5.35 ppm. The ^{13}C NMR spectrum indicated the presence of 15 signals, including one carbonyl group, and seven quaternary carbon signals. The ^{13}C NMR spectrum is shown in Figure 8. The carbon signals were observed for seven methine signals at δc 103.2 (C-3), 99.2 (C-6), 94.3 (C-8), 128.8 (C-2' & 6'), 116.3 (C-3' & 5'), and seven quaternary carbon signals at δc 164.1 (C-2), 161.5 (C-5), 164.5 (C-7), 157.7 (C-9), 104.0 (C-10), 121.5 (C-1'), 161.8 (C-4'). One carbonyl signal was also observed at 182.1 (C-4). From the basis of the observed melting point, some physicochemical tests, and all spectral data compared with reported data of apigenin (Kalpana and Rajasekaran 2018), the isolated compound AAT-2 was identified as apigenin ($C_{15}H_{10}O_5$).

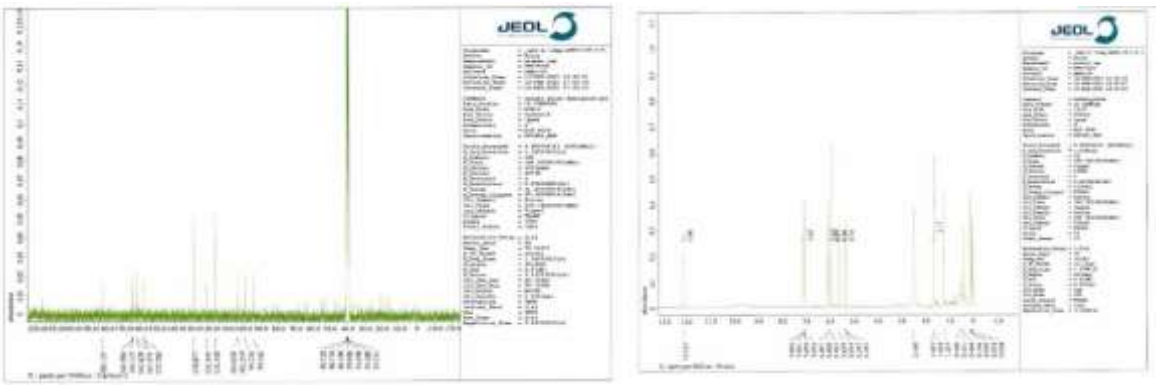

Figure 8. ^{1}H NMR (DMSO-d_6, 400 MHz) and ^{13}C NMR (DMSO-d_6, 100 MHz) spectra of apigenin AAT-2

Compound **AAT-2** (Apigenin): A pale yellow crystal crystallized from pet-ether/EtOAc, (1:1) mp: 345 ℃.; FT IR (ν, cm^{-1}): 3274 (ν_{O-H}), 1650 ($\nu_{C=O}$), 1604,1555,1495 ($\nu_{C=C}$), 1267 (ν_{C-O-C}), 1015 (δoop(C-H)), UV$_{max}$ (MeOH) nm: 268, 338; NaOAc nm: 275,368; NaOAc + H_3BO_3 nm: 269, 344; $AlCl_3$ nm: 276, 340, 381; $AlCl_3$ + HCl nm: 276, 381; NaOH nm: 275,393.^{1}H NMR (400 MHz, DMSO-d_6) δ_H (ppm): 5.94(s, 1H, H-3), 12.1(s,1H, Ar-OH), 5.35 (d, J = 1.6 Hz, 1H, H-6), 5.64 (d, J = 2 H, 1H ,H-8), 7.09 (d, J = 8.4 Hz, 2H, H-2', 6'), 6.09 (d, J = 8.4 Hz, 2H, H-3', 5').

^{13}C NMR (100 MHz, DMSO-d_6) δ_C (ppm): 94.3 (C-8), 99.2 (C-6), 103.2 (C-3), 104 (C-10), 115.9 (C-3' and 5'), 121.5 (C-1'), 128.5 (C-2' and 6'), 157.7 (C-9), 161.5 (C-5), 161.8 (C-4'), 164.1 (C-2), 182.1 (C-4).

Structure Elucidation of Antidiabetic Active Isolated Compound AAT-3

The diabetic active compound AAT-3, (0.75 %) yield was isolated as yellow crystals from ethyl acetate extract of *B. monnieri,* using a solvent system (PE: EA 1:1). The R_f value is 0.4. It may be a flavonoid compound because it gave off a red colour when treated with Mg/HCl and a brown colour when reacted with 10 % $FeCl_3$. The UV-vis spectrum of AAT-3 showed the flavonoid bands II and I in methanol at 254 nm and 351 nm. This absorption band may be a flavone (bands II 210-280 and band I 310-350). The addition of 2M NaOH shifted the band at λ_{max} 351 nm to 404 nm, i.e., a 53 nm shift of band I, suggesting the presence of an OH group at position 4′. On the other hand, the addition of NaOAc shifted the band at λ_{max} 254 nm to 267 nm, i.e., 13 nm shifted from band II, suggesting the presence of a hydroxy group at position 7. The further addition of H_3BO_3 caused a +23 nm shift of band I, relative to the spectrum of AAT-3 in MeOH solution, suggesting the presence of the *o-di*hydroxy group on the B ring. The presence of

$AlCl_3$ showed a bathochromic in the band I of 55 nm (351 nm to 406 nm) which exhibited *o-di*-OH on the B ring (3'-OH and 4'-OH) adjacent to the C=O group. The presence of an OH group in position 5 was exhibited (Figure 9). After the addition of HCl, the UV-vis spectral properties in various shift reagents of AAT-3 were found to be identical to those of 5, 7, 3' and 4' tetrahydroxy flavone (Rahate and Rajasekaran, 2018).

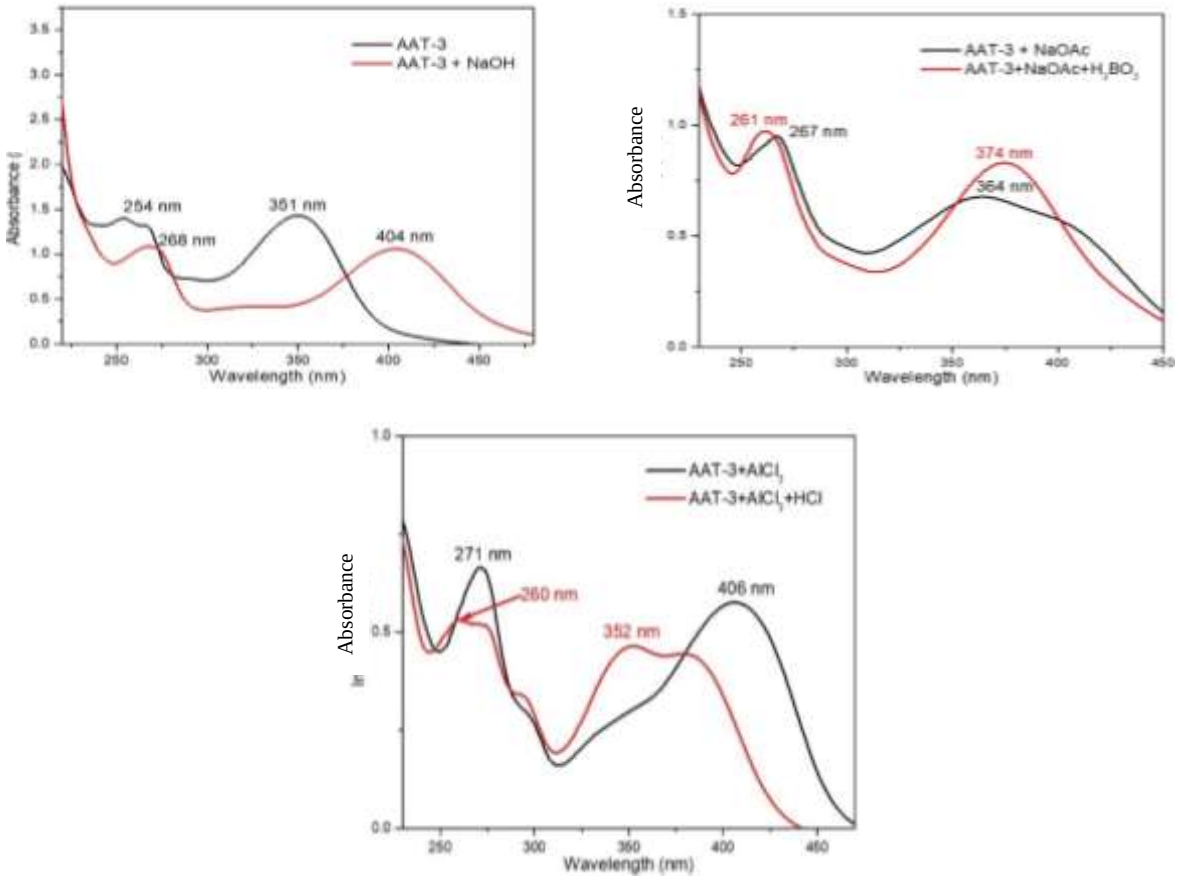

Figure 9. UV spectra of an isolated compound Luteolin (AAT-3) by using shift reagents

In the FT IR spectrum of compound AAT-3, the absorption bands that occurred at 3295 cm^{-1} and 3070 cm^{-1} were indicated due to the O-H stretching band of the phenolic group and the C-H stretching of the aromatic ring. At 1649 cm^{-1}, the C=O stretching of an unsaturated carbonyl group appeared. The bands at 1604 cm^{-1}, 1555 cm^{-1}, and 1495 cm^{-1} were assigned for the C=C stretching of an aromatic ring. The absorption band at 1364 cm^{-1} was due to the O-H bending of the phenolic group, and the absorption bands at 1254 cm^{-1} and 1117 cm^{-1} appeared due to the stretching of the cyclic C-O-C group. The absorption band at 1162 cm^{-1} was assigned as the C-O stretching of the phenolic group. The band at 861 cm^{-1} =C-H out of plane bending vibration of the aromatic system (Figure 10).

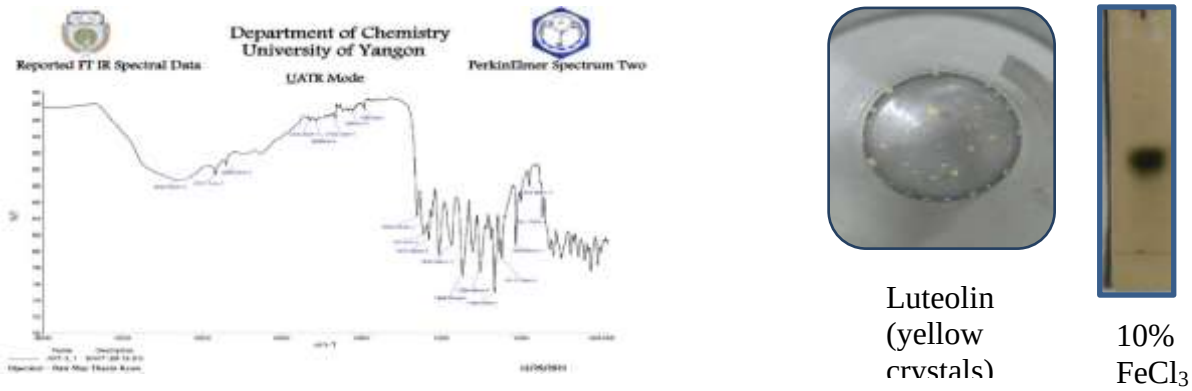

Figure 10. FT IR spectrum of an isolated compound Luteolin (AAT-3)

The ^{1}H NMR spectrum (400 MHz, DMSO-d_6) of the isolated compound AAT-3 showed ten proton signals (Figure 11). A doublet of the doublet with ortho and meta coupling constant (J = 2.4, 8.0 Hz) appeared at δ 7.37 ppm, representing a proton of 6'. A doublet at δ 7.34 ppm (J = 2.4 Hz) was a characteristic of the H-2' proton. In addition, the H-5' proton was observed as a doublet (J = 8.8 Hz) at δ 6.84 ppm. A singlet at δ 6.61ppm was attributed to a proton of H-3. Two singlets at 6.38 and 6.13 ppm corresponded to protons on H-8 and H-6.

The ^{13}C NMR spectrum indicated the presence of 15 signals, which included one carbonyl group, eight quaternary carbon signals, and six methine carbon signals. The ^{13}C NMR spectrum is shown in Figure 11. The carbon signals were observed for six methine signals at δc 145.73 (C-3'), 118.99 (C-6'), 113.36 (C-2'), 102.87 (C-3), 98.82 (C-6) and 93.83 (C-8), eight quaternary carbon signals at δc 164.12 (C-7), 163.88 (C-2), 161.47 (C-5), 157.27 (C-9), 121.49 (C-1'), 116 (C-5'), 103.69 (C-10). One carbonyl signal was also observed at 182.66 (C-4). From the basis of the observed melting point, some physicochemical tests, and all spectral data compared with the reported data of luteolin (Puspalata *et al.*, 2019), the isolated compound AAT-3 was identified as luteolin ($C_{15}H_{15}O_6$).

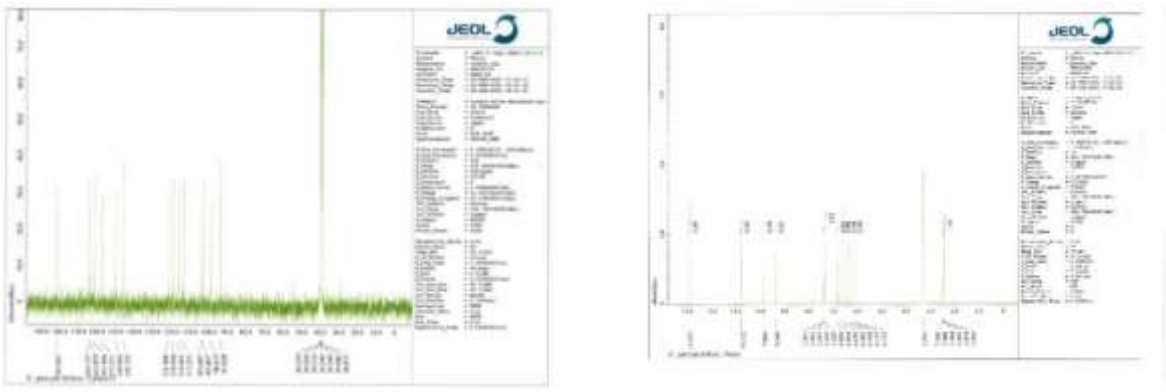

Figure 11. ^{1}H NMR (DMSO-d_6, 400 MHz) and ^{13}C NMR (DMSO-d_6, 100 MHz) spectra of AAT-3

Compound **AAT-3** (Luteolin): A yellow crystal crystallized from PE:EtOAc, mp: 325℃.; FTIR (ν cm^{-1}): 3295(ν_{O-H}), 1649($\nu_{C=O}$), 1611,1577, 1432($\nu_{C=C}$), 1254, 1117 (ν_{C-O-C}), 861(δop (C-), UV_{max} (MeOH) nm: 254, 351; NaOAc nm: 267,364; NaOAc+ H_3BO_3 nm: 261, 374; $AlCl_3$ nm: 271, 406 ; $AlCl_3$ + HCl nm: 260, 352; NaOH nm: 268, 404.^{1}H NMR (400 MHz, DMSO-d_6) δH (ppm): 6.61(s,1H, H-3), 12.92, 10.77, 9.87, 9.349,(s,1H, 5, 7,4', 3'-OH), 7.367 (dd, J =2.4, 8 Hz, 1H, H- 6'), 7.335 (d, J = 2.4 Hz,1 H, H-2'), 6.836 (d, J = 8.8 Hz, 1H, H-5'), 6.382 (d, J = 1.6 Hz,1H, H-8), 6.127 (d, J =1.6 Hz, 1H, H-6) ^{13}C NMR (100 MHz, DMSO-d_6) δ_C (ppm): 93.8

(C-8), 98.8 (C-6),102.88 (C-3),103.69 (C-10) 145.73 (C-3') 121.49 (C-1') 116.01 (C-5'), 118.99(C-'), 113.36 (C-2'), 157.27 (C-9), 161.47 (C-5), 149.68 (C-4'), 164.12 (C-7), 163.88 (C-2), 181.C-4).

The structures of two isolated compounds AAT-2 as apigenin and AAT-3 as luteolin are shown in Figure 12.

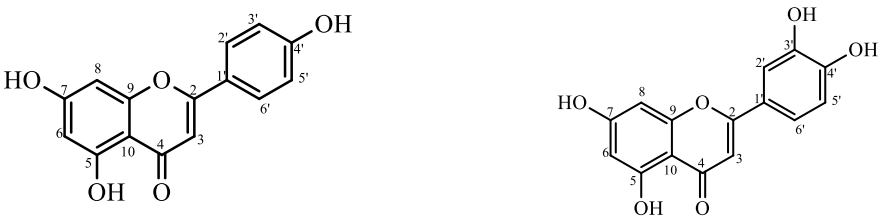

Figure 12. Structures of isolated compounds: AAT-2 (Apigenin) and AAT-3 (Luteolin)

Conclusion

The present study deals with the isolation and identification of apigenin and luteolin from aerial parts of *B, monnieri* and screening for *in vitro* antidiabetic activity. The extraction of phenolic compounds from aerial parts of *B, monnieri* was done by using 70 % ethanol, and the resulting extract was divided into pet ether, ethyl acetate, and water-soluble portions. Apigenin and luteolin were isolated from the ethyl acetate portion by column chromatography. Its structure was identified by modern spectroscopic methods. The ethanol and watery extracts possessed antidiabetic activity due to their α-amylase inhibitory effects (IC_{50}= 54.09 μg/mL, 78.14 μg/mL) and α-glucosidase inhibitory effects (IC_{50} = 62 μg/mL, 91.66 μg/mL) comparable with the standard drug metformin (IC_{50} = 45.31 μg/mL, 50.79 μg/mL). On the other hand, the isolated compounds apigenin and luteolin possessed antidiabetic activity due to their α-amylase inhibitory effects (IC_{50}= 1.049 μg/mL, 0.75 μg/mL) and α-glucosidase inhibitory effects (IC_{50} = 0.558 μg/mL, 0.507 μg/mL) comparable with the standard drug metformin (IC_{50} = 0.497 μg/mL, 0.44 μg/mL). The higher percent enzyme inhibition with the lowest IC_{50} value, the percent inhibition of ethanol extract and luteolin was nearly the same as the percent inhibition of standard metformin.

Acknowledgements

The authors would like to express their profound gratitude to the Department of Higher Education (Lower Myanmar), Ministry of Education, Yangon, Myanmar, for giving them the opportunity to do this research and the Myanmar Academy of Arts and Science for allowing them to present this paper.

References

Ei Shoubaky. G.A., M. Mohamed, H. M. ADaim, H. M. Mohamed, and E. A. Salem. (2016).” Isolation and Identification of a Flavone Apigenin from Marine Red Alga Acanthophora spicifera with Antinociceptive and Anti-Inflammatory Activities”. *Journal of Experimental Neuroscience,* vol.10, pp. 21-29

Ghosh, T., T. K. Maity and J. Singh. (2011). “Antihyperglycemic Activity of Bacosine, A Triterpene from *Bacopa monnieri*, in Alloxan-induced Diabetic Rats”. *Planta Med*., vol.77, pp. 804-808

Kajaria, D., S. Tiwari, J. Tripathi, Tripathi, and Y. Ranjana. (2013) “*In-vitro* α Amylase and Glycosidase Inhibitory Effect of Ethanolic Extract of Antiasthmatic Drug-Shirishadi”. *J. Adv. Pharm. Technol. Res*., vol.4, pp. 206–209

Khadayat, K., P. M Bishnu, G. Hira Gautam, G. Sajani and P. Niranjan. (2020). “Evaluation of the α-Amylase Inhibitory Activity of Nepalese Medicinal Plants Used in the Treatment of Diabetes Mellitus.” *Clinical Phytoscience*, vol.6(34), pp. 1-8

Kim, J., T. Hyun, and M. Kim. (2011).” The Inhibitory Effects of Ethanol Extract from Sorghum, Foxtail Millet and Proso Millet on Glucosidase and α-Amylase activities.” Food α- α Chemistry, vol. 124, pp. 1647-51

Lal, S and B. Baraik. (2019).” Phytochemical and Pharmacological Profile of *Bacopa monnieri* an Ethnomedical Plant”. *JPSR,* vol.10(3), pp. 1001-1013

Mogale, A. M., L. S. Lebelo, N. Thovhogi, A. N. de Freitas, and L. J. Shai. (2011) “*α*-Amylase and *α*-Glucosidase Inhibitory Effects of *Scleroderma Birrea* [(A. Rich.) Hochst.] Subspecies *caffra* (Sond) Kokwaro (Anacardiaceae) Stem-bark Extracts,” *African Journal of Biotechnology*, vol. 10(66), pp. 15033–15039

Ogunwande, A., T. Matsui, T. Fujise, and K. Matsumoto. (2007) “*α*-Glucosidase Inhibitory Profile of Nigerian Medicinal Plants in Immobilized Assay System,” *Food Science and Technology Research*, vol.13(2), pp. 169–178

Oyedemi,S.O., B.O. Oyedemi, Ijeh,I.I.,Ohanayarem,P.E.,Coopoosamy,R.M.,and Aiyegoro,O.A.(2017). “Alpha-Amylase Inhibition and Antioxidative Capacity of Some Antidiabetic Plants Used by the Traditional Healers in Southeastern Nigeria”. *The Scientific World Journal*, vol.10, pp. 1-11

Puspalata, B., P. Parajuli, P. P. Ramesh, and K. S. Jae. (2019). “Microbial Biosynthesis of Antibacterial Chrysoeriol in Recombinant *Escherichia coli* and Bioactivity Assessment.” *Catalysts,* vol.9, pp.1-15

Rahate, K. P., and A. Rajasekaran. (2018).” Isolation and Identification of Flavone Aglycones in Roots of Desmostachya Bipinnata Stapf*”. Indian J Pharm Sci*, vol.80(3), pp. 551-556

Williams, G. (2013). “Possible Effect of Diatary Polyphenol on Sugar Absorption and Digestion”. *Molecular Nutr Food Res*, vol. 57, pp. 48-57

PREPARATION, CHARACTERIZATION AND ANTIMICROBIAL ACTIVITY OF BIONANOCOMPOSITES OF COPPER OXIDE NANOPARTICLES BASED CARBOXYMETHYL CELLULOSE DERIVED FROM ASPARAGUS STALK END

Win Pa Pa Phyo[1], Aung Than Htwe[2], Yamin Thet[2], Hninn Wutt Yee Htun[2],

Margaret Hkawn Taung[2]

Abstract

Green, sustainable bionanocomposites have the potential to be useful in diagnostic and biomedical applications. In the present study, a series of copper oxide nanoparticles-based carboxymethyl cellulose (CuCMC) bionanocomposites with different weight ratios of carboxymethyl cellulose (CMC) derived from asparagus stalk end to copper oxide nanoparticles (CuO NPs) were prepared. The prepared bionanocomposite of copper oxide nanoparticles based carboxymethyl cellulose (CuCMC) material was characterized by using XRD, FT IR, UV-Visible, SEM and TG-DTA techniques. SEM, and XRD studies indicated the in situ generation of CuO NP in the carboxymethyl cellulose matrix. FT IR analysis confirmed the presence of both CuO NPs and CMC. TG-DTA results indicated that the CMC content of CuCMC was between 61.9 and 73.6 % by weight. Finally, the synthesized CuO, CMC, and CuCMC were tested for their antimicrobial activity. The results obtained from those different studies revealed that carboxymethyl cellulose and copper oxide bionanocompsite can be used effectively for biomedical applications.

Keywords: Copper oxide nanoparticles, carboxymethyl cellulose, antimicrobial activity, bionanocomposite

Introduction

Nanocomposites are materials which consist of two components, with one of them having dimensions in the nanometer range (10^{-9} m). As environmental problems worsen, more and more emphasis has been placed on green chemistry. Asparagus *(Asparagus officinalis* L.*)* is a nutritious and perennial vegetable continuously used as an antifungal, anticancer, and anti-inflammatory herbal medicine in Asia. In the processing of asparagus, the spears, which are 2-3% of the total weight of the asparagus, are typically processed into three types of products: canned, fresh, and frozen. The processing residues were used for animal feed and produced low-value products due to their high cellulose content. As a result, tons of asparagus stalk ends are produced as an agricultural by-product, which can pollute the environment. It is a rich source of celluloses which can be isolated from the asparagus stalk end (Klunklin *et al.,* 2021). Carboxymethyl cellulose (CMC), one of the most important cellulose derivatives, is obtained by chemical modification of natural cellulose. It is a linear, long-chain, water-soluble ionic polysaccharide derived from cellulose. In addition, the purified cellulose is white to cream-coloured as well as tasteless and odourless, and it is a free-flowing powder. Furthermore, carboxymethyl cellulose has an acid fusion, meaning that CMC is an anionic polyelectrolyte, CMC has many interesting properties when dissolved in an aqueous solution, but this depends on the CMC grade and the solution condition.

Due to its water-soluble heteropolysaccharides with high molecular weight properties, CMC is often blended with starch to provide a desirable mixture, enhance product quality and stability, control moisture, and also improve water mobility (Hong, 2013).

Copper oxide nanoparticles are technically interesting because of their physical and chemical properties, such as high temperature superconductors, batteries, gas sensors, solar energy

[1] Department of Chemistry, University of Yangon, Myanmar
[2] Department of Chemistry, University of Yangon, Myanmar

conversion, and low-cost and low-toxicity antibacterial properties. It can also be used as an antibacterial agent (Peternela *et al*., 2018). Recently, much interest has been focused on the preparation of antimicrobial bionanocomposite materials due to their excellent biomedical relevance. These antibacterial agents have great potential to inhibit the growth of microorganisms and to save the environment.

In this respect, copper-based materials are attractive alternatives because they are known to have important antibacterial activity in addition to being low cost and easy to release from the human body. The advantage of copper nanoparticles is that they oxidize to form copper oxide nanoparticles. It mixes easily with polymers and macromolecules and is relatively stable in terms of both chemical and physical properties. Therefore, copper-based nanocomposites are very important (Yadollahi *et al*., 2015).

Materials and Methods

Asparagus stalk ends were purchased from the local market. Copper (II) sulphate pentahydrate ($CuSO_4.5H_2O$), sodium hydroxide (NaOH), hydrogen peroxide (H_2O_2), sodium silicate (Na_2SiO_3), isopropanol (C_3H_8O), monochloroacetic acid (MCA), methanol (CH_3OH), acetic acid (CH_3COOH), ethanol (C_2H_5OH), hydrochloric acid (HCl), and sulphuric acid (H_2SO_4) were supplied by the Department of Chemistry, University of Yangon, Myanmar. Where necessary, distilled water was used with all the chemicals in this study.

Preparation of Copper Oxide (CuO) Powder

The copper (II) sulphate pentahydrate was used to prepare copper oxide nanoparticles according to the well-known co-precipitation method with some modifications. In brief, $CuSO_4.5H_2O$ (12.48 g) was dissolved in 250 mL of distilled water and stirred continuously. And then, 5M sodium hydroxide (NaOH) solution was added dropwise into the copper(II) sulphate pentahydrate solution until the pH 12 solution was reached. The colour of the solution changed from green to bluish green and finally to black as the reaction proceeded. For 6 h, the solution was continuously stirred at 85 ºC. Then, the solution was centrifuged at 8000 rpm for 10 min. The synthesized CuO NPs were washed free of alkali metals several times with distilled water until they reached a neutral state (pH 7). This was washed again with ethanol and dried in the oven at 60 ºC for 8 h. After that, the dried CuO NPs were calcined in a muffle furnace at 500 ºC for 4 h to achieve stable CuO NPs. This was crushed with a mortar and pestle and sieved with a 90 µm size screen. Finally, the samples were stored in a sealed bottle and placed in a desiccator for further use.

Preparation of Carboxymethyl Cellulose Derived from Asparagus Stalk End

Cellulose from dried asparagus stalk end powder was extracted according to the method of Klunklin *et al.,* 2021. Briefly, the dried powder sample of asparagus stalk end was treated at 100 °C for 3 h with a ratio of cellulose to 10 % (w/v) NaOH solution at 1:20 (w/v). The black slurry was filtered and rinsed with cold distilled water until neutral (pH 7) rinsed water was obtained. To obtain the cellulose fiber, the washed fibre residue was dried in an oven at 55 °C for 24 h. The dried fibre residue was bleached with 6 % sodium silicate and 50 % hydrogen peroxide on magnetic stirrer for 3 h. The white cellulose was obtained and dried in an oven at 55 °C for 24 h. The bleached cellulose was then ground using a mortar and pestle and sieved through a 90 µm size mesh. The bleached cellulose powder was stored in a sealed bottle.

The cellulose powder was then modified to carboxy methyl cellulose by alkalization and esterification processes. In briefly, 100 mL of concentrations of NaOH at 40 % (w/v) and 500 mL of isopropanol were blended with 10 g of cellulose powder extracted from asparagus stalk

ends, and this was stirred for 1.5 h. Subsequently, the carboxymethylation reaction was carried out. 15g of monochloroacetic acid was added while stirring and stirred further for 1.5 h. This obtained solution was covered with aluminium foil and placed in an oven at 55 °C for 3 h. And then, two phases appeared. The solid phase was suspended in 66.67 mL of absolute methanol and neutralized with 90 % acetic acid. This neutral solution was filtered through the Buchner funnel. The product was soaked in 200 mL of 70 % v/v ethanol for 10 min and washed 5 times with distilled water. And then the product was washed again with 200 mL of absolute methanol. CMC was obtained and dried in an oven at 55 ºC for 12 h.

Preparation of Copper Oxide Nanoparticles Based Carboxymethyl Cellulose Bionanocomposite (CuCMC)

A 1 g of copper oxide powder was dissolved in 2.5 mL of epichlorohydrin and 30 mL of 25% (v/v) acetic acid solution and stirred continuously at room temperature for 12 hours to form a green-coloured CuO NPs mixture solution. The five different amounts of CMC (0.1, 0.2, 0.3, 0.4, and 0.5 g) were added to the prior CuO NPs mixture solution, and then the mixed polymer composite solution was stirred at room temperature for 30 min. This was allowed to stand for 24 h to obtain CuCMC bionanocomposite. Finally, the obtained CuCMC was dried in an oven at a temperature of 60 ºC for 12 h and powdered by using a mortar and pestle. A series of CuCMC bionanocomposites are coded as CuCMC(0.1)(0.1 g of CMC), CuCMC(0.2) (0.2 g of CMC), CuCMC(0.3) (0.3 g of CMC), CuCMC(0.4) (0.4 g of CuCMC) and CuCMC(0.5) (0.5 g of CMC), respectively.

Characterization

The surface morphology of bionanocomposite materials was studied using SEM (EVO-18, Germany) at 7 kV. The dried sample film was cut, sputter-coated with EVO-18 using platinum, and viewed through the microscope. Fourier transform infrared spectrophotometer (Shimadzu, Japan) was used. The resolution was 1 cm^{-1} and the scanning was performed in the range of 400–4000 cm^{-1}. The X-ray diffraction (XRD) measurements of CuO NPs, CMC, and CuCMC bionanocomposites were recorded using a Rigaku D/Max 220 X-ray diffractometer (Rigaku, Japan) with a detector operating under a voltage of 40.0 kV and a current of 30.0 mA using Cu K_α radiation (λ= 0.15418 nm). The recorded range of 2θ was 10-80 º and the scanning speed was 6 º/min. The thermal stability of CuO, CMC, and CuCMC bionanocomposites was evaluated by a simultaneous TG-DTA (DTG-60 H) operated under a nitrogen atmosphere.

Results and Discussion

Characterization of CuCMC Bionanocomposites

X-ray diffraction analysis

Figure 1 shows the XRD patterns of CuO NPs, CMC, and CuCMC bionanocomposites. As seen in Figure 1(a), the diffractive region of CuO NPs is observed at 2θ values of 35.69º, 38.75º, 48.48º,61.69º,66.01º and 68.23º, respectively, and the corresponding Miller indices are (110), (111), (112), (202), (311), and (113) planes. The higher intensity values of 2θ for CuO indicate that the mixed phase has a major proportion of CuO with a highly oriented crystalline structure. Using Scherrer's equation, the average crystallite size of CuO NPs was found to be 18.46 nm. In Figure 1(b), pure CMC shows characteristic peaks at around 2θ values of 19.71º, 31.75º, and 45.83º, which indicate the amorphous and crystalline structures. The strength of hydrogen bonding and crystallinity contribute to the microstructure of CMC material. Figure 1(c) shows that the main diffractive region of all CuCMC is found with a weak broad peak at 2θ value of 34.10º, 37.14º, 46.58º, 50.32º, 55.99º, 59.52º, 64.98º, 66.66º, 70.81º and 73.25º which are

assigned to the crystal planes of (110), (111), (112), (200), (020), (202), (220), (311), (113) and (400). These values confirmed the presence of two crystalline phases of CuO and Cu_2O. When incorporation of CuO into the CMC chemical structure of the CMC hydrogels changes due to overlap of biopolymer diffraction, it indicates that there was mainly physical interaction but scarcely a chemical reaction between CMC and CuO NPs (Alothman *et al.*, 2020). The calculated mean crystallite sizes of the CuCMC(0.1), CuCMC(0.2), CuCMC(0.3), CuCMC(0.4), and CuCMC(0.5) were found to be 50.88 nm, 55.28 nm, 57.06 nm, 59.43 nm, and 64.33 nm, respectively. The higher the amount of CMC, the larger the crystallite size of CuCMC nanoparticles produced.

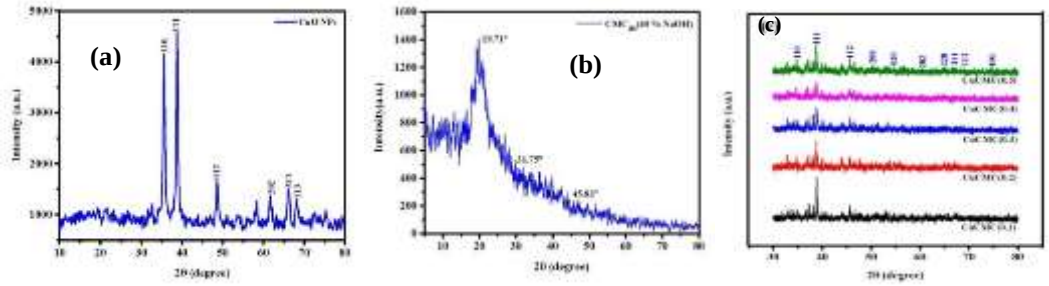

Figure 1. XRD patterns of pure (a) CuO NPs, (b) CMC, and (c) CuCMC bionanocomposites

FT IR spectroscopy

FT IR experiments were carried out to investigate the interaction between CuO and CMC. As shown in Figure 2(a), in the spectrum of CuO, the peaks at 3414, 1632, and 608 cm^{-1} correspond to O-H stretching vibration, C=O stretching, and Cu-O vibration, respectively (Luna *et al*., 2015). In the spectrum of CMC in Figure 2(b), there is one characteristic absorption band at 1588 cm^{-1}, which corresponds to the carboxyl group (COO-), where the hydroxyl group was replaced with the carboxyl group after etherification (Pormsila *et al*., 2019). As seen in Figure 2(c), the CuCMC spectra show peaks at 3469, 3472 cm^{-1} (O-H stretching), and 1595 cm^{-1}, as well as a superposition band assigned to the C=O stretching vibration. 1423 cm^{-1} is due to the CH_2 scissors, and 1052 cm^{-1} assigned to the C-O-C of aliphatic ether (Basta *et al.*, 2021). Moreover, the band corresponding to the Cu-O stretching vibration shifts to a lower wavenumber, 626 cm^{-1}.

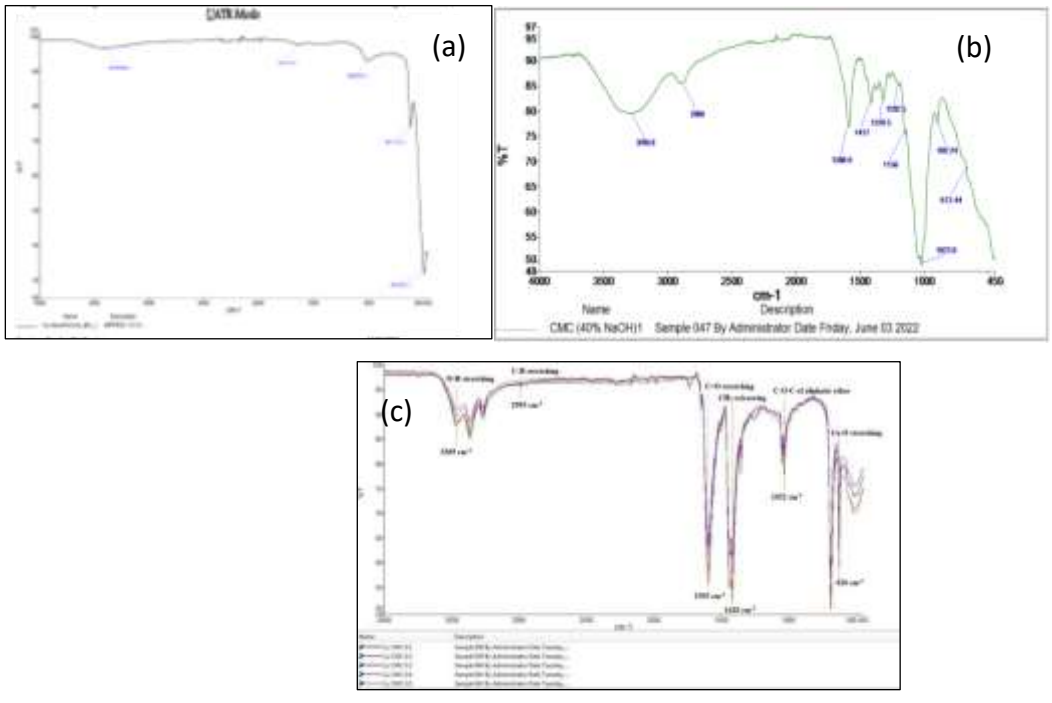

Figure 2. FT IR spectra of (a) CuO NPs, (b) CMC and (c) CuCMC bionanocomposites

UV-vis absorption spectra

The UV-Vis spectrum (Figure 3(a)) of pure CuO NPs shows absorption peaks at 272 nm. The CuCMC bionanocomposite shows 228 nm, 247 nm, and 260 nm. It was found that the intensity of the CuCMC bionanocomposite was lower than that of CuO. After attachment with CMC, the peaks of CuO have shown a bathochromic shift. This shift in absorption maxima might be attributed to the formation of nanoscale particles. Optical absorption is an important tool to obtain the optical energy band gap of crystalline and amorphous materials. The fundamental absorption corresponds to the electron excitation from the valence band to the conduction band and can be used to determine the nature and value of the optical band gap. The absorption spectrum reveals that the increase in concentration of CuCMC NPs produces a shift in the absorption peak and results in a high band gap. The absorption peak in the UV region was used to study the shifting in the optical energy band gap for CuCMC NPs at 25 ˚C. The optical energy band gap, E_g, is calculated from the relation:

$$(\alpha h\nu) = B(h\nu - E_g)^n$$

where hν is the photon energy, B is the constant, and n is the power factor and that takes 1/2, 2, 3/2, and 3 for direct allowed, indirect allowed, direct forbidden, and indirect forbidden transitions, respectively.

Figure 3(b) shows that the optical band gap for CuO NPs is 3.18 eV, 3.31 eV for CuCMC(0.1), 3.38 eV for CuCMC(0.2), 3.43 eV for CuCMC(0.3), 3.49 eV for CuCMC(0.4), and 3.54 eV for CuCMC(0.5). CMC addition, as shown in the figure, raises the optical band gap from 3.31 eV to 3.54 eV. This may be attributed to salt complexation with the polymer matrix in addition to the expected nanoparticle aggregation. The absorption decreases and the optical band gap increases due to charge transfer transitions. The prepared CuCMC NPs in the present study are expected to be more useful in photonic and electronic device applications.

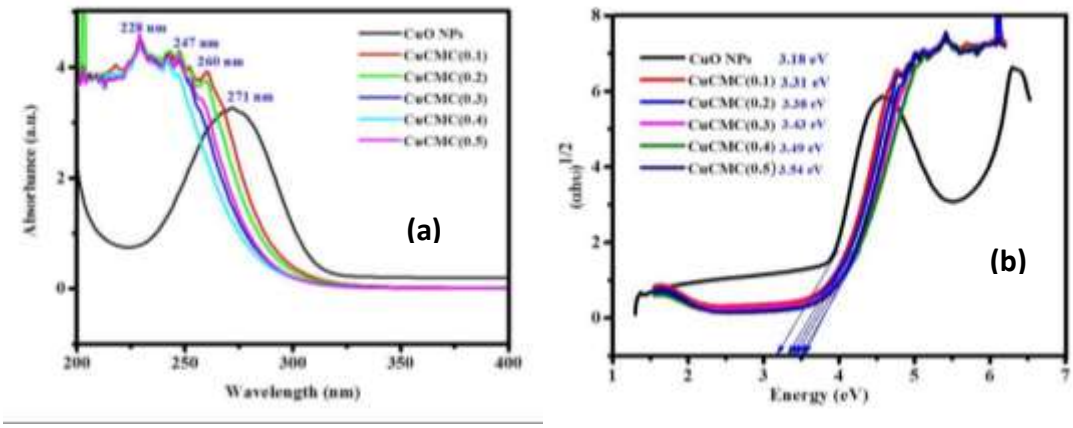

Figure 3. (a) UV spectra (b) plots of *hv* vs $(\alpha hv)^{1/2}$ of CuO NPs and CuCMC bionanocomposites

SEM Analysis

The morphology of the prepared CuO, CMC, and CuCMC was investigated by the scanning electron microscopy technique. The surfaces of the CuO, CMC and CuCMC display a generally smooth morphology, as shown in Figures 4 (a) to (g), indicating that the CuO nanoparticles are uniformly aggregated and clustered. CMC was found to be rod-like or ribbon-shaped and CuCMC bionanocompsites were found to be cube-like structures. In the case of using a surface with some pores, its chelation with CMC appears as a surface coated with a white fibrillar layer of CMC (Basta *et al.*, 2020).

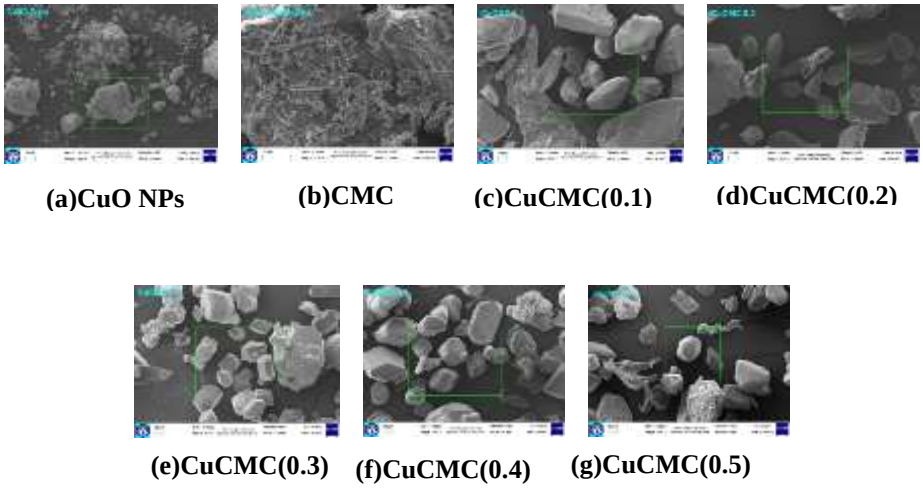

Figure 4. SEM images of (a) CuO NPs, (b) CMC, and (c,d,e,f,g) CuCMC bionanocomposites

TG-DTA Analysis

The thermogravimetric analysis was used to investigate the thermal stability of pure CuONPs, CMC, and five different ratios of CuCMC composite powder (CuCMC0.1, CuCMC0.2, CuCMC0.3, CuCMC0.4, and CuCMC0.5). The thermal stability of CuO NPs was observed due to a weight loss of 0.938% within the temperature range of 38 ℃ to 340 ℃, as shown in Figure 5(a). This is attributed to the thermal decomposition of unstable groups containing oxygen and the evolution of CO_2 gas. Figure 5(b) depicts CMC's thermogram, which shows weight loss in four stages. The first stage occurs in the temperature range of 37 ºC to 59 ºC with 2.88 % weight loss. This is a result of moisture evaporation. In the second stage, the temperature range between 59 ºC to 76 ºC was observed to have an 8.65 % weight loss. This is attributed to the volatile organic compounds with low molecular weight. In the third stage, a loss of weight of 17.31 % was observed to take place within the temperature range of 76 ºC to 158 ºC. At this stage, weight loss may be due to the volatile organic compounds with low molecular weight. The fourth stage occurred at temperatures ranging from 158 ℃ to 238 ℃, with a weight loss of 46.15 %. This is due to the decarboxymethylation of CMC with the elimination of CO_2 and the temperature range between 300 ºC to 600 ºC is due to the residual organic fractions. The total weight loss of the CMC is 74.99 %.

The thermograms of all CuCMC composites are shown in Figures 5(c) to 5(g), with weight loss in three stages. The temperature ranges from 38 ℃ to 157 ℃ in the first stage, with weight loss of 0.98 % in CuCMC(0.1), 6.50 % in CuCMC(0.2), 7.84 % in CuCMC(0.3), 6.71 % in CuCMC(0.4), and 7.06 % in CuCMC(0.5). There is an evaporation of water. The second stage was observed to lose 15.69 % in CuCMC(0.1), 12.99 % in CuCMC(0.2), 15.69 % in CuCMC(0.3), 20.14 % in CuCMC(0.4), and 20.14 % in CuCMC(0.5) at temperatures ranging from 157 ℃ to 238 ℃. This is due to the decomposition of the substituted sites in the methylated derivatives. In the third stage, the temperature ranges from 238 ℃ to 600 ℃, with a weight loss of 45.19 % in CuCMC (0.1). The broad exothermic peaks at 229 ℃, 240 ℃, 229 ºC, 229 ºC, and 272 ℃ correspond to 45.47% in CuCMC(0.2), 47.06 % in CuCMC(0.3), 47.00 % in CuCMC(0.4), and 35.58 % in CuCMC(0.5). At this stage, weight loss is due to the depolymerization and pyrolytic processes of the main polymer chains. The total weight loss percents of CuCMC bionanocomposites were in the range of 61.9-73.6%. The results show that the maximum weight loss percent of CuO NPs is lower than that of CuCMC bionanocomposites.

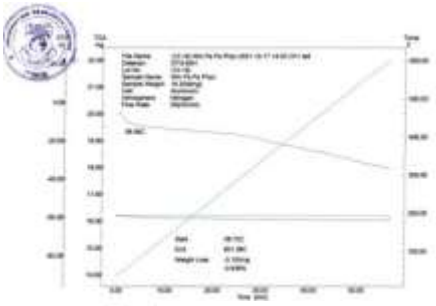

(a) CuO NPs

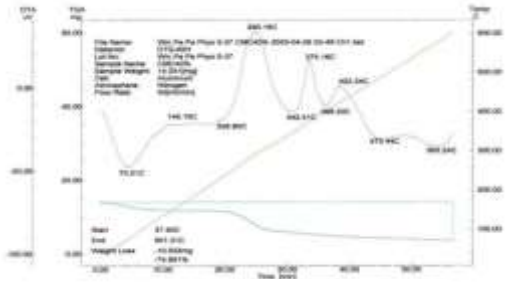

(b) CMC

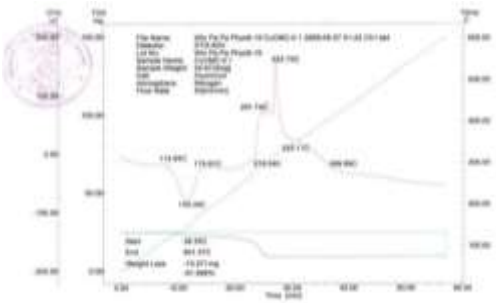

(c) CuCMC(0.1)

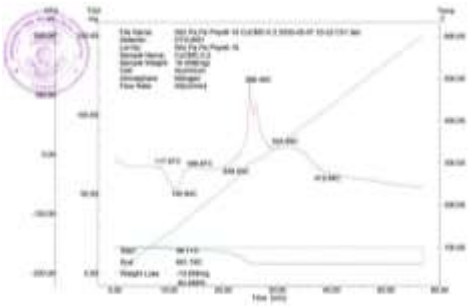

(d) CuCMC(0.2)

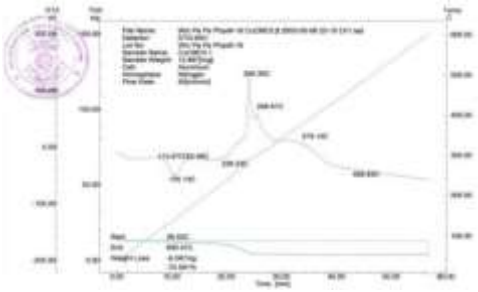

(e) CuCMC(0.3)

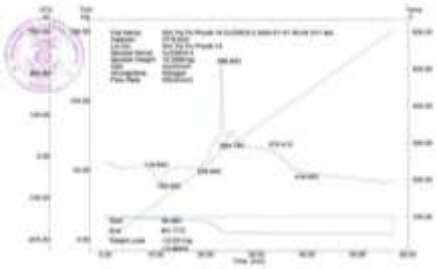

(f) CuCMC(0.4)

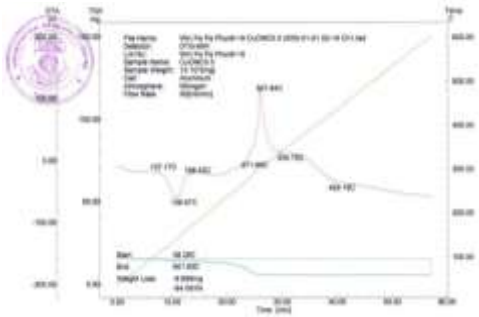

(g) CuCMC(0.5)

Figure 5. (a) TG curves (b) DTA curves for CuO NPs and CuCMC Bionanocomposites

Antimicrobial Activity

Screening the antimicrobial activity of three samples of nanoparticles was done by the ager well diffusion method. In this investigation, the nanoparticles were tested against eight microorganisms, namely *Bacillus subtilis*, *Staphylococcus aureus, Pseudomonas fluorescens, Bacillus pumilus, Candida albicans, Escherichia coli, Agrobacterium tumefaciens,* and *Micrococcus luteus.* The inhibition zone diameter, including the filter paper, showed the degree of antimicrobial activity. The larger the inhibition zone diameter, the higher the antimicrobial activity. The inhibition zones of nanoparticles against the eight microorganisms tested are shown in Figure 6, and the observed data are summarized in Table 1.

From the results, CuO NPs and CuCMC(0.5) NPs had antimicrobial activity, but CMC did not show any antimicrobial activity. It was found that CuO NPs possessed an 11~14 mm inhibition zone against *C. albicans*, *P. fluorescens*, and *S. aureus*, respectively, whereas CuCMC(0.5) exhibited an inhibition zone diameter range of 30-36 mm against all tested microorganisms. The antimicrobial activity of CMC did not show activity. It can be concluded that, according to the antimicrobial activity, the CuCMC(0.5) NPs may be intended to be used as an antibiotic agent.

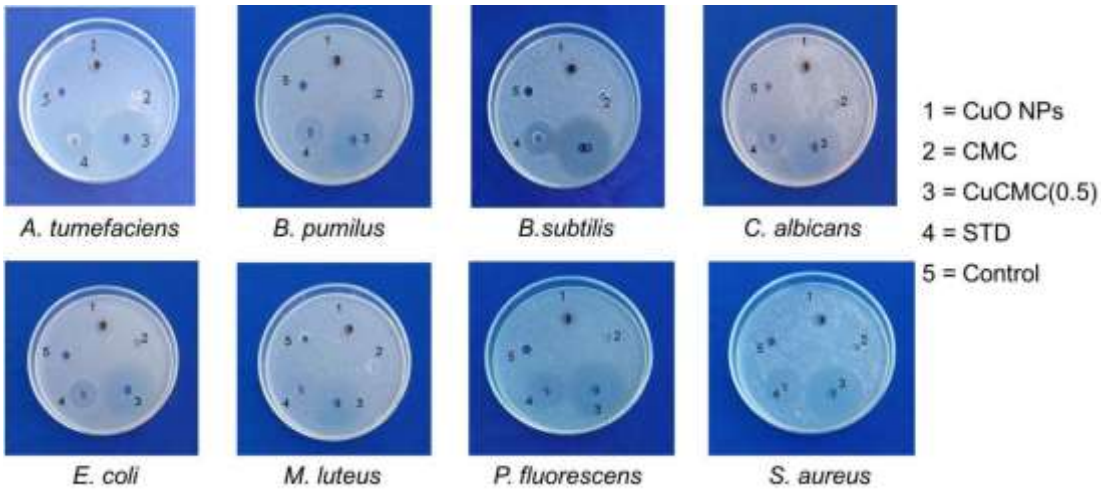

Figure 6. Antimicrobial activity of CuO NPs, CMC and CuCMC on eight microorganisms by agar well diffusion method

Table 1. Inhibition Zone Diameters of CuO, CMC, and CuCMC NPs Against Microorganisms by Agar Well Diffusion Method

Tested microorganisms	Inhibition zone diameters (mm)			
	CuO NPs	CMC	CuCMC(0.5)	*STD
A. tumefaciens	-	-	32	23
B. pumilus	-	-	30	21
B. subtilis	-	-	34	21
C. albicans	14	-	34	22
E. coli	-	-	36	20
M. leteus	-	-	36	18
P. fluorescens	11	-	35	22
S. aureus	11	-	35	23

*STD, for bacterial = choramphenicol, for fungus = Nystatin; (-) = not detected

Agar well diameter ~8 mm

10 mm ~14 mm = weak activity; 15 mm~19 mm = moderate activity; 20 mm and above = potent

Conclusion

The bionanocomposites of copper oxide nanoparticles based on carboxymethyl cellulose were successfully prepared by the co-precipitation method. It is observed that CuO NPs are dispersed on a molecular scale in the CMC matrix, and some interactions occur between the CMC and CuO NPs. In CuCMC bionanocomposites, FT IR showed the strong absorption band of the Cu-O bond at 626.96 cm^{-1}. The XRD patterns confirmed the formation of CuO NPs with a size range of 50.88–64.33 nm within the CMC matrix. SEM images confirmed the linking and grafting of CuCMC. SEM measurements revealed that the higher the CMC content, the larger the average diameter. All the results demonstrated that copper oxide was well-dispersed in the CMC matrix. TG-DTA measurements indicated the homogeneous dispersion of CuO within the CMC polymer matrix. The synthesized bionanocomposite was found to have greater thermal stability. The presence of both components of the bionanocomposite was confirmed by UV-Vis and FT-IR spectral studies. These studies also indicate a strong interaction between CuO and CMC in the bionanocomposites. The antimicrobial activity was measured by the agar well diffusion method. The CuCMC0.5 has more potent antimicrobial activity than the other two samples of CuO NPs and CMC. The main contribution of the present research is that the synthesis of copper-based carboxymethyl cellulose bionanocomposite may be used in the biomedical field.

Acknowledgements

The authors would like to thank Professor Dr Ni Ni Than, Head of Department of Chemistry, University of Yangon, for giving us permission to present this research paper at the Paper Reading Session organized by the Myanmar Academy of Arts and Science. We would like to acknowledge Professors Dr Ye Myint Aung, Dr Myat Kyaw Thu, Dr San San Aye and Dr Nyan Tun, Department of Chemistry, University of Yangon, for their valuable suggestions and advice throughout this research work. Finally, we are also thankful to Universities' Research Center, West Yangon University and Pathein University, for providing XRD, TG-DTA, SEM, and FT IR facilities.

References

Alothman, Z. A., A. Y. Badjah, O. M. L. Alharbi, and I. Ali. (2020). "Copper Carboxymethyl Cellulose Nanoparticles for Efficient Removal of Tetracycline Antibiotics in Water". *Environmental Science and Pollution Research*, vol. 27, pp. 42960-42968

Basta, A. H., V. F. Lotfy, and C. Eldewany. (2021). "Comparison of Copper-crosslinked Carboxymethyl Celluose Versus Biopolymer-based Hydrogels for Controlled Release of Fertilizer". *Polymer-plastics and Materials*, vol. 10, pp. 1884-1897

Hong, K. M. (2013). *Preparation and Characterization of Carboxymethyl Cellulose from Sugarcane Bagasse*. BSc(Hons:) Project Report, Department of Chemical Science, Universiti Tunku Abdul Rahman, pp.8-19

Klunklin, W., K. Jantanasakulwong, Y. Phimolsiripol, N. Leksawasdi, P. Seesuriyachan, T. Chaiyaso, C. Insomphun, S. Phongthai, P. Jantrawut, S. R. Sommano, W. Punyodom, A. Reungsang, T. M. P. Ngo, and P. Rachtanapun. (2021). "Synthesis, Characterization, and Application of Carboxymethyl Cellulose from Asparagus Stalk End". *Polymers*, vol. 13 (81), pp. 1-15

Luna, I. Z., L. N. Hilary, A. M. S. Chowdhury, M. A. Gafur, N. Khan, and R. A. Khan. (2015). "Preparation and Characterization of Copper Oxide Nanoparticles synthesized via Chemical Precipitation Method". *Open Access Library Journal*, vol. 2 (3), pp. 1-8

Peternela, J., M. F. Silva, M. F. Vieira, R. Bergamasco, and A. M. S. Vieira. (2018). "Synthesis and Impregnation of Copper Oxide Nanoparticles on Activated Carbon through Green Synthesis for Water Pollutant Removal". *Materials Research*, vol. 21(1), pp. 1-11

Pormsila, W., D. Kongsantear, and P. Prasongsuk. (2019). "Production and Characterization of Carboxymethyl Cellulose from Orange Rind". *RMUTP Research Journal*, vol,13(1), pp.127-138

Yadollahi, M., I. Gholamali, H. Namazi, and M. Aghazadeh. (2015). "Synthesis and Characterization of Antibacterial Carboxymethylcellulose/CuO Bio-Nanocomposite Hydrogels". *International Journal of Biological Macromolecules*, vol. 73, pp. 109-114

ENVIRONMENTALLY EFFECTIVE PREPARATION AND CHARACTERIZATION OF CELLULOSE DIACETATE FILM DERIVED FROM WASTE CIGARETTE FILTERS

May Thazin Kyaw[1], Ngwe Sin[1], Aung Than Htwe[2], Hninn Wutt Yee Htun[2],Yamin Thet[2]

Abstract

Cigarette waste pollutes the environment and is a problem that must be solved. However, such waste can be recycled by converting it into raw materials for the production of new products. The purpose of this study is to focus on a simple and low-cost method to transform waste cigarette filters into cellulose diacetate (CDA) films, which can be used in packaging films. Furthermore, waste must be recycled in order to be reused. In this paper, cellulose diacetate films derived waste cigarette filters with different volume ratios of glycerol, (0.25, 0.50, 0.75, and 1.00 mL) glycerol as the plasticizer (CDAG) have been successfully prepared by the solvent evaporating method of the CDA and CDAG films were determined. The physical parameters, the mechanical properties, the degree of swelling and water uptake. The prepared CDA films were characterized using XRD, SEM, FT IR and TG DTA analysis. From the FT IR analysis, the characteristic absorption peaks of CDA and CDAG films clearly showed that the two polymers were well mixed. According to TG-DTA analysis, the thermal stability of the CDA blended film was found to be slightly higher. The antimicrobial activity of CDA and CDAG films was investigated by agar-disc diffusion method. Subsequently, the biodegradable nature of the prepared CDA and CDAG films was studied through the soil burial test. Finally, the prepared CDA and CDAG films can be used as packaging materials.

Keywords: Cigarette waste cellulose diacetate, glycerol, antimicrobial activity, biodegradable nature

Introduction

Cigarette waste has polluted the environment due to the non-biodegradability and toxic substances found in cigarette filters. The reuse of cigarette waste is a hot topic in today's society. Many countries and regions have proposed relevant policies and methods for trying to collect waste cigarettes, but reusing waste cigarettes remains a challenge (Zhang *et al.*, 2020). Cellulose is a linear carbohydrate polymer with long chains of β-D glucopyranose units linked by β-1**,**4-glycosidic bonds**.** It is considered to be one of the most abundant molecules in the biosphere. As one of the most commercially important cellulose derivatives, cellulose acetate (CA) is widely used in the manufacture of plastics, textiles, filter tows, films, or membranes (Arroyo *et al.*, 2020). Cellulose acetate, an organic ester, is a bio-based polymer with excellent mechanical properties. Its general properties can be adjusted by adding small-molecule plasticizers that are also needed for treatment. Over the last few decades, various types of plasticizers based on glycols, phthalates, acetates, and citrates have been incorporated into CA (Erdmann *et al.*, 2021). Cellulose and its derivatives have been used in a wide range of applications due to their abundant sources, excellent biodegradability, and effective renewability. Cellulose acetate is one of the most important cellulose esters and is widely used in the manufacturing industry owing to its excellent all-around properties (Boulven *et al*. 2019).

CA is mainly synthesized via acetylation and hydrolysis reactions, and it can result in a desirable degree of substitution (DS). Based on its DS value, CA is typically classified as cellulose diacetate (CDA, DS =2.2–2.7) or cellulose triacetate (CTA, DS=3) (Wang *et al.*, 2017). Traditional plasticization of the CDA has been performed using traditional plasticizers such as phthalates, glycerol derivatives, and phosphates. This plasticization often leads to problems caused by the bleeding of plasticizers with harmful properties and decomposition products. In this regard,

[1] Department of Chemistry, University of Yangon, Myanmar
[2] Department of Chemistry, University of Yangon, Myanmar

there have been several attempts to use aliphatic polyesters as a plasticizer for cellulose acetate (CA). With this situation in mind, we recently sought to find new plasticizers and plasticization processes that could provide biodegradable thermoplastic polymers from CA (Lee and Shiraishi, 2001). Plasticizers can lower the glass transition temperature of CA and reduce the intramolecular force between polymer chains, resulting in a softer and more flexible polymer matrix (Cindradewi *et al.*, 2021). To improve the processing of CA, some studies have explored several eco-friendly plasticizers such as Triacetin (TA), Triethyl citrate (TC), glycerol, and polyethylene glycol (PEG) (Teixeira *et al.*, 2021). These plasticizers are biodegradable, non-toxic, and have been approved as plasticizers for many polymers. TA and TC are two of the most common eco-friendly plasticizers that have been used for CA. TA and CA share the same side functional groups: acetyl groups. It has been demonstrated that TC can improve the stiffness and brittleness of CA films (Lee and Shiraishi, 2001). The addition of plasticizers to the CA matrix reduces tensile strength (Phuong *et al.*, 2014). Therefore, it could impede the function of CA bio-plastics in specific industries.

Materials and Methods

Waste cigarettes were collected from domestic waste. Glycerol and glacial acetic acid were purchased from the British Drug House (BDH) Chemical Ltd., England. All of the chemicals used in this study were of analytical grade. In all investigations, the recommended standard methods and techniques involving both conventional and modern methods were used.

Preparation of Cellulose Diacetate (CDA) Film

The CDA films were prepared via the solution casting method. Firstly, collected waste cigarette filters were washed with ethanol and hot water several times and then dried at 60 °C. Secondly, the above waste cigarette filters were dissolved in glacial acetic acid at a ratio of 1:15 (w/w) and then treated using an overhead stirrer for 4 h to form a homogeneous emulsion. Subsequently, the different volumes of 0.25, 0.50, 0.75, and 1.00 mL glycerol were added to above emulsion. In addition, the sample without glycerol was used as a comparison. Finally, the obtained solution was poured onto a melamine plate and dried at room temperature to form CDA films. In this work, as-prepared samples were denoted as CDA, CDAG-0.25, CDAG-0.50, CDA-0.75, and CDAG-1.00 according to the volume of glycerol, respectively.

Physical Parameter Measurement of CDA and CDAG Solutions

Determination of pH

Each sample solution was placed into separate beakers. The pH of the solution was measured by using a pH meter at room temperature (Htwe *et al.*, 2021).

Determination of specific gravity

A SG density bottle (50 cm^3) was washed and cleaned with distilled water, thoroughly dried and subsequently weighed. Then the SG bottle was filled with distilled water at room temperature. The stopper was firmly inserted in the bottle, and excess distilled water exiting from the capillary of the stopper was wiped carefully with a piece of tissue paper. Then the bottle containing water was weighed. In order to determine the specific gravity of the sample, the bottle was thoroughly dried and filled with the different CDA solutions at room temperature. The excess solution from the capillary was wiped with the piece of tissue paper and weighed. The specific gravity of different samples was calculated using the following Equation (1) (Htwe *et al.*, 2021).

$$\text{Specific gravity (SG)} = \frac{W_3\text{-}W_1}{W_2\text{-}W_1} \times \text{density of liqud} \qquad (1)$$

where, W_1 is the weight of the density bottle in grams, W_2 is the total weight of the density bottle with distilled water in grams and W_3 is the total weight of the density bottle with sample solution in grams.

Determination of viscosity

About 50 cm^3 of sample solution was placed into the viscometer cup. The solution was kept in a constant temperature bath at 30 ºC and was measured the rotational viscosity (cPs) with VISCO viscometer (Htwe *et al.*, 2021). A VISCO 6800-E07 viscometer, ATAGO, Japan was used for determining the viscosity.

Determination of transparency

The transparency of edible film was measured using a UV spectrophotometer at a wavelength of 550 nm. Film transparency is measured using the method of Bao *et al*. (2009) and the transparency of CDA and CDAG films was calculated using the formula (2):

$$T = A_{550}/x \qquad (2)$$

where, T is transparency, A_{550} is absorbance at a wavelength of 550 nm, and x is film thickness (mm).

Determination of Physicomechanical Properties

The tensile strength, elongation at break and tear strength of the samples were measured on the Tensile testing machine (Hourns Field 5000E), Cutter (Wallace) at room temperature with the rate of moveable jaw 100 mm/min according to JIS K 7127 (1987). Three samples were measured and average values were reported (Htwe *et al.*, 2013).

Determination of Water Uptake (%)

The films to be tested were cut into 1" × 1" size. The cut films were immersed in distilled water at room temperature for the specified period of time. The films were removed from distilled water in a beaker, blotted gently with tissue paper, weighed, and then put back into beaker for the next measurement. The water uptake of different samples was calculated using the Equation (3) (Htwe *et al.*, 2021).

$$\text{Water uptake (\%)} = \frac{W_2\text{-}W_1}{W_1} \times 100\ \% \qquad (3)$$

where, W_1 is the weight of completely dried sample and W_2 is the weight of a swelled sample in distilled water at room temperature for 1 hour.

Determination of Degree of Swelling

The films to be tested were cut into 1" × 1" size. The films were immersed in distilled water at room temperature for the specified period of time. The films were removed from distilled water in a beaker, blotted gently with tissue paper, weighed, and then put back into the beaker for the next measurement. The procedure was continued until no more water was absorbed. Based on these values, swelling (%) was determined. Each experiment was replicated three times. The degree of swelling was determined according to Equation (4).

$$\text{Degree of swelling (\%)} = \frac{W_s - W_d}{W_s} \times 100\ \% \qquad (4)$$

where, W_s and W_d represent the weight of the films after and prior to immersion. All the experiments were carried at room temperature.

Characterization

The surface morphology of CDA materials was studied using SEM (JOE-JSM-5610 LV model, Japan). SEM images of samples were collected under an accelerating voltage of 5 kV. A Fourier transform infrared spectrophotometer (Shimadzu, Japan) was used. The resolution was 4 cm^{-1} with 64- time scanning, and the scanning was performed in the range of 4000–400 cm^{-1}. The X-ray diffraction (XRD) measurements of the different CDA films were recorded using a Shimadzu 8000 X-ray diffractometer (Shimadzu, Japan) with a detector operating under a voltage of 40.0 kV and a current of 30.0 mA using Cu Kα radiation (λ = 0.15418 nm). The recorded range of 2θ was 5–40°, and the scanning speed was 6°/min. The thermal properties of CDA films were characterized by thermogravimetric analysis (TGA) on a thermogravimetric analyzer (Rigaku Thermoplus TG 8120) in the range of 30-600°C at a heating rate of 10°C min^{-1} under N_2 flow.

Antimicrobial activity of CDA Films

The antimicrobial activity of CDA film was carried out by agar disc diffusion method at Pathein University, Myanmar. Eight microorganisms, namely *Escherichia coli, Candida albicans, Bacillus subtilis, Staphylococcus aureus, Pseudomonas fluorescens, Agrobacteriumb tumefaciens, Bacillus pumilus,* and *Micrococcus luteus* were used for this test.

Biodegradable Nature of CDA Films

Biodegradation of prepared CDA film was determined by soil burial test, and weight loss and morphology were examined. The films were cut into 1″ x 1″ dimensions. The films were then accurately weighed and buried in soil at a depth of 5 cm. They were taken out from the soil at an interval of 2 weeks.

Results and Discussion

Physical Parameters of CDA and CDAG Solutions

Figure 1 shows the physical parameters (pH, specific gravity, and refractive index) of different CDA solutions. From the value of pH, it can be observed that different CDA solutions are slightly acidic solutions in the range of 3.13 to 3.50. The specific gravity of different CDA solutions is in the range of 1.12 to 1.14. It can be seen that there are no significant changes in specific gravity. The refractive indices of different CDA solutions are around 1.38. The viscosity of CDA solution is 980.4 cPs for CDA, 915.2 cPs for CDAG-0.25, 912.8 cPs for CDAG-0.50, 912.8 cPs for CDAG-0.75, and 1020.1 cPs for CDAG-1.00 at 25 °C. Thus, all physical parameters of CDAG solutions showed slightly different values.

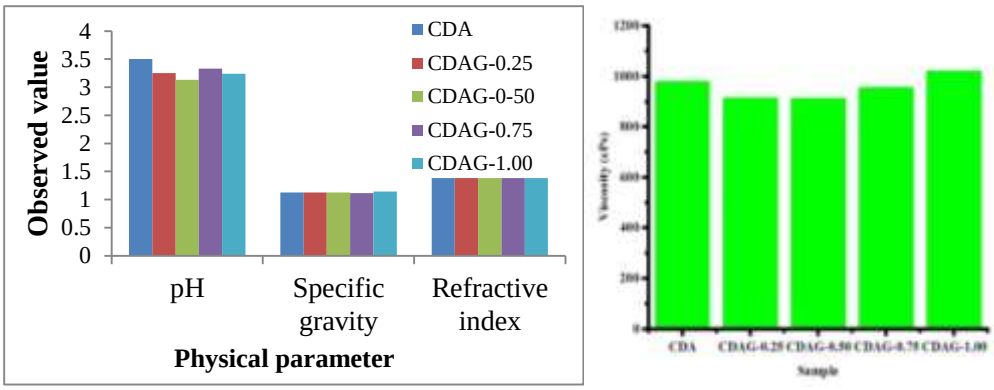

Figure 1. Physicochemical properties of CDA and CDAG solutions

Transparency of CDA and CDAG Films

Transparency is an aesthetic for marketing edible films. Transparency values represent the level of clarity of the films produced (Mustapa *et al.,* 2017). The results of the analysis presented in Figure 2 show that glycerol concentration had a significant effect on the transparency of edible films. The average transparency of CDA film in each treatment is CDAG0 (11.1 %), CDAG0.25 (11.6 %), CDAG0.5 (10.9 %), CDAG0.75 (10.3 %), and CDAG1 (9.8 %).

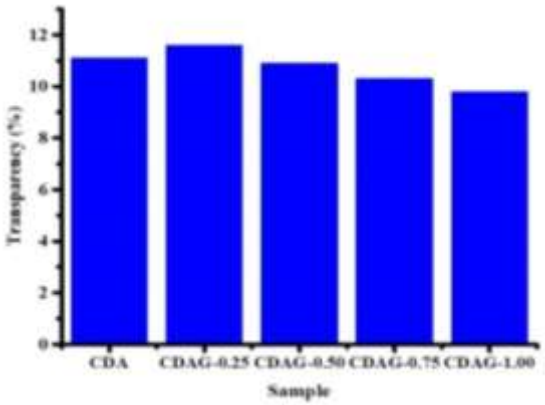

Figure 2. The transparency percentage of CDA and CDAG films

Physicomechanical Properties of CDA and CDAG Films

The physicomechanical properties in terms of tensile strength, elongation at break (%), and tear strength are important parameters which reveal the nature of films. The physicomechanical properties of different CDA films are presented in Figure 3. The thickness of CDA films is in the range of 0.01 mm to 0.05 mm. Tensile strength increased from 8.3 MPa to 52.5 MPa. As shown in figure 3(a), the tensile strengths of the CDA, CDAG-0.25, CDAG-0.50, CDAG-0.75, and CDAG-1.0 films were 8.3, 15, 28, 39.2, and 52.5 MPa, with elongation at break values of 3, 4.2, 8, 5.2, and 6 %, respectively. It can be seen that the tensile strength of all CDAG-0.25, CDAG-0.5, CDAG-0.75, and CDAG-1.0 films was much higher than that of CDA film, and the elongation at break of the former was longer. The sample of CDAG-1.0 with an elongation at break of 6 % had a maximum tensile strength of 52.5 MPa. Interestingly, the tensile strength declined sharply, although the elongation at break continued to increase when the content of glycerol was increased. These results demonstrate that the flexibility of as-prepared films can be improved with an increase in glycerol content. The tear strength is another mechanical property of the nature of films. Figure 3(b) shows the profile of tear strength versus glycerol content. It was found that the tear strength of CDAG film increased significantly and progressively from 0 to 0.75 % v/v glycerol content.

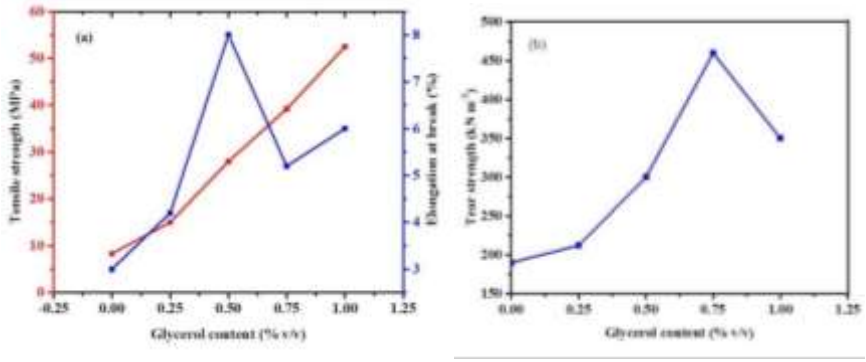

Figure 3. (a) Tensile strength and elongation at break and (b) tear strength of CDA and CDAG films as a function of glycerol concentration

Water Uptake (%)

The degree of water uptake was investigated with increasing immersion time. It was found that the water uptake of all samples was increased by increasing the glycerol content at 50 min. When a film was used as a biodegradable material, one of the most important parameters was water uptake. The water uptake was the amount of water entrapped in the matrix, including bound water (Htwe *et al.*, 2013). Figure 4 shows the water uptake percent for CDAG films. The water uptake of different CDAG films was significantly different according to the various ratios of glycerol compared to those of CDA films. CDAG 0.75 had the highest degree of water uptake content (85.71%) at 50 minutes. The water uptake degree of every CDAG film increased with increasing time. The water uptake may impart stickiness and durability.

Aspect of Degree of Swelling (%)

The degree of swelling of CDAG films is shown in Figure 5 as a function of immersion time in distilled water at room temperature. For a given blended film composition, the degree of swelling mostly increased with increasing immersion time. It can also be observed that the degree of swelling increased with increasing glycerol content in the blended film. The maximum value for the degree of swelling of the CDAG 0.75 film was 45 % at 50 minutes.

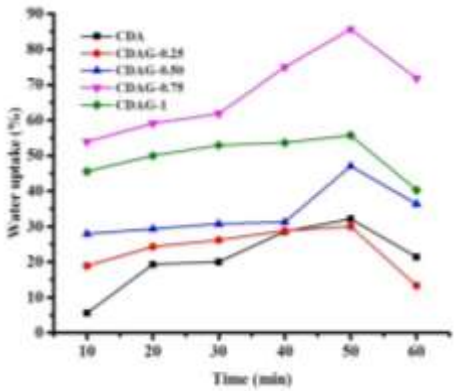

Figure 4. Degree of water uptake percent of CDA and CDAG as a function of contact time

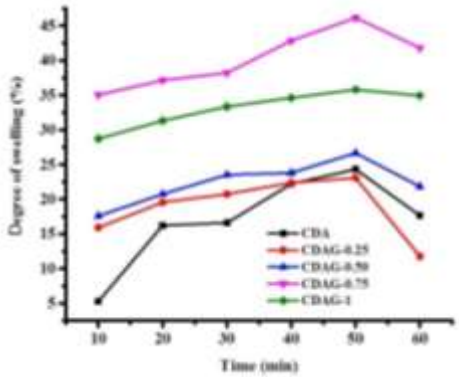

Figure 5. Degree of swelling percent of CDA and CDAG as a function of contact time

Characterization

In this study, CDA films with different ratios of glycerol were chosen and characterized by FT IR and TG-DTA analysis. After that, antimicrobial properties and biodegradable nature of the chosen blend films were determined by the agar disc diffusion method and the soil burial method.

FT IR spectroscopy

Figure 6 depicts the FTIR spectra of CDA, CDAG-0.25, CDAG-0.50, CDAG-0.75, and CDAG-1.00. The CDA film had several distinguishing bands at approximately 1735 cm^{-1}, 1367 cm^{-1}, 1231 cm^{-1}, and 1023 cm^{-1} (Wang *et al.,* 2017). These bands correspond to the stretching vibration of C=O in acetyl groups, the symmetric bending vibration of C-H in methyl groups, the asymmetric stretching vibration of C-O-C in ester groups, and the stretching vibration of C-O-C in the pyranose ring (Rambaldi *et al.*, 2014; Vallejos *et al,* 2012). Because glycerol is an alcohol with a chemical structure that contains CH and OH groups, its incorporation into cellulose acetate may have increased the interactions between the two compounds in the bands that represent these attributes. Because the plasticizer's OH group is available for possible interactions, hydrogen bonds between the OH groups of CA and glycerol may form. In contrast, glycerol has two more OH groups that will not be available for interactions. As a result, the prominent OH band could be related to the increased amount of OH in the film as a result of the glycerol addition (Goncalves *et al.*, 2019). It was found that adding glycerol increased the intensity of the band at 3319 cm^{-1}, corresponding to the stretching vibration of O-H groups. Because glycerol contains O-H groups, hydrogen bonds may form between glycerol and the CDA film. Furthermore, O-H groups that are not involved in glycerol interactions result in a higher content of O-H groups in the CDA film (David and Gong, 2018).

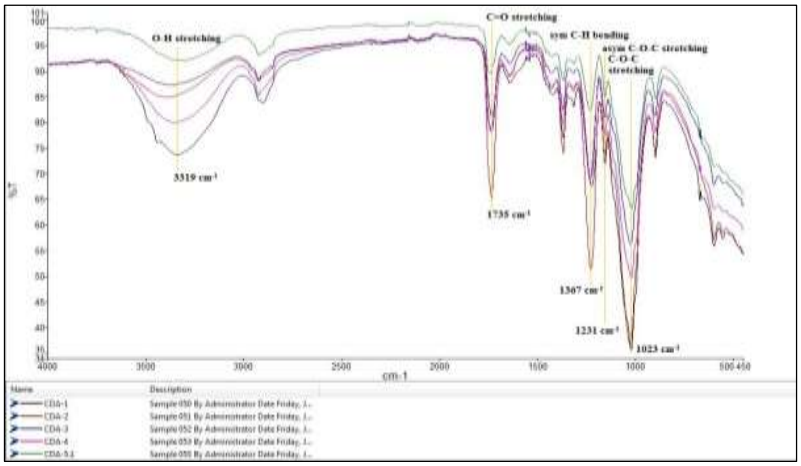

Figure 6. FT IR spectra of CDA and CDAG films

Table 1. The Wavenumber Assignment of CDA and CDAG Films

Samples	C-C & C-H bend	C-O-C stretch	Asym C-O-C stretch	Symmetric C-H bend	C=O stretch	CH stretch	OH stretch
CDA	902.24	1023.80	1227.60	1370.60	1731.60	2904.30	3333.30
CDAG0.25	898.67	1023.80	1224.00	1370.60	1735.20	2922.10	3383.30
CDAG0.50	898.67	1023.80	1227.60	1367.00	1735.20	2925.70	3354.70
CDAG0.75	898.67	1020.20	1234.70	1370.60	1738.80	2918.60	3347.60
CDAG1.0	895.10	1023.80	1231.10	1367.00	1735.20	2922.10	3319.00

* Wang *et al.* 2017 ; Rambaldi *et al.* 2014 ; Goncalves *et al.*, 2019

X-ray diffraction analysis

The XRD patterns of CDA, CDAG-0.25, CDAG-0.5, CDAG-0.75, and CDAG-1.0 are shown in Figure 7. There was an obvious peak at 21.9 for CDA/glycerol films, and the CDA peak at 21.9 was much weaker. This research shows that a single CDA film has low crystallinity and that glycerol can improve the crystallinity of composite films. Glycerol can disrupt the CDA chain arrangement and form hydrogen bonds between them. Figure 8 depicts an illustration of the glycerol-CDA reaction process. Glycerol disrupts CDA chain arrangement, and then-OH groups in glycerol combine with oxygen-containing groups in CDA chains to form hydrogen bonds (Zhang *et al.*, 2020).

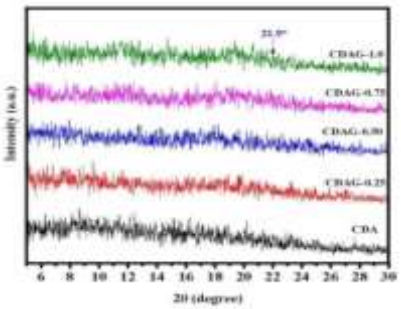

Figure 7. XRD patterns of different CDAG films

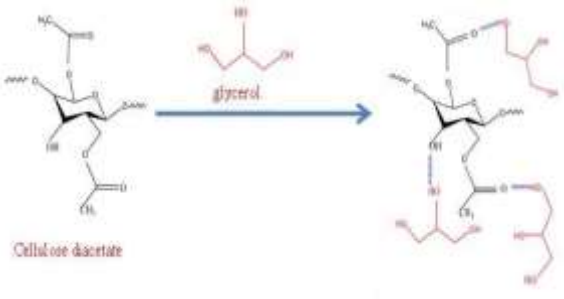

Figure 8. The illustration for the reaction of glycerol and CDA chains (Zhang *et al.*, 2020)

SEM Analysis

The morphology of the prepared CDA, CDAG-0.25, CDAG-0.50, CDAG-0.75 and CDAG-1.0 was examined using scanning electron micrographs (SEM). The surfaces of CDA, CDAG-0.25, CDAG-0.50, CDAG-0.75, and CDAG-1.0 have a generally smooth morphology, as shown in Figures 9a-e. It was found that CDA film had a smoother surface than other films (Figure. 9a). However, some small pores and depressions were found on the surface of CDA/glycerol films (in Figure. 9b-e). Furthermore, as the glycerol content increased from 0.25 % to 1.0 %, the number of pores also increased. The surface morphologies of the films changed slightly when the glycerol content exceeded 1.0%. This is because glycerol-adsorbed water evaporates during the drying process of CDA films (Zhang *et al.*, 2020).

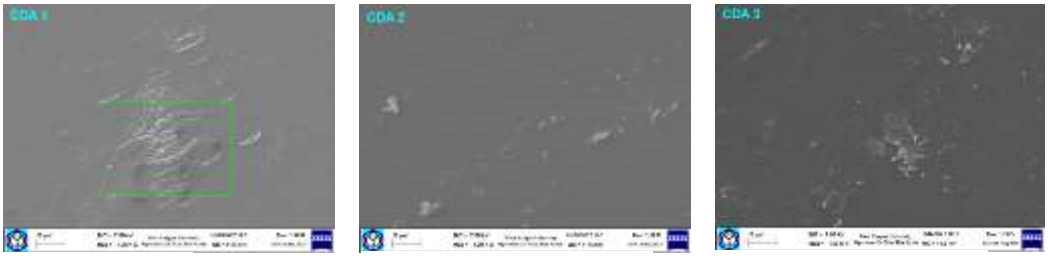

(a) CDA (b) CDAG-0.25 (c) CDAG-0.50

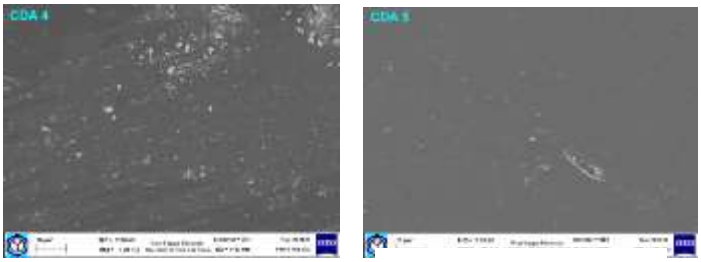

(d) CDAG-0.75 (e) CDAG-1.00

Figure 9. SEM images of CDA and different CDAG films

TG-DTA analysis

The thermal stability of CDA films with varying glycerol ratios (CDAG-0.25, CDAG-0.50, CDAG-0.75, and CDAG-1.00) was investigated using thermogravimetric analysis, as shown in Figures 10(a) and (b). As seen in Figures 10(a) and (b), the thermal stability of as-prepared CDAG films was assessed by TGA and DTG. As shown in Figure. 10(a), the thermal decomposition of CDA film includes two main stages. Firstly, CDA film has a total weight loss of 2.61 % in the range of 39 °C to 150 °C. This is due to evaporation of water. When the temperature exceeded 280 °C, the polymer chains for the CDA began to decompose, losing 83.88% of their weight, resulting in exothermic peaks in Figure 9(b) at 347 °C and 503 °C. Figure 10(a) shows the thermal degradation of CDAG films, which behave similarly to CDA films, in three stages: the first stage shows a total weight loss of 5.85% for CDAG-0.25, 4.26% for CDAG-0.50, 5.80% for CDAG-0.75, and 4.69% for CDAG-1.00 in the range of 39 °C to 150 °C. This is due to the evaporation of water on the film and moisture in glycerol. In the second stage, the loss in weight of 82.42 % for CDAG-0.25, 80.35 % for CDAG-0.50, 73.71 % for CDAG-0.75 and 79.60 % for CDAG-1.00 were observed to take place within the temperature range of 288 °C to 380 °C. Sharp exothermic peaks are shown in Figure 9(b) at 363 °C (CDAG-0.25), 347 °C (CDAG-0.50), 336 °C (CDAG-0.75), and 353 °C (CDAG-1.00). This is due to the thermal degradation of glycerol molecules. According to the CDAG curves in Figure 10(a), the third stage temperature range between 380 °C and 600 °C lost 4.76% for CDAG-0.25, 12.75% for CDAG-0.50, 12.43% for CDAG-0.75, and 9.52% for CDAG-1.00, corresponding to exothermic peaks at 456 °C (CDAG-0.25 in Figure 10(b)) and 486 °C (CDAG-0.50 in Figure 9(b)), 446 °C (CDAG-0.75 in Figure 10(b)) and 486 °C (CDAG-1.00 in Figure 10(b)). This is due to the thermal degradation of CDA chains. Interestingly, it was found that the residual weight of CDA films after adding glycerol increased. However, the weight loss of CDAG films was greater than that of CDA film before 300 °C, which was attributed to the evaporation of water in glycerol. The added plasticizer reduces the intermolecular forces between CDA chains (Zhang *et al.*, 2020).

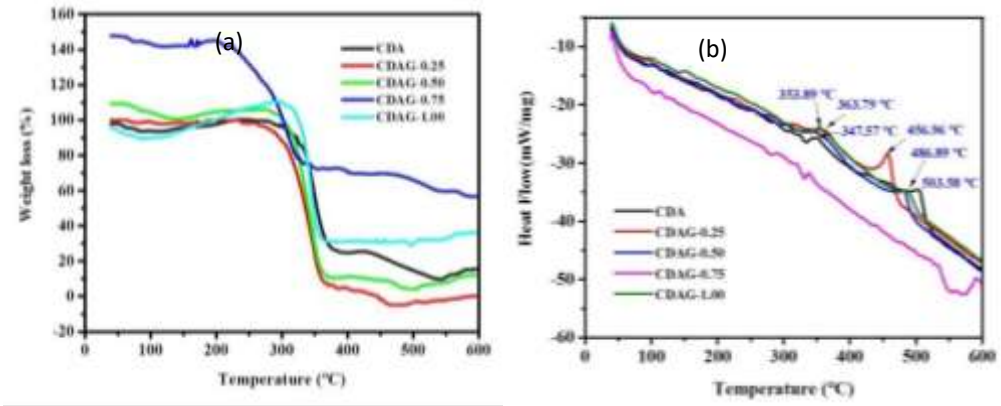

Figure 10. (a)TG curves (b) DTA curves for CDA and CDAG films

Antimicrobial Activity of CDA and CDAG Film

Pure CDA and CDAG films were screened for antimicrobial activity against eight different pathogenic microbes (Figure 11). It was observed that all of the films did not show any antimicrobial activity except *Bacillus subtilis* and *Escherichia coli* for CDA film and *Escherichia coli* for CDAG-0.25 film against all of the microorganisms tested. Eight microorganisms with the

inhibition zone diameter ranging below 10 mm for all of the films. According to results, CDA and CDAG-0.25 films possessed pronounced activity against *Bacillus subtilis, and Escherichia coli.*

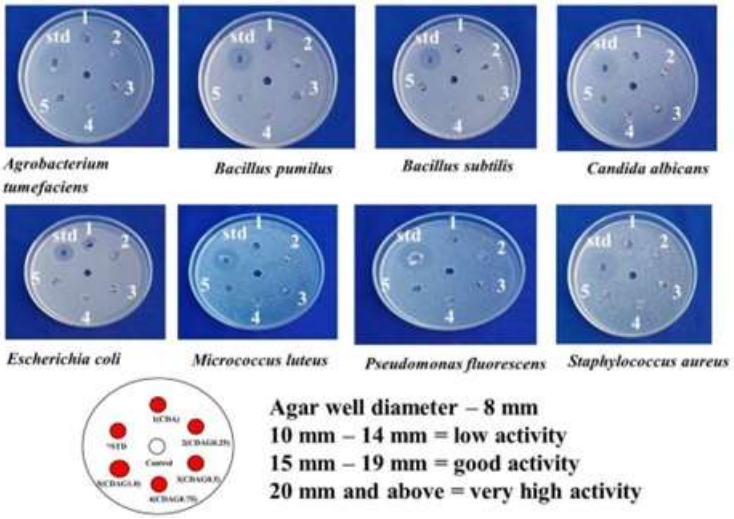

Figure 11. Photo records showing inhibition zone due to the effect of CDA and CDAG films

Biodegradation test by soil burial

The biodegradability of CDA and CDAG films was tested by the soil burial method under natural soil condition (pH = 6.95). As described above, environmental effects mentioned in this work are moisture and soil which may be favorable conditions for the microbial growth (Gu *et al.*, 2000). Soil burial is a traditional method to test samples for degradation because of its similarity to actual condition of waste disposal. Uniformly sized samples were buried in the soil from waste disposal. The physical appearances of blended films after buried in the soil are shown in Figure 12.

Figure 12 shows biodegradation nature of different CDAG films within one month interval. There, the weight loss was about 10.3%, 14.1 %, 10.2%, 15.2 % and 14.4 % of CDA, CDAG-0.25, CDAG-0.50, CDAG-0.75, and CDAG-1.00 after 2nd week. After 4 weeks, it was found that the weight loss was about 84.2 %, 89.6 %, 90.2 %, 91.0 % and 90.6 % of CDA, CDAG-0.25, CDAG-0.50, CDAG-0.75, and CDAG-1.00. It can be seen with slight degradation, before 2 weeks. However, quite deformation of CDA film appeared after 2 weeks. From this investigation, it was expected that these films would be degradable in soil in more than one month. One of the objectives of the development of CDA is to remove easy-to-throwaway materials from degradable plastic to alleviate the waste disposal problem through environmental degradation.

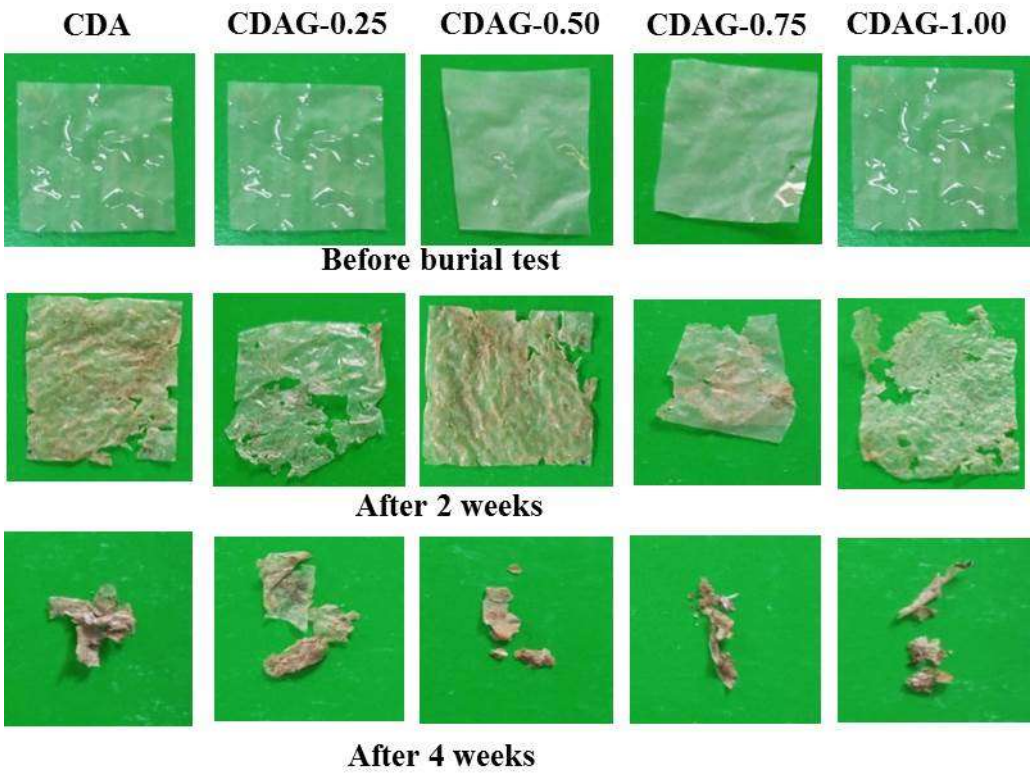

Figure 12. The physical appearances of CDA and CDAG films

Conclusion

Waste cigarette filters were recycled to prepare an excellent cellulose diacetate film. Glycerol significantly improved the mechanical properties of CDA films. When the glycerol volume content was 1 mL, the as-prepared film with a 6% elongation at break had the highest tensile strength of 52.5 MPa. Furthermore, the swelling and water uptake of the film demonstrated a higher degree of hydration, as measured by swelling and water uptake, which can be varied by varying the volume percentage of glycerol in the film matrix. FT IR and XRD analysis indicated that hydrogen bonds were formed between CDA chains and glycerol. From TG-DTA analysis, CDAG films exhibited better thermal stability. SEM images revealed that glycerol caused the formation of small pores in films, and the number of pores increased as the glycerol content increased. The CDA and CDAG films were tested for their antimicrobial activities by using the agar disc diffusion method. It can be noted that all of the microbial agents that came into contact with films did not possess pronounced activity. By using the soil burial techniques, it was found that a significant deformation of CDA and CDAG films had occurred at 4 weeks. According to these results, CDA and CDAG films can be made from used cigarette filters and are a good replacement for packaging film.

Acknowledgements

The authors owe their gratitude to Professor Dr Ni Ni Than, Head of Department, Department of Chemistry, University of Yangon, Yangon, Myanmar, for her stimulating suggestions.

References

Arroyo, F. D., C. F. Guerrero, and U. L. Silva. (2020). "Thin Films of Cellulose Acetate Nanofibers from Cigarette Butt Waste". *Progress in Rubber Plastics and Recycling Technology*, vol. 36(1), pp. 3-17

Bao, S., S. Xu, and Z. Wang. (2009). " Antioxidant Activity and Properties of Gelatin Films Incorporated with Tea Polyphenol-Loaded Chitosan Nanoparticles". *Journal of the Science of Food and Agriculture*, vol. 89, pp. 2692-2700

Boulven, M., G. Quintard, A. Cottaz, C. Joly, A. Charlot, and E. Fleury. (2019). "Homogeneous Acylation of Cellulose Diacetate: Towards Bioplastics with Tuneable Thermal and Water Transport Properties". *Carbohydrate Polymers*, vol. 206, pp. 674-684

Cindradewi, A. W., R. Bandi, C. W. Park, J. S. Park, E. A. Lee, J. K. Kim, G. J. Kwon, S. Y. Han, and S. H. Lee. (2021). "Preparation and Characterization of Cellulose Acetate Film Reinforced with Cellulose Nanofibril". *Polymers*, vol. 13(2990), pp. 1-14

David, B.K.L., and H. Gong. (2018). "Highly Stretchable and Transparent Films Based on Cellulose". *Carbohydr. Polym.*, vol. 201, pp. 446-453

Erdmann, R., S. Kabasci, and H. P. Heim. (2021). "Thermal Properties of Pasticized Cellulose Acetate and Its Relaxation Phenomenon**".** *Polymers,* vol. 13(1356), pp. 1 – 14

Goncalves, S. M., D. C. dos Santos, J. F. G. Motta, R. R. dos Santos, D. W. H. Chavez, and N. R. de Melo. (2019). "Structure and Functional Properties of Cellulose Acetate Films Incorporated with Glycerol". *Carbohydrate Polymers*, vol. 209, pp. 190-197

Htwe, A. T., M. Htwe, S. Maung, and M. N. Tun. (2021). "Study on Biodegradable and Antimicrobial Properties of Biowaste Chitin-Polyvinyl Alcohol Blended Film". *ASEAN Engineering Journal*, vol. 11(3), pp. 127-139

Htwe, A. T., S. Tun, K. A. May, and K. M. Naing. (2013). "Studies on preparation, characterization and application of pH-sensitive biodegradable chitosan-polyvinyl alcohol hydrogel". *Jour. Myan. Acad. Arts & Sc,* vol. XI(1), pp. 127-140

Lee, S. H., and N. Shiraishi. (2001). "Plasticization of Cellulose Diacetate by Reaction with Maleic Anhydride, Glycerol, and Citrate Esters during Melt Processing". *Journal of Applied Polymer Science*, vol. 81, pp. 243-250

Phuong, V. T., S. Verstichel, P. Cinelli, I. Anguillesi, M. B. Coltelli, and A. Lazzeri. (2014). "Cellulose Acetate Blends- Effect of Plasticizers on Properties and Biodegradability". *J. Renew. Mater.*, vol. 2, pp. 35-41

Rambaldi, D.C., C. Suryawanshi, C. Eng, and F.D. Preusser. (2014). "Effect of Thermal and Photochemical Degradation Strategies on the Deterioration of Cellulose Diacetate". *Polym.Degrad. Stab.*, vol. 107, pp. 237-245

Teixeira, S. C., R. R. A. Silva, T. V. Oliveira, P. C. Stringheta, M. R. M. R. Pinto, and N. D. F. F. Soares. (2021). "Glycerol and Triethyl Citrate Plasticizer Effects on Molecular, Thermal, Mechanical, and Barrier Properties of Cellulose Acetate Films". *Food Bioscience*, vol. 42(101202), pp. 1-10

Vallejos, M.E., M.S. Peresin, and O.J. Rojas. (2012). "All Cellulose Composite Fibers Obtained by Electrospinning Dispersions of Cellulose Acetate and Cellulose Nanocrystals". *J. Polym. Environ.*, vol. 20, pp. 1075-1083

Wang, W., T. Liang, H. Bai, W. Dong, and X. Liu. (2017). "All Cellulose Composites Based on Cellulose Diacetate and Nanofibrillated Cellulose Prepared by Alkali Treatment". *Carbohydrate Polymers*, vol. 179, pp. 297-304

Zhang, Q., C. Fang, Y. Cheng, J. Chen, Z. Huang, and H. Han. (2020). "Construction and Properties of Cellulose Diacetate Film". *Cellulose*, vol. 27, pp. 8899-8907

STUDY ON PHOTOCATALYTIC PROPERTIES OF BISMUTH OXYCHLORIDE CATALYSTS

Aye Aye Lwin[1], Aung Khaing[2]*, Aung Than Htwe [2]

Abstract

Well-crystallized flake-like bismuth oxychloride nanoparticles (BiOCl NPs) were successfully synthesized by a solvothermal process using bismuth(III) nitrate pentahydrate ($Bi(NO_3)_3.5H_2O$) and potassium chloride (KCl) with various ratios of ethanol and distilled water (10:90, 25:75, 50:50, 75:25, and 90:10 v/v). The synthesized BiOCl NPs were characterized by using XRD, SEM, UV-visible, FT IR and TG-DTA analysis. Degradation of Rhodamine B and Eriochrome Black T in aqueous media was estimated spectrophotometrically in the visible range at 553 and 545 nm, respectively. Among them, BiOCl-4 showed the highest photodegradation performance under UV light exposure due to the formation of nanosheets. The mechanism of synthesized BiOCl-4 is evaluated by conduction band and valence band values. So, the synthesized BiOCl NPs can be used as photocatalysts in the photodegradation of aqueous organic dyes.

Keywords: BiOCl NPs, solvothermal process, photodegradation, organic dyes

Introduction

Nanoparticles (NPs) are assigned as nanoentries whose size ranges from 1 to 100 nm. According to their smaller size, nanoparticles present a much higher specific surface area because the total surface area of a particle is inversely proportional to its diameter. Nanoparticles have promising potential for use in various applications due to their unusual characteristics compared to bulk materials. Nanotechnology is used in the creation, investigation, and application of new types of materials, called nanomaterials. Nanomaterials are used in industrial chemistry, agriculture engineering, pharmaceutics, and medicine (Dudchenko *et al.*, 2022). Bismuth oxychloride nanoparticles were used to degrade pollutants such as pesticides, antibiotics, heavy metal ions, and microorganisms. BiOCl nanoparticles have a unique layered structure, electronic properties, optical properties, good photocatalytic activity, and stability (Wang *et al*., 2022).

Bismuth oxyhalides, BiOX (X= Cl, Br, I), have been found useful in various applications because of their optical properties, such as as photocatalysts. BiOX belongs to the V-VI-VII groups of compound semiconductors with a tetragonal system. The structure of BiOX is known to have a layered structure that is constructed by combining the halide ion layer and the bismuth oxygen layer (Tripathi *et al*., 2015). It has exhibited wide applications as a pigment in the cosmetic industry, a photocatalyst in degrading organic pollutants, and for optoelectronic and photovoltaic devices, e.g., light-emitting diodes, lasers, and solar cells (Cao *et al.*, 2009). Bismuth oxychloride (BiOCl), with a band gap energy of 3.5 eV, has been used as a catalyst for the oxidative cracking of hydrocarbons and photoluminescent materials. BiOCl nanoparticles can be an efficient photocatalyst for decomposing methyl orange under UV light.

Materials and Methods

Bismuth (III) nitrate pentahydrate, $Bi(NO_3)_3.5H_2O$, potassium chloride (KCl), ethanol, (EtOH) and ammonia (NH_3) were of analytical grade and used directly without further purification. Distilled water was used throughout all the experiments.

[1] Department of Chemistry, University of Yangon, Myanmar
[2] Department of Chemistry, University of Yangon, Myanmar

Synthesis of BiOCl NPs

To synthesize the first sample of BiOCl, 100 mL of bismuth nitrate solution was prepared by dissolving 4 g of $Bi(NO_3)_3.5H_2O$ in the first solvent, i.e., ethanol: water: (10:90), and 50 mL of KCl solution was prepared by dissolving 0.75 g of KCl in (10:90) ($EtOH:H_2O$). $Bi(NO_3)_3.5H_2O$ solution was taken in a conical flask and placed on the magnetic stirrer. KCl solution was allowed to flow into the Bi $(NO_3)_3.5H_2O$ solution in the conical flask at 2.5 mL min^{-1} with continuous stirring. After the complete addition of 50 mL KCl solution, 5 mL of 25 % NH_3 solution was added to maintain the pH of the mixture at 2, and stirring was further continued for 10 h to ensure the completion of the reaction, i.e., the precipitation of bismuth oxychloride. The resulting precipitates were collected by filtration and washed several times with distilled water for complete removal of undesirable water-soluble products. Solid compound so obtained was subsequently dried at 80 ˚C for 24 h in an oven. The above procedure was repeated to synthesize four other samples of BiOCl using the solvent composition ethanol: water as 25:75, 50:50, 75:25, and 90:10 (v/v).

Characterization

The crystal phases of the BiOCl NPs were analyzed by using an X-ray powder diffractometer (XRD). The surface morphology of synthesized samples was observed with scanning electron microscope (SEM) (EVO-18, Probe Micro Analyzer, Germany). Fourier transform infrared spectroscopy (FT IR) was measured for functional group estimation using (FT IR-8400, PerkinElmer GX system; USA). The wavelengths of maximum absorption of synthesized BiOCl NPs were determined by UV-Vis spectroscopy (UV-mini 1240). Finally, the weight loss of BiOCl NPs was measured by using TG-DTA.

Photocatalytic Activity

The photocatalytic efficiency of BiOCl NPs was assessed with a degradation of Rhodamine B (RhB) and Eriochrome Black T (EBT) using Ultraviolet light irradiation. In a process, 30 mg of BiOCl NPs were added to 50 mL of solution containing 200 mgL^{-1} RhB and EBT dye concentration. The solution was stirred for 30 min in the dark. After that, the solution was exposed to UV light. The 3 mL each of RhB and EBT dye samples were taken at 3 min intervals and instantly centrifuged at 1000 rpm for 2 min to isolate the photocatalyst particles. Finally, absorbance of the dye sample was noted at UV visible spectrophotometer at 553 nm (RhB) and 545 nm (EBT) wavelengths.

Results and Discussion

Structure of BiOCl NPs

X-ray power diffraction peaks were analyzed to investigate the phase structure of synthesized BiOCl NPs, as shown in Figure 1. The diffraction peaks of synthesized samples appear at 2θ values, which match with (hkl) values according to entry card no. (96-450-9950) corresponding to the tetragonal system, respectively (Sharma *et al*., 2015). Four characteristic peaks of BiOCl were observed around 2θ of 11.98˚, 25.81˚, 32.48˚, and 34.50˚ corresponding to Miller indices of (001), (101), (110), and (012) planes, respectively, which are in good agreement with the planes of BiOCl obtained from the entry card number. XRD data confirmed the formation of a crystalline tetragonal phase of BiOCl NPs . Using Scherrer's equation, the average crystallite sizes were determined to be 19.98 nm for BiOCl-1, 28.86 nm for BiOCl-2, 20.24 nm for BiOCl-3, 32.23 nm for BiOCl-4, and 21.24 nm for BiOCl-5.

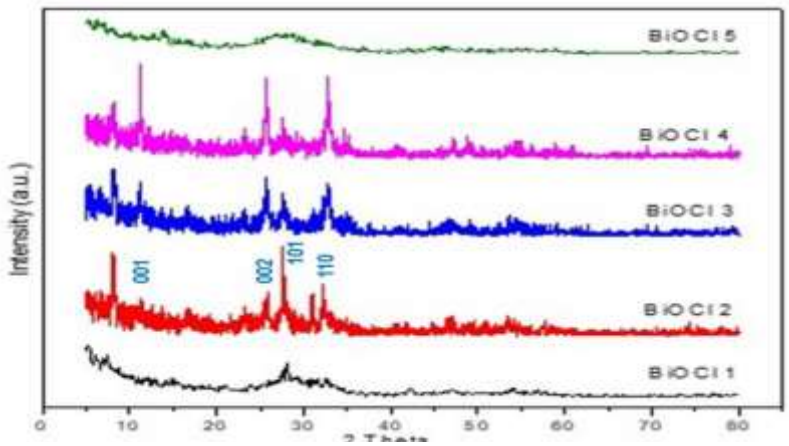

Figure 1. XRD patterns of synthesized BiOCl

FT IR Spectroscopy

The results of the FT IR spectra analysis of the synthesized BiOCl-1, BiOCl-2, BiOCl-3, BiOCl-4, and BiOCl-5 samples are shown in Figure 2. As shown in Figures 2(a to e), the absorption bands of all BiOCl samples were observed in the range 1400-1600 cm^{-1}, which can be assigned to the skeletal stretching vibration mode of Bi-Cl. The characteristic peak of 1155 cm^{-1} can be assigned to the stretching vibration mode of Bi-Cl, and 512 cm^{-1} can be assigned to the vibration mode of Bi-O (Seddigi *et al*., 2017).

UV-Vis Absorption Spectra

The UV-Vis spectra (Figure 3) of BiOCl NPs show absorption maxima between 210 and 275 nm due to the n to π* electronic transition of synthesized BiOCl NPs. The other peak of 254 nm was due to the ethanol solvent effect (Silverstein and Webster, 1998; Schwartz, 1965).

Morphology of BiOCl NPs

Figure 4 shows the SEM images of synthesized BiOCl-1 to 5 NPs in different solvents by the solvothermal method, respectively. These images were obtained at a 7 kV accelerating voltage with 20,00 times magnification. The synthesized samples consisted of a large number of flake- like nanosheets. According to SEM images, the porosity of BiOCl-1 has the highest value compared to other samples.

But BiOCl-4 has the highest flake-like nanosheet and cluster of aggregation because it depends on the ethanol- solvent ratio (75:25). BiOCl-1 is bulky and clustered in its amorphous form. BiOCl-2 has a bulky shape with aggregation. BiOCl-3 belongs to a flake-like aggregation cluster. BiOCl-5 has a rod-like shape and a cluster of nanorod.

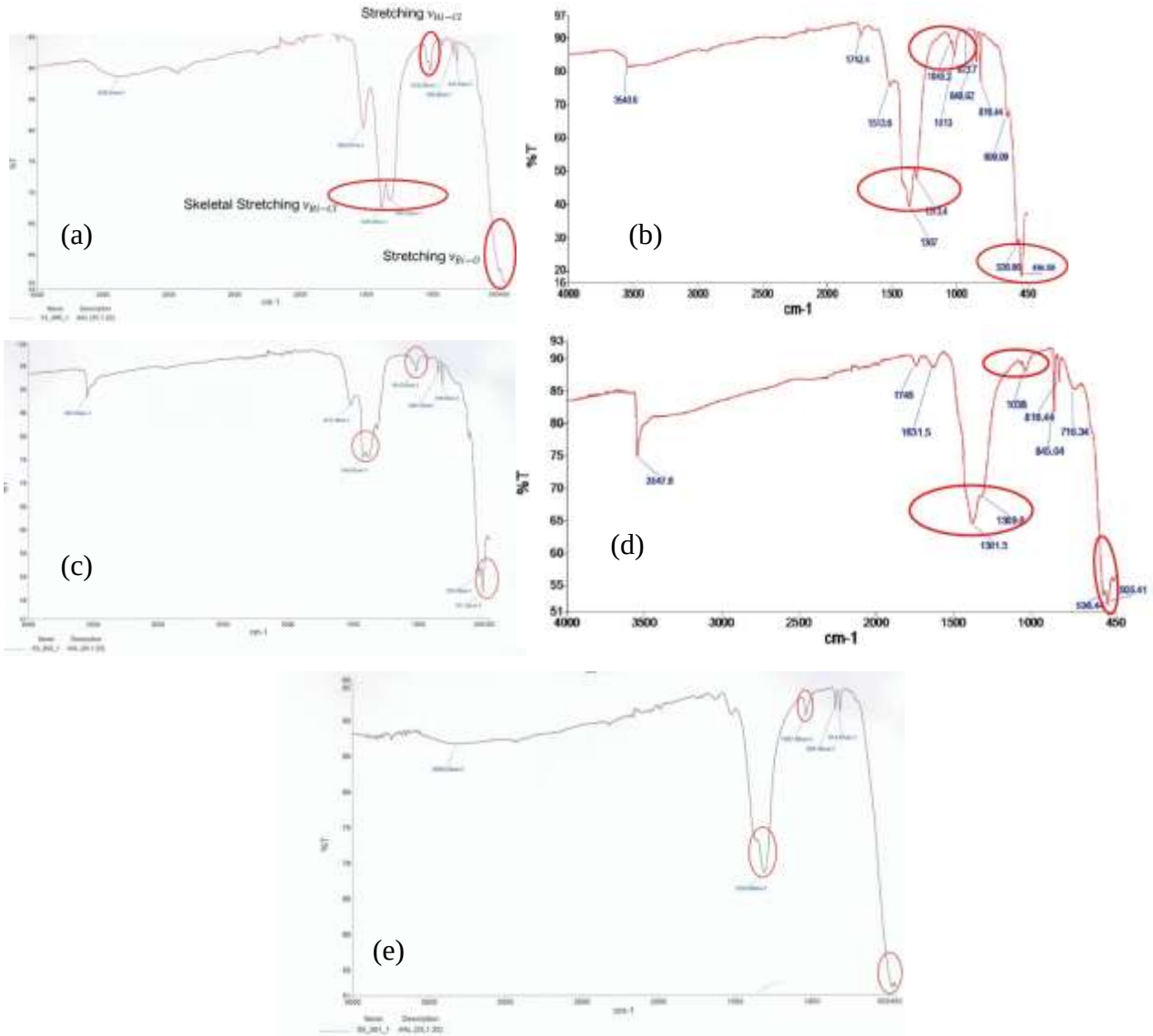

Figure 2. FT IR spectra of (a) BiOCl-1, (b) BiOCl-2, (c) BiOCl-3, (d) BiOCl-4, and (e) BiOCl-5

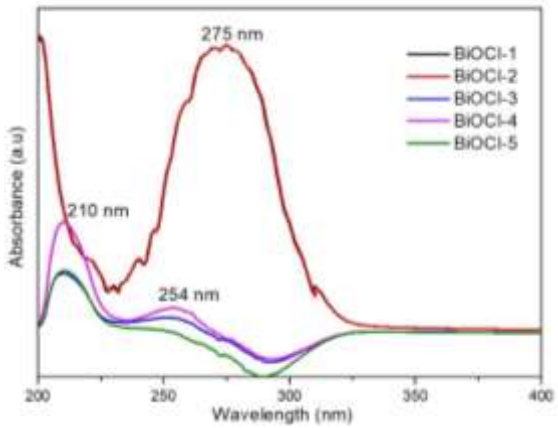

Figure 3. UV-vis spectra of synthesized BiOCl NPs

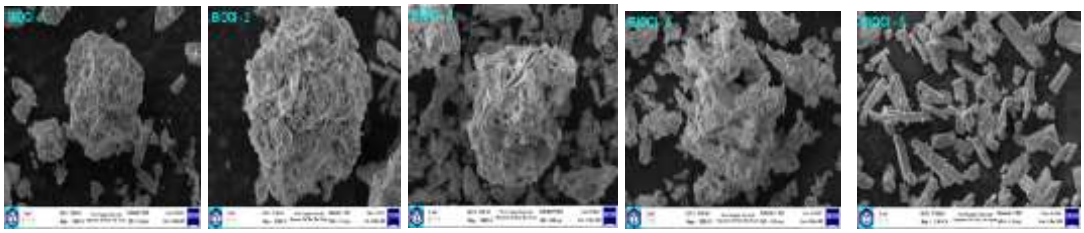

Figure 4. SEM images of BiOCl NPs

Optical Properties of Synthesized BiOCl NPs

As the ethanol solvent increases to 75 %, the absorption wavelength of BiOCl-4 increases to 254 nm. The band gap energy of semiconductor can be calculated approximately by using the Tauc Plot, $(\alpha h\nu)^2$ vs $h\nu$, where α, h, and ν are the absorption coefficient, Planck's constant, and light frequency, respectively. As can be seen in Figure 5, E_g values of BiOCl NPs gradually decrease with increasing ratio of the ethanol to 90 %, changing from 4.06 to 3.6 eV as determined from a plot of $(\alpha h\nu)^2$ vs $h\nu$. According to the literature, the common band gap value of BiOCl is 3.2 eV. In this work, the band gap value of BiOCl NPs reduced from 4.06 eV to 3.7 eV. It can be compared with the literature value of 3.2 eV; the band gap value of synthesized BiOCl-4 is in close agreement with the earlier reports (Tripathi *et al*., 2015). From these results, it can be deduced that all the synthesized BiOCl NPs 1 to 5 have suitable band gaps to be activated by ultraviolet light for photocatalytic decomposition of organic and inorganic pollutants.

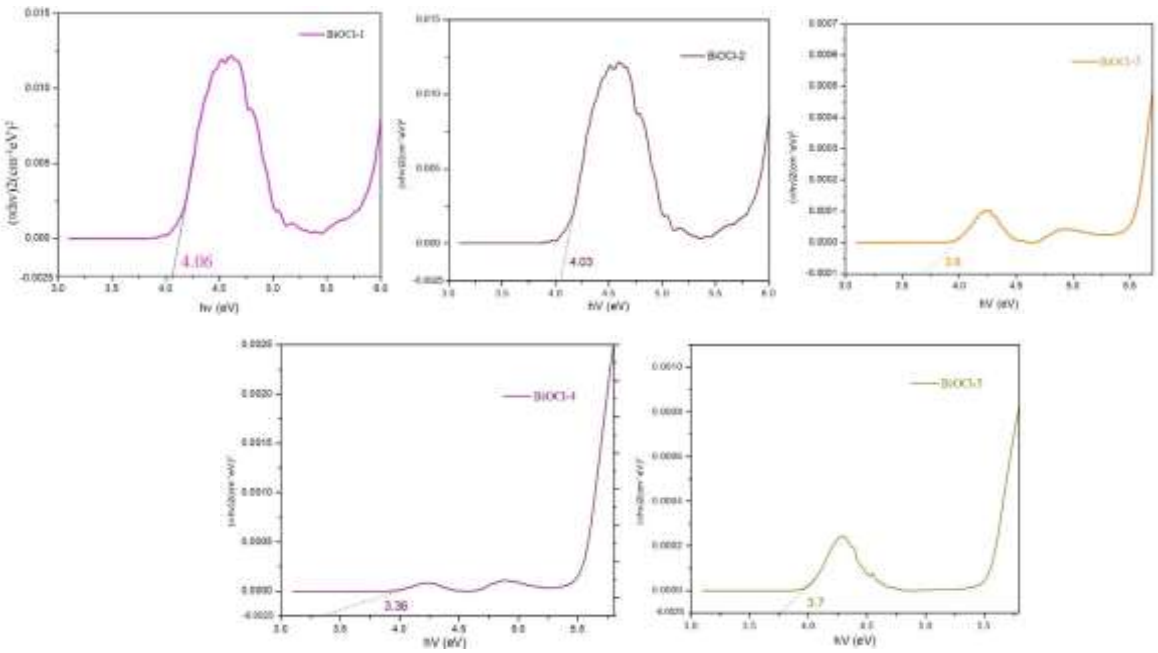

Figure 5. Tauc plots of BiOCl NPs 1 to 5

Thermogravimetric analysis

Thermogravimetric (TG) and differential thermal analysis (DTA) thermograms of synthesized BiOCl NPs were carried out at room temperature up to 80 ºC. TG-DTA thermogram profiles of the BiOCl NPs are shown in Figure 6(a to e). All of the BiOCl NPs cause weight loss in three stages. The first stage range is about 38 ºC to 88 ºC with weight loss of 0.93 % for BiOCl-1, 1.34 % for BiOCl-2, 0.41 % for BiOCl-3, 0.49 % for BiOCl-4, and 1.69 % for BiOCl-5. There is a loss of surface water.

In the second stage of the temperature range between 88 ºC and 216 ºC the weight losses were observed to be 10.30 % for BiOCl-1, 6.01 % for BiOCl-2, 3.48 % for BiOCl-3, 2.15 % for BiOCl-4, and 2.38 % for BiOCl-5. This is due to the evaporation of water and the surface of NO_3 group adsorbed on the BiOCl NPs. The third stage is the weight loss of 7.81 % for BiOCl-1, 3.00 % for BiOCl-2, 2.99 % for BiOCl-3, 2.54 % for BiOCl-4, and 3.90 % for BiOCl-5 which were observed to take place within the temperature range of 218 ºC to 329 ºC. At this stage, the weight loss may be due to complete combustion of residue at an exothermic temperature of about 314 ºC.

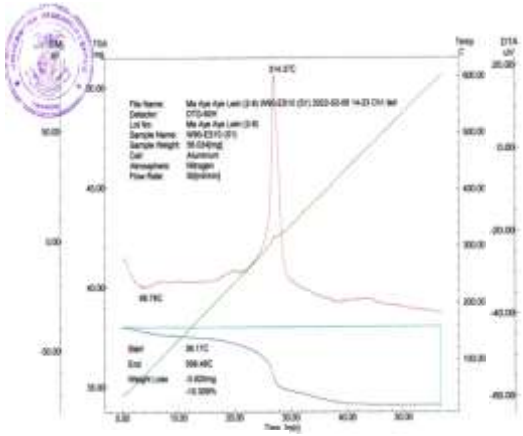

(a) BiOCl-1

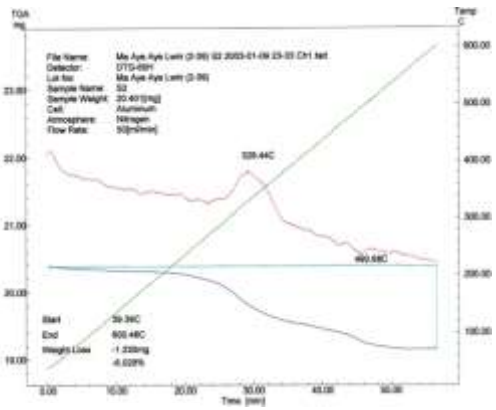

(b) BiOCl-2

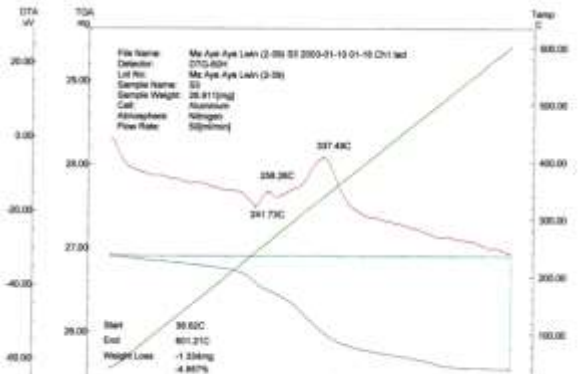

(c) BiOCl-3

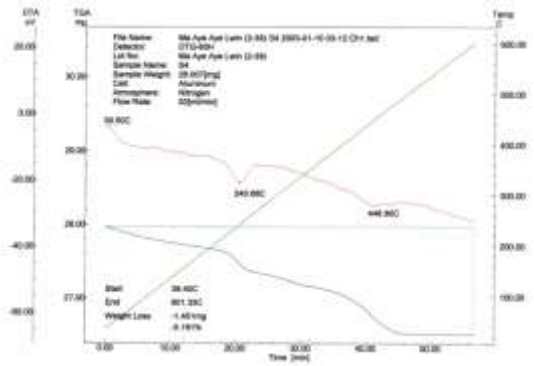

(d) BiOCl-4

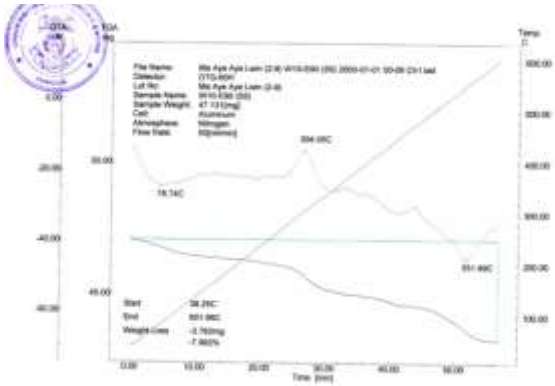

(e) BiOCl-5

Figure 6. TG -DTA thermogram of BiOCl NPs

Photocatalytic Performance of BiOCl NPs on RhB and EBT

The photocatalytic activity of the synthesized BiOCl NPs was evaluated by the estimation of RhB and EBT present in the solution after different durations of ultraviolet light exposure, which were subsequently related to the amount of dye degraded in a specific interval of time under identical exposure conditions. For synthesized samples, the photocatalytic performance was gradually enhanced as the ethanol ratio increased from 10% to 75%. Among all the samples, the concentrations of BiOCl-3 (~0.0509) and BiOCl-4 (~0.0063) showed the highest photocatalytic activity of ~0.0063 on RhB and the concentration of BiOCl-4 (~0.015) and BiOCl-5 (~0.051) showed the highest photocatalytic activity of ~0.015 on EBT. As seen in Figure 7, the catalytic efficiency can achieve ~100 % removal within 1 h on RhB and 30 min on EBT. The ethanol ratio was increased to 75 %, leading to an increase in photocatalytic degradation activity.

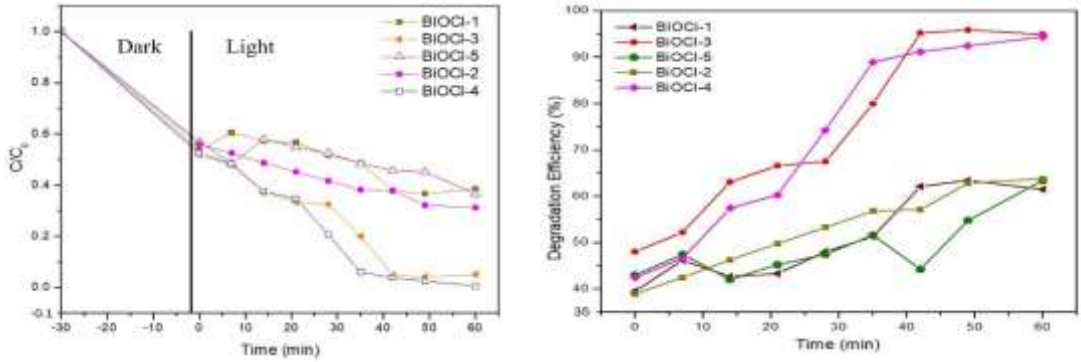

(a)

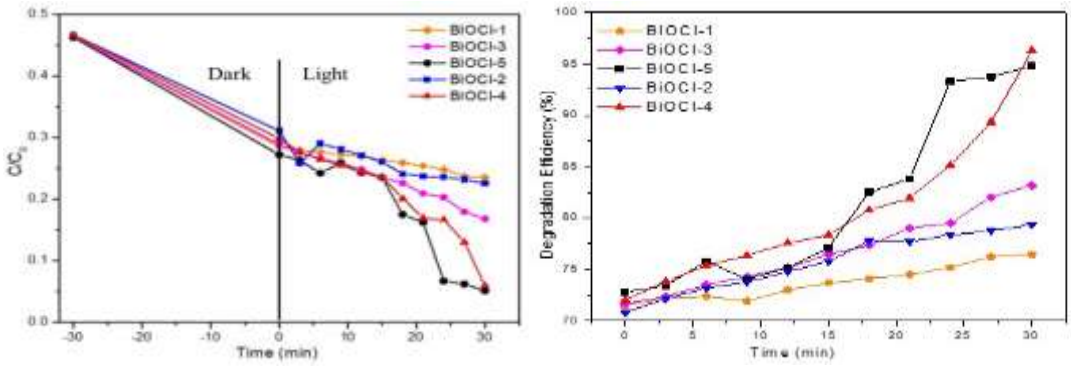

(b)

Figure 7. Comparison of photocatalytic activity and degradation efficiency of BiOCl 1 to 5 for degradation performance with (a) RhB and (b)EBT under UV light irradiation

Mechanism of Photocatalytic Activity of Synthesized BiOCl-4 NPs

The mechanism of the photocatalytic activity of BiOCl-4 can be attributed to electron and hole recombination. The conduction band (CB) and valence band (VB) for a semiconductor can be calculated according to the following theoretical empirical formulae

$$E_{CB} = \chi - E^e - 0.5E_g$$

$$E_{VB} = E_{CB} + E_g$$

where E_{CB} is the conduction band (CB) energy; χ is the absolute electronegativity of the constituent atoms, expressed as the arithmetic mean of the atomic electron affinity and the first ionization energy; E^e is the energy of free electrons on the hydrogen scale (~4.5 eV); E_g is the band gap energy of the semiconductor; E_{VB} is the valence band (VB) energy. The band gap energy value for BiOCl-4 is 3.36 eV (Table 1).

Table 1. Absolute Electronegativity, Calculated Conduction Band, Valence Band and Band Gap energy for BiOCl-4

Semiconductors	Absolute electronegativity (χ) (eV)	Calculated CB energy (eV)	Calculated VB energy (eV)	Band gap energy, E_g (eV)
BiOCl-4	6.36	0.46	3.82	3.36

When the BiOCl nanosheet is irradiated by UV light, holes in the VB will be created as the electrons in the VB get excited and jump to the CB (Dan-Iya and Soylu, 2019). The generated electrons (e^-) react with dissolved oxygen molecules in the aqueous solution to produce superoxide anion radicals ($O_2^{\bullet -}$), while the positively charged holes (h^+) can react with hydroxide anions (OH^-) derived from water to make hydroxyl radicals ($OH^\bullet$). Degradation of the RhB and EBT dye molecules to make degradation products (CO_2, H_2O) took place through their reaction with the superoxide anion and hydroxyl radicals (Figure 8). Based on the above results, a possible photocatalytic pathway for BiOCl was proposed, as outlined as below.

$$BiOCl + h\nu \rightarrow BiOCl(h^+) + BiOCl(e^-)$$
$$O_2 + e^- \rightarrow O_2^{\bullet -}$$
$$h^+ + OH^- \rightarrow OH^\bullet$$
$$h+ + H_2O \rightarrow OH^\bullet + H^+$$
$$O_2^{\bullet -} \text{ or } OH^\bullet + \text{organic dye} \rightarrow \text{degradation products}$$

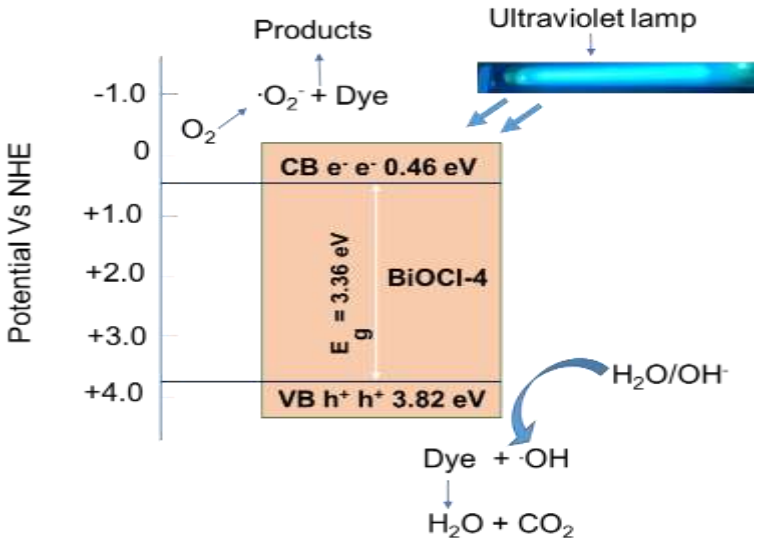

Figure 8. Schematic diagram of the photocatalytic mechanism for the dye degradation under ultraviolet light

Conclusion

Well-crystallized flake-like bismuth oxychloride (BiOCl) nanosheets were successfully synthesized by a solvothermal process. The XRD diffractogram of BiOCl NPs showed the major diffraction peaks at Miller indices of (001), (101), (110), and (012). The average crystallite sizes of BiOCl NPs obtained from the Debye-Scherrer equation were found to be in the range of 19.92 to 32.23nm. The SEM images of BiOCl NPs revealed that BiOCl-4 had the highest number of flake-like nanosheets. According to UV spectra, BiOCl NPs showed wavelengths of maximum

absorption ranging from 210-275 nm activity due to n to π* electronic transition of BiOCl NPs. FT IR spectra showed the functional groups of synthesized BiOCl NPs. TG-DTA thermogram showed the total weight loss percentages of BiOCl NPs were 3.48 to 10.30 %. BiOCl-4 showed the highest photocatalytic due to lower band gap values than other samples. These results indicated that BiOCl NPs may be suitable photocatalysts for wastewater and industrial textile wastewater treatment due to their enhanced photocatalytic activities.

Acknowledgements

The authors would like to thank Professor Dr Ni Ni Than, Head of Department of Chemistry, University of Yangon, for giving us permission to present this research paper at the Paper Reading Session organized by Myanmar Academy of Arts and Science. We would like to acknowledge Professors Dr Ye Myint Aung, Dr Myat Kyaw Thu, Dr San San Aye and Dr Nyan Tun, Department of Chemistry, University of Yangon for their valuable suggestions and advice throughout this research work. Finally, we are also thankful to, Universities' Research Center, West Yangon University and Pathein University, for providing XRD, TG-DTA, SEM, and FT IR facilities.

References

Cao, S., C. Guo, Y. Lv, Y. Guo, and Q. Liu. (2009). "A Novel BiOCl Film with Flowerlike Hierarchical Structure and Its Optical Properties". *Nanotechnology*, vol. 20, pp. 1-7

Dan-Iya, B.I., and Soylu, G.S.P. (2019). "Preparation and Characterization of Bismuth Oxychloride Nanoparticles for The Development of Photocatalytic Performance". *J. Indian Chem. Soc*., vol. 96, pp.1205-1209

Dudchenko, N, S. Pawar, I. Perelshtein, and D. Fixler. (2022). "Magnetite Nanoparticles: Synthesis and Application in Optics and Nanophotonics". *Materials*, vol. 15, pp. 1-34

Schwartz, J.C.P (Ed) (1965). *Physical Methods in Organic Chemistry*. London: Robert Cunningham and Sons, Ltd.

Seddigi, Z.S., M. A. Gondal, U. Baig, S. A. Ahmed, M.A. Abdulaziz, E. Y. Danish, M. M. Khaled, and A. Lais. (2017). "Facile Synthesis of Light Harvesting Semiconductor Bismuth Oxychloride Nano Photo-catalysts for Efficient Removal of Hazardous Organic Pollutants". *PLOS ONE*, vol.12(2), pp. 1-19

Sharma, I. D., G. K. Tripathi, V. K. Sharma, S. N. Tripathi, R. Kurchania, C. Kant, A. K. Sharma, and K. K. Saini. (2015). "One-pot Synthesis of Three Bismuth Oxyhalides (BiOCl, BiOBr, BiOl) and their Phytocatalytic Properties in Three Different Exposure Conditions". *Cogent Chemistry*, vol. 1, pp. 1-15

Silverstein, R.M., and Webster, F. X. (1998). *Spectrometric Identification of Organic Compounds*. New York: 6th edition John Wiley and Sons

Tripathi, G. K., K. K. Saini, and R. Kurchania. (2015). "Synthesis of Nanoplate Bismuth Oxychloride – A Visible Light Active Material". *Optics and Spectroscopy*, vol. 119, pp. 656-663

Wang, L., Y. Liu, G. Chen, M. Zhang, X. Yang, R. Chen, and Y. Cheng. (2022). "Bismuth Oxychloride Nanomaterials Fighting for Human Health; From Photodegradation to Biomedical Application". *Crystal*, vol. 12, pp. 1-23

PREPARATION, CHARACTERIZATION AND ANTIMICROBIAL PROPERTIES OF CHITIN BASED POLYVINYL ALCOHOL BLENDED FILMS

Aung Than Htwe[1], Maung Htwe[1], May Myat Noe[1,2] , Khine Phyu Phyu Thant[1,3]

Abstract

In this research, high strength chitin (CT) - based polyvinyl alcohol (PVA) blended films were prepared by adding different amounts of PVA to chitin dissolved in an aqueous formic acid solution and then by a solvent evaporating technique at room temperature. All prepared blended films have smooth surfaces, are highly transparent, and pale yellow in colour. The physical parameters, the mechanical properties, the degree of swelling and water uptake the prepared blended films were determined. The swelling and water uptake of the blended membrane have a higher degree of hydration, as measured by swelling and water uptake, which can be altered by varying the weight percent of PVA in the membrane matrix. From FT IR analysis, the characteristic absorption peaks of the CT-based PVA blended film clearly showed that the two polymers were blended. A SEM micrograph of CT-based PVA blended films showed homogeneous and amorphous phases. The XRD patterns of the CT-based PVA blended films also exhibited crystallinity. According to TG-DTA analysis, the thermal stability of the CT-based PVA blended were found to decrease. All of the prepared CT-based PVA blended films showed effective antimicrobial activities. The prepared CT-based PVA blended films exhibited excellent biocompatibility and safety in the environment and may also be intended for use in burning dressings and packaging materials.

Keywords: Chitin, polyvinyl alcohol, mechanical properties, antimicrobial activity

Introduction

Because of the ever-increasing production of polymers, which causes environmental pollution, the current problem of polymer utilization is becoming more and more pressing. This problem can be solved by developing biodegradable polymer materials that decompose under environmental conditions to produce harmless byproducts. The most efficient and economically profitable research trend in this field appears to be the production of polymer materials by combining synthetic and natural, biodegradable materials (Rogovina *et al*., 2011). Biopolymers such as cellulose, chitin, and chitosan are abundant. They are primarily obtained from the exoskeletons of crustaceans such as shrimp, but they can also be obtained from fungi and some insect wings. It is widely known. Poly (vinyl alcohol) (PVA) is a nontoxic, water-soluble synthetic polymer with good film-forming ability due to its large number of hydroxyl groups, which allows it to react with a wide range of functional groups (Hefian *et al*., 2010). Polymer blending is a useful method for creating new materials with desired properties, and there has been significant scientific and commercial progress in the field of polymer blends (Cascone, 1997; Fukae *et al*., 1990).

In this paper, chitin/PVA blend films were created by solution-casting chitin and PVA solutions in concentrated formic acid at various compositional ratios. The physical properties, thermal properties, mechanical properties, morphology, and swelling behaviour of blended compositions were investigated.

[1] Department of Chemistry, University of Yangon, Myanmar
[2] Department of Applied Chemistry, Graduate School of Engineering, Osaka University, Japan
[3] Department of Chemistry and Biochemistry, Waseda University, Japan

Materials and Methods

Chitin and Polyvinyl alcohol (Molecular weight 20, 000, degree of hydrolysis 98%) were purchased from the British Drug House (BDH) Chemical Ltd., England. All other chemicals used were of analytical reagent grade. In all investigations, the recommended standard methods and techniques involving both conventional and modern methods were provided.

Preparation of Chitin-Polyvinyl Alcohol (CT-PVA) Blended Films

Chitin solution 2 % w/v was prepared by dissolving 2 g of chitin (CT) in 100 ml of 90 % v/v formic acid with frequent stirring for 30 minutes at room temperature to get a clear solution. The five different amounts of PVA samples (2 g, 4 g, 6 g, 8 g, and 10 g) were added to each beaker containing 100 ml of 2% chitin solution by thoroughly stirring the mixed polymer for about 30 minutes to obtain a series of CT-PVA blends. The blended polymer solutions were kept for sufficient time to remove any bubble formation and were cast onto a cleaned and dried melamine plate at room temperature. The melamine plates containing the blend solution were left for about 3 days to obtain CT-PVA blended films. After drying, the membranes were easily removed from the melamine plates and immersed in a 1 M NaOH solution to remove residual materials. They were then washed with distilled water to remove alkali and unreacted materials, and finally dried at room temperature. The prepared sample was coded as CT-PVA2 for 2 g of PVA, CT-PVA4 for 4 g of PVA, CT-PVA6 for 6 g of PVA, CT-PVA8 for 8 g of PVA, and CT-PVA10 for 10 g of PVA, respectively.

Physical Parameter Measurement of CT-PVA Blended Solution

The details of the measurement of the physical parameters such as pH, specific gravity and viscosity of the different CT-PVA solutions have been reported earlier (Aung Than Htwe *et al*., 2021).

Determination of Mechanical Properties

The details of the measurement of tensile strength, elongation at break and tear strength of the samples have been described earlier (Aung Than Htwe *et al*., 2021). The tensile strength (TS), elongation at break (EB), and tear strength of films were determined using the UCT-5T model (UTM (Orientec Co. Ltd.)). The sample sheets were cut using an ASTM D638 M-III dumbbell cutter. The test conditions were 27 °C temperature, 65 % humidity in the test chamber, 1 mm/min tensile velocity, and 10% load cell scale of 50 N. The sample thickness was measured in three positions, namely, the top, middle, and bottom of the membrane. The thickness value was averaged according to the thickness of the sample. The formula of the TS used as shown in Eq. (1):

$$TS = \frac{F_{max}}{A} \quad (1)$$

where TS is tensile strength (MPa); F_{max} is the force of TS (N); and A is sample surface area (mm^2) (Hidayati *et al.*, 2021).

The elongation at break was calculated by dividing the deformation at the moment of rupture by the initial length of the sample, according to equation (2).

$$R = \frac{L}{C_i} \times 100 \quad (2)$$

where R is elongation at rupture expressed in %; L is distance at moment of rupture expressed in mm; and C_i is initial sample length in mm (Goncalves *et al.*, 2019).

Determination of Water Uptake (%)

The water uptake (%) of the as-prepared films was determined by measuring the weight of the films after immersion in distilled water for 0–60 min in comparison with the dry weight of the films before the immersion. The water uptake (%) was calculated according to the following relationship:

$$\text{Water uptake (\%)} = [W_s\text{-}W_d/W_d] \times 100\ \%, \quad (3)$$

where W_s and W_d represent the weight of the films after and before immersion. It is important to note that all the experiments were carried out at room temperature.

Determination of Degree of Swelling

The swelling behaviour of the as-prepared films was studied by measuring the weight of the films after immersion in distilled water for 0–60 min in comparison with the dry weight of the films before the immersion. The degree of swelling was calculated according to the following relationship:

$$\text{Degree of swelling (\%)} = [W_s\text{-}W_d\ /W_s] \times 100\ \%, \quad (4)$$

where W_s and W_d represent the weight of the films after and before to immersion. It is important to note that all the experiments were carried at room temperature.

Characterization

The prepared blend films were analysed by FTIR in a wide range of wavelengths between 400 cm^{-1} and 4000 cm^{-1} with a resolution of 1 cm^{-1} and 3 scans/sample. A Perkin Elmer GX System FT-IR spectrophotometer was used. A SEM study of the prepared blend films was carried out by JSM–5610 LV. Scanning Electron Microscope, JEOL at 20 kV. The dried sample film was cut and was sputter coated with platinum using a microscope sputter coater and viewed through the microscope. An X-ray powder diffractometer (XRD) was used to perform X-ray diffraction studies with Ni filtered Cu Kα X-ray radiation. Thermo gravimetric analysis was carried out in a nitrogen atmosphere at a heating rate of 20.0 $kJmin^{-1}$ and scanning from 40 ^oC to 600 ^oC. Thermogravimetric analysis was carried out in a nitrogen atmosphere at a heating rate of 15 °C/min up to a temperature range of 1400 °C on the DTG-60H thermal analyzer.

Determination of Antimicrobial Test

The different chitin based PVA blended films were tested with *Bacillus subtilis, Staphylococcus aureus, Pseudomonus aeruginosa, Bacillus pumilus, Candida albicans* and *E. coli* species to investigate the nature of antimicrobial activity. The details procedure of the antimicrobial test has been reported earlier (Aung Than Htwe *et al*., 2021).

Results and Discussion

Physical Properties of CT- Based PVA Solution

Figure 1 indicates the physical parameters of CT- based different amounts of PVA blended solutions. The measuring parameters are pH, specific gravity and viscosity. From the value of pH of CT-based different amount of PVA blended solutions are slightly acidic and distilled water in the range of 4 to 5. The specific gravity is 1.163 in CT-PVA2, 1.345 in CT-PVA4, 1.348 in CT-PVA6, 1.374 in CT-PVA8 and 1.282 in CT-PVA10, respectively. It can be seen that increasing the PVA content, Causes a slight increase in the specific gravity. The viscosity value is 6.86 cPs in CT-PVA2, 14.45 cPs in CT-PVA4, 34.93 cPs in CT-PVA6, 69.45 cPs in CT-PVA8 and 150.6 cPs

in CT-PVA10. It is observed that the higher the PVA content, the higher the viscosity. Thus, all physical parameters of CT-PVA blended solutions showed obviously significant values.

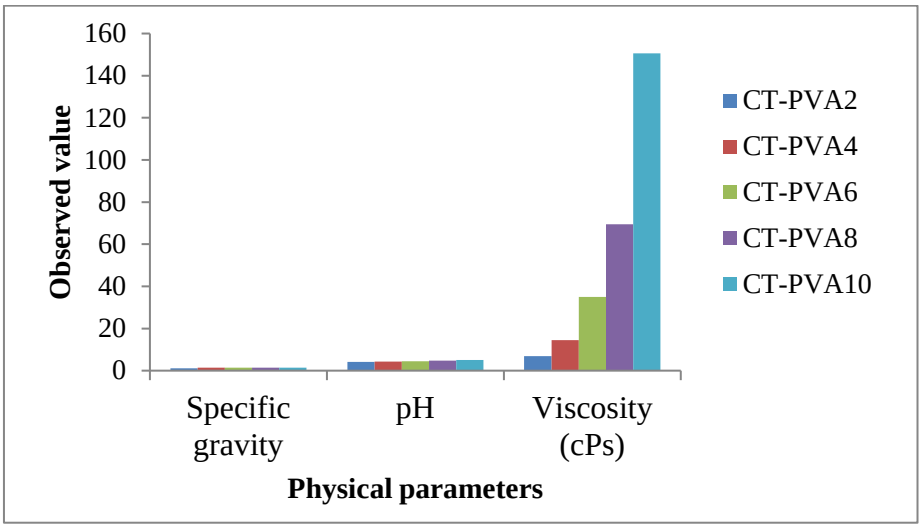

Figure 1. The physical parameter of the chitin based polyvinyl alcohol blended solutions

Mechanical Properties of CT- Based PVA Films

The mechanical properties in terms of tensile strength, elongation at break (%), tear strength are important parameters which reveal the nature of films. The mechanical properties of CT based PVA blended films are presented in Figure 2. The thickness values of CT- based PVA blended films were 0.12 mm in CT-PVA2, 0.27 mm in CT-PVA4, 0.40 mm in CT-PVA6, 0.50 mm in CT-PVA8 and 0.70 mm in CT-PVA10. It was found that as the amount of PVA content increased, the thickness also increased. The tensile strength values of CT- based PVA blended films were 4.4 MPa in CT-PVA2, 2.7 MPa in CT-PVA4, 2.3 MPa in CT-PVA6, 1.7 MPa in CT-PVA8 and 1.2 MPa in CT-PVA10, respectively. Tensile strength of CT based PVA blended films decreased from 4.4 MPa to 1.2 MPa. The percent elongation at break was 205 % in CT-PVA2 content, however, it was significantly increased to 444 % in CT-PVA4 and then to 529 % in CT-PVA6. As seen in Figure 2, the tensile strength and % elongation values are flexible in CT-PVA6. The tear strength is another mechanical property of the nature of films. It indicated that the tear strength of CT- based PVA blended films significantly decreased from 34.7 kN/m in CT-PVA2 to 11.0 kN/m in CT-PVA8. It can be concluded that according to the mechanical properties such as tensile strength, percent elongation at break, tear strength, and thickness, among CT based PVA blended films, CT-PVA6 has the highest value of mechanical properties.

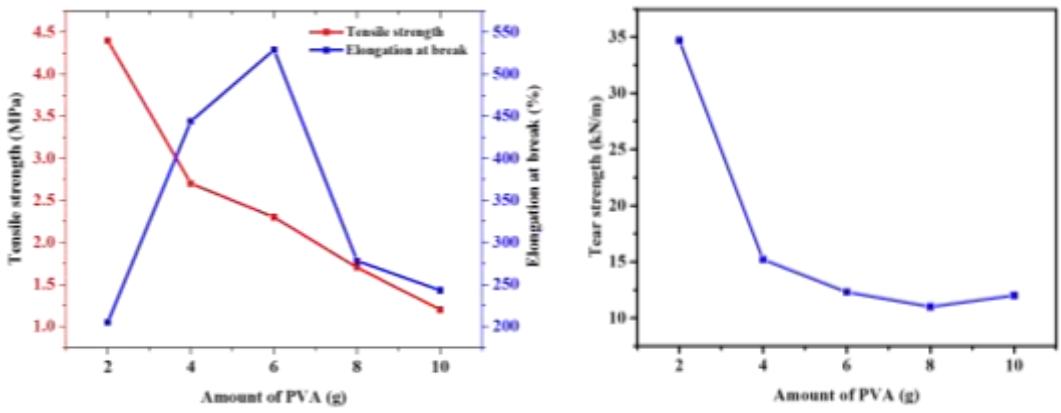

Figure 2. The mechanical properties of chitin based PVA blended films

Degree of Swelling (%) Behaviour

The degree of swelling of CT-based PVA blended films are shown in Figure 3 as a function of immersion time in distilled water at room temperature. As shown in figure, with increasing PVA content, the ultimate degree of swelling before 50 min of immersion time of CT-PVA blend films were found to increase from ca. 75.3 to ca. 84.6 %, when PVA content increased from 2 g to 8 g. After 50 min, all of the blended films were found in deswelling nature. The maximum value for the degree of swelling of CT-PVA6 blended film has 84.6 % at 50 min. The fact is attributed to a more rigid network formed by the inter-intra polymer chain reactions that have occurred, reducing the flexibility and number of hydrophilic groups of hydrogel which is unfavourable to the swelling rate. So, these results correspond to the hydrogel mechanism. The PVA chains are physically entangled with the chitin chains, forming a hydrogel network (Özturk, 2011).

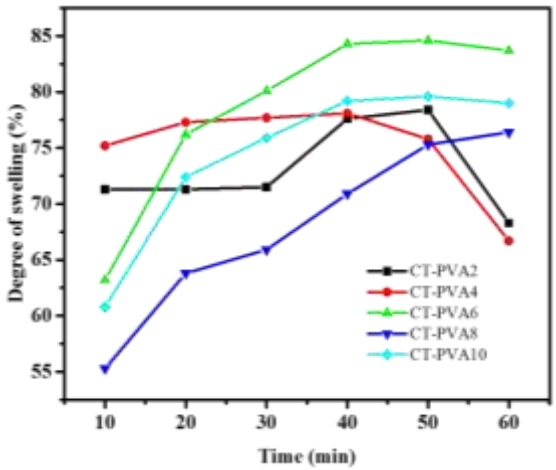

Figure 3. The degree of swelling of chitin based PVA blended films

Water Uptake (%)

The degree of water uptake was investigated with increasing immersion time. The water uptake as a function of time for CT-PVA hydrogel film is shown in Figure 4. As seen in the figure, the water uptake of CT-PVA blended film was significantly different according to the amount of PVA content. The water uptake was the amount of water entrapped in the matrix, including bound water. CT-PVA6 had the highest degree of water uptake content (550.9 %) at 50 min. The water uptake may impart stickness and durability.

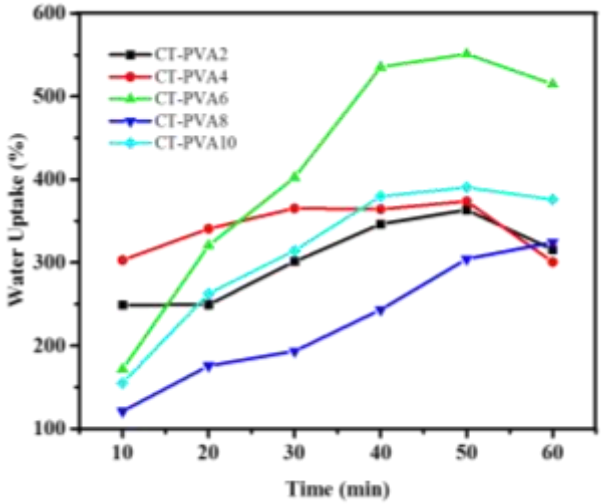

Figure 4. The water uptake (%) of chitin-based PVA blended films

Characterization

FT IR analysis

The FTIR spectra of chitin-based PVA films are presented in Figures 5 and Table 1. As can be seen, the increase in the PVA concentration in the blended films caused a decrease in the intensity of the band arising from NH bending (amide II) at 1416 cm^{-1} of chitin. Also, an increase in the intensity of CH group at around 2939 cm^{-1} was found as the PVA content increased. As seen in figures, all of the blended films are agreement with the range of absorption peak to the references peak range.

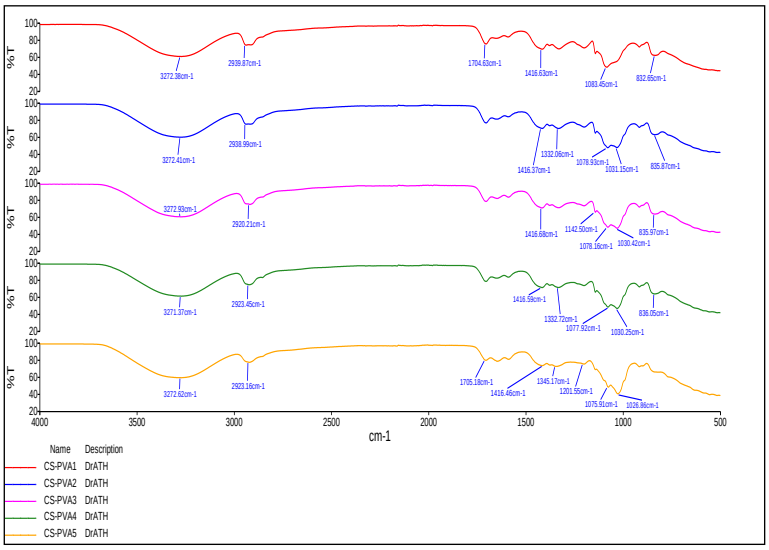

Figure 5. FTIR spectra of chitin-based PVA blended films

Table 1. FT IR Characteristic Bands of Chitin based PVA Blended Films

Samples	C-C & C-H bend	C-OH stretch	CH	NH amide I	C=O amide I	CH stretch	OH stretch
CT-PVA2	832.65	1083.45	1332.02	1416.63	1704.63	2939.87	3272.38
CT-PVA4	835.87	1078.93	1332.06	1416.37	1703.68	2938.99	3272.41
CT-PVA6	835.97	1078.16	1332.67	1416.68	1703.65	2920.21	3272.93
CT-PVA8	836.05	1077.92	1332.72	1416.59	1704.43	2923.45	3271.37
CT-PVA10	836.02	1075.91	1345.17	1416.46	1705.18	2923.16	3272.62

Ref: Lee *et al*.(1996), Nakamoto (1970)

SEM analysis

Morphological tests of the films were performed by using SEM technique. The SEM images for (a) CT-PVA2, (b) CT-PVA4, (c) CT-PVA6, (d) CT-PVA8 and (e) CT-PVA10 films are shown in Figure 6. It can be found that all of the blended films exhibited homogeneity showing a certain miscibility between chitin and PVA. Finally, the SEM clarifications have supported the measured mechanical and thermal properties of the biocomposite films.

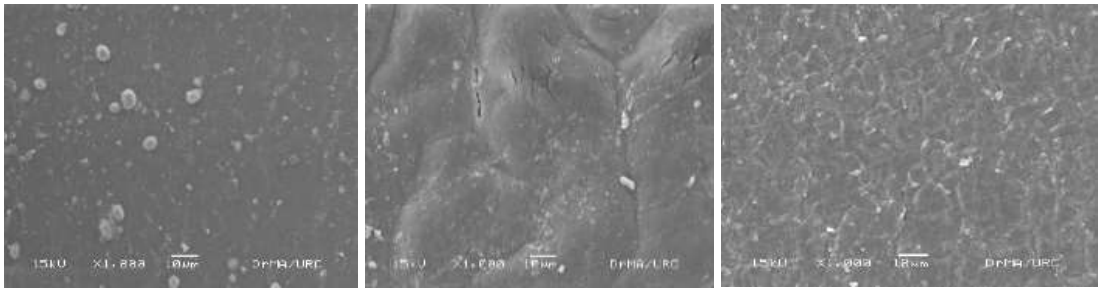

(a) CT-PVA2 (b) CT-PVA4 (c) CT-PVA6

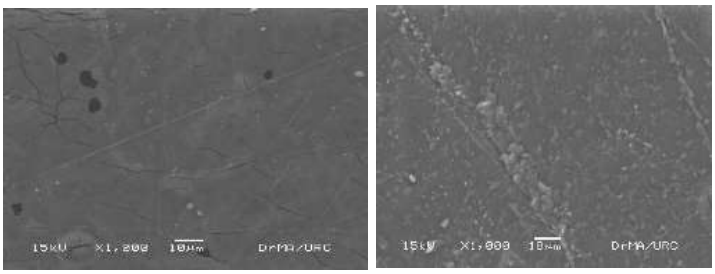

(d) CT-PVA8 (e) CT-PVA10

Figure 6. The SEM images of the surface of chitin-based PVA blended films

XRD analysis

X-ray diffractograms of the chitin/PVA binary blend, are shown in Figure 7. Hema, Ramya, and Sudha (2012) reported that the two characteristic crystalline peaks of pure chitin were found at 2θ =9.32° and 19.25°, corresponding to the (010) and (020) and (110) planes, respectively. When PVA crystallized in a monoclinic unit cell, the main peaks in the XRD pattern should appear at the 2θ angles of 11.3, 19.7, 22.9, 28, 32.5, and 40.9° (Peesan, 2003). As seen in Figure 4(a) to (e), in all of the chitin-based PVA blended films, the peak of the hydrated crystalline structure of chitin at 9.32° is absent, and the strong 19.2° peak with (110) plane is diminished. It illustrates that existence of PVA decreases the crystallinity of chitin in the binary blend. Lastly, it can be deduced that the XRD patterns would be expressed as simply mixed patterns of different components in the mechanical and thermal blending cases.

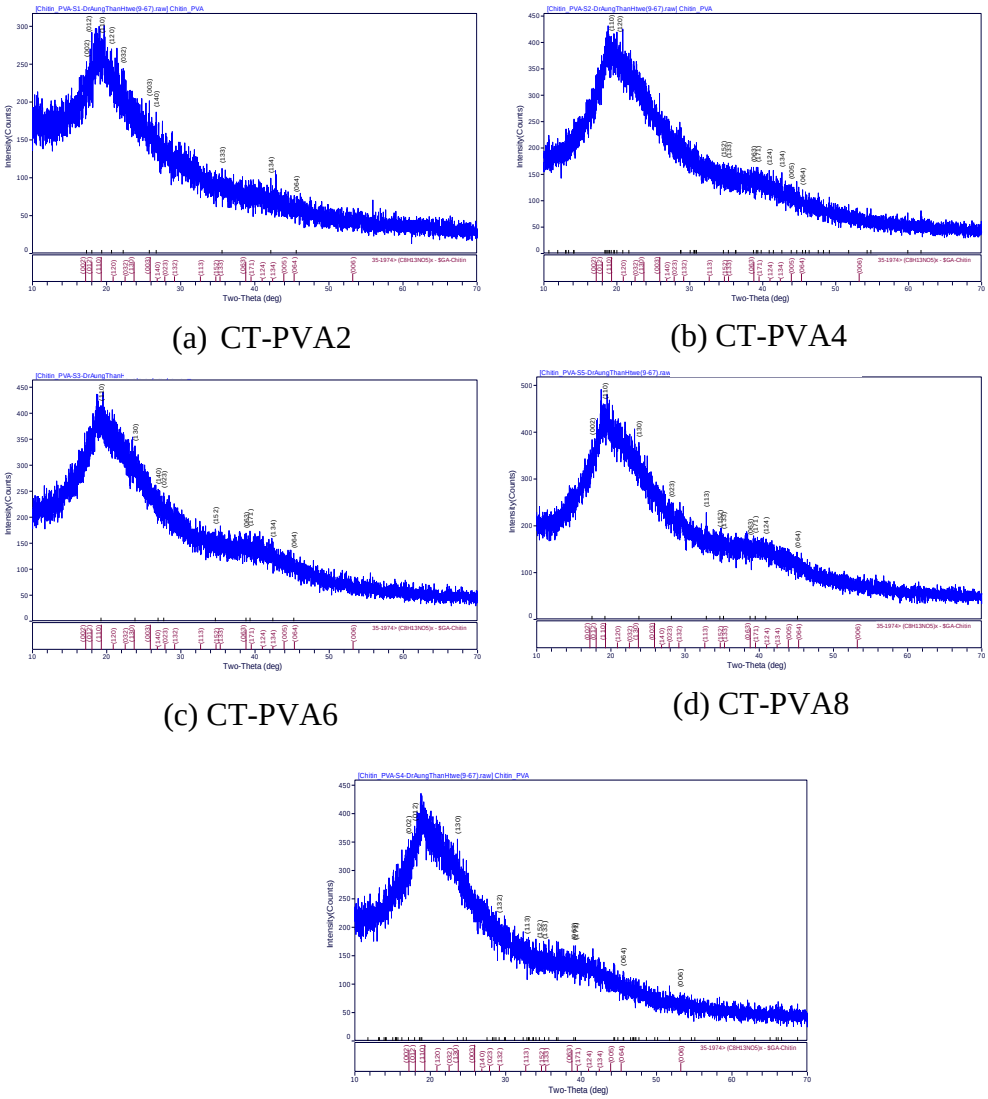

(a) CT-PVA2 (b) CT-PVA4

(c) CT-PVA6 (d) CT-PVA8

(d) CT-PVA10

Figure 7. X-ray diffraction patterns of chitin-based PVA blended films

Thermogravimetric analysis

TGA is a useful technique to assess the thermal stability of polymers and polymers blends. The decomposition and thermal stability of chitin and blended films were determined from thermograms, as shown in Figure 8. As seen in Figure 8, the CT-PVA2, CT-PVA4, CT-PVA6, CT-PVA8 and CT-PVA10 films have weight loss in four stages. The first stage ranges from 39°C to 50°C; weight loss was 15.83% in CT-PVA2, 15.99% in CT-PVA4, 10.69% in CT-PVA6, 5.54% in CT-PVA8 and 6.53% in CT-PVA10. There is a loss of absorbed water. In the second stage, in the temperature range between 150°C to 290°C, was observed as 27.70% in CT-PVA2, 21.32% in CT-PVA4, 26.72 % in CT-PVA6, 16.64 % in CT-PVA8 and 19.59% in CT-PVA10. This is due to the evaporation of some organic materials. In the third stage, weight loss of 31.66% in CT-PVA2, 53.30% in CT-PVA4, 48.10% in CT-PVA6, 49.92% CT-PVA8 and 39.18% in CT-PVA10 was observed to take place within the temperature range of 290°C to 378°C. In this stage, weight loss is due to partial decomposition of chitin and PVA polymer. The fourth stage ranges between about the temperature range of 378°C to 600°C with 15.83% in CT-PVA2, 5.33% in CT-PVA4, 10.6 % in CT-PVA6, 24.96% in CT-PVA8 and 32.64% in CT-PVA10. There is complete degradation of chitin and PVA polymer.

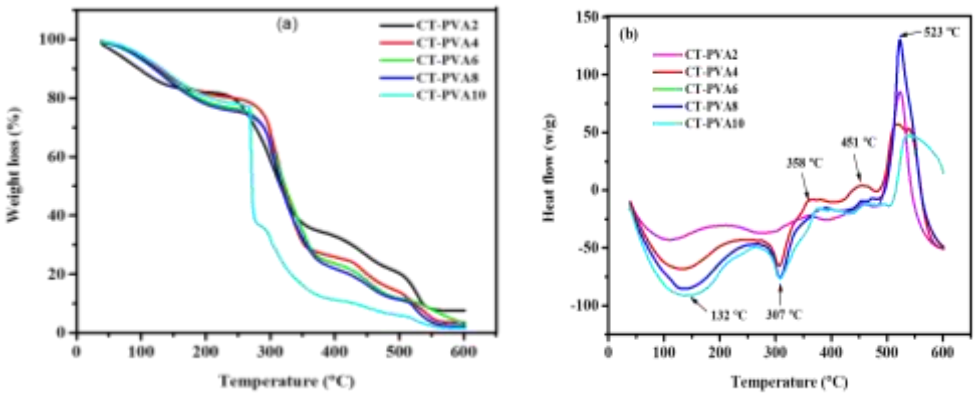

Figure 8. (a) TGA curves and (b) DTA curves of chitin-based PVA blended films

Antimicrobial Activity

Antimicrobial activity of CT-PVA2, CT-PVA4, CT-PVA6, CT-PVA8 and CT-PVA10 films are shown in Figure 9 and Table 2. As seen in Figure 9 and Table 2, antimicrobial tests of all blended films were performed on the agar medium. As a result of the blended films, they all have antimicrobial activity. It can be concluded that according to the antimicrobial activity, the blended CT-PVA film may be intended for use as burn dressing and food packaging materials.

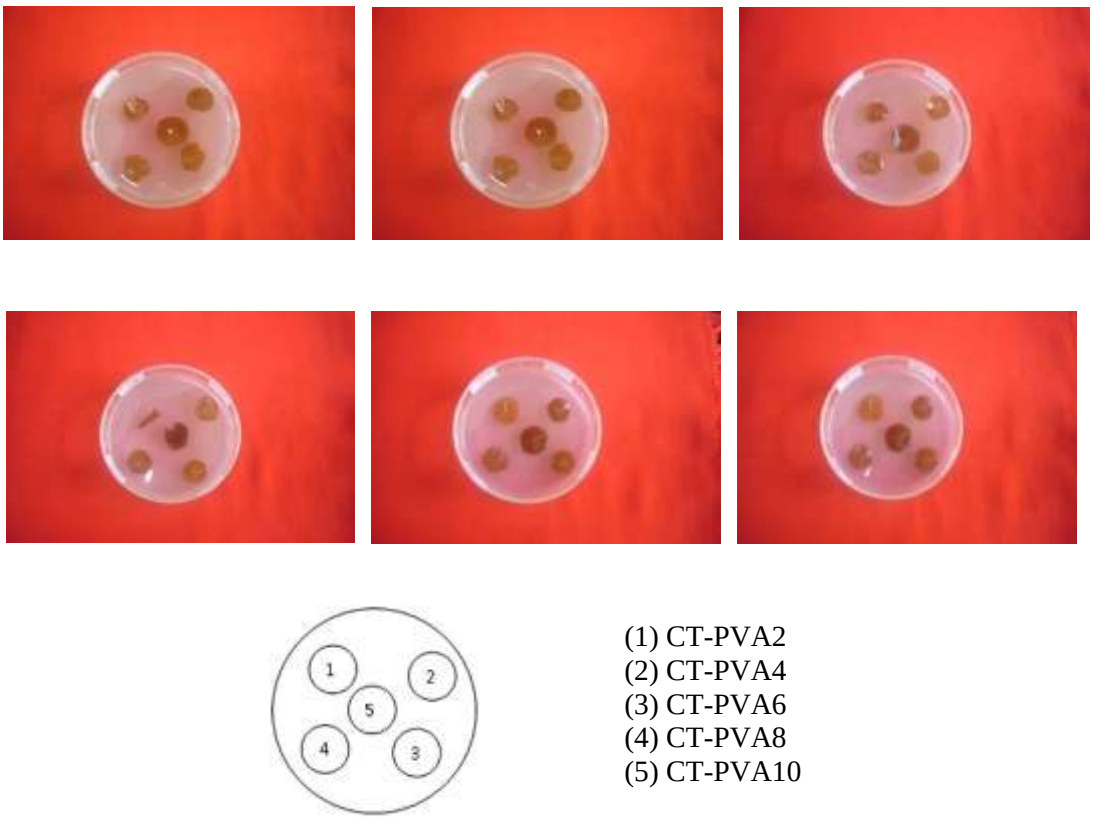

Figure 9 Antimicrobial activity of prepared chitin-based PVA blended films

Table 2 Antimicrobial Activity of CT-PVA Blended Film by Agar Disc Diffusion Method

No	Microorganism	Samples				
		CT-PVA2	CT-PVA4	CT-PVA6	CT-PVA8	CT-PVA10
1	*Bacillus subtilis*	++	++	++	+	++
2	*Staphylococcus aureus*	++	++	++	+	++
3	*Pseudomonas aeruginosa*	++	++	++	+	++
4	*Bacillus pumilus*	++	++	++	+	++
5	*Candida albicans*	++	++	++	+	++
6	*E.coli*	++	++	++	+	++

Disc diffusion (mm) ≥ 21(+++) susceptible, 17.20(++) intermediate, ≤16(+) resistant

Conclusion

In this study, polymer blend membranes of chitin-based polyvinyl alcohol were prepared by blending, casting and solvent evaporating techniques. All prepared CT-based PVA blended films showed a plain, clear, smooth surface, were flexible, highly transparent, and were of a light-yellow colour. The swelling and water uptake of blend membrane has a higher degree of hydration, as measured by swelling and water uptake, which can be altered by varying the weight percent of PVA in the membrane matrix. FT IR analysis showed that there exist intermolecular interactions between CT and PVA. The SEM analysis showed that all of the blended films exhibited homogeneity showing a certain miscibility between chitin and PVA. The XRD patterns also showed a reduction of crystallinity of chitin as diffused rings in the blend, but hold amorphous nature. From TG-DTA analysis, the thermal stability of CT-based PVA blended films was found to decrease and the weight loss to increase. The properties of various types of CT-based PVA blended films were tested on their antimicrobial activities by using agar disc diffusion method. It can be noted that all of the microbial agents that come in contact with films are active. According to these results, the prepared CT-based PVA blended films could be used as burn dressing and food packaging materials.

Acknowledgements

The authors feel indebted to Professor and Head Dr Ni Ni Than, Department of Chemistry, University of Yangon, Yangon, Myanmar, for her stimulating suggestions.

References

Aung Than Htwe, Maung Htwe, Soe Maung, and Myint Naing Tun. (2021). "Study on Biodegradable and Antimicrobial Properties of Biowaste Chitin-Polyvinyl Alcohol Blended Film". *ASEAN Engineering Journal*, vol. 11(3), 127-139

Cascone, M.G. (1997). "Dynamic-mechanical Properties of Bioartificial Polymeric Materials". *Polymer International*, vol. 43, pp. 55-69

Fukae, R., T. Yamamoto, O. Sangen, M. Saso, M. Kakot, and M. Kamachi. (1990). "Dynamic Mechanical Behaviour of Poly(Vinyl Alcohol) Film with High Syndiotacticity". *Polymer Journal*, vol. 22, pp. 636-637

Goncalves, S.M., D.C. Santos, J.F.G. Motta, R.R. Santos, D.W.H. Chavez, and N.R. Melo. (2019). "Structure and Functional Properties of Cellulose Acetate Films Incorporated with Glycerol". *Carbohydrate Polymers*, vol. 209, pp. 190-197

Hefian, E.A., M.M. Nasef, and A.H. Yahaya. (2010). "The Preparation and Characterization of Chitosan/Poly (Vinyl Alcohol) Blended Films". *E-Journal of Chemistry*, vol. 7(4), pp. 1212-1219

Hidayati, S., Zulferiyenni, U. Maulidia, W. Satyajaya, and S. Hadi. (2021). "Effect of Glycerol Concentration and Carboxymethyl Cellulose on Biodegradable Film Characteristics of Seaweed Waste". *Heliyon*, vol. 7, pp. 1-8

Lee, Y.M., S.H. Kimt, and S.J. Kimt. (1996). "Preparation and Characterization of β-Chitin and Polyvinyl Alcohol Blend". *Polymer*, vol. 37(26), pp. 5897-5905

Nakamoto, K. (1970). Infrared Spectra of Inorganic and Coordination Compound. New York, Second Edition, JOHN WILEY&SONS, 191.

Öztürk, B. (2011). Preparation and Characterization of Crosslinked Chitosan Based Hydrogels. MSc (Thesis), Graduate School of Natural and Applied Sciences of Dokuz Eylül University.

Peesan, M., R. Rujiravanit, and P. Supaphol. (2003). "Characterization of Beta-Chitin/Polyvinyl Alcohol Blend Films". *Polymer Testing*, vol. 22, pp. 381-387

Rogovina, S.Z., C.V. Alexanyan, and E.V. Prut. (2011). "Biodegradable Blends Based on Chitin and Chitosan: Production, Structure, and Properties". *Journal of Applied Polymer Science*, vol. 121, pp. 1850-1859

INVESTIGATION OF SOME BIOACTIVITIES AND PHYTOCONSTITUENTS FROM THE PEELS OF *DIMOCARPUS LONGAN* LOUR. (LONGAN)

Kay Khine Win Swe[1], Prema[2], Zin Thu Khine[3], Ni Ni Than[4*]

Abstract

The aim of the present work is to investigate the total phenolic contents, antioxidant, cytotoxic, and anti-arthritic activities, and phytoconstituents of *Dimocarpus longan* Lour. (Longan) peel (LGP). The total phenolic content of ethanol and watery extracts from LGP was determined by the Folin-Ciocalteu Reagent (FCR) method. Total phenolic content was found to be the highest in ethanol extract (176.12 ± 0.15) μg/mL. The *in vitro* antioxidant activity of ethanol and watery extracts of LGP was assessed by the DPPH free radical scavenging assay. The IC_{50} values were found to be 70.52 μg/mL for the watery extract and 8.77 μg/mL for the ethanol extract of LGP. The cytotoxicity of the watery and ethanol extracts was evaluated by a brine shrimp lethality bioassay. From these results, the LD_{50} values of watery and ethanol extracts were found to be non- toxic at the 1000 μg/mL concentration. The anti-arthritic activity of watery and ethanol extracts screened by the egg albumin method. According to the data, the watery extract (IC_{50} = 97.77 μg/mL) is more potent than standard diclofenac sodium (IC_{50} = 57.57 μg/mL) in anti-arthritic activity. By silica gel column chromatographic separation technique, two steroids, one terpenoid and a steroidal carboxylic acid were isolated from petroleum ether extract of LGP and characterized by physico-chemical properties and the FT IR spectroscopic method.

Keywords: *Dimocarpus longan* Lour., antioxidant activity, cytotoxicity, anti-arthritic activity

Introduction

Medicinal plants play a crucial role in the development of potent therapeutic agents. Natural products from plants, animals and minerals are the basis of the treatment of human diseases. Today, about 80 % of individuals in developing countries still rely on traditional medicine based largely on species of plants and animals for their primary health care. Herbal medicines are currently in demand and their popularity is increasing day by day. Currently, 80 % of the world population depends on plant-derived medicine for the primary line of primary health care and human alleviation because it has no side effects (Dipak et al., 2012). Longan (Dimocarpus longan lour.), commonly known as dragon's eye is an important evergreen fruit crop grown in tropical and subtropical regions. It belongs to the sapindaceae family and widely distributed in Myanmar, China, Vietnam, Thailand, India, Philippines, and other Southeast Asian countries. The main world longan-producing countries are China, Vietnam, and Thailand. This fruit has been used as traditional medicine in other countries. It is rich in carbohydrates, protein, fiber, fat, vitamin C, amino acids, and minerals. Different parts can be used to treat or prevent different types of diseases. It is a good source of polyphenolic compounds. Its active compounds possess anti-arthritic, antioxidant, anti-hyperglycemic, anticancer, antidote, and other activities (Shahrajabian et al., 2019). Therefore, the present work aimed to investigate some bioactivities and phytoconstituents from the peels of Dimocarpus longan Lour. (Longan).

[1] Department of Chemistry, University of Yangon, Myanmar
[2] Department of Chemistry, University of Yangon, Myanmar
[3] Department of Chemistry, Sagaing University, Myanmar
[4] Department of Chemistry, University of Yangon, Myanmar

Materials and Methods

Plant materials

Longan fruits were collected from July to August, 2021 in Sagaing Township, Sagaing Region, Myanmar. The collected sample was identified as Dimocarpus longan Lour. (Longan) fruits at the Botany Department, University of Yangon. The sample was cleaned by washing thoroughly with water and peeled off. Then the fresh peel was cut into small pieces and air-dried at room temperature. The dried samples were ground into powder by a grinding machine, sieved, and stored in an airtight container for further use.

Preparation of crude extracts for biological activities

About 20 g of dried powder sample was extracted three times with 95 % ethanol (each time with 100 mL). Extraction time was allowed for six hours and then filtered. Then, the solvent was removed by the rotary evaporator, providing the ethanol extract. To obtain watery extract, 20 g of dried powder samples was separately soaked in 100 mL of distilled water. It was then concentrated by evaporating the solvent on a water bath to get a watery extract. In this way, crude extracts were obtained. The crude extracts were dried and kept in a refrigerator for a few weeks.

Determination of total phenol contents (TPC) as gallic acid equivalent

The total phenolic content was determined by the Folin-Ciocalteu method. Each extracted sample solution (0.5 mL) was added 5 mL of FC reagent (1:10) and incubated for 5 min. To each tube, 4 mL of 1 M sodium carbonate solution was added, the tubes were kept at room temperature for 15 min, and the UV absorbance of the reaction mixture was read at λ_{max} 765 nm. The blank solution was prepared as in the above procedure by using distilled water instead of the sample solution. Total phenolic content was estimated as micrograms of gallic acid equivalent per milligram (μg GAE/mg) of crude extract (Hishamuddin *et al*., 2020).

Determination of Antioxidant Activity by DPPH Free Radical Scavenging Assay

Preparation solutions

DPPH (2 mg) was thoroughly dissolved in 100 mL of 95 % ethanol. This solution was freshly prepared in the brown-coloured reagent bottle and stored in the fridge for no longer than 24 h. Each of the tested samples (ethanol and watery extracts) (10 mg) was thoroughly mixed with 10 mL of ethanol. The stock solution was obtained. This stock solution was twofold serially diluted with ethanol to obtain the desired concentrations: 3.91, 7.81, 15.63, 31.25, 62.5, and 125 μg/mL.

Determination of antioxidant activity

DPPH free radical scavenging activity was determined by a spectrophotometric method. The control solution was prepared by mixing 1.5 mL of DPPH solution and 1.5 mL of ethanol in the brown bottles. The sample solution was also prepared by mixing thoroughly 1.5 mL of DPPH solution with 1.5 mL of the test sample solution. These bottles were incubated at room temperature and were shaken on the shaker for 30 min. After 30 min, the absorbance of each solution was measured at 517 nm by using a spectrophotometer (Hishamuddin *et al*., 2020). Absorbance measurements were done in triplicate for each solution, and the percent inhibition of oxidation was calculated by the following equation.

$$\% \text{ RSA} = \frac{(A_{control} - A_{sample}) \times 100}{A_{control}}$$

where

% RSA = % radical scavenging activity
$A_{Control}$ = Absorbance of control solution
A_{Sample} = Absorbance of sample solution

Determination of Cytotoxicity by Brine Shrimp Lethality Bioassay

Preparation of solutions

Accurately weighed 5 mg of each sample (ethanol extract, watery extract, potassium dichromate and caffeine) was separately dissolved in 5 mL of distilled water to obtain a respective stock solution (1000 µg/mL). Desired concentrations (1000, 100, 10, 1 µg/mL) of each solution were prepared from this stock solution by tenfold serial dilution with distilled water.

Procedure

The brine shrimp (*Artemia salina*) were used in this study for a cytotoxicity bioassay. Artificial sea water (3.8 % (w/v) NaCl) was prepared by dissolving (38 g) of sodium chloride in 1 L of distilled water. Brine shrimp cysts (0.5 g) were put into 1 L of artificial sea water in a bottle. This bottle was placed near a lamp. Light is essential for the cysts to hatch. Brine shrimp cysts required to hatch constant supplied oxygen and 24 h incubation at room temperature. 9 mL of artificial seawater and 1 mL of different concentrations of samples and standard solutions were added to each chamber. Alive brine shrimp (10 nauplii) were then taken with a pasteur pipette and placed into each chamber. They were incubated at room temperature for about 24 h. After 24 h, the number of dead or survival brine shrimps were counted and the estimation of cytotoxicity was done by 50 % lethality dose (LD_{50}) (Singh *et al*., 2015). The control solution was prepared as in the above procedure by using distilled water instead of the sample solution.

Determination of Anti-arthritic Activity by Egg Albumin Method

The reaction mixture (5 mL) consisted of 0.2 mL of egg albumin (from fresh hen's egg), 2.8 mL of phosphate buffered saline (PBS, pH 6.4) and 2 mL of varying concentrations of crude extracts of Longan so that final concentrations became 100, 200, 400, 800 and 1000 µg/ mL. Similar volume of double-distilled water served as control. Then the mixtures were incubated at 37 ˚C in an incubator for 15 min and then heated at 70 ˚C for 5 min. After cooling, their absorbance was measured at 660 nm. Diclofenac sodium was used as a reference drug (Sunmathi *et al*., 2016). The percentage inhibition of protein denaturation was calculated by using the following formula:

$$\% \text{ inhibition} = \frac{(A_{control} - A_{sample}) \times 100}{A_{control}}$$

where

$A_{Control}$ = Absorbance of control solution
A_{Sample} = Absorbance of sample solution

Extraction and Isolation of Compounds

The air-dried powder sample of LGP (1 kg) was macerated with ethanol (3 × 1 L) at room temperature for about two weeks by sonication. method. The extract was concentrated under reduced pressure at 60 ˚C. The extract was partitioned with PE and EtOAc successively. The PE

fraction (5 g) was separated by a column chromatographic method, eluting successively with PE only, PE: EtOAc (9:1 to 1:5 v/v), EtOAc only, and EtOAc: MeOH (9:1 to 1:1 v/v) as a solvent system. Then, ten fractions were obtained. The collected fractions were monitored by TLC, and similar fractions were combined into 10 fractions: F-1 (f_{1-19}), F-2 (f_{20-125}), F-3 ($f_{126-216}$), F-4 ($f_{217-250}$), F-5 ($f_{251-324}$), F-6 ($f_{325-337}$), F-7 ($f_{-338-356}$), F-8 ($f_{357-365}$), F-9 ($f_{366-372}$), and F-10 ($f_{366-372}$) based on TLC analysis. From these fractions, four compounds were isolated. Fractions F-2, F-3, F-4, and F-5 were further chromatographed on silica gel columns by using PE: EtOAc (19:1 to 5:1, v/v) to get compound **A** (30.40 mg), compound **B** (20.32 mg), compound **C (**55.65 mg), and compound **D** (18.76 mg), respectively. The isolated compounds **A**–**D** were characterized by their physico-chemical properties and FT IR spectroscopic method.

Results and Discussion

Total Phenolic Content of Crude extracts of Longan Peels

In the present investigation, the total phenolic contents of crude extracts of Longan peels were estimated by the Folin-Ciocalteu method. Gallic acid (3, 4, 5-trihydroxybenzoic acid) was used to construct a standard calibration curve for total phenol content estimation. Total phenolic content (TPC) was expressed as microgram of gallic acid equivalent (GAE) per milligram of crude extract (µg GAE/mg) (Table 1 and Figure 1).

According to the results, the total phenolic content (TPC) (µg GAE/mg) of ethanol extract (176.12 ± 0.15) µg GAE/mg was found to be higher than that of watery extract (76.22 ± 0.45) µg GAE/mg (Table 2 and Figure 2).

Table 1. The Absorbance of Standard Gallic Acid Solution at λ_{max} 765 nm

No.	Concentration (µg/mL)	Absorbance at λ_{max} 765 nm
1	3.125	0.603
2	6.25	0.373
3	12.5	0.252
4	25	0.194
5	50	0.164
6	100	0.147

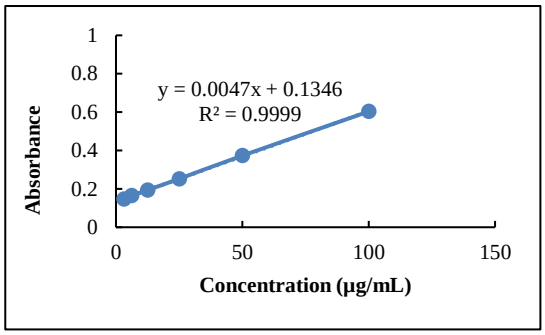

Figure 1. A calibration curve of gallic acid standard curve

Table 2. Total Phenol Contents of Crude Extracts of Longan Peels

Extracts	TPC (µg GAE/mg ±SD)
Watery	76.22 ± 0.45
Ethanol	176.12 ± 0.15

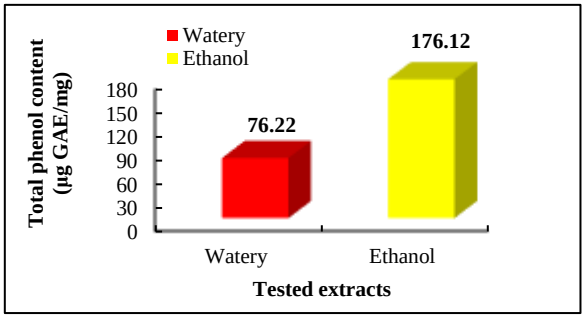

Figure 2. Histogram of total phenolic content of ethanol and watery extracts of longan peels

Antioxidant Activity of Crude Extracts of Longan Peels by DPPH Free Radical Scavenging Assay

Longan peels are a good source of phenolic compounds, as their potential antioxidants and antioxidants activity depend on the content of phenolic compounds. The antioxidant activity of ethanol and watery extracts of LGP was studied by the DPPH free radical scavenging assay. IC_{50} values were observed to be 70.52 µg/mL for watery extract and 8.77 µg/mL for ethanol extract. The largest scavenging activity to scavenge the DPPH radical was observed in ethanol extract, which inhibited 50 % of free radicals at the concentration (IC_{50}) of 8.77 µg/mL. Because of the phenolic content, the ethanol extract is more effective than watery extract. The results are shown in Table 3 and Figures 3 and 4. The ethanol extract possessed less antioxidant activity than standard ascorbic acid (4.41 µg/mL).

Table 3. Average % RSA Inhibition and IC_{50} Values of Crude Extracts of Longan Peels

Tested samples	% RSA ± SD of different concentrations (µg/mL)						IC_{50} (µg/mL)
	3.91	7.81	15.63	31.25	62.5	125	
Watery extract	11.42 ±0.11	17.26 ±0.19	21.22 ±0.26	26.36 ±0.45	37.03 ±0.31	55.91 ±0.05	70.52
Ethanol extract	20.43 ±0.06	47.41 ±0.21	64.97 ±0.38	80.74 ±0.41	82.06 ±0.51	83.33 ±0.29	8.77
Std. Ascorbic acid	46.15 ±0.03	75.81 ±0.28	79.12 ±0.16	85.93 ±0.32	87.37 ±0.37	87.62 ±0.00	4.41

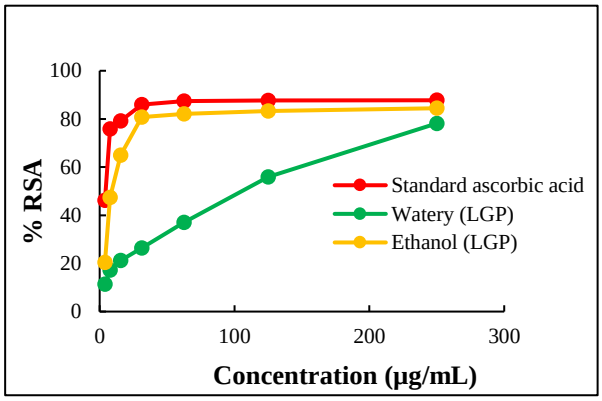

Figure 3. Mean % inhibition versus concentration of different extracts of longan peels

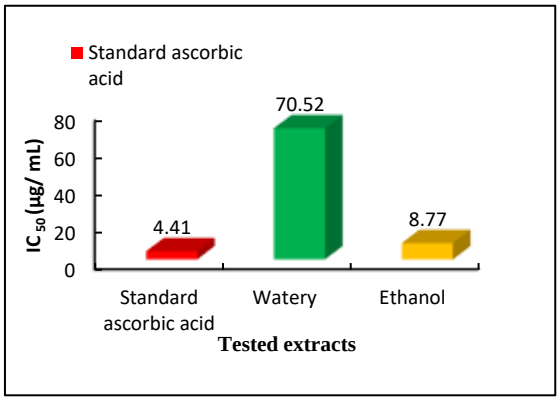

Figure 4. IC_{50} values of standard ascorbic acid and crude extracts of longan peels

Cytotoxicity of Crude Extracts of Longan Peels

The cytotoxicity of watery and ethanol extracts of LGP was evaluated by the brine shrimp lethality bioassay. The organisms used were brine shrimp (*Artemia salina*). The cytotoxicity of watery and ethanol extracts of selected plants is shown in Table 4. From these results, the LD_{50} values of watery and ethanol extracts were found to be greater than 1000 µg/mL. LD_{50} values of crude extracts, less than 1000 µg/mL was toxic (active) and greater than 1000 µg/mL was non-toxic (inactive). Therefore, watery and ethanol extracts have no cytotoxic effect.

Table 4. Cytotoxicity of Different Concentrations of Crude Extracts of Longan Peels against *Artemia salina* (Brine Shrimp)

Tested Samples	% of Dead Brine Shrimp in Different Concentrations of Sample (µg/mL)				LD_{50} (µg/mL)
	1	10	100	1000	
Watery extract	20.00±0.00	23.33±0.58	40.00±0.58	40.00±0.00	> 1000
Ethanol extract	13.33±0.00	13.33±0.00	16.67±0.58	46.67±0.58	> 1000
Std. $K_2Cr_2O_7$	43.33±0.58	46.67±0.58	76.67±0.58	100±0.00	19.99
Std. caffeine	0.00±0.00	13.33±0.58	23.33±0.58	33.33±0.58	>1000

Anti-arthritic Activity of Crude Extracts of Longan Peels

One of the well-documented causes of inflammatory and arthritic diseases is denaturation of tissue proteins. The effect of watery and ethanol extracts of LGP was evaluated against denaturation of egg albumin, showed 97.77 µg/mL and 347.41 µg/mL respectively (Table 5). According to the results, the IC_{50} value of the watery extract of LGP is lower than ethanol but higher than standard diclofenac sodium, 57.57 µg/mL. The lower the IC_{50} value, the higher anti-arthritic activity. Therefore, the watery extract of LGP has more anti-arthritic potency than ethanol extract. So, it can be concluded that a watery extract of LGP can serve as an anti-arthritic agent.

Table 5. Average % Protein Denaturation and IC_{50} Values of Crude Extracts of Longan Peels

Tested Samples	% Protein Denaturation ± SD of different concentrations (µg/mL)						IC_{50} (µg/mL)
	31.25	62.5	125	250	500	1000	
Watery extract	34.98 ±0.10	41.29 ±0.09	56.75 ±0.00	61.67 ±0.09	86.09 ±0.02	90.20 ±0.23	97.77
Ethanol extract	27.10 ±0.04	44.62 ±0.21	43.92 ±0.00	47.38 ±0.01	54.14 ±0.00	74.40 ±0.29	347.41
Std. Diclofenac sodium	34.87 ±0.03	52.84 ±0.34	54.65 ±0.10	60.57 ±0.03	65.20 ±0.07	78.83 ±0.00	57.57

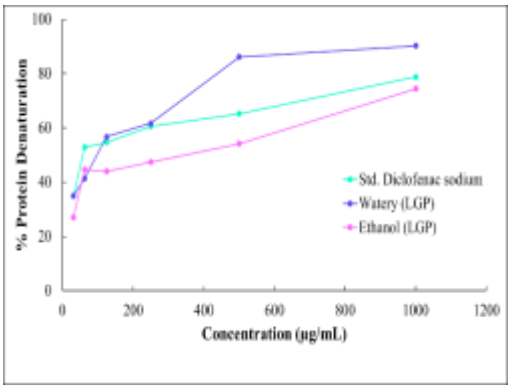

Figure 5. Mean % inhibition versus concentration of different extracts of longan peel

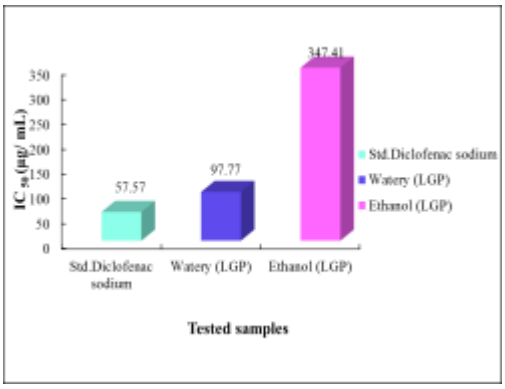

Figure 6. IC_{50} values of crude extracts of longan peels

Some Physico-chemical Properties of the Isolated Compounds

By silica gel column chromatographic separation, four compounds were isolated from the PE extract of LGP. They were characterized by melting point, FT IR, comparison with reported data. Compound **A** was synthesized as a colourless needle crystal PE: EtOAc (19:1 v/v) (R_f = 0.4, Hex: CH_2Cl_2, 4:1 v/v, m.pt 255-260 ˚C, 0.002 % yield). It is UV inactive. It is soluble in PE, $CHCl_3$ and CH_3OCH_3 but insoluble in EtOAc, MeOH, EtOH, and H_2O. In the chemical test, it gave a green colour when treated with Libermann-Burchard solution due to the presence of steroids and a brown spot appeared when tested with iodine vapour because of the C=C present. In the FT IR data, Figure 7(a) indicated the presence of asymmetric and symmetric C-H stretching and bending vibration of sp^3 hydrocarbons at 2925, 2858 cm^{-1} and 1460, 1389 cm^{-1}, respectively. The carbonyl group of C=O stretching vibration was observed at 1714 cm^{-1}. The cyclic ether of C-O stretching bands was displayed at 1190, 1109, and 1073 cm^{-1} and C-H out of plane bending vibration was displayed at 924, 794 cm^{-1}. According to the results, compound **A** may be considered a steroid compound.

Compound **B** (R_f = 0.6, PE: EtOAc (9:1) v/v, m.pt 290 ˚C, 0.001% yield) was obtained as a colourless crystal. It is UV inactive. It is soluble in PE, $CHCl_3$, and CH_3OCH_3 but insoluble in EtOAc, MeOH, EtOH, and H_2O. According to the pink colouration that was observed when treated with acetic anhydride and conc: H_2SO_4. Therefore, compound **B** may be considered a terpenoid. The FT IR spectrum of compound **B** (Figure 6 (b)) showed absorption bands at 3620, 3466 cm^{-1} and 1360, 1256 cm^{-1} due to the presence of alcoholic -OH stretching and bending bands (Silverstein *et al*., 2015), respectively. The bands at 2929, 2872cm^{-1} and 1449, 1385 cm^{-1} were appeared due to the asymmetric and symmetric C-H stretching and bending vibrations of sp^3 hydrocarbons, respectively. The bands at 1174, 1049, and 1020 cm^{-1} could be presented as C-O stretching vibration of alcohol groups, and C-H out of plane bending vibration was observed at 981, 920, 791, and 620 cm^{-1}, respectively. Therefore, compound **B** may be considered a terpenoid.

Compound **C** (R_f = 0.6, PE: EtOAc (5:1) v/v, m.pt 139-140 ˚C, 0.003 % yield) was obtained as a colourless needle crystal. It is soluble in PE, $CHCl_3$ and CH_3OCH_3, EtOAc but insoluble in MeOH, EtOH, and H_2O. Compound **C** visualized green colouration with Libermann-Burchard solution due to the presence of steroid. Moreover, the TLC behaviour of compound **C** was found to be identical with that of *β*-sitosterol in any solvent system. Therefore, compound **C** may be *β*-sitosterol. In the FT IR spectrum of compound **C** Figure 6 (c) due to O-H stretching of the alcoholic group, broadband can be seen at 3473 cm^{-1} and bending vibration at 1367 cm^{-1}. The asymmetrical and symmetrical C-H stretching vibrations of $–CH_2$ and $–CH_3$ groups may be assigned to 2933, 2865 cm^{-1} and bending vibrations at 1464 cm^{-1}. The olefinic group of C=C stretching vibration is at 1687 cm^{-1}. At 1385 cm^{-1}, it appeared due to the CH_3 deformation of the isopropyl group. The cyclic alcohol of C−O stretching vibration occurred at 1023, 1049, 1174 cm^{-1} and the bands of 920, 959 cm^{-1} were designated as the C-H deformation of out of plane bending in benzene. All the results, such as melting point, R_f value, chemical properties, and FT IR spectral data of compound **C** were found to be similar to those of reported *β*-sitosterol (Azeez *et al*., 2018). As a result, the isolated compound C could be assigned as *β*-sitosterol.

Compound **D** (R_f = 0.6, PE: EtOAc, 5:1 v/v, m.pt 130-140 ˚C, 0.001% yield) was obtained as a colourless needle crystal PE: EtOAc (9:1 v/v). It is soluble in PE, $CHCl_3$ CH_3OCH_3 and EtOAc but insoluble in MeOH, EtOH, and H_2O. Compound **D** gave a green colour with Libermann-Burchard solution and a yellow colour with Bromocresol green because it is the steroid compound. Therefore, compound **D** may be considered as steroid acid. In the FT IR spectrum of compound **D** Figure 6 (d), the carboxylic acid of O-H stretching vibration for the COOH group indicated the absorption band at 3473 cm^{-1} and 1360 cm^{-1}, respectively. The

asymmetrical and symmetrical C-H stretching and bending vibrations of $–CH_2$ and $–CH_3$ groups were assigned at 2933, 2869 cm^{-1} and 1442, 1385 cm^{-1}, respectively. The C=O of carboxylic acid for the COOH group was displayed at 1710 cm^{-1}. The C-O stretching of the alcoholic O-H group was observed at 1220, 1049, and 1020 cm^{-1}, respectively. C-H out of plane bending vibration was shown at 981, 920, 709, and 530 cm^{-1}, respectively. According to the results, compound **D** may be considered a steroidal carboxylic acid.

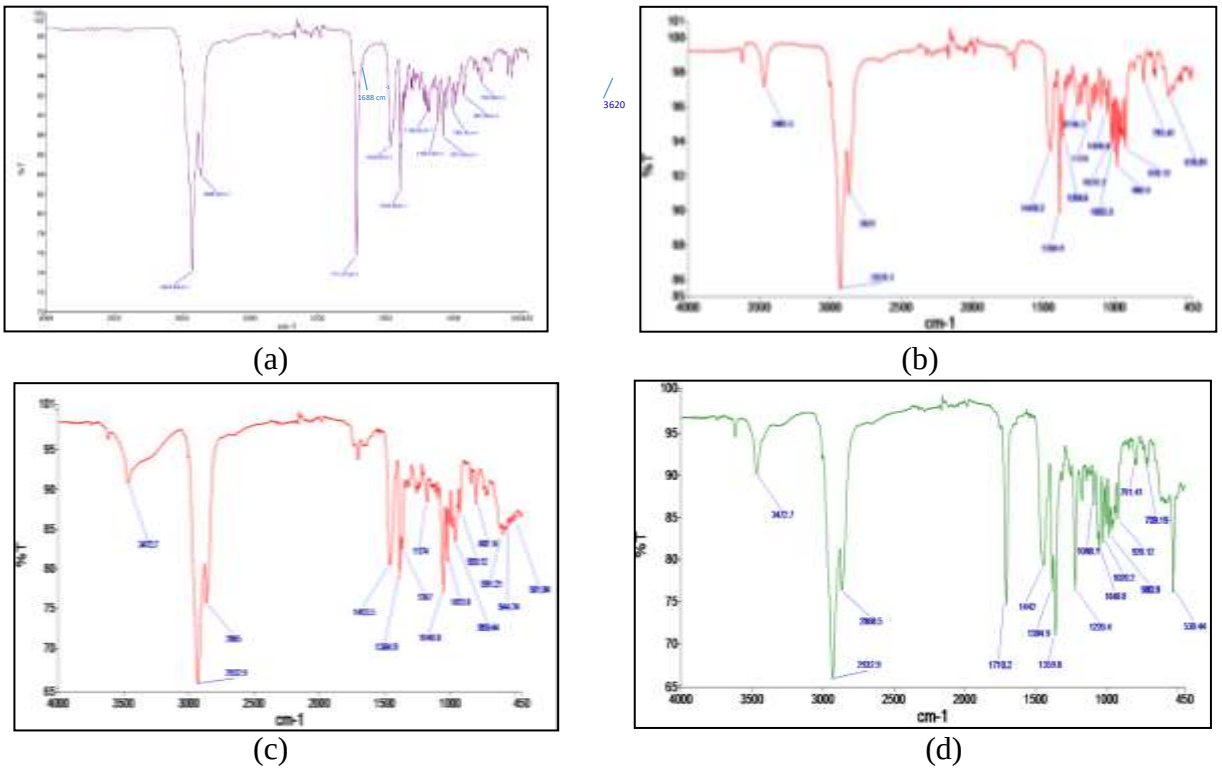

Figure 7. FT IR spectra of isolated (a) compound A, (b) compound B, (c) compound C and (d) compound D from PE extract of longan peels

Conclusion

The present research work deals with the first report for the investigation of total phenol contents, antioxidant, cytotoxicity, and anti-arthritic activities and phytoconstituents of *Dimocarpus longan* Lour. (Longan) peels. Based on the data, EtOH extract (176.12 ± 0.15 µg GAE/mg) was found to possess a higher total phenol content than watery extract (76.22 ± 0.45) µg GAE/mg). The antioxidant activity of the ethanol extract (IC_{50} = 8.77 µg/mL) is more effective than that of the watery extract. According to the cytotoxic effect, ethanol and watery extracts from LGP were observed to be free from toxic effects up to 1000 µg/mL dose. In terms of anti-arthritic activity, the watery extract (IC_{50} = 97.77 µg/mL) was more effective than the ethanol extract but slightly lower than the standard diclofenac sodium (IC_{50} = 57.57 µg/mL). On silica gel column chromatographic separation, four compounds were isolated from the PE crude extract of the LGP. Four compounds such as a steroid (**A**, m.pt 255-260 ˚C, 0.002 % yield), a terpenoid (**B**, mpt 290 ˚C, 0.001% yield), β-sitosterol (**C**, mpt 138-140 ˚C, 0.003% yield), and a steroidal carboxylic acid (**D**, mpt. 130-140 ˚C, 0.001% yield) were isolated. The information about the chemical composition and biological investigation described in this report might be useful in the formulation of corresponding traditional medicines.

Acknowledgements

The authors would like to express their profound gratitude to the Ministry of Education, Department of Higher Education (Yangon), for provision of opportunity to do this research and Myanmar Academy of Arts and Science for allowing to present this paper.

References

Azeez, R. A., I. S. Abaas, and E. J. Kadhim. (2018). "Isolation and Characterization of *β*-sitosterol from *Elaeagnus angustifolia* Cultivated in Iraq". *Asia Journal of Pharmaceutical and Clinical Research*, vol. 11(11), pp. 442-446

Dipak, G., P. Axay, C. Manodeep, and K. Jagdish. (2012). "Phytochemical and Pharmacological Profile of *Punica granatum*: An Overview". *International Research Journal of Pharmacy*, vol. 3(2), pp. 65-68

Hishamuddin, S. N. A., Q. Q. Amir, A. H. Mohamed, and N. R. Said. (2020). "Extraction of Bioactive Compounds from Longan Peel by Using Solvent Extraction Method and its Antioxidant Activity". *ASM Science Journal*, vol. 13(6), pp. 60-65

Shahrajabian, M. H., W. Sun, and Q. Cheng. (2019). "Modern Pharmacological Actions of Longan fruits and their usages in Traditional Herbal Remedies". *Journal of Medicinal Plants Studies*, vol. **7**(4), pp. 179-185

Silverstein, R. M, F. X. Webster, D. J. Kiemle, and D. L. Bryce. (2015). *Spectrometric Identification of Organic Compounds.* New York: 8th Ed., John Wiley and Sons, Inc., pp. 71-125.

Singh, M. P., J. Singh, and Rajesh. R. (2015). "Brine Shrimp Cytotoxic Assay for Polyherbal Formulation of *Moringa oleifera, Viola odorata, Allium sativum*". *International Journal of Innovative Pharmaceutical Sciences and Research*, vol. 3(12), pp. 1639-1643

Sunmathi, D., R. Sivakumar, and K. Ravikumar. (2016). "*In vitro* Anti-inflammatory and Antiarthritic Activity of Ethanolic Leaf Extract of *Alternanthera sessilis* (L.) R.BR. ex DC and *Alternanthera philoxeroides* (Mart.) Griseb". *International Journal of Advances in Pharmacy, Biology and Chemistry*, vol. 5(2), pp. 109-115

VIRAL PROTEIN R INHIBITORS FROM SOME MEDICINAL PLANTS COLLECTED IN MYANMAR

Prema[1], Hnin Htet Wai Nyunt[2], Yi Yi Win[3], Daw Hla Ngwe[4], Hiroyuki Morita[5]

Abstract

The aim of the study is to identity a viral protein R (Vpr) inhibitor from the bioactive selected medicinal plants collected in Myanmar. Their methanol and chloroform extracts were tested separately for their inhibitory effect on Vpr activities on the TREx-HeLa-Vpr cells. The chloroform extracts of P. javanica wood, G. sherwoodiana rhizomes, and *K. candida* roots and rhizomes showed the most potent anti-Vpr activities with cell proliferation percentages of 178%, 160%, and 160% at 10 µg/mL, respectively. Then, the thirty-nine compounds were isolated from these three bioactive samples, identified by UV, FT IR, NMR, HR-ESI-MS, and CD. Five new quassinoids (**1**-**5**), together with ten known compounds (**6**-**15**) were isolated from the active chloroform extract of the *P. javanica* wood. Isolated quassinoids **1**-**4**, **6**-**9**, and 10 displayed potent anti-Vpr activity, with the cell proliferation rate ranging from 148% to 181%, at the 5 µM concentration. Then, two new homodrimane type sesquiterpenoids (**16** and **17**), a new 16-norlabdane diterpenoid (**18**), two new naturally occurring compounds (**19** and **20**), together with eleven known compounds (**21**-**31**) were isolated from the chloroform extract of the *G. sherwoodiana* rhizomes. The isolated compounds **16**, **18**, **19**, **23**, **24**, **27**, and **29** showed moderate anti-Vpr activities at a concentration of 10 µM. In addition, three new compounds (**32**-**34**), together with five known compounds (**35**-**39**) were isolated from the chloroform extract of the *K. candida* roots and rhizomes. All of the isolated compounds showed moderate anti-Vpr activities on the TREx-HeLa-Vpr cells. Among the isolated compounds, **32** and **34**-**38** possessed higher anti-Vpr activity than **33** and **39**.

Keywords: Anti-Vpr activities, *P. javanica* wood, *G. sherwoodiana* rhizomes, *K. candida* roots and rhizomes, isolated compounds

Introduction

Viral protein R (Vpr) is a small basic protein (14 kDa) of 96 amino acids found in HIV-1, HIV-2, and the simian immunodeficiency virus (SIV), and plays an important role in the virus life cycle. Vpr seems to be essential for viral replication in non-dividing cells such as macrophages. It has several functions, including cell cycle arrest at G2/M phase, modulation of CD4 T cell apoptosis, nuclear import of the pre-integration complex (PIC), nuclear localization, cation selective channel activity, and transcriptional activation of HIV-1 LTR and other heterologous promoters (Morellet *et al*., 2003). Considering these functions, the Vpr inhibitor is one of the possible target molecules for anti-HIV drugs. Myanmar is the second largest country in Southeast Asia, and about half of the land area is covered with forest. Approximately 11,800 species belonging to 273 families of plants have been recorded in the Myanmar flora (Kress *et al.*, 2003). Several of these plant species are used in traditional cosmetics and/or folk medicine. However, most of the scientific evidence for the bioactivities of these medicinal plants and phytochemical constituents is still behind the scenes. In previous studies, we reported the chemical constituents such as isopimarane diterpenoids, picrasane quassinoids, terpenoids, iridoids, and bis-iridoid glycosides with potent anti-Vpr activities (Win *et al*., 2016). These results motivated me to continue the search for new Vpr inhibitors as a part of the anti-HIV drug discovery from Myanmar's natural resources. In this study, 11 species of plants, including *Picrasma javanica* wood (Simaroubaceae), *Stemona burkillii* tuber (Stemonaceae), *Zanthoxylum rhetsa* trunks

[1] Department of Chemistry, University of Myitkyina, Myanmar
[2] Department of Chemistry, Dagon University, Myanmar
[3] Department of Chemistry, Hpa-An University, Myanmar
[4] Department of Chemistry, University of Yangon, Myanmar
[5] Institute of Natural Medicine, University of Toyama, Japan

(Rutaceae), and eight rhizomes from the Zingiberaceae family, including *Amomum corynostachyum*, *Curcuma aeruginosa*, *C. comosa*, *C. petiolata*, *Globba sherwoodiana*, *Kaempferia candida*, *K. parvilora*, and *Zingiber zerumbet,* were collected in Myanmar, and their methanol and chloroform extracts with three different concentrations were tested separately for their inhibitory effect on Vpr activities on the TREx-HeLa-Vpr cells. Furthermore, the chloroform extracts of the *P. javanica* wood, *G. sherwoodiana* rhizomes, and *K. candida* roots and rhizomes showed the most potent anti-Vpr activities without any cytotoxicity on the Vpr-induced cells.

Picrasma javanica Blume. is a bitter, medium-sized rainforest tree belonging to the Simaroubaceae family. It is locally known as 'Nann-paw-kyawt' in Myanmar. The plant is found spanning Southeast Asia, Papua New Guinea, India, Indonesia, the Solomon Islands, and Myanmar. *P. javanica* stem bark and leaves are widely used for the treatment of malaria in traditional medicine in Myanmar, Indonesia, Thailand, and northern India. The stem bark and leaves contain quassinoids, indole alkaloids, coumarins, sesquiterpenes, and triterpenes. *P. javanica* extracts and their constituents reportedly possess various biological properties; antimalaria, antioxidant, thrombolytic, cytotoxicity, antibacterial, antiproliferative, membrane stability, hypoglycemic, and anti-Vpr activities (Saiin and Sirithunyalug, 2017, and Win *et al*., 2016).

Globba sherwoodiana (Zingiberaceae) is a small perennial herb from 38 to 45 cm in height with compact rhizomes and tall leafy shoots. It was identified as a new species in 2012 based on its obvious morphology. In Myanmar, it is cultivated and locally known as 'Padein Gno'. *G. sherwooiana* is also cultivated in Thailand and India. The flowers of *G. sherwoodiana* are sold in markets and used for Buddhist offerings in Myanmar and Thailand. The previous phytochemical studies revealed that the genus *Globba* contains labdane diterpenoids, sesquiterpenoids, steroids, lipids, and phenolic compounds. Labdane diterpenoids were reported to possess antibacterial and antifungal activities (Shaaria *et al*., 2009).

The genus *Kaempferia* L. belongs to the Zingiberaceae family and comprises approximately 60 species distributed worldwide. Among them, *K. candida* is a 45-60 cm tall perennial herb that is distributed in Myanmar and Thailand. Its roots are small, tuberous, oblong, and pale brown in colour, and inflorescences are numerous, with white-yellow flowers emerging directly from rhizomes. It grows in the burnt bamboo forest along roadside and teak plantations in both shady and sunny habits. In Myanmar, it is locally known as "Pa-dat-sa", and the young inflorescences and tuberous roots are consumed as a fresh vegetable (Jenjittikul and Larsen, 2000). Previous studies on the plant species of the genus *Kaempferia* have reported the isolation of several sesquiterpenes, diterpenes, diarylheptanoids, essential oils, steroids, flavonoids, and phenolic compounds. These compounds have been reported to possess anticancer, anti-obesity, antimicrobial, antioxidant, anti-inflammatory, anticholinesterase, anti-mutagenicity, and anti-Vpr activities (Win *et al*., 2016; and Chawengrum *et al*., 2018). To the best of our knowledge, the investigation of phytochemical constituents and biological activities of *G. sherwoodiana* and *K. candida* has not been reported yet.

Therefore, this study focused on the isolation and characterization of Vpr inhibitors from three Myanmar plants: *P. javanica* wood, *G. sherwoodiana* rhizomes, and *K. candida* roots and rhizomes.

Materials and Methods

Extraction and Preparation of Test Solution

Eleven plant samples were dried at room temperature and coarsely powdered. The dried powder was macerated with methanol and chloroform to obtain methanol and chloroform crude extracts. After the solvent was evaporated under reduced pressure, the crude extract was dissolved in DMSO and used for the anti-Vpr activities, according to the published procedure.

In Vitro Anti-Vpr Activity Against TREx-HeLa-Vpr Cells

Cell culture and Transfection: TREXTM-HeLa cells were grown in α-minimal essential medium (α-MEM, Wako) supplemented with 10% fetal bovine serum (FBS, Nichirei Bioscience), 1% antibiotic antimycotic solution (Sigma–Aldrich), and 5 μg/mL of blasticidin at 37 °C under a 5 % CO_2 and 95 % air atmosphere. When the cells were 40–50 % confluent, the inducible expression vector (Vpr-c-myc-His6), pc DNA4/TO plasmid encoding full-length Vpr from HIV-1NL4-3 (Genbank) and c-myc-His6-Tag provided by Professor Ikuro Abe at the University of Tokyo, were co-transfected with pcDNA6/TR into TREx-HeLa cells using the calcium chloride transfection method. The medium was supplemented with 200 μg/mL of zeocin, and the culture was continued to select a single stable cell line expressing both the Tet repressor and Vpr genes. Screening the assay system: The anti-Vpr activities of the extracts and the isolated compounds with the three different concentrations were tested on the Vpr induced TREx-HeLa cells, as described previously. Briefly, TREx-HeLa-Vpr cells (12×10^3 cells/well) were seeded in 48-well plates and cultured in Minimum Essential Medium (α-MEM) at 37 °C with a 5% CO_2 and 95% air atmosphere for 24 h. After 24 h of culture, tetracycline solution (50 μL of 10 μg/mL) was added to induce Vpr expression, and the cells were incubated further for 24 h. After incubation, three different concentrations of the extracts and compounds (50 μL) were added to the wells and incubated for 48 h. Afterwards, a 10% MTT solution (50 μL) was added to each well and further incubated for 3 h. The supernatant was then removed, and DMSO (200 μL) was added to each well and incubated for 10–15 min. The absorbance was measured with a microplate reader at 570 nm. The cell proliferation was calculated, and the data was expressed as mean values and standard deviation by the following equation: cell proliferation (%) = 100 × [Abs (treated cell) - Abs (blank)/Abs (control cell)-Abs (blank)]. The cytotoxicities of the extracts and compounds were also evaluated using the same MTT method, without tetracycline induction. Damnacanthal (Dam) was used as a positive control.

General Experimental Procedures

Specific optical rotations were determined by the JASCO P2100 polarimeter (Japan) at standard room temperature (22 °C). Ultravoilet (UV) spectra were recorded on a NanoDrop TM 2000C spectrophotometer (Thermo Fisher Scientific, Waltham, MA, USA) in methanol. Circular dichroism (CD) spectra were recorded on a JASCO-J-805 spectropolarimeter (Japan) in methanol. Fourier-transform infrared (FT IR) spectra were recorded on a JASCO FT/IR-460 Plus spectrometer (Japan). Melting points were measured with a YANACO melting point apparatus (Japan) and are uncorrected. Nuclear magnetic resonance (NMR) spectra were recorded at 500 MHz (^{1}H NMR) and 125 MHz (^{13}C NMR) on a JEOL ECA500II spectrometer (Wako Pure Chemical Industries, Ltd., Osaka, Japan) in $CDCl_3$. High-resolution mass spectrometry (HR-ESI-MS) data was taken on a SHIMADZU LCMS-IT-TOF (Shimadzu, Kyoto, Japan) spectrometer. Normal phase silica gel (silica gel 60 N, spherical, neutral, 40–50 μm; Kanto Chemical, Tokyo, Japan) and reversed phase silica gel (Cosmosil 75C18-OPN; Nacalai Tesque, Kyoto, Japan) were used for open column chromatography (C.C.). Thin layer chromatography (TLC) was performed using silica gel GF254 precoated (Merck) plates. Reverse-phase HPLC column chromatography

with COSMOSIL 5C18-AR-II (10 × 250 mm) columns was used for separation on an Agilent Technologies 1260 quat pump with a JEOL detector. The absorbance for the biological assay was measured at 570 nm by SH-1200 Microplate Reader (Corona, Hitachinaka, Japan).

Plant Materials for Isolation

The *P. javanica* wood was collected from Kayin State (September 2016), fresh *G. sherwoodiana* rhizomes (10.0 kg) were collected from Pyin Oo Lwin Township, Mandalay Region (October 2018), and fresh (5.0 kg) *K. candida* roots and rhizomes were collected from Pathein Township, Ayeyawady Division (June 2018), Myanmar. The samples were identified by Dr. Khin Cho Cho Oo and Dr. New Ni Tun, botanists at the Department of Botany, University of Yangon. The samples were washed, cut into small pieces, air dried at room temperature, and made into powder by using a grinding machine, and stored in airtight container.

Extraction and Isolation Procedure of Three Selected Samples

The dried powdered *P. javanica* wood sample (1.0 kg) was macerated in methanol (5.0 L × 5) for 2 h with sonication. 97.6 g of methanol extract was obtained after filtration and removal of the solvent by a rotary evaporator, and it was triturated in 50 mL of water and successively partitioned with chloroform to obtain (43.3 g) extract. The chloroform extract (42.4 g) was subjected to normal phase silica gel open C.C., using solvent systems composed of *n*-hexane: $CHCl_3$ and $CHCl_3$: MeOH, to give seven main fractions (F1-F7) after TLC profiling. The fractions (F1-F5) were further subjected to a series of chromatographic separation: **1** (6.0 mg), **2** (20.0 mg), **3** (2.0 mg, R_f = 0.50), **4** (7.9 mg, R_f = 0.34), **5** (0.4 mg, tR 52.0 min), **6** (1.1 g), **7** (45.0 mg), **8** (7.0 mg, tR 42.00 min), **9** (15.0 mg, tR 47.00 min), **10** (17.0 mg, tR 60.5 min), **11** (80.0 mg, tR 74.0 min), **12** (123.0 mg), **13** (2.0 mL/min, tR = 21.65 min, 10.0 mg), **14** (19.0 mg), and **15** (2.0 mL/min, tR = 11.23 min, 5.0 mg) totaling fifteen compounds, were obtained. The dried powder rhizomes of *G. sherwoodiana* (3.2 kg) were extracted with chloroform by sonication (7.0 L, 90 min, × 5) at room temperature to give a residue (80.4 g). The chloroform extract (80.0 g) was subjected to silica gel C.C. eluted with *n*-hexane: EtOAc including (9.5:0.5 to only EtOAc) and EtOAc: MeOH (9:1 and 7:3) to give ten main fractions (F1 to F10) after TLC profiling. From fractions F2, F3, F5, F6, F7, and F8, **16** (25.0 mg), **17** (10.0 mg), **18** (11.0 mg), **19** (5.0 mg), **20** (20.0 mg), **21** (1.5 mg), **22** (2.0 mg), **23** (30.0 mg), **24** (25.7 mg), **25** (0.9 mg), **26** (2.0 mg), **27** (35.0 mg), **28** (5.0 mg), **29** (10.0 mg), **30** (1.0 mg), and **31** (7.2 mg), totaling sixteen compounds, were obtained. by silica gel C.C, eluted with an *n*-hexane: CH_2Cl_2: EtOAc (40:40:1 and 20:20:1). The dried powdered roots and rhizomes of *K. candida* (1.4 kg) were extracted with methanol (7.0 L, 90 min × 5) at room temperature by sonication, and it was evaporated under reduced pressure to obtain the extract (158.0 g). The residue was suspended in water and partitioned with chloroform (500 mL×8) to yield a chloroform soluble fraction (37.1 g). The chloroform extract (36.0 g) was chromatographed on a silica gel C.C. with gradient elution using *n*-hexane: EtOAc (9:1 to EtOAc only) to yield five fractions (F1-F5), which were combined based on TLC analysis. The fractions (F2-F5) were chromatographed by normal phase silica gel C.C. eluted with *n*-hexane: EtOAc and EtOAc: $CHCl_3$ (7:3 and 1:1) as solvent systems, to give eight compounds, **32** (2.5 mg), **33** (5.0 mg), **34** (2.5 mg), **35** (59.3 mg), **36** (10.0 mg), **37** (11.3 mg), **38** (11.0 mg), and **39** (50.0 mg).

DFT/TDDFT Calculations

A conformation based on the X-ray crystallographic structure of compound-**10** was optimized, using RI-DFT at the M06-L/TZVP level of theory. Excited states calculations (oscillator and rotatory strengths) were performed on the optimised ground state geometry at the

TDDFT M06-L/augcc-pVTZ level of theory. All DFT and TDDFT calculations were performed using Turbomole 7.1.

Results and Discussion

Anti-Vpr Activity of Various Crude Extracts of Eleven Medicinal Plants

In this study, methanol and chloroform extracts (Figures 1 and 2) of 11 species of plants were collected in Myanmar and tested separately for their inhibitory effect on Vpr activities on the TREx-HeLa-Vpr cells. The screening results revealed that the chloroform extracts possessed stronger anti-Vpr activities than the methanol extracts. Furthermore, the chloroform extracts of the *P. javanica* wood, *G. sherwoodiana* rhizomes, and *K. candida* roots and rhizomes showed the most potent anti-Vpr activities without any cytotoxicity on the Vpr-induced cells, with cell proliferation percentages of 178 %, 160 %, and 160 % at 10 μg/mL, respectively.

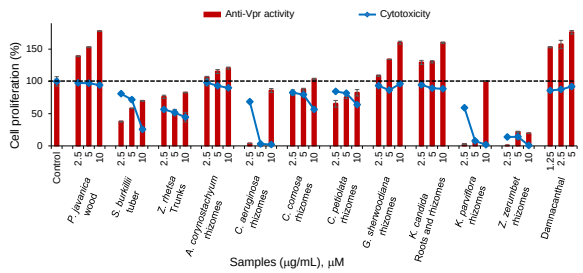

Figure1. Inhibitory effects of the chloroform extract of tested samples and positive control, damnacanthal, on Vpr expression. Data are represented as mean ± SD (n = 3)

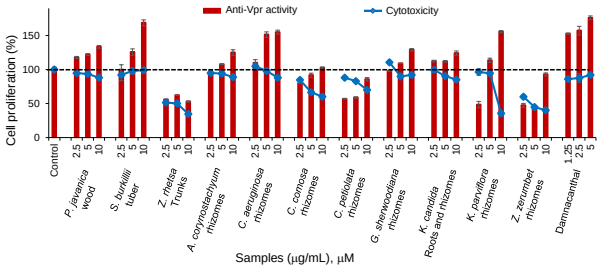

Figure 2. Inhibitory effects of the methanol extract of tested samples and positive control, damnacanthal, on Vpr expression. Data are represented as mean ± SD (n = 3)

Structure Elucidation of Isolated Compounds (1-15) from the Wood of *P. javanica*

Five new quassinoids (**1-5**) together with ten known compounds (**6-15**) (Figure 3) were isolated from the active chloroform extract of the wood of *P. javanica*.

(16*R*)-Methoxyjavanicin B (1): white amorphous powder; $[\alpha]_D^{22}$ −14.9° (*c* 0.1, MeOH); CD (*c* 0.01, MeOH): 245 (Δε −5.75), 268 (Δε 19.11) nm; UV (MeOH) λ_{max}: 218, 259 nm; IR (KBr) ν_{max}: 2945, 2839, 1690, 1638, 1454, 1370, 1213, 1130, 1042 cm^{-1}; ^1H NMR (500 MHz, $CDCl_3$) δ_H 5.46 (dd, *J* = 5.7, 2.3 Hz, H-3), 2.12 (dt, *J* = 18.9, 5.7 Hz, H-4*α*), 2.21 (m, H-4*β*), 2.44 (m, H-5), 1.57 (dt, *J* = 14.3, 2.9 Hz, H-6*α*), 1.86 (m, H-6*β*), 3.31 (t, *J* = 2.9 Hz, H-7), 3.17 (s, H-9), 1.96 (dd, *J* = 12.6, 4.6 Hz, H-14), 1.67 (dt, *J* = 12.6, 2.9 Hz, H-15*α*), 2.03 (m, H-15*β*), 4.35 (dd, *J* = 9.7, 2.9 Hz, H-16), 1.48 (s, H_3-18), 1.05 (s, H_3-19), 1.82 (s, H_3-20), 3.55 (s, 2-OCH_3), 3.64 (s, 12-OCH_3), 3.46 (s, 16-OCH_3); ^{13}C NMR data (125 MHz, $CDCl_3$) δ_C 197.9 (C-1), 149.4 (C-2), 109.6 (C-3), 27.4 (C-4), 36.5 (C-5), 29.4 (C-6), 77.6 (C-7), 39.1 (C-8), 46.7 (C-9), 46.2 (C-10), 193.2 (C-11), 148.4 (C-12), 137.9 (C-13), 49.8 (C-14), 32.5 (C-15), 102.7 (C-16), 11.6 (C-18), 21.9 (C-19), 15.3 (C-20), 55.1 (2-OCH_3), 59.2 (12-OCH_3), 56.2 (16-OCH_3); HR-ESI-MS: *m/z* 391.2100 $[M+H]^+$ (calcd. for $C_{22}H_{31}O_6$, 391.2115) (Prema *et al*., 2019)

(16*S*)-Methoxyjavanicin B (2): colorless solid; m.p. 228–230 °C; $[\alpha]_D^{22}$ +14.3° (*c* 0.1, MeOH); CD (*c* 0.01, MeOH): 244 (Δε −5.82), 268 (Δε 19.11) nm; UV (MeOH) λ_{max}: 219, 260 nm; IR (KBr) ν_{max}: 2941, 2840, 1690, 1639, 1453, 1369, 1213, 1042 cm^{-1}; ^1H NMR (500 MHz, $CDCl_3$) δ_H 5.46 (dd, *J* = 5.7, 2.3 Hz, H-3), 2.10 (dt, *J* = 18.3, 5.7 Hz, H-4*α*), 2.23 (m, H-4*β*), 2.35 (m, H-5), 1.44

(dt, *J* = 14.4, 2.9 Hz, H-6*α*), 1.90* (m, H-6*β*), 3.60 (t, *J* = 2.9 Hz, H-7), 3.17 (s, H-9), 2.28 (dd, *J* = 12.6, 4.6 Hz, H-14), 1.88 (dt, *J* = 12.6, 2.9 Hz, H-15*α*), 1.93* (m, H-15*β*), 4.78 (brd, *J* = 2.9 Hz, H-16), 1.50 (s, H_3-18), 1.07 (s, H_3-19), 1.84 (s, H_3-20), 3.58 (s, 2-OCH_3), 3.64 (s, 12-OCH_3), 3.37 (s, 16-OCH_3); ^{13}C NMR data (125 MHz, $CDCl_3$) δ_C 198.4 (C-1), 149.4 (C-2), 109.5 (C-3), 27.4 (C-4), 36.8 (C-5), 29.2 (C-6), 69.4 (C-7), 38.9 (C-8), 46.0 (C-9), 46.1 (C-10), 193.0 (C-11), 148.4 (C-12), 139.5 (C-13), 44.1 (C-14), 31.1 (C-15), 97.7 (C-16), 11.5 (C-18), 22.2 (C-19), 15.4 (C-20), 55.0 (2-OCH_3), 59.2 (12-OCH_3), 54.7 (16-OCH_3); HR-ESI-MS: *m/z* 391.2070 $[M+H]^+$ (calcd. for $C_{22}H_{31}O_6$, 391.2115) (Prema *et al*., 2019)

Javanicinol A (3): white amorphous powder; $[\alpha]_D^{22}$ +14.8° (*c* 0.1, MeOH); CD (*c* 0.01, MeOH): 230 (Δ*ε* −12.13), 280 (Δ*ε* 7.29), 332 (Δ*ε* −4.39) nm; UV (MeOH) λ_{max}: 219, 250 nm; IR (KBr) ν_{max}: 3428, 2945, 2844, 1720, 1640, 1452, 1384, 1250, 1034 cm^{-1}; ^{1}H NMR (500 MHz, $CDCl_3$) δ_H 3.79 (dd, *J* = 12.6, 2.9 Hz, H-3), 1.79* (m, H-4*α*), 1.87 (dt, *J* = 12.6, 2.9 Hz, H-4*β*), 1.58 (tt, *J* = 12.6, 2.9 Hz, H-5), 1.76* (m, H-6*α*), 1.98 (ddd, *J* = 14.3, 12.6, 2.9 Hz, H-6*β*), 4.24 (t, *J* = 2.9 Hz, H-7), 3.04 (s, H-9), 2.39 (dd, *J* = 12.0, 6.9 Hz, H-14), 2.57 (dd, *J* = 18.3, 12.0 Hz, H-15*α*), 2.98 (dd, *J* = 18.3, 6.9 Hz, H-15*β*), 1.61 (s, H_3-18), 1.19 (s, H_3-19), 1.89 (s, H_3-20), 3.47 (s, 2*α* -OCH_3), 3.41 (s, 2*β*-OCH_3), 3.63 (s, 12-OCH_3); ^{13}C NMR data (125 MHz, $CDCl_3$) δ_C 204.2 (C-1), 101.1 (C-2), 74.9 (C-3), 33.8 (C-4), 33.0 (C-5), 28.8 (C-6), 82.1 (C-7), 37.1 (C-8), 47.6 (C-9), 49.0 (C-10), 190.8 (C-11), 148.4 (C-12), 139.7 (C-13), 47.4 (C-14), 31.6 (C-15), 168.8 (C-16), 11.4 (C-18), 23.0 (C-19), 15.8 (C-20), 51.8 (2*α*-OCH_3), 51.9 (2*β*-OCH_3), 59.7 (12-OCH_3); HR-ESI-MS: *m/z* 445.1850 $[M+Na]^+$ (calcd. for $C_{22}H_{30}O_8Na$, 445.1833) (Prema *et al*., 2020)

Javanicinol B (4): white amorphous powder; $[\alpha]_D^{22}$ −15.9° (*c* 0.1, MeOH); CD (*c* 0.01, MeOH): 234 (Δ*ε* −3.26), 264 (Δ*ε* 7.09), 330 (Δ*ε* −4.47) nm; UV (MeOH) λ_{max}: 217, 249 nm; IR (KBr) ν_{max}: 3378, 2940, 2842, 1722, 1638, 1451, 1380, 1249, 1035 cm^{-1}; ^{1}H NMR (500 MHz, $CDCl_3$) δ_H 4.18 (t, *J* = 2.9 Hz, H-3), 1.59 (dt, *J* = 14.3, 2.9 Hz, H-4*α*), 2.15 (td, *J* = 14.3, 2.9 Hz, H-4*β*), 2.32 (tt, *J* = 14.3, 2.9 Hz, H-5), 1.73 (dt, *J* = 14.9, 2.9 Hz, H-6*α*), 2.00 (ddd, *J* = 14.9, 14.3, 2.9 Hz, H-6*β*), 4.23 (t, *J* = 2.9 Hz, H-7), 3.14 (s, H-9), 2.39 (dd, *J* = 12.6, 6.9 Hz, H-14), 2.60 (dd, *J* = 18.3, 12.6 Hz, H-15*α*), 2.95 (dd, *J* = 18.3, 6.9 Hz, H-15*β*), 1.62 (s, H_3-18), 1.19 (s, H_3-19), 1.88 (s, H_3-20), 3.32 (s, 2*α* -OCH_3), 3.34 (s, 2*β*-OCH_3), 3.62 (s, 12-OCH_3); ^{13}C NMR data (125 MHz, $CDCl_3$) δ_C 204.9 (C-1), 101.9 (C-2), 70.6 (C-3), 29.9 (C-4), 34.2 (C-5), 28.8 (C-6), 82.4 (C-7), 37.0 (C-8), 47.8 (C-9), 50.5 (C-10), 191.1 (C-11), 148.4 (C-12), 139.7 (C-13), 47.7 (C-14), 31.6 (C-15), 168.9 (C-16), 11.3 (C-18), 23.5 (C-19), 15.7 (C-20), 52.2 (2*α*-OCH_3), 48.2 (2*β*-OCH_3), 59.7 (12-OCH_3); HR-ESI-MS: *m/z* 445.1811 $[M+Na]^+$ (calcd. for $C_{22}H_{30}O_8Na$, 445.1833) (Prema *et al*., 2020)

4-Keto-(16*S*)-methoxyjavanicin B (5): white amorphous powder; $[\alpha]_D^{22}$ +20.8° (*c* 0.1, MeOH); CD (*c* 0.01, MeOH): 215 (Δ*ε* 3.35), 249 (Δ*ε* −3.53), 273 (Δ*ε* 9.93), 337 (Δ*ε* −1.99), 370 (Δ*ε* 2.36) nm; UV (MeOH) λ_{max}: 213, 259 nm; IR (KBr) ν_{max}: 2936, 2848, 1723, 1678, 1637, 1608, 1445, 1386, 1264, 1051 cm^{-1}; ^{1}H NMR (500 MHz, $CDCl_3$) δ_H 5.77 (s, H-3), 3.13 (dd, *J* = 18.3, 5.7 Hz, H-5), 2.06 (dt, *J* = 14.9, 3.4 Hz, H-6*α*), 1.96* (m, H-6*β*), 3.72 (t, *J* = 3.4 Hz, H-7), 3.42 (s, H-9), 2.35 (dd, *J* = 12.6, 5.2 Hz, H-14), 1.87 (ddd, *J* = 14.5, 5.2, 3.4 Hz, H-15*α*), 1.98* (m, H-15*β*), 4.78 (brd, *J* = 3.4 Hz, H-16), 1.49 (s, H_3-18), 1.07 (s, H_3-19), 1.85 (s, H_3-20), 3.77 (s, 2-OCH_3), 3.63 (s, 12-OCH_3), 3.35 (s, 16-OCH_3); ^{13}C NMR data (125 MHz, $CDCl_3$) δ_C 196.8 (C-1), 162.9 (C-2), 108.9 (C-3), 197.7 (C-4), 50.2 (C-5), 22.6 (C-6), 68.4 (C-7), 38.6 (C-8), 45.9 (C-9), 49.8 (C-10), 192.1 (C-11), 148.2 (C-12), 141.5 (C-13), 44.3 (C-14), 30.9 (C-15), 97.5 (C-16), 16.2 (C-18), 22.0 (C-19), 15.6 (C-20), 56.6 (2-OCH_3), 59.5 (12-OCH_3), 54.8 (16-OCH_3); HR-ESI-MS: *m/z* 405.1900 $[M+H]^+$ (calcd. for $C_{22}H_{29}O_7$, 405.1908) (Prema *et al*., 2020)

Javanicin F (**6**), Javanicin B (**7**), Picrajavanicin B (**8**), Picrajavanicin C (**9**) (Win *et al*., 2015) Picrajavanicin H (**10**), Picrajavanicin M (**11**), Picrasin A (**12**) (Win *et al*., 2016), Canthin-3-one (**13**) (Koike and Ohmoto, 1985), Lanosta-7,24-dien-3-one (**14**) (Nana *et al*., 2012), and Scopoletin (**15**) (Darmawan *et al*., 2012) are shown in Figure 3.

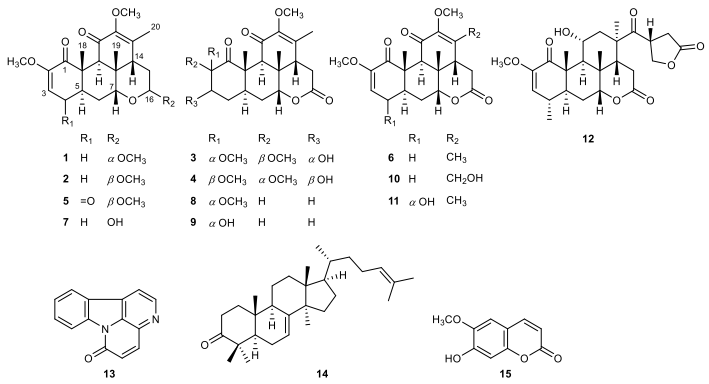

Figure 3. Structures of compounds1-15 isolated from the chloroform extract of P. javanica.

Anti-Vpr Activities of Isolated Compounds from *P. javanica* Wood

The anti-Vpr activities of all isolated compounds (**1-4** and **6-15**) were screened for their inhibition of growing the TREx-HeLa-Vpr cells with the three different concentrations of 1.25, 2.5, and 5 μM (Figure 4). The anti-Vpr activities of the isolated compounds **1**, **2**, **3**, **4**, and **13-15** were investigated for the first time. Compound **5** was not screened for anti-Vpr activity due to the insufficient yield. Among the tested compounds, all isolated compounds showed potent anti-Vpr activities without showing any cytotoxicity at 5 μM. The % cell proliferation of the anti-Vpr activities of all tested compounds and Dam were 165 % (**1**),167 % (**2**), 168 % (**3**), 163 % (**4**), 162 % (**6**), 181 % (**7**), 159 % (**8**), 170 % (**9**), 148 % (**10**), 142 % (**11**), 134 % (**12**), 153 % (**13**), 104 % (**14**), 128 % (**15**), and 176 % (Dam) at the 5 μM concentration, respectively. The previous study reported that quassinoid compounds **6**–**12** exhibited potent anti-Vpr activities on the TREx-HeLa-Vpr cells, which are similar to the assay results in this study.

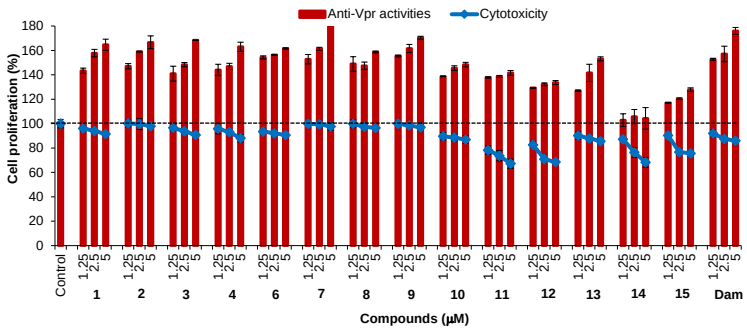

Figure 4. Anti-Vpr activities of 1–15 from *P. javanica*. Data are represented as mean ± SD (n = 3)

In the structure-activity relationship (SAR), the presence of a methyl group at C-13 and a hydroxy group at C-16 of the C-20 type quassinoids was found to be important for their potent anti-Vpr activities, as previously reported. Moreover, comparisons of the structure and activity of **1**, **2**, and **7** with neoquassin type suggested that **1** and **2** have slightly weaker anti-Vpr activities than **7** at the 1.25 μM concentration. These results revealed that the presence of the methoxy group at C-16 was the most essential for Vpr inhibitory activities, as seen by comparing **2** and **7**. In contrast, the anti-Vpr activities of **1** and **2** showed the same value of (%) cell viability, suggesting

that C-16 epimers do not affect their potencies. On the other hand, quassin types **3**, **4**, and **9** revealed that **3** and **4** had slightly weaker activities than **9** at the 1.25 μM concentration. This observation indicated that the absence of the *β*-methoxy group and/or the hydroxy group at C-2 in the quassin type quassinoid may play a critical role in enhancing the anti-Vpr activity.

Structure Elucidation of Isolated Compounds (16-31) from the Rhizomes of *G. sherwoodiana*

Three new compounds (**16-18**), two new naturally occurring compounds (**19-20**), and eleven known compounds (**21-31**) (Figure 5) were isolated from the chloroform extract of the *G. sherwoodiana* rhizomes.

Globbatone A (16): pale yellowish oil; $[\alpha]_D^{22}$ +41.7° (*c* 0.1, $CHCl_3$); UV (MeOH) λ_{max}: 208, 218 nm; IR (KBr) ν_{max} 3313, 2925, 2855, 1729, 1465, 1372, 1266, 1181, 1032 cm^{-1}; ^1H NMR (500 MHz, $CDCl_3$) δ_H 1.71* (m, H-1*α*), 1.00 (td, *J* = 13.2, 4.2 Hz, H-1*β*), 1.58 (dt, *J* = 13.2, 3.4 Hz, H-2*α*), 1.49 (m, H-2*β*), 1.38 (m, H-3*α*), 1.17 (td, *J* = 13.2, 4.2 Hz, H-3*β*), 1.09 (dd, *J* = 12.9, 2.7 Hz, H-5), 1.71* (m, H-6*α*), 1.31 (qd, *J* = 12.9, 4.2 Hz, H-6*β*), 2.38 (ddd, *J* = 12.9, 4.2, 2.4 Hz, H-7*α*), 1.97 (dt, *J* = 12.9, 4.2 Hz, H-7*β*), 1.71* (m, H-9), 1.83 (m, H-11a), 1.71* (m, H-11b), 4.22 (m, H-16a), 3.98 (m, H-16b), 3.86 (t, *J* = 5.5 Hz, H_2-3′), 2.56 (t, *J* = 5.5 Hz, H_2-2′), 4.84 (brs, H-12a), 4.54 (brs, H-12b), 0.88 (s, H_3-13), 0.81 (s, H_3-14), 0.68 (s, H_3-15); ^{13}C NMR (500 MHz, $CDCl_3$) δ_C 39.1 (C-1), 19.4 (C-2), 42.1 (C-3), 33.7 (C-4), 55.6 (C-5), 24.4 (C-6), 38.2 (C-7), 148.2 (C-8), 53.1 (C-9), 39.5 (C-10), 23.2 (C-11), 106.7 (C-12), 33.6 (C-13), 21.8 (C-14), 14.4 (C-15), 64.8 (C-16), 173.1 (C-1′), 36.8 (C-2′), 58.4 (C-3′); HR-ESI-MS *m/z* 331.2225 $[M+Na]^+$ (calcd. for $C_{19}H_{32}O_3Na$, 331.2244) (Prema *et al*., 2020)

Globbatone B (17): pale yellowish oil; $[\alpha]_D^{22}$ +20.5° (c 0.1, $CHCl_3$); UV (MeOH) λ_{max}: 208, 218 nm; IR (KBr) ν_{max} 2934, 2830, 1735, 1465, 1378, 1266, 1181, 1035 cm^{-1}; ^1H NMR (500 MHz, $CDCl_3$) δ_H 1.72* (m, H-1*α*), 1.00 (td, *J* = 12.8, 4.2 Hz, H-1*β*), 1.55 (dt, *J* = 13.3, 3.4 Hz, H-2*α*), 1.48 (m, H-2*β*), 1.38 (m, H-3*α*), 1.17 (td, *J* = 13.3, 4.2 Hz, H-3*β*), 1.08 (dd, *J* = 12.8, 2.7 Hz, H-5), 1.72* (m, H-6*α*), 1.30 (qd, *J* = 12.8, 4.2 Hz, H-6*β*), 2.38 (ddd, *J* = 12.8, 4.2, 2.4 Hz, H-7*α*), 1.96 (dt, *J* = 12.8, 4.2 Hz, H-7*β*), 1.72* (m, H-9), 1.83 (m, H-11a), 1.72* (m, H-11b), 4.24 (m, H-16a), 3.95 (m, H-16b), 8.03 (s, 4′-CHO), 4.43 (td, *J* = 6.3, 0.6 Hz, H_2-3′), 2.67 (t, *J* = 6.3 Hz, H_2-2′), 4.83 (brs, H-12a), 4.53 (brs, H-12b), 0.86 (s, H_3-13), 0.79 (s, H_3-14), 0.67 (s, H_3-15); ^{13}C NMR (500 MHz, $CDCl_3$) δ_C 39.1 (C-1), 19.4 (C-2), 42.2 (C-3), 33.7 (C-4), 55.6 (C-5), 24.4 (C-6), 38.2 (C-7), 148.1 (C-8), 53.1 (C-9), 39.5 (C-10), 23.0 (C-11), 106.7 (C-12), 33.7 (C-13), 21.8 (C-14), 14.4 (C-15), 64.9 (C-16), 170.5 (C-1′), 33.8 (C-2′), 59.5 (C-3′), 160.7 (C-4′); HR-ESI-MS *m/z* 359.2208 $[M+Na]^+$ (calcd. for $C_{20}H_{32}O_4Na$, 359.2193) (Prema *et al*., 2020)

Globbatone C (18): pale yellowish oil; $[\alpha]_D^{22}$ +50.4° (*c* 0.1, $CHCl_3$); UV (MeOH) λ_{max}: 214, 267 nm; IR (KBr) ν_{max} 3353, 2934, 2840, 1762, 1720, 1649, 1462, 1380, 1279, 1188, 1026 cm^{-1}; ^1H NMR (500 MHz, $CDCl_3$) δ_H 1.70* (m, H-1*α*), 1.05 (td, *J* = 13.6, 3.4 Hz, H-1*β*), 1.60 (m, H-2*α*), 1.50 (m, H-2*β*), 1.37 (m, H-3*α*), 1.17 (td, *J* = 13.3, 4.1 Hz, H-3*β*), 1.03 (dd, *J* = 12.8, 1.9 Hz, H-5), 1.70* (m, H-6*α*), 1.32 (qd, *J* = 12.8, 5.0 Hz, H-6*β*), 2.36 (m, H-7*α*), 1.93 (td, *J* = 12.8, 5.0 Hz, H-7*β*), 1.54 (brd, *J* = 2.3 Hz, H-9), 1.87 (m, H-11a), 1.53 (m, H-11b), 2.56 (dd, *J* = 9.0, 3.6 Hz, H-12a), 2.29 (m, H-12b), 2.62 (dd, *J* = 9.5, 4.8 Hz, H-14), 3.82 (t, *J* = 4.8 Hz, H-15), 4.81 (brs, H-17a), 4.42 (brs, H-17b), 0.85 (s, H_3-18), 0.79 (s, H_3-19), 0.67 (s, H_3-20); ^{13}C NMR (500 MHz, $CDCl_3$) δ_C 39.1 (C-1), 19.4 (C-2), 42.2 (C-3), 33.7 (C-4), 55.6 (C-5), 24.5 (C-6), 38.3 (C-7), 148.4 (C-8), 56.3 (C-9), 39.9 (C-10), 17.4 (C-11), 42.5 (C-12), 212.5 (C-13), 44.5 (C-14), 58.0 (C-15), 106.4 (C-17), 33.7 (C-18), 21.8 (C-19), 14.4 (C-20); HR-ESI-MS *m/z* 315.2293 $[M+Na]^+$ (calcd. for $C_{19}H_{32}O_2Na$, 315.2295) (Prema *et al*., 2020)

(*E*)-Labda-8(17),12-dien-15,16-olide (**19**) (Sheeja and Nair, 2014), γ-Bicyclohomofarnesen-12-ol (**20**) (Boukouvalas and Wang, 1988), 13,14,15,16-tetranor-8(17)-labden-12-al (**21**) (Kumar and

Chein, 2014), Zerumin (**22**) (Xu *et al*., 1995), 16-oxo-(8)17–12-labdadien-15,11-olide (**23**) (Shaaria *et al*., 2009), Amoxanthin A (**24**) (Win *et al*., 2017), Sceptrumlabdalactone A (**25**) (Ali *et al*., 2011), Coronarin D ethyl ether (**26**), Coronarin D methyl ether (**27**) (Chimnoi *et al*., 2008), Pahangensin B (**28**), (*E*)-Labda-8(17),12-dien-15,16-dial (**29**) (Win *et al*., 2017), Calcaratarin A (**30**), and Kravanhin B (**31**) (Yin *et al*., 2013).

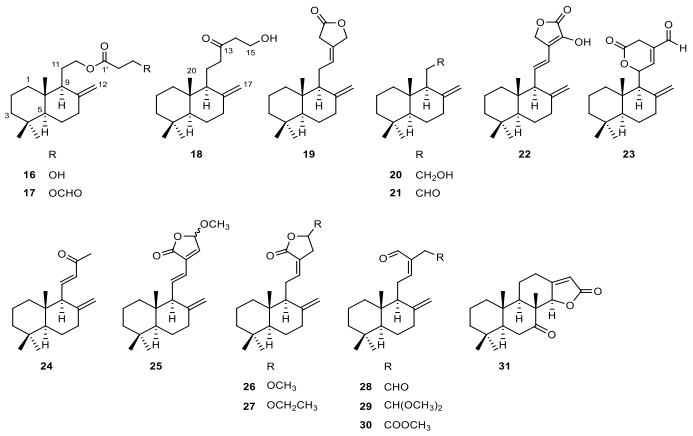

Figure 5. Structures of compounds 16-31 isolated from the chloroform extract of *G. sherwoodiana*

Anti-Vpr Activities of Isolated Compounds from *G. sherwoodiana* Rhizomes

Except for **21**, **22**, **25**, **26**, and **30** with insufficient yields, the anti-Vpr activities of **16**–**20**, **23**, **24**, **27**–**29**, and **31** (2.5, 5, 10 μM) were screened. The results (Figure 6) showed that **16**, **18**-**27**, and **29**-**31** had moderate anti-Vpr activities, although **31** possessed a weak cytotoxic effect at the concentration of 10 μM. In contrast, **17** and **20** were found to slightly inhibit the Vpr activity, without any cytotoxicity. Compared with the other tested compounds, **28** did not inhibit the Vpr activity in the TREx-HeLa-Vpr cells. The order of the anti-Vpr activities of the isolated compounds and positive control Dam at the 10 μM concentration was Dam (141%) > **27** (130 %) =**18** (129 %) > **23** (123 %) = **31** (122 %) > **29** (120 %) = **19** (119 %) = **16** (118 %) > **24** (116 %) > **20** (103 %) > **17** (92 %) > **28** (58 %), respectively. However, the isolated compounds **16**, **18**, **19**, **23**, **24**, **27**, **29**, and **31** had weaker anti-Vpr activities as compared to Dam.

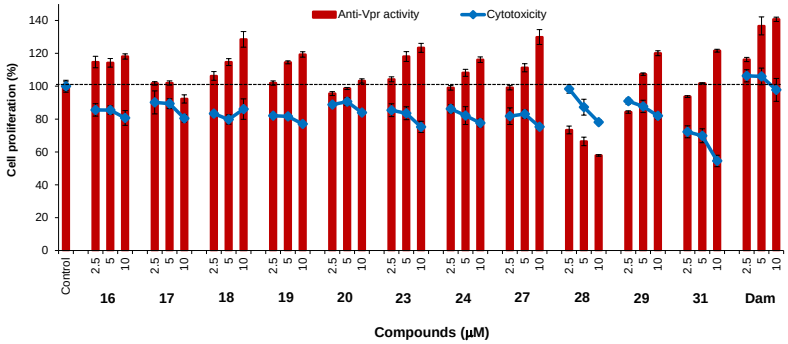

Figure 6. Anti-Vpr activities of 16–31 from *G. sherwoodiana*. Data are represented as mean ± SD (n = 3).

The structure–activity relationship (SAR) study of homodrimane sesquiterpenes revealed that **16** possessed stronger activity than those of **17** and **20**, suggesting that the presence of the hydroxypropionate group at C-12 was important for increasing the activities. Comparisons of the 8(17)-eomethylene labdane diterpenoids, **18**, **19**, **23**, **24**, **27**, and **31** revealed the higher potency of

28, suggesting that the presence of the lactone ring and carbonyl group could be the important functionalities to enhance the activity.

Structure Elucidation of Isolated Compounds (32-39) from the Roots and Rhizomes of *K. candida*

Three new compounds (**32-34**), together with five known compounds (**35**-**39**) (Figure 7) were isolated from the chloroform extract of the *K. candida* roots and rhizomes.

7-Hydroxymustakone (32): colorless oil; $[\alpha]_D^{22}$ –58.6° (*c* 0.1, $CHCl_3$); UV (MeOH) λ_{max}: 205, 218, 229, 260 nm; IR (KBr) ν_{max} 3440, 2928, 2865, 1725, 1661, 1460, 1380, 1164 cm^{-1}; ^1H NMR (500 MHz, $CDCl_3$) δ_H 2.57 (dd, *J* = 6.9, 1.1 Hz, H-1), 5.79 (d, *J* = 1.5 Hz, H-3), 2.62 (dd, *J* = 6.9, 1.5 Hz, H-5), 2.69 (s, H-6), 1.92 (m, H-8*α*), 1.64 (m, H-8*β*), 1.89 (m, H-9*α*), 1.78 (m, H-9*β*), 1.73 (sept, *J* = 6.9 Hz, H-11), 0.92 (d, *J* = 6.9 Hz, H_3-12), 0.88 (d, *J* = 6.9 Hz, H_3-13), 2.04 (s, H_3-14), 0.99 (s, H_3-15); ^{13}C NMR data (125 MHz, $CDCl_3$) δ_C 57.6 (C-1), 203.1 (C-2), 121.9 (C-3), 170.3 (C-4), 49.8 (C-5), 60.5 (C-6), 76.1 (C-7), 29.3 (C-8), 34.5 (C-9), 57.4 (C-10), 36.7 (C-11), 16.9 (C-12), 16.4 (C-13), 23.9 (C-14), 20.2 (C-15); HR-ESI-MS: *m/z* 257.1515 $[M+Na]^+$ (calcd. for $C_{15}H_{22}O_2Na$, 257.1512) (Prema *et al*., 2020)

15-Hydroxynerolidol (33): colorless oil; $[\alpha]_D^{22}$ +18.0° (*c* 0.1, $CHCl_3$); UV (MeOH) λ_{max}: 211, 218, 228, 276 nm; IR (KBr) ν_{max} 3397, 2926, 2871, 1720, 1643, 1448, 1380, 1063 cm^{-1}; ^1H NMR (500 MHz, $CDCl_3$) δ_H 5.38 (dd, *J* = 17.3, 2.3 Hz, H-1a), 5.29 (dd, *J* = 10.8, 2.3 Hz, H-1b), 5.82 (dd, *J* = 17.3, 10.8 Hz, H-2), 1.65 (m, H-4a), 1.53 (m, H-4b), 2.12 (m, H-5a), 1.99 (m, H-5b), 5.13 (m, H-6), 1.97 (m, H_2-8), 2.04 (m, H_2-9), 5.06 (m, H-10), 1.59* (s, H_3-12), 1.66 (s, H_3-13), 1.59* (s, H_3-14), 3.48 (dd, *J* = 21.8, 10.8 Hz, H_2-15); ^{13}C NMR data (125 MHz, $CDCl_3$) δ_C 115.5 (C-1), 140.9 (C-2), 76.5 (C-3), 36.9 (C-4), 22.1 (C-5), 124.4 (C-6), 136.2 (C-7), 39.8 (C-8), 26.8 (C-9), 124.2 (C-10), 131.7 (C-11), 25.9 (C-12), 17.9 (C-13), 16.2 (C-14), 69.1 (C-15); HR-ESI-MS: *m/z* 261. 1814 $[M+Na]^+$ (calcd. for $C_{15}H_{26}O_2Na$, 261. 1825) (Prema *et al*., 2020)

Kaempcandiol (34): white amorphous solid; $[\alpha]_D^{22}$ +46.0° (*c* 0.1, $CHCl_3$); UV (MeOH) λ_{max}: 209, 219, 223 nm; IR (KBr) ν_{max} 3440, 2934, 2865, 1702, 1652, 1542, 1523, 1457, 1396, 1161, 1067 cm^{-1}; ^1H NMR (500 MHz, $CDCl_3$) δ_H 1.69 (m, H-1*α*), 1.06 (td, *J* = 12.9, 3.7 Hz, H-1*β*), 1.55 (m, H-2*α*), 1.48 (m, H-2*β*), 1.38 (m, H-3*α*), 1.18 (td, *J* = 12.9, 3.7 Hz, H-3*β*), 1.16 (dd, *J* = 12.9, 2.7 Hz, H-5), 1.72 (m, H-6*α*), 1.31 (qd, *J* = 12.9, 4.2 Hz, H-6*β*), 2.39 (ddd, *J* = 12.9, 4.2, 2.7 Hz, H-7*α*), 2.03 (td, *J* = 12.9, 5.6 Hz, H-7*β*), 2.08 (m, H-9), 1.70 (m, H_2-11), 4.45 (dd, *J* = 10.0, 4.9 Hz, H-12), 6.32 (s, H-16a), 5.89 (s, H-16b), 4.85 (s, H-17a), 4.59 (s, H-17b), 0.87 (s, H_3-18), 0.79 (s, H_3-19), 0.66 (s, H_3-20); ^{13}C NMR data (125 MHz, $CDCl_3$) δ_C 39.1 (C-1), 19.5 (C-2), 42.2 (C-3), 33.8 (C-4), 55.6 (C-5), 24.5 (C-6), 38.4 (C-7), 148.9 (C-8), 52.4 (C-9), 39.4 (C-10), 31.3 (C-11), 70.1 (C-12), 142.9 (C-13), 170.3 (C-14), 126.6 (C-16), 106.2 (C-17), 33.8 (C-18), 21.9 (C-19), 14.8 (C-20); HR-ESI-MS: *m/z* 305.2122 $[M-H]^-$ (calcd. for $C_{15}H_{25}O_2$, 305.2122) (Prema *et al*., 2020)

Mustakone (**35**) (Nyasse *et al*., 1988), Coronadiene (**36**) (Win *et al*., 2017), Aromaticane J (**37**) (Dong *et al*., 2017), Longpene A (**38**) (Xu *et al*., 2015), and Docosyl ferulate (**39**) (Nishiyama *et al*., 2019).

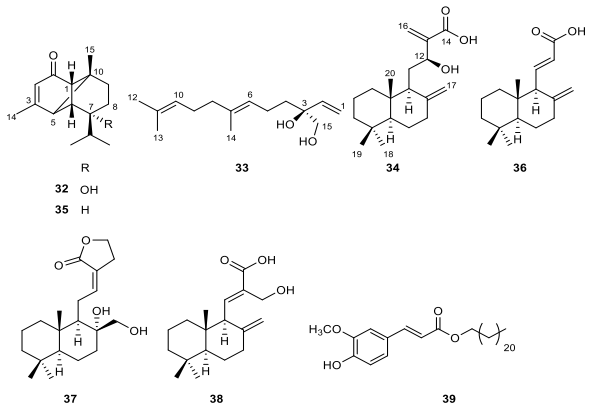

Figure 7. Structures of compounds 32-39 isolated from the chloroform extract of *K. candida*

Anti-Vpr Activities of Isolated Compounds from *K. candida* Roots and Rhizomes

All isolated compounds **32**-**39** and positive control Dam (Figure 8) were screened for their anti-Vpr activity in TREx-HeLa-Vpr cells. Compounds **32** and **34**-**39** possessed potent anti-Vpr activities at the 5 μM concentration, without showing any cytotoxicity. Compound **33** exhibited moderate anti-Vpr activities at the 5 μM concentration, although this compound possessed a weak cytotoxic effect. The anti-Vpr activities of tested compounds and Dam were 159 % (Dam), 136 % (**32**), 113 % (**33**), 131 % (**34**), 137 % (**35**), 129 % (**36**), 135 % (**37**), 134 % (**38**), and 120 % (**39**) at the 5 μM concentration, respectively.

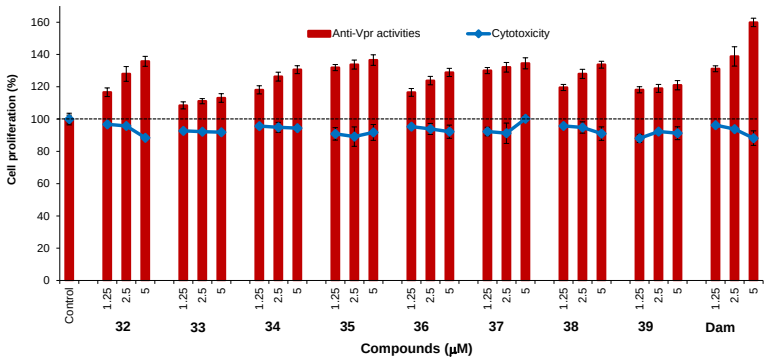

Figure 8. Anti-Vpr activities of 32–39 from *K. candida*. Data are represented as mean ± SD (n = 3).

SAR of sesquiterpenes **32** and **35** showed stronger anti-Vpr activities than **33**, suggesting that tricyclic sesquiterpenes with *α*, *β*-unsaturated ketone group at C-2 could be potential candidates for the anti-Vpr activities. On the other hand, the labdane diterpenes **34** and **36**-**38** possessed potent anti-Vpr activities, revealing that the presence of tertiary carboxylic acid and 8(17)-exomethylene and/or hemiacetal groups may play essential roles for anti-Vpr activities.

Conclusion

In this study, the chemical investigation of the active chloroform extracts of the *P. javanica* wood, *G. sherwoodiana* rhizomes, and *K. candida* roots and rhizomes led to the isolation of 39 compounds, including eleven new ones, namely (16*R*)-methoxy javanicin B (**1**), (16*S*)-methoxyjavanicin B (**2**), javanicinols A and B (**3** and **4**), 4-keto-(16*S*)-methoxyjavanicin B (**5**), globbatones A-C (**16**-**18**), 7-hydroxymustakone (**32**), 15-hydroxynerolidol (**33**), kaempcandiol

(**34**), two new naturally occurring (*E*)-labda-8(17),12-dien-15,16-olide (**19**) and γ-bicyclohomofarnesen-12-ol (**20**), and 26 known compounds **6**–**15**, **21-31**, **35-39**. The biological screening suggested that most of the quassinoids, bicyclic and/or tricyclic sesquiterpenes, and labdane diterpenes showed potent anti-Vpr activities. In addition, except for triterpenoid **14**, three minor constituents (**13**, **15**, and **39)** had anti-Vpr activities, with the less cytotoxic effect on the TREx-HeLa-Vpr cells. These results suggested that the three skeletons could be crucial for the development of anti-HIV-1 drug. The findings will also contribute to the scientific development of Myanmar's traditional medicine, especially in areas concerned with the disease of AIDS.

Acknowledgements

The authors would like to thank the Department of Higher Education, the Ministry of Education and the University of Yangon for some support in doing this research. This work was supported in part by Grants-in-Aid for Scientific Research from the Ministry of Education, Culture, Sports, Science, and Technology, Japan. We would like to acknowledge Professor Dr Hiroyuki Morita (Takahashi Industrial and Economic Research Foundation), Institute of Natural Medicine, University of Toyama. Finally, one of the authors, the corresponding author, is also thankful to the Japanese Government (Monnukagakusho: MEXT Scholarship), for financial support for her PhD study.

References

Ali, Z. C., T. Okpekon, F. Roblot, C. Bories, M. Cardao, J. C. Jullian, E. Poupon and P. Champy. (2011). "Labdane Diterpenoids from *Aframomum sceptrum*: NMR Study and Antiparasitic Activities". *Phytochemistry Letters*, vol. 4, pp. 240-244

Boukouvalas, J., and J. X. Wang. (1988). "Structure Revision and Synthesis of a Novel Labdane Diterpenoid from *Zingiber ottensii*". *Phytotherapy Research*, vol. 2, pp. 33-36

Chawengrum, P., J. Boonsombat, P. Kittakoop, C. Mahidol, S. Ruchirawat, and S. Thongnest. (2018). "Cytotoxic and Antimicrobial Labdane and Clerodane Diterpenoids from *Kaempferia elegans* and *Kaempferia pulchra*". *Phytochemistry Letters*, vol. 24, pp. 140–144

Chimnoi, N., S. Pisutjaroenpong, L. Ngiwsara, D. Dechtrirat, D. Chokchaichamnankit, N. Khunawutmanotham, C. Mahidol, and S. Techasakul. (2008). "Labdane Diterpenes from the Rhizomes of *Hedychium coronarium*". *Natural Product Research*, vol. 22(14), pp. 1249-1256

Darmawan, A., S. Kosela, L. B. S. Kardono, and Y. M. Syah. (2012). "Scopoletin, a Coumarin Derivative Compound Isolated from *Macaranga gigantifolia* Merr". *Journal of applied pharmaceutical science*, vol. 2, pp. 175-177

Dong, S., B. Li, W. Dai, D. Wang, Y. Qin, and Y. Zhang. (2017). "Sesqui- and Diterpenoids from the Radix of *Curcuma aromatic*". *Journal of Natural Products*, vol. 80, pp. 3093–3102

Jenjittikul, T. and K. Larsen. (2000). "*Kaempferia candida* Wall. (Zingiberaceae), a New Record for Thailand". *Thai Forest Bulletin (Botany)*, vol. 28, pp. 45-49

Koike, K., and T. Ohmoto. (1985). "Carbon-13 Nuclear Magnetic Resonance Study of Canthin-6-one Alkaloids". *Chemical and Pharmaceutical Bulletin*, vol. 33, pp. 5239-5244

Kress, W. J., R. A. DeFilipps, E. Farr and D. Y. Y. Kyi. (2003). "*A Checklist of the Trees, Shrubs, Herbs, and Climbers of Myanmar* (revised from the original works by J. H. Lace, R. Rodger, H. G. Hundley and U Chit Ko Ko on the "*List of Trees, Shrubs, Herbs and Principal Climbers etc. Recorded from Burma*")". Contributions from the United States National Herbarium, vol. 45, pp. 1–590

Kumar, C. N. S. S. P. ,and R. J. Chein. (2014). "Synthesis of Labdane Diterpenes Galanal A and B from (+)-Sclareolide". *Organic Letters*,vol. 16, pp. 2990-2992

Morellet, N., S. Bouaziz, P. Petitjean, and B. P. Roques. (2003). "NMR Structure of the HIV-1 Regulatory Protein VPR". *Journal of molecular biology*, vol. 327, pp.215-227

Nana, F., L. P. Sandjo, F. Keumedjo, P. Ambassa, R. Malik, V. Kuete, V. Rincheval, M. I. Choudhary and B. T. Ngadjui. (2012). "Ceramide and Cytotoxic Constituents from *Ficus glumosa* Del. (Moraceae)". *Journal of the Brazilian Chemical Society*, vol. 23, pp. S1–S9

Nishiyama, Y., Y. Noda, N. Nakatani, N. Shitan, T. Sudo, A. Kato and P. B. Chalomutiso. (2019). "Structure of Constituents Isolated from the Bark of *Cassipourea malosana* and their Cytotoxicity against a Human Ovarian Cell Line". *Journal of Natural Medicines*, vol. 73, pp. 289–296

Nyasse, B., R. Ghogomu, T. B. L. Sondengam, M. T. Martin and B. Bodo. (1988). "Mandassidione and Other Sesquiterpenic Ketones from *Cyperus articulates*". *Phytochemistry*, vol. 27, pp. 3319–3321

Prema, T. Kodama, H. H. W. Nyunt, H. Ngwe, I. Abe, and H. Morita. (2020). "Anti-Vpr Activities of Sesqui- and Diterpenoids from the Aerial Parts of *Kaempferia candida*. *Journal of Natural Medicines*, vol. 75(3), pp. 489-498

Prema, T. Kodama, C. P. Wong, A. H. El-Desoky, H. H. W. Nyunt, H. Ngwe, I. Abe, and H. Morita. (2020). "Anti-Vpr Activities of Homodrimane Sesquiterpenoids and Labdane Diterpenoids from *Globba sherwoodiana* Rhizomes". *Fitoterapia*, ,vol. 146, pp. 104705

Prema, C. P. Wong, T. Kodama, A. E. Nugroho, A. H. El-Desoky, M. D. Awouafack, Y. Y. Win, H. Ngwe, I. Abe, and H. Morita. (2020). "Three New Quassinoids Isolated from the Wood of *Picrasma javanica* and their Anti-Vpr Activities". *Journal of Natural Medicines*, vol. 74, pp. 571-578

Prema, C. P. Wong, A. E. Nugroho, M. D. Awouafack, Y. Y. Win, N. N. Win, H. Ngwe, H. Morita, and H. Morita. (2019). "Two New Quassinoids and Other Constituents from *Picrasma javanica* Wood and their Biological Activities". *Journal of Natural Medicines*, vol. 73, pp. 1-8

Saiin, C., and B. Sirithunyalug. (2017). "Review of the Chemical Structures and Antimalarial Activities of Indole Alkaloid Isolated from *Picrasma javanica* Bl". *Advancement in Medicinal Plant Research*, vol. 5, pp. 29-36

Shaaria, K., Maulidiania, C. Paetzb, J. Stanslasa, F. Abasa, and N. H. Lajisa. (2009). "Naturally Occurring Labdane Diterpene and Benzofuran from *Globba pendula*". *Natural Product Communications*, vol. 4, pp. 1031-1036

Sheeja, A. D. B., and M. S. Nair. (2014). "Facile Isolation of (*E*)-Labda-8(17),12-dien-15,16-dial from *Curcuma amada* and its Conversion to Other Biologically Active Compounds". *Indian Journal of Chemistry*, vol. 53, pp. 319-324

Thongam, B., B. Konsam, and N. Sarangthem. (2013). "*Globba sherwoodiana* (Zingiberaceae) – A New Record for India from Manipur". *Rheedea*, vol. 23, pp. 34-36

Win, N. N., T. Ito, Ismail, T. Kodama, Y. Y. Win, M. Tanaka, H. Ngwe, Y. Asakawa, I. Abe, and H. Morita. (2015). "Picrajavanicins A-G, Quassinoids from *Picrasma javanica* Collected in Myanmar". *Journal of Natural Products*, vol. 78, pp. 3024-3030

Win, N. N., T. Ito, Ismail, T. Kodama, Y. Y. Win, M. Tanaka, H. Okamoto, H. Imagawa, H. Ngwe, Y. Asakawa, I. Abe, and H. Morita. (2016). "Picrajavanicins H-M, New Quassinoids from *Picrasma javanica* Collected in Myanmar and their Antiproliferative Activities". *Tetrahedron*, vol. 72, pp. 746-752

Win, N. N., T. Ito, H. Ngwe, Y. Y. Win, Prema, Y. Okamoto, M. Tanaka, Y. Asakawa, I. Abe, and H. Morita. (2017). "Labdane Diterpoids from Curcuma amada Rhizomes Collected in Myanmar and their Antiproliferative Activities". *Fitoterapia*, vol. 122, pp. 34-39

Win, N. N., T. Ito, Y. Y. Win, H. Ngwe, T. Kodama, I. Abe and H. Morita. (2016). "Quassinoids: Viral Protein R Inhibitors from *Picrasma javanica* Bark Collected in Myanmar for HIV infection". *Bioorganic and Medicinal Chemistry Letters*, vol. 26, pp. 4620-4624

Xu, H. X., D. Hui, and K. Y. Sim. (1995). "The Isolation of a New Labdane Diterpene from the Seeds of *Alpinia zerumbet*". *Natural Product Letters*, vol. 7, pp. 29-34

Xu, J., F. Ji, J. Kang, H. Wang, S. Li, D. Q. Jin, Q. Zhang, H. Sun, and Y. Guo. (2015). "Absolute Configurations and NO Inhibitory Activities of Terpenoids from *Curcuma longa*". *Journal of Agricultural and Food Chemistry*, vol. 63, pp. 5805−5812

Yin, H., J. G. Luo, and L. Y. Kong. (2013). "Tetracyclic Diterpenoids with Isomerized Isospongian Skeleton and Labdane Diterpenoids from the Fruits of *Amomum kravanh*". *Journal of Natural Products*, vol. 76, pp. 237-242

COMPARATIVE STUDIES ON PHYTOCHEMICAL CONSTITUENTS AND SOME BIOLOGICAL ACTIVITIES OF THE SEEDS, FRUITS, LEAVES, AND BARK OF *ZIZIPHUS MAURITIANA* LAM. (ZEE)

Thet Thet Mon[1], Prema[2], Khin Chaw Win[3], Ni Ni Than[4]

Abstract

The aim of this research is to isolate bioactive compounds and to investigate some biological activities, such as antioxidant, α-amylase and antimicrobial activity, of the fruits, seeds, bark and leaves of *Ziziphus mauritiana* Lam. (Zee). According to the phytochemical tests, Zee bark and leaves have more secondary metabolites than other. By thin layer and silica gel column chromatographic methods, lupeol was isolated from the ethyl acetate extract of the seeds and identified by the nuclear magnetic resonance (NMR) spectroscopic method. The antioxidant activity of bark of ethanol extract (IC_{50} = 2.51 μg/mL) and watery extract (IC_{50} = 3.30 μg/mL) was found, and Zee leaves of ethanol extract (IC_{50} = 3.10 μg/mL) and watery extract (IC_{50} = 2.11 μg/mL) were detected. In α-amylase activity, the percent inhibition of α-amylase activity of ethanol extracts of fruits, seeds, bark and leaves has good activity, but water extracts have mild activity. According to antimicrobial activity, the ethanol extracts of all four portions have good activity.

Keywords: *Ziziphus mauritiana*, Lupeol, Antioxidant, α-Amylase, Antimicrobial activity

Introduction

The medicinal plants have very complex chemical constituents called secondary metabolites, which make them very important in the field of therapeutics. The folkloric system, which is mostly based on phytotherapy, is still used by around 80 % of the world's population. Zee scientifically known as *Ziziphus mauritiana* Lam. is one of the plant family Rhamanacae. Genus is *Ziziphus* and species is *mauritiana.* Myanmar name is Zee Chin. It is grown in dry places and is found in India, Pakistan and China (Perez *et al*., 1990). It can be found in the middle part of Myanmar. The genus Z*iziphus* comprises approximately 170 species and is important in the treatment of various diseases. In Myanmar, Zee seeds were exported to China and Korea for medicinal uses. The fruit is variable shape and size. It can be oval, oblong or round and can be 1-1.5 in long depending on the variety. Its leaves are used in the treatment of liver diabetic, asthma, gonorrhea, and fever. The fruits have been used as anodyne, sedative, tonic, anticancer, potent wound healer. All parts of this plant are extremely effective against various types of diseases (Song, *et al*., 2010).

Hence, *Ziziphus mauritiana* Lam. (Zee) was chosen for this study because it has a variety of biological activities and bioactive chemical constituents, as well as a lack of scientific reports on locally grown Zee plants. In this research work, the isolation of some phyto-constituents and investigation of antioxidant activity, α-amylase activity, and antimicrobial activity of the seeds, fruits, leaves, and bark of Zee were carried out on the respective crude extracts.

Materials and Methods

Plant Materials

The four parts of Zee sample were collected from Kyaukpadaung Township, Mandalay region during April in 2018. After collection the sample was confirmed at Department of Botany,

[1] Department of Chemistry, Myingyan University
[2] Department of Chemistry, Myitkyina University
[3] Department of Chemistry, University of Distance Education, Yangon
[4] Department of Chemistry, University of Yangon

University of Yangon. The four parts of Zee sample were cleaned and air dried at room temperature. The dried samples were cut into small pieces and were ground into powder by using a grinding machine. The powdered samples were stored in airtight container to prevent contamination and were kept for the isolation of organic compounds and screening biological activities.

Phytochemical Screening

Preliminary phytochemical tests such as alkaloids, flavonoids, terpenoids, steroids, glycosides, organic acids, starch, phenolic compounds, saponins, tannins, carbohydrates, cyanogenic glycosides, reducing sugars, and α-amino acids tests were carried out according to the appropriate reported methods (Sofowora, 2000).

Isolation and Identification of Phytochemical Constituent from Ethyl acetate Extract of Seeds of Zee by Column Chromatography

Dried powdered bark sample (1 kg) was percolated in 1 L of 70 % ethanol for one week and filtered. This procedure was repeated three times. Then the filtrate was concentrated by using a vacuum rotatory evaporator to give an ethanol extract (100 g). Then the ethanol extract was defatted by using petroleum ether and the defatted ethanol extract was successively partitioned between ethyl acetate and water. The ethyl acetate layer was concentrated under reduced pressure using a vacuum rotatory evaporator. Ethyl acetate crude extract (45 g) from the seeds of Zee was subjected to column chromatographic separation using silica gel (63-210 µm mesh). Gradient elution was performed successively with the PE: EtOAc system in the ratios of 20:1, 15:1, 9:1, 5:1, 3:1, 1:1, 1:2, and 1:5 v/v followed by ethyl acetate only and methanol only. Successive fractions obtained were combined on the basis of their behavior on TLC. Finally, eight main fractions, F-I to F-VIII, were obtained. When the fraction F-IV was evaporated and washed with petroleum ether, a white powder of the compound A in 65 mg was obtained. The isolated compound was then identified using its physicochemical properties and modern spectroscopic techniques such as ^{1}H NMR and ^{13}C NMR and compared with the reported data. The NMR spectra of the isolated compound were measured at Division of Natural Product Chemistry, Institute of Natural Medicine, and University of Toyama, Japan.

Screening of Antioxidant Activity of Ethanol and Watery Extracts of Seeds, Fruits, Leaves, and Bark of Zee

In this experiment, DPPH (2 mg) was thoroughly dissolved in ethanol (100 mL). This solution was freshly prepared in the brown coloured reagent bottle. Each of the tested samples (2 mg) and 10 mL of ethanol were thoroughly mixed by shaker. The mixture solution was filtered, and the stock solution was obtained. By adding ethanol, the sample solutions in different concentrations of 125, 62.5, 31.25, 15.62, 7.81, 3.91, and 1.95 µg/mL were prepared from the stock solution. The effect on the DPPH radical was determined using the method of Marinova and Batchvarov (2011). The control solution was prepared by mixing 1.5 mL of 50 µM DPPH solution with 1.5 mL of ethanol using a shaker. The test sample solution was also prepared by mixing thoroughly 1.5 mL of 50 µM DPPH solutions and 1.5 mL of each sample solution. The mixture solutions were allowed to stand at room temperature for 30 min. Then, the absorbance of each solution was measured at 517 nm by a UV-visible spectrophotometer (GENESYS 10 S UV-VIS, China). Absorbance measurements were done in triplicate for each concentration, and the mean values so obtained were used to calculate the percent inhibition of oxidation. The capability to scavenge the DPPH radical was calculated by using the following equation:

$$\%\,\mathrm{RSA} = \frac{A_c - (A - A_b)}{A_c} \times 100$$

Where, %RSA = Radical Scavenging Activity
A_c = absorbance of the control (DPPH only) solution
A_b = absorbance of the blank (ethanol + Test sample solution) solution
A = absorbance of the test sample solution

Determination of *α*-Amylase Inhibition Potency

In *α*-amylase assay, the starch-iodine method was used. First 2 mL of (0.5 %) substrate starch solution and 1 mL of tested solution (Acarbose standard drug, ethanol extract and aqueous extract) of 250, 125, 62.5, 31.25, 15.62, 7.81, 3.91 and 1.95 µg/mL were added in a bottle and these mixtures was incubated for 3 min at room temperature. To start the reaction, 1 mL of *α*-amylase was added in above solution followed by incubated for 15 min at room temperature. To stop the reaction, 4 mL of 0.1 M HCl was added in this mixture and to detect the reaction, 1 mL of Iodine-iodide indicator (1 mM) was added in this mixture. Absorbance was read at 650 nm by UV spectrophotometer in the visible region. The control solution was prepared as above procedure by using phosphate buffer (0.02 M) instead of drug solution. All the experiments were done in triplicate. Percent inhibition of each sample solution was calculated by using the following formula.

$$\%\ \text{inhibition} = \frac{A_{\text{control}} - A_{\text{sample}}}{A_{\text{control}}} \times 100$$

Where,

$A_{control}$ = the absorbance of the control solution
A_{sample} = the absorbance of sample solution

Standard deviation (SD) and 50 % inhibition concentration (IC_{50}) value in µg/mL were calculated by computer excel program.

Screening of Antimicrobial Activity of Various Crude Extracts of the Seeds, Fruits, Leaves, and Bark of Zee by Agar Well Diffusion Method

The screening of antimicrobial activity of various crude extracts such as pet-ether, ethyl acetate, ethanol, and watery extracts of the four parts of *Ziziphus mauritiana* L. were carried out by agar well diffusion method at Department of Botany, Pathein University, Myanmar. Six microorganisms such as *Bacillus subtilis, Staphylococcus aureus, Pseudomonas aeruginosa, Bacillus pumilus, Candida albicans,* and *Escherichia coli* were used for this test (Perez *et al*., 1990).

Results and Discussion

Types of Phytochemicals Present in Seeds, Fruits, Leaves, and Bark of Zee

In order to find out the types of phytochemical constituents present in the four portions of *Z. mauritiana* L., preliminary phytochemical tests were carried out according to the reported procedure. From the data findings, it was observed that various secondary metabolites such as alkaloids, terpenoids, steroids, glycosides, organic acids, phenolic compounds, saponins, tannins, and carbohydrates were present, however cyanogenic glycosides, flavonoids, starch, and reducing sugars were not detected in the samples. It can be found as cyanogenic glycosides in leaves sample.

According to these results, it can be seen that the bark and leaves samples might contain potent bioactive secondary metabolites.

Isolation and Identification of Compound from Ethyl acetate Extract of Zee seeds

Compound A was isolated as a white crystal (R_f = 0.6, *n*-Hexane: EtOAc, 4:1 v/v) from the ethyl acetate extract of the seeds by silica gel column chromatographic separation. Compound A is soluble in chloroform and chloroform and methanol mixtures but insoluble in pet-ether, ethanol, and acetone. According to FT IR spectrum data (Figure 1), 3315 cm^{-1} (-OH stretching vibration of hydroxyl group), 3095 cm^{-1} (=C-H stretching), 2923 cm^{-1} and 2852 cm^{-1} (C-H asymmetric and symmetric stretching), 1638 cm^{-1} (=C-C stretching), 1452 cm^{-1} (C-H bending of CH_2), 1379 cm^{-1} (C-H bending of CH_3 group), and 1043 cm^{-1} (C-O stretching vibration) can be found.

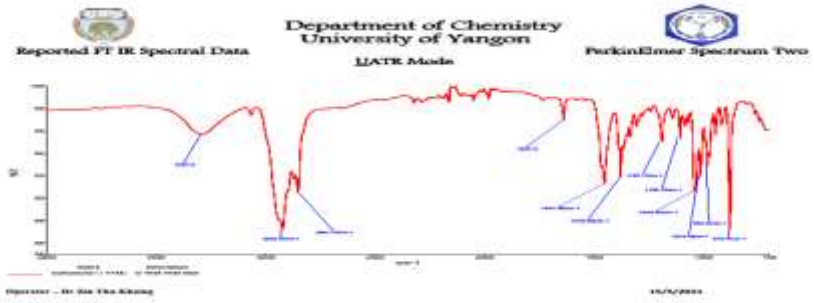

Figure 1. FT IR spectrum of isolated compound A

The structural elucidation of isolated compound A was determined by NMR spectroscopy. The ^{1}H NMR (400 MHz, $CDCl_3$) spectrum of compound A (Figure 2) indicated that the signals at δ_H 4.68, 4.56 (d, *J* = 1.9 Hz, H_2-29), 2.37 (m, H-19), 1.37 (t, *J* = Hz, H-18), 1.02 (d, *J* = Hz, H-15), 3.19 (dd, *J* = Hz, H-3), 0.91 (s, H_3-23), 0.69 (t, *J* = Hz, H-5), and 1.67 (s, H_3-30). The ^{13}C NMR (400 MHz, $CDCl_3$) spectrum of compound A (Figure 3) revealed the presence of 30 carbon signals, which were further classified into 7 methyl carbons at δ_C 27.4 (C-23), 15.4 (C-24), 16.1 (C-25), 15.9 (C-26), 14.5 (C-27), 17.9 (C-28), and 19.3 (C-30), 11 methylene carbons at δ_C 38.8 (C-1), 28.4 (C-2), 18.3 (C-6), 34.3 (C-7), 20.9 (C-11), 25.1 (C-12), 27.4 (C-15), 35.6 (C-16), 29.8 (C-21), 39.9 (C-22), and 109.3 (C-29), 6 methine signals at δ_C 78.9 (C-3), 55.3 (C-5), 50.4 (C-9), 38.0 (C-13), 48.3 (C-18), and 47.9 (C-19), and 6 quaternary carbon signals at δ_C 38.7 (C-4), 40.8 (C-8), 37.1 (C-10), 42.8 (C-14), 42.9 (C-17), and 150.9 (C-20). The ^{1}H and ^{13}C NMR spectral data of compound A were identical with the reported NMR spectral data of lupeol (Mahato *et al*., 1994). Therefore, the structure of the isolated compound A was assigned as lupeol, and its molecular formula is $C_{30}H_{50}O$ (Figure 4).

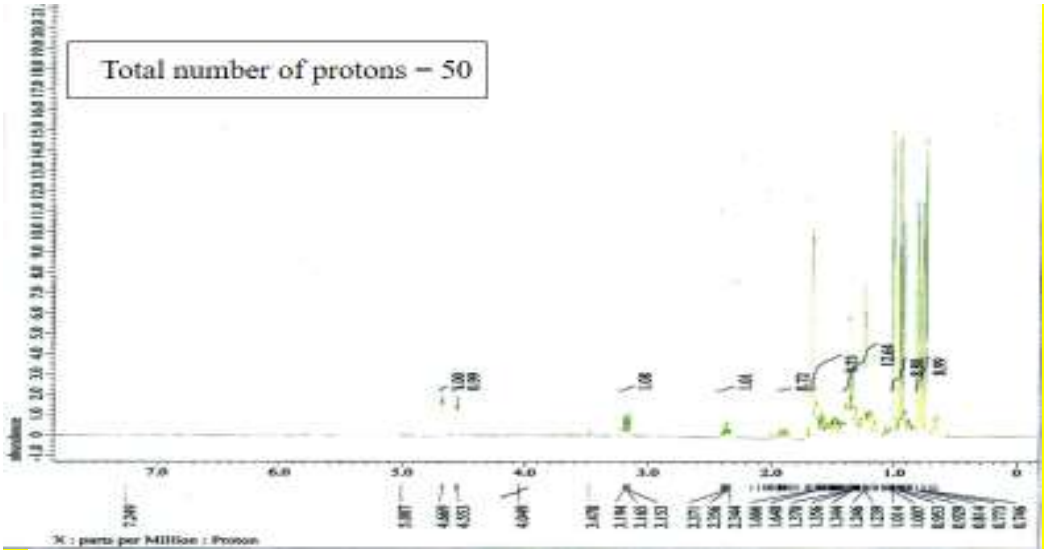

Figure 2. ^{1}H NMR spectrum (400 MHz, $CDCl_3$) of compound A

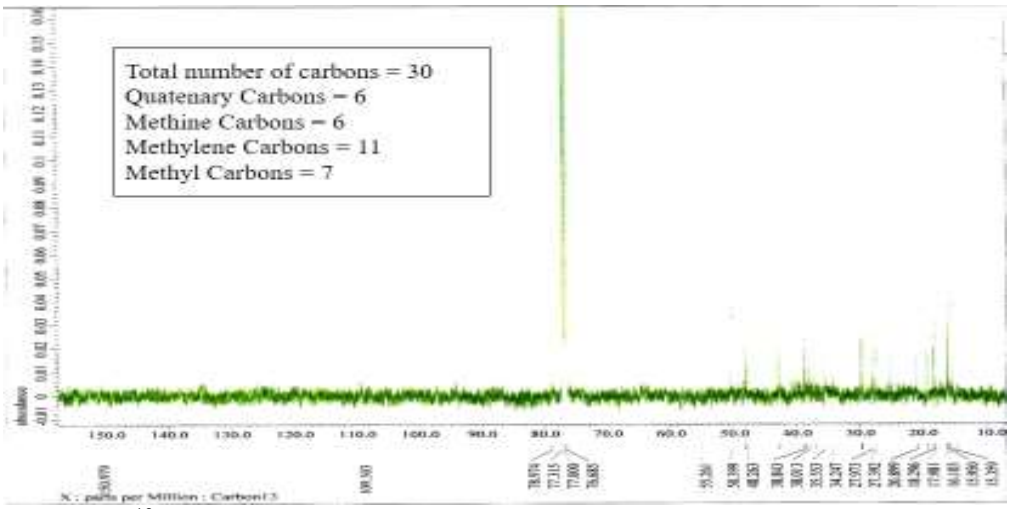

Figure 3. ^{13}C NMR spectrum (100 MHz, $CDCl_3$) of compound A

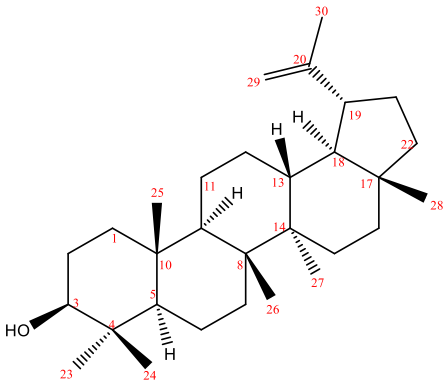

Figure 4. Structure of lupeol ($C_{30}H_{50}O$)

Antioxidant Activity of Crude Extracts of Fruits, Seeds, Bark and Leaves of Zee

The antioxidant activity was measured in terms of hydrogen donation or radical scavenging ability of the ethanol and watery extracts of the samples by using the stable radical DPPH. The radical scavenging activity of standard ascorbic acid and the results are shown in Table 1 and Figures 5 and 6. From these observations, the radical scavenging activity of Zee Bark of ethanol extract (IC_{50} = 2.51 μg/mL) and watery extract (IC_{50} = 2.11μg/mL) was found and Zee leaves of ethanol extract (IC_{50} = 2.51 μg/mL), watery extract (IC_{50} = 3.30 μg/mL) were detected. According to these results, Zee bark and leaves have more potent activities than other portions.

Table 1. % Radical Scavenging Activity and IC_{50} Values of Crude Extracts of Zee Fruits, Seeds, Bark and Leaves by DPPH Radical Scavenging Assay

No.	Samples	Extracts	% Inhibition ± SD at Different Concentration (μg/mL)						IC_{50} (μg/mL)
			1.95	3.91	7.81	15.62	31.25	62.5	
1	Fruits	EtOH	46.18 ± 0.75	48.76 ± 0.23	50.09 ± 0.34	52.06 ± 0.96	53.58 ± 0.27	54.45 ± 0.38	7.54
		Watery	28.05 ± 0.43	34.76 ± 0.16	37.74 ± 0.32	39.99 ± 0.21	45.32 ± 0.48	51.15 ± 0.21	56.34
2	Seeds	EtOH	38.93 ± 0.68	41.41 ± 0.94	45.45 ± 0.63	50.87 ± 0.71	52.62 ± 0.28	54.41 ± 0.55	14.58
		Watery	44.12 ± 0.21	45.41 ± 0.16	46.51 ± 0.16	48.21 ± 0.28	52.11 ± 0.32	55.19 ± 0.48	22.79
3	Bark	EtOH	48.58 ± 0.48	53.54 ± 0.21	55.05 ± 0.62	56.61 ± 0.29	60.56 ± 0.36	67.63 ± 0.41	2.51
		Watery	43.11 ± 0.68	53.08 ± 0.50	56.15 ± 0.50	59.50 ± 0.44	60.65 ± 0.16	64.78 ± 0.25	3.30
4	Leaves	EtOH	47.11 ± 0.89	52.02 ± 0.21	61.62 ± 0.16	64.97 ± 0.14	73.55 ± 0.92	78.65 ± 0.14	3.10
		Watery	49.77 ± 0.60	52.48 ± 0.94	56.75 ± 0.08	60.93 ± 0.48	67.54 ± 0.57	69.05 ± 0.16	2.11
5	Standard	Ascorbic acid	48.39 ± 0.76	54.68 ± 0.95	60.61 ± 0.96	78.42 ± 1.03	85.72 ± 0.08	87.47 ± 0.28	2.45

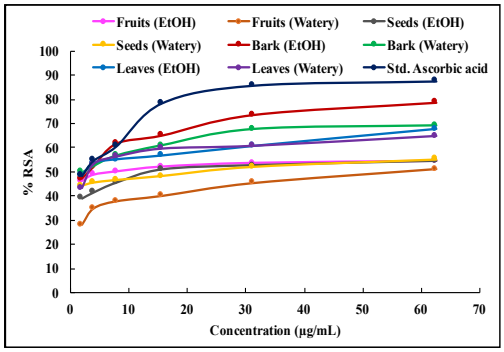

Figure 5. A plot of % DPPH free radical scavenging activity *vs* different concentrations of various crude extracts of Zee

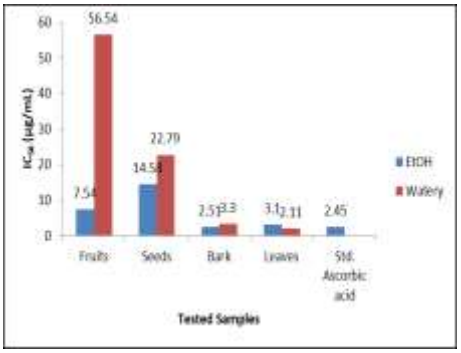

Figure 6. A bar graph of IC_{50} values of Ze Fruits, Seeds, Bark and Leave (DPPH free radical scavenging assay)

α-Amylase Enzyme Inhibition Activity of Seeds, Fruits, Bark and Leaves of *Z. mauritiana* Lam.

The *α*-amylase inhibitory activity of seeds, fruits, bark, and leaves of zee was investigated. The percentage inhibition of the *α*-amylase by ethanol and watery extracts was studied in concentrations of (125, 62.5, 31.25, 15.62, 7.81, 3.92, and 1.95 µg/mL), respectively. The percentage inhibition of the sample on *α*-amylase enzyme activity increased with the increasing concentration. The percentage inhibitions of *α*-amylase activity of ethanol extracts from all four portions have good activity, but water extracts have mild activity. These observations are dedicated in Figures 7 and 8, and Table 2.

Table 2. α-Amylase Inhibition % and IC_{50} Values of the Crude Extracts of Four Tested Samples of Zee and Standard Acarbose

Samples	Extracts	% Inhibition ± SD at Different Concentration (µg/mL)							IC_{50} (µg/mL)
		1.95	3.91	7.81	15.62	31.25	62.5	125	
Fruits	EtOH	39.87 ± 0.61	46.95 ± 0.62	52.27 ± 0.21	53.25 ± 0.41	56.42 ± 0.35	60.1 ± 0.10	64.32 ± 0.27	6.14
	Watery	34.07 ± 0.48	35.71 ± 0.44	43.07 ± 0.51	52.94 ± 0.55	55.67 ± 0.06	62.55 ± 0.99	67.68 ± 0.68	13.29
Seeds	EtOH	46.71 ± 0.71	52.31 ± 0.25	54.71 ± 0.17	58.25 ± 0.39	61.08 ± 0.33	63.08 ± 0.33	67.67 ± 0.22	3.10
	Watery	35.85 ± 0.91	39.74 ± 0.62	45.11 ± 0.24	48.03 ± 0.41	52.19 ± 0.18	58.41 ± 2.27	65.88 ± 0.27	23.02
Bark	EtOH	37.67 ± 0.54	50.74 ± 0.45	53.29 ± 0.48	55.53 ± 0.28	59.03 ± 0.4	64.63 ± 0.14	67.41 ± 0.26	3.79
	Watery	22.64 ± 0.80	33.68 ± 0.23	36.43 ± 0.45	45.16 ± 0.24	48.41 ± 0.43	50.52 ± 0.22	54.53 ± 0.31	54.74
Leaves	EtOH	49.45 ± 0.27	52.93 ± 0.06	56.32 ± 0.15	57.39 ± 0.05	58.52 ± 0.35	59.37 ± 0.1	61.30 ± 0.04	2.26
	Watery	41.67 ± 0.36	48.5 ± 0.37	52.51 ± 0.24	55.18 ± 0.22	56.55 ± 0.40	58.55 ± 0.33	60.32 ± 0.21	5.37
Std.	Acarbose	44.84 ± 0.41	52.27 ± 0.24	58.88 ± 0.42	65.13 ± 0.06	66.65 ± 0.12	71.61 ± 0.12	79.99 ± 0.12	3.31

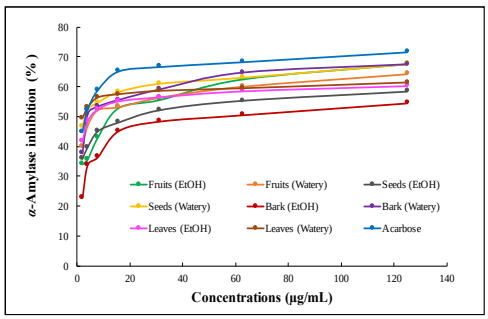

Figure 7. α-Amylase inhibition percent of tested samples of Zee

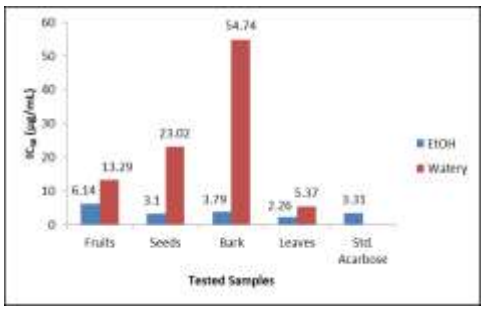

Figure 8. A bar graph of IC_{50} values of α-amylase activity of tested samples of Zee

Antimicrobial Activity of Crude Extracts of the Fruits, Seeds, Bark, and Leaves of Zee

Four crude extracts such as pelidem ether, ethyl acetate, ethanol and watery extracts, from four parts of the samples were subjected to screening for antimicrobial activity against six different pathogenic microbes using the agar well diffusion method. This method is based on the zone diameter, including the well diameter, in millimeter (mm). The larger the zone diameter, the higher the activity. According to the results, the ethanol extracts of all four portions have good activity, but watery extracts have mild activity. The resultant data are shown in Table 3.

Table 3. Inhibition Zone Diameters of Various Extracts of the Seeds, Fruits, Leaves and Bark of Zee against Six Microorganisms by Agar Well Diffusion Method

No.	Microorganisms	Samples	Diameter of inhibition zone (mm) in various crude extracts			
			PE	EtOAc	EtOH	H_2O
1	*B. subtilis*	Fruits	13	32	35	18
		Seeds	-	11	15	-
		Bark	15	15	15	19
		Leaves	13	23	15	18
2	*S. aureus*	Fruits	13	30	33	17
		Seeds	-	12	16	-
		Bark	18	17	16	19
		Leaves	18	24	16	17
3	*P. aeruginosa*	Fruits	17	33	35	26
		Seeds	-	12	14	-
		Bark	17	19	18	20
		Leaves	18	23	18	14
4	*B. pumilus*	Fruits	15	25	35	24
		Seeds	-	12	16	-
		Bark	19	19	17	19
		Leaves	16	23	14	16
5	*C. albicans*	Fruits	18	27	32	24
		Seeds	-	11	18	-
		Bark	19	17	17	20
		Leaves	15	22	16	20
6	*E. coli*	Fruits	13	28	34	20
		Seeds	-	12	17	-
		Bark	15	18	18	20
		Leaves	13	23	15	13

Diameter of agar well = 8 mm
10 mm - 14 mm = weak activity
15 mm - 19 mm = moderate activity
20 mm - above = potent activity

Conclusion

From the overall assessment concerning the investigation of phytochemicals and biological activities on the seeds, fruits, bark, and leaves of *Z mauritiana* Lam. the following inferences could be deduced. Lupeol was isolated from the ethyl acetate extract of the seeds by using silica gel column chromatographic separation technique. The bark and leaves of both extracts possessed greater antioxidant activity than those of other portions. According to the α-amylase activity, ethanol extracts of seeds, bark, and leaves have good α-amylase activity; however, other extracts

showed mild activity. For antimicrobial activity, pet-ether, ethanol, ethyl acetate and watery extracts of fruits, bark and leaves showed good antimicrobial activity against all tested microorganisms whereas seeds of ethanol extract and ethyl acetate extract have mild activity and then pet- ether extract and watery extract did not show antimicrobial activity. In conclusion, the four portions of Zee were found to have rich chemical constituents. According to the experimental result, the present study will contribute that four portions of *Ziziphus mauritiana* Lam. can be used in the traditional medicinal formulation for the treatment of many diseases.

Acknowledgements

The authors would like to express their profound gratitude to the Department of Higher Education (Lower Myanmar), Ministry of Education, Yangon, Myanmar, for provision of opportunity to do this research and Myanmar Academy of Arts and Science for allowing to present this paper. Greatful thanks are also to Professor Dr Hiroyuki Morita, Institute of Natural Medicine, University of Toyama for his help for NMR spectroscopic measurements.

References

Atta, E. M., N. H. Mohamedm, and A. A. M. Abdelgawad. (2017). "Antioxidant: An Overview on the Natural and Synthetic Types". *Journal of Natural and Synthetic antioxidants*, vol. 6 (8), pp. 365-375

Balouiri, M., M. Sadiki, and S. K. Ibnsouda. (2016). "Methods for *in Vitro* Evaluating Antimicrobial Activity". *Journal of Pharmaceutical Analysis*, vol. 6, pp. 71–79.

Chandrasekhar, N., V., Siddartha, and B., Venkateswarlu, (2012). "Evaluation of Antimicrobial Activity of Flower Extracts of *Allamanda cathartica* L." *International Journal of Pharma World Research*, vol. 3 (2), pp. 1-20

Mahato, S.B., and A. P. Kundu. (1994). "^{13}C NMR Spectra of pentacyclic triterpenoids – a compilation and some salient features." India Institute of Chemical Biology, vol. 37 (6), pp. 1517-1575

Marinova, G., V., and Batchvarov, (2011). "Evaluation of the Methods for Determination of the Free Radical Scavenging Activity by DPPH". *J.Agric. Sci*., vol. 17, pp.11-24

Perez, C., M., Paul, and P., Bazerque, (1990). "Antibiotic Assay by Agar Well Diffusion Method.". *Alta BioMed Group Experiences,* vol. 15, pp. 113-115

Sofowora, E. A. (2000). "Phytochemical Screening of Nigerian Medicinal Plants". *J. Intergrative Med*., vol. 41, pp. 234-24

Song, F. L., R. Y., Gan, Y., Zhang, Q., Xiao, L., Kuang, and H. B. Li, (2010). "Total Phenolic Contents and Antioxidant Capacities of Selected Chinese Medicinal Plants". *Int. J. Mol. Sci.*, vol. 11, pp. 2367-2372

Supaluk, P., P. Saraban, R. Cherdtrakulkiat, S. Ruchirawat, and V. Prachayasittikul. (2010). "New Bioactive Triterpenoids and Antimalarial Activity of *DIOSPYROS RUBRA LEC." EXCLI Journal,* vol. 9 (10), pp. 1611-2156

Xiao, Z., R. Storms, and A. Tsang. (2006). "A Quantitative Starch-iodine Method for Measuring Alpha-amylase and Glucoamylase Activities". *Journal of Analytical Biochemistry*, vol. 351 (1), pp. 146–148

Yang, X. W., M. Z. Huang, Y. S. Jin, L. Sun, Y. Song, and H. S. Chen. (2012). "Phenolic from Bidens Bipinnata and their Amylase Inhibitory Properties". *Journal of Fitoterapia*, vol. 83 (7), pp.1169-1175

Zou, Y., and Y. Zhao. (2015). "Chemical Composition and Radical Scavenging Activity of Melanin from *Auricularia auricula* Fruiting Bodies". *J. of food Science and Technology*, vol. 35 (2), pp. 253-258

STRUCTURE ELUCIDATION OF AN ISOLATED COMPOUND FROM THE HENLIN HOT SPRING DERIVED THERMOPHILIC BACTERIAL STRAIN AND ANTIBACTERIAL ACTIVITY

Sann Myint Oo[1], Thinn Myat Nwe[2], Myint Myint Sein[3]

Abstract

The thermophilic bacterial strain No. 21 which was obtained from the Department of Biotechnology, Mandalay Technical University, showed antagonistic activity against *S. aureus* (MRSA). Ethyl acetate crude extract was prepared from the strain fermentation broth. A pure Organic compound (SMOo) was isolated as a colourless oily form (250 mg) from ethyl acetate extract by chromatographic separation methods. The chemical structure of the isolated compound was identified by using modern spectroscopic techniques such as FT IR, ^{1}H NMR, COSY, ^{13}C NMR, HMQC, DEPT, HMBC and EI-MS. In addition, the antibacterial activity of the isolated compound was investigated by the agar well diffusion method and the isolated compound showed significant inhibitory activity on *S. aureus* (MRSA).

Keywords: thermophilic bacterial strain, antagonistic activity, antibacterial activity, spectroscopic data

Introduction

Infectious disease outbreaks become a challenge of worldwide nowadays. It is also the major cause of death which leads the 25% of all causes per year. Recently, antibacterial drugs have become less effective or even ineffective, resulting in an accelerating global health security emergency that is rapidly outpacing available treatment options (WHO, 2014). Natural products isolated from microorganisms have not only been the source of most of the antibiotics currently on the market but also the largest contributors to drugs in the history of medicine. To obtain antimicrobials from microorganisms, many scientists are trying to study unusual habitats for the discovery of new bioactive compounds (Harvey *et al*., 2001).

An extremophile is an organism that thrives in physically or geographically extreme conditions that are detrimental to most life on earth (Rampelotto, 2010). Over the last year, the extremophile with different categories, thermophiles (high temperature), acidophiles (low pH), alkaliphiles (high pH), halophiles (high salinity), and psychrophiles (low temperature) have the capability to produce new bioactive compounds under extreme or unusual conditions (Tango and Islam, 2002). Thermophilic bacteria (optimum growth temperature of 50 °C or above) have attracted great attention among extremophiles because they are sources of new bioactive metabolites (Singh *et al*., 2011). Hot water springs are situated throughout the length and breadth of India and Myanmar, at places with boiling water (e.g., Manikaran, Himachal Pradesh and Helin, an Ancient city of Myanmar) (Win Min Thant, 2008).

In 2010, a detailed experimental work for determination of antibacterial activity and isolation of a pure compound (SMOo) from the thermophilic bacterial strain No. 21 was reported (Sann Myint Oo *et al*., 2010). The suggested structure was mainly determined by FT IR spectroscopy at that time. In this paper, the complete structure of isolated compound, a phthalate derivative, is reported by extensive NMR spectroscopy. Phthalate derivatives are colourless liquid chemicals that have been used as plasticizers to improve the plasticity and the flexibility of materials. They can also be synthesized by plants and bacteria or fungi, and many studies have reported different biological activities of these compounds (Ortiz & Sansinenea, 2018).

[1] Department of Chemistry, Kalay University
[2] Department of Chemistry, University of Mandalay
[3] Department of Chemistry, University of Mandalay

Materials and Methods

Strain Collection

The ten isolated thermophiles which respond to antagonistic activities were provided by the Department of Biotechnology, Mandalay Technical University. They were cultured using the sample collected from the Henlin hot spring (Temp. 51°C and pH 5-6), the ancient city of Myanmar (Win Min Thant, 2008). Among them, the effective strain No. 21 showing the antagonistic activity on *S. aureus* (MRSA) was selected for this research work.

Fermentation of the Effective Strain

280 mL of inoculum was cultured from the selected strain at 90 rpm and room temperature for two days. For the production of a bioactive compound, the inoculum (280 mL) was transferred to the fermenter (5 L) containing 2.8 L of the prepared broth (antibiotic producing peptone medium). Running condition as impeller rotation, OD and temperature fixed at 220 rpm, 12.5 and 30 ºC was performed. The fermentation process was derived for 96 hours (Crueger *et al*., 1989).

Isolation and Purification of a Bioactive Compound

The fermentation broth was extracted three times with ethyl acetate (1:1, v/v). The ethyl acetate extract was separated from an aqueous phase by separating funnel. It was then concentrated by using a rotary evaporator and evaporated to dryness at room temperature to obtain the crude extract. The crude extract (750 mg) was fractionated using column chromatographic separation packed with silica gel and eluted with *n*-hexane gradually enriched with ethyl acetate to afford 42 fractions. Then, these fractions were confirmed for purity and homogeneity by analytical TLC. The fractions with the same R_f values were combined to give four fractions (I-IV). Among these combined fractions, the combined fraction (I) was rinsed by re-dissolving in *n*-hexane for further purification. It was checked by TLC for purity [*n*-Hexane: EtOAc, 9:1 (v/v)] (Sann Myint Oo *et al*., 2010).

Structural Elucidation of a Bioactive Compound

FTIR spectrum of an isolated compound was measured at the Department of Chemistry, University of Mandalay. ^{1}H NMR, COSY, ^{13}C NMR, HMQC, DEPT, HMBC, and EI-MS spectra were also determined at Meijo University, Nagoya, Japan. The isolated compound was elucidated by using the above spectroscopic techniques.

Screening of Antibacterial Activity of Isolated Compound

The antibacterial activity of isolated compound was determined on tested organism, *S. aureus* (MRSA), by agar well diffusion and agar drop diffusion methods. *n*-Hexane solvent was used as control. 1.05 g of Muller-Hinton and 1.5 g agar were dissolved in the sterilized beaker containing 50 mL of distilled water. It was then stirred with magnetic stirrer and sterilized by autoclaving at 121 °C for 15 minutes. After sterilization of medium, 20 mL of this medium was poured on the sterilized petridishes. The medium was then allowed to harden and dried in microwave oven at 40 °C for ten minutes. 0.1 mL of tested organism was inoculated into 20 mL of medium at 40 °C for four hours and swabbed onto the Muller-Hinton agar pate. Using a 5 mm punch, a well was made on the agar plate. An isolated compound (SMOo) solution (25 μL) that are dissolved in *n*-hexane was introduced into the well and dropped on the agar plate. It was incubated in an incubator at 27 °C for 24 hours. After incubation, the clear zone of agar well diffusion was measured and recorded (Collin, 1965).

Results and Discussion

Isolated Organic Compound from the Bacterial Fermentation Broth

The combined fraction (I) separated from the ethyl acetate extract (1.67 g) by column chromatographic method gave one spot on TLC with R_f value of 0.66 [*n*-Hexane: EtOAc, 9:1 (v/v)] and UV active. A pure colourless oily form (250 mg, 31.2% based on theyl acetate exract) was obtained.

Identification of Isolated Compound

FT IR spectrum (Figure 1) of the isolated compound showed the presence of the sp^2 =C-H stretching of the alkenic group at 3070 cm^{-1}. The absorption bands appeared at 2958, 2931 and 2873 cm^{-1} were responsible for the C-H stretching vibrations of sp^3 hydrocarbon. The sharp peak at 1728 cm^{-1} indicated the carbonyl stretching of the ester carbonyl group (-C=O). The conjugated C=C stretching of the aromatic ring was associated with the bands of 1600 and 1581 cm^{-1}. The intense peaks at 1272, 1122 and 1072 cm^{-1} attributed to the –C-(C=O)-O- stretching vibration of the ester group whereas those at 767, 705 and 651 cm^{-1} were corresponding to the =C-H bending vibration of an olefinic group.

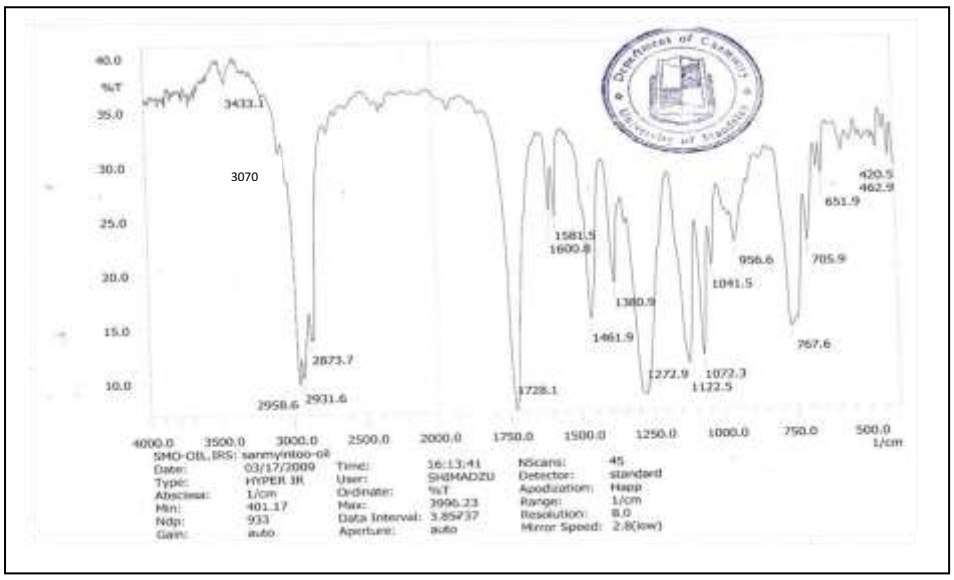

Figure 1. FT IR spectrum of the isolated compound

The ^{1}H NMR spectrum (Figure 2) displayed the characteristic aromatic proton signals of the *o*-disubstituted benzene ring [7.70 (2H, dd, *J* = 8.8 and 3.2 Hz, H-3 and H-6)] and [7.52 (2H, dd, *J* = 8.8 and 3.2 Hz, H-4 and H-5]. Two similar ester moieties were evidenced at 4.21 (4H, *m*, H-1'), 1.68 (2H, *m*, H-2'), 1.34-1.43 (16H, *m*, H-3',4',5' and 7') and 0.91 (12H, *t*, H-6' and H-8'). The ^{13}C NMR (Figure 3), HMQC (Figure 4) and DEPT (Fiture 5) spectra exhibited a total of 12 carbon signals, including characteristic signals due to an ester carbonyl at δ_C 167.7 (COO-), aromatic quaternary carbon at δ_C 132.4 (C-1 and C-2), two aromatic methine carbons at δ_C 130.8 (C-4 and C-5), 128.8 (C-3 and C-6), ester oxygen bearing methylene carbon at δ_C 68.1 (C-1'), one sp^3 methine carbon at δ_C 38.7 (C-2'), four methylene carbons at δ_C 30.3 (C-3'), 28.9 (C-4'), 22.9 (C-5'), 23.7 (C-7') and two methyl carbons at δ_C 14.0 (C-6') and 10.9 (C-8').

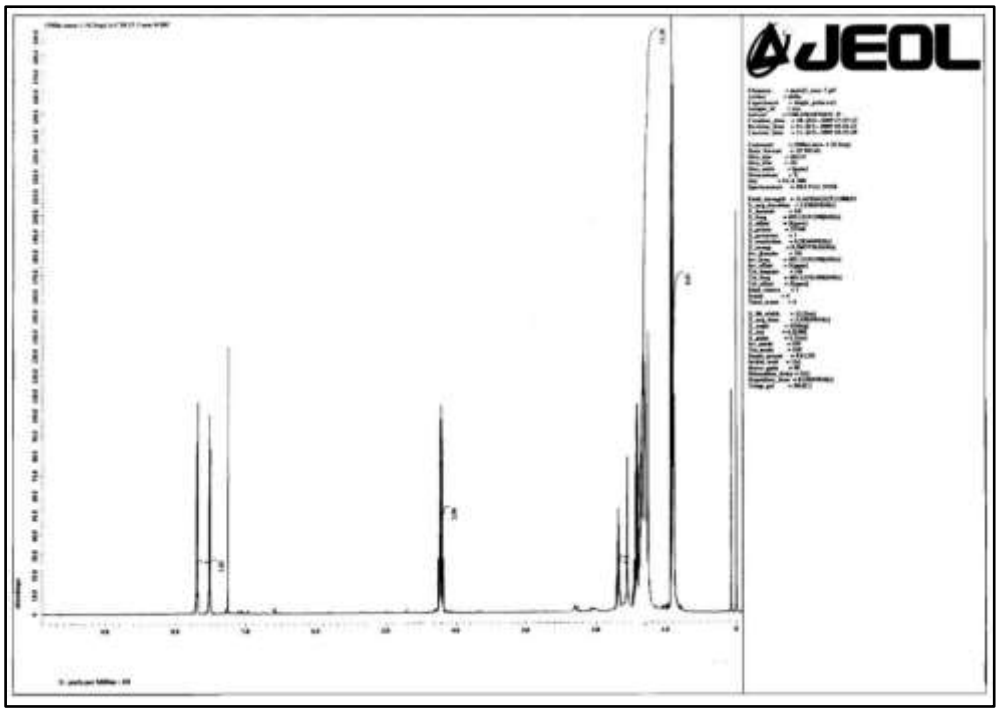

Figure 2. ^{1}H NMR spectrum ($CDCl_3$, 500 MHz) of the isolated compound

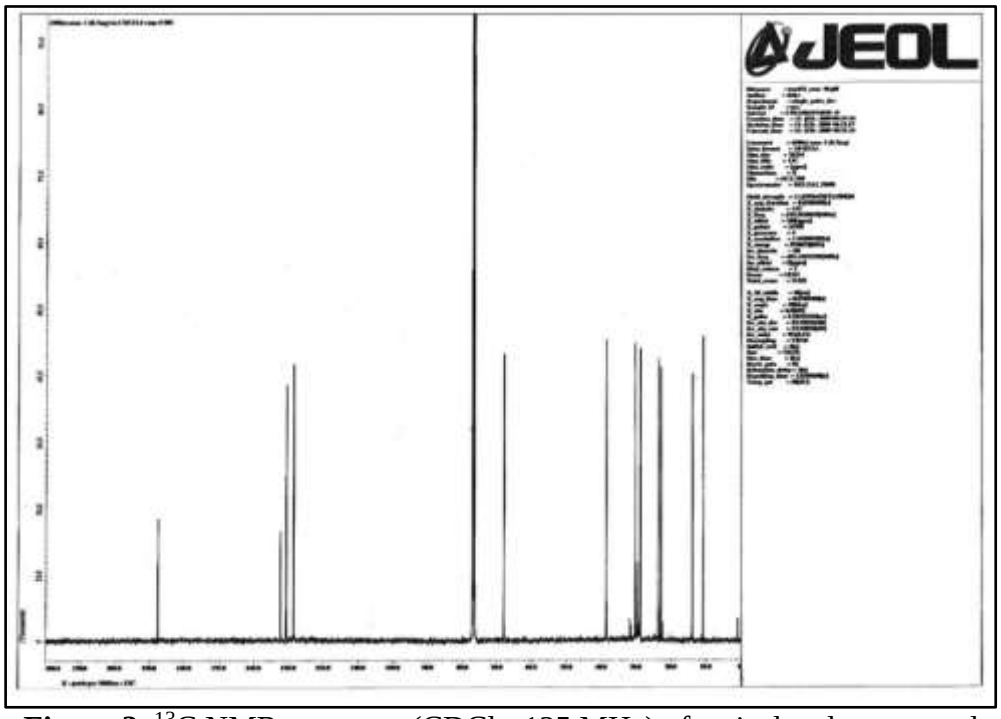

Figure 3. ^{13}C NMR spectrum ($CDCl_3$, 125 MHz) of the isolated compound

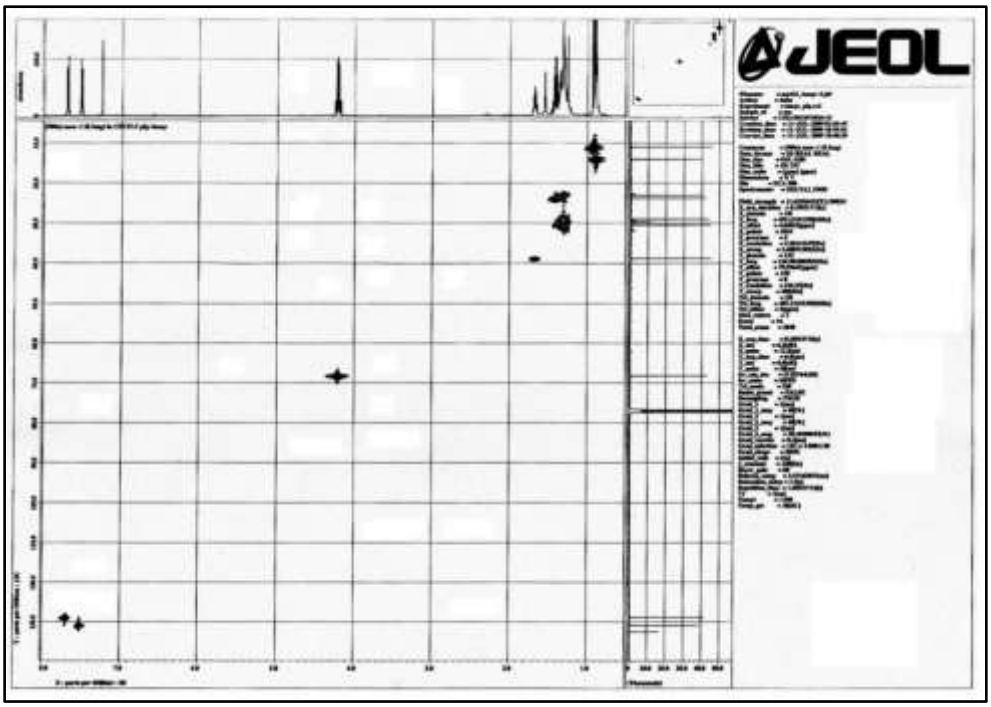

Figure 4. HMQC spectrum of the isolated compound

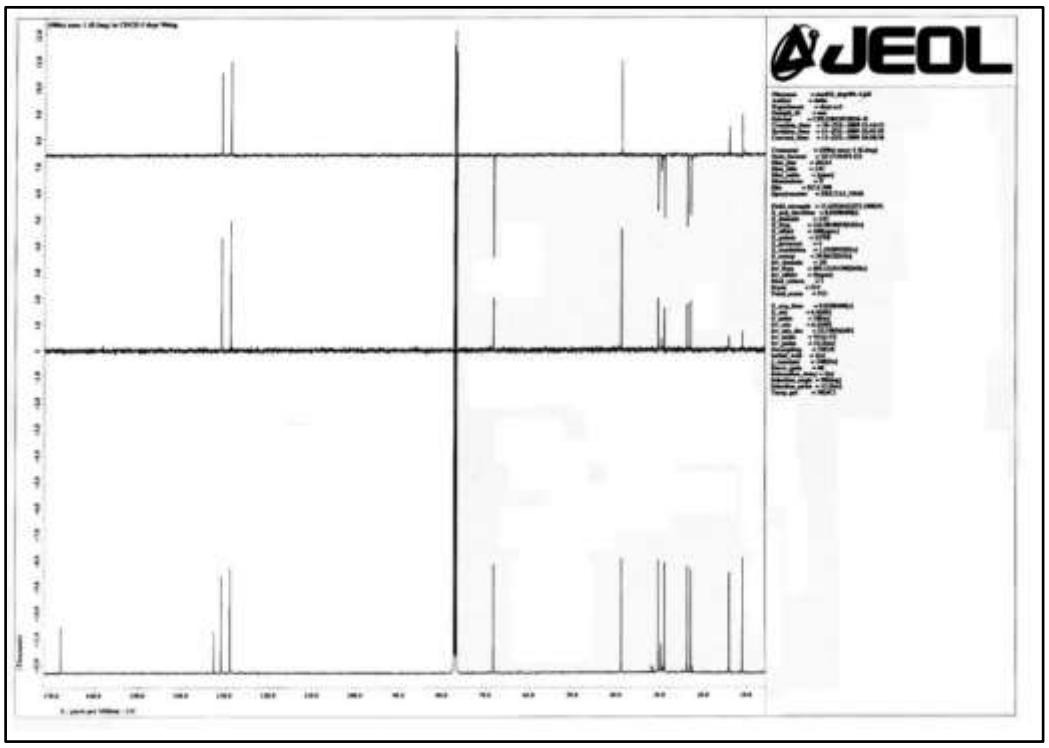

Figure 5. DEPT spectrum of the isolated compound

Moreover, the $^{1}H–^{1}H$ COSY spectrum (Figure 6) on the isolated compound indicates the presence of two partial structures which are ortho-disubstituted benzene ring and ester oxygen-bearing 2-ethyl hexoxy group. In the ^{1}H and ^{13}C NMR, and HMBC (Figure 7) spectra, the ester oxygen-bearing methylene protons [4.21 (4H, *m*, H-1')] in 2-ethyl hexoxy group respond long range coupling with the ester carbonyl carbon at 167.7 (COO-) extending the ester moiety in the

isolated compound. Two similar ester moieties are achieved due to the presence of double proton integration numbers and carbon intensity lines. The three fragments, one ortho-disubstituted benzene ring and two ester groups, are connected by HMBC correlation between the aromatic protons at 7.70 and ester carbonyl carbon at 167.7. Based on the above evidence, the structure of the isolated compound was identified to be bis (2-ethyl hexyl) phthalate as shown in Figure 8.

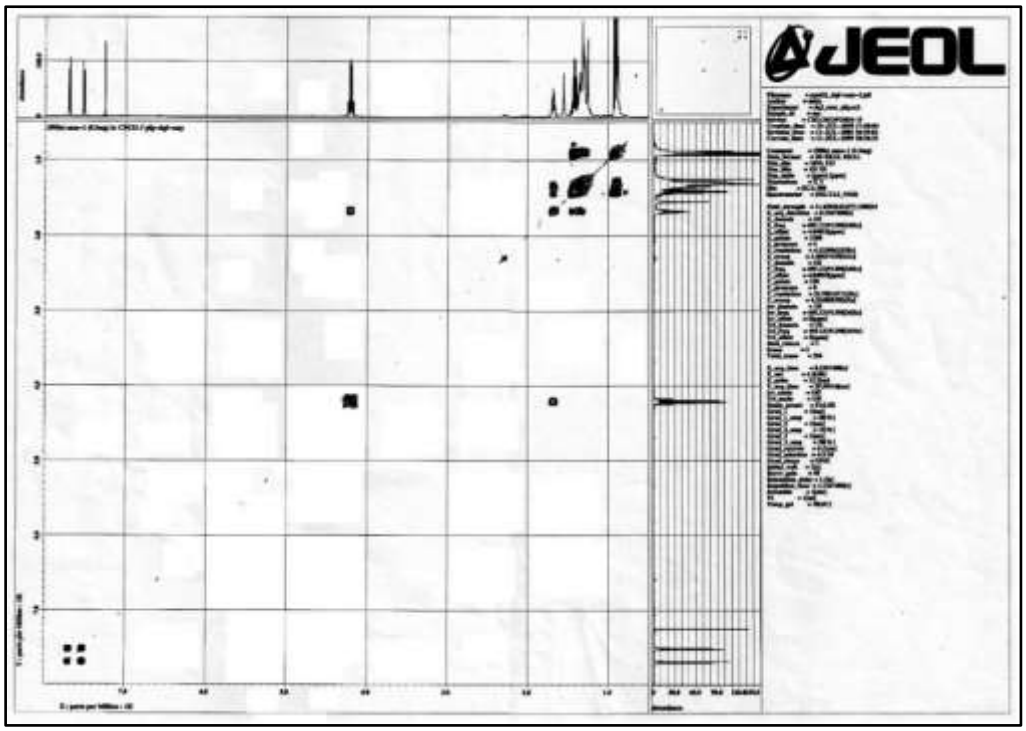

Figure 6. $^{1}H–^{1}H$ COSY spectrum of the isolated compound

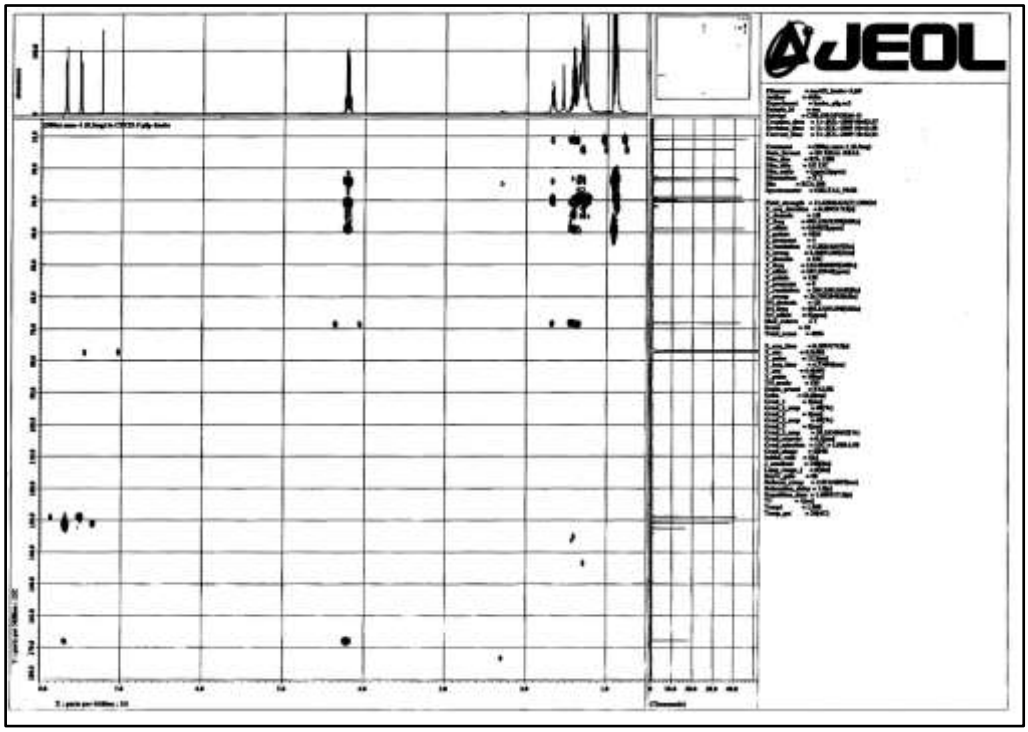

Figure 7. HMBC spectrum of the isolated compound

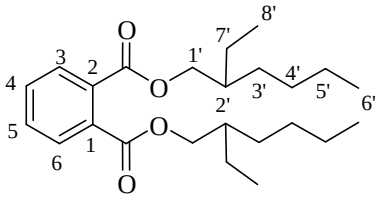

Figure 8. Chemical structure of the isolated compound

In the EI-MS of compound (Figure 9), the ions at *m/z* 149, 167 and 279 may correspond to the following fragments ***a, b*** **and** ***c***, respectively as seen in Figure 10. The molecular ion peak is present at *m/z* 390.

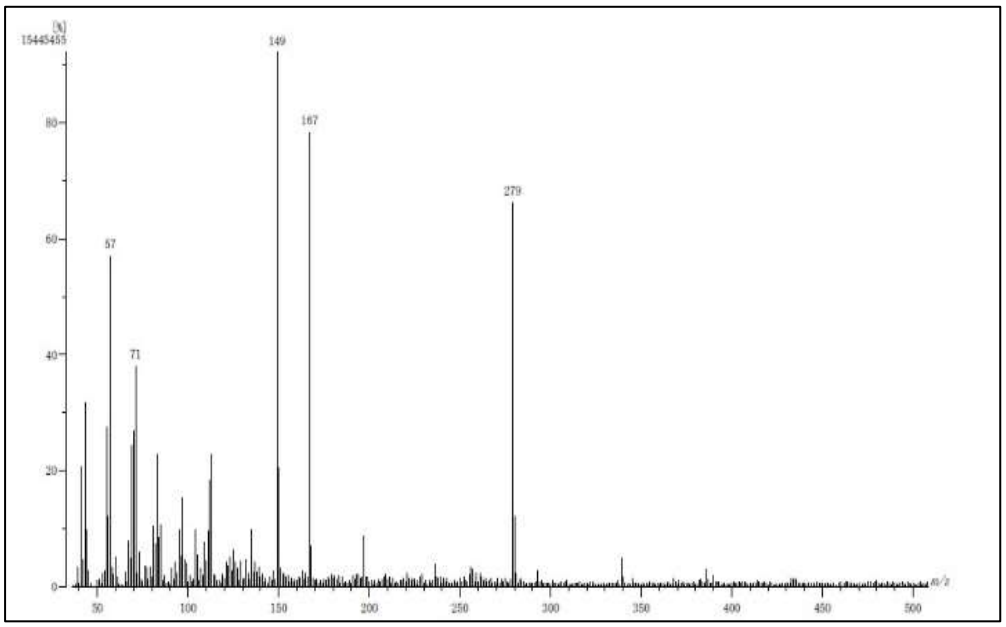

Figure 9. EI-MS spectrum of the isolated compound

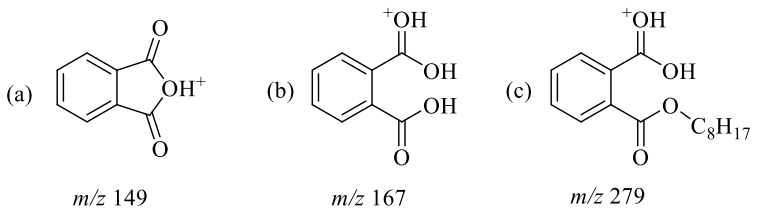

m/z 149 *m/z* 167 *m/z* 279

Figure 10. EI-MS analysis of the isolated compound

Based on NMR, including observation of HMBC correlation, mass spectral data and comparison of the spectral data with those reported in the literature (Rao *et al.*, 2000), the isolated compound (SMOo) could be confirmed as bis (2-ethyl hexyl) phthalate.

It was found that the reported spectral data of di- 2-ethyl hexyl phthalate isolated from *Cassia auriculata* leaves are expressed in Table 1 (Rao *et al.*, 2000).

Table 1. The ^{1}H (500 MHz), ^{13}C (125 MHz) NMR and DEPT Spectral Data of the Isolated Compound (SMOo) in $CDCl_3$

Position	^{1}H (J in Hz)		^{13}C (δ)		DEPT
	Isolated compound	Literature data[R]	Isolated compound	Literature data[R]	
1,2	-	-	132.4	132.4	C
3,6	7.70 (2H, *dd*, *J* = 8.8 and 3.2Hz)	7.75 (2H, *dd*, *J* = 7.5 and 1.5Hz)	128.8	128.7	CH
4,5	7.52 (2H, *dd*, *J* = 8.8 and 3.2Hz)	7.55 (2H, *dd*, *J* = 7.5 and 1.5Hz)	130.8	130.8	CH
1'	4.21 (4H, *m*)	4.25 (4H, *d*)	68.1	68.1	CH_2
2'	1.68 (2H, *m*)	1.65 (2H, *m*)	38.7	38.7	CH
3'	1.34-1.43 (4H, *m*)[a]	1.3 (4H, *m*)	30.3	30.3	CH_2
4'	1.34-1.43 (4H, *m*)[a]	1.3 (4H, *m*)	28.9	28.9	CH_2
5'	1.34-1.43 (4H, *m*)[a]	1.3 (4H, *m*)	22.9	22.9	CH_2
6'	0.91 (6H, *t*)[a]	0.91 (6H, *t*)	14.0	14.0	CH_3
7'	1.34-1.43 (4H, *m*)[a]	1.3 (4H, *m*)	23.7	23.7	CH_2
8'	0.91 (6H, *t*)[a]	0.91 (6H, *t*)	10.9	10.9	CH_3
COO-	-	-	167.7	167.7	C

[R]Rao *et al.*, 2000
[a]Overlapped

Antibacterial Activity of the Isolated Compound

The antibacterial activity of the isolated compound (SMOo) was investigated by the agar well diffusion method and found to possess high inhibitory activity (18 mm, +++) on *S. aureus* (Figure 11). *n*-Hexane as control did not show activity (-) on the tested organism.

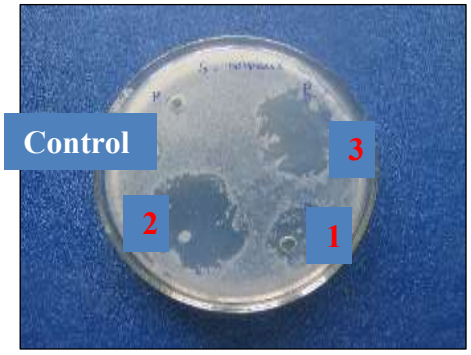

Figure 11. Antibacterial Screening of the isolated compound

Agar well = 5 mm
No activity = 5 mm (-)
Low activity = 5-10 mm (+)
Medium activity = 10-15 mm (++)
High activity = Above 15 mm (+++)

(1): Agar well diffusion method
(2) and (3): Agar-drop diffusion method
Control: *n*-Hexane

Conclusion

In the research work, the selected thermophilic bacterial strain No. 21 was found to produce a potent bioactive compound. The isolated compound (SMOo) with the molecular formula of $C_{24}H_{38}O_4$, showed the antibacterial activity. The bioactive compound (SMOo) was able to be elucidated as a well-known organic compound, di- (ethyl hexyl) phthalate (DEHP), by using spectroscopic data.

Acknowledgements

The authors are extremely grateful to Dr. Mya Aye, Rector (Rtd.), University of Mandalay for his help measuring spectra of a compound. We are thankful to Dr. Yoshiaki Takaya, Associate Professor, Meijo University, Nagoya, Japan for NMR spectra. We must particularly express my gratitude to Dr. Win Min Thant, Director, Biotechnology Research Department, Kyaukse for his excellent and skilful technical assistance, valuable suggestion and close guidance concerning my research work.

References

Collin, C.H. (1965). *Microbiology Methods*. London*:* 5th Edition, Butterworth and Col, Publishers Ltd.,

Crueger, W., and A. Crueger. (1989). *BIOTECHNOLOGY*: *A Textbook of Industrial Microbiology*, New Delhi 2nd Edition, Panima Publishing Corporation

Harvey, I., Y. Cormier, C. Beaulieu, V.N. Akimov, A. Mériaux, and C. Duchaine. (2001). "Random Amplified Ribosomal DNA Restriction Analysis for Rapid Identification of Thermophilic Actinomycete-like Bacteria Involved in Hypersensitivity Pneumonitis," *Syst. Appl. Microbiol*., vol. 24 (2), pp. 277-284

Ortiz A., and E. Sansinenea. (2018). "Di-2-ethylhexylphthalate may be a Natural Product, rather than a pollutant," *Journal of Chemistry*, vol. 1, pp. 1-7

Rampelotto, P. H. (2010). "Resistance of Microorganisms to Extreme environmental Conditions and its Contribution to Astrobiology," *Sustainability*, vol. 2 (6), pp. 1602-1623

Rao, G.N., P.M. Kumar, V.S. Dhandapani, T.R. Krishna, and T. Hayashi. (2000). "Constituents of *Cassia auriculata*," *Fitoterapia,* vol. 71 (1), pp. 82-83

Sann Myint Oo, Hla Myo Min and Myint Myint Sein. (2010). "The Investigation into Bioactive Secondary Metabolite Isolated from Extreme Strain No. 21", *Universities Research Journal*, vol. 3 (5), pp. 259-272

Singh, G. A., Bhalla, P. Kaur, N. Capalash, and P, Sharma. (2011). "Laccase from Prokaryotes: A New Source for an Old Enzyme," *Reviews in Environmental Science and Biotechnology*, vol. 10 (4), pp. 309-326

Tango, M.S.A., and M.R. Islam. (2002). "Potential of Extremophiles for Biotechnological and Petroleum Applications," *Energy Sources*, vol. 24 (6), pp. 543-559

Win Min Thant (2008). *Investigation of the Extreme Bacteria and Their Antifungal Activity Focusing on Agriculture Sector*, Ph.D. Dissertation, Department of Biotechnology, Mandalay Technological University

World Health Organization (WHO). (2014). *Antimicrobial Resistance: Global report on Surveillance*, Switzerland: WHO Press

STUDY ON KINETIC PROPERTIES OF CATALASE ISOLATED FROM *CORIANDRUM SATIVUM* L. LEAVES

Tin Zar Ni Tun[1], Myat Kyaw Thu[2], Wai Lin Oo[3]

Abstract

Isolation and purification of catalase enzyme from *Coriandrum sativum* L. leaves were performed by ammonium sulphate precipitation followed by dialysis and gel filtration chromatography on Sephadex G-100. The catalase activity of the final purification steps was measured by following the dismutation of H_2O_2 spectrophotometrically using an extinction coefficient for H_2O_2 at 439 nm of 0.0113 mM^{-1} cm^{-1}. The effect of substrate concentration and enzyme concentration on the catalase-catalyzed reaction was studied. The K_m value was calculated to be 5.1420×10^{-3} M H_2O_2, and the V_{max} value was found to be 0.1308 M min^{-1} using the plot of Lineweaver-Burk. The activation energy (E_a) of the catalase-catalyzed reaction was calculated to be 2.978 kcal mol^{-1}. The reaction order (n) of the catalase-catalyzed reaction was found to be the first-order reaction. The catalase activity decreased with each hour of incubation in buffers with different pH values and temperatures. After 3 h of incubation at 40 ºC, the catalase activity was almost completely lost.

Keywords: catalase enzyme, ammonium sulphate precipitation, *gel filtration chromatography*, K_m, V_{max}, E_a, reaction order

Introduction

Antioxidants found in nature are enzymatic and non-enzymatic antioxidants. They all work together in collaboration to equalize oxidative stress. In all living cells, enzymes were found to be very necessary. They impact the rate at which a biochemical reaction achieves equilibrium (Susmitha *et al*., 2016). Catalase (EC 1.11.1.6) is the first discovered and potent antioxidant enzyme that catalyzes the disintegration of hydrogen peroxide into water and dioxygen (Demir *et al.*, 2008). It is broadly spread among a diversity of life forms, consisting of plants, animals, and microbes, and is usually away from anaerobic organisms. They play crucial roles in promoting health by forming part of our bodies' primary system of defence against free radical damage (Dumen and Kaya, 2013). Catalase holds an important place in the enzymatic world because of its use in various industries and medicines. The main role of catalase in cells is to protect against the accumulation of hydrogen peroxide (H_2O_2) up to a toxic level that forms as a by-product of the metabolic process that occurs in a living system. It also finds diverse industrial applications in textiles, waste treatment, cosmetics, and as a disinfectant agent, while in the analytical field it is used as a source of H_2O_2 (Farhan *et al.*, 2016).

Since ancient times, there has been a growing interest in plants. *Coriandrum sativum* has a very effective antioxidant profile, showing radical scavenging activity, hydroxyl radical scavenging activity, superoxide dismutation, etc. The present study aimed to study the kinetic behaviour of the purified catalase enzyme isolated from *Coriandrum sativum* L. leaves.

[1] Department of Chemistry, University of Yangon
[2] Department of Chemistry, University of Yangon
[3] Department of Chemistry, University of Yangon

Materials and Methods

Sample Collection

Coriander leaf samples were collected from Hledan Market, Kamayut Township, Yangon Region. Then, identification of the sample was done at the Department of Botany, University of Yangon. Sample extraction and purification were performed at the Analytical Chemistry Research Laboratory, Department of Chemistry, University of Yangon.

Materials

The chemicals required and catalase assay reagents were purchased from Sigma-Aldrich, England. All the chemicals used in this work were analytical grade. In all examinations, the recommended standard methods and techniques involving both conventional and modern methods were provided.

Sample Preparation, Extraction, and Purification of Catalase Enzyme from *Coriandrum sativum* L. Leaves

A 30 g of fresh coriander leaves were washed with tap water, air dried, cut, and homogenized with a 150 mL phosphate buffer (pH 7.0) solution. It was blended with an electrical blender and filtered. The suspensions were centrifuged for about 30 min at 5500 rpm. And then the precipitate was discarded, and the supernatant was collected. Solid ammonium sulphate was slowly added to this supernatant to obtain 20 % saturation. To homogenize it for complete dissolution, it was stirred for 2 h in ice. After 2 h, the mixture was centrifuged again for about 30 min and the precipitate was discarded. Solid ammonium sulphate was slowly added to this filtrate to obtain 20-70 % saturation, and after standing overnight, the precipitated protein-containing catalase enzyme was collected by centrifugation for about 30 min. The precipitate was dissolved in phosphate buffer (pH 7.0), and then the catalase enzyme was dialyzed through a dialysis bag in the same buffer for 5 h, with two changes of the buffer during dialysis. For further purification of catalase, the dialyzed enzyme sample was put onto the column filled with Sephadex G-100 equilibrated with the phosphate buffer at a flow rate of 1.5 mL/7 min. Eluates were collected in 1.5 mL tubes (Gholamhoseinian *et al*., 2006).

Catalase Enzyme Assay

For the enzyme assay, the catalase activity of the purified sample was measured spectrophotometrically by monitoring the reduction in absorbance at 439 nm. To stop the reaction, a cobalt bicarbonate solution was used. Although other methods of measuring catalase activity have been developed, this method is free from the interference that results from the presence of amino acids, proteins, sugars, and fats in the studied sample. Catalase was assayed by its depletion of hydrogen peroxide under slight modification. One unit is the amount of enzyme that decomposes one micromole of H_2O_2 per minute under the assay conditions (Hadwan, 2018).

Kinetic Studies of Catalase Enzyme

The values of K_m and V_{max} were determined using different concentrations of hydrogen peroxide (2.5 mM – 35 mM) as a substrate. The reaction order and activation energy of the catalase-catalyzed reaction were also evaluated.

Determination of pH Stability and Thermostability of Catalase Enzyme

Firstly, 0.5 mL of purified catalase with phosphate buffer pH 7 was placed in a water bath at temperatures of 20, 30, and 40 ℃. For pH stability, the enzyme solution was mixed with a

pH (6, 7, and 8) phosphate buffer solution at room temperature. After the above treatment, enzyme activity was examined at incubation times of 0, 1, 2, and 3 h under the assay conditions.

Effect of Enzyme Concentration

To study the effect of enzyme concentration, the activities of the catalase enzyme were examined using different concentrations of enzyme solution in a 10 mM phosphate buffer at pH 7.

Results and Discussion

Catalase enzyme from *Coriandrum sativum* L. leaves was extracted by (20-70) % ammonium sulphate precipitation method. Purification was achieved by dialysis and gel filtration chromatography on Sephadex G-100. Each 1.5 mL fraction after purification with Sephadex G-100 was estimated for enzyme activity and protein content. Fractions with high catalase activity were pooled and stored at 4℃. Catalase activity was found to be 31221 μmol min^{-1} in a total volume of purified enzyme of 15 mL. The total protein content was determined by the Biuret method, and it was observed to be 85.59 mg. The specific activity was calculated as 364.77 μmol min^{-1} mg^{-1}.

Effect of Substrate Concentration on Catalase Enzyme-catalyzed Reaction

In the present study, the velocities of enzyme reactions measured at varying levels of hydrogen peroxide concentration and their reciprocal values are shown in Table 1. The Michaelis-Menten plot of V vs. [S] is shown in Figure 1. The catalase enzyme reaction was followed by a hyperbolic curve. The concentration of hydrogen peroxide was increased, and the rate of reaction also increased, until a point was reached where the enzyme was working as fast as it could, that is, transforming its maximum number of hydrogen peroxide molecules each minute. At this point, the enzyme is said to be saturated with substrate, and further increases in the concentration of hydrogen peroxide would not increase the rate of reaction. The enzyme could not have worked faster. For a more accurate estimation, K_m and V_{max} values were computed using statistical and various graphical methods (Figures 2, 3, 4, and 5), and the values are presented in Table 2.

Table 1. Relationship between Substrate Concentration and Velocity of Catalase Enzyme-catalyzed Reaction

[S] (M)	-[S] (M)	1/[S] (M^{-1})	V (M min^{-1})	1/V (M^{-1} min)	V/[S] (min^{-1})	[S]/V (min)
0.0025	-0.0025	400.0000	0.0435	22.9885	17.4000	0.0575
0.0050	-0.0050	200.0000	0.0627	15.9489	12.5400	0.0798
0.0100	-0.0100	100.0000	0.0804	12.4378	8.0400	0.1244
0.0150	-0.0150	66.6667	0.0944	10.5932	6.2933	0.1589
0.0200	-0.0200	50.0000	0.1062	9.4162	5.3100	0.1883
0.0250	-0.0250	40.0000	0.1121	8.9206	4.4840	0.2230
0.0300	-0.0300	33.3333	0.1143	8.7489	3.8100	0.2625
0.0350	-0.0350	28.5714	0.1217	8.2169	3.4771	0.2876

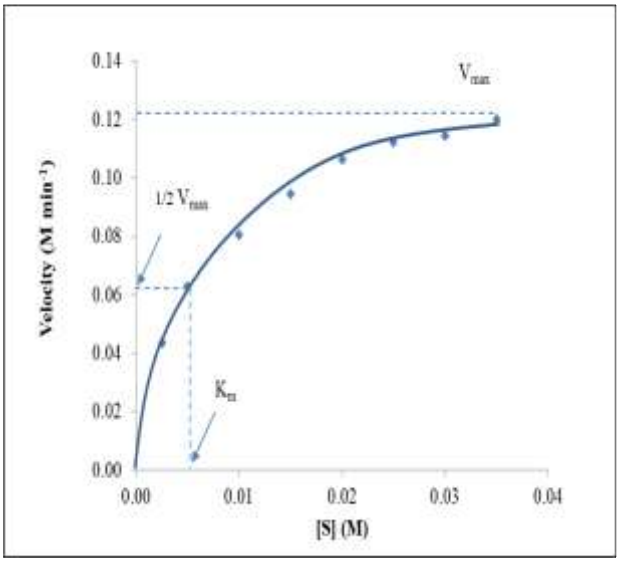

Figure 1. Michaelis-Menten plot of catalase enzyme-catalyzed reaction

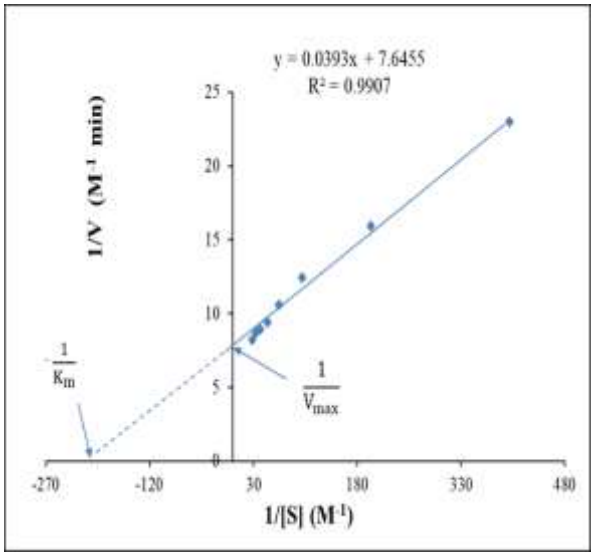

Figure 2. Lineweaver-Burk plot of 1/V vs. 1/[S] for catalase enzyme-catalyzed reaction

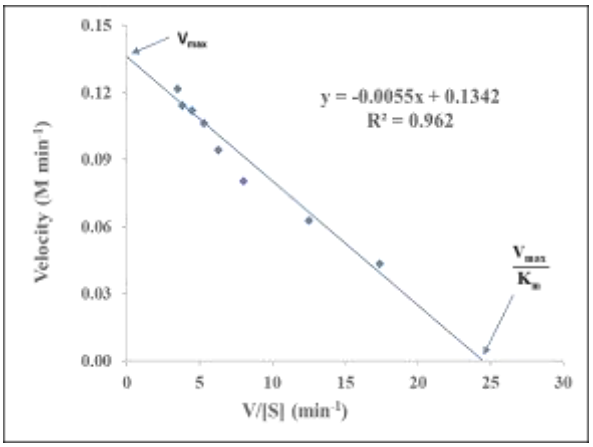

Figure 3. Eadie-Hofstee plot of catalase enzyme-catalyzed reaction

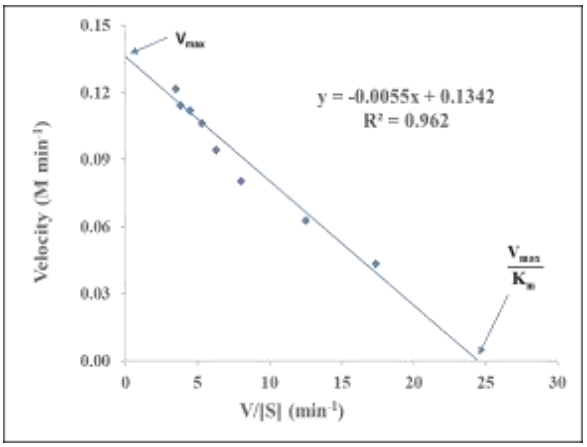

Figure 4. Hanes-Wilkinson plot of catalase enzyme-catalyzed reaction

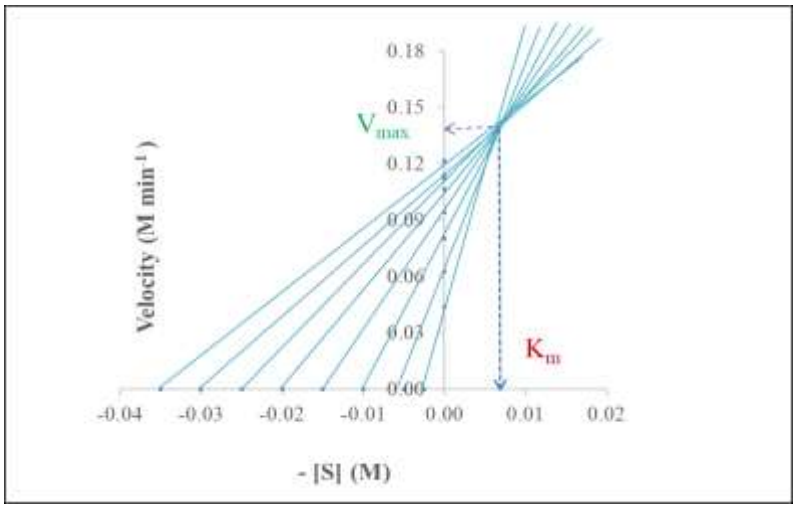

Figure 5. Eisenthal-Cornish Bowden plot of catalase enzyme-catalyzed reaction

Table 2. Representation of V_{max} and K_m Values of Catalase Enzyme Using Statistical and Graphical Methods

Methods	Statistical		Graphical	
	$K_m \times 10^3$ (M)	V_{max} (M min^{-1})	$K_m \times 10^3$ (M)	V_{max} (M min^{-1})
Michaelis-Menten	-	-	5.0000	0.1230
Lineweaver-Burk	5.1420	0.1308	5.1410	0.1308
Eadie-Hofstee	5.5167	0.1342	5.5000	0.1348
Hanes-Wilkinson	6.8160	0.1426	6.6557	0.1416
Eisenthal-Cornish Bowden	-	-	6.3000	0.1360

Reaction Order of Catalase-catalyzed Reaction

A reaction specified by the transformation of one molecule of A to one molecule of B with no impact from any other reactant or solvent is a first-order reaction (Martin *et al*., 1993). In this study, the 'n' value was determined from the plot of Log $V/(V_{max} - V)$ vs. Log [S] for catalase activity using the linear regression method (Table 3 and Figure 6). The reaction order (n) was observed to be a first-order reaction due to the evaluated value being 1.1702.

Table 3. Reaction Order for Catalase Enzyme-catalyzed Reaction

No.	Log [S]	Log $V/(V_{max} - V)$
1	-2.6021	-0.3025
2	-2.3010	-0.0359
3	-2.0000	0.2028
4	-1.8239	0.4139
5	-1.6989	0.6352
6	-1.6021	0.7778
7	-1.5229	0.8406
8	-1.4559	1.1263

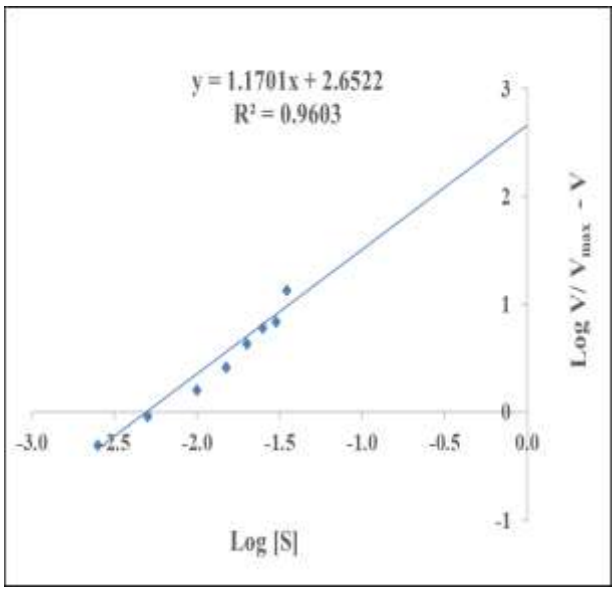

Figure 6. Plot of by log V/V_{max} -V as a function of log [S] of catalase-catalyzed reaction

Activation Energy of Catalase-Catalyzed Reaction

Enzymes lower the activation energy of the chemical reactions that they catalyze, and the reaction proceeds at a faster rate. Activation energy determination was performed using the relation between reaction velocity and temperature (Table 4). There is an increase in temperature and a faster reaction velocity. From the plot of Log V vs 1/T (Figure 7) the evaluated E_a value was found to be 2.978 kcal mol^{-1}.

Table 4. Relationship between Catalase Enzyme Velocity and Temperature of the Solution at pH 7

Temperature (°C)	1/T x 10^3 (K^{-1})	Velocity (M min^{-1})	Log V
10	3.5336	0.0822	-1.0851
20	3.4130	0.0870	-1.0605
25	3.3557	0.0999	-3.3570
30	3.3003	0.1188	-3.0534

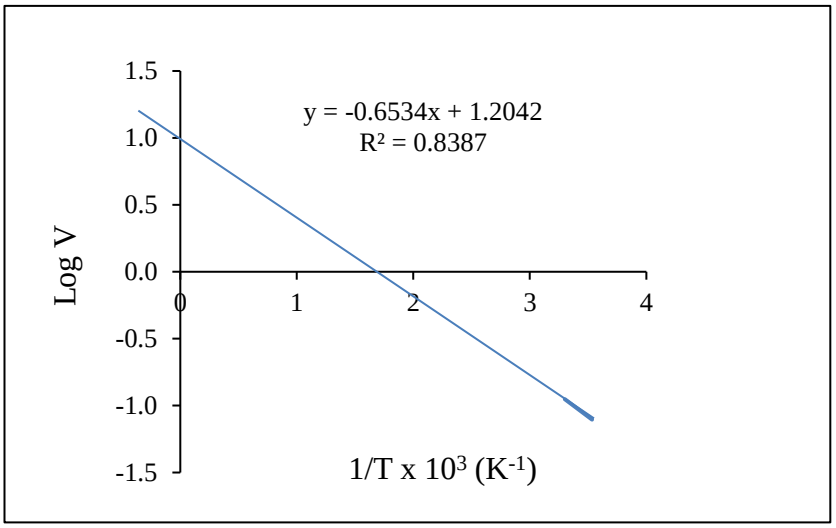

Figure 7. Plot of Log V as a function of 1/T for the determination of E_a

pH Stability and Thermostability of Catalase Enzyme

Stability means the maintenance of a defined functional state (chemical and structural properties that are needed for activity) under extreme conditions. To be a thermostable protein means to be resistant to changes in protein structure due to applied heat (Jaenicke and Bohm, 1998). For the determination of the pH stability of catalase activity in buffers with different pH values, an incubation period of 0–3 h was used. The data results are shown in Table 5 and Figure 8. The catalase activity of each buffer retained over half of its activity after 1 h of incubation. However, activity decreased 24.76 %, 31.11 %, and 28.21 % of its original activity for 3h of incubation.

The thermostability of catalase activity was also investigated using a particular pH of 7 at temperatures of 20, 30, and 40 ºC (Table 6). It can be seen clearly in Figure 9 that the catalase activity at 30 ºC was relatively stable, whereas at 20 ºC and 40 ºC, activity was reduced to 21.21 % and 9.80 % respectively.

Table 5. Relationship between Relative Activity of Catalase Enzyme and Incubation Time at Different pH Values

pH	Incubation time (h)	Catalase activity (μmol min^{-1} mL^{-1})	Relative activity (%)
6.0	0	1239.19	100.00
	1	601.89	48.57
	2	377.66	30.48
	3	306.85	24.76
7.0	0	2124.32	100.00
	1	1428.01	67.22
	2	1227.38	57.78
	3	660.89	31.11
8.0	0	1841.08	100.00
	1	1144.77	62.18
	2	920.54	50.00
	3	519.28	28.21

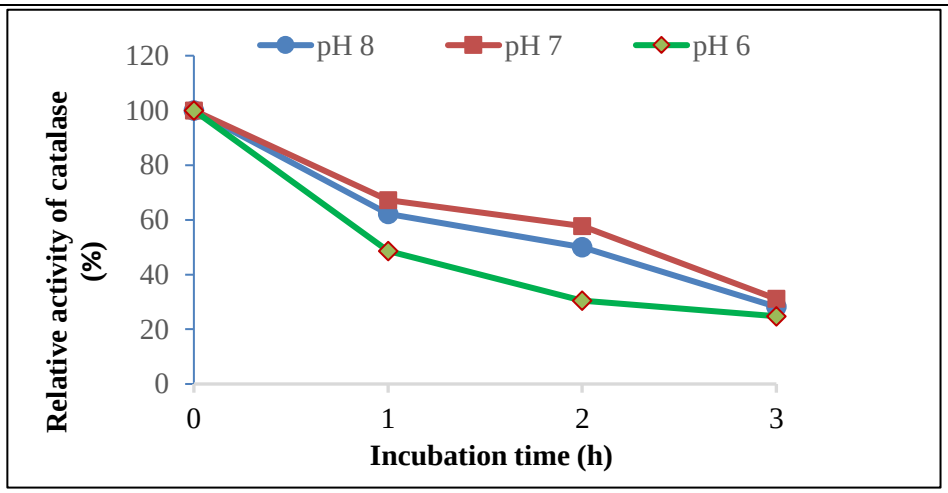

Figure 8. Plot of relative activity of catalase as a function of incubation at different pH values

Table 6. Relationship between Relative Activity of Catalase Enzyme and Incubation Time at Different Temperatures

Temperature (°C)	Incubation time (h)	Catalase activity (μmol min^{-1} mL^{-1})	Relative activity (%)
20	0	1947.29	100.00
	1	778.92	40.00
	2	578.29	29.69
	3	413.06	21.21
30	0	2195.13	100.00
	1	1062.16	48.39
	2	708.11	32.26
	3	625.49	28.49
40	0	1805.67	100.00
	1	613.69	33.99
	2	247.84	13.73
	3	177.03	9.80

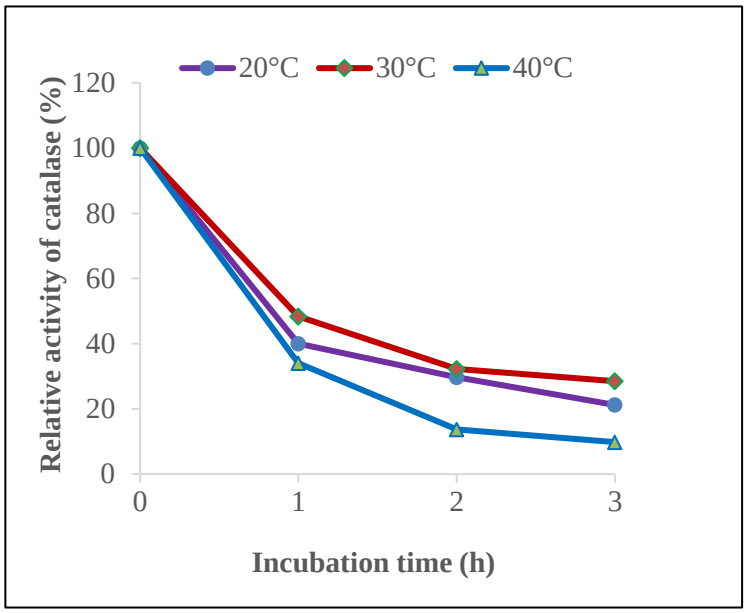

Figure 9. Plot of relative activity of catalase as a function of incubation at different temperature values

Effect of Enzyme Concentration on Catalase-catalyzed Reaction

As the concentration of an enzyme increases, the rate at which the substrate is changed also increases (Henrickson *et al*., 2007). Using different concentrations of enzyme ranging from 5.5 % to 7.5 %, the activities of catalase were examined.

Table 7. Relationship between Catalase Enzyme Activity and Enzyme Concentration

No.	Catalase enzyme concentration (%)	Catalase activity (μmol min^{-1} mL^{-1})
1	5.5	404.96
2	6.0	444.60
3	6.5	478.60
4	7.0	504.08
5	7.5	535.24

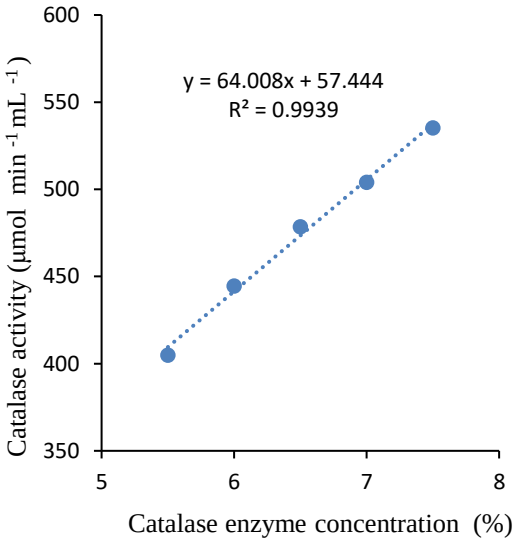

Figure 10. Plot of catalase enzyme activity as a function of enzyme concentration

According to Table 7, it was found that there was a direct relationship between enzyme concentration and catalase activity. The velocity of the reaction increased when the concentration solution was increased. An increase in enzyme concentration causes a decrease in colour intensity due to hydrogen peroxide depletion.

Conclusion

In this research, purified catalase enzyme was isolated from mature green *Coriandrum sativum* L. leaves. The total catalase activity and protein content of purified catalase were computed to be 31221 μmol min^{-1} and 85.59 mg, respectively. The values of K_m and V_{max} were treated statistically using the linear regression method. It was confirmed with various graphical methods: Michaelis-Menten, Lineweaver-Burk, Eadie-Hofstee, Hanes-Wilkinson, and Eisenthal-Cornish Bowden. In various methods of investigation, the values of K_m and V_{max} were seen as nearly the same. For the Lineweaver-Burk plot, the K_m and V_{max} values of catalase were found to be 5.1420×10^{-3} M and 0.1308 M min^{-1}, respectively. The reaction order (n) for catalase was computed to be 1.1702, proving that the reaction order is first order. The activation energy (E_a) of catalase-catalyzed reaction was calculated to be 2.978 kcal mol^{-1}. In the pH stability estimation of catalase activity, activity decreased by 24.76 %, 31.11 %, and 28.21 % of original activity, for pH 6, 7, and 8, respectively, for a 3h incubation at room temperature. The thermostability study on catalase activity revealed that the activity at 30 ºC was relatively stable. After 3 h of incubation at 40 ºC, the catalase enzyme lost nearly all of its original activity. The catalase activity was found to have a linear relationship with different enzyme concentrations.

Acknowledgements

The authors would like to thank the Department of Higher Education, Ministry of Education, Yangon, Myanmar. We would like to express our sincere thanks to Dr Tin Maung Tun (Rector) and Dr Khin Chit Chit, Dr Cho Cho, and Dr Thidar Aye (Pro-Rectors), University of Yangon. Our warmest thanks are also extended to Professor Dr Ni Ni Than, Head of the Department of Chemistry, University of Yangon, for her kind encouragement, permission to submit this paper and many helpful suggestions.

References

Demir, H., T.A. Coban, and M. Ciftci. (2008). "Purification and Characterization of Catalase Enzymes from Coriander (*Coriandrum sativum*) Leaves". *Asian Journal of Chemistry*, vol. 20 (3), pp. 1927-1936

Duman, Y.A., and E. Kaya. (2013). "Three-Phase Partitioning as a Rapid and Easy Method for the Purification and Recovery of Catalase from Sweet Potato Tubers (*Solanum tuberosum*)". *Applied Biochemistry and Biotechnology*, vol.170, pp. 1119-1126

Farhan, L.O., S.A. Mustafa, and A.S. Hameed. (2016). "Partial Purification and Characterization of Catalase from Banana Peels". *Baghdad Science Journal*, vol. 12 (2), pp. 392-398

Gholamhoseinian, A., N. Ghaemi, and F. Rahimi. (2006). "Partial Purification and Properties of Catalase from *Brassia Oleracea Capitata*". *Asian Journal of Plant Sciences*, vol. 5 (5), pp. 827-831

Hadwan, M.H. (2018). "Simple Spectrophotometric Assay for the Measuring Catalase Activity in Biological Tissues". *BMC Biochemistry*, vol. 19 (7), pp. 1-8

Henrickson, C.H., L.C. Byrd, and N.W. Hunter. (2007). *A Laboratory Manual for General, Organic and Biochemistry*. New York: 5th Edition, McGraw-Hill Co., pp. 357-378

Jaenicke, R. and G. Bohm. (1998). "The Stability of Proteins in Extreme Environments". *Current Opinion in Structural Biology*, vol. 8 (6), pp. 738-748

Martin, D.W., P.A. Mayes, and V.W. Rodwell. (1993). *Harper's Review of Biochemistry*. California:18th Edition, Lange Medical Pub.

Susmitha, S., P. Meenambigai, R.S. Gowri, K.U. Hima, and R. Vijayaraghavan. (2016). "Purification of Catalase Enzyme from *Nostoc* and its Physicochemical Properties". *International Journal of Microbiological Research*, vol. 7 (1), pp. 30-35

PHOTOCATALYTIC EFFECTS OF ZINC OXIDE NANOPARTICLES ON DEGRADATION OF ROSE BENGAL DYE

Phyu Phyu Myint[1] and Myat Kyaw Thu[2]

Abstract

ZnO nanoparticles were synthesized by using the co-precipitation method with the precursors Zn (CH3COO)2, 2H2O, and NaOH. Three different lighting environments-darkness, daylight, and sunlight—were used in this study to examine how ZnO nanoparticles affected the photocatalytic degradation of rose bengal dye solutions. The effects of contact time, dye concentration, and catalytic dosage were studied to better understand the photocatalytic process. The photocatalytic activities of ZnO nanoparticles were investigated at three pH values: 4, 7, and 10. The optimum degradation was found to be 96.483% after 2 h of contact time at a pH of 7 under sunlight. The optimum concentration of the dye solution was determined to be 10 ppm, and the photodegradation percent under sunlight at a pH of 7 was found to be 96.003%. The optimal ZnO nanoparticle dosage was 0.30 g, and the percentage of colour deterioration was calculated to be 98.113% at a pH of 7. The photocatalytic activity of ZnO was highest at a pH of 7, compared to pHs of 4 and 10.

Keywords: ZnO nanoparticles, co-precipitation method, photodegradation, rose bengal dye

Introduction

Zinc oxide (ZnO) nanoparticles (NPs), as a cheap, nontoxic semiconductor with a wide direct band gap (3.37 eV), are a promising material for different applications such as photocatalysts and photodetectors. Zinc oxide is an amphoteric oxide. Zinc oxide is widely used in different areas because of its unique photocatalytic, electrical, dermatological, and antibacterial properties (Becherri et al.,2008). Today, the entire world is facing a major problem of water pollution, which is caused in different ways. Dyes from different textile, dyeing, and printing industries are one type of pollutant, as these industries discharge their influent into nearby natural water resources without any treatment. In recent years, due to industrialization, there has been a rapid increase in the release of pollutants from industries into water bodies. Industries mainly responsible for polluting water bodies are food, textiles, dyeing, chemicals, printing, etc. Out of these industries, the main source of water pollution is the dyeing industry. Discharge from these industries has a deleterious effect on aquatic flora and fauna and renders water toxic and unfit for use. Also, due to their persistent nature, they remain in the environment for a very long period of time (Kaur and Singhal, 2014). Pure zinc oxide is a white powder, but in nature it occurs as the rare mineral zincite (Battez et al., 2008), which usually contains manganese and other impurities that confer a yellow to red colour. It is nearly insoluble in water, but it will dissolve in most acids, such as hydrochloric acid. Nanoparticles have widespread applications in various fields such as science, technology, and medicine due to their unique physicochemical and biological properties (Taghizadeh et al., 2020). Today, nanotechnology is operating in various fields of science via its operation on materials and devices using different techniques at the nanometer scale. Nanoparticles are a part of nanomaterials that are defined as single particles 1-100 nm in diameter (Khan et al., 2022). A nanoparticle is the most fundamental component in the fabrication of a nanostructure and is far smaller than the world of everyday objects that are described by Newton's laws of motion but bigger than an atom or a simple molecule that are governed by quantum mechanics. Nanoparticles are of great interest because of their extremely small size and large surface to volume ratio (Iravani, 2011). Scientists around the world have recently become interested in nanotechnology because of its potential applications in a wide range of fields, including catalysis, gas sensing, renewable energy,

[1] Department of Chemistry, Dagon University
[2] Department of Chemistry, University of Yangon

electronics, medicine, diagnostics, medication delivery, cosmetics, the construction industry, and the food industry.

Materials and Methods

Preparation of ZnO nanoparticles

Zinc oxide (ZnO) nanoparticles (NPs) were synthesized by the co-precipitation method at 300 ˚C. Zinc acetate dihydrate and sodium hydroxide were used as the starting materials for preparing the zinc oxide nanoparticles. In brief, zinc acetate dihydrate and sodium hydroxide were dissolved in deionized water to form two transparent solutions with 0.5 M and 1 M concentrations, respectively. These solutions were poured into a beaker at room temperature. The mixture was stirred for 2 h, during which a white precipitate formed in the solution. The precipitation was then separated after centrifugation. Finally, ZnO nanoparticles were obtained by washing with deionized water and acetone and drying at 300 ˚C.

Preparation of rose bengal dye solution

A stock solution of 100 ppm rose bengal dye was prepared by dissolving 0.1g of rose bengal dye in deionized water in a 1 L volumetric flask and making up to the mark with deionized water. By dilution of rose bengal stock solution, various concentrations of 10, 20, 30, 40, 50, and 60 ppm dye solutions were obtained.

Photocatalytic degradation study on rose bengal dye

The spectrophotometric method was employed for the degradation study of rose bengal dye. Firstly, the wavelength of maximum absorption of the rose bengal dye solution was determined by measuring the absorbance values over the range of 400 to 650 nm. To determine the residual concentration of dye, a calibration curve was constructed by measuring the absorbance values of 10, 20, 30, 40, and 50 ppm dye solutions.

The effect of contact time on degradation was studied by adding 0.05 g of ZnO NPs into each of the beakers containing 50 mL of a 10 ppm rose bengal dye solution (pH 4). The mixture was stirred in darkness for 30 min prior to the experiment to maintain equilibrium between the adsorption and desorption processes between dye molecules and the nanoparticle surface. After 30 min, the dye solutions with ZnO nanoparticles were placed under sunlight irradiation. The residual absorbance of the solution was measured at intervals of 20 min in the range of 20 to 120 min. The above experiment was also carried out in daylight and darkness. To study the effect of the initial concentration of dye solution, concentrations were varied between 10 and 60 ppm while other conditions were kept constant. Similarly, to study the effect of dosage of ZnO NPs on rose bengal dye, dosages of 0.05, 0.10, 0.15, 0.20 ,0.25, and 0.30 g were used. The pH influence on the photodegradation of the dye was studied by doing experiments at pH 7 and 10.

Percentages of rose bengal photodegradation were calculated by the following formula:

$$\%\text{Degradation} = \frac{(C_0 - C)}{C_0} \times 100$$

where (C_0) denotes the initial concentration, while (C) indicates the final concentration.

Results and Discussion

Wavelength of Maximum Absorption and Calibration Curve of Rose Bengal Dye Solution

The wavelength of maximum absorption is typically used for the analysis. The wavelength of maximum absorption (λ_{max}) must be determined before employing UV-visible spectrophotometry to quantify a chemical. The absorption spectra of rose bengal dye solution were obtained at six different concentrations of 0, 10, 20, 30, 40, and 50 ppm in the wavelength region of 400-800 nm. The wavelength of maximum absorption was found to be 510 nm (Figure 1). The calibration curve was constructed by plotting absorbance vs. concentration. A standard calibration curve for rose bengal dye solution was constructed by plotting absorbance vs. six different concentrations of 0, 10, 20, 30, 40, and 50 ppm of rose bengal dye solution at 510 nm (Figure 2 and Table 1). The curve was observed to be linear, and it passed through the origin, so Beer's Law was obeyed (R^2=0.9969).

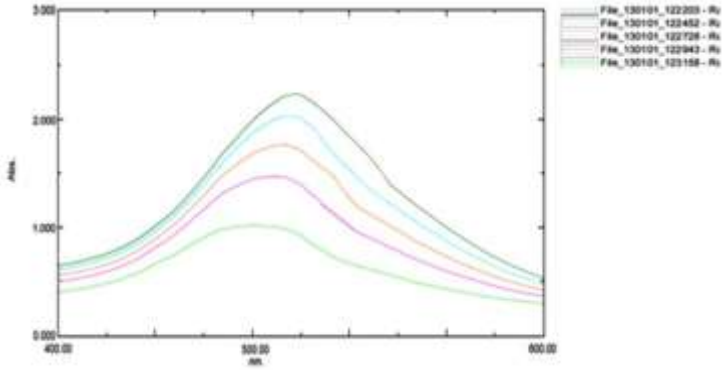

Figure 1. The wavelength of maximum absorption spectra of rose bengal dye

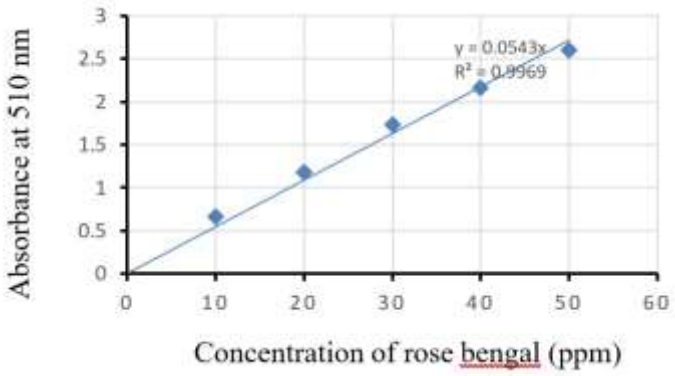

Figure 2. Calibration curve of rose bengal dye

Table 1. Relationship Between Absorbance and Concentration of Rose Bengal Dye Solution

No.	Concentration (ppm)	Absorbance at 510 nm
1	0	0.000
2	10	0.668
3	20	1.179
4	30	1.734
5	40	2.165
6	50	2.595

Photocatalytic Activity of ZnO NPs

Effect of contact time

The effect of contact time on the degradation of rose bengal dye solutions was investigated at different contact times (20–120 min) at pH 4. The presence of ZnO photocatalyst was tested in the dark, as shown in Table 2 and Figure 3. ZnO NPs had just a little effect on dye degradation in the dark, i.e., 10.703% of rose bengal dye decomposed photochemically within 2 h. Under daylight and sunlight conditions, a time-dependent decrease in the absorbance occurred with an increase in the degradation percentages of rose bengal dye. In daylight, 35.183% of rose bengal was degraded after 2 h of contact time. Furthermore, the rose bengal dye had almost completely degraded (95.044%) under sunlight in just 2 h. In the absence of a ZnO NPs catalyst, rose bengal degradation under three conditions exhibited little degradation.

Table 2. Degradation of Rose Bengal Dye using ZnO Nanoparticles with Different Contact Times at pH 4

No.	Contact time (min)	Degradation (%)		
		In dark	Daylight	Sunlight
1	0	0	0	0
2	20	1.387	19.425	64.915
3	40	2.576	21.407	71.645
4	60	4.955	27.849	83.349
5	80	7.234	29.335	88.701
6	100	8.225	31.615	92.460
7	120	10.703	35.183	95.044

Concentration of rose bengal dye = 10 ppm,
Dosage = 0.05 g,
Volume of dye solutions = 50 mL, pH 4

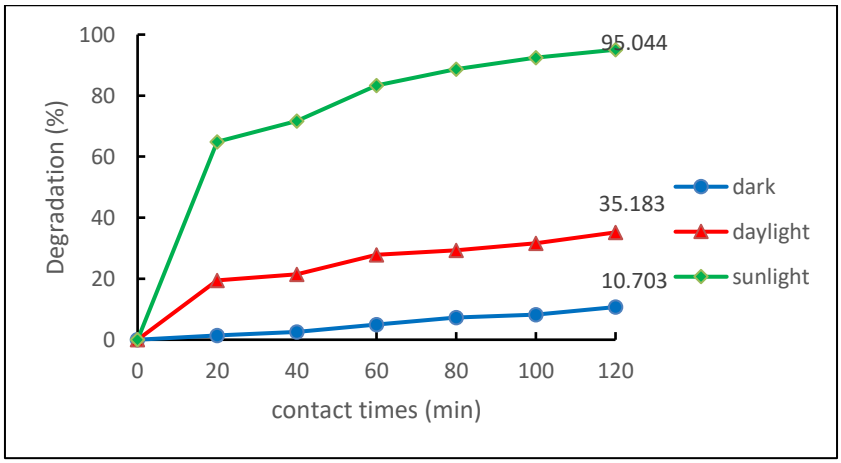

Figure 3. A plot of contact times vs. degradation (%) of ZnO nanoparticles on rose bengal dye at pH 4

The effects of contact time on the degradation of rose bengal dye solutions were also investigated at pH 7 and pH 10. The resulting data and the corresponding graphs are depicted in Table 3 and Figure 4 for pH 7 and in Table 4 and Figure 5 for pH 10. At these pH values, similar degradation patterns like pH 4 were observed. After 2 h of contact time, the degradation percent of rose bengal at pH 7 was found to be 96.483%, compared to 95.044 and 95.253% at pH 4 and 10 under sunlight, respectively. Moreover, the degradation percentages of rose bengal in daylight were 35.183, 41.743, and 40.261% for 2 h of contact time at pH 4, 7, and 10, respectively. In dark

conditions, the degradation percentages of rose bengal were 22.344% and 18.003% at pH 7 and pH 10, respectively, during 2 h of contact time. In all three conditions, the highest degradation percentage of rose bengal was found at pH 7, compared to the other two pH values.

Table 3. Degradation of ZnO Nanoparticles on Rose Bengal Dye with Contact Times at a pH of 7

No.	Contact Time (min)	Degradation (%)		
		In dark	Daylight	Sunlight
1	0	0.000	0.000	0.000
2	20	2.140	6.116	77.675
3	40	5.045	12.385	81.192
4	60	9.021	19.418	84.097
5	80	10.856	28.593	88.837
6	100	19.418	37.155	94.189
7	120	22.344	41.743	96.483

Concentration of rose bengal dye = 10 ppm,
Dosage = 0.05 g,
Volume of dye solutions = 50 mL, pH 7

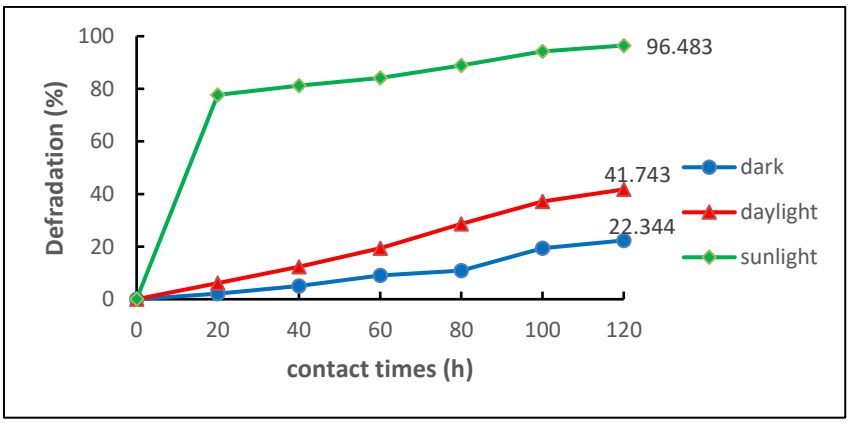

Figure 4. A plot of contact times (h) vs. degradation (%) of ZnO on rose Bengal dye at a pH of 7

Table 4. Degradation of ZnO Nanoparticles on Rose Bengal Dye with Different Contact Times at a pH of 10

No.	Contact time (min)	Degradation(%)		
		In dark	Daylight	Sunlight
1	0	0.000	0.000	0.000
2	20	2.945	10.149	71.849
3	40	6.873	14.729	73.813
4	60	8.674	20.621	79.541
5	80	12.929	28.150	84.779
6	100	14.402	34.369	92.144
7	120	18.003	40.261	95.253

Concentration of rose bengal dye = 10 ppm,
Dosage = 0.05 g,
Volume of dye solutions = 50 mL, pH 10

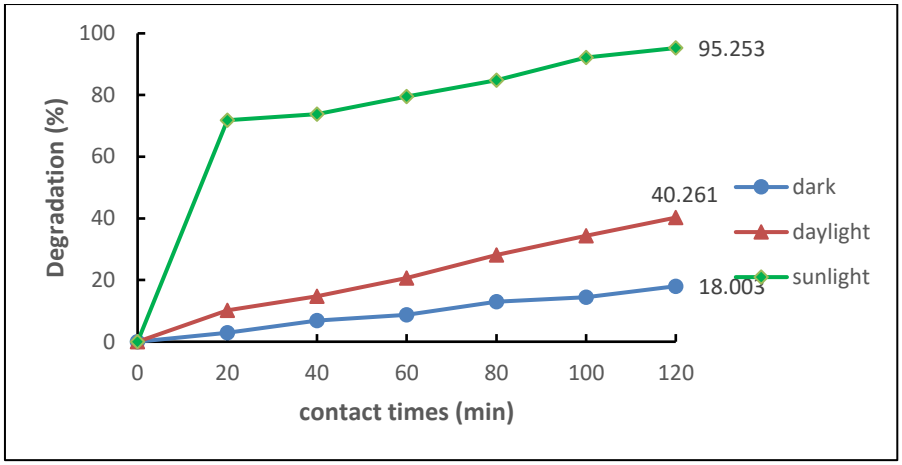

Figure 5. A plot of contact times (min) vs. degradation (%) of ZnO nanoparticles on rose Bengal dye at a pH of 10

Effect of the concentration of dye solution

The effect of the concentration of dye solution on photocatalytic degradation was also investigated at pH 4. It was found that in all three conditions, the degradation percent decreased as the concentration of dye solution increased (Table 5 and Figure 6). In daylight and in sunlight, as the concentration of dye increases, keeping the photocatalyst constant, the catalyst surface gets saturated. The intense colour of the dyes does not permit light to reach the ZnO photocatalyst. The dye molecules covered the active sites of ZnO NPs, and the degradation percent of the dye decreased. Using zinc oxide nanoparticles, the lower the concentration of rose bengal dye, the higher the degradation percentage of rose bengal dye.

Table 5. Effect of ZnO Nanoparticles on Degradation of Different Concentrations of Rose Bengal Dye at a pH of 4

No.	Concentration (ppm)	Degradation (%)		
		In Dark	Daylight	Sunlight
1	0	0	0	0
	10	7.366	19.153	94.860
2	20	7.331	17.640	91.408
3	30	6.673	16.102	83.558
4	40	5.727	14.411	80.046
5	50	5.258	12.284	79.555
6	60	2.665	9.684	77.765

Dosages = 0.05 g,
Volume of dye solutions = 50 mL,
Contact time = 2 h, pH= 4

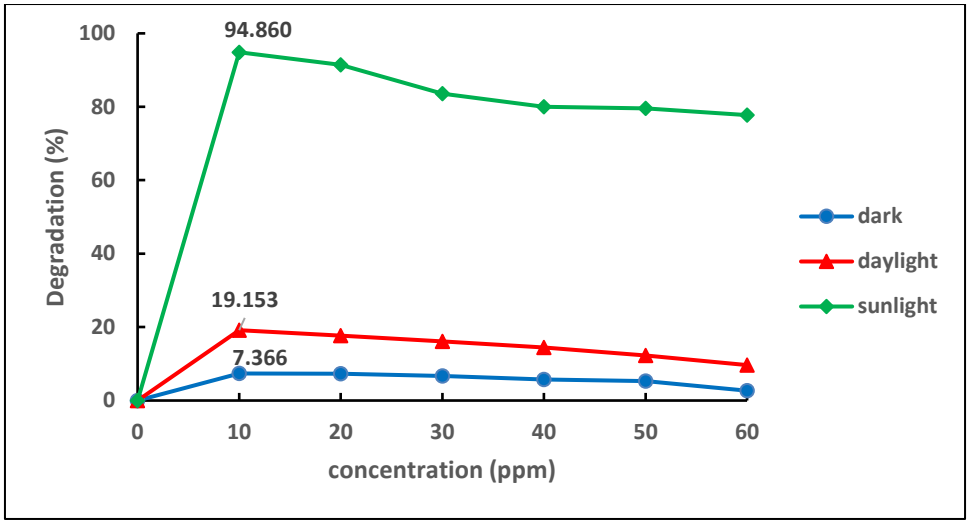

Figure 6. A plot of concentration (ppm) vs. degradation (%) of ZnO nanoparticles on rose bengal dye at a pH of 4

The effects of the concentration of rose bengal dye on the photocatalytic degradation were also studied at pH values of 7 (Table 6 and Figure 7) and 10 (Table 7 and Figure 8). As expected, the increased initial concentration of the dye solution has a negative impact on percent degradation. The same number of reactive radicals were generated on the surface of ZnO, but more and more dye molecules were adsorbed on its surface. Thus, the number of reactive radicals available for attack decreases, and photodegradation decreases. Among three different pH values, the degradation of dye was highest at pH 7 under sunlight (84.451%).

Table 6. Degradation of ZnO Nanoparticles on Rose Bengal Dye with Concentrations at a pH of 7

No.	Concentration (ppm)	Degradation (%)		
		In dark	Daylight	Sunlight
1	0	0	0	0
2	**10**	9.769	16.607	96.003
3	20	7.784	14.517	94.890
4	30	7.427	13.984	93.580
5	40	6.927	12.955	90.958
6	50	3.938	11.371	87.262
7	60	1.776	10.484	84.451

Dosages = 0.05 g,
Volume of dye solutions = 50 mL,
Contact time = 2 h, pH= 7

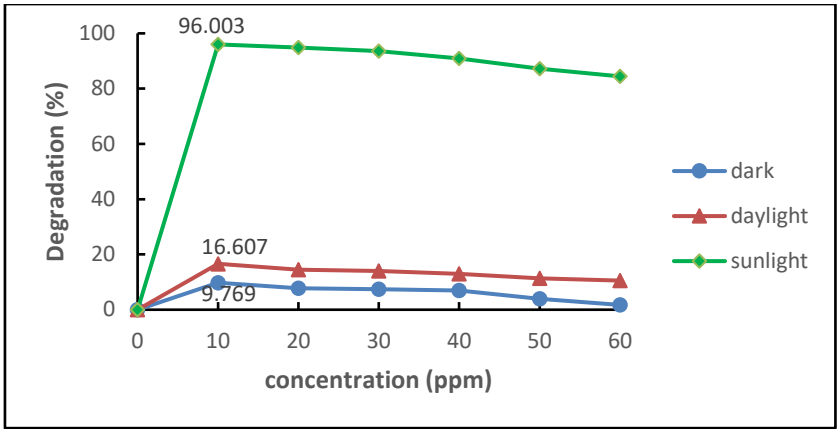

Figure 7. A plot of concentration (ppm) vs. degradation (%) of ZnO nanoparticles on rose Bengal dye at a pH of 7

Table 7. Degradation of Rose Bengal Dye using ZnO Nanoparticles with Different Concentrations pH 10

Sr No.	Concentration (ppm)	Degradation (%)		
		In Dark	Daylight	Sunlight
1	**0**	0	0	0
2	**10**	15.898	30.365	95.389
3	20	14.340	26.200	94.323
4	30	12.692	20.476	92.847
5	40	10.398	19.064	88.561
6	50	8.769	15.384	85.692
7	60	5.286	12.124	84.044

Dosages = 0.05 g,
Volume of dye solutions = 50 mL,
Contact time = 2 h, pH= 7

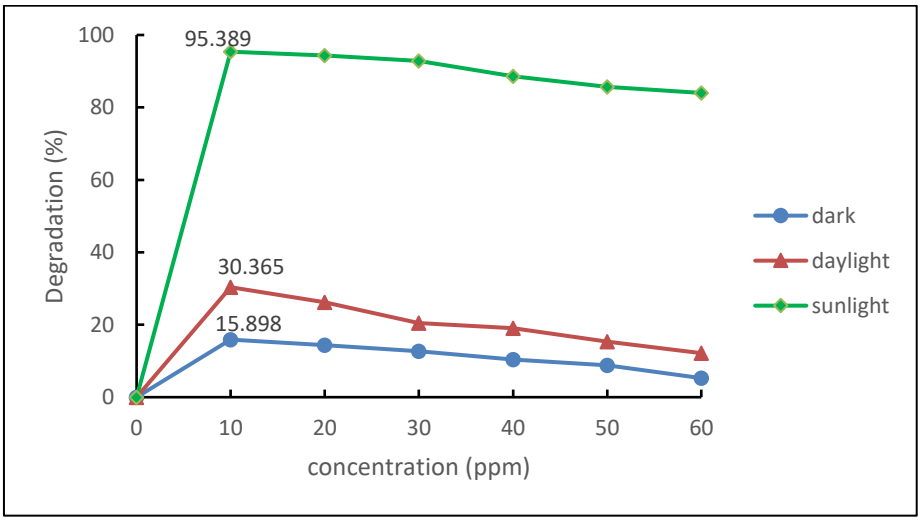

Figure 8. A plot of concentration vs. degradation (%) of ZnO nanoparticles on rose Bengal dye at a pH of 10

Effect of the dosage of ZnO nanoparticles

The effect of the dosage of ZnO on the degradation of 10 ppm of rose bengal dye solutions was investigated at pH 4. In this study, as the catalyst dosage was increased from 0.05 to 0.30 g, the percentage degradation of the dye was found to increase. Table 8 and Figure 9 show that the higher the dosage of zinc oxide nanoparticles, the higher the degradation of rose bengal dye in all three conditions. The increase in the dosage of ZnO increased the number of active sites on the photocatalytic surface, thus increasing the number of hydroxyl radicals (Wang *et al.*, 2007). The highest degradation of rose bengal was found to be 97.348% under sunlight, compared to 37.315 % in darkness and 64.454 % in daylight.

Table 8. Degradation of Rose Bengal Dye using ZnO Nanoparticles with Different Dosages Condition (pH4)

No.	Weight of ZnO (g)	Degradation percent(%)		
		Daylight	In dark	Sunlight
1	0.05	5.014	52.064	83.775
2	0.10	9.734	58.259	85.103
3	0.15	16.799	58.849	88.348
4	0.20	21.091	61.061	91.592
5	0.25	30.383	62.094	95.280
6	0.30	37.315	64.454	97.348

Concentration of rose bengal dye = 10 ppm
Volume of dye solutions = 50 mL,
Contact time = 2 h, pH 4

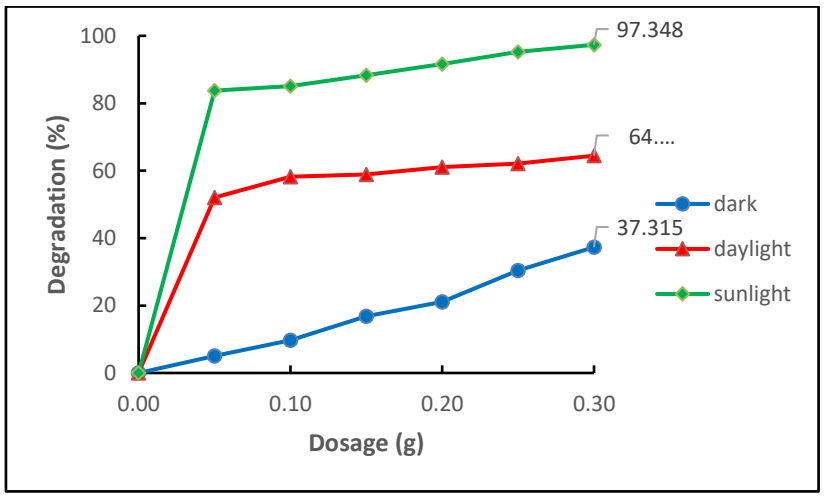

Figure 9. A plot of dosage (g) vs. degradation (%) of ZnO nanoparticles on rose bengal dye at a pH of 4

Table 9 and Figure 10 depict the degradation of rose bengal at pH 7, and Table 10 and Figure 11 show the degradation of rose bengal at pH 10 by ZnO. As the amount of ZnO increases, the surface area of the catalyst increases; hence, the adsorption of dye molecules over the surface of ZnO increases, which increases the percent degradation. The highest degradation percentage of rose bengal was found to be 98.113% at pH 7 under sunlight when compared to 97.348% at pH 4 and 95.505 % at pH 10.

Among three pH values, the photocatalytic activity of ZnO on the degradation of rose bengal was highest at pH 7 under sunlight. It may be explained as follows: at low pH, the anionic dye molecules remain in their protonated form, and the ZnO surface also possesses a positive charge due to the adsorption of H^+ ions. Hence, the dye molecules and ZnO repel each other. This results in low degradation efficiency. As pH increases to 7, the repulsion between ZnO and dye molecules decreases and the degradation efficiency increases. At pH 10, the surface of ZnO is negatively charged and again repels dye molecules. So, degradation efficiency decreases (Kumawat *et al*., 2012).

Table 9. Degradation of ZnO Nanoparticles on Rose Bengal Dye with Dosages at a pH of 7

No.	Weight of ZnO (g)	Degradation (%)		
		In dark	Daylight	Sunlight
1	0	0	0	0
2	0.05	5.525	19.137	90.431
3	0.10	8.490	20.350	91.239
4	0.15	11.590	21.832	93.126
5	0.20	12.803	23.450	94.878
6	0.25	15.363	27.892	97.574
7	0.30	20.889	34.905	98.113

Concentration of rose bengal dye = 10 ppm
Volume of dye solutions = 50 mL,
Contact time = 2 h, pH 7

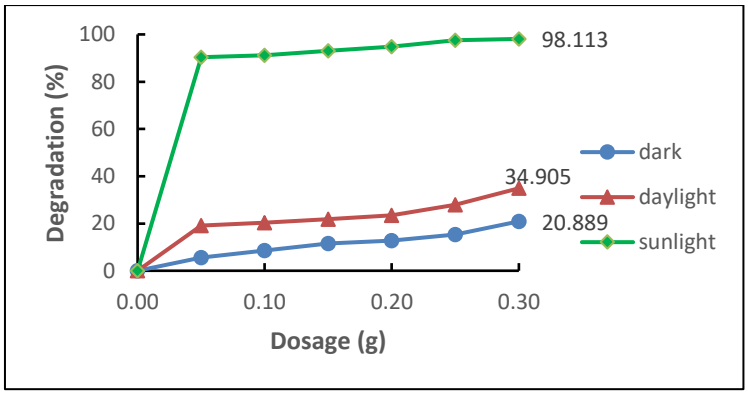

Figure 10. A plot of dosage (g) vs. degradation (%) of ZnO nanoparticles on rose Bengal dye at a pH of 7

Table 10. Degradation of Rose Bengal Dye using ZnO Nanoparticles with Different Dosages pH 10

No.	Weight of ZnO (g)	Degradation (%)		
		In dark	Daylight	Sunlight
1	0	0	0	0
2	0.05	3.720	13.643	87.131
3	0.10	8.837	19.224	91.472
4	0.15	13.646	27.906	93.333
5	0.20	17.984	31.937	94.108
6	0.25	21.05	35.193	95.193
7	0.30	23.255	39.222	95.505

Concentration of rose bengal dye = 10 ppm,
Volume of dye solutions = 50 mL,
Contact time = 2 h, pH 10

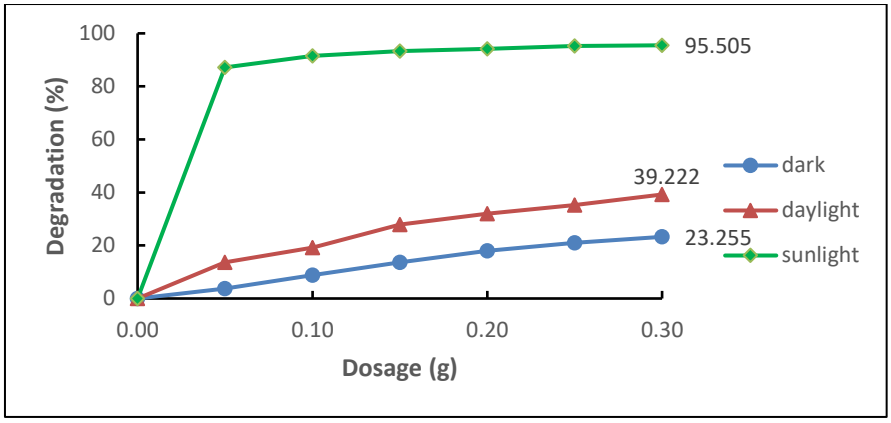

Figure 11. A plot of dosage (g) vs. degradation (%) of ZnO nanoparticles on rose bengal dye at a pH of 10

Conclusion

This study used a rose Bengal dye solution at various pH levels (4, 7, and 10) to examine the colour degradation efficiency of synthesized ZnO nanoparticles in the dark, in daylight, and in sunlight. The variable parameters (contact times, concentrations, and dosages) of synthesized ZnO nanoparticles were used in those conditions. In sunlight at a pH of 7, the colour degradation efficiencies of the produced ZnO nanoparticles on solutions of rose bengal dye were found to be more than 90%, indicating their high photocatalytic activity. At pH 7, ZnO nanoparticles exhibit the best photocatalytic behaviour (as compared to pH 4 and 10). ZnO was found to be an efficient photocatalyst for the degradation of rose bengal dye. From this study, ZnO nanoparticles can be utilized to treat wastewater from industrial zones as an effective colour degradation agent.

Acknowledgements

The authors would like to express their profound gratitude to the Department of Higher Education, Ministry of Education, Yangon, Myanmar, for providing the opportunity to do this research, and the Myanmar Academy of Arts and Science for allowing a presentation of this paper.

References

Battez, A.H., A., R.González, J.L. Viesca, J.E.Fernández, J.M. Díaz Fernández, A.Machado, R.Chou, and J.Riba. (2008). "CuO, ZrO_2 and ZnO Nanoparticles as Antiwear Additive in Oil Lubricants". Wear, vol.265(3-4), pp. 422-428

Becheri,A., M. Dürr, P. L. Nostro and P. Baglioni.(2008). "Synthesis and Characterization of Zinc Oxide Nanoparticles: Application to Textiles as UV-absorbers". *Journal of Nanoparticle Research*, vol. 10, pp. 679–689

Iravani, S. (2011). "Green Synthesis of Metal Nanoparticles Using Plants". *Green Chem*, 13, 2638-2650

Kaur,J., and S.Singhal. (2014). "Heterogeneous Photocatalytic Degradation of Rose Bengal: Effect of Operational Parameters**".** *Physical B: Condensed Matter***,** vol. 450, pp.49-53

Khan, Y., H.Sadia, S.Z. A. Shah, M.N.Khan, A.A.Shah, N. Ullah, M.F. Ullah, H. Bibi, O.T. Bafaqeeh, N.B.Khedher, S.M.Eldin,B.M.Fadl, and M.I.Khan..(2022). "Classification, Synthetic, and Characterization Approaches to Nanoparticles, and Their Applications in Various Fields of Nanotechnology: A Review". *Catalysts*, vol.*12(3)*, pp.1-27

Kumawat,R., I. Bhati, and R. Ameta.(2012). "Role of some Metal Ions in Photocatalytic Degradation of Rose Bengal Dye". Indian Journal of Chemical Technology, vol.19, pp.191-194

Taghizadeh,S.M., N. Lal , A. Ebrahiminezhad , F. Moeini , M. Seifan , Y. Ghasemi, A. Berenjian.(2020). "Green and Economic Fabrication of Zinc Oxide (ZnO) Nanorods as a Broadband UV Blocker and Antimicrobial Agent". *Nanomaterials*, vol. *10(*3), pp.530-541

Wang, H., C. Xie, W. Zhang, S.Cai , Z.Yang, and Y. Gui. (2007). "Comparison of Dye Degradation Efficiency using ZnO Powders with Various Size Scales. *J. Hazard. Mater*., vol.141, pp. 645-652

SYNTHESIS AND CHARACTERIZATION OF NANO ALUMINIUM OXIDE FROM WASTE ALUMINIUM CANS

Naw Yoon Eimzi Tun[1], Hnin Yu Wai[2]

Abstract

The majority of the energy drinks are labelled as "canning" (in which aluminum sheet is commonly used). Can is a waste material that pollutes our environment. This research aims to take advantage of aluminium waste cans (Coca Cola) by using them as raw materials for preparing alumina (Al_2O_3) by the co-precipitation method. The synthesis of α-Al_2O_3 from waste aluminium cans is presented in this study. The proposed technique was the precipitation of aluminum chloride with NaOH to produce aluminium hydroxide. The obtained Al $(OH)_3$ was washed, crushed, and dried at 105 °C, and then it was converted to alumina by calcination using different calcination temperatures (500, 600, 700 and 800°C) for 2 h. The prepared aluminium oxide nanoparticles were characterized by EDXRF, FT IR, SEM and XRD techniques. The γ-Al_2O_3 phase was found in the sample calcined at 600 °C, according to XRD data. The methodology has the capability to produce nano-alumina powder; the average crystal size was 30.05– 51.49 nm. Furthermore, the SEM image of these samples revealed that the γ-Al_2O_3 phase had an irregular spherical shape. Thus, the use of waste aluminium can precursors simplifies the process, and the synthesized alumina is a valued added material.

Keywords*:* Waste aluminium can, co-precipitation method, nano-alumina

Introduction

Aluminium is one of the most valuable component materials of municipal refuse in terms of cigarette and candy casings, cans, wrapping foil, doors, siding, car machine and body portions, icy food dishes, pie plates and other various domestic waste. Aluminium waste is known by various names, including dross, salt cake, baghouse fines, and others. Aluminium waste recycling is important to the environment (Nada *et al.*, 2017). Aluminium waste can be recycled to yield numerous beneficial products (such as alumina). Therefore, many studies have focused on the use of waste for several applications. Aluminium oxide (Al_2O_3) is the only oxide formed by the metal aluminium. Aside from α-Al_2O_3, other types of metastable alumina include ρ, γ, η, θ, δ, χ and κ-Al_2O_3 (Noor *et al.*, 2019).

Alumina has many appealing properties, which make the material interesting for applications in many different areas. It is a very hard substance, and its hardness is exceeded only by diamond and a little artificial material (Hosseini and Khosravi, 2016). Al_2O_3 is an electrical insulator with high thermal conductivity; it is also used in the glass industry as a catalyst and as filler. Alumina adsorbents are widely used as desiccants in both heated (temperature swing adsorption) and heatless (pressure swing adsorption) dryers (Bayus *et al.*, 2016).

In addition, alumina is widely used as an adsorbent to remove dissolved pollutants from contaminated water (Kumar *et al.*, 2006). Accordingly, in the present work, the synthesis of nano alumina powder is achieved by the simple and cost effective, co-precipitation method using NaOH as precipitant and aluminium waste as raw material in order to get rid of those wastes by turning it into a useful product (Das *et al.*, 2007)

In the present research, alumina nanomaterials were synthesized by the sol-gel method using waste aluminium cans as a precursor.

[1] Department of Chemistry, University of Yangon
[2] Department of Chemistry, Maubin University

Materials and Methods

Synthesis of Aluminium Oxide

Waste aluminium cans (Coca Cola) were boiled in a water bath at 100 °C for 30 min, and then treated with acetone to remove dyes and the internal covering polymer before being cut up into aluminium pieces. The obtained aluminium pieces were treated with a digestive substance, hydrochloric acid, in concentrations of 2, 4 and 6 M, each on its own, as follows: Five grams of prepared aluminium pieces were weighed and then they were digested in 100 mL of hydrochloric acid. The sample was stirred by a magnetic stirrer for 60 min to obtain an $AlCl_3$ solution. The aluminium chloride solution was filtered to remove the impurities. And then, NaOH solution (5M) was added dropwise, producing aluminium hydroxide. The precipitate was washed several times with distilled water. The precipitate was then filtered, dried at 90 °C for 24 h and calcined at four different temperatures ranging from 500 to 800 °C for 2 h. Finally, aluminium oxide nanoparticles were obtained.

Characterization of Prepared Aluminium and Aluminium Oxide

The purity of aluminium and alumina was characterized by an Energy Dispersive X-Ray Fluorescence spectrometer (EDXRF -700 spectrometer, Shimadzu, Japan), and the measurement was performed in accordance with the recommended standard as reported in the EDXRF spectral catalogue. The functional groups of prepared alumina were evaluated by FT IR spectrometer. The surface morphology of the prepared sample was studied with a Scanning Electron Microscope (JSM-5610, JEOL Ltd., Japan). The prepared alumina was identified and characterized by X-Ray Diffraction Spectrometer (Regaku X-ray diffractometer, RINI 2000/PC software, Cat. No. 9240 J 101, Japan) in accordance with the recommended standard as reported in the catalogue.

Results and Discussion

Characterization of Waste Aluminium Cans and Prepared Aluminium Oxide Materials

EDXRF analysis

The elemental compositions of waste aluminium cans and prepared alumina were confirmed by EDXRF analysis. The relative abundance of elements in the waste aluminium can (Coca Cola) is shown in Table 1 and Figure 1. The purity percent of aluminium (Al) is 95.30 % and it is the main constituent in waste aluminium can. The purity of aluminium oxide present in prepared alumina samples at different HCl concentrations and different calcination temperatures was evaluated by EDXRF and the results are shown in Figures 2- 4 and Tables 2-4. The prepared alumina materials contained 37.09 to 56.14 % alumina (Al_2O_3).

Table 1. Relative Abundance of Elements in Waste Aluminium Can (Coca Cola)

Elements	Relative abundance (%)
Mg	0.935
Al	**95.300**
Si	0.661
P	0.425
S	0.056
Ti	0.034
V	0.013
Cr	0.038
Mn	1.240
Fe	0.719
Co	0.007
Ni	0.011
Cu	0.263
Zn	0.102
Ga	0.015

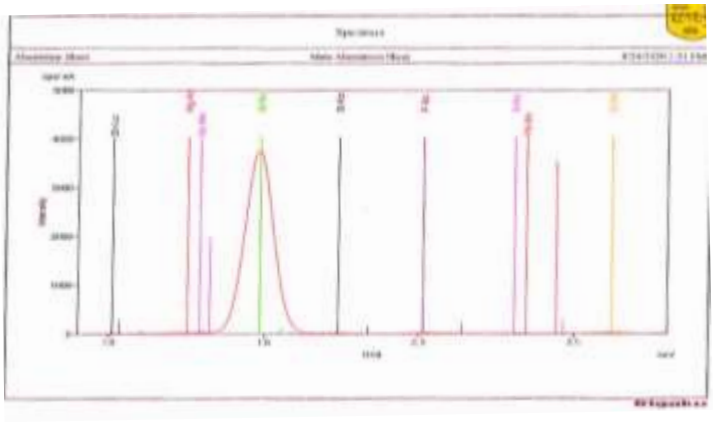

Figure 1. EDXRF spectrum of aluminium waste can (Coca Cola)

Table 2. EDXRF Analysis of Elements Present in Al_2O_3 Powder at Different Calcination Temperatures for 2 M HCl

Calcined temperature (°C)	Relative abundance (%)
500	52.27
600	42.04
700	37.09
800	56.14

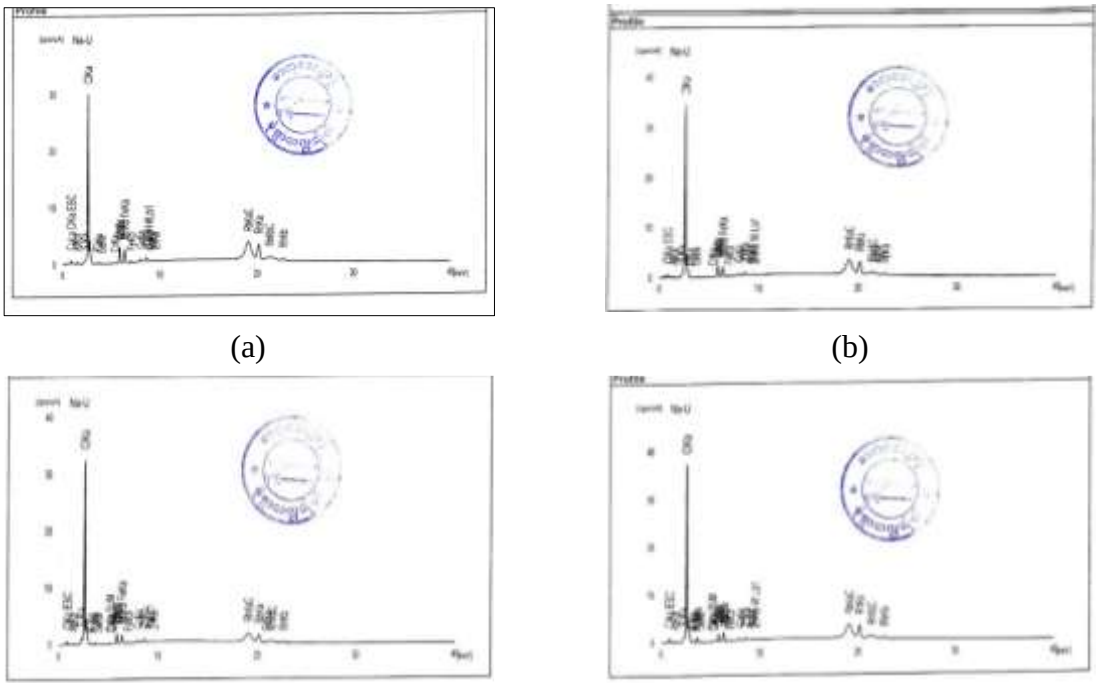

(a) (b)

(c) (d)

Figure 2. EDXRF spectra of prepared Al_2O_3 nanoparticles calcined at (a) 500 °C, (b) 600 °C, (c) 700 °C and (d) 800 °C for 2 M HCl

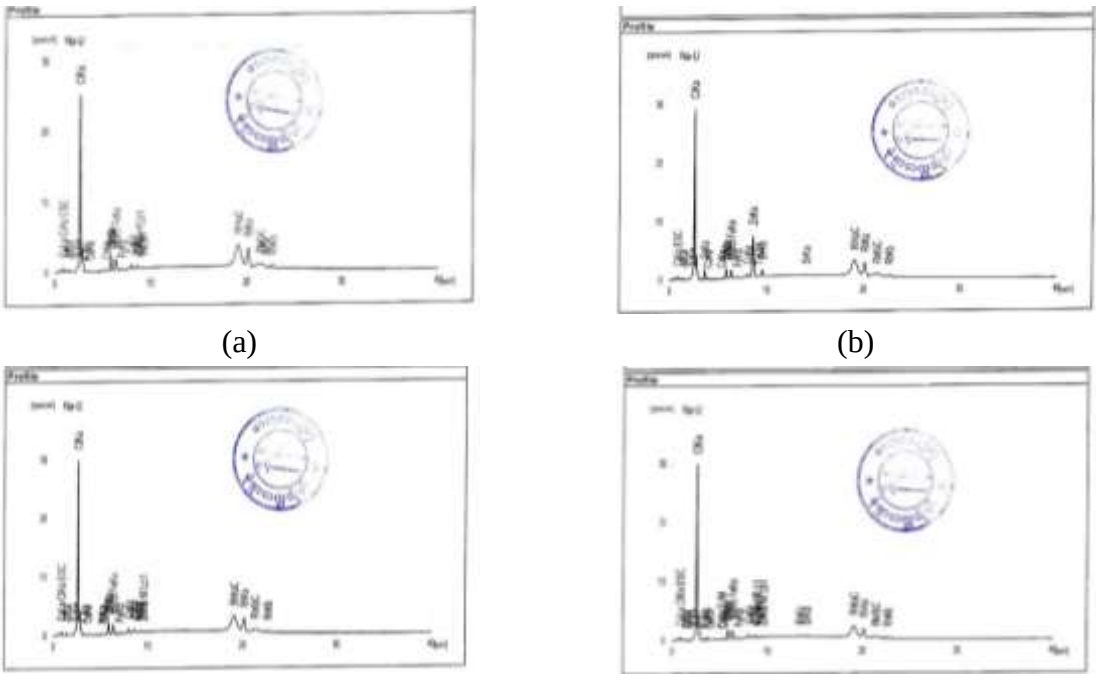

(a) (b)

(c) (d)

Figure 3. EDXRF spectra of prepared Al_2O_3 nanoparticles calcined at (a) 500 °C, (b) 600 °C, (c) 700 °C and (d) 800 °C for 4 M HCl

Table 3. EDXRF Analysis of Elements Present in Al_2O_3 Powder at Different Calcination Temperatures for 4 M HCl

Calcined Temperature (°C)	Relative abundance (%)
500	56.14
600	48.54
700	53.79
800	41.15

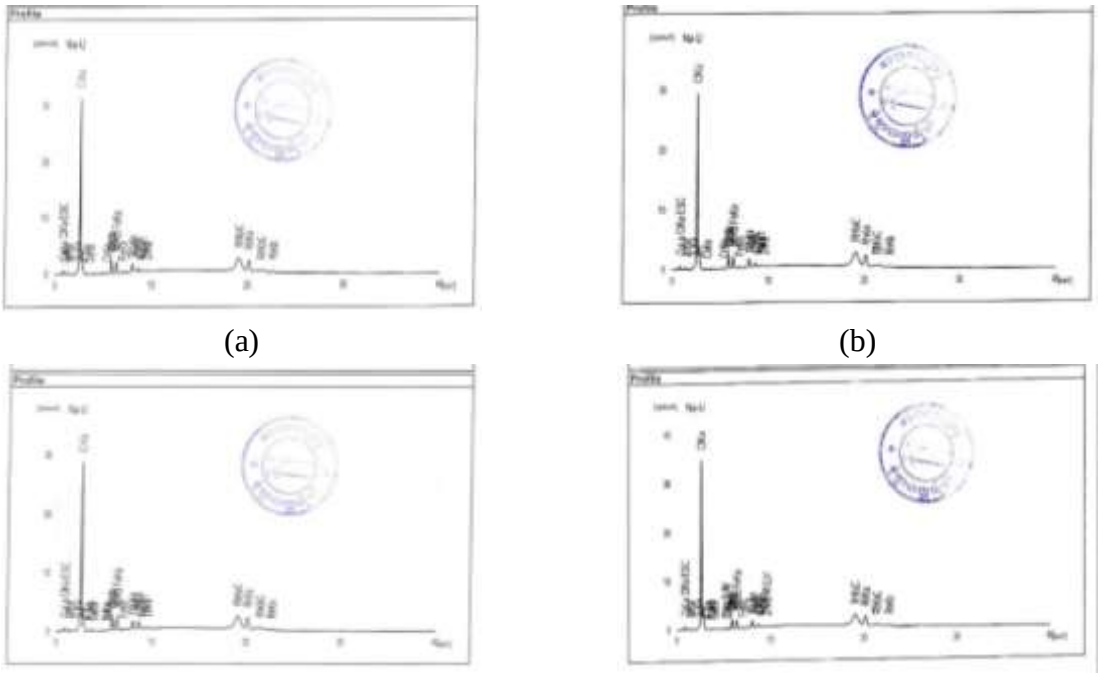

(a) (b) (c) (d)

Figure 4. EDXRF spectra of prepared Al_2O_3 powder calcined at (a) 500 °C, (b) 600 °C, (c) 700°C and (d) 800 °C for 6 M HCl

Table 4. EDXRF Analysis of Elements Present in Al_2O_3 Powder at Different Calcination Temperatures for 6 M HCl

Calcined temperature (°C)	Relative abundance (%)
500	47.40
600	47.14
700	53.29
800	38.01

FT IR analysis of selected Al_2O_3 nanoparticles

FT IR spectrum of selected aluminium oxide nanoparticles is shown in Figure 5. The characteristic peaks of aluminium oxide were depicted in Table 5. The Peaks at 611 $cm^{-1}$and 631 cm^{-1} are assigned to the aluminium oxide stretching. The peak at 1128.36 cm^{-1}indicates the triply

degenerative vibrational mode of chloride ion. The peaks at 1639.49 $cm^{-1}$and 3473.80 cm^{-1} are assigned to the bending and stretching vibration mode of O-H.

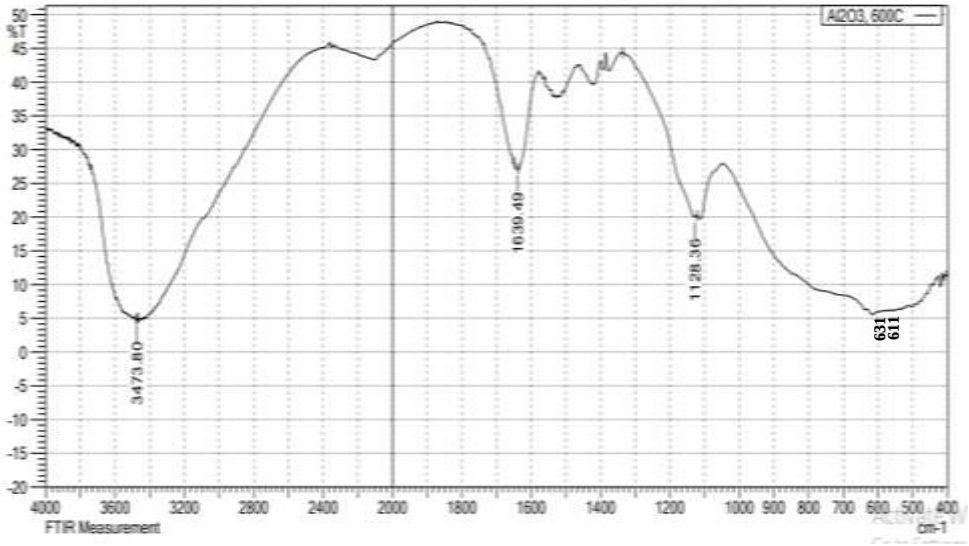

Figure 5. FT IR analysis of selected Al_2O_3 nanoparticles

Table 5. FT IR Band Assignment of Prepared Alumina

Wavenumber (cm^{-1})		Band assignments
Prepared alumina	***Literature**	
3473.80	3526	O-H stretching
1639.49	1646	O-H bending
1128.36	1127	Triply degenerative vibrational mood of Chloride ion
611	615	Al-O stretching
631	636	Al-O stretching

* Manyasree *et al.*, 2018

SEM analysis of prepared Al_2O_3

The morphology of prepared alumina was examined by the SEM analysis, and the SEM image is shown in Figure 6. The surface morphology of aluminium oxide consists of smaller crystal agglomerates. It is apparent that this feature influences the final crystal size of calcined samples, as can be seen in Figure 6. Heat-treated powders at 600 °C for 2 h form agglomerates of submicrometer crystals. From the XRD results, the measured crystal size was 30.05 to 51.49 nm for obtained alumina samples from aluminum hydroxide.

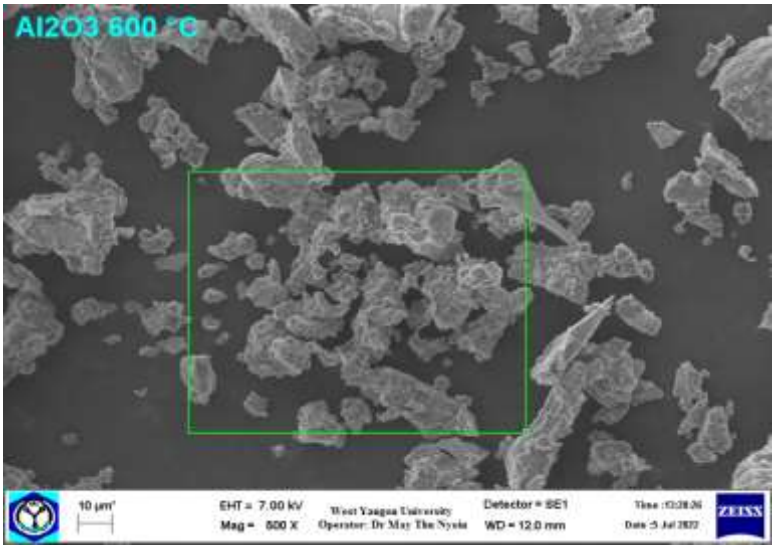

Figure 6. SEM microphotograph of selected Al_2O_3 nanoparticles

XRD analysis

The XRD diffraction patterns of different calcination temperatures and different concentrations of hydrochloric acid are shown in Tables 6, 7, and 8 and Figures 7, 8, and 9. As shown in figures, the XRD peaks can be assigned to alumina structure characterized by 2θ values at 31°, 45°, and 66°, respectively. It was obvious from Figure 7 that those increasing calcinations temperature to 600ºC showed a comparable pattern with the characteristic peaks located at 2θ of 31.27°, 45.01°, 64.22° and 65.78°, respectively.

Table 6. XRD Data of Prepared Alumina Using 2 M HCl

No.	Calcined Temperature (°C)	2θ values (degree)	Average crystallite size (nm)	Crystal system
1	500	27.15,31.49,45.25,56.01, 65.78	48.89	Cubic
2	600	31.27, 45.01, 56.01, 64.22, 65.78	33.73	Cubic
3	700	31.34,45.04,53.48, 56.09, 65.82	30.05	Cubic
4	800	31.59,45.33,56.33, 66.09	47.99	Cubic

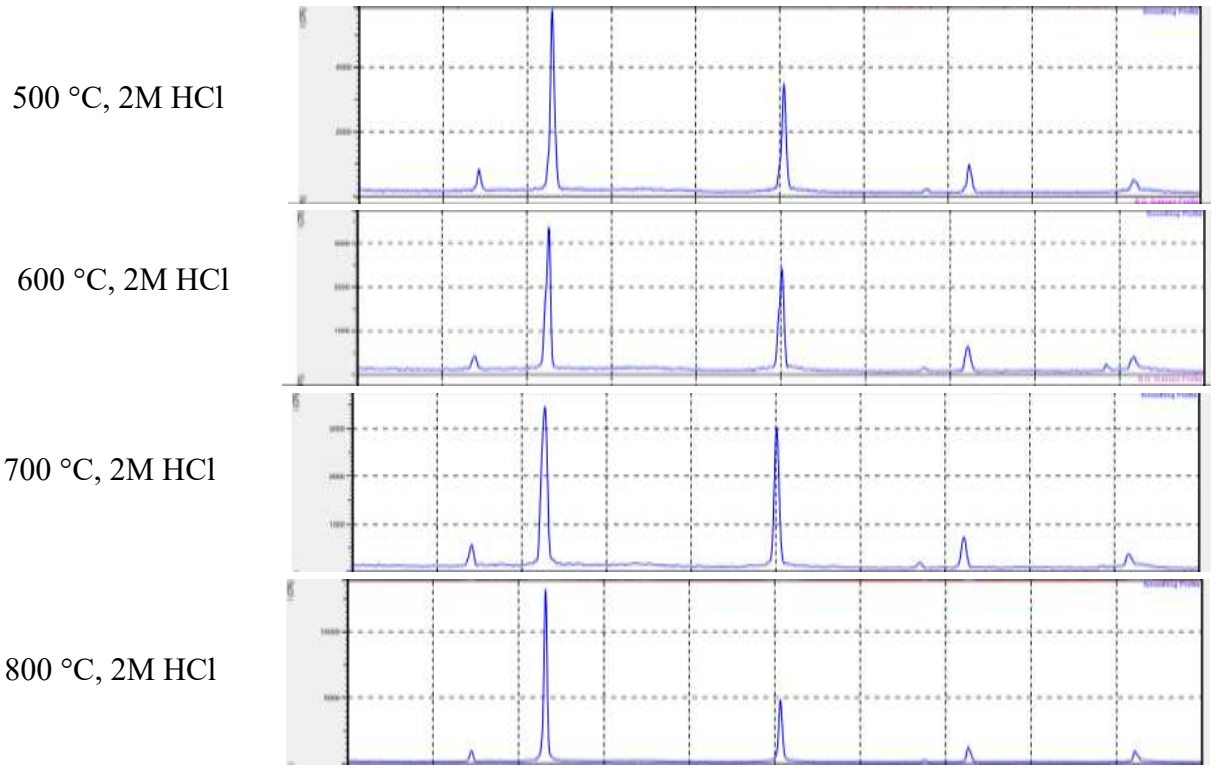

Figure 7. X-ray diffractograms of prepared Al_2O_3 nanoparticles calcined at 500°C, 600°C, 700°C and 800°C using 2 M HCl

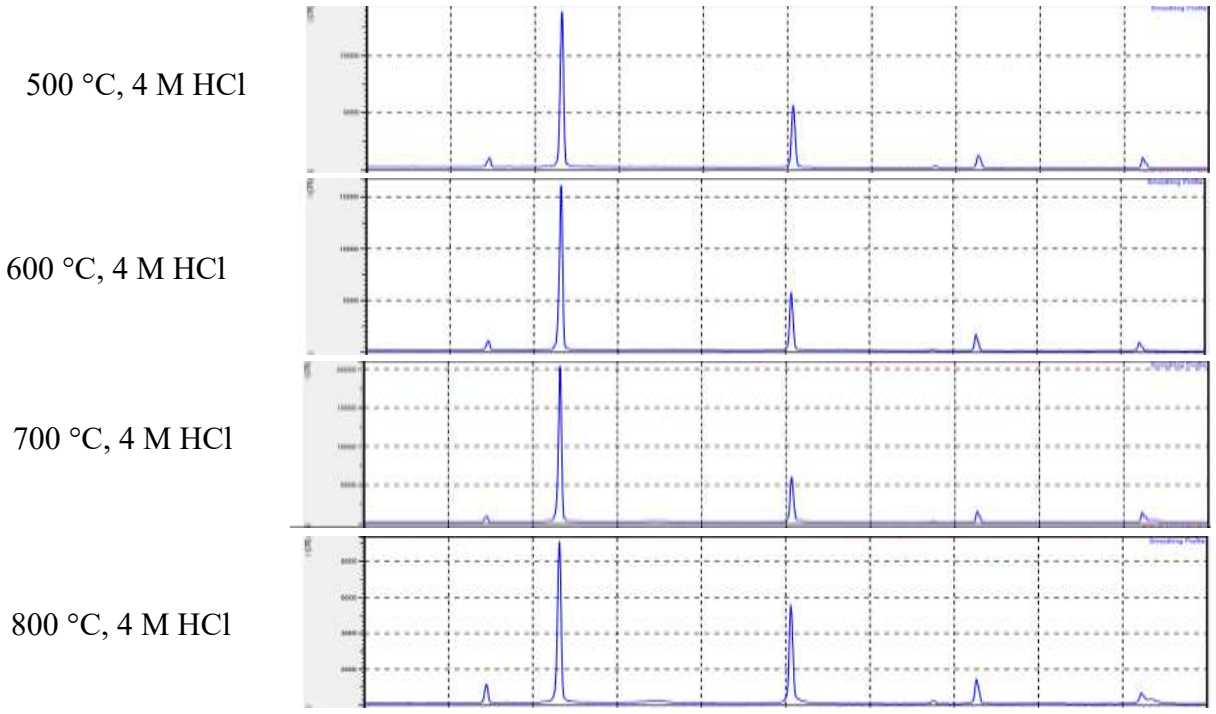

Figure 8. X-ray diffractograms of prepared Al_2O_3 nanoparticles calcined at 500 °C, 600 °C, 700°C and 800 °C using 4 M HCl

Table 7. XRD Data of Al_2O_3 Nanoparticles Using 4 M HCl

No.	Calcined Temperature (°C)	2θ values (degree)	Average crystallite size (nm)	Crystal system
1	500	31.60,45.33,56.33, 66.11	48.03	Cubic
2	600	31.63,45.34,56.36, 66.11	50.56	Cubic
3	700	31.63,45.33,56.34, 66.10	51.97	Cubic
4	800	31.58,45.31,56.33, 66.11	34.17	Cubic

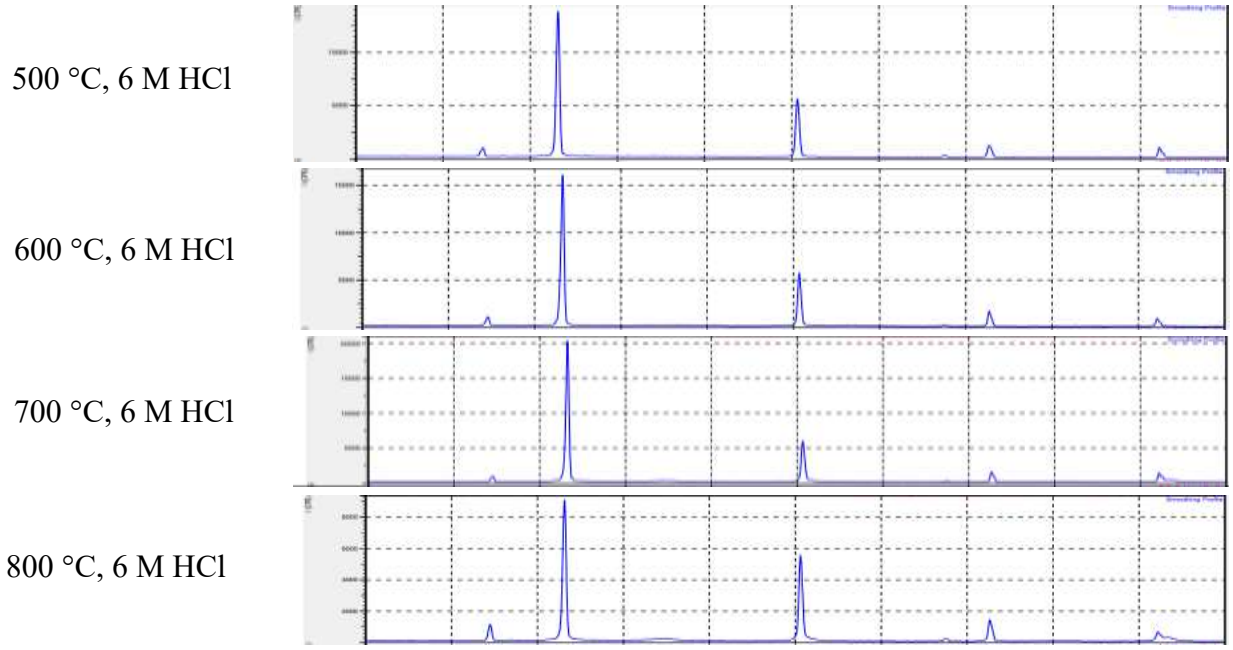

Figure 9. X-ray diffractograms of prepared Al_2O_3 nanoparticles calcined at 500 °C, 600°C, 700 °C and 800 °C using 6 M HCl

Table 8. XRD Data of Al_2O_3 Nanoparticles Using 6 M HCl

No.	Calcined Temperature (°C)	2θ values (degree)	Average crystallite size (nm)	Crystal system
1	500	31.62,45.39, 56.38, 66.14	44.98	Cubic
2	600	31.61,45.35, 56.38, 66.13	51.49	Cubic
3	700	31.19,45.13,55.97,64.25,65.73	53.77	Cubic
4	800	31.33,45.08, 56.08, 65.88	46.40	Cubic

The relationships between calcination temperature and crystallite sizes of samples are illustrated in Tables 6, 7, and 8. The crystallite sizes showed an increasing trend from 30.05 to 51.97 nm with increasing the calcination temperature from 500 to 700 ºC; however, the crystallite size was significantly decreased at 800 °C for three different concentrations of HCl. It can be proved that the prepared alumina contains alumina nanoparticles. Moreover, it contains noticeable that alumina calcined at 550, 600, and 700 ºC had identical XRD peaks positions and cubic crystal structure.

Conclusion

Starting with waste aluminium cans, alumina was synthesized. The current study demonstrated the feasibility of recycling waste aluminium cans into valuable nanoparticles of alumina via co-precipitation. FT IR spectra of selected aluminium oxide nanoparticles have shown that the peaks at 611 cm^{-1} and 631 cm^{-1} were assigned to Al-O (Al_2O_3) stretching. According to the XRD results, the smallest size of alumina nanoparticles was found at 2 M HCl and calcination temperature at 600°C, and its crystallite size is 33.73 nm in comparison with 30.05 nm of higher temperature (800°C), considering the energy saving aspect. The obtained alumina crystalline powders had crystallite sizes ranging from 30 to 52 nm indicating that the prepared alumina composed of alumina nanoparticles. It can be considered that this type of compound is a good candidate for the green light because its preparation is simple, has a low economic cost, and reduces the environmental pollution of waste cans.

Acknowledgements

The authors would like to express deepest gratitude to the Department of higher Education, Ministry of Education, Yangon, Myanmar, for providing the opportunity to do this research and the Myanmar Academy of Arts and Science for allowing us to present this paper. Thanks, are also due to all necessary research facilities provided by Department of Chemistry, West Yangon University for FT IR and SEM and the support and help of the Universities Research Center (URC) for XRD and ED XRF.

References

Bayus, J., C. Ge, and B. Thorn. (2016). "A Preliminary Environmental Assessment of Foil and Metallized Film Centered Laminates". *Resources Conservation and Recycling*, vol. 115, pp. 31-41

Das, B. R., B. Dash, and B. C. Tripathy, I. N. Bhattacharya and S.C. Das. (2007). "Production of Eta-alumina from Waste Aluminium Dross". *Minerals Engineering*, vol. 20, pp. 252-258

Hosseini, S. Y., and M. R. Khosravi-Nikou. (2016). "Synthesis and Characterization of Nano-sized γAl_2O_3 for Investigation the Effect of Temperature on Catalytic Dehydration of Methanol to Dimethyl Ether". *Part A: Recovery, Utilization, and Environmental Effects*, vol. 38, 914-920

Kumar, S., R. Kumar, and A. Bandopadhyay. (2006). "Innovative Methodologies for the Utilisation of Wastes from Metallurgical and Allied Industries", *Journal of Resources-conservation-and-recyclin*, vol. 48, 301-314

Manyasree, D. A., P. A. Kiranmayi, and K. R. Ravi. (2018). "Synthesis, Characterization and Anteribacterial Activity of Aluminium Oxide Nanoparticles". *International Journal of Pharmacy and Pharmaceutical Sciences*, vol. 10, pp. 32-35

Nada, S. A., S. Hussein, and W. A. Abdulnabi. (2017). "Recycling Waste Cans to Nano Gamma Alumina: Effect of the Calcination Temperature and pH". *International Journal of Current Engineering and Technology*, vol. 7(1), pp. 82-88

Noor, A. G., N. A. Mohammed, and E. S. Dawood. (2019). "Preparing of Alumina from Aluminum Waste". *International Journal of Innovative Science and Research Technology*, vol. 4, pp. 326-331

OPTIMIZATION FOR COLOUR REMOVAL PROPERTY OF PREPARED REDUCED GRAPHENE OXIDE (rGO)

Su Myat Htay[1], Ye Myint Aung[2], Yee Mun Than[3]

Abstract

In this study, the modified Hummer process was used to synthesize graphene oxide (GO) from graphite powder. Later, GO was chemically reduced to form reduced graphene oxide (rGO) nanoparticles using hydrazine hydrate as the reducing agent. Techniques such as XRD, FT IR, UV-visible, SEM, and EDX were used to characterize the prepared rGO. Malachite green (MG), a cationic dye, was employed as a model dye contaminant to study the colour removal efficiency of rGO. In order to assess the optimal values of the important parameters, including the initial dye concentration, pH, contact time, and rGO dosage, batch adsorption tests were conducted. For the purpose of removing the colour of malachite green utilizing synthesized rGO, the optimum conditions were found to be 10 ppm of MG concentration, pH 4, 60 min of contact time, and 0.06 g of adsorbent dosage.

Keywords: graphite, reduced graphene oxide, modified Hummer process, hydrazine hydrate, malachite green

Introduction

Dye and pigment pollution has been a significant problem on a global scale and is likely to get worse in the environment. Dyes are coloured, toxic, and non-biodegradable. They affect humans and other living beings when they enter the food chain (Hassan and Nemr, 2017). To treat this effluent, several physical, chemical, and biological decolourization methods are employed. Among them, adsorption gives the best result for removing coloured materials. Recently, graphene oxide (GO) and reduced graphene oxide (rGO) have been employed for the removal of organic pollutants and dyes from industrial effluents (Yusuf *et al.*, 2015). Graphite, one of many allotropes of carbon, can provide great potential in many applications, such as electronic and functional nanocomposites (Hidayah *et al*., 2017). A single atomic plane layer of graphite is called graphene. Graphene can be produced from graphite using chemical vapour deposition (CVD) and mechanical or chemical methods (Zaaba *et al*., 2017). Graphene Oxide (GO) is prepared from the oxidation of graphite powder by Modified Hummer's Method (Mindivan, 2016). The oxidation of graphite in protonated solvents leads to graphite oxide, which consists of multiple stacked layers of graphene oxide. GO has a similar hexagonal carbon structure to graphene but also contains hydroxyl, alkoxy, carbonyl, carboxylic acid, and other oxygen-based functional groups (Smith *et al*., 2019). GO was synthesized and characterized using various analytical techniques and exploited as an adsorbent for rapid removal of malachite green dye from the aqueous solution (Mohamadi *et al*., 2016). These are usually considered one kind of chemically derived graphene, just like GO. Hydrazine hydrate ($H_2NNH_2.H_2O$), one of the reducing agents used in the chemical reduction of exfoliated graphene oxide sheets, was found to be the most effective in synthesizing extremely thin graphene-like sheets. As oxygen atoms are taken out, the rGO becomes less hydrophilic and precipitates. The main objective of the research was to prepare reduced graphene oxide from graphite and examine how effectively it adsorbed the cationic dye malachite green after being exposed to it.

[1] Department of Chemistry, Dagon University
[2] Department of Chemistry, University of Yangon
[3] Department of Chemistry, University of Yangon

Materials and Methods

Sample Collections

In this research, graphite powder (extra pure, purchased from China Aladdin Industry Corporation), sodium nitrate ($NaNO_3$), sulphuric acid (H_2SO_4), potassium permanganate ($KMnO_4$), hydrogen peroxide(H_2O_2), and hydrochloric acid (HCl) were procured from BDH. The chemicals used were of analytical reagent grade.

Synthesis of Graphene Oxide

A modified Hummer process was used to make graphene oxide from powdered graphite. Briefly, 120 mL of concentrated sulphuric acid was mixed with 5 g of graphite and 5 g of $NaNO_3$. Using an ice bath, the mixture was kept cool-about 5 °C-while being ultrasonically processed for an hour. After that, 15 g of KMnO4 was slowly added to the mixture. For a homogenous mixture, the mixture was then ultrasonically agitated for 1 h in an ultrasonic bath. The mixture was then progressively given 250 mL of distilled water, and it was ultrasonically processed for an hour. The mixture was then brown in colour. The colour of the mixture changed to a light brown hue. The mixture was then given an additional 100 mL of deionized water, and it was agitated for 1 h at 90 °C. To produce a pale-yellow suspension, 50 mL of hydrogen peroxide and 100 mL of purified water were mixed. The remaining $KMnO_4$ and MnO_2 produced in the solution were also converted to colourless soluble salts when hydrogen peroxide was added, changing the colour of the solution from brown to light yellow.

Synthesis of Reduced Graphene Oxide (rGO)

To synthesize rGO 100 mL of distilled water were mixed with 0.1 g of GO. The mixture was heated at 95˚C for 12 h with 1 mL of hydrazine hydrate. The rGO was obtained from the mixture as a black powder after filtering. Multiple repetitions of distilled water washing were performed on the finished product.

Characterization of Reduced Graphene Oxide

Modern methods were used to characterize the reduced graphene oxide. The presence of the crystalline phase in the sample was evaluated by X-ray Diffraction (XRD, Rigaku, /max 2200, Japan). In order to identify the functional groups, present in the sample, a Fourier Transform Infrared (FT IR) spectrometer was used. Scanning Electron Microscopy (SEM, JOEL-JSM-5610, Japan, Ion Sputter-JEC-1600) was employed for the morphological examination. The relative elemental abundance was determined using the Energy Dispersive X-Ray (EDX) method. UV-visible spectrophotometer (Shimadzu: UV-1800) was used to measure the absorbance of dye solutions.

Colour Removal of Malachite Green Dye Solution by the Prepared Reduced Graphene Oxide

In this study, the effectiveness of colour removal by reduced graphene oxide was examined. Malachite green (MG) (1000 ppm) stock solution was made in distilled water. Serial dilution was used to create a series of standard MG solutions. A spectrophotometer was used to measure the absorbance of dye solutions between the wavelengths of 400 and 800 nm. Plotting the absorbance against the concentration of the malachite green solution allowed for the construction of the standard calibration curve.

Determination of the Optimum Conditions for Colour Removal of MG Dye

Effects of initial dye concentration, pH, contact time, and dosage of adsorbent on colour removal of MG dye were studied utilizing the prepared rGO. The following equation was used to determine the percentage of MG that was coloured and removed by rGO.

$$\text{Colour removal percent} = \frac{C_o - C_t}{C_o} \times 100$$

where C_o and C_t are concentrations of MG at initial and at time t, respectively.

Effect of Initial Concentration of Malachite Green

In separate conical flasks, precisely weighed samples (0.06 g each) were placed. Each conical flask was then filled with 50 mL of a dye solution with concentrations of 10, 20, 30, 40, and 50 ppm. The mixtures were shaken for 120 min, after which the sampling mixture was immediately centrifuged for 20 min at 200 rpm. After the removal of the dye solution, the remaining absorbance of the malachite green solution was measured at 617 nm by using a spectrophotometer.

Effect of pH on the Removal of Malachite Green

In the pH range of 2 to 10, the impact of pH on the adsorption capacity of rGO was determined by the initial pH value of the solution (10 ppm), which was adjusted with 0.1 M HCl or 0.1 M NaOH using a pH meter. In separate conical flasks, precisely weighed samples (0.06 g each) and 50 mL of dye solutions were added to each conical flask and agitated using an electric shaker. After 20 min, the mixture was immediately centrifuged at 200 rpm for 20 min. The absorbance of malachite green was measured at 617 nm by using a spectrophotometer.

Effect of Contact Time on the Removal of Malachite Green

In separate conical flasks, precisely weighed samples (0.06 g each) were placed. Then 50 mL of 10 ppm dye solution were added to each conical flask and agitated using an electric shaker at intervals of 30 min, 60 min, 90 min, 120 min, and 150 min, respectively. The sample mixture was immediately centrifuged at 200 rpm for 20 min. A spectrophotometer was used to measure the absorbance of the residual dye solution.

Effect of Dosage of Reduced Graphene Oxide for the Removal of Malachite Green

Different masses (0.02, 0.04, 0.06, 0.08, and 0.10) of the prepared rGo sample were placed in the conical flasks, and 50 mL each of 10 ppm malachite green solutions were added. The mixture were agitated using an electric shaker for 1 h at room temperature in order to achieve perfect equilibrium. Centrifugation was used to separate the sample solutions from the sorbent for 20 min at 200 rpm. The absorbance of the residual malachite green solution was determined at 617 nm by the spectrophotometer.

Results and Discussion

X-ray Diffraction (XRD) Analysis

With an interlayer distance of 0.334 nm, the strong and distinct diffraction peak (002) of graphite powder was seen at a 2θvalue of 26.52° (Figure 1). It is found in Figure 2 that the distinctive diffraction peak (001) of GO was displaced to a 2θ value of 10.48°, indicating that the graphite was completely oxidized into GO (Cui *et al*., 2011). When graphite oxidizes and transforms into GO, the XRD peak should change from 2θ value of 26^o to 11^o (Zaaba *et al*., 2017).

With a d-spacing of 0.84 nm, the GO interlayer distance also increased. When compared to the graphite sample, the XRD pattern of the rGO sample in Figure 3 shows dominating and broad peaks at around 2θ value of 25.14° and a d-spacing of about 0.35 nm, which suggests a small difference (0.334 nm). These results showed that after the reduction process used to synthesize few-layer graphene, the crystalline structure could be retained (Jiao *et al.*, 2017).

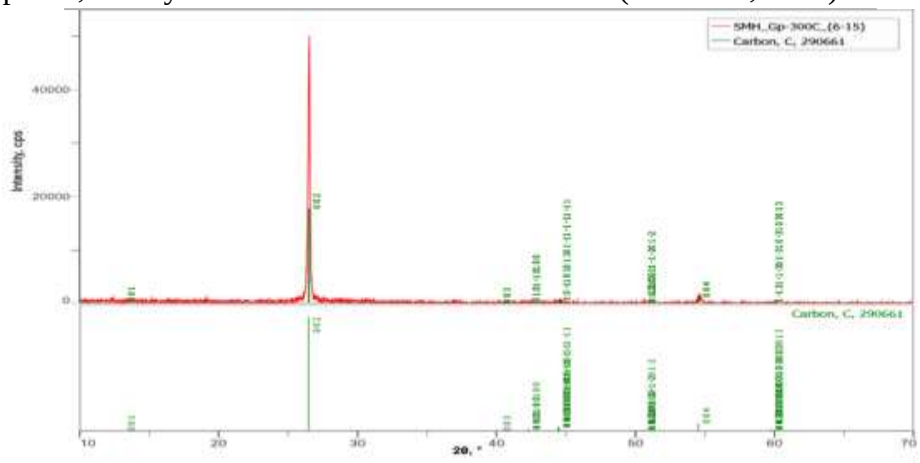

Figure 1. X-ray diffractogram of graphite powder

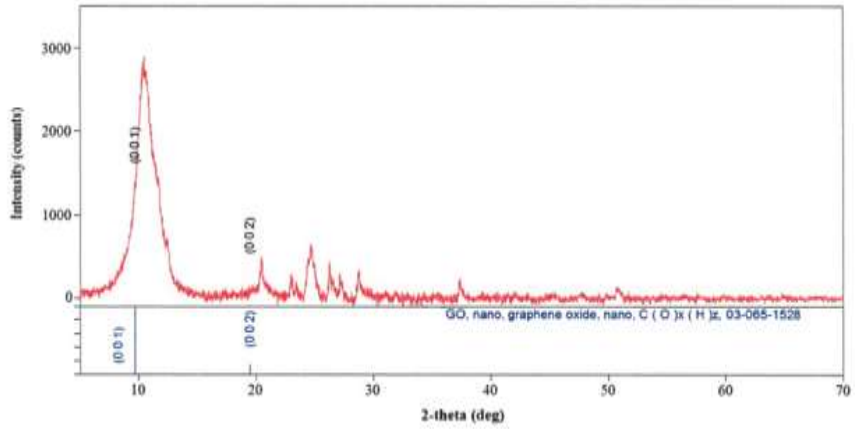

Figure 2. X-ray diffractogram of prepared GO

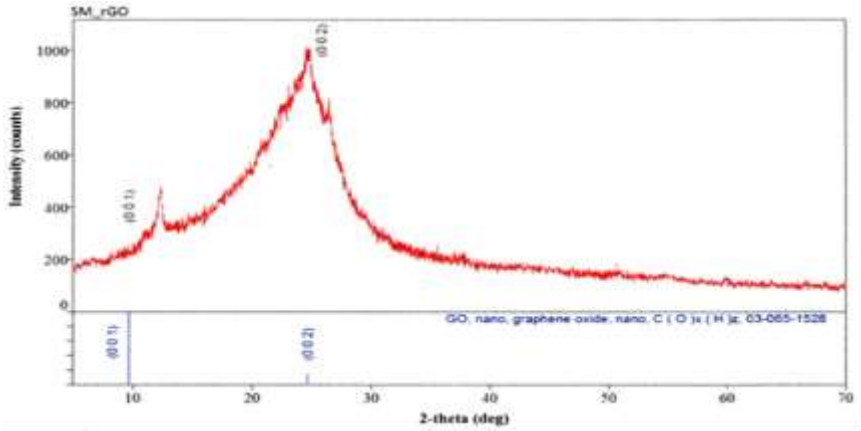

Figure 3. X-ray diffractogram of prepared rGO

Fourier Transform Infra-Red (FT IR) Analysis

The FT IR spectrum of rGO is presented in Figure 4. The spectrum shows no sharp peaks, confirming the efficient reduction of rGO. The peak at 1555 cm^{-1} corresponds to the aromatic C=C stretching of rGO (Ickecan *et al*., 2017). The procedure of hydroxyl and carboxyl functionality removal could be efficiently facilitated by chemical reduction.

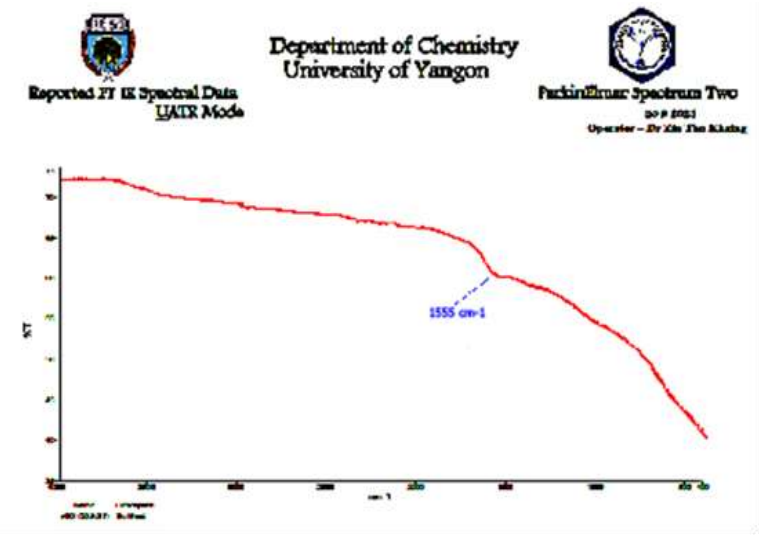

Figure 4. FT IR spectrum of reduced graphene oxide

UV Spectroscopic Measurement

The UV spectroscopic measurement was performed between 200 and 400 nm (Figure 5). The rGO absorption peak was found at 280 nm, which was in accordance with the literature value of 279 nm (Hidayah *et al*., 2017). Li *et al*. (2008) reported that the absorption peak of GO was 238 nm. After the reduction of GO, there was a redshift towards a higher wavelength of 280 nm. The shift was due to the π-π* transition of the graphitic C-C ring (Low *et al*., 2015).

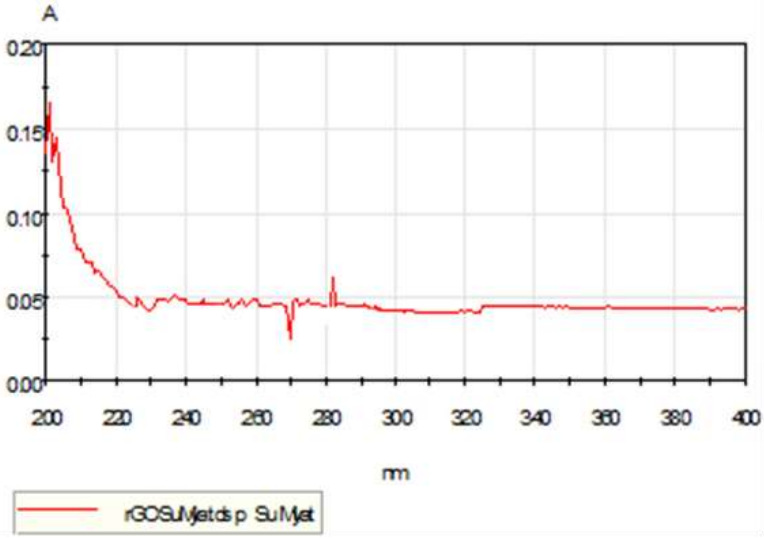

Figure 5. UV absorption spectrum of rGO

Scanning Electron Microscopic (SEM) Analysis

The SEM measurement was carried out to analyze the morphology of the prepared rGO (Figure 6). The SEM micrograph produced a substantially enlarged image of a surface of material. Graphene oxide that has undergone chemical reduction using hydrazine hydrate is seen in the micrograph. Sheets that had been crumpled and piled on the rGO surface formed disordered structural material.

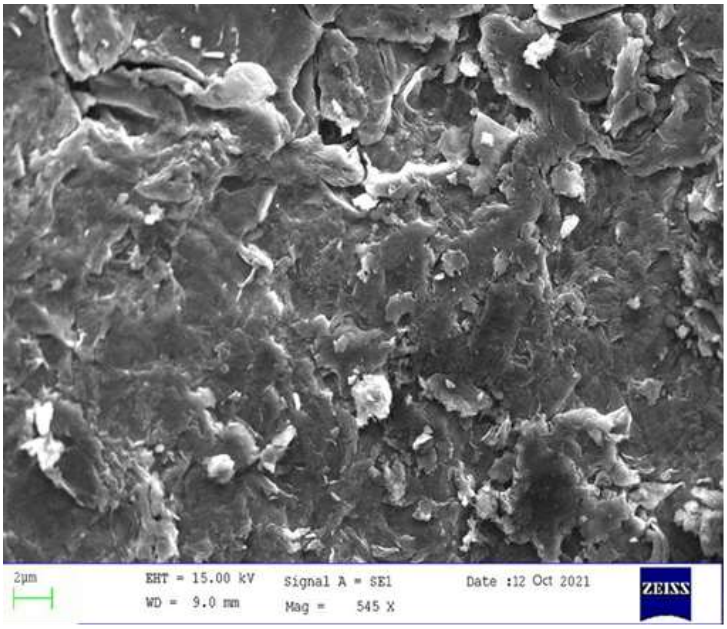

Figure 6. SEM micrograph of reduced graphene oxide (rGO)

Energy Dispersive X-Ray (EDX) Analysis

The Energy Dispersive X-Ray (EDX) spectrometer was used to determine the elements that made up the prepared rGO (Figure 7 and Table 1). According to EDX analysis, the elemental composition of carbon and oxygen in rGO was determined to be 86.65% and 13.35%, respectively. After GO was reduced, the carbon to oxygen atomic ratio was 6.4, with 13.35% of oxygen still present.

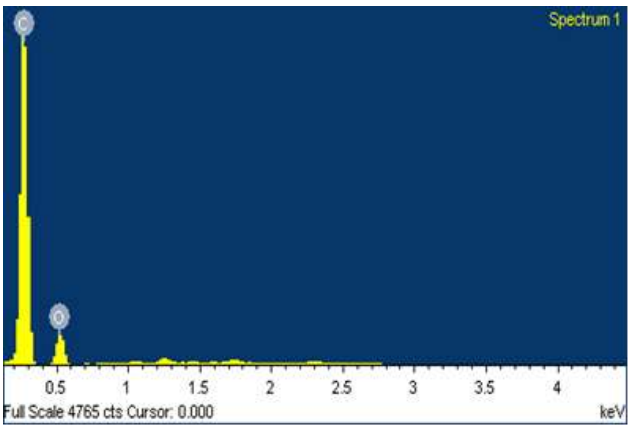

Figure 7. EDX spectrum of reduced graphene oxide (rGO)

Table 1. The Elemental Compositions in Graphene Oxide

Element	Weight %	Atomic %
C	86.65	89.63
O	13.35	10.37

The Wavelength of Maximum Absorption of Malachite Green

In this work, the absorption spectra of MG Dye at various concentrations were recorded in the wavelength range of 400-800 nm. It was observed that the wavelength of maximum absorption of MG dye solution was 617 nm (Figure 8).

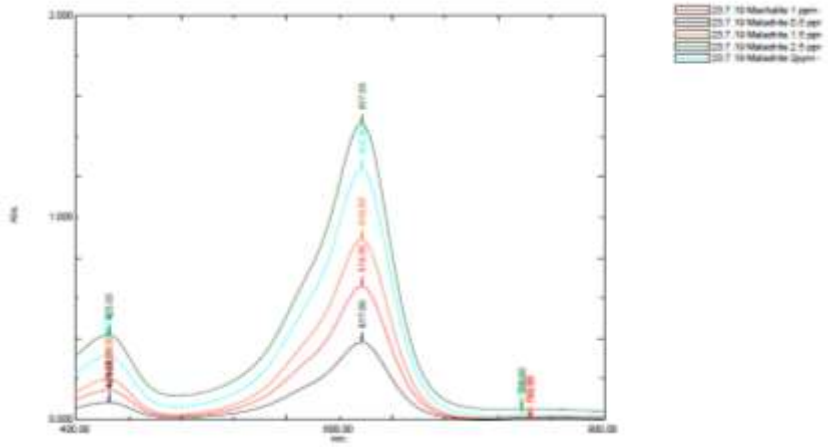

Figure 8. Wavelength of maximum absorption of malachite green

The Optimum Conditions for Colour Removal of MG Dye using Prepared rGO
Effect of initial concentration

The effect of the initial concentration of MG dye on the adsorption process was well studied. The initial concentration of MG dye in the solution was varied such as, 10, 20, 30, 40, and 50 ppm at pH 7 in the experiment using 0.06 g of prepared rGO. The maximum colour removal efficiency was obtained at the initial concentration of MG dye (10 ppm). The removal percent decreased from 90.66 % to 89.37 % as the concentration of MG increased from 10 to 50 ppm (Figure 9 and Table 2).

Table 2. Effect of Initial Concentration of Malachite Green

	Concentration (ppm)	Percent Removal (%)
1	10	90.66
2	20	90.46
3	30	89.99
4	40	89.86
5	50	89.37

The volume of dye solution = 50 mL
Weight of sample (GO) = 0.06 g
Contact Time = 60 min
Temperature = room temperature
pH = 7

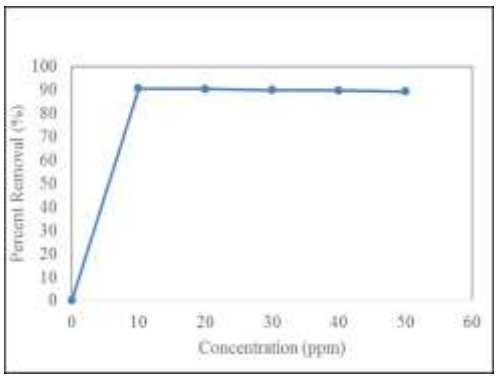

Figure 9. Effect of initial concentration of malachite green

Effect of pH

The effect of pH (2, 4, 6, 8, and 10) on the removal of MG dye by using prepared rGO was carried out for 60 min at room temperature. The maximum colour removal efficiency was obtained at pH 4 by using 0.06 g of prepared rGO (Figure 10 and Table 3).

Effect of contact time

The effect of contact time on dye by rGO was studied by varying the contact time to 30, 60, 90, 120, and 150 min on a rotary shaker. Rapid adsorption took place within the first 30 min of contact time, and the colour removal of 92.26 % was achieved using 0.06 g of prepared rGO at room temperature and pH 7 (Figure 11 and Table 4). After 60 min, the highest colour removal percent of 95.47 % was attained, followed by a slight decrease in colour removal percent of 94.00 % after 90 min.

Table 3. Effect of pH on the Removal of Malachite Green

No.	pH	Percent removal (%)
1	2	90.83
2	4	94.56
3	6	91.66
4	8	90.42
5	10	89.99

The volume of dye solution = 50 mL
Concentration = 10 ppm
Weight of sample = 0.06 g
Contact Time = 60 min
Temperature = room temperature

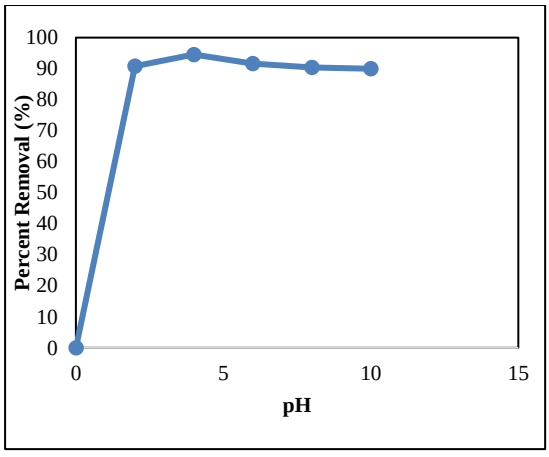

Figure 10. Effect of pH on the removal of malachite green

Table 4. Effect of Contact Time on the Removal of Malachite Green

No.	Time (min)	Percent removal (%)
1	30	92.26
2	60	95.47
3	90	94.00
4	120	91.23
5	150	90.41

The volume of dye solution = 50 mL
The concentration of dye solution = 10 ppm
Weight of sample = 0.06 g
Temperature = room temperature
pH = 7

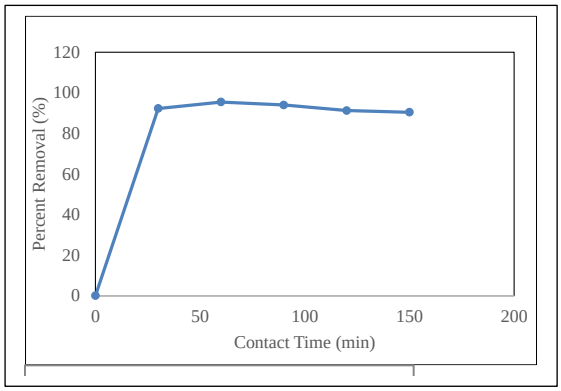

Figure 11. Effect of contact time on the removal of malachite green

Effect of dosage

The dosage of the adsorbent was varied in the range of 0.02 to 0.10 g (0.02, 0.04, 0.06, 0.08, and 1.00 g) while keeping the initial concentration of 10 ppm of MG at 60 min. The removal efficiency of MG increased from 90.10 to 96.05 % by an increase of rGO from 0.02 g to 0.06 g due to the increase in the adsorption sites. However, a further increase in the mass of rGO decreased the colour removal percent due to the desorption of the MG dye molecule from the adsorbent surface. The maximum colour removal percent was observed at a dosage of 0.06 g of prepared rGO (Figure 12 and Table 5).

Table 5. Effect of Dosage of Reduced Graphene Oxide for Removal of Malachite Green

No.	Dosage (g)	Percent removal (%)
1	0.02	90.10
2	0.04	92.23
3	0.06	96.05
4	0.08	94.41
5	0.10	92.88

Volume of dye solution = 50 mL
Concentration of dye solution = 10 ppm
Time = 60 min
Temperature = room temperature
pH = 7

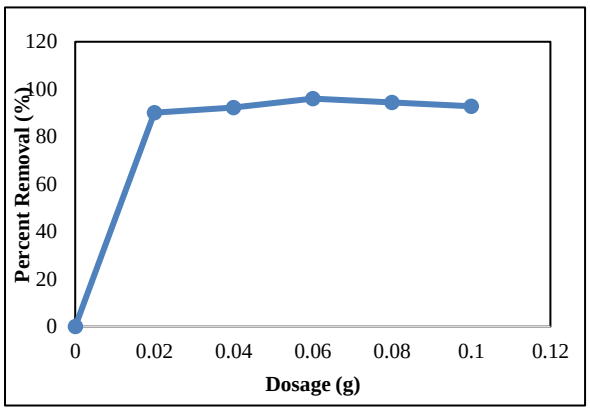

Figure 12. Effect of Dosage of Graphene Oxide for Removal of Malacchite Green

Conclusion

Reduced graphene oxide was successfully prepared by oxidizing graphite by modified Hummer's method followed by reduction with hydrazine hydrate. The prepared rGO was characterized by XRD, FT IR, SEM, UV-visible spectroscopy, and EDX. The dominant and

broad peak at an approximately 2θ value of 25.14° in the XRD pattern, the absence of epoxy and alkoxy groups in the FT IR spectrum, and the appearance of the UV absorption peak at 280 nfm confirmed the prepared sample as rGO. The removal of malachite green dye from the aqueous solutions by adsorption with rGO has been experimentally determined. The effects of the initial concentration of MG dye, pH, contact time, and adsorbent dose on the removal of MG by prepared rGO were investigated.The maximum removal percent of MG by prepared rGO was found to be 96.05% at pH 7 for 60 min and initial concentration of 10 ppm MG and 0.06 g of prepared rGO. Due to these unique properties, reduced graphene oxide, meets the needs of various applications.

Acknowledgements

The authors would like to thank the Department of Higher Education, Ministry of Education, Yangon, Myanmar. We would like to express our sincere thanks to Dr Tin Maung Tun (Rector) and Dr Khin Chit Chit, Dr Cho Cho, and Dr Thidar Aye (Pro-Rectors), University of Yangon. Our warmest thanks are also extended to Professor Dr Ni Ni Than, Head of the Department of Chemistry, University of Yangon, for their kind encouragement, permission to submit this paper, and many helpful suggestions.

References

Cui, P., J. Lee, E. Hwang, and H. Lee, (2011). "One-pot Reduction of Graphene Oxide at Subzero Temperatures". Chem. Commun., vol. 47(45), pp.12370-12372

Hassaan, M. A., and A.E. Nemr. (2017). "Health and Environmental Impacts of Dyes: Mini Review". *American Journal of Environmental Science and Engineering*, vol. 1(3), pp. 64-67

Hidayah, N. M. S., W.W. Liu, C.W. Lai, N.Z. Noriman, C.S. Khe, U. Hashiman, and H.C. Lee. (2017). "Comparison on Graphite, Graphene Oxide and Reduced Graphene Oxide: Synthesis and Characterization". *AIP Conference Proceeding*, vol. 1892(1), pp. 150002-1 - 150002-8

Ickecan, D., R. Zan, and S. Nezir. (2017). "Eco-Friendly Synthesis and Characterization of Reduced Graphene Oxide". *Journal of Physics: Conference Series*, vol. 902, 012027

Jiao, X., Y. Qiu, L. Zahng, and X. Zahng.(2017). "Comparison of the Characteristic Properties of Reduced Graphene Oxides Synthesized from Natural Graphites with Different Graphitization Degrees". *RSC Adv*., vol.7, pp. 52337-52344

Li, D., M.B. Muller, S. Gilje, R.B. Kaner, and G.G. Wallace. (2008). "Processable Aqueous Dispersions of Graphene Nanosheets". *Nat Nano*, vol.3 (2), pp.101-105

Low, F.W., C.W. Lai, and S.B. Abd Hamid. (2015). "Easy Preparation of Ultrathin Reduced Graphene Oxide Sheets at A High Stirring Speed". *Ceram. Int*., vol.41(4), pp. 5798-5806

Mindivan, F. (2016). "The Synthesis and Characterization of Graphene Oxide (GO) And Reduced Graphene Oxide (RGO)". *Machines, Technologies, Materials*, vol. 2, pp.51-54

Mohamadi, A. S., M. Skrkhosh, Z. Atafar, M. Avazpour,S. Nazari, S. Rezaei, S.M.Mohseni, and B.Baziar. (2016). "Removal of Malachite Green, a Hazardous dye using Graphene Oxide as an Adsorbent from Aqueous Phase". *Journal of Chemical and Pharmaceutical Research*, vol.8(3), pp. 624-633

Smith, A. T., A.M. Lachance, S. Zeng, B. Liu, and L. Sun. (2019). "Synthesis, Properties, and Applications of Graphene Oxide/Reduced Graphene Oxide and Their Nanocomposites". *Nano Materials Science*, vol. 1, pp. 31-47.

Yusuf, M., F.M. Elfghi, S.A. Zaidi, E.C. Abdullah, and M.A. Khan. (2015). "Applications of Graphene and Its Derivatives as An Adsorbent for Heavy Metal and Dye Removal: A Systematic and Comprehensive Overview". *RCS Advances*, vol.5, pp. 50392-50420

Zaaba, N. I., K.L. Foo, U. Hashim, S.J. Tan, W. Liu, and C.H.Voon. (2017). "Synthesis of Graphene Oxide Using Modified Hummers Method: Solvent Influence". *Procedia Engineering*,vol.184, pp. 469-477

Zeng, F., Z. Sun, X. Sang, D. Diamond, K.T. Lau, X. Liu, and D. S. Su. (2011). "In Situ One-Step Electrochemical Preparation of Graphene Oxide Nanosheet-Modified Electrodes for Biosensors". *Chem. Sus*. vol.4(11), pp. 1587-1591

PREPARATION AND INVESTIGATION OF SOME PHYSICOCHEMICAL PARAMETERS IN *ANABAS TESTUDINEUS* (NGA PYAE MA) FISH SAUCE SUPPLEMENTED WITH PAPAIN ENZYME

Nwe Mar Lin[1], Yee Mun Than[2], Myat Kyaw Thu [3]

Abstract

In this study, the fish sauce was prepared using the papain enzyme from the mature green leaves of *Carica papaya* L. The papain enzyme was isolated using ammonium sulphate precipitation (20%–70%). Fish samples of *Anabas testudineus* (Nga Pyae Ma) from the local market in Maubin Township, Ayeyarwady Region, were obtained for this investigation. Fish sauces were produced both with and without the papain enzyme. This study revealed how the physicochemical characteristics of fish sauce containing papain changed during fermentation, including pH (6.2 -7.0), refractive index (1.375-1.386), specific gravity (1.174-1.178), sodium chloride (19.59-20.27 %), total nitrogen (1.34-1.93 %), protein (8.38-12.06 %), formal amino nitrogen (0.60-1.00 %), and degree of hydrolysis (44.78-51.81 %). When compared to those without papain enzyme, it was found that fish sauces containing papain enzyme produced the most favorable outcomes. These results show that the use of papain to speed up the production of fish sauce is important.

Keywords: *Carica papaya*, papain, ammonium sulphate precipitation method, *Anabas testudineus*, fish sauce

Introduction

Climbing perch (*Anabas testudineus)* is a commercially important fish in Asian countries, mostly in Bangladesh, China, India, Malaysia, Pakistan, Sri Lanka, and Thailand. Also, it is used as a valuable food fish in different parts of the world (Hossain *et al*., 2015). Climbing perch is rich in iron and copper, which are essential for haemoglobin synthesis, and also contains easily digestible polyunsaturated fat and essential amino acids. This fish distribution is almost everywhere: in swamp waters, lakes, reservoirs, rivers, and other puddles. This fish can be caught throughout the year, with the spawning season at the beginning of the rainy season (Pahmi and Slamat, 2020).

Fish sauces are clear brown liquids produced by the fermentation of underutilized fish species with high salt contents (Tsai *et al*., 2006). Because of its high salt concentration, fermentation is one of the techniques used to preserve perishable fish. In Thailand, they are known as nampla, patis in the Philippines, kecap ikan or bakasang in Indonesia, badu in Malaysia, nuocnam in Vietnam and Cambodia, and nganpya ye in Myanmar. The process of fermenting traditional fish sauce is conducted by a combination of reactions, which are salting, enzyme hydrolysis, and bacterial fermentation. Fish sauce fermentation can be accelerated by the addition of enzymes (usually papain, bromelain, or bacterial proteases) (Beddows *et al*.,1979). Fish sauce is an enzymatic hydrolysate from fish tissue fully preserved by salt. It provides highly nutritious animal protein, vitamins, minerals, and an umami taste.

The main aim of this research is to isolate the papain enzyme from *Carica papaya* L. leaves, prepare fish sauce samples with and without papain, and investigate the changes in physicochemical parameters in fish sauces during fermentation.

[1] Department of Chemistry, University of Yangon
[2] Department of Chemistry, University of Yangon
[3] Department of Chemistry, University of Yangon

Materials and Methods

Materials

In this research work, Nga Pyae Ma fish samples were collected from local markets in Maubin Township, Ayeyarwady Region. All other chemicals used were of analytical reagent grade.

Sample Preparation

Fish samples were removed from the skin, scales, and bones. The fillets obtained were washed in running tap water and cut into smaller blocks.

Extraction of Papain Enzyme from Papaya Leaves

Papaya leaf samples (44 g) were mixed with 1000 mL of pH (7.4) phosphate buffer and stirred for 2 h at room temperature. And then, solid ammonium sulphate 113.34 g (20 % saturation) were slowly added to this extract on ice. After that, 337.34 g (70% saturation) were slowly added and stirred in ice for 2 h. After standing overnight, the precipitate containing papain enzyme was collected by centrifugation for 30 min at 5000 rpm (Maria, 2016).

Fermentation of Fish Sauce

The prepared fish sample (1 kg) was mixed with 0.3 % w/w papain in a jar. After 2 h 20 % (w/w) sodium chloride was added and then thoroughly mixed (Ooshiro *et al*., 1981). For control, the above procedure was carried out except that enzyme was not added. The prepared fish sauces with papain enzyme and without papain enzyme were stored at room temperature. The sauces were subjected to analysis after 30 days.

Determination of Physical Properties in Fish Sauce Samples

pH values were determined by a pH meter which was first standardized with standard buffer solutions of pH 4.6 and pH 6.8. Refractive indices were determined by a refractometer. The total dissolved solid contents were determined by the oven drying method. An accurately weighed fish sauce sample (5 mL) was put into a crucible and then weighed. The crucible was dried in the oven for half an hour, cooled in a desiccator, and weighed. Then the crucible was placed into the oven for 30 min, cooled in the desiccator, and weighed. The procedure was continued until a constant weight was obtained. From the difference in weights, the amount of total dissolved solids was calculated (AOAC, 1995).

Determination of Chemical Properties in Fish Sauce Samples

Mohr's titration may be used for the determination of chloride in a neutral solution by titration with a standard silver nitrate solution (Vogel, 1969). Total nitrogen and protein contents were determined by the Kjeldahl and Conway methods. (Conway, 1962)

Total nitrogen acts as an indicator of the protein content in fermented fish sauce. By multiplying by 6.25, the protein contents of the fish sauce were obtained. Formol Animo nitrogen was determined by the titrimetric method. The Sorensen method (AOAC, 1995), based on titration with formaldehyde, was used for quantifying the amino nitrogen. The degree of hydrolysis was calculated from amino nitrogen (AN) and total nitrogen (TN) using the Sorensen method (Harrimann *et al*., 2013).

Results and Discussion

Preparation of Nga Pyae Ma Fish Sauce with and without Papain Enzyme

Papain is a proteolytic enzyme from the cysteine protease family. Responsible for breaking down proteins, papain is an enzyme present in papaya and is used for breaking down meat fibres. It is used as a meat tenderizer, since the enzyme can break down muscle fibers in tough meat, leaving it tender (Trivedi *et al.*, 2013). In this study, papain was extracted from mature papaya leaves for the preparation of fish sauce. Papain (1.5 g) was obtained. Fish sauce fermentation began by mixing Nga Pyae Ma fish samples with papain enzyme (0.3%) for 2 h and adding 20 % salt at room temperature. The papain enzyme was not added to the control fish sauce. All volumes of fish sauce increased during fermentation. During fermentation, fish tissue in the presence of papain hydrolyzes more rapidly than that without papain. After fermentation for 180 days, the total volume of fish sauce supplemented with enzyme was 300 mL and found to be greater than that of fish sauce without enzyme (258 mL) (Table 1). During fermentation, fish tissue was gradually hydrolyzed by papain, indicating the activity of proteolytic enzymes.

Table 1. Total Volume of Nga Pyae Ma Fish Sauces during Fermentation

Fermentation time (Days)	Total volume (mL) (with papain)	Total volume (mL) (without papain)
180	300	258

Physical Properties in Nga Pyae Ma Fish Sauces

pH is an important parameter that affects the fermentation process (Siti, 2015). The changes in pH values of the fish sauce during fermentation are shown in Table 2 and Figure 1. As can be seen from the table, the pH value of fish sauces was found to increase during the 90-day period of fermentation and then stabilize. Therefore, it can be generally concluded that pH changes as a function of time in the early stages of fermentation. pH was found to be 7.0 in fish sauce supplemented with papain and 7.2 in that without papain after 180 days of fermentation. pH values in fish sauce with enzyme supplements were lower than those without enzymes. These observed values agreed closely with those reported as pH 7 (Koochekian and Moini, 2009), and pH 6.4-6.9 (Koffi-Nervy *et al*., 2011).

The changes in refractive indices of the fish sauce samples with and without papain enzyme during fermentation are shown in Table 3 and Figure 2. As can be seen from the table, the refractive indices of fish sauces were found to slightly increase during fermentation. During fermentation, the increase in the refractive index of fish sauce supplemented with papain was from 1.375 to 1.386 and, without papain, from 1.371 to 1.379. The changes in refractive indices of both fish sauce samples were not noticeable throughout the fermentation.

The changes in specific gravities of the fish sauce samples with and without papain enzyme during fermentation are shown in Table 4 and Figure 3. Specific gravities of fish sauces with and without papain were 1.174 and 1.172, respectively. However, after fermentation for 180 days, the specific gravities of all fish sauces were found to be comparable. Specific gravities of fish sauces with and without papain were 1.178 and 1.176, respectively. The increased specific gravity was due to the greater solubility of amino acids and small peptides at higher temperatures. In this research, the specific gravity of fish sauce supplemented with papain was slightly higher than without the papain enzyme.

In this study, total dissolved solids in Nga Pyae Ma fish sauces with and without papain were 29.2 % and 28.4 %, respectively, after 30 days of fermentation. Total dissolved solids in fish sauce supplemented with papain were higher than those without the enzyme. After 180 days of fermentation, total dissolved solids in fish sauces with and without papain were, respectively, 33.8 % and 32.2 % (Table 5 and Figure 4). It can be seen that the total dissolved solids content of the fish sauce supplemented with papain was slightly higher than that of the fish sauce without enzyme.

Table 2. Changes of pH of Nga Pyae Ma Fish

Fermentation time (Days)	pH (with papain)	pH (without papain)
30	6.2	6.3
60	6.4	6.5
90	6.6	6.7
120	6.8	7.0
150	6.9	7.2
180	7.0	7.2

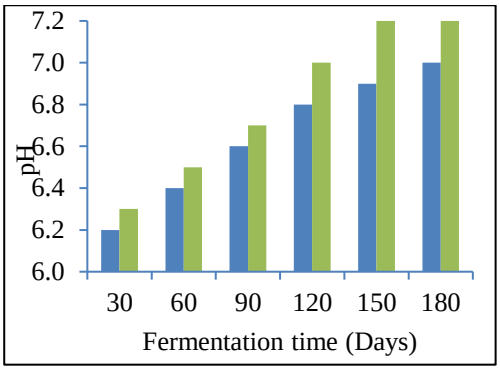

Figure 1. Changes of pH of Nga Pyae Ma fish sauces during fermentation

Table 3. Changes of Refractive Index of Nga Pyae Ma Fish Sauces during Fermentation

Fermentation time (Days)	Refractive index (with papain)	Refractive index (without papain)
30	1.375	1.371
60	1.377	1.373
90	1.379	1.373
120	1.380	1.375
150	1.382	1.376
180	1.386	1.379

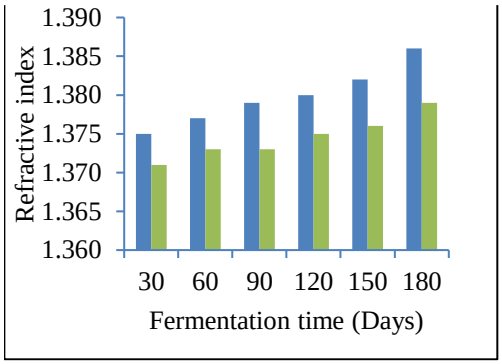

Figure 2. Changes of refractive index of Nga Pyae Ma Fish sauces during fermentation

Table 4. Changes of Specific Gravity of Nga Pyae Ma Fish Sauces during Fermentation

Fermentation time (Days)	Specific gravity (with papain)	Specific gravity (without papain)
30	1.174	1.172
60	1.174	1.173
90	1.175	1.174
120	1.176	1.175
150	1.178	1.176
180	1.178	1.176

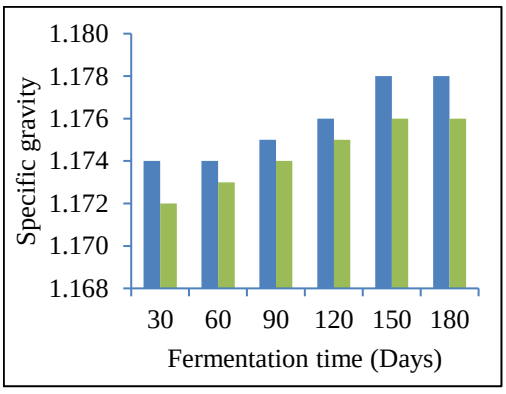

Figure 3. Changes of specific gravity of Nga Pyae Ma fish sauces during fermentation

Table 5. Changes of Total Dissolved Solids of Nga Pyae Ma Fish Sauces during Fermentation

Fermentation time (Days)	Total dissolved solids (%) (with papain)	Total dissolved solids (%) (without papain)
30	29.2	28.4
60	31.0	29.2
90	31.8	30.0
120	33.2	31.6
150	33.2	31.6
180	33.8	32.2

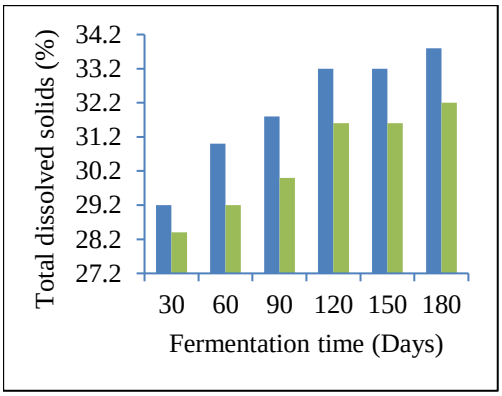

Figure 4. Changes of total dissolved solids of Nga Pyae Ma fish sauces during fermentation

Sodium Chloride Content in Nga Pyae Ma Fish Sauce Samples

The fish-to-salt ratio is another factor affecting fish sauce quality. Salt controls the type of microorganisms and retards or kills some pathogenic microorganisms during fermentation. In this research, the salt content was found to increase during a 90 - day period of fermentation. After that, the sodium chloride content in both sauces was found to decrease. The decrease may be due to the increase in volume of fish sauce. Sodium chloride contents were 20.27 % and 20.60 % in fish sauces with and without papain enzyme, respectively (Table 6 and Figure 5). In this research, higher sodium chloride contents were found in the control than those in the enzyme supplement sauce.

Total Nitrogen in Nga Pyae Ma Fish Sauce Samples

The soluble nitrogen components, including proteins, peptides, and amino acids, were generated by the activities of the proteolytic enzyme. Nitrogenous compounds in fish sauce are composed of protein and nonprotein nitrogenous compounds such as free amino acids, nucleotides, peptides, ammonia, urea, and TMAO. Total nitrogen increased dramatically during the fermentation period, especially in the first four months, and then remained relatively constant in the following six months (Brillantes *et al*., 2002). In this research, the total nitrogen content was found to increase during fermentation. After 180 days of fermentation, the total nitrogen of fish sauces with and without papain enzyme was found to be 1.93 % and 1.81 %, respectively (Table 7 and Figure 6). Total nitrogen in fish sauce with enzyme was higher than in fish sauce without enzyme. The total nitrogen content in liquid is also one of the most important quality factors for fish sauce and is used as an indicator to determine the price of fish sauce in Thailand (Lopetchart *et al.*, 2001).

Table 6. Changes of Sodium Chloride Contents of Nga Pyae Ma Fish Sauces during Fermentation

Fermentation time (Days)	Sodium chloride contents (%) (with papain)	Sodium chloride contents (%) (without papain)
30	19.59	19.89
60	20.19	20.49
90	21.39	21.70
120	21.09	21.39
150	20.60	20.87
180	20.27	20.60

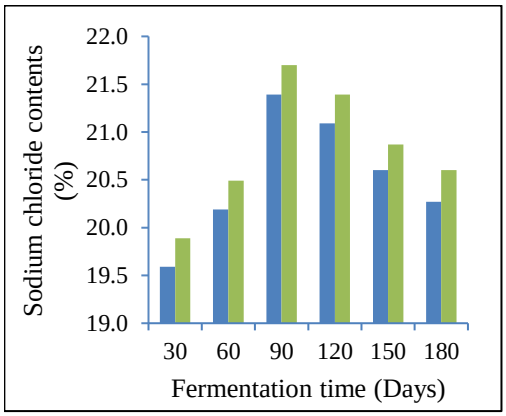

Figure 5. Changes of sodium chloride contents of Nga Pyae Ma fish sauces during fermentation

Table 7. Changes of Total Nitrogen Contents of Nga Pyae Ma Fish Sauces during Fermentation

Fermentation time (Days)	Total nitrogen contents (%) (with papain)	Total nitrogen contents (%) (without papain)
30	1.34	0.82
60	1.66	0.89
90	1.78	1.34
120	1.81	1.66
150	1.90	1.77
180	1.93	1.81

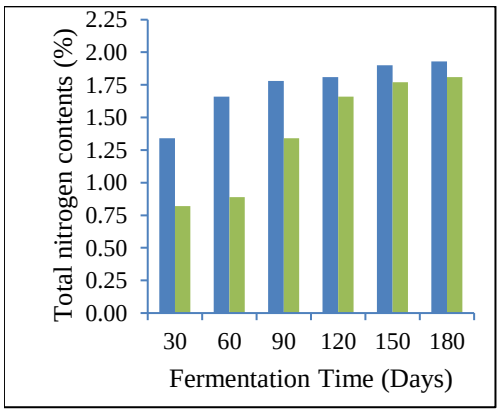

Figure 6. Changes of total nitrogen contents of Nga Pyae Ma fish sauces during fermentation

Protein Percentage in Nga Pyae Ma Fish Sauce Samples

The protein content of fish sauces was found to increase during fermentation and to become more stabilized in the later stages, i.e., after 180 days (Table 8 and Figure 7). The protein contents of fish sauce with papain enzyme were increased to 8.38 % - 12.06 % and without papain enzyme to 5.13 % - 11.31 % during fermentation. The protein contents of fish sauce with an enzyme supplement were higher than those of fish sauce without an enzyme. These observed values agreed closely with those reported to have a protein content of 12.3 % (Gildberg *et al*., 2007) and a protein content of 10.17–10.51% (Poernomo *et al*., 1984).

Formol Amino Nitrogen in Nga Pyae Ma Fish Sauce Samples

Ammonia nitrogen is suitable as a relational index for fish sauce to better understand its quality and character. Amino nitrogen is usually used as an indicator of the degree of fermentation (Lopetcharat *et al.*, 2001). The amino nitrogen represents the number of amino groups in fish sauce. An increase in amino nitrogen concentration is related to the degradation of

the polypeptide (Tungkawachara *et al.,* 2003). In this work, the formal amino nitrogen contents of fish sauce with papain enzyme were increased to 0.60 – 1.00 % and without papain enzyme to 0.32 – 0.82 % during fermentation. The formal amino nitrogen of fish sauce supplemented with enzyme was higher than that of fish sauce without enzyme (Table 9 and Figure 8).

Table 8 Changes of Protein Contents of Nga Pyae Ma Fish Sauces during Fermentation

Fermentation time (Days)	Protein contents (%) (with papain)	Protein contents (%) (without papain)
30	8.38	5.13
60	10.38	5.56
90	11.13	8.38
120	11.31	10.38
150	11.88	11.06
180	12.06	11.31

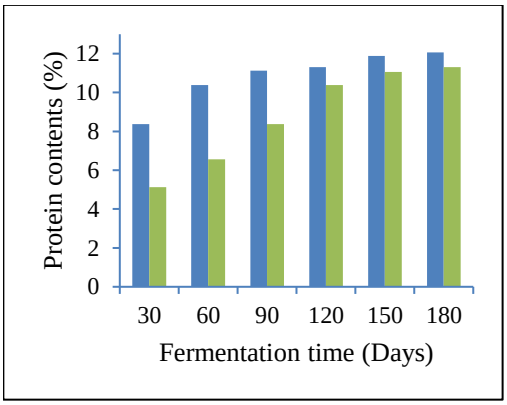

Figure 7. Changes of protein contents of Nga Pyae Ma fish sauces during fermentation

Table 9 Changes of Formol Amino Nitrogen Nga Pyae Ma Fish Sauces during Fermentation

Fermentation time (Days)	Formol amino nitrogen (%) (with papain)	Formol amino nitrogen (%) (without papain)
30	0.60	0.32
60	0.76	0.36
90	0.82	0.54
120	0.86	0.67
150	0.93	0.75
180	1.00	0.82

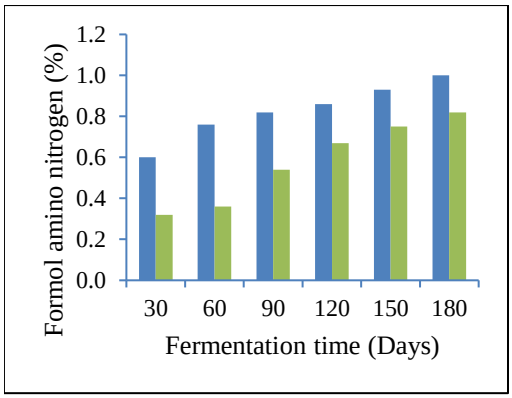

Figure 8. Changes of formol amino nitrogen of Nga Pyae Ma fish sauces during fermentation

Degree of Hydrolysis in Nga Pyae Ma Fish Sauce Samples

The degree of hydrolysis is defined by the proportion of cleaved peptide bonds in the protein hydrolysate. The degree of hydrolysis represents the extent of the hydrolytic degradation of the protein in the sample (Siti *et al*., 2015). During fermentation, the degree of hydrolysis in fish sauce with papain enzyme, increased from 44.78 % to 51.81 %, and without papain enzyme, it increased from 39.02 % to 45.31 % (Table 10 and Figure 9). The degree of hydrolysis increases during fermentation. A high degree of hydrolysis indicates a much greater amount of a complex compound will be cut down into a smaller compound (Siti *et al*., 2015). The degree of hydrolysis was greater in fish sauce supplemented with papain enzyme than in fish sauce without papain.

Table 10. Changes of Degree of Hydrolysis of Nga Pyae Ma Fish Sauces during Fermentation

Fermentation time (Days)	Degree of hydrolysis (%) (with papain)	Degree of hydrolysis (%) (without papain)
30	44.78	39.02
60	45.78	40.45
90	46.07	40.30
120	47.51	40.36
150	48.95	42.37
180	51.81	45.30

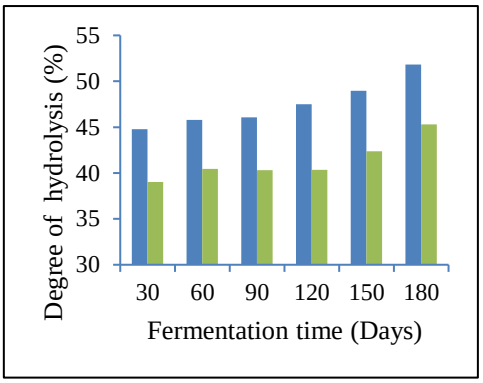

Figure 9. Changes of degree of hydrolysis of Nga Pyae Ma fish sauces during fermentation

Quality of the Prepared Fish Sauce

The prepared fish sauce samples were found to be clear, brown liquids that were rich in salt. Some properties of fish sauce samples prepared in this study were compared to the reported value of fish sauce (Table 11). The pH values of prepared fish sauces were neutral, and commercial fish sauces were slightly acidic. The salt contents of the prepared fish sauce were lower than those of commercial fish sauces. Total nitrogen, protein contents, formal amino nitrogen, and degree of hydrolysis in fish sauce supplemented with papain were found to be the highest among the others.

Table 11. Comparison of the Physicochemical Properties of Nga Pyae Ma Fish Sauce and Commercial Fish Sauces

Properties	Fish sauce (with papain)	Fish sauce (without papain)	Mingalar Daung	Shwe Pwar	Sein Gae
pH	7.0	7.2	5.8	5.3	5.7
Sodium Chloride (%)	20.27	20.6	25.91	27.12	25.01
Total Nitrogen (%)	1.93	1.81	1.69	0.77	1.6
Protein (%)	12.06	11.31	10.56	4.81	10.5
Formol Amino Nitrogen (%)	1.00	0.82	0.75	0.27	0.71
Degree of Hydrolysis (%)	51.81	45.3	44.38	35.06	42.26

Conclusion

The effect of papain supplements on the preparation of fish sauce was investigated in this research. Papain (EC 3.4.22.2) was isolated from mature green *Carica papaya* L. leaves by ammonium sulphate precipitation. During fermentation, pH values gradually increased and stabilized after 150 days. The refractive index and specific gravity slightly increased throughout the fermentation, but the increase was negligible whether the fish sauces were supplemented with papain or not. Higher sodium chloride contents were found in the control than those in the enzyme supplement sauce. Total dissolved solids, total nitrogen, formol nitrogen, and protein contents in fish sauce with enzyme supplements were higher than those without enzymes. The degree of hydrolysis in fish sauce with papain was found to be higher than without papain. Compared to commercial fish sauces, the prepared fish sauces with papain showed the most satisfactory results.

Based on these findings, fish sauces with papain enzymes were produced in less time than those without papain. This study showed that the prepared papain enzyme could be used as a meat tenderizing agent and to improve the quality of the fish sauce.

Acknowledgements

The authors would like to thank the Myanmar Academy of Arts and Science for allowing them to present this paper and Professor and Head Dr Ni Ni Than and Professor Dr Ye Myint Aung, Department of Chemistry, University of Yangon, and Professor and Head Dr Thandar Aung, Department of Chemistry, Meiktila University, for their kind encouragement.

References

AOAC. (1995). *Official Methods of Analysis.* Washington, D.C: 16th Ed. Association of Official Agricultural Chemists, 2

Beddows, C. G., A. G. Ardeshir, and W. J. Daud. (1979). "Biochemical Changes Occurring during the Manufacture of Budu". *J. Sci. Food Agric*, vol. 30, pp. 1097-1103

Brillantes, S., S. Paknoi, and A. Totakien. (2002). "Histamine Formation in Fish Sauce Production". *Journal of Food Science*, vol. 67, pp. 2090-2097

Conway, E. J. (1962). *Microdiffusion Analysis and Volumetric Error*. London: Crosby Lockwood and Son, Ltd., p. 9

Gildberg, A., J. Wichaphon, S. Lertsiri, A. Assavanig, N. K. Sorensen, and C. Thongthai. (2007). "Chemical Organoleptic Comparison of Fish Sauce Made from Cold Water Species and Typical Thai Fish Sauce". *Journal of Aquatic Food Product Technology*, vol. 16 (3), pp. 31-41

Harriman, A. M., P. C. S. Marialice, D. M. S. Viviane, R. S. Mauro, C. S. S. Cristina, and N. S. Josianne. (2013). "Correlation between the Degree of Hydrolysis and the Peptide Profile of Whey Protein Concentrate Hydrolysates: Effect of the Enzyme Type and Reaction Time". *American Journal of Food Technology.*, vol. 8(1), pp. 1-16

Hossain, M. Y., M. A. Hossen, M. N. U. Pramanik, Z. F. Ahmed, K. Yahya, M. M. Rahman and, J. Ohtomi. (2015). "Threatened Fishes of the World: *Anabas testudineus* (Bloch, 1792)". *Croatian Journal of Fisheries*, vol. 73, pp. 128-131

Koffi-Nevry, R., T. S. T. Ouina, M. Koussemon, and K. Brou. (2011). "Chemical Composition and Lactic Microflora of Adjuevan, A Traditional Ivorian Fermented Fish Condiment". *Pakistan J. N.*, vol. 10(4), pp. 332-337

Koochekian, S. A., and S. Moini. (2009). "Producing Fish Sauce from Caspia Kilka*". Iranian Journal Fisheries Sciences*, vol. 8(2): pp. 155-162

Lopetcharat, K., Y. J. Choi, J. W. Park, and M. A. Daeschel. (2001). "Fish Sauces Products and Manufacturing – A Review". *Food Rev. International*, vol. 17(1): pp. 65-88

Maria, G. M. P. (2016). " The Role and Efficiency of Ammonium Sulphate Precipitation in Purification Process of Papain Crude Extract". *Procedia Chemistry*, vol. 18, pp. 127 – 131

Ooshiro, Z., T. Ok, H. Une, S. Hayashi, and T. Itakura. (1981). "Study on Use of Commercial Proteolytic Enzymes in Production of Fish Sauce". *Mem. Fac. Fish.*, vol. 30, pp. 383-394

Pahmi, A., and S. Slamat. (2020). "Comparison of the Performance of Climbing Perch *Anabas testudineus* Bloch Filial 2 Fry and Natural Fry Treated in Acidic Swamp Waters, Jejangkit Village, South Kalimantan". *Journal of Suboptimal*, vol. 9(1), pp. 23-30

Poernomo, A., T. D. Suryaningrum, F. Ariyanic, and S. Putro. (1984). "Studies on the Nutritive Value and Microbiology of Traditional Fishery Products". *Laporan Penelitian Teknologi Perikanan*, vol. 30, pp. 9-19

Siti, M. S., I. Maria, and S. Jansen. (2015). "Protein Analysis of Canned Legumes by using Visible Spectrophotometry and Kjeldahl Method". *International Journal of Pharm Tech Research*, vol. 8(6), pp. 258-264

Trivedi, V., R. P. S. Rathore, P. R. Kamble, M. Goyal, and N. Singh. (2013). "Pepsin, Papain and Hyaluronidase Enzyme Analysis: A Review". *Int. J. Res. Phar. & Sci*, vol. 3(1), pp. 01-18

Tsai, Y. H., C. Y. Lin, L. T. Chein, T. M. Lee, C. I. Wei, and D. F. Hwang. (2006). "Histamine Contents of Fermented Fish Products in Taiwan and Isolation of Histamine-forming Bacteria". *Food Chemistry.*, vol. 98, pp. 64-70

Tungkawachara, S., J. W. Park, and Y. J. Choi. (2003). "Biochemical Properties and Consumer Acceptance of Pacific Whiting Fish Sauce". *J. Food Sci*, vol. 68, pp. 855-860

Vogel, A. I. (1969). *A Textbook of Quantitative Inorganic Analysis.* London: Longmans Green and Co., pp. 346-351

INVESTIGATION OF SOME PHYTOCHEMICAL AND BIOLOGICAL ACTIVITIES OF *OROXYLUM INDICUM* (L.) BENTH (KYAUNG-SHA) FRUITS

Aung Kyaw Min[1,2], Tin Aung Kyaw[3], War War May Zin[4], San San Aye[5], Cho Cho Than[6]

Abstract

The present research is concerned with some phytochemical and biological investigation of crude extracts from *Oroxylum. Indicum* (L.) (Kyaung sha) fruits. Preliminary phytochemical investigations by test tube methods revealed the presence of alkaloids, α–amino acids, carbohydrates, flavonoids, glycosides, organic acids, phenolic compounds, reducing sugars, saponins, steroids, tannins, and terpenoids, and the absence of starch in the tested samples. The total phenol contents of watery extract of fruits were determined by the Folin-Ciocalteu reagent (FCR) method. Gallic acid (3,4,5-trihydroxy benzoic acid), was used to construct a standard calibration curve for total phenol. TPC contents (μg GAE/mg) were found to be the highest content (51.28 ± 0.41). The total flavonoid contents of watery extract of fruits were determined by the aluminum chloride method. Quarcetin was used to construct a standard calibration curve for total flavonoid. TFC contents (mg QE/g) were found to be highest content (36.05 ± 1.2). The watery and ethanol extracts of the fruits were observed to possess antioxidant capacity by the DPPH assay method, with the watery extract having more potent antioxidant activity (IC_{50} = 18.28 μg/mL) than other tested samples. Moreover, the watery extract also exhibits higher antidiabetic activity, expressed in terms of α-amylase inhibitory (IC_{50} = 106.85 μg/mL than other tested samples. In the antimicrobial screening by agar well diffusion method, petroleum ether and ethyl acetate extracts were found to possess high activity against all tested microorganism with the inhibition zone diameters ranging between 18 mm ~ 23 mm but other crude extracts of fruits had mild activity. According to the result, *O. indicum* (Kyaung sha) fruits contain the highest amount of phytochemical constituents, so these selected fruits have more portent antioxidant, antidiabetic, and antimicrobial effects.

Keywords: *Oroxylum indicum* (L.) Bent, phytochemical constituents, antioxidant, antidiabetic, antimicrobial activity

Introduction

Natural products such as plants have been used for the treatment of different diseases for thousands of years. Global plants have been used as medicines in Egypt, China, India and Greece and in many countries from ancient time and an extraordinary number of modern drugs have been developed from them (Haroon, 2014). Medicinal plants remain on to be a central therapeutic assist used for alleviating ailments of human race. Over the last 2500 years, here have been very strongly built traditional systems of medicine such as Ayurvedic, and the Unani (Hong-Fang *et al.*, 2009). These plants restrain materials that can be utilized for useful purposes, of which are originators for the synthesis of drugs. Plenty of research work has been carried out on a number of medicinal herbs as well as they have been initiate to have definite action on the respiratory, nervous, circulatory, digestive and urinary organisms, sexual organs, skin, hearing, vision, and taste (Fabricant and Farnsworth, 2001). The exploration for anti-cancer means on or after plant sources started during the 1950s. Moreover, like other countries in Myanmar, there are a lot of research has been done and some research is still going on as it is to be mentioned that till

[1] Department of Chemistry, University of Yangon
[2] Department of Chemistry, Pathein University
[3] Department of Chemistry, Pathein University
[4] Department of Chemistry, Pathein University
[5] Department of Chemistry, University of Yangon
[6] Department of Chemistry, Pathein University

now the best source of anticancer agents is medicinal plant. Traditional medicines from readily available medicinal plants offer great potential for the discovery of new anticancer drugs. Most of plants contain glycosides, alkaloids, terpenoids, flavonoids, etc., that are frequently implicated as having anticancer effect. In Myanmar, valuable medicinal plants are found abundantly, most of them have not been scientifically investigated yet. In this study, our attention has been focused on the Myanmar bitter medicinal fruits, *Oroxylum indicum* (L.) Bent (Myanmar name: Kyaung-sha) was selected (Figure 1). These plants have been widely used as a traditional Myanmar medicine. Some reported chemical constituents of fruits of Oroxylum indicum (L.) Bent are shown in Figure 2 (Dinda *et al.*,2015).

Family	Bignoniaceae
Botanical name	Oroxylum indicum (L.) Benth
English name	midnight horror, Indian trumpet flower
Myanmar name	Kyaung sha
Part used	Fruits

Figure 1. Photographs of *Oroxylum indicum* (L.) Benth (Kyaung-sha) Fruits

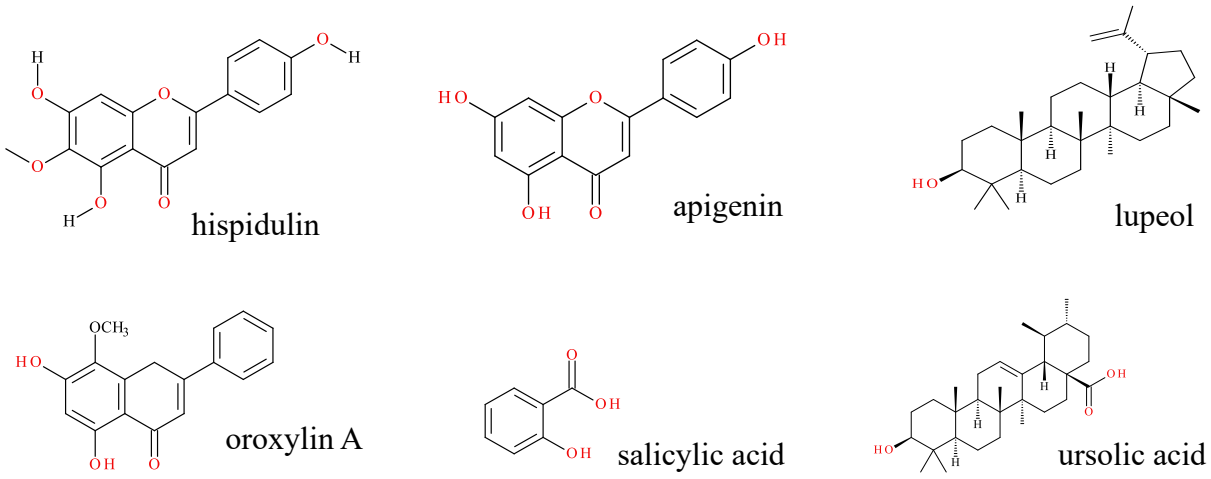

Figure 2. Some reported chemical constituents of *Oroxylum indicum* (L.) Benth (Kyaung-sha) Fruits

The main aim of this research was to investigate some phytochemical constituents from the fruits of *Oroxylum indicum* (L.) Benth (Kyaung-sha) and to evaluate some biological activities such as antimicrobial activity, antioxidant activity and antidiabetic activity.

Materials and Methods

Sample Collection

The fruits sample of *Oroxylum indicum* (L.) Benth (Kyaung-sha) was collected from Pathein Township, Ayeyawady Region in October, 2020. After being collected, the scientific name of the sample was identified by authorized botanists at Botany Department, Pathein University.

Sample Preparation

The fresh sample was cleaned and washed with water and then air-dried. The dried sample was ground using grinding machine. And then this powdered sample was kept in the sealed air-tight container to prevent moisture changes and other contamination. It was then used without further purification or refining.

Preparation of crude extracts by direct extraction methods for screening of some biological activities

Each dried powdered sample (2 g) was extracted with 50 mL of petroleum ether (60-80 °C) for 6 h by using a Soxhlet extractor. The filtrate was concentrated by removal of the solvent under reduced pressure to give the respective petroleum ether crude extract. The ethyl acetate, 95% ethanol, and watery extracts were prepared by similar manner mentioned in the above procedure. Each extract was dried at normal pressure in a water bath and stored in the refrigerator for screening some biological activities.

Preliminary Phytochemical Test

A few gram of dried powder of selected sample was subjected to the tests of alkaloids, α-amino acids, carbohydrates, flavonoids, glycosides, organic acids, phenolic compounds, reducing sugars, saponins, starch, tannins, steroids, terpenoids according to the standard procedures (Harborne, 1984).

Determination of Chemical Constituents of the Watery Extract of *Oroxylum indicum* (L.) Benth (Kyaung-sha) Fruits

(a) Determination of total phenol content by Folin-Ciocalteu Reagent (FCR) method

The total phenol content (TPC) of watery extract of *Oroxylum indicum* (L.) Benth (Kyaung-sha) fruits were estimated by Folin-Ciocalteu (FC) method according to the procedure described by Song *et al.*, (2010). The extract solution (1000 µg/mL) was mixed with 5 mL of F-C reagent (1:10) in a test tube and incubated for about 5 min. To each test tube, 4 mL of 1 M sodium carbonate was added and the test tubes were kept at room temperature for 15 min and UV absorbance of reaction mixture was measured at λ_{max} 765 nm. The blank solution was prepared as the above procedure by using distilled water instead of sample solution. Total phenol content was estimated as milligram gallic acid equivalent per gram (mg GAE/g) of extract.

(b) Determination of total flavonoid content by aluminium chloride method

The total flavonoid content (TFC) of watery extract of *Oroxylum indicum* (L.) Benth (Kyaung-sha) fruits was estimated by Aluminium Chloride method according to the procedure described by Song *et al.* (2010). The extract solution (1000 µg/mL) was mixed with 1.5 mL of methanol, 0.2 mL of 1% $AlCl_3$ solution and 2.8 mL of distilled water. The absorbance of reaction mixture was measured at λ_{max} 415 nm. The blank solution was prepared as the above procedure by using distilled water instead of sample solution. Total flavonoid content was estimated as milligram quercetin equivalent per gram (mg QE/g) of extract.

Investigation of Some Biological Activities of Crude Extracts of *Oroxylum indicum* (L.) Benth (Kyaung-sha) Fruits

(a) Determination of antioxidant activity of crude extracts of *Oroxylum indicum* (L.) Benth (Kyaung-sha) fruits

In this experiment, DPPH (2 mg) was thoroughly dissolved in ethanol (100 mL). This solution was freshly prepared in the brown coloured reagent bottle and stored in the fridge for no longer than 24 h. The crude extracts of *O. indicum* (2 mg) and 10 mL of ethanol were thoroughly mixed by shaker. The mixture solution was filtered and the stock solution was obtained. By adding with ethanol, the sample solutions in different concentrations of 200, 100, 50, 25, 12.5, 6.25 and 3.125 μg/mL were prepared from the stock solution. The effect on DPPH radical was determined by using the method of Marinova and Batchvarov (2011). The control solution was prepared by mixing 1.5 mL of 50 μM DPPH solution and 1.5 mL of ethanol using shaker. The test sample solution was also prepared by mixing thoroughly 1.5 mL of 50 μM DPPH solutions and 1.5 mL of each sample solution. The mixture solutions were allowed to stand at room temperature for 30 min. Then, the absorbance of each solution was measured at 517 nm by using UV-1650 spectrophotometer. Absorbance measurements were done in triplicate for each concentration and then mean values so obtained were used to calculate percent inhibition of oxidation. The capability to scavenge the DPPH radical was calculated by using the following equation:

$$\% \text{ RSA} = \frac{A_{control} - (A_{sample} - A_{blank})}{A_{control} \times 100}$$

Where, %RSA = Percent of Radical Scavenging Activity

$A_{control}$ = absorbance of the control (DPPH only) solution

A_{blank} = absorbance of the blank (EtOH + Test sample solution) solution

A_{sample} = absorbance of the test sample solution

(b) Determination of antidiabetic activity of crude extracts of *Oroxylum indicum* (L.) Benth (Kyaung-sha) fruits

Determination of α-amylase inhibitory activity

In alpha amylase assay, the starch-iodine was used. First 2 mL of (0.5%) substrate starch solution and 1 mL of tested solution (Acarbose standard drug and crude) of seven different concentrations such as 200, 100, 50, 25, 12.5, 6.25, and 3.125 μg/mL were added in a bottle and this mixture was incubated for 3 min at room temperature. To start the reaction, 1 mL of α-amylase was added to the above solution followed by incubated for 15 min at room temperature. To stop the reaction, 4 mL of 0.1M HCl was added to this mixture, and to detect the reaction, 1 mL of iodine-iodide indicator (1 mM) was added to the mixture. Absorbance was read at 650 nm by UV spectrophotometer in the visible region. The control solution was prepared as the above procedure by using phosphate buffer (0.02M, pH 6.5) instead of drug solution.

All the experiments were done in triplicate. Percent inhibition of each sample solution was calculated by using the following formula. Standard deviation (SD) and 50% inhibition concentration (IC_{50}) value in μg/mL were calculated by computer excel program.

$$\% \text{ Inhibition} = \frac{A_{Sample} - A_{Control}}{A_{Sample}} \times 100$$

Where,

$A_{control}$ = the absorbance of the control solution

A_{sample} = the absorbance of sample solution

(c) Determination of antimicrobial activity of crude extracts of *Oroxylum indicum* (L.) Benth (Kyaung-sha) fruits

The antimicrobial activity of crude extracts of *Oroxylum indicum* (L.) Benth (Kyaung-sha) fruits was determined against eight strains of microorganisms such as *Agro tumefaciens* (NITE 09678), *Bacillus pumilus* (IFO 12092), *Bacillus subtilis* (IFO 90517), *Candida albicans (*NITE 09542), *Escherichia coli* (AHU 5436), *Micro luteus* (NITE 83297), *Pseudomonas fluoresens* (IFO 94307) and *Staphylococus aureus* (AHU 8465) by employing the agar well diffusion method. To prepare the agar plate, firstly, peptone (0.5 g) and sodium chloride (0.25 g) were mixed in distilled water and made up to 100 mL with distilled water. The pH of this solution was adjusted to 7.2 with a 0.1 M sodium hydroxide solution, and 1.5 g of agar was added. Nutrient agar medium was prepared according to method described by Cruick (1975). Briefly, nutrient agar was boiled, and 20-25 mL of the medium was poured into a test tube, plugged with cotton wool, and autoclaved at 121 ºC for 15 min. Then the tubes were cooled down to 60 ºC and poured into sterilized petri dishes, and 0.1 mL of spore suspension was also added to the dishes. The agar was allowed to set for 30 min, after which a 10 mm plate agar well was made with the help of a sterilised cork borer. After that, about 0.1 mL of each of the prepared extract solutions was introduced into the agar well and incubated at 37 ºC for 24 h. The inhibition zone (clear zone) appeared around the agar well, indicating the presence of antimicrobial activity. The extent of antimicrobial activity was measured from the inhibition zone diameter of. The measurements were conducted at Botany Department, Pathein University.

Results and Discussion

Phytochemical Constituents

The phytochemical tests revealed that alkaloids, α-amino acids, carbohydrates, flavonoids, glycosides, organic acids, phenolic compounds, reducing sugars, saponins, steroids, tannins and terpenoids were found to be present but starch was absent in fruits of *Oroxylum indicum* (L.) Benth (Kyaung-sha).

Total Phenol and Total Flavonoid Contents of Watery Extract of *Oroxylum indicum* Fruits

The total phenol content of the watery extract of *Oroxylum indicum* (L.) Benth (Kyaung-sha) fruits was determined with spectrophotometric method by using Folin-Ciocalteu reagent. The total phenol content of the watery extract of *Oroxylum indicum* (L.) Benth (Kyaung-sha) fruits was 51.28 ± 0.41 mg GAE/g. The total flavonoid content of sample was determined with spectrophotometric method by aluminium chloride reagent and was found to be 36.05 ± 1.2 mg QE/g. The results are shown in Table1.

Table 1. Total Phenol and Total Flavonoid Contents of Watery Extract of *Oroxylum indicum* (L.) Benth (Kyaung-sha) Fruits

Chemical Constituents	Contents
Total Phenol Content (mg GAE ± SD)/mg of extract	51.28 ± 0.41
Total Flavonoid Content (mg QE ± SD)/g of extract	36.05 ± 1.2

According to the experimental results, phenol and flavonoid compounds were detected in watery extract of selected sample. Besides their established antioxidant activity, many phenolic

compounds may exhibit significant antimicrobial activity. Since many plant extracts are rich in phenolic compounds, this is of particular interest for the development of natural alternatives to synthetic preservatives in food and cosmetic applications. Flavonoids are also present as a potent water-soluble antioxidant and free radical scavengers, which prevent from the oxidative cell damage and also have strong anticancer activity. It also helps in managing diabetes induced oxidative stress.

Antioxidant Activity of Crude Extracts of *Oroxylum indicum* (L.) Fruits by DPPH Assay

The antioxidant activity was measured in terms of hydrogen donating or radical scavenging ability of the watery and ethanol extracts of selected sample by using the stable radical DPPH. The results are shown in Table 2. The watery extract of selected fruit was found to be the low (IC_{50}) value 18.28 μg/mL than the ethanol extract of selected fruit, low IC_{50} value indicate the more potent antioxidant activity. However, the watery and ethanol extracts of selected sample were weaker activity than the standard ascorbic acid (IC_{50} = 1.08 μg/mL).

Table 2. Antioxidant Activity of Watery and Ethanol Extracts of *Oroxylum indicum* (L.) Benth (Kyaung-sha) Fruits by DPPH Assay

Samples (Extracts)	% RSA (mean ± SD) in different concentrations (μg/mL)							IC_{50} (μg/mL)
	3.125	6.25	12.5	25	50	100	200	
Watery	31.78 ± 0.54	34.63 ± 0.54	45.25 ± 0.83	55.53 ± 0.15	69.43 ± 0.26	88.43 ± 0.40	97.93 ± 0.26	18.28
Ethanol	34.37 ± 0.54	39.64 ± 0.26	42.57 ± 0.54	47.15 ± 0.26	58.89 ± 0.54	65.54 ± 0.26	73.32 ± 0.26	31.07

Andiabetic (α-Amylase Inhibitory) Activity of Crude Extracts of *Oroxylum indicum* Fruits

Hyperglycemia has been a classical risk in the development of diabetes and the complications associated with diabetes. Therefore, control of blood glucose levels is critical in the early treatment of diabetes mellitus and reduction of macro and microvascular complications. One therapeutic approach is the prevention of carbohydrate absorption after food intake, which is facilitated by inhibition of enteric enzymes including *α*-glucosidase and *α*-amylase present in the brush borders of intestine. In this study, the *α*-amylase inhibitory activity of *Oroxylum indicum* (L.) Benth (Kyaung-sha) fruits was investigated. The inhibitory effects of watery and ethanol extracts were analyzed. The percentage inhibition of *α*-amylase by watery and ethanol extracts was studied in a concentration range of 3.125-200 μg/mL. The percentage inhibition of the sample on *α*-amylase enzyme activity increased with increasing the concentrations. From the percentage inhibition, the respective IC_{50} values for the watery and ethanol extracts were calculated and the results are respectively tabulated in Table 3. The watery and ethanol extracts of bitter selected plant were also explored for *in vitro α*-amylase inhibition and their activity was compared with that standard of the anti-diabetic drug, acarbose. The 50% α–amylase inhibition potency (IC_{50}) of watery and ethanol extracts of the selected sample ranged between 106.85-153.98 μg/mL, indicating that crude extracts possessed potent *α*-amylase inhibition activity but these extracts has a lower inhibition activity than standard acarbose (IC_{50} =20.92 μg/mL).

Table 3. IC_{50} Values of Watery and Ethanol Extracts of *Oroxylum indicum* (L.) Benth (Kyaung-sha) Fruits by α-Amylase Inhibition Assay

Samples (Extracts)	% Inhibition in different concentrations (µg/mL)							IC_{50} (µg/mL)
	3.125	6.25	12.5	25	50	100	200	
Watery	4.07 ± 0.20	7.29 ± 0.32	10.10 ± 0.30	23.13 ± 0.34	46.35 ± 0.16	49.43 ± 0.10	57.75 ± 0.07	106.85
Ethanol	7.29 ± 0.32	16.04 ± 0.26	20.77 ± 0.24	37.62 ± 0.15	45.29 ± 0.11	48.32 ± 0.57	65.99 ± 0.04	153.98

Screening of Antimicrobial Activity of Various Crude Extracts of *Oroxylum indicum* Fruits

Screening of the antimicrobial activity of various crude extracts such as petroleum ether, ethyl acetate, 80 % ethanol, and watery extracts of *Oroxylum indicum* (L.) Benth (Kyaung-sha) fruits was done by employing the agar well diffusion method (Table 4 and Figure 3). In this study, the samples were tested on eight pathogenic microorganisms, such as *Agro tumefaciens, Bacillus pumilus, Bacillus subtilis, Candida albicans, Escherichia coli, Micro luteus, Pseudomonas fluoresens* and *Staphylococus aureus.* From these results, it was found that the watery extract of the selected sample did not exhibit any antimicrobial activity against all tested microorganisms, whereas the petroleum ether, ethyl acetate, and ethanol extracts of the selected sample exhibited inhibition zone diameters ranging from 13 ~ 22 mm, respectively, against all tested microorganisms. The selected sample of ethanol extract showed less activity, while petroleum ether and ethyl acetate extracts were observed to be most effective in antimicrobial activity. Therefore, all the crude extracts of the selected sample, except the watery extract of *Oroxylum indicum* (L.) Benth (Kyaung-sha) fruits, exhibited antimicrobial activity against all microorganisms tested. Among the crude extracts, petroleum ether and ethyl acetate extracts from the *Oroxylum indicum* fruits showed the most pronounced antimicrobial activity against all microorganisms tested. However, the selected sample possesses smaller inhibition zone diameters than the standard antimicrobial drug chloramphenicol (29 ~ 30 mm).

Table 4. Inhibition Zone Diameters of Crude Extracts by Agar Well Diffusion Method

Microorganism	Inhibition zone diameters (mm)				
	H_2O	EtOH	EtOAc	PE	STD
A. tumefaciens	-	14	20	21	29
B. pumilis	-	14	18	20	29
B. subtilis	-	15	20	23	29
C. albicans	-	13	19	21	30
E. coli	-	14	20	21	29
M. luteus	-	14	18	20	29
P. fluorescens	-	15	20	22	29
S. aureus	-	14	19	21	30

Agar well diameter (8 mm) No activity (-)

10 mm – 14 mm = weak activity (+)

15 mm – 19 mm = moderate activity (++)

20 mm and above = potent activity (+++)

STD = chloramphenicol

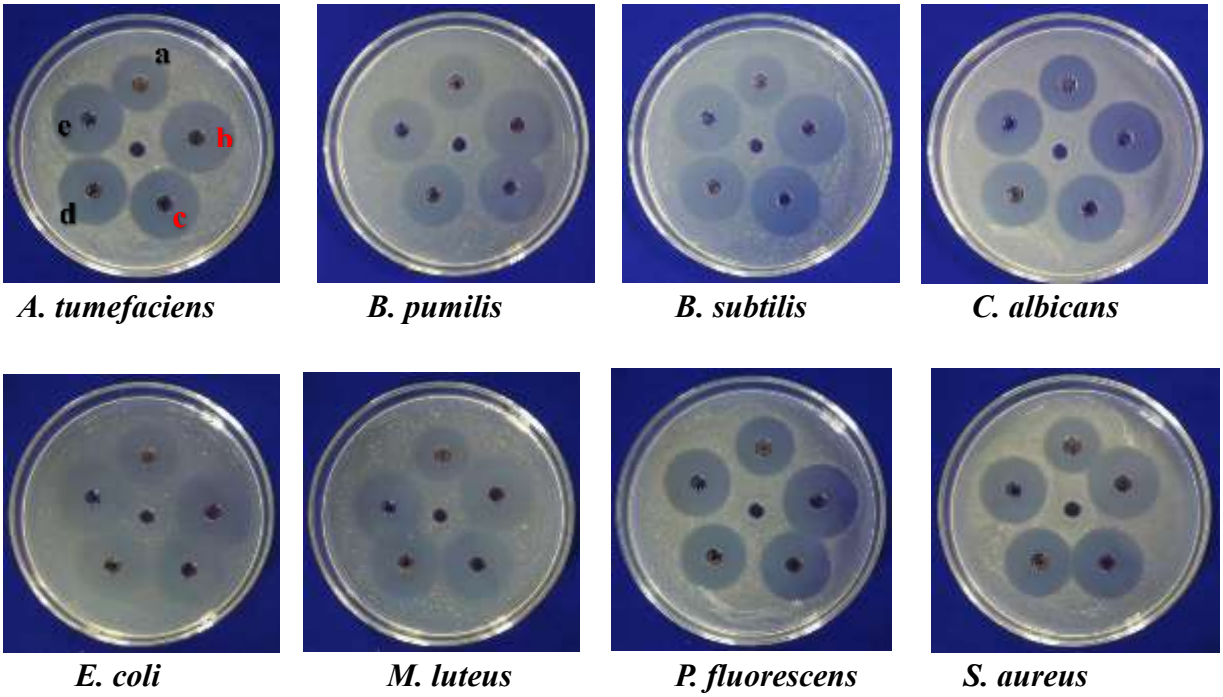

a= H_2O, b= EtOH, c= EtOAc, d= PE & e= Standard

Figure 3. Screening of antimicrobial activity of the crude extracts by agar well diffusion method

Conclusion

The following inferences could be deduced from the overall assessment of the chemical and biological investigation on the fruits of *Oroxylum indicum* (L.) Benth (Kyaung-sha). In the preliminary phytochemical results, alkaloids, α-amino acids, carbohydrates, flavonoids, glycosides, organic acids, phenolic compounds, reducing sugars, saponins, steroids, tannins, and terpenoids were found to be present, but starch was absent in the selected sample. According to the chemical investigation, the watery extract of the selected sample contains significant amounts of TPC (51.28 ± 0.41 mg GAE/mg) and TFC (36 ± 1.4 mg QE/g). The extracts showed the high antimicrobial activity (13 mm ~ 22mm) against *Agro tumefaciens, Bacillus pumilus, Bacillus subtilis, Candida albicans, Escherichia coli, Micro luteus, Pseudomonas fluoresens* and *Staphylococus aureus* due to the presence of flavonoids and phenols. The watery and ethanol extracts of the selected sample also showed DPPH free radical scavenging activity IC_{50} = 18.28 mg/mL and IC_{50} = 31.07 μg/mL respectively, as antioxidant activity. The watery and ethanol extracts of the selected sample possessed the antidiabetic activity due to its α-amylase inhibitory effects (IC_{50}= 106.85 μg/mL and IC_{50}= 153.98 μg/mL respectively). The result obtained from this research indicated that the tested crude extracts of *Oroxylum indicum* (L.) Benth (Kyaung-sha) fruit may play an important role in medicinal properties used *in vitro* and may be effective.

Acknowledgements

The authors would like to express their profound gratitude to the Department of Higher Education (Lower Myanmar), Ministry of Education, Yangon, Myanmar, for provision of opportunity to do this research and Myanmar Academy of Arts and Science for allowing to the presentation of paper. Our deepest gratitude is expressed to Dr Than Htun, Rector, Pathein University, for his encouragement, kind guidance, and kind help to do this research. We wish to thank Dr Myint Myint Khaine, Dr Nay Aung, and Dr Nilar Kyu, Pro-Rectors, Pathein University for their invaluable advice and encouragement. Thanks, are also extended to Dr Hnaung Hnaung Win and Dr Ei Ei Khaine (Professors), Department of Chemistry, Pathein University, for their suggestions and provision of research facilities at the Department of Chemistry, Pathein University.

References

Basma, A. A., Z. Zakaria, L. Y. Latha and S. Sasidharan. (2011). "Antioxidant Activity and Phytochemical Screening of the Method Extracts of *Euphorbia hirta* L.", *Journal of Tropical Medicine*, vol. 8 (8), pp. 386-390

Dinda, B., I. S. Sarma, and M. Rudrapaul. (2015). "*Oroxylum indicum* (L.) Kurz, an Important Asian Traditional Medicine: from Traditional Uses to Scientific Data for its Commercial Exploitation". *J Ethnopharmacol*, vol 161, pp. 255–278

Calixto, J. B. (2019). "The Role of Natural Products in Modern Drug Discovery". *An. Acad. Bras. Cienc*, vol. 2, pp. 91-95

Cruickshank, R. (1975) *Medical Microbiology: A Guide to Diagnosis and Control of Infection*. Edinburgh: E and S Livingston Ltd. p. 888

Deka, D. C., K. Vimal, P. Chandan, and K. Kamal. (2013). "*Oroxylum indicum* a Medicinal Plant of North East India: An Overview of Its Nutritional, Remedial, and Prophylactic Properties''. *Journal of Applied Pharmaceutical Science*, vol. 3 (1), pp. 104-112

Fabricant, D. S and N.R.Farnsworth. (2001). "The Value of Plants Used in Traditional Medicine for Drug Discovery". National Library of Medicine*, vol. 109 (1), pp. 69-75*

Harborne, J. B. (1984). "Phytochemical Methods and A Guide to Modern Technique of Plant Analysis". London: Chapman and Hall, pp. 37-222

Haroon, K. (2014). "Medicinal Plants in Light of History: Recognized Therapeutic Modality". *Topical Review Article*, vol. 19(3), pp. 216-219

Hong, F. J., J. L. Xue, and Y.Z. Hong. (2019). "Natural Products and Drug Discovery. Can Thousands of Years of Ancient Medical Knowledge Lead Us to New and Powerful Drug Combinations in the Fight Against Cancer and Dementia?" National Library of Medicine, vol. 10 (3), pp. 194-200

Marinova, G. V., and Batchvarov, V. (2011). "Evaluation of the Mehthods for Determination of the Free Radical Scavenging Activity of DPPH". *Bulgarian Journal of Agricultural Science*, vol. 17, pp. 11-24

Newman, D.J., and G.M. Cragg. (2020). "Natural Products as Sources of New Drugs Over the Nearly Four Decades from 01/1981 to 09/2019". *J. Nat. Prod*, vol. 83, pp. 770–803

Song, F. L., Gan, R. Y., Zhang, Y., Xiao, Q., Kuang, L., and Li, H. B. (2010). "Total Phenolic Contents and Antioxidant Capacities of Selected Chinese Medicinal Plants". *Int. J. Mol. Sci*, vol. 11, pp- 2367-2372

NOVEL COBALT SULFIDE-ETHYLENEDIAMINE NANOSHEETS FOR ADSORPTION-ASSISTED HEXAVALENT CHROMIUM REMOVAL*

Win Thi Yein[1], Qun Wang[2]

Abstract

Hexavalent chromium, Cr (VI), contamination of wastewater is a great threat to living organisms and environment. Hence, the innovative advancement in the removal of Cr(VI) from wastewater is urgently on demand. The current research studied the influence of morphological and structural properties of CoS nanoadsorbents on the adsorption efficiency of Cr(VI) removal. The prepared CoS nanoadsorbents were synthesized with one-pot solvothermal/hydrothermal route without using toxic and harmful chemical reagents. The morphological and structural properties of prepared CoS nanoadsorbents were investigated by using various analytical techniques including Scanning Electron Microscopy (SEM), X- ray Diffraction (XRD) and FT-IR spectroscopy. The inorganic-organic hybrid CoS/En-nanoflowers gave the highest Cr(VI) removal efficiency from aqueous liquid compared to that of its counterparts such as CoS-nanorods and CoS-nanoflowers within 40 min. The Cr(VI) adsorption capacity of CoS/En-nanoflowers was found to be 87.7 mg/g and the adsorption process followed the pseudo-second-order kinetic model. Based on the theory of hard and soft acid-base (HSAB) and zeta potential results, the mechanism of Cr(VI) removal was suggested as electrostatic attraction between CoS/En surface and Cr(VI).

Keywords: inorganic-organic hybrid, nanosheets, adsorption, hexavalent chromium, electrostatic attraction

Introduction

Hexavalent chromium, Cr (VI), pollution has become the most critical problem in recent years due to its high toxicity in human health and its persistence in the environment (Gupta et al., 2021). Various conventional methods including chemical precipitation, electrolysis, ion exchange, reverse osmosis, coagulation, and adsorption are being used as pollutants mitigation for the removal of Cr(VI). Among these, adsorption method is a low cost and high-efficiency technology to remove heavy metals. The conventional carbon adsorbents require high activation energy. The modified adsorbents either by crosslinking, grafting, changing the chemical form or through engineered composite materials have been put forward as a way to cost effective, and enhance the adsorption capacities (Manyangadze et al., 2020).

Compared to using conventional carbon adsorbents, inorganic-organic hybrid nanoadsorbents open up a new avenue towards the treatments of heavy metals contaminated wastewater. Recently, two-dimensional (2D) layered materials are gaining enormous interest as nanoadsorbent because of its high surface area and distinct layer structure (Wu et al., 2015). Non-layered cobalt sulfides possessing diverse chemical formulae (Co_mS_n) and various crystalline phases are difficult to design the atomically-thin 2D structure (Yein et al., 2018). Organic amine template-assisted fabrication is prominent to design nonlayered 2D atomically thin layer building blocks into 3D hierarchical structures through self-assembling growth process. There are researches on the fabrication of inorganic-organic metal sulfide-amines as alternative electrocatalysts for efficient energy conversion technologies (Liu et al., 2014; Ma et al., 2017). However, to our knowledge, the inorganic-organic hybrid CoS nanosheets used as a nanoadsorbent is rarely investigated to remove Cr(VI) from aqueous solution.

---

* Best Paper Award Winning Paper in Industrial Chemistry (2022)

[1] Department of Industrial Chemistry, University of Yangon

[2] School of Chemistry and Chemical Engineering, Harbin Institute of Technology, Harbin, China

Thus, the objectives of the present study are as follows: to fabricate CoS nanoadsorbents with different morphological and structural properties; to assess the adsorption efficiency of CoS nanoadsorbents on the Cr(VI) removal; and to gain deep insight into the adsorption mechanism of inorganic-organic hybrid CoS nanoadsorbent.

Materials and Methods

Materials

All the reagents used in this work were analytical grade without further purification. Cobalt acetate tetrahydrate ($Co(OAc)_2{\cdot}4H_2O$), thiourea ($SC(NH_2)_2$), ethylenediamine (En), potassium dichromate ($K_2Cr_2O_7$), hydrochloric acid (HCl) and sodium hydroxide (NaOH) were purchased from Shanghai Aladdin Bio-Chem Technology Co., Ltd. Deionized water was used as the solvent.

Methods

Preparation of CoS/En-nanoflowers

In a typical procedure, 0.10 mol of cobalt acetate tetrahydrate, and 0.15 mol of thiourea were dissolved into a volume ratio of ethylenediamine and water (V_{En}: V_{H2O}- 9:1) under vigorous stirring for 30 min. The solution was transferred into 20 mL Telfon-line stainless steel autoclave and heated at ~180˚C for 12 h. The resultant black product was collected and washed several times with distilled water and absolute ethanol. Finally, it was dried at ~70˚C for 12 h and ground to obtain the powder form. It was denoted as CoS/En-flowers.

Preparation of CoS-nanoflowers

As a comparison, CoS-nanoflowers were synthesized in the identical procedure as mentioned above, with the same molar ratio of reagents and similar steps with the different volume ratio of ethylenediamine and water (V_{En}: V_{H2O}- 1:9) as solvent.

Preparation of CoS-nanorods

As a comparison, CoS-nanorods were fabricated in the identical procedure as mentioned above, with the same molar ratio of reagents and similar steps with pure water (V_{H2O}-10) as solvent without adding ethylenediamine (En) as solvent.

Characterization

The morphologies of the samples were examined by Hitachi field emission scanning electron microscope (FESEM, SU8100) at the accelerating voltage of 5.0 kV. The structure of the samples was determined by X-ray diffraction (XRD) on Rigaku D/max-2000 diffractometer. The functional groups in the samples were identified by using FT-IR spectroscopy (FT-IR-8400S, Shimadzu). Surface charges of samples were analyzed by a Zeta potential (Nano-ZS90 nanoparticle analyzer, Malvern Instruments Ltd.,).

Batch Adsorption Experiments

Typically, 100 mg/L stock Cr(VI) solution was prepared by dissolving 0.1 g of potassium dichromate in 1.0 L of water (Vaddi et al., 2022). 100 mg of CoS samples were dispersed in 100 mL solution with a concentration of 100 mg/L of Cr(VI) solution and then the pH of Cr (VI) solution was adjusteds with 0.1 M HCl and 0.1M NaOH. The pH adjusted Cr(VI) solution was stirred in the dark for 120 min to reach the adsorption-desorption equilibrium. At a definite time interval, the suspensions were centrifuged, and the supernatant solution was taken to measure the

residual Cr(VI) concentration at 350 nm wavelength by using UV-Vis spectrophotometer (UV-1700, Shimadzu).

Mathematical Equations

The Cr(VI) removal efficiency of CoS samples was calculated by the following equation.

$$\text{Removal Efficiency (\%)} = \frac{C_o - C_e}{C_o} \times 100\ \% \qquad (1)$$

Where C_0 (mg/L) is the initial concentration of Cr(VI); C_t (mg/L) and C_e (mg/L) is the concentration of Cr(VI) ions at time *t* and equilibrium *e*. Kinetic models named pseudo-first-order and pseudo-second-order models were simulated for Cr(VI) adsorption on the adsorbent surface.

$$\log(q_e - q_t) = \log q_e - \frac{k_1 t}{2.303} \qquad \text{(Pseudo – first – order)} \qquad (2)$$

$$\frac{t}{q_t} = \frac{1}{k_2 q_e^2}\ \frac{t}{q_t} \qquad \text{(Pseudo – second – order)} \qquad (3)$$

Where q_e and q_t are the adsorbent absorption capacity (mg g^{-1}) at equilibrium and time. Moreover, k_1 and k_2 are the reaction rate constants (min^{-1} and g mg^{-1} min^{-1}) for the pseudo-first-order and pseudo-second-order, respectively.

Results and Discussion

In the present study, the influence of solvent compositions on the morphological and structural properties of CoS samples were identified by serial microscopic and spectroscopic techniques. Firstly, the morphologies of CoS samples were examined by using SEM technique. Interestingly, when pure water was used as solvent medium, the morphology of the product was composed of nanorods as shown in Figure 1(a). In contrast, the volume ratio of En to water (1:9) under the identical conditions produced highly interconnected nanosheets assembled to form peony-flower-like structure CoS, named as CoS-nanoflowers as shown in Figure 1(b and c). The results indicated that the combination of a trace amount of En changed the sheet-like nanostructures of CoS. As shown in Figure 1(d and e), a similar morphology was seen, when the volume ratio of En to water (9:1) was used and named as CoS/En-snanoflowers. This is due to the fact that the structure directing roles of organic amine influences on the formation and geometry of layered superstructures (Ma et al., 2017). The photo-picture of real peony flower is shown in Figure 1(f).

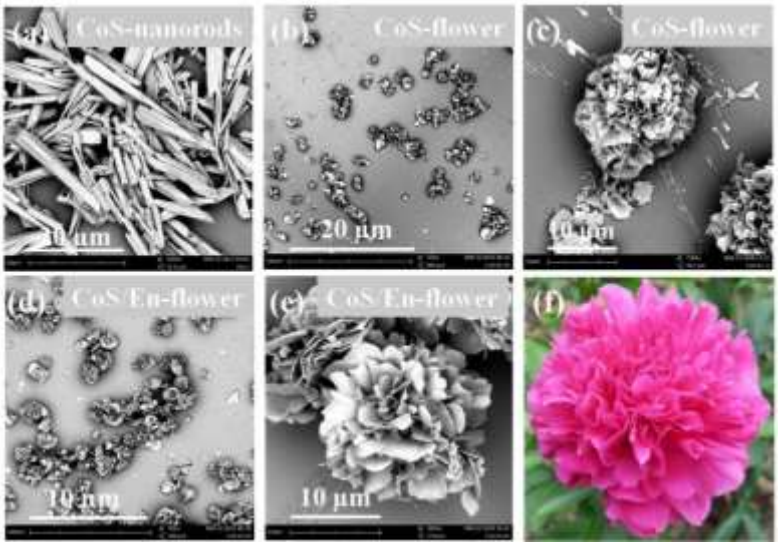

Figure 1 SEM images of (a) CoS-nanorods, (b,c) peony flower-like CoS, (d,e) peony flower-like CoS/En, and (f) photo picture of peony flower in nature

To validate the crystal structure of CoS samples, XRD analyses were performed. As shown in Figure 2(a, curve i), the diffraction peaks at 2θ=30.4˚, 35.1˚, 46.6˚, and 54.2˚ in the XRD patterns correspond to respective (100), (101), (102) and (110) planes of CoS and matched well with the standard hexagonal CoS (space group of P63/mmc(194) (JCPDS no-75-0605). No other peaks from other phases were detected, implying high purity and single-phase crystallization of the product and no attached organic amine in the crystal structure of CoS nanorods. The XRD patterns of CoS-nanoflowers fabricated with V_{En}:V_{H2O}-1:9 are similar with that of CoS-nanorods as illustrated in Figure 2(a, curve ii). This is due to the fact that a small amount of En affects the morphology rather than crystal structure. Compared with the crystal structure of CoS-nanorods and CoS-nanoflowers, crystal structure of CoS/En-nanoflowers was different. The corresponding XRD patterns displayed in Figure 2(a, curve iii) stated that CoS–En inorganic–organic hybrid was mainly composed of amphorous CoS, considering the covalent organic-inorganic hybrid materials-based CoS layers coordinated through the bonding of the nitrogen atoms of ethylenediamine (En) (Gordillo et al., 2012).

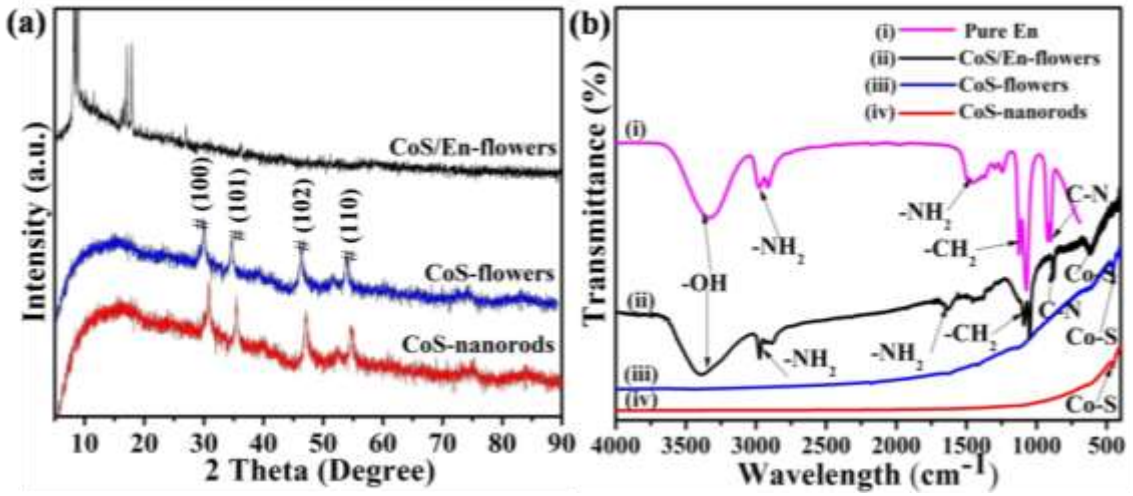

Figure 2 (a) XRD patterns and (b) FT-IR spectrum of CoS samples including CoS/En nanoflowers, CoS-nanoflowers and CoS-nanorods

In order to attest the above statement, FT-IR spectroscopic measurements were carried out to confirm the preferential binding of the amine ligands to cationic sites on the surface of nanocrystals at growth stage as seen in Figure 2(b). The pure ethylenediamine (En) in pure liquid state is the *trans*-conformation structure which represented as broad and strong vibration bands in FT-IR spectra as shown in Figure 2(b, curve i). The standard spectrum of pure En shows characteristic bands corresponding to broad N–H deformation and stretching vibration at 3088 cm^{-1} and 1612 cm^{-1}. $–CH_2–$ deformation vibration was visible at 1280–1520 cm^{-1}, and 1065 cm^{-1} was assigned to C–N stretching (Hunyaid et al., 2017). As shown in Figure 2(b, curve ii), because of the chemical bonding between Co^{2+} and the N atom of En, the stretching vibration band of the N–H shifted to the frequency around 2967 cm^{-1} indicating that the amine groups of En is grafted on the inorganic crystal (Kang et al., 2017). Moreover, the new peak represented for Co–S stretching vibration appeared at 616 cm^{-1} which was indicative of the CoS/En formation. In FT-IR spectrum of CoS-nanoflowers, the absence of vibration bands of N–H represented that there was no amine group of En attached with CoS sample as displayed in Figure 2(b, curve iii). Additionally, the band at 582 cm^{-1} was attributed to Co–S stretching vibration in CoS phase. In CoS-nanoflowers formation, a small amount of En couldn't have the strong tendency of En binding in CoS crystal and En molecule could easily dissolve out in the reaction medium resulting in the pure CoS crystal. Considering a similar morphology, using a large amount of En was the decisive factor to give the amine functionalized CoS sample. In Figure 2(b, curve iv), almost all of the distinct peaks of En molecules haven't been seen in CoS-nanorods when water was used as solvent medium indicating that high purity CoS were obtained. Therefore, based on the above discussion of XRD and FT-IR analyses, the complete phase transformation occurred during the one-pot solvothermal/ hydrothermal route.

Considering the SEM images of Figure 1, the XRD patterns and FT-IR spectra of Figure 2, the sequential formation mechanism of peony flower-like CoS/En nanosheets could be proposed. It is well known that ethylenediamine (En) is a strong tridentate amine ligand with two $–CH_2$ groups to form chelates with metal ions in aqueous solutions. From the point of crystal formation mechanism, an ethylenediamine (En) molecule having a pair of binding sites for a Co^{2+} ion produced a chemically stable complex $[Co(En)_x]^{2+}$ as written in Equation (6). Thiourea, sulfur precursor, acts as the reducing agent and reacted with water to form a sulfide ion ($S^{2–}$) as described in Equation (7) and (8). The reduced sulfide ion would react with $[Co(En)_x]^{2+}$ to form CoS/En as shown in Equation (9). Therefore, organic amine template-assisted fabrication was prominent to design nonlayered 2D atomically thin layer building blocks into 3D hierarchical structures through self-assembling growth process.

$$Co(CH_3COO)_2 + m\ (En \longrightarrow Co(En)_m(CH_3COO)_2 \quad (4)$$

$$H_2N–S–NH_2 \xrightarrow{\triangle} H_2S + HN=C=NH \quad (5)$$

$$H_2S \xrightarrow{\triangle} S^{2–} + H_2 \quad (6)$$

$$Co(En)_m(CH_3COO)_2 + S^{2–} \longrightarrow CoS(En)_m + 2(CH_3COO)^{–} \quad (7)$$

After a deep insight into a variety of CoS nanoadsorbents formation, the adsorption test was carried out by using different CoS samples. The adsorption efficiency toward Cr(VI) was evaluated at pH 5 through monitoring UV-Vis absorption spectra as shown in Figure 3(a). It is obvious that both CoS-nanorods and CoS-flowers gave less adsorption performance towards Cr(VI), with the removal efficiency of 30.8 mg/g and 64.3 mg/g, respectively. However, the obtained adsorption performance of Cr (VI) over CoS/En-nanoflowers exhibited much higher activity than that of its counterparts. Its adsorption efficiency of Cr(VI) reached to 87.7 mg/g within 40 min. A relatively high adsorption was obtained using CoS/En-nanoflowers as compared to those of CoS-nanorods

and CoS-nanoflowers that might be due to the morphological influence and activation of amine groups on adsorbent surface. Figure 3(b) represents the time-dependent UV-Vis absorption spectra of CoS/En-nanoflowers toward Cr(VI) concentration. With the increase in adsorption time, the absorption peak at 350 nm assigned to the Cr(VI) ions decreased gradually which demonstrated the adsorption capacity of Cr(VI) ions over CoS/En-nanoflowers at pH 5.

The time dependent adsorption rate is crucial factor for practical application. In order to better explore the adsorption kinetics of Cr(VI) ions, two kinetic models including pseudo-first-order (Eq- 4) and pseudo-second-order (Eq-5) were established and fitted with the experimental adsorption performance data of CoS/En-nanoflowers. The kinetic behavior of the adsorption process was studied at pH 5. The kinetic data were shown to be 0.071 min^{-1} and 0.00130 g mg^{-1} min^{-1}, respectively. The pseudo-second-order kinetic model showed the best correlated coefficient value ($R^2 > 0.995$) as compared with that of pseudo-first-order ($R^2 > 0.935$).

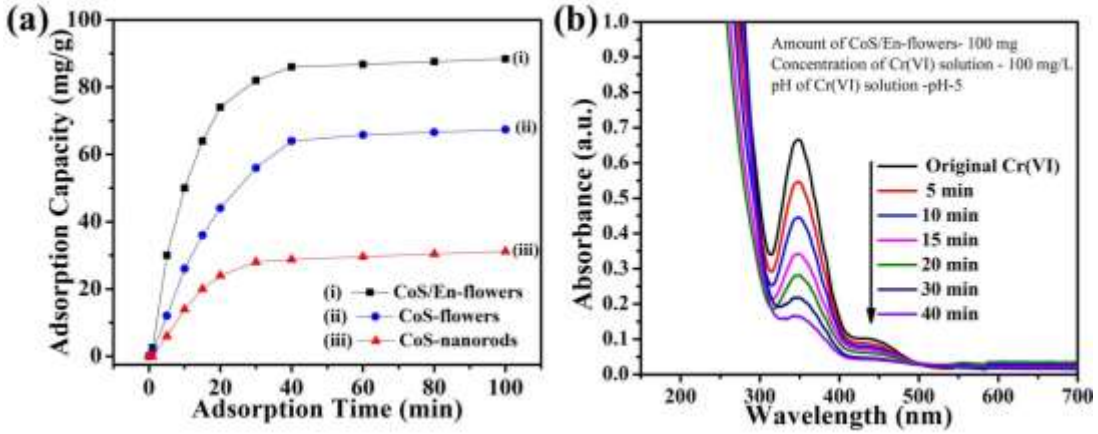

Figure 3 (a) Cr(VI) adsorption performances on (i) CoS/En-nanoflowers, (ii) CoS-nanoflowers, (iii) CoS-nanorods at pH 5, (b) time dependent UV-Vis absorption spectra of Cr(VI) adsorption over CoS/En-nanoflowers at pH 5

The effect of pH strongly influences on the removal efficiency of Cr(VI) over adsorbents. The major Cr(VI) species exists mainly as $Cr_2O_7^{2-}$ and $HCrO_4^-$ in low pH solution, and were mainly in the form of CrO_4^{2-} in natural aqueous solution. The variation of solution pH may not only cause the change in protonation degree of the amine groups grafted on the CoS surface but also can change the forms of Cr(VI) ions in water (Pakade et al., 2019). The experiments on the effect of pH on the Cr(VI) adsorption over CoS/En-nanoflowers were conducted. The removal of Cr(VI) ions decreased with increase in pH. It can be found that the maximum adsorption capacity was 90.8 mg/g and 87.7 mg/g in pH 2 and pH 5 aqueous solutions within 40 min. Conversely, at pH 8, much lower amounts of Cr(VI) (58.30 mg/g) were adsorbed on the CoS/En-nanoflowers under similar experimental conditions. The above investigations on the adsorption performance of CoS/En-nanoflowers found that the electrostatic interaction played a vital role in capturing negatively charged Cr(VI). To prove the interaction between the CoS/En-nanoflowers and the Cr(VI), the Zeta potential measurements over CoS/En-nanoflowers before and after adsorption were performed at different pHs. The surface charges of CoS/En-nanoflowers were revealed by Zeta potential as tabulated in Table (1). It can be seen that the surface of CoS/En-nanoflowers had positive charges when pH was less than 6 that was due to the fact that amine group ($–NH_2$) created more active sites on the CoS surface for H^+ ions of the solution at low pH. So, the coverage of H^+ ions tended to give the positive charge surface of amine grafted CoS showing the positive values of +8.8 mV and +6.5 mV at pH 2 and 5 before adsorption. The increased positive charges on the surface were conducive to the adsorption of negatively charged Cr(VI) at low pH. The negatively charged Cr(VI) ions covered on the surface of CoS/En-nanoflowers showing the changes in surface charges after adsorption. Therefore, the surface charge of CoS/En-nanoflowers was distinctly

changed to negative charges (–13.2 mV and –10.8 mV) at pH 2 and 5 after adsorption performances. This was attributed to the fact that, the electrostatic attraction between the Cr(VI) (e.g., $Cr_2O_7^{2-}$ and $HCrO_4^-$) and the amine functionalized CoS/En nanoflowers was taken, resulting in a dramatic enhancement of the adsorption capacity. However, at pH 8, the potential of CoS/En-nanoflowers reached the negative value of –16.8 mV and –18.5 mV before and after adsorption. The concentration of ^-OH ions in the alkali solution had a tendency to repulse $–NH_2$ group of the amine grafted CoS surface resulting in more negative charges. There was the repulsion force between the negatively charged surface of CoS/En-nanoflowers and the Cr(VI) (e.g., CrO_4^{-2}) at pH 8 showing less amount of Cr(VI) adsorption.

Table (1) Zeta Potential of CoS/En-Nanoflowers at Different pH Values Before and After Adsorption

pH	Surface Charge (mV)	
	Before Adsorption	After Adsorption
2	+8.8	–13.2
5	+6.5	–10.8
8	–16.8	–18.5

Above observation revealed that the adsorption of Cr(VI) over CoS/En-nanoflowers was obviously described as the electrostatic attraction between the positive charge amine groups on the surface of adsorbent and the negative charge Cr(VI). On the other hand, according to the theory of hard and soft acid-base (HSAB), Cr (VI) is a hard acid and easy to form a stable complex with a hard alkali like amine and the interaction between Cr(VI) and amine has a high complexation rate. So, CoS/En-nanoflowers exhibited a high adsorption toward Cr(VI). The synthesis route of CoS/En-nanoflowers and tentative adsorption mechanism of Cr(VI) on CoS/En-nanoflowers is illustrated in Figure 4.

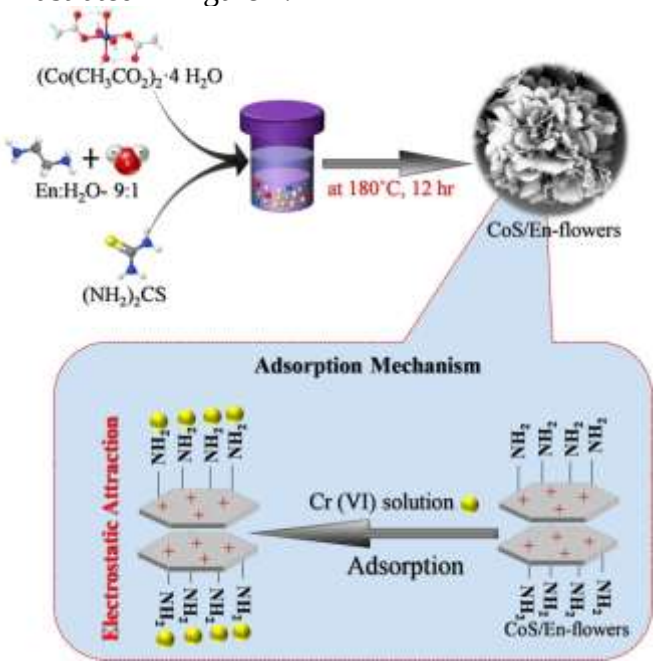

Figure 4 Schematic illustration of processing steps of CoS/En-flowers adsorbent and mechanism of Cr(VI) ions adsorption on amine functionalized CoS surface

Conclusion

In summary, inorganic-organic hybrid peony flower-like CoS nanosheets could be used as a nanoadsorbent for the removal of toxic Cr(VI) from aqueous liquid. CoS/En-nanoflowers exhibited a high adsorption efficiency and fast adsorption rate at pH 5 compared to that of its counterparts. The maximum adsorption capacity of the CoS/En-nanoflowers was found to be 87.7 mg/g within 40 min. Based on the zeta potential results at different pH, the adsorption mechanism investigation described that the main driving force for capturing Cr(VI) was the electrostatic interaction between the surface of adsorbent and Cr(VI).

Acknowledgements

This work was supported by the National Natural Science Foundation of China (Grant Nos. 51173033, 51572060, 51502062) and Excellent Youth Foundation of Heilongjiang Scientific Committee (No. JC2015010).

References

Gordillo, A. H., F. Tzompantzi, and R. Gomez, (2012) "Enhanced Photoreduction of Cr(VI) using ZnS(en)0.5 Hybrid Semiconductor" *Catalysis Communications*, Netherlands, vol. 19, pp.51-55.

Gupta, A., V. Sharma, K. Sharma, V. Kumar, S. Choudhary, P. Mankotia, B. Kumar, H. Mishra, A. Moulick, A. Ekielski, and P. K. Mishra, (2021) "A review of Adsorbents for Heavy Metal Decontamination: Growing Approach to Wastewater Treatment" *Materials (Basel)*, United Kingdom, vol. 14, pp.1-45.

Hunyaid, D., E. Majzik, J. Matyasi, J. Balla, A. Domjan, A. Szegedi, and I. M. Szilayi, (2017) "WO3–EDA Hybrid Nanoplates and Nanowires: Synthesis, Characterization, Formation Mechanism and Thermal Decomposition" *RSC Advance*, United Kingdom, vol. 7, pp.46726-46737.

Kang, H. J., and J. H. Kim, (2017) "Utilization of a ZnS(en)0.5 Photocatalyst Hybridized with a CdS Component for Solar Energy Conversion to Hydrogen" *Power Technology*, United Kingdom, vol. 28, pp. 2438-2444.

Liu, Y. W., H. Cheng, M. J. Lyu, S. J. Fan, Q. H. Liu, and W. H. Zhang, (2014) "Low Overpotential in Vacancy-Rich Ultrathin CoSe2 Nanosheets for Water Oxidation" *Journal of The American Chemical Society*, United States, vol. 136, pp.15670-15675.

Manyangadze, M., N. H. M. Chikuruwo, T. B. Narsaiah, C. S. Chakra, M. Radhakumari, and G. Danha, (2020) "Enhancing Adsorption Capacity of Nano-Adsorbents via Surface Modification: A Review" *South African Journal of Chemical Engineering*, Netherlands, vol 31, pp.25-32.

Ma, T., F. Zhou, T. W. Zhang, H. B. Yao, T. Y. Fu, Z. L. Yu, L. L. Li, and S. H. Yu, (2017) "Large-Scale Syntheses of Zinc. Sulfide. (Diethylenetriamine)0.5 Hybrids as Precursor for Sulfur Nanocomposites Cathodes" *Angewandte Chemie International Edition*, United Kingdom, vol 56, pp.11836-11840.

Pakade, V. E., N. T. Tavengwa, and L. M. Madikizela, (2019) "Recent Advances in Hexavalent Chromium Removal from Aqueous Solutions by Adsorptive Methods" *RSC Advances*, United Kingdom, vol. 9, pp. 26142–26164

Wu, X., R. Xu, R. J. Zhu, R. Wu, and B. Zhang, (2015) "Converting 2D Inorganic-Organic ZnSe-DETA Hybrid Nanosheets into 3D Hierarchical Nanosheets based ZnSe Microspheres with Enhanced Visible-Light-Driven Photocatalytic Performances" *Nanoscale*, United Kingdom, vol. 7, pp. 9752-9759.

Yein, W. T., Q. Wang, J. Z. Wu, X. H. Wu, (2018) "Converting CoS-TEA Hybrid Compound to CoS Defective Ultrathin Nanosheets and Their Enhanced Photocatalytic Property" *Journal of Molecular Liquids*, Netherlands, vol. 268, pp. 273-283.

DEVELOPMENT OF A NOVEL MATERIAL MONTMORILLONITE SUPPORTED BISMUTH VANADATE NANORODS HETEROSTRUCTURE WITH HIGHLY EFFICIENT PHOTOCATALYTIC ACTIVITY FOR THE TREATMENT OF DYE

Phyu Phyu Tun*

Abstract

Clay minerals supported semiconductor based photocatalysts have drawn wide attention for its economical, feasible and excellent reaction activity in photocatalytic process and for the detoxification of environmental pollutants. In this study, visible-light responsive montmorillonite (MMT) supported BiVO4 heterostructure photocatalyst having superb photocatalytic activity was synthesized via typical hydrothermal method. The optimum nanocomposite with 40 wt% BiVO4/MMT exhibited around 4.17 times higher photodecomposition efficiency for Methylene-blue (MB) over the as-synthesized bare BiVO4, respectively. The enhancement of photocatalytic activity could be credited to sound absorption of visible light spectrum due to the narrow bandgap of BiVO4, formation of additional active sites and enlarged specific surface area facilitated by MMT support, and strong interface interaction between BiVO4 and MMT which is confirmed by XPS analysis. The catalyst efficiently performed well over a wide pH scale range 3-10 in the photodecomposition process. Moreover, the possible photocatalytic mechanism of BiVO4/MMT nanocomposite towards the degradation progress was discussed and inferred that both •O2- and •OH were dominant reactive species. The study might provide insight in designing visible-light driven clay minerals supported semiconductor based photocatalyst system for the wastewater treatment and environmental remediation.

Keywords: Photocatalytic action; Bismuth vanadate; Montmorillonite; Methylene-blue

Introduction

The prominent increase in the application of antibiotics and organic pollutants, and their direct emissions have emerged as a big threat to human health and global environment (Huang et al. 2015). Various types of technologies have been introduced for the detoxification of these environmental pollutants, in which semiconductor-based photocatalysis is one of the most lucrative, green, excellent reaction activity, low cost and highly stable technology for the decomposition of environmental contaminants. Visible light responsive photocatalysis efficiently harnesses the visible light spectrum from the abundant solar energy and convert the pollutants into harmless products. The different approaches and tactics have been developed to attain this motive, like heterojunction structure formation, morphological modification, impurity doping, coupling semiconductor, and co-catalyst loading (Long, Cai, and Kisch 2008; Wang et al. 2012; Tsuzuki et al. 2019). In recent years, although varieties of semiconductor photocatalysts have been recognized for photocatalytic removal of antibiotics and organic dyes, visible light-responsive photocatalysis having excellent activity are still in demand.

Amongst several photocatalysts, bismuth-based semiconductor materials are one of the promising photocatalyst due to their proficient exploitation of visible light, nontoxicity and high chemical stability. Recently, Bismuth Vanadate ($BiVO_4$) has attracted wide attention, is a metal oxide n-type semiconductor, reveals superb photocatalytic activity under visible light spectrum and has relatively narrow band gap for monoclinic scheelite (2.4-2.5 eV) crystalline form. The foundation of such improved visible-light photo reactivity of $BiVO_4$ led by the transformation from a valence band created by Bi 6s or a Bi 6s and O 2p hybrid orbital to a V 3d conduction band and its narrower bandgap. Additionally, as compared to similar semiconductors (e.g. In_2O_3

* Department of Industrial Chemistry, West Yangon University, Myanmar

or TiO_2), the estimated effective masses of electrons and holes of $BiVO_4$ is lower, resulting in the principle of an enriched separation and migration course of electron/hole pairs (Zhao, Li, and Zou 2011; Park, McDonald, and Choi 2013; Walshetal.2009).

Recent researches have been reported that interlinking semiconductor with apposite substrate such as carbon spheres, graphene, fly ash chemosphere's, multi-walled carbon nanotube and clay minerals owns many enhancements in photocatalytic action; improvement in the activity of semiconductor potential, formation of more active sites, aversion particle aggregation, enhancement the adsorption ability of pollutants and larger specific surface area. Montmorillonite (MMT) is the 2:1 layer structure clay mineral member of smectite clay family, formed one octahedral Al-O (Mg-O) sheet sandwiching between two tetrahedral Si-O sheets Thus, by incorporating $BiVO_4$ on MMT surface as support can attain improved visible light responsive photocatalytic activities. MMT matrix boost in the formation of more active centers with large surface area, which inhibits in the loss of catalyst through recycling and recovery process which marks more effective in practical applications (Tun et al. 2020).

This study created a $BiVO_4$/MMT nanocomposite by hydrothermally embedding nanosized $BiVO_4$ on sheets of montmorillonite matrix. As a model pollutant, methylene blue (MB) was selected, and the photocatalytic effectiveness of a synthetic photocatalyst under visible-light irradiation on the removal of MB was examined. A series of photocatalysts prepared by varying the content of $BiVO_4$ and their influence on photocatalytic activity was analyzed, and some other influencing factors were also evaluated.

Materials and Methods

Materials

The pristine Montmorillonite K-10, bismuth (III) nitrate pentahydrate (Bi $(NO_3)_3.5H_2O$), ammonium metavanadate (NH_4VO_3), nitric acid (HNO_3), urea and ammonium hydroxide ($NH_3.H_2O$) were used and obtained from Suzhou, Jiangsu Province, China for this study. All chemicals were analytical grade and used without any additional purification. Distilled water and deionized water were used as required in the experiments.

Preparation of Photocatalyst

The $BiVO_4$/MMT photocatalysts were synthesized by hydrothermal method. Approximately 2 mmol of (Bi $(NO_3)_3.5H_2O$) was dissolved in 15 ml of HNO_3 solution, and titled as A. After magnetic stirring for 30 min, a white color solution was formed. Simultaneously, 2 mmol of NH_4VO_3 was dispersed in 15 ml of HNO_3 solution and continuously stirred for 30 min and titled as B. A bright yellow turbid solution was formed after mixing solution A and B. That solution was added to 2 g of MMT solution prepared by dissolving in 50 ml of distilled water and ultrasonicated for 1 h. Then, the mixture was vigorously stirred for 1 h at room temperature. Afterwards, 0.75 g urea was mixed to the combined solution and $NH_3.H_2O$ was used to adjust the solution pH to 7. The mixture was transferred into a Teflon-lined stainless-steel vessel and subsequently heated at 200 ºC for 6 h. After that, the resulting material was washed with distilled water and dried for 8 h in a hot air oven at 70 ºC. Next, as-prepared $BiVO_4$/MMT nanocomposite was calcined at 400 ºC for 3 h and the final $BiVO_4$/MMT photocatalyst was obtained. In order to investigate the photocatalytic performance, ratios of $BiVO_4$/MMT nanocomposites, 10%, 20%, 40%, and 60% $BiVO_4$/MMT were synthesized via the similar process by changing the amounts of $BiVO_4$, and denoted as BVO/M-10, BVO/M-20, BVO/M-40 and BVO/M-60 respectively. For comparison dedications, the pristine material $BiVO_4$, was prepared without adding MMT.

Characterization

The X-ray diffraction (XRD) analysis (DW-XRD-Y3000) was performed to analyze the crystal plane and phase structure. The morphology and size of as-synthesized photocatalysts were examined by Scanning Electron Microscope (SEM) (JSM 5610LV). As-prepared sample morphologies and microstructures were investigated by transmission electron microscopy (TEM) (HT7800) along with an energy-dispersive X-ray (EDX) at 200kV accelerating voltage. Fourier transform infrared (FT-IR) spectroscopy (EGA4000) was used to analyze the presence of structural units and functional groups. The X-ray photoelectron spectroscopy (XPS) (ULVAC-PHI 5000, Shimadzu.Japan) study was performed using an ESCALAB II XPS system with a source of monochromatic Mg Kα and a neutralizer of charge. The Brunauer-Emmett-Teller (BET) (Horiba SA-9600) was used to measure the surface area and porosity. The catalysts absorption surface was defined by the UV-visible spectrophotometer (UV2550, 200-800 nm, Shimadzu,Japan) (DRS).

Results and Discussion

XRD Analysis

Fig. 1 illustrates the XRD pattern of the prepared samples to observe the crystal plane and phase structure. The MMT matrix displayed strong typical diffraction peak at 2θ degree ~8º could be fixed to (0 0 1) crystal plane that demonstrates the interlayered-stacking structure characteristics in MMT (Djowe et al. 2013). The observed diffraction peaks at 2θ value 18.91, 28.89, 30.57, 34.55, 35.12, 39.81, 42.44, 46.76, 50.40 and 53.39 in the pattern of $BiVO_4$ which can be indexed as (0 1 1), (1 2 1), (0 4 0), (2 0 0), (0 0 2), (2 1 1), (0 5 1), (2 4 0), (2 0 2) and (1 6 1) crystal planes, respectively, are well matched with standard monoclinic $BiVO_4$ (JCDPS file no. 14-0688). The XRD pattern of all BVO/M nanocomposite samples unveiled the diffraction peaks of $BiVO_4$. Moreover, the diffraction peak d (0 0 1) intensity of BVO/M composite get weaken and moved towards the higher 2θ value signifying that $BiVO_4$ is well overloaded on the surface of MMT structure.

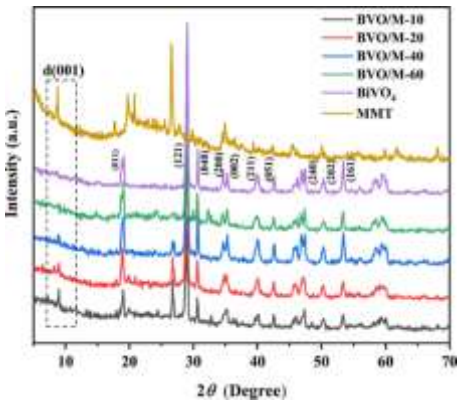

Figure.1. XRD patterns of MMT, pure $BiVO_4$ and a series of $BiVO_4$/MMT nanocomposites.

Morphological Interpretation

The surface morphological study of prepared nanocomposites was conducted by SEM and HR-TEM analysis. In MMT (Figure. 2a), layered platelet like structure comprising microscale flakes in aggregated morphology was witnessed while in pure $BiVO_4$ (Figure. 2b), leaf like with branches and trunks were observed. The $BiVO_4$ nanoparticles with average particle size 129 nm are dispersed over the surface and interspace of MMT. Upon incorporation of $BiVO_4$ on MMT surface, the trunks and branches of the $BiVO_4$ disappeared showing nanorod like

structure and partially crackdown layered structure of MMT were observed in the BVO/M-40 nanocomposite (Figure. 2c, d). Moreover, the HR-TEM images Figure. 2e, f reflect the lattice phase and crystallographic plane of BVO/M-40 nano-composite. The identified lattice spacing of 0.212 nm and 0.467 nm corresponds to the (0 5 1) and (0 1 1) crystallographic plane of $BiVO_4$ respectively, which is in good agreement with the XRD analysis. The energy dispersive X-ray analysis (Figure. 3) validates that as synthesized BVO/M-40 nanocomposite consists of Bi, O, V, Si, Al, Mg and Fe as dominant species which shows the sound evidence of the successful synthetization of $BiVO_4$/MMT nanocomposite.

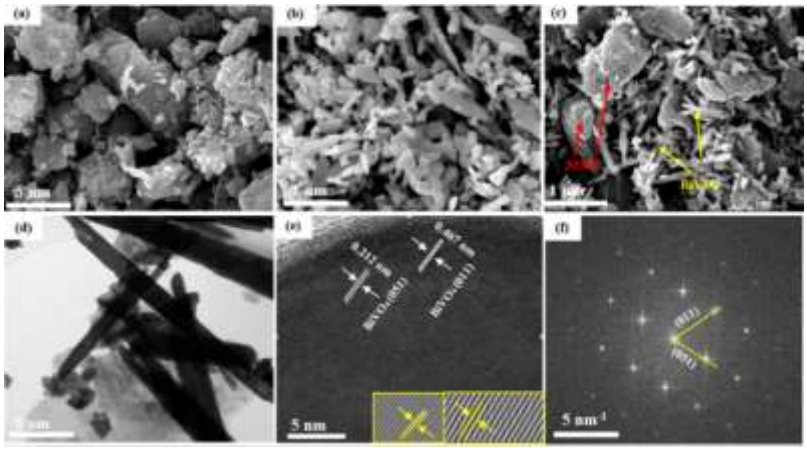

Figure.2. SEM images of (a) MMT, (b) $BiVO_4$, (c) $BiVO_4$/MMT, and (d) TEM images, (e) HRTEM image of $BiVO_4$/MMT, the insets are HRTEM image of lattices of $BiVO_4$, and (f) Selective area electron diffraction (SAED) showing well resolved lattice fringes of $BiVO_4$.

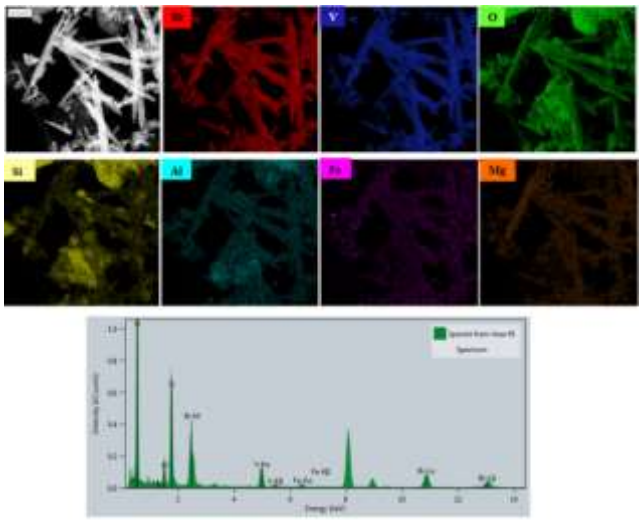

Figure.3. The HRTEM image of $BiVO_4$/MMT and the corresponding EDX mapping images

BET Analysis

N_2 adsorption examination was performed to determine the porosity and specific surface area of as-synthesized photocatalysts (Fig.4). The BJH curves appear to be type IV isotherms and display a H3 hysteresis loop, which indicates mesoporosity in the photocatalyst (2-50 nm) (Manova et al. 2010). The pore size distribution graph further ratified the mesoporous size distribution in the materials (inset in the Fig. 4) and have majority of the available pores smaller

than 10 nm. The BET surface area and pore volume of MMT were calculated to be about 248.01 m^2/g and 0.397 cm^3/g and the composite BVO/M-40 were approximately 247.02 m^2/g and 0.416 cm^3/g, respectively (Table 1). Upon overloading $BiVO_4$, the specific surface area of BVO/M-40 nanocomposite was maintained at high level with no drastic fall down. The BET surface area of BVO/M-40 nanocomposite is higher than $BiVO_4$ NPs (80.2 m^2/g) that suggests interlaminar configuration and sound adsorption ability of MMT which constructed extra active centers and enlarged specific surface area.

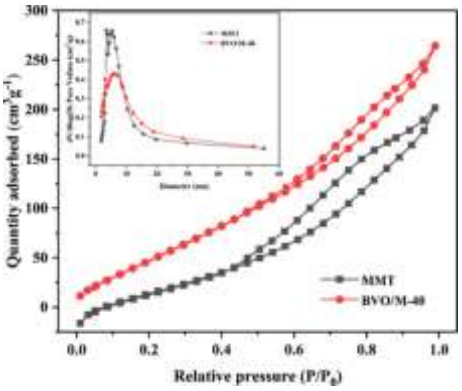

Figure 4. N_2 adsorption-desorption isotherms and the pore size distribution plot of montmorillonite and $BiVO_4$/MMT-40 nanocomposite.

Table 1 BET specific surface area and pore size data of the MMT and BVO/M-40 nanocomposite.

Sample	S_{BET} (m^2/g)	Pore Volume (cm^3/g)	Pore Size (nm)
Pure MMT	248.01	0.397	6.4
BVO-M/40 nanocomposite	247.02	0.416	6.7

UV- Visible DRS

Figure. 5a shows how the photo-absorption abilities of as-synthesized photocatalysts were investigated using UV-visible spectroscopy. The MMT matrix displayed 250-350 nm broadband absorption characteristics. These bands might be allocated to charge transferal band for the existing ions in the clay mineral octahedral layer (Rao and Mishra 2002).

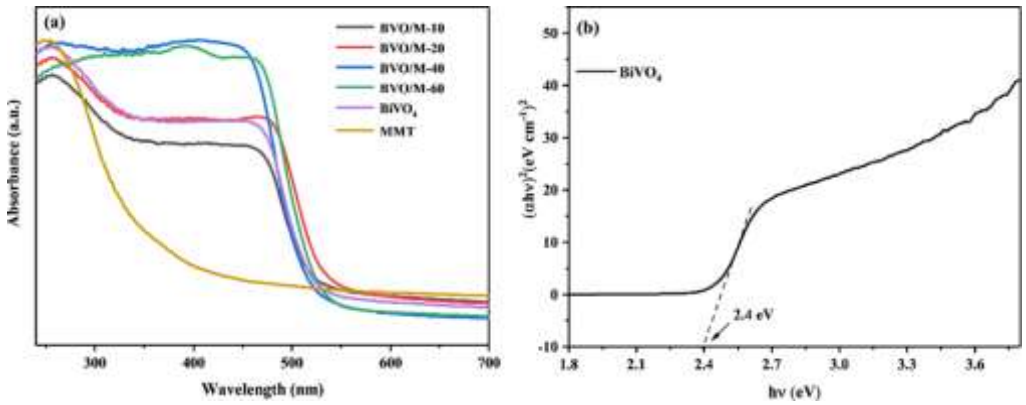

Figure.5. (a) UV-vis Diffuse reflectance spectra of MMT, $BiVO_4$, and a series of $BiVO_4$/MMT composites and (b) Plot of $(\alpha h\nu)^2$ versus photon energy hν for $BiVO_4$.

The configuration of Si-O tetrahedron silicate layers in the clay are not capable of absorbing light in the range of 200–700 nm except when the transition-metal ions or the silicate

structure exists in the exchanging interlayers. The pure $BiVO_4$ show absorption band edge ~530 nm and displayed fair visible-light absorption. All the $BiVO_4$/MMT photocatalysts exhibited the strong photonic absorbance in 350-550 nm region, signifying visible-light absorbance is because of the intrinsic band gap transition. The band gap (E_g) of $BiVO_4$ were measured by the Tauc-plot equation;

$$(\alpha h\nu)^2 = A(h\nu - E_g)^n$$

Where $h\nu$ is the energy of the strike photon (eV), α is the absorbance coefficient, E_g band gap (eV) and whereas A stands for a constant respectively. Here, the value of n is taken as 1 for direct transition of $BiVO_4$. The estimated band gap of $BiVO_4$ was 2.4 eV (Fig.5b). This analysis reflected that BVO/M-40 nanocomposite could proficiently exploit the visible light.

XPS –Analysis

The high-resolution XPS spectra analysis was conducted to inspect the oxidation state and surface composition of BVO/M nanocomposites. Fig. 6a shows the XPS survey spectra of BVO/M-40, which validated the existence of O, V, Bi, Al, Si and C, as key elements in the nanocomposite. In the spectrum of $BiVO_4$, Bi 4f display two peaks at binding energies 164.4 and 159.1 eV corresponding to the peaks of Bi $4f_{7/2}$ and Bi $4f_{5/2}$ in as Bi^{3+} state respectively. While BVO/M nanocomposite exhibited the peaks of Bi $4f_{7/2}$ and Bi $4f_{5/2}$ at binding energies 164.2 and 158.99 eV (Fig. 6b). The slight backward shift in binding energy of 0.2 eV along with decreased intensities in BVO/M nanocomposite reflects strong interaction. In the XPS spectra of Bi 4f, no other peaks were further detected, that inferred bismuth occurred in only +3 oxidation state. The XPS peaks of $BiVO_4$ could be fitted into two peaks of V $2p_{3/2}$ and V $2p_{1/2}$ at binding energies 516.63 and 524.17 eV respectively (Fig.6c), and can be ascribed to the surface V^{5+} species . In fig. 6d, the XPS of O 1s of the $BiVO_4$ fitted into two peaks at binding energies at 531.74 and 530.66 eV which could be correspond to the Bi-O and V-O bond in the sample respectively. The O 1s spectra of BVO/M-40 display three peaks at 532.20 and 531.60 and 529.80 eV, these peaks might be ascribed to the Bi-O bond, V-O bond and Metal-O bond on the surface of MMT in the BVO/M nanocomposite, respectively. In BVO/M composite, an additional form of oxygen was found and also the peaks slightly shifted and increased the binding energies as that of $BiVO_4$ which shows the strong interaction between $BiVO_4$ and MMT structure.

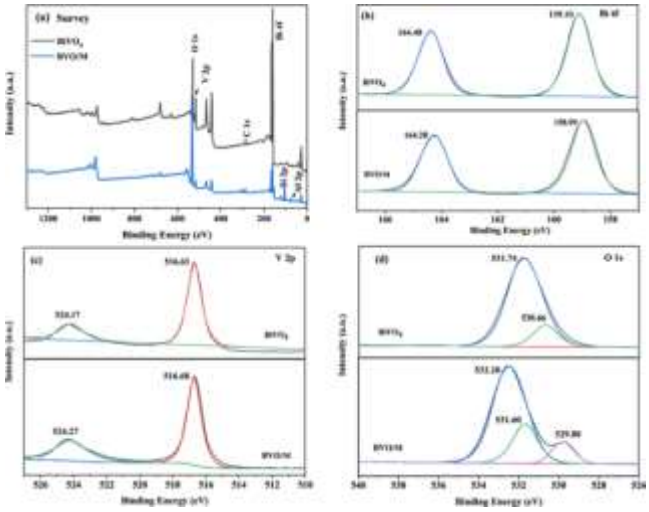

Figure.6. XPS spectra of $BiVO_4$ and $BiVO_4$/MMT-40 nanocomposite: (a) survey spectra, (b) Bi 4f spectra, (c) V 2p spectra, and (d) O 1s spectra.

FT-IR and Raman Analysis

The FT-IR spectra of as-synthesized BVO/M-40 and MMT are presented in Fig. 7a to analyze the presence of structural units and functional groups. Both samples display the distinctive absorption points of MMT in the FT-IR spectra. The spectrum of BVO/M-40 exhibits peaks at 3435, 1632, 1062, 740, 525 and 470 cm^{-1}, which are indexed to the characteristics of MMT. The bands at 3622 and 3437 cm^{-1} of MMT could be related to the characteristic stretching vibrations of –OH and adsorbed H_2O on the surface of clay, respectively. The band at 1637 cm^{-1} denotes the bending vibration and stretching of adsorbed water molecule. The tough robust absorption band at 1051 cm^{-1} is credited to Si–O stretching vibration. The absorption peaks of nanocomposite at 749 cm^{-1} and 810 cm^{-1} can be allotted to asymmetric and symmetric stretching/bending vibration of V–O (García-Pérez, Sepúlveda-Guzmán, and Martínez-de la Cruz 2012). The adsorption band at 525 cm^{-1} might display stretching vibration of Bi–O.

Additionally, Raman spectroscopy analysis was also conducted to further probe the structural vibration and bonding in metal-oxide group. Fig. 7b depicts the Raman spectra of MMT, pure $BiVO_4$ and BVO/M-40 nanocomposite. The Raman spectra of $BiVO_4$ exhibits six distinctive observable vibrational band peaks at 216, 331, 371, 644, 710 and 834 cm^{-1} that are correlated to vibrational characteristics of the VO_4 tetrahedron (Sandhya Kumari et al. 2013). The strong Raman band at 834 cm^{-1} was ascribed to the shorter symmetric V–O stretching band and weak peaks at 710 and 644 cm^{-1} could be attributed to the long and short asymmetric V–O stretching bands respectively. The symmetric and asymmetric bending bands of VO_4 tetrahedron appeared at 371 and 331 cm^{-1} respectively (Sandhya Kumari et al. 2013), and while peak at 216 cm^{-1} detected by external modes. The V–O stretching vibration band has moved to lower frequency at 828 cm^{-1} and considerably declined in BVO/M-40 nanocomposite with respect to pure $BiVO_4$ toughest peak at 834 cm^{-1}. This reflects strong synergetic interaction between MMT and tetrahedron VO_4 structure of $BiVO_4$.

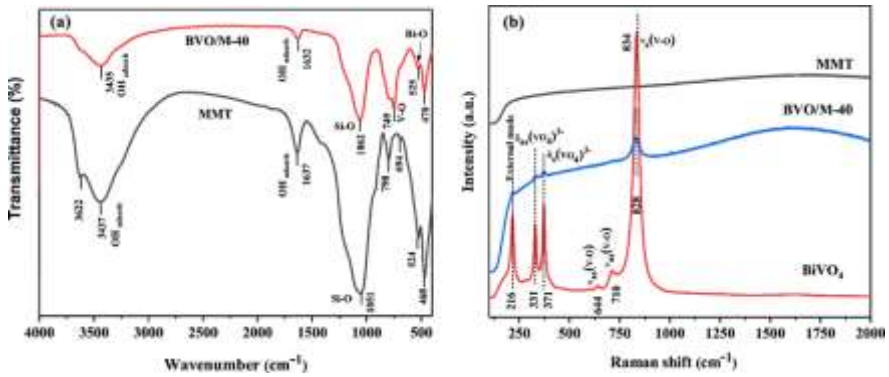

Figure.7. (a) FT-IR spectra of pristine MMT and $BiVO_4$/MMT-40 nanocomposite and (b) Raman spectra of pure BiVO4 and BiVO4/MMT-40 nanocomposite.

Photocatalytic performance for the degradation of MB and influencing factors

The photocatalytic efficiencies of as-prepared catalysts were further investigated through degrading MB (10 mg/L) under visible-light illumination (Fig. 8a). The photo-degradation of MB was virtually completely disregarded during blank test and the BVO/M-40 nanocomposite revealed fair adsorption capacity in the dark state. The photocatalytic efficiency of BVO/M-40 nanocomposite was highest among all other catalyst samples, where complete degradation of MB occurs in 30 min. Furthermore, the photocatalytic degradation of MB unveiled pseudo first order

reaction kinetics (ln (C_t/C_0) = kt). As depicted in Fig.8b BVO/M-40 nanocomposite displays utmost photodecomposition and has highest apparent rate constant k towards MB and pursue the order: BVO/M-40 (0.096 min^{-1}) > BVO/M-60 (0.044 min^{-1}) > BVO/M-20 (0.033 min^{-1}) > BVO/M-10 (0.028 min^{-1}) > $BiVO_4$ (0.023 min^{-1}) > MMT (0.008 min^{-1}).

The influence of pH was inspected on photodegradation efficiency of MB by BVO/M-40 nanocomposite photocatalyst with adjusting pH scale range 3-10. As displayed in graph Fig. 9a, the photo discoloration efficiency on MB steadily decrease from 100% to 75% while adjusting elevation of pH scale 3 to 10. The optimum discoloration efficiency was at pH 3 and all the experiments were performed at pH 3 for MB. The reaction activity of as prepared BVO/M-40 photocatalyst is suitable for wide pH range.

Additionally, the photocatalytic activity of BVO/M-40 was further assessed by considering different initial concentration of MB. As demonstrated in Fig. 9b, the photodegradation proficiency consecutively drop on increasing its concentration from 10 mg/L to 50 mg/L. However, the discoloration efficiencies of MB were still above 65%. The reduction might be due to hindrance in light absorption by the catalyst caused by excess MB molecules which restraint in the formation of oxidative agent. The impression of catalyst dosages in photocatalytic decomposition of MB were also evaluated (Fig. 9c). The minimal fall down in photo discoloration efficiency was observed while increasing the concentration of catalyst 0.5 g/L to 1.0 g/L. It might be due to reaction turbidity in the system.

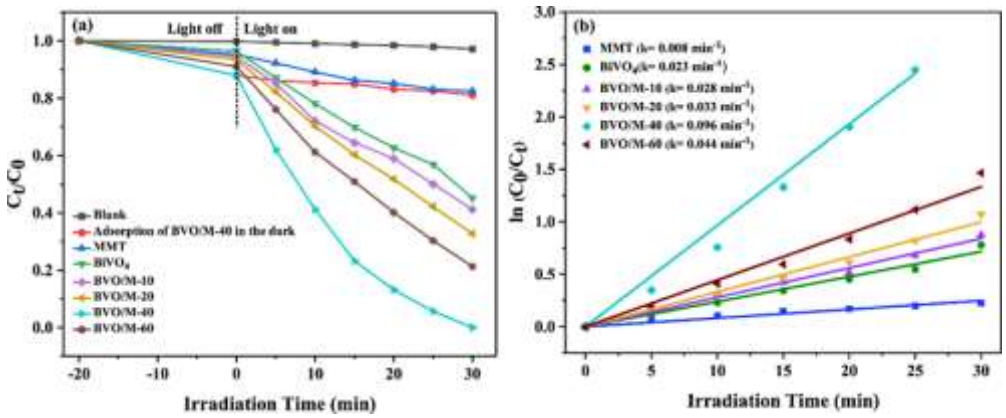

Figure.8. (a) Degradation efficiency of MB (20 mg/L), and (b) the relationship between ln (C_0/C_t) and irradiation time with pseudo first order reaction rate constant.

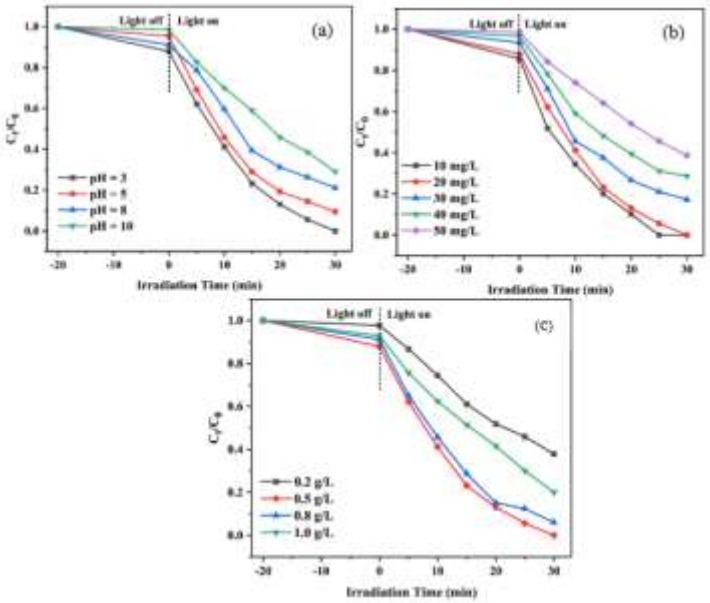

Figure.9. (a) Effect of pH, and (b) Effect of initial MB concentration, and (c) Effect of catalyst dosage on the degradation of MB in photocatalytic process.

Photocatalytic Mechanism

The mechanism for the extremely improved photocatalytic scheme can be put forward in Fig. 10 on the grounds of the above-mentioned experimental study. As BVO/M-40 nanocomposite was irradiated under visible light, $BiVO_4$ NPs get photo-excited producing e^-/h^+ pairs by forming holes in valence band (VB) and electrons in conduction band (CB). The excited electrons may reduce the O_2 molecules adsorbed on the surface of BVO/M into anionic superoxide radical ($^\bullet O_2^-$) that can oxidize the contaminants as well as parts of $^\bullet O_2^-$ can combine with H^+ to generate H_2O_2 which further undergoes to reductive decomposition in the reaction system to produce hydroxide radicals ($^\bullet OH$). As formed $^\bullet OH$ and $^\bullet O_2^-$ radicals are strong oxidizing agents to decompose MB directly. In addition, some amount of photoinduced holes in the VB of $BiVO_4$ oxidizes the H_2O/OH^- in the reaction system by interfacial charge transfer to form hydroxide radicals ($^\bullet OH$) radicals. On the other side, the photo-excited electrons in the CB of $BiVO_4$ can also be trapped by Al atoms present in the montmorillonite structure. In fact, MMT matrix performs like electron acceptors because of the existence of Lewis acid (Al atoms). The trapped electrons from these aluminum sites then moved to the adsorbed O_2 molecules in the solutions. As a consequence, the recombination reaction of photogenerated e^-/h^+ pairs by hopping mechanism of electrons are delayed. Moreover, MMT enables many active centers for the adsorption of organic molecules, averts the aggregation of photocatalyst and its support reduces the high turbidity of the solution. It also provides easiness during recovery and separation process of photocatalyst.

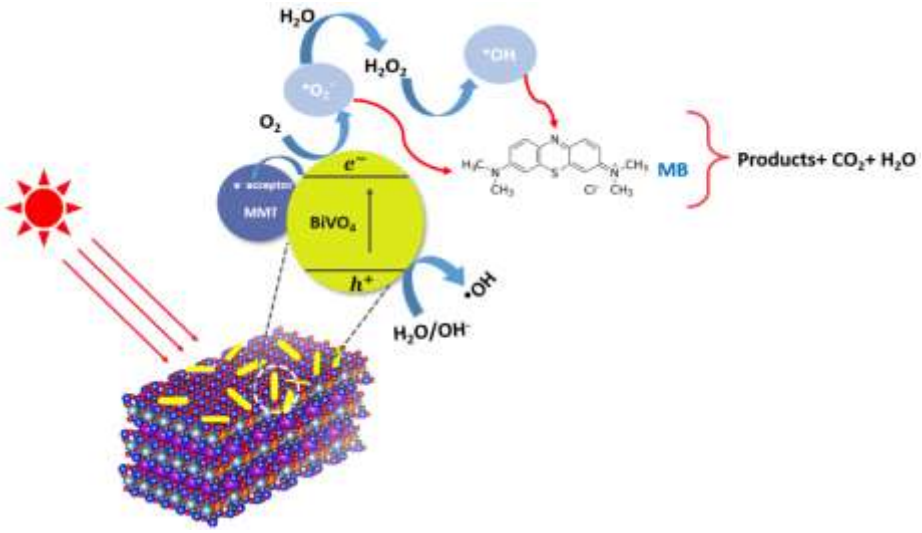

Figure.10. Schametic depiction of proposed mechanism for eletron-hole separation of $BiVO_4$/MMT composite under visible light irradiation.

Conclusion

A series of $BiVO_4$/MMT nanocomposites were developed by a one-step hydrothermal process, a competitive synthesis of novel and active photocatalysts were employed to decompose the dye MB as a model of evolving contaminant. The results confirmed that optimized BVO/M-40 nanocomposite exhibited superior photocatalytic activity than that of $BiVO_4$, MMT and BVO/M photocatalyst, which were clarified by the characterization of the as-prepared specimens through conducting XRD, HRTEM, XPS, BET, FT-IR, and UV-Vis DRS analysis. The efficient visible-light harvesting and interface interaction between the $BiVO_4$ and MMT synergism to enhance the photocatalytic performance that were revealed by UV-Vis DRS and XPS analysis. BET exploration suggested MMT support facilitates in the creations of more active centres and enlarged surface area for photocatalytic action. The catalyst unveiled a high-quality photocatalytic action over a broad pH 3-10 range. This is the promising properties for the as-synthesized photocatalyst for the decontamination of the wastewater toxins and also insights to design effective photocatalysts for the environmental remediation.

Acknowledgements

The author wishes to express her sincere gratitude to the Chinese Scholarship Council (CSC) for providing funding for her PhD grant.

The author would like to acknowledge Dr. Khin Thida, Rector of West Yangon University. I am very grateful to Professor Dr. Thin Thin Khaing, Head of the Department of Industrial Chemistry, West Yangon University, for giving me permission to present this research paper at Research Paper Reading Session organized by Myanmar Academy of Arts and Science.

I express my deepest gratitude to my esteemed research supervisor Professor Dr. Zhang Gaoke, School of Resources and Environmental Engineering, Wuhan University of Technology, for his continuous support, encouragement, and insightful guidance.

References

Djowe, Antoine Tiya, Samuel Laminsi, Daniel Njopwouo, Elie Acayanka, and Eric M. Gaigneaux. 2013. 'Surface Modification of Smectite Clay Induced by Non-thermal Gliding Arc Plasma at Atmospheric Pressure', Plasma Chemistry and Plasma Processing, 33: 707-23.

García-Pérez, U. M., S. Sepúlveda-Guzmán, and A. Martínez-de la Cruz. 2012. 'Nanostructured BiVO4 photocatalysts synthesized via a polymer-assisted coprecipitation method and their photocatalytic properties under visible-light irradiation', Solid State Sciences, 14: 293-98.

Huang, Manhong, Fangfang Qi, Jue Wang, Qi Xu, and Li Lin. 2015. 'Changes of bacterial diversity and tetracycline resistance in sludge from AAO systems upon exposure to tetracycline pressure', Journal of Hazardous materials, 298: 303-09.

Liu, Yuxi, Hongxing Dai, Jiguang Deng, Lei Zhang, and Chak Tong Au. 2012. 'Three-dimensional ordered macroporous bismuth vanadates: PMMA-templating fabrication and excellent visible light-driven photocatalytic performance for phenol degradation', Nanoscale, 4: 2317-25.

Long, Cai, and Horst Kisch. 2008. 'Visible Light Induced Photoelectrochemical Properties of n-BiVO4 and n-BiVO4/p-Co3O4', The Journal of Physical Chemistry C, 112: 548-54.

Manova, Elina, Pilar Aranda, M. Angeles Martín-Luengo, Sadok Letaïef, and Eduardo Ruiz-Hitzky. 2010. 'New titania-clay nanostructured porous materials', Microporous and Mesoporous Materials, 131: 252-60.

Park, Y., K. J. McDonald, and K. S. Choi. 2013. 'Progress in bismuth vanadate photoanodes for use in solar water oxidation', Chemical Society Reviews, 42: 2321-37.

Rao, G. Ranga, and Braja Gopal Mishra. 2002. 'Mixed Al/Ce oxide pillaring of montmorillonite: XRD and UV-VIS diffuse reflectance study', Reaction Kinetics and Catalysis Letters, 75: 251-58.

Sandhya Kumari, L., P. Prabhakar Rao, A. Narayana Pillai Radhakrishnan, Vineetha James, S. Sameera, and Peter Koshy. 2013. 'Brilliant yellow color and enhanced NIR reflectance of monoclinic BiVO4 through distortion in VO4− tetrahedra', Solar Energy Materials and Solar Cells, 112: 134-43.

Tsuzuki, Takuya, Rongliang He, Aaron Dodd, and Martin Saunders. 2019. 'Challenges in Determining the Location of Dopants, to Study the Influence of Metal Doping on the Photocatalytic Activities of ZnO Nanopowders', Nanomaterials, 9.

Tun, Phyu Phyu, Junting Wang, Thinn Thinn Khaing, Xiaoyong Wu, Gaoke Zhang, Journal of Alloys and Compounds. 2020. 'Fabrication of functionalized plasmonic Ag loaded Bi2O3/montmorillonite nanocomposites for efficient photocatalytic removal of antibiotics and organic dyes', 818: 152836.

Walsh, Aron, Yanfa Yan, Muhammad N. Huda, Mowafak M. Al-Jassim, and Su-Huai Wei. 2009. 'ChemInform Abstract: Band Edge Electronic Structure of BiVO4: Elucidating the Role of the Bi s and V d Orbitals', ChemInform, 40.

Wang, Donge, Rengui Li, Jian Zhu, Jingying Shi, Jingfeng Han, Xu Zong, and Can Li. 2012. 'Photocatalytic Water Oxidation on BiVO4 with the Electrocatalyst as an Oxidation Cocatalyst: Essential Relations between Electrocatalyst and Photocatalyst', The Journal of Physical Chemistry C, 116: 5082-89.

Zhao, Z., Z. Li, and Z. Zou. 2011. 'Electronic structure and optical properties of monoclinic clinobisvanite BiVO4', Physical Chemistry Chemical Physics, 13: 4746-53.

BIOENERGY STUDY ON GRASS (*Pennisetum Hordeorides* Lam.)

Nay Yee Nyunt Oo[1], Win Thi Yein[2], Soe Soe Than[3]

Abstract

Hydrothermal treatment is one of the environmentally friendly methods for the conversion of biomass into valuable end products such as biofuel, hydrochar and biochar. In this research work, hydrothermal treatment of grass (*Pennisetum hordeorides* Lam.) was carried out at 100°C to 140 ˚C for 20 min to 40 min as the preliminary step to provide bioenergy products such as bioethanol and biochar. The maximum reducing sugar content of liquid fraction, 43.46 mg/mL was achieved after hydrothermal treatment at 110 ˚C for 30 min and further yeast fermentation of reducing sugar was accomplished to obtain 2% by volume of bioethanol. Carbonization of solid residue after hydrothermal treatment was conducted for biochar at different temperatures (300 °C, 400 °C and 500 °C) and times (0.5 hr, 1 hr, 2 hr, 4 hr, 8 hr). Characterization of grass such as cellulose, hemicellulose, and lignin contents before and after hydrothermal treatment was conducted. High heating value (HHV) and energy densification were evaluated for energy values of biochar. The maximum HHV (26.78 MJ/kg) and energy densification (1.28) had resulted for the carbonization temperature of 500 °C for 2 hr. The changes in surface morphology and functional groups in raw grass, HTG and biochar were observed by Scanning Electron Microscopy (SEM) and by Fourier Transform Infrared Spectroscopy (FTIR).

Keywords: hydrothermal treatment, bioethanol, carbonization, biochar

Introduction

Transformation of biomass to energy is a sustainable solution to reduce greenhouse gas emissions and the secondary as well as tertiary biomass can be substituted for fossil fuels. Bioenergy is related to the process heat (thermal energy used for residential, commercial, or industrial applications), biopower (conversion of biomass into electric power intended to stationary application), and biofuels (chemicals derived from biomass designated for transportation purpose) (Brown, 2014). Bioethanol and biochar are regarded as the bioenergy providing substances with the significant characteristics of structural composition, rich in carbon and renewable content (Kandasamy et al., 2021). Several technologies to convert biomass into useful products are mainly categorized to thermochemical (non-catalytic) route and biological (catalytic) route (Garba, 2020).

Thermochemical biomass conversion processes involve combustion (heating the biomass in the presence of oxygen), gasification (partial biomass oxidation at 700 ˚C - 900 ˚C), pyrolysis (heating the biomass at 300 ˚C - 900 ˚C under the absence of oxygen), torrefaction (low-temperature pyrolysis) and carbonization (two types - flash and hydrothermal processing) (Kumar et al., 2020). Hydrothermal treatment has been extensively studied as a first step for a biorefinery due to its environmentally friendly advantages over other treatments (del Río et al., 2020). This co-production of high value-added products and bioethanol allows the reduction of capital costs involved in the lignocellulosic biomass processing (Du et al., 2020, Aristiz´abal-Marulanda & Cardona, 2021).

The present study intended to explore the potential bioenergy of grass (*Pennisetum hordeorides* Lam.). Bioethanol and biochar were prepared by further processing of liquid and solid portions resulting from hydrothermal treatment of grass stems. Fermentation of liquid portion and carbonization of solid residue were carried out for bioethanol and biochar, respectively. Scanning Electron Microscopy (SEM) and Fourier Transform Infrared (FTIR) analyses of grass stems before and after hydrothermal treatment and biochar were conducted for the surface morphology and

[1,2] Department of Industrial Chemistry, University of Yangon

[3] Department of Industrial Chemistry, University of Yangon

functional groups present. Proximate composition of grass stems before and after hydrothermal treatment, strength of bioethanol, and high heating value (HHV) of biochar were analysed.

Materials and Methods

Raw Materials

Grasses (*Pennisetum hordeorides* Lam.) as shown in Figure (1) were harvested from the campus of East Yangon University, Yangon Region. *Saccharomyces cerevisiae* – baker's yeast was purchased from Supershell Chemical Dealer, 27th street, Pabedan Township.

Figure (1) Grass (*Pennisetum hordeorides* Lam.)

Methods

Processing of Bioethanol and Biochar

Grass stems were cleaned, and chopped into small pieces and then air-dried for 2 hr until the moisture content was 10-12%. Hydrothermal treatment of crushed grass stems was conducted in a 100 mL, polytetrafluoroethylene (PTFE) lined stainless steel synthesis reactor. The amount of biomass and distilled water were added into the reactor with solid to liquid ratio of 1:9 (w/v). Then the reactor was securely sealed and placed in a hot air oven. The treatment was conducted at various temperatures of 100 – 140 ºC and heating times (20 - 40 min). After the hydrothermal treatment was completed, the reactor was cooled and the broth was subjected to vacuum filtration for the separation of liquid and solid residue. Fermentation of liquid fraction was carried out using *Saccharomyces cerevisiae* – baker's yeast for production of bioethanol. pH of the liquid portion was maintained at pH 5.6 and 3 g/L of yeast was used in fermentation. After fermentation, bioethanol was separated by distillation. The strength of bioethanol was measured by portable alcohol meter (ATAGO AL-21 Alpha Handheld Alcohol Refractometer, 0 to 21%). Meanwhile, the solid residue was carbonized in a muffle furnace at various temperatures of 300 °C, 400 °C and 500 °C for 0.5 hr, 1 hr, 2 hr, 4 hr, and 8 hr, respectively. The resulting solid residue biochar was washed with water for several times and dried.

Determination of Reducing Sugar Content of Liquid Fraction during Hydrothermal Process

Reducing sugar content of liquid fraction resulting from hydrothermal treatment was determined by Lane and Eynon's method (Pearson, 1976). The liquid was titrated with standard Fehling solutions A and B using methylene blue as indicator.

Characterization of Grass Before and After Hydrothermal Treatment

The air-dried biomass was pulverized in a grinder into -16 mesh size particles. Proximate composition such as extractive matter, lignin content, holocellulose, hemicellulose and cellulose content of grass before and after hydrothermal treatment was determined.

Determination of Extractive Matter

The procedure for determination of extractive matter was conducted according to the method of ISO 14453:2014. Extractive matter present in the samples was determined by carrying out solvent extraction with acetone in Soxhlet apparatus at 90˚C for 2 hr. The sample was taken out, dried and weighed.

Determination of Acid Insoluble Lignin

Acid insoluble lignin of the extractive free sample was determined based on the Klason Method. 72% H_2SO_4 was used for hydrolysis of biomass for lignin until complete hydrolysis was assured by further hydrolysis with 4% H_2SO_4. The solid residue was collected, dried and weighed for acid insoluble lignin.

Determination of Holocellulose, Hemicellulose and Cellulose Content

Holocellulose content in extractive free sample was determined by TAPPI T9-wd -75. Extractive free sample was hydrolyzed with a mixture of acetic acid and 80% sodium chlorite solution at 90˚C for 1 hr. The complete hydrolysis was assured by adding of a mixture of acetic acid and 80% sodium chlorite solution. The filtered residue was dried and weighed for holocellulose. Holocellulose obtained from above was further hydrolyzed with 17.5% sodium hydroxide solution. The residue was neutralized with 1M acetic acid to pH 7, dried and weighed for hemicellulose. Cellulose content can be calculated by subtracting hemicellulose content from the holocellulose content.

Characterization of Biochar

Volatile Matter content (VM), ash content and Fixed Carbon content (FC) were analyzed by ASTM-D1762-84 method for its high heating energy value and energy densification value.

Determination of Volatile Matter (VM)

Volatile matter was determined by igniting the sample in a muffle furnace at 850°C for 10 min. The weight loss was the amount of all volatile matter.

Determination of Ash Content

The dried sample was incinerated in a muffle furnace at 750 °C for 6 hr. The residue was weighed for ash content.

Determination of Fixed Carbon Content (FC)

The fixed carbon of samples was calculated by the subtraction of the sum of ash and volatile matter contents from 100.

Determination of High Heating Value (HHV)

The HHVs of samples were estimated using the following equation of Kieseler et al., 2013.

$$HHV\ (MJ/kg) = 0.4108FC + 0.1934VM - 0.02111Ash$$

Determination of Energy Densification

Energy densification was calculated with the ratio of HHV of biochar and HHV of biomass described by Fan et al., 2018.

Scanning Electron Microscopy (SEM) and Fourier Transform Infrared Spectroscopy (FTIR) Analyses

Changes in surface morphology and the functional group of raw grass, HTG and biochar were analyzed by Scanning Electron Microscopy (SEM) (EVO-18, ZEISS, Germany) and by Fourier Transform Infrared Spectroscopy (FTIR) (IR Tracer-100, SHIMADZU, Japan) at the Department of Chemistry, West Yangon University, Htantabin Township, Yangon Region.

Results and Discussion

The hydrothermal treatment of grass stem was conducted for the purpose of energy providing intermediate products by varying the treatment temperature and time. Figure (2) and Figure (3) show the effect of temperature and time on the reducing sugar content of liquid fraction. Maximum amount of reducing sugar, 43.46 mg/mL was obtained by the hydrothermal treatment at 110˚C for 30 min. Table (1) presents the proximate composition of grass stems before and after hydrothermal treatment. Cellulose and lignin contents in raw grass (*Pennisetum hordeorides* Lam.) were ranged to the similarity of those contents of switchgrass and mixed grass (27-35% cellulose, 12-21% hemicellulose, 15-20% lignin) cited in Williams et. al., (2017) whereas hemicelllulose content was different from that of the value mentioned in literature. High cellulose content represents the potential component for the conversion into biochar (Waliszewska et al., 2021). After hydrothermal treatment, degradation of biomass was proved by increase in lignin content of 23.12% and cellulose content of 23.98%, respectively in solid residue as shown in Table (1). Simultaneously, release of reducing sugar was observed in the liquid fraction with the evidence of decrease in hemicellulose content of 13.21% found in solid residue. Soluble fractions of cellulose and hemicellulose in liquid fraction may consist of six carbon sugars (hexose) and five carbon sugar (pentose). As a result, hexoses were fermented to ethanol and pentoses were resistant to fermentation that was processed by baker's yeast. A few microorganism strains were confirmed for fermentation of pentose sugars (Liu, 2005). The strength of bioethanol by yeast fermentation of liquid fraction resulting from hydrothermal treatment was found to be 2% by volume. This result could be compared with the conventional treatment method such as acid hydrolysis using concentrated sulphuric acid followed by yeast fermentation. 3.83 % by volume of bioethanol was achieved by conc: H_2SO_4 treatment (3.4% conc: H_2SO_4, at 100˚C for 86 min) in which 61.08 ± 7.84 mg/g of reducing sugar was resulted (Soe Soe Than, 2014). Harsh acid treatment of grass stem reached to release more reducing sugar that gave slightly higher strength of bioethanol when compared to novel method of hydrothermal treatment.

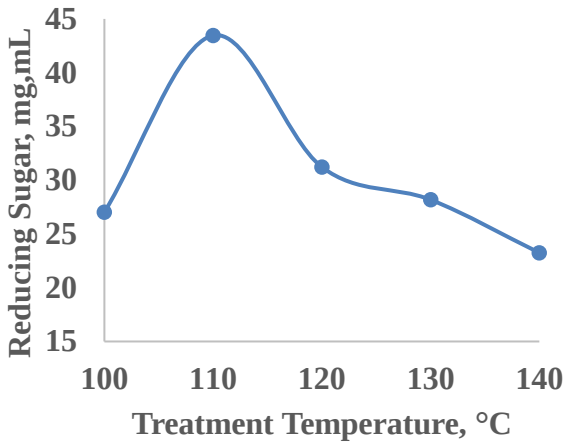

Figure (2) Effect of Treatment Temperature on Reducing Sugar Content

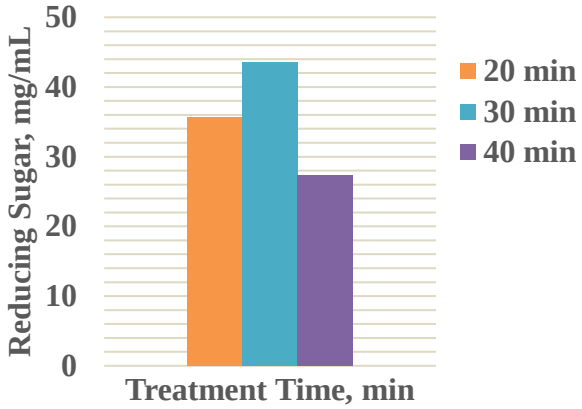

Figure (3) Effect of Treatment Time on Reducing Sugar Content

Table (1) Composition of Grass Before and After Hydrothermal Treatment

Composition (%)	Grass Stem (dry basis)	
	Raw grass	**Solid residue after hydrothermal treatment (HTG)**
Lignin	19.72	24.28
Holocellulose	60.7	65.15
Hemicellulose	27.18	23.59
Cellulose	33.53	41.57

Figures (4) and Figure (5) depict the effect of carbonization temperature and time on High Heating Value (HHV) of biochar obtained from cellulose and lignin rich residue after hydrothermal treatment (HTG). HHV can be supposed to the energy content of biomass which is an essential parameter for the assessment of a combustion system. HHV is determined, based on the results of proximate analysis of ash content, volatile matter content, and fixed carbon content. The highest result was observed at carbonization temperature of 500˚C for 2 hr. Thus, the higher temperature of carbonization from 300˚C - 500˚C would increase HHV from 22.57 MJ/kg to 26.78 MJ/kg for a residence time of 2 hr. The longer residence time (4 hr to 8 hr) caused slight decrease in HHV of biochar. It may be due to increase in ash content of biochar with longer carbonizing time. According to the experimental results, the increment of carbonization temperature (300-500˚C) for time (0.5 – 8 hr) was observed with gradually decrease in the amount of volatile matter and increase the ash content. When compared to HHV of raw grass, HTG, and biochar as shown in Figure (6), HHV of biochar was significantly large. It was due to increase in cellulose and lignin contents in solid residue by hydrothermal treatment.

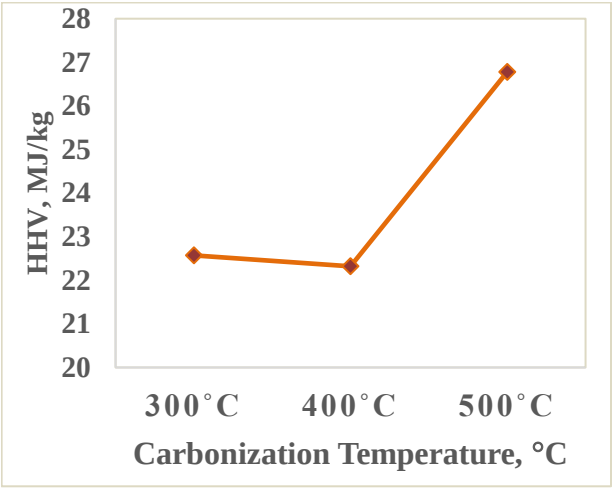

Figure (4) HHV of Biochar at Different Carbonization Temperature for 2hr

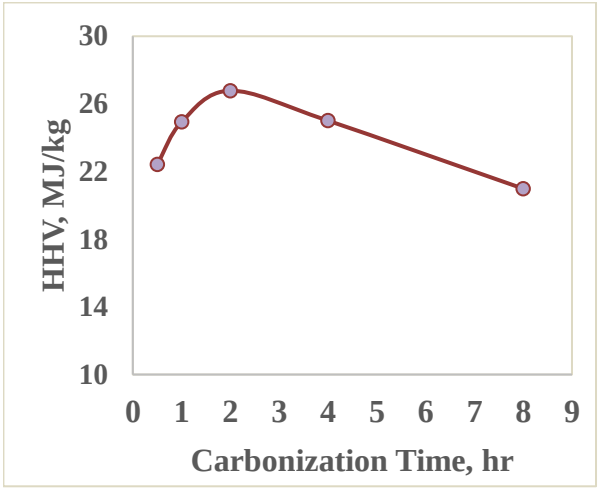

Figure (5) HHV of Biochar at Different Carbonization Time at 500˚C

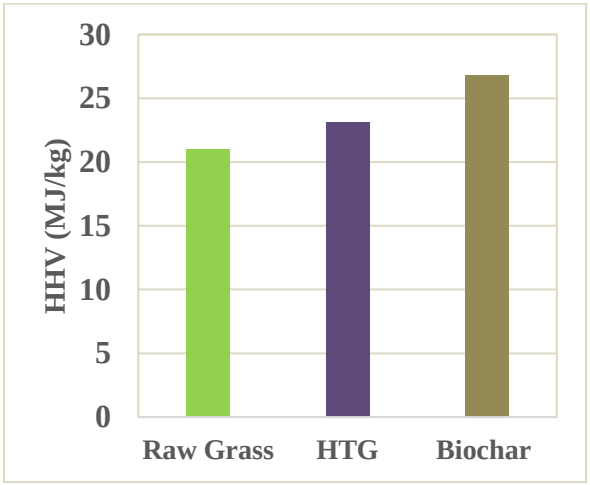

Figure (6) HHV of Raw Grass, HTG and Biochar

As can be seen in Figure (7), the highest energy densification was observed as 1.28 at the carbonization temperature of 500˚C for 2 hr. Zhang et al., (2015) and Liu et al., (2018) also stated that the conversion of biomass to biochar needs proper carbonization temperature and time. If the carbonization temperature and/or residence time is higher than the suitable carbonization condition, most of the organic compounds are susceptible to change into ash. On the other hand, biomass could not be completely converted to the volatile compounds and underwent decomposition of organic compounds. The observed results were consistent with the statement of Mäkelä et al., (2015). It has been reported that higher temperature led to increase the degradation of hemicellulose, cellulose, and lignin which was accompanied by decarboxylation of biomass components. Consequently, a desirable decrease in oxygen content of the solid enabled increasing energy densification in biomass. HHV and energy densification are important assessment to evaluate the success of biochar produced from biomass (Elaigwu and Greenway, 2019 and Fan et. al., 2018). The maximum amount of HHV and energy densification indicate the destruction of low energy chemical components with the production of high energy components.

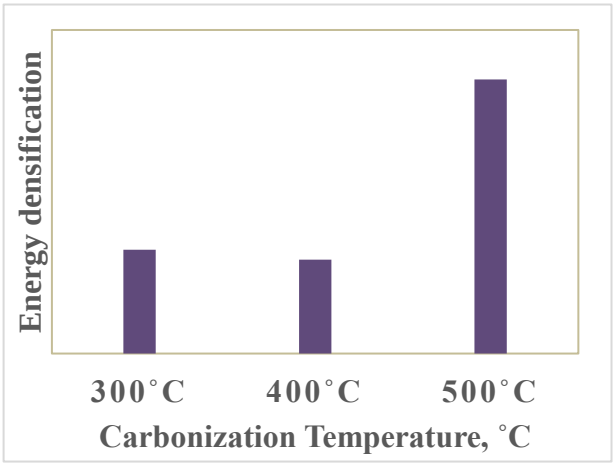

Figure (7) Energy Densification of Biochar

The surface morphology changes in raw grass, HTG and biochar were studied by Scanning Electron Microscopy (SEM). As shown in Figure (8), raw grass exhibited a smooth surface structure, but it was evident with fragmentation and fibrillation by the appearance of a higher number of droplets like structures in solid residue after hydrothermal treatment (HTG). After carbonization, the surface of biochar became rough and porous when compared with that of HTG after hydrothermal treatment. It may be due to the stresses gained by the hydrothermal treatment and carbonization. Yang et. al., (2015) and Nizamuddin, (2017) reported that the decomposition of hemicellulose, cellulose and lignin can attribute to the coarseness of the surface of the biomass. It may be associated with the removal of hemicellulose by hydrothermal treatment and the droplets observed on the surface of HTG could be due to the increase of some residues accompanied by lignin modification. Under the carbonization condition, the small pores and fragments were gradually formed on the surface of biochar because of the release of volatile matters. Moreover, the regular pore structures were found in biochar because elevated temperature and increased residence time enhanced the decomposition of the cellulose and hemicellulose as well as a small amount of lignin components (Fan et al., 2018).

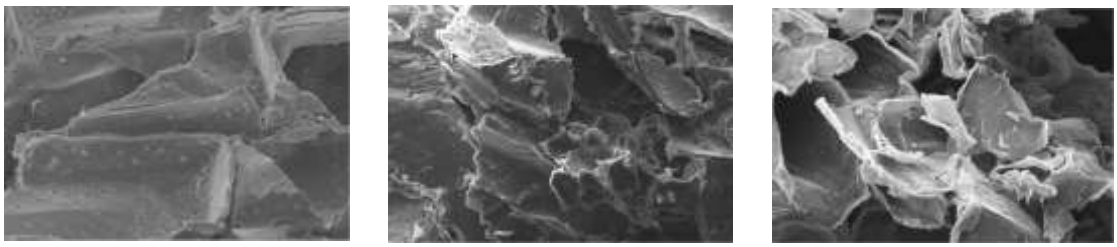

(a) (b) (c)

Figure (8) Scanning electron microscopy images for (a) Raw grass, (b) HTG (c) Biochar

FTIR spectra of biomass before and after hydrothermal treatment and biochar (after carbonization of solid residue) are depicted in Figure (9). The absorption band within the range of 3,500–3,000 cm^{-1} indicated that the stretching of O–H groups of hydroxyl and carboxyl groups present in grass stems before and after hydrothermal treatment and biochar. It can also be found that the peaks between 2000-1660 cm^{-1} of C–H stretching vibration for the methylene groups, the absorption band nearly 1500 cm^{-1} of C=C stretching vibration for the aromatic compound, the peak at 1732 cm^{-1} and 1248 cm^{-1} of C=O and C-O bond in acetyl ester groups

exhibited for before and after the treatment of grass. The significant appearance of absorption bands at 1600 cm^{-1} and around 1480 – 1350 cm^{-1} indicated the C-H of alkane group and C=C of aromatic groups in HTG and biochar. When compared with FTIR spectra of grass before and after hydrothermal treatment, the intensity of peaks around 3390 cm^{-1} became slightly diminished for HTG. This was due to the disruption of hydrogen bonds in cellulose (Buranov and Mazza, 2010). The appearance of a band around 2900 cm^{-1} (2,920 cm^{-1}, 2899 cm^{-1}) in HTG distinctly indicated diminishing intensity than that of raw grass. Kumar et al., (2009) reported the statement that the band around 2900 cm^{-1} was ascribed to C–H stretching vibration within the methylene portions of the cellulose. The bands at 1732 cm^{-1} and 1248 cm^{-1} for HTG showed a relative decrease in the intensity than that of raw grass. Nitsos et al., (2021) stated that the corresponding components of acetyl ester units might be present in hemicellulose and also described that decrease in the intensity of bands after hydrothermal treatment. It indicated the dissolution of hemicellulose from biomass and its deacetylation (Pandey, 1999). The absorption band around 1515 cm^{-1} indicates the presence of the aromatic ring in lignin (Colom et al., 2003). Nongthombam et al., (2017) observed that a small increase in the intensity of the peak at 1515 cm^{-1} could be attributed to the enhancement of the lignin concentration in the treated biomass samples. In the case of biochar, the intensity of the peaks at 3396 cm^{-1}, 2900 cm^{-1}, 1732 cm^{-1} and 1248 cm^{-1} were greatly diminished than that of HTG because of the degree of deoxygenation and dehydration during carbonization and after carbonization. The intensity of C=C and C-O stretching vibration was weakened after carbonization, indicating that lignin was partially decomposed (Fan et al., 2018).

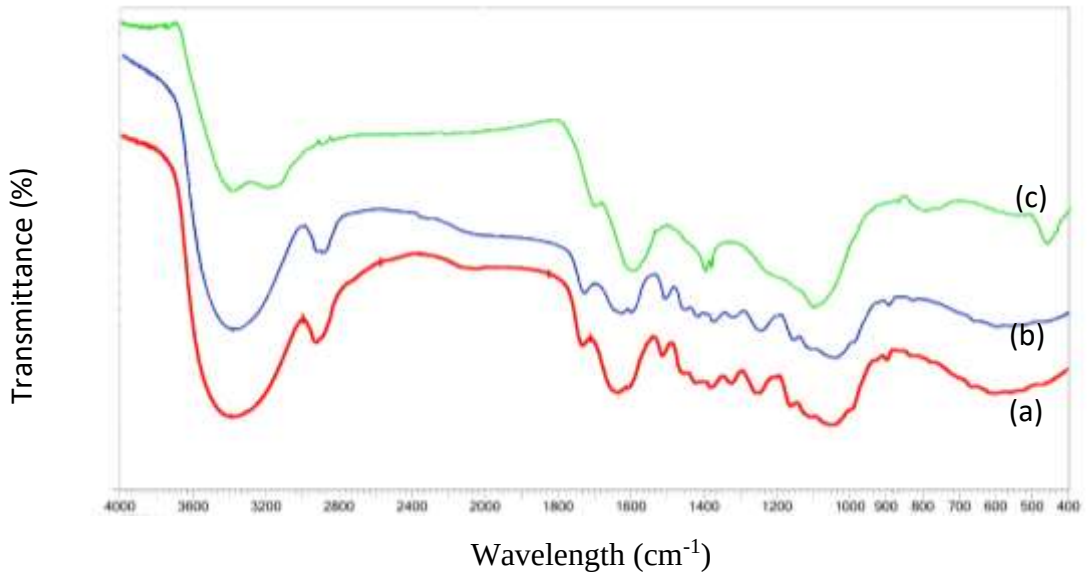

Figure (9) Fourier Transform Infrared (FTIR) Spectra for (a) Raw Grass, (b) HTG (c) Biochar

Conclusion

Hydrothermal treatment is an environmentally friendly method and it can discharge zero net waste. In this research, the potential bioenergy such as bioethanol and biochar from grass (*Pennisetum hordeorides* Lam.) was studied using hydrothermal treatment followed by fermentation of liquid fraction and by carbonization of solid fraction. Hydrothermal liquefaction of grass into soluble fractions of cellulose and hemicellulose was carried out at different temperatures and different times. The effective hydrothermal treatment at 110˚C for

30 min gave for maximum amount of fermentable sugar without any further treatment method of biomass. It was also evident that changes in composition of grass such as cellulose, hemicellulose, and lignin contents were observed for raw grass and HTG. 2% by volume of bioethanol was accomplished by direct fermentation of liquid fraction using Baker's yeast. Carbonization of HTG at 500˚C for 2 hr presented the maximum HHV and energy densification for the prepared biochar from grass. HHV (26.78 MJ/kg) of biochar prepared from grass can be compared with the HHV of lignite (~16.077MJ/kg), subbituminous coal (~23.26 MJ/kg) and bituminous coal (grade C) (~25.05MJ/kg) (Schweinfurth, 2009). Therefore, hydrothermal treatment method can support the process conversion of biomass into bioenergy.

Acknowledgements

The authors greatly acknowledge the receipt of research funding for this project (2020-2022) from the Department of Higher Education, Ministry of Education, Myanmar.

References

Aristiz´abal-Marulanda, A. and C.A. Cardona, (2021) "Experimental production of ethanol, electricity, and furfural under the biorefinery concept." *Chemical Engineering Science,* vol. 229.

Brown R. C. and T. R. Brown, (2014) *Biorenewable Resources Engineering New Products from Agriculture.* Second Edition, John Wiley & Sons, Inc, Low State Press, USA.

Buranov, A. U., and G. Mazza, (2010) "Extraction and characterization of hemi-celluloses from flax shives by different methods." *Carbohydr. Polym.* vol. 9, pp. 17–25.

Colom, X., F. Carrillo, F. Nogués, and P. Garriga, (2003) "Structural analysis of photodegraded wood by means of FTIR spectroscopy." *Polymer. Degradation and Stability,* vol. 80, pp. 543–549.

Del Río P. G., B. Gull, J. Wu, J. Saddler, G. Garrote, and A. Romani, (2022) "Current breakthroughs in the hardwood biorefineries: hydrothermal processing for the co-production of xylooligosaccharides and bioethanol." *Bioresource Technology,* vol. 343.

Du C., Y. Li, Z. Han, T. Yuan, W. Yuan and J. Yu, (2020) "Production of bioethanol and xylitol from non-detoxified corn cob via a two-stage fermentation strategy" *Bioresources Technology,* vol. 310, https://doi.org/ 10.1016/j. biortech.2020.123427.

Elaigwu S. E. and G. M. Greenway, (2019) "Characterization of energy-rich hydrochars from microwave-assisted hydrothermal carbonization of coconut shell." *Waste and Biomass Valorization,* vol 10, pp. 1979–1987.

Fan F., Z. Yang, H. Li, Z. Shi and H. Kan, (2018) "Preparation and properties of hydrochars from macadamia nut shell via hydrothermal carbonization." *Peer review Journal: Royal Society Open Science*, vol. 5.

Garba A., (2020) *Biomass Conversion Technologies for Bioenergy Generation: An Introduction*. Intech Open, *DOI: http://dx.doi.org/10.5772/intechopen.93669*

Kandasamy S., K. Devarayan, N. Bhuvanendran, B. L. Zhang, Z. He, M. Narayan, T. Mathimani, S. Ravichandran and A. Pugazhendhi, (2021) "Acceleration the product of bio-oil from hydrothermal liquefaction of microalgae via recycled bichar-supported catalysts." *Journal of Environmental Chemical Engineering*, vol. 9, http://doi.org/10.1016/j.jece.2021.105321.

Kieseler S., Y. Neubauer, and N. Zobel, (2013) "Ultimate and Proximate Correlations for Estimating the Higher Heating Value of Hydrothermal Solids." *Journal of Energy and Fuel*, vol. 27.

Kumar A., T. Bhattacharya, S. M. M. Hasnain, A. K. Nayak and M. S. Hasnain, (2020) "Applications of biomass-derived materials for energy production, conversion, and storage." *Materials Science for Energy Technologies*, vol. 3, pp 905–920.

Kuma R., and V. Strezov, (2021) "Thermochemical production of bio-oil: A review of downstream processing technologies for bio-oil upgrading, production of hydrogen and high value-added products." *Renewable and Sustainable Energy Reviews*, https://doi.org/10.1016/j.rser.2020.110152

Liu C. and C. E. Wyman, (2005) "Partial Flow of Compressed-Hot Water Through Corn Stover to Enhance Hemicellulose Sugar Recovery and Enzymatic Digestibility of Cellulose." *Bioresource Technology*, vol. 96, pp 1978-1985.

Liu Z, W. Niu, H. Chu, T. Zhou and Z. Niu, (2018) "Effect of the carbonization temperature on the properties of biochar produced from the pyrolysis of crop residues." *Peer-Reviewed Article, Bioresources*, vol. 13, pp 3429-3446.

Mäkelä M., V. Benavente, and A. Fullana, (2015) "Hydrothermal carbonization of lignocellulosic biomass: Effect of process conditions on hydrochar properties." *Journal of Applied Energy*, vol. 155, pp 576-584.

Nitsos C.K., K. A. Matis, and K. S. Triantafyllidis, (2012) "Optimization of hydrothermal Pretreatment of lignocellulosic biomass in the bioethanol production process." *ChemSubChem (Chemistry Substainability Energy Materials)*, vol 6, issue 1, pp 110-132.

Nizamuddin S, H. A. Baloch, G. J. Griffin, N. M. Mubarak, A. W. Bhutto, R. Abro, S. A. Mazari and B. S. Ali, (2017) "An overview of effect of process parameters on hydrothermal carbonization of biomass." *Journal of Renewable and Sustainable Energy Reviews.* vol. 73, pp1289–1299.

Pandey K. K., (1999) "A study of chemical structure of soft and hardwood and wood polymers by FTIR spectroscopy." *Journal of Applied Polymer Science*, vol. 71, pp 1969.

Pearson. D., (1976) *The chemical analysis of foods*. 7th Edition, J & A Chruchill 104, Gloucester Place, London.

Schweinfurth, S.P., (2009) *An introduction to coal quality*, in Pierce, B.S., and Dennen, K.O., eds., The National Coal Resource Assessment Overview: U.S. Geological Survey Professional Paper 1625–F, Chapter C.

Soe Soe Than, (2014) "Assessment of ethanol preparation by acid hydrolysis and fermentation of grasses." *Journal of Myanmar Academy of Arts & Science*, vol. 9, pp 479-487.

Waliszewska, B., M. Grzelak, E. Gaweł, A. Spek-D´zwigała, A. Sieradzka, and W. Czekała, (2021) "Chemical Characteristics of Selected Grass Species from Polish Meadows and Their Potential Utilization for Energy Generation Purposes." *Energies*, vol.14, pp 1669. https://doi.org/10.3390/en14061669

Williams C. L., R. M. Emeerson and Tumuluru, (2017) *Biomass compositional analysis for conversion to renewable fuels and chemicals.* Chapter 11 - The book: Biomass Volume Estimation and Valorization for Energy, http://www.intechopen.com/books/biomass-volume-estimationand-valorization-for-energy.

Yang W, T. Shimanouchi, M. Iwamura, Y. Takahashi, R. Mano, K. Takashima, T. Tanifuji and Y. Kimura, (2015) "Elevating the fuel properties of *Humulus lupulus, Plumeria alba, and Calophyllum inophyllum* L. through wet torrefaction" *Fuel* vol. 146, pp 88–94. (doi:10.1016/j.fuel.2015.01.005)

Zhuang, X., W. Wang, Q. Yu, W. Qi, Q. Wang, X. Tan, G. Zhou, and Z. Yuan, (2016) "Liquid hot water pretreatment of lignocellulosic biomass for bioethanol production accompanying with high valuable products" *Bioresource Technology*, vol. 199, pp 68–75.

INSTRUCTIONS TO AUTHORS

Presentation: Manuscripts (MS) should be typed on one side of **quarto or A4 size paper**. Typing should be single spaced, with a one-inch margin all around. A CD of the paper should be submitted together with two print-outs. In general, the text should be organized according to the following outline:

(i) Title
(ii) Abstract
(iii) Materials & Methods/ Premises / Hypotheses
(iv) Results / Findings
(v) Discussion
(vi) Summary/ Conclusion
(vii) Acknowledgements
(viii) References

The body of the text should be printed in **font size 12**, and those of the Abstract, Acknowledgement and References should be printed in **font size 10.** The relative importance of the **headings** in the text should be indicated as follows:

First Order	-	CENTRE HEADING, All Capitals
Second Order	-	Centre Heading, Capitals & lower case
Side Heading	-	Capitals & lower case, not indented (bold – faced)
Run-in heading	-	Capitals & lower case, indented (bold-faced)

Title. The title should describe the contents of the article adequately and concisely and should be typed in **font size 14.**

Author's name. Capital & lower case. The designation of the first author and email (where the number of authors is more than two) and the name of the institution where the work was carried out should be given at the bottom of the title page; but academic degree of the author is not necessary.

Abstract. The main points of the paper, including its findings and conclusions, should be highlighted in the abstract; it should not contain more than 300 words. Add email address for making further contact with the author; evaluation of the paper should be typed in **font size 10**.

Keywords: Between 3-7 keywords highlighting the main points should be listed below the abstract.

References. References should be presented in alphabetical order, beginning with the surname first for the senior author and surname last for the other authors, followed by the year of publication. Examples of references are given below:

To a paper: Rabinowitz, A., Than Myint, email, Tun Khaing, and S. Rabinowitz, (1999)"Description of the Leaf Deer (*Muntiacus Putaoensis),* a New Species of Muntjac from Northern Myanmar" *Journal of Zoology,* London, vol.249, pp.427-435.

To a book: Corbet, G.B., & J.E. Hill, (1992) *The mammals of the Indomalayan Region.* Oxford, Oxford University Press.

To a thesis: May Soe Thu (1995) *Taxonomy of Offshore Fishes Caught by Bottom Trawl Operations in Myanmar Waters.* M.Sc. Thesis Zoology Department, Yangon University (Unpublished).

N.B. If the manuscript submitted is from a thesis, its format should be revised to conform to the instructions of the Myanmar Journal of Arts & Science presented here. **Pagination** should commence from the title page except when they are used to identify the affiliated instructions, and cite unpublished material. **Footnotes** should be avoided wherever possible. The MS, including illustrations and references, should not exceed **15 pages** for Arts and related subjects and **10 pages** for Science in length. Please kindly follow this limit in your final manuscript.

MYANMAR ACADEMY OF ARTS AND SCIENCE
EXECUTIVE COMMITTEE

President : Dr Thet Lwin
Vice-Presidents : Dr Maung Kyaw, Dr U Win
Secretary : Dr Win Tun
Joint Secretaries: Dr Tin Maung Tun, Dr Aye Aye Khaing, Dr Tin Tin Htwe

Executive Members

Dr Myo Thant Tyn	Dr Daw Than Nwe
Dr Tin Nyo	Daw Carole Ann Chit Tha
Dr Khin Than Oo	Daw Khin Lat
Dr Hla Pe	Dr Maung Thin

Publication Committee

Dr Thet Lwin	(Chairman)	Dr Maung Kyaw	(Vice-Chairman)
Dr U Win	(member)	Dr Daw Than Nwe	(member)
Dr Tin Nyo	(member)	Daw Carole Ann Chit Tha	(member)
Daw Khin Lat	(member)	Dr Hla Pe	(member)
Dr Maung Thin	(member)	Dr Khin Than Oo	(Joint Secretary)
Dr Myo Thant Tyn	(Secretary)		

Editorial Board

Dr Maung Kyaw	(Chairman)	Dr Myo Thant Tyn	(member)
Dr Daw Than Nwe	(member)	Dr Tin Nyo	(member)
Dr Khin Than Oo	(member)	Daw Khin Lat	(member)
Dr Hla Pe	(member)	Dr Maung Thin	(member)
Dr U Win	(Secretary)	Daw Carole Ann Chit Tha	(Joint Secretary)

Coordinators for International Academies

Daw Carole Ann Chit Tha	Dr Maung Kyaw
Dr Myo Thant Tyn	Dr Daw Than Nwe
Dr Tin Nyo	Dr Tin Maung Tun
Dr Tin Tin Htwe	